BLAST HARDENING OF CURTAIN WALL MULLIONS WITH INFILLED CEMENTITIOUS MATERIALS

Rasha Alayash

Thesis submitted to the University of Ottawa
in partial fulfillment of the requirements for the
Doctor of Philosophy
in Civil Engineering

uOttawa

Department of Civil Engineering
Faculty of Engineering
University of Ottawa

June 2025

ABSTRACT

Glass façades and curtain walls are frequently employed in the construction industry as part of building envelopes. They offer several functional benefits, such as a pleasing architectural look, energy optimization, acceptable fire resistance, and low maintenance cost. However, they are typically designed for wind pressures and pose a high risk when exposed to blast loads. The glass panes that make up the building envelope are held up by aluminum frames, which consist of vertical elements, referred to as mullions, and horizontal elements, referred to as transoms. Critical infrastructure, such as important government facilities, embassy buildings, office complexes, and industrial facilities that have curtain walls may be vulnerable to blast loads. Experience with such blast loads demonstrates the need for in-depth experimental and analytical studies, especially on mullion hardening as they play the primary role in carrying blast loads to the structural substrate. Literature reviews show that there has been limited prior study on mullion strengthening/hardening. The goal of the current investigation is to develop innovative hardening methods for curtain wall mullions involving infilled cementitious materials to endure impulsive blast loads of high intensity.

A combined experimental and analytical study recently conducted at the University of Ottawa revealed that the aluminum mullions of glazed curtain walls sustain severe damage because of their weakness and high deformation demands. Lack of mullion strength and inadequate connections between the vertical and horizontal mullions under blast loads were identified as the major contributors to the unfavorable performance of such walls.

The current research project consists of experimental and analytical tasks. The experiments were carried out at the University of Ottawa's Shock Tube Facility. The hardening technology that was researched entails the filling of curtain wall mullions with different types of cementitious materials with and without additional reinforcement. The tests comprise of commercially available hollow aluminum sections as mullions, filled with high-strength mortar (HSM) or engineered cementitious composites (ECC). Some of the mullions were reinforced with steel wires or steel chains inserted as internal reinforcement, others were reinforced externally with carbon fibre reinforced polymer (CFRP) sheets. A total of 16 mullion tests were performed.

They were exposed to incrementally increasing blast loads to assess the improvements in strength and deformability. Following the tests, analytical research was conducted with the primary goal of validating the experimental findings and the assumption of full composite action between the aluminum mullion and the filling materials. Resistance functions were developed to conduct nonlinear single degree of freedom (SDOF) dynamic analysis. In addition, an analytical parametric investigation was conducted under selected threat scenarios to expand the results.

The results indicate that filling aluminum mullions with selected cementitious materials increase strength and deformability of mullions under blast loads. The infill material provides additional compressive resistance while controlling local buckling of the aluminum sections. Cement-based materials with fibres, such as ECC provides additional tensile capacity and deformability adding further to the resistance of the mullions. The additional reinforcement provided internally, in the form of steel cables or steel chains, and externally in the form of CFRP sheets provide further enhancement of the resistance in tension, generating superior performance of curtain wall mullions under high blast loads. The design and construction procedure provided at the end of the current research project provides guidance to practicing engineers and security professionals to mitigate blast risk in modern buildings.

ACKNOWLEDGMENT

First and foremost, I would like to express my deepest gratitude to my supervisor, Professor **Murat Saatcioglu**, for his invaluable guidance, unwavering support, and insightful mentorship throughout my PhD journey. His expertise and encouragement have been instrumental in shaping both my academic and personal growth.

I am profoundly grateful to my family for their endless love and support. To my **mother and sisters,** thank you for always believing in me and for being my pillars of strength during the most challenging times. Your words of encouragement have carried me through.

To **my husband**, your patience, understanding, and constant encouragement have meant the world to me. Thank you for standing by my side and for sharing in both the sacrifices and the triumphs of this journey.

To **my two sons**, you are my greatest source of inspiration. Your laughter, curiosity, and love gave me strength and perspective when I needed it most. This achievement is as much yours as it is mine.

I would also like to extend my heartfelt thanks to my dear friends and colleagues, **Abla, Usama and Kelechi**, for their friendship, encouragement, and support throughout this journey. Your presence made the difficult days lighter and the achievements even more meaningful.

A special note of appreciation is extended to **His Excellency Dr.Wadee Batti,** Ambassador of the Republic of Iraq in Ottawa, for his kind support and encouragement. His recognition of academic achievement and his commitment to the advancement of Iraqi scholars abroad have been deeply inspiring.

I would also like to extend my sincere appreciation to all those who have supported and contributed to this research in various ways but whose names are not individually mentioned here.

This thesis would not have been possible without the support of every one of you. Thank you from the bottom of my heart.

LIST OF CONTENT

LIST OF TABLES

LIST OF FIGURES

NOTATIONS AND ACRONYMS

AL - Aluminum

ASTM - American Society for Testing and Materials

CFAT - Carbon Filled Aluminum Alloy Tubes

CFRP - Carbon Fiber Reinforced Polymer

CFST - Concrete-Filled Steel Tubes

DAS - Data Acquisition System

DLF - Dynamic load factor

ECC - Engineering Cementitious Composite

E_{al} - Modulus of elasticity of aluminum

F_y - Yield strength of material

HSM - High Strength Mortar

HSS - Hallow steel section

IGU - Insulated Glass Unit

I_r - Peak reflected impulse

K_{LM} - Load mass factor

LVDT - Linear Variable Displacement Transducer

M - Mullion

MDOF - Multiple Degrees of Freedom

P_r - Peak reflected pressure

R_m - Elastic yield resistance

SDOF - Single Degree of Freedom

TNT - Trinitrotoluene

UFC - Unified Facilities Criteria

Θ - Support rotation

μ - Ratio of maximum deformation to the deformation at yield

CHAPTER 1. INTRODUCTION

1.1 General

Modern building construction frequently includes glass façade /curtain wall components as a component of the building envelope. This system has many benefits, such as a pleasing architectural look, optimizing building energy use, possible fire resistance, and low maintenance requirements. However, they happen to be vulnerable to potential terrorist attacks in the form of bomb explosions and associated shock waves. The literature review shows that there has been limited prior study on mullion strengthening/hardening against blast loads. The goal of the current investigation is to create hardening methods for curtain wall mullions to endure impulsive blast loads of high intensity.

1.2 Background of the Study

For both functional and aesthetic reasons, glass façades and curtain walls are frequently employed in the construction of modern buildings. Often, the glass panes that make up the building envelope are held up by aluminum mullions, protecting the structure from exterior environmental factors such as the impacts of weather (heat and cold), safety against intrusions, and other architectural requirements. Critical government facilities and office buildings could be highly susceptible to explosions and planned terrorist attacks such as bombings. Experience with the effects of such blast loads on vital infrastructure demonstrated the need for an in-depth experimental and analytical study for the protection of curtain wall façade and its components to withstand high blast loads.

The experimental and analytical study conducted recently at the University of Ottawa revealed that the aluminum mullions of glazed curtain walls sustain severe damage as a result of their weakness and lack of inelastic deformability. Both the lack of mullion strength and inadequate connections between the vertical mullions and horizontal transoms under blast loads were major contributors to the unfavorable performance of such walls. Injuries and fatalities are common when the failure of building facades and window systems occurs under blast loads. There

are many previous examples of such bombing incidents such as the 1995 Oklahoma City Bombing, the 2011 Oslo Regjering Skvartalet bombing, and the 2015 Mexico City Hospital gas explosion. The bulk of injuries and fatalities in such incidents have been noted to be brought on by flying debris and building component disintegration, including shattered glass. Most human casualties and injuries can be attributed to shattered glass windows, wall fragments, and other unsecured objects that are propelled toward the occupants, rather than by the air blast wave or the bomb container fragments themselves, according to post-event investigations of such incidents. Glass is especially vulnerable in such circumstances due to their comparatively low strength. The construction of blast-resistant curtain walls has been a research focus for many researchers, manufacturers, security people, and government authorities all over the world to improve human protection against blast loads. In new and modern office, commercial, and public buildings curtain walls are frequently used (Zhang et al., 2015). They are made up of a variety of materials. These materials include load-bearing elements of most modern glass curtain wall systems in the form of aluminum extrusions, which come in a variety of alloys depending on the design loads and safety criteria such as glass (vision and spandrel), aluminum panels in sheets, plates, or as composite materials consisting of stone - usually granite - marble or other items such as louvers, operable windows and fiber-reinforced concrete (FRC) panels (Allana, 2012).

The most important issue for glass curtain walls is the prevention of glass from being shattered under blast loads. There are different preventative measures against such threats including the use of laminated glass with an intermediate elastic layer. Internal laminates such as PVB layers installed between glass panes keep glass shards intact upon breakage. Another method of keeping broken glass shards together is the installation of protective films on the inner pane of glass. This film is applied on the surface and provides a protective layer that can be utilized on monolithic glass units, IGUs (insulated glass units), or laminated glass panes. The protective film is glazed using several glazing techniques. The most popular glazing types are mechanical glazing utilizing metal elements along the perimeter of window frames, or wet glazing using structural silicon (Alameer, 2020). While reducing the risk of fragmentation of windowpanes is vital, the window frames must be anchored to the substrate with sufficient strength so that the windows do not fly in as a whole when subjected to blast loads.

1.3 Problem Definition and Research Needs

The blast-resistance of curtain walls in critical infrastructures needs to be investigated by structural engineers if the building is assessed to have threats for terrorist bomb attacks. Curtain walls are architectural elements designed for wind loads with little or no blast resistance. The behavior of curtain walls, especially the performance of their mullions, has not been thoroughly documented despite some previous studies on window glazing and the overall performance of blast-resistant window systems. Furthermore, it is not obvious how various retrofit methods developed for existing buildings involving the use of a combination of aluminum and steel on vertical and horizontal mullions would perform. Some of these techniques negatively affect the esthetic appearance of curtain walls with externally welded steel plates and tend to become labor-intensive. There exist research gaps for developing practical and structurally sound hardening techniques for use in blast-resistant curtain wall mullions. An alternative to covering existing aluminum mullions with steel sections is to infill the mullions with strong and rigid material, such as a cementitious material to increase strength while also improving inertia resistance associated with increased mass. The strength can be further increased with internal steel reinforcement as well as externally applied fiber-reinforced polymer (FRP) sheets. This is a concept that has not been investigated in the past, though it offers a clear potential for use in practice. The infill material needs to be investigated in terms of its strength and deformability under extreme loads. Both experimental and analytical research is needed to develop the technology.

1.4 Objective and Scope

The main objective of the proposed research project is to develop structurally sound, practical, and economically viable hardening techniques for curtain wall mullions for use in blast-resistant buildings involving the use of different types of cementitious materials and additional internal or external reinforcement. The proposed research has experimental and analytical components with the following tasks forming the scope:

- Literature review to verify the state of the art on blast-resistant curtain wall mullions.
- Selection of two sizes of aluminum mullions used in practice for experimental investigation using the shock-tube facility at the University of Ottawa.
- Selection of two cementitious infill materials for improved strength and mass, consisting of high-strength mortar (HSM) and engineering cementitious composites (ECC).
- Use of additional reinforcement in terms of internally placed high-strength wires, high-strength chains, and externally placed carbon fiber reinforced polymer (CFRP) materials.
- Testing, construction, and instrumentation of 16 full-size curtain wall aluminum mullions under simulated blast loading using the University of Ottawa Shock Tube. Twelve of the specimens are full-size curtain wall mullions comprising mullions filled with high-strength mortar (HSM) with and without different strengthening techniques such as steel wires and steel chains inserted as internal reinforcement in addition to the use of CFRP sheets as external reinforcement. The remaining four specimens are mullions filled with ECC, two of which are reinforced externally with CFRP sheets.
- Evaluation of test data based on the assessment of mullion reinforcement behavior and retrofit system performance, in addition to the specific behavior of various hardening materials used, while also investigating the effects of test parameters.
- Development of resistance functions for the hardening techniques considered in the experimental phase for use in analytical research.
- Use of non-linear single-degree-of-freedom (SDOF) dynamic analysis method to validate the resistance functions and the applicability of the SDOF method of analysis for use in practice.
- Analytical parametric investigation to expand the effects of design parameters, such as the mullion size, percentage of internal steel, infill material type, and external CFRP thickness beyond the test data to generate design information.
- Development of a design and construction methodology for hardening curtain wall mullions using infill cementitious materials and additional reinforcement.

1.5 Research Methodology

The proposed research comprises experimental and analytical phases. The experimental phase includes tests of full-size aluminum mullions under simulated blast loads using a shock tube as a blast simulator. The mullions are filled with either high-strength mortar (HSM) or engineered cementitious composites (ECC). They will either be simply supported or fixed at the supports, and some will contain different types of additional reinforcement.

The first stage of the experiments includes nine aluminum mullions to be tested with simple supports. Two different size mullions are tested, having either 51mm x 127mm x 3mm or 51mm x 152mm x 4.8mm rectangular sections. One mullion of each size is filled with ECC without any additional reinforcement. The remaining seven mullions are filled with HSM: two without any additional reinforcement, two with high-strength cables as internal reinforcement, two with internal steel chains as reinforcement, and one mullion with external CFRP reinforcement.

The mullions are instrumented to measure deflections and strains. High-speed cameras are utilized to record different positions of the mullions during blast load applications.

The analytical phase of research is intended to expand the results obtained through testing. Non-linear single degree of freedom (SDOF) dynamic analysis is conducted in this phase. Resistance functions are established first, followed by the validation of the methodology against the recorded test data. The analysis is used to undertake a parametric study to assess the effects of design parameters consisting of mullion size, percentage and type of internal steel reinforcement, infill material type, and external CFRP thickness. Finally, a design procedure is developed based on the experimental and analytical phases of research for use in practice.

CHAPTER 2. LITERATURE REVIEW

2.1 General

Previous research in the area of blast-resistant curtain walls includes experimental and numerical studies to understand the effects of blast loading on curtain walls. Research on blast-resistant window systems was also conducted, showing the performance of common elements, such as glass panes and window frames. In most of these studies, the failure modes of glass windows/panes were related to the glass panel flexural bending. Some research was also conducted on glazed glass with protective security films, displaying membrane action after the breakage of glass. The behavior of the supporting aluminum frames and mullions was investigated, including their connections to frame elements and their substrates. A limited number of research projects were conducted on blast-resistant curtain walls, providing some understanding of the behavior of curtain walls. Additional information and guidance were also provided in recently published books on blast engineering.

This chapter presents an overview of blast loads, blast analysis, and the mechanisms of load resistance in curtain wall systems, while also providing a review of previous literature on the topic.

2.2 Blast Loading and Blast Effects on Structures

2.2.1 Explosives

Explosives consist of specific chemical compositions that can detonate in the presence of high ambient temperature or sufficient heat source within the mass itself. Blasts involving chemical reactions can be classified based on their reaction rate. An oxidation reaction that propagates at a rate less than the speed of sound is referred to as “deflagration.” In contrast, the reaction front that propagates supersonically, usually many times faster than the speed of sound is termed “detonation.” Explosions are classified as “High Explosives,” or “Low Explosives.” High explosives are materials that are intended to produce detonations with supersonic reaction fronts. The initial pressure of an explosion is 10-30 GPa with a temperature of 3000-4000 C° (Smith, 1994). The reactions proceeding through the explosive are self-sustaining if the charge is of sufficient

diameter and properly initiated. Reaction rate, or detonation velocity, varies with material type and is a key factor in detonation pressure for a given material. Detonation velocities typically range from 3000 to 30,000 ft/s (1–9 km/s). High explosives can be classified by their sensitivity to initiation as primary, secondary, and tertiary explosives.

Low explosives are energetic materials that do not typically detonate and are used to produce gas, smoke, flash, or sound. Both solid and liquid rocket propellants, gun propellants, and black powder are examples of low explosives. The relatively low reaction rates of these materials result in low blast pressure output because they typically don't detonate.

High-explosive detonations are of interest to structural engineers, as they may affect structures. They can result from accidents or intentionally triggered events. Accidents involving high explosives can occur during the processing, handling, and transportation of explosives. Intentional detonations include explosives testing, military weapons, demolition of building infrastructure, specialized cutting and explosive forming, as well as acts of terror. The explosives used for terrorist bombing are high explosives. The supersonic combustion (oxidation) of a high explosive generates a blast shock wave. It also generates heat from combustion.

Explosives in their normal state come in the form of solids, liquids, or gases (Uddin, 2010). They are also categorized as being physical, nuclear, or chemical. An example of a physical explosive is a cylinder of compressed gas, or a vessel designed to contain fluids under pressure. They have the potential to create hazardous overpressures and fragments if the vessel fails while under pressure. In nuclear explosions, the energy release occurs due to the redistribution of protons and neutrons in the interacting nuclei of atoms. In chemical explosions, rapid oxidation of fuel elements (carbon and hydrogen atoms) occurs.

2.2.2 Types of Blast Shock Waves

Three different types of blast shock waves may impact structures as governed by the location of detonation (Karlos, 2013). These are illustrated in Figure 2.1 and are listed below:

- **Free-air bursts**: The blast waves are formed as spherical waves that move from the charging source towards the structure. The detonation propagates in the air far from any reflecting surface.
- **Air bursts:** During the detonation process, the blast wave hits the ground and propagates in a spherical form reaching the structure.
- **Surface bursts:** The explosive charge explodes close to the ground surface. The blast waves directly hit the ground and propagate hemi-spherically outwards, before they impact the structure.

2.2.3 Blast Wave Formation and Blast Parameters

The primary parameters of blast loading are charge weight (size of bomb), usually expressed as the weight of explosives in pounds (lbs) or kilograms (kg), and standoff distance, expressed distance between the center of the explosion and the target. Figure *2.2* shows the blast wave generated from intensive free air detonation on a stand-off distance R. The wave takes a period to arrive called t_a (arrival time). Meanwhile, the velocity U_s decreases gradually. However, the pressure commences to increase from the ambient pressure P_a to the maximum pressure known as peak overpressure P_{so}. The positive phase duration is called t_d which is the period of pressure increase, and this duration is followed by an immediate decrease which represents the negative phase duration. The negative phase is generated by an instantaneous return, and it is known as t_d^-. Furthermore, the maximum pressure is named as p_0^- and the area under the positive pressure curve is known as positive impulse I (Ngo et al., 2007).

2.2.4 Blast Waves Reflection

Reflected pressure (P_r) is generated when a blast shock wave arrives and interacts with the surface of an object. An example is overpressure reflecting from the surface of a wall or other building components, which is not parallel to the direction of the wave propagation. There is no

difference in the shape of the pressure-time relationship between the incident and reflection pressures. However, the peak of the reflected pressure is multiple times higher than the peak of the incident pressure. The main parameters relating to the reflected pressure are the incident wave and the angle of the surface. The main factor that affects the duration of the reflected pressure is the size of the surface (Krauthammer, 2008).

2.3 Non-Linear Dynamic Analysis Methods

The dynamic motion of a structure or a structural element that results from a blast shock wave can be described by the equation of motion in the form of a differential equation. Dynamic motion can be affected by multiple degrees of freedom (MDOF), where each degree of freedom reflects the effect of a different mode shape (Rolater, 2022), it is usually sufficiently accurate to describe the response of a structural element to blast loads by selecting a single ordinate, resulting in a single degree of freedom (SDOF) system. The SDOF method of analysis provides acceptably accurate results for analysis and design under blast loads (Biggs, 1964).

The SDOF system represents the primary mode of deformation. It is possible to come up with a static load that results in the same deformation shape. This is referred to as the equivalent static force. The structural properties of a component can be approximated and used along with equivalent static loads to conduct static analysis, which provides a convenient analysis technique for design purposes.

2.3.1 Single-Degree-of-Freedom (SDOF) Analysis

A structural element can be idealized as a SDOF system, which can be expressed as a single mass-single spring system, set into motion either by a concentrated force, an initial displacement, or an initial velocity. This is illustrated in Figure 2.3, which shows an element with distributed mass and distributed forcing function that can be represented by a mass-spring model subjected to a time varying concentrated force. The term *m* represents mass, k represents stiffness, and F(t) represents the forcing function. F(t) is obtained by multiplying the blast pressure P by the tributary surface area of beam *A.* The term *u(t)* is the displacement of the mass while ü in Eq. 2.1

is the acceleration of the mass. The time-variant forcing function in terms of pressure variation is represented by *P(t).*

$$m\ddot{u}(t) + ku(t) = AP(t) \qquad 2.1$$

In idealizing the behavior of an element as a SDOF system, the distributed mass of a structural element is transformed into an equivalent single mass. Similarly, the stiffness of the element can be transformed into a spring stiffness. These transformations can be done by employing transformation factors, using the principles of the conservation of energy, as described in the next section.

The forcing function used for blast analysis often corresponds to the positive phase of reflected pressure $P_r(t)$, which can be idealized as a linear function. Figure 2.4 illustrates the positive phase of blast loading (UFC-03-340-02, 2008) which is idealized as a linearly decreasing forcing function ease in computations. It consists of a forced vibration and free vibration phases. Eq. 2.2 represents the forcing function within the force vibration phase where P_r is the maximum reflected pressure, and t_d is the duration of the positive phase of pressure. The impulse generated by the forcing function (*I*) can be calculated as the area under the pressure-time relationship. It is defined by Eq. 2.3.

$$P_r(t) = P_r\left(1 - \frac{t}{t_d}\right) \qquad 2.2$$

$$I = \int_0^{t_d} P_r(t)dt = \frac{P_r\, t_d}{2} \qquad 2.3$$

The following expression can be obtained if Eq. 2.2 is substituted into Eq. 2.1.

$$m\ddot{u}(t) + ku(t) = AP_r\left(1 - \frac{t}{t_d}\right) \qquad 2.4$$

The solution of Eq. 2.4 consists of a complimentary solution (for the homogeneous part of the equation) and a particular solution due to the forcing function. Consequently, the forced vibration phase of response within $0 \le t \le t_d$ has the solution given in Eq. 2.5, which is a function of initial displacement u_o and initial velocity v_o at $t = 0$. The frequency of the SDOF system can be expressed as $\omega = \sqrt{\frac{k}{m}}$.

$$u(t) = \left(u_o - \frac{AP_o}{k}\right)\cos\omega t + \frac{\left(v_o + \frac{AP_o}{kt_d}\right)}{\omega}\sin\omega t + \frac{AP_o}{k}\left(1 - \frac{t}{t_d}\right) \quad 2.5$$

The solution for the free vibration phase (when $t \geq t_d$) can be written as follows in terms of the initial displacement and initial velocity.

$$u(t) = u_{t_d}\cos\omega(t - t_d) + \frac{v_{t_d}}{\omega}\sin\omega(t - t_d) \quad 2.6$$

The term u_{td} and v_{td} represent displacement and velocity at $t = t_d$, respectively.

2.3.2 Equivalent SDOF system

This section describes the transformation of a multi-degree of freedom system into a single degree of freedom system with a lumped mass and a spring stiffness under a concentrated blast force. The single equivalent ordinate is represented by the maximum displacement through the displacement-time history of the structure. Therefore, the distributed mass is represented by a lumped mass at the same position of the equivalent ordinate. The distributed force is also represented by an equivalent concentrated force.

The distributed mass is converted to an equivalent lumped mass by setting the kinetic energy associated with the distributed mass to that of the lumped mass and then finding the ratio between the two as the transformation factor for mass k_m. This is illustrated in the equation below:

$$k_M = \frac{\int_0^L \bar{m}\Phi(x)^2 dx}{\bar{m}L} \quad 2.7$$

The term $\bar{m}$ represents mass per unit length of the component having a distributed mass and a shape function $\Phi(x)$, which defines the deflected shape associated with the first mode response.

The transformation of the distributed load to a single point load can be performed by setting the work done by the distributed force to that of the concentrated force and then finding the ratio between the two as the transformation factor for load k_L. The load factor k_L is defined by the following equation:

$$k_L = \frac{\int_0^L P\Phi(x)dx}{PL} \quad 2.8$$

The resistance of an element is the internal force that will try to restore the element to its unloaded static position. In elastic systems R = ku. The stiffness is equal to the total load of the same distribution which would cause a unit deflection at the point where the deflection "u" is equal to that of the equivalent system. Because the deflection caused by the load is directly proportional to stiffness, the Resistance Factor k_R is always equal to the Load Factor k_L, i.e., $k_R = k_L$.

$$k_M m\ddot{u}(t) + k_R R\big(u(t)\big) = k_L A P(t) \quad 2.9$$

Dividing all terms with k_L results in Eq. 2.10.

$$k_{LM} m\ddot{u}(t) + R\big(u(t)\big) = A P(t) \quad 2.10$$

Where the load mass factor (K_{LM}) is defined as a ratio of the mass factor to the load factor as illustrated in the equation below:

$$k_{LM} = \frac{k_M}{k_L} \quad 2.11$$

The equation of motion of a SDOF can be defined by Eq. 2.13 in terms of K_{LM}. The derivations of transformation factors for distributed systems having different support conditions are illustrated in Biggs (1964) and UFC-03-340-02 (2008).

2.4 Review of Materials Used in the Current Investigation

A review of existing information on the materials planned for use in the current investigation was conducted in an effort to understand their behavior before undertaking the research project. The scope of the proposed research involves hardening of aluminum mullions by using high compressive strength filler materials such as high-strength mortar (HSM) and engineered cementitious composites (ECC) which have the additional advantage of possessing inelastic deformability and providing either internal or external reinforcement. The internal reinforcement is to be placed inside the filler material (either in HSM or ECC) and the external reinforcement is to be placed outside of the aluminum mullion. An important requirement for the internal reinforcement is its flexibility (ability to bend) so that it can be inserted in existing mullions.

Therefore, high-strength wire and high-strength chains are considered as internal reinforcing material. The external reinforcement considered is fibre reinforced polymer (FRP) strips of jackets to be placed on the aluminum mullions. Therefore, the properties of these materials are reviewed in this section, i.e., those of the aluminum, HSM, ECC, steel wires, steel chains, and FRP. Furthermore, the literature review on bond strength characteristics of FRP on aluminum is included.

2.4.1 Aluminum Mullion

Aluminum material is preferred for some applications as a building material due to its architecturally pleasant appearance, lightweight, and corrosion resistance. The strength of aluminum is considered to be high relative to its weight and easy to use in complex designs (Mondolfo, 1976). It has widely been used in engineering applications since the end of the 19th century. One common use is for window frames and curtain wall mullions. Aluminum is classified as the second most plentiful metallic component (Davis, 1993).

Aluminum is alloyed with different metals to enhance its strength when used for different functions, such as building facades to resist wind loads and transfer loads onto structural frames (Kissell, 1995). The flexural behavior of aluminum alloy beams is affected by post-yield material properties such as strain hardening and ductility (Moen et al., 1999). There are various cross-sectional shapes with different effectiveness under different loading. An experimental study was conducted by Su et al. (2014) on bending of aluminum alloy square and rectangular hollow sections with simple supports. Three-point loads were applied on 14 specimens and four-point loads were applied on 15 specimens consisting of 6061-T6 and 6063-T5 heat-treated aluminum alloys with a thickness varying between 2.8 mm to 20.5 mm as shown in Figure 2.5. The results indicated that the capacities achieved were well beyond the fully plastic moment resistance.

Several studies were carried out by Huang & Zhang (2018) to examine the deformation modes and strength of aluminum by applying a three-point load on thin-walled rectangular tubes. The main parameters were the span, the diameter of the punch, and the cross-section configuration. A numerical study was also conducted to compare the test results with those obtained numerically. The results showed that the geometric parameters influence the deformed shape,

as well as the force and bending moment responses of beams. Different deformation modes of hollow sections were observed. This is shown in Figure 2.6, which illustrates the buckling of the tube at the middle span and the indentation of the tube under bending. Regarding the span length effect, Figure 2.7 shows the indentation behavior of the tube with s/b=1. At 1<s/b<3, the deformation mode changes from indentation to bending with progressively developing indentation. It is noted that larger s/b ratios result in higher peak bending moments and larger rotation angles. The thickness of the thin-walled tubes has a significant influence on the bending response. Figure 2.8 illustrates the deformed shapes of tubes with various thicknesses. It is noticeable that the diameter of the punch varies and decreases with the increase of the thin-walled tube. The section width was also investigated as the third parameter, the effects of which are illustrated in Figure 2.9. An early collapse can be noticed on the tube with a large section width. This was also accompanied by a larger initial maximum bending moment. The researchers concluded that the higher ratio of a/b is preferable for the aluminum tubes for higher energy absorption because the mass is smaller and the load is distributed uniformly (Huang & Zhang, 2018).

2.4.2 Engineering Cementitious Composites (ECC)

Engineered Cementitious Composites is a special form of fibre-reinforced concrete (FRC) where the interface between the fibers and the matrix is engineered to interact together when the load is applied to the composite material. Generally, tension-softening behavior is observed in all FRCs immediately after the crack formation, as the cracks widen and the load bearing decreases. This tension-softening phenomena in FRCs is an advantage in comparison with normal concrete that fails by fracture. Fibers in FRC help bridge the cracks, creating a quasi-brittle response. It is known that the elastic limit reaches approximately 0.01% strain for both FRC and normal concrete. The main difference between ECC and FRC is the behavior after the first cracking. FRC shows tension-softening while ECC shows strain-hardening as shown in Figure 2.10 (Bentur, 2007).

A comparison was carried out between the ECC and ultra high-performance concrete (UHPC) by Li (2019) in terms of tensile strain capacity and ductility. UHPC showed a tensile strain capacity

of up to 0.2% or less while ECC showed a tensile strain capacity of more than 2%. This is shown in Figure 2.11. Additionally, there is a similarity between ECC and metallic materials in terms of their stress-strain relationships, which indicates tensile strain hardening beyond the yield strength. Therefore, ECC is known as Strain-Hardening Cementitious Composites (SHCC) as well. As a result, ECC shows ductility (strain capacity at peak strength) two orders higher than normal concrete. The compressive strength of ECC ranges from a few MPa up to over 200 MPa for ultra-high strength ECC, which is used in structures subjected to impact or blast loading. The high compressive strength of the high-strength concrete is achieved by the tight packing of particles while the high compressive strength of ECC is obtained by the mechanical interactions generated between the fibers and the matrix. This broad study that deals with this design is known as the micromechanics of ECC (Li, 2019).

The orientation of PVA fibers within the ECC mixture has a big role in governing bearing stresses and bridging micro-cracks. A study was conducted by Thanh et al. (2021) on fiber orientation, indicating that a higher fiber orientation factor can be attained in thin specimens rather than the thick ones. Moreover, short polyvinyl alcohol (PVA) fibers mixed with ECC mixture, created a unique class of high-performance fibre-reinforced cementitious material, which generates tensile strain capacities of up to 5% with less than 2% fibers (Thanh et al., 2021 as cited in Serna et al., 2020 b).

Another study was carried out by Thanh et al. (2021) to examine the bond between ECC and steel reinforcing bars. The results showed no effect of PVA fiber content on the peak stress of the mixture. Moreover, the bond strength between ECC and steel bars increases with the increase in bar diameter. Furthermore, the crack width was controlled effectively by PVA fiber bridging (Magalhães et al. 2021, as cited in Serna et al., 2020a).

Generally, studies proved that mixing fiber with concrete provides high ductility (Scheffler et al., 2017). Khandelwal & Rhee (2020) indicated that the increase in fiber dosage increases the mechanical properties of the composite. ECC tensile behavior is important for the design of airport runways and structures affected by earthquake and blast loads.

Li et al. (2021) investigated the effects of high strain rates on the tensile performance of KEVLAR fiber and steel grid-polyvinyl alcohol (PVA) fiber-reinforced ECC using dynamic tensile tests at medium strain rates. The volume percentages of both types of fibers were 0%, 0.5%, 1%, 1.5%, and 2% of the ECC matrix. The results showed ductile behavior of PVA-ECC, while a brittle behavior was obtained in KEVLAR-ECC. As a result, it was concluded that adding fibers such as PVA fiber into the mix can improve the tensile peak stress for the ECC composite. ECC structural members, such as beams, columns, and walls show significant structural strength, energy absorption, and ductility in addition to fracture energy under cycling and monotonic loading. Typically, ECC composites with short and randomly distributed fibers can attain tensile strain hardening and multi-cracking after the first crack. This is illustrated in Figure 2.12 (Yu & Dai, 2009).

The impact capacity of ECC material can be improved by appropriate design. Maalej et al., (2012) examined hybrid ECC behavior by incorporating 0.5% steel and 1.5% polyethylene fibers by volume and applying a series of uniaxial tests at varying strain rates. The results showed that under dynamic tensile loading multiple cracking and large strain capacity were obtained. Moreover, the high fracture energy of the hybrid ECC eliminated fragmentation and spalling. An additional series of tests conducted by Zain et al. (2018), showed that all ECC mixes considered gained a minimum of 1.8 times the compressive strength of normal concrete. The fiber contents range between 1.5% and 2.5% improved ECC modulus and toughness. However, the researchers reported that this level of increased fiber content can have a negative effect on compressive strength.

2.4.3 HSM (High Strength Mortar)

Mortar is a material used in masonry construction to fill the gaps between masonry units such as bricks, concrete blocks, and stones. It is a mixture of sand, a binder material such as cement or lime, and water. Cementitious mortars are mixed from a combination of ordinary Portland cement, hydrated lime, and sand, typically at a 1:1:6 proportion. The cement provides the binder, and the hydrated lime provides workability. The hydrated lime does not bind the materials, and it is different than hydraulic lime. A lime mortar is typically a mixture of hydraulic lime and sand. Hydraulic lime is a binder that sets hard and binds the sand in much the same way

as cement and is completely different from the hydrated lime used in cementitious mortars which simply provides workability. The proportion of hydraulic lime to sand in a lime mortar mix varies according to the strength of the lime itself and varies between producers. There are many ready-mixed mortars available for use in industry.

Portland cement mortar is made by mixing Portland cement with sand and water. It is similar to concrete without the coarse aggregate. High-strength mortar can be made using similar proportions of materials as high-strength concrete. High-strength concrete is described by the American Concrete Institute as concrete with compressive strength higher than 6000 psi, which is about 41.37 MPa. High-strength Concrete has a low water-cement ratio, which affects its workability. Therefore, superplasticizers are used to improve workability. Silica fume (with fine particles) is used to increase the strength of concrete (Mehta, 2014). The use of high-strength/high-performance concrete has increased in recent years. High-strength mortar can be produced using a similar mix design as high-strength concrete except for the use of coarse aggregate. The high strength and high performance of mortar mainly come from the dense microstructure and low permeability of the material (Aydın et al., 2008).

2.4.4 High Strength Reinforcement

The strength of reinforcement used in concrete has increased over the years. ACI-318 and CSA A23.3 codes and standards have accepted the use of higher-grade reinforcement with strengths higher than 400 MPa. In the current research project, because of the practical difficulties of inserting re-bars in existing aluminum mullions, flexible reinforcement, either in the form of high-strength cables or high-strength chains has been adopted. There is extensive research conducted in the past on both materials and a detailed review of them is beyond the scope of current research, except for establishing their stress-strain relationships, which are of importance as they affect the strength of hardened mullions.

2.4.5 Carbon Fiber Reinforced Polymer (CFRP)

The use of FRP material in the construction industry for strengthening, rehabilitating and retrofitting of structural and non-structural building elements has increased during the last three

decades. The FRP comprises of high strength fibers embedded in a matrix resin. FRP has many advantages such as high strength, lightweight, excellent durability performance, stiffness, fatigue, and corrosion resistance. Additionally, it is easy to assemble, which is useful for the repair or strengthening of structures. Lately, several studies proved that carbon FRP (CFRP) is the most effective material for steel strengthening in comparison with other types of FRP materials such as those made with glass or aramid fibers (Al-Saidy et al., 2007). The use of CFRP in the construction industry has been researched extensively with a large volume of research data. CFRP has been selected in the current research project among other types of reinforcing materials for external application.

2.4.6 Bond Between Aluminum and Surface-Bonded CFRP

Zhu et al. (2019) investigated the bond strength between aluminum alloys and CFRP sheets. An Al/CFRP/Al laminate was examined using three types of aluminum alloy AA6061. The surface of the aluminum was prepared before the CFRP application. The preparation included sanding, surface modification, and anodizing to increase the bond strength between the two materials as illustrated in Figure 2.13. The main parameter that affects the bond strength was reported to be the macro roughness of the metal surface. It was also indicated that the large surface area of contact generates high bond strength with resin. The interlocking influence could be weak when the width and depth of the grooves on the surface are either very small or very big. Scanning Electron Microscopy (SEM) test was performed to examine the effect of anodizing on AA6061 surfaces. Anodizing was observed to generate a nanoporous structure that covered the surface. This type of structure improves the wettability of CFRP on AA6061 in addition to the mechanical anchoring influence between AA6061 and CFRP. In addition, a good chemical bond is created between epoxy resin and anodized AA6061. The shear strength of Al/CFRP/Al laminates was also improved by surface modification after anodizing reached 54.9 MPa. Meanwhile, the bond strength was reduced by 2.2% with the Al alloy surface (Zhu et al., 2019).

Another strengthening mechanism was examined by Wang et al. (2018), which was the ultrasonic vibration-strengthened adhesive bonding method. This method improved the bond

strength by 40% to 60%. Additionally, bonding gaps were well-filled by the adhesive when ultrasonic vibration is used (Wang et al., 2018).

A study was carried out by Zhou et al. (2014) to examine the flexural rigidity and load-carrying capacity of aluminum beams after the application of CFRP layers as illustrated in Figure 2.14. This strengthening technique was improved by using a hybrid bond technique with mechanical fastening. Four-point bending tests were conducted to observe the flexure behavior of the retrofitted beam. It was reported that both the flexural rigidity and the load-carrying capacity were enhanced. The flexural rigidity was increased up to 32.8% while the flexural capacity was increased by 31.1 %. The researchers also reported that the hybrid bond method of CFRP applied on aluminum specimens was more efficient than equivalent steel specimens (Zhou et al., 2014).

The advantage of CFRP application on aluminum was reported in a study performed by (P. Feng et al., 2016). The researchers showed that the bilinear behavior for aluminum members retrofitted with CFRP helped in mitigating failure as shown in Figure 2.15. Significant improvement was observed in axially loaded members of CFRP–Al hybrid tubes. This is shown in Figure 2.16.

Shin et al. (2014) investigated the behavior of aluminum beams retrofitted with CFRP sheets under three-point bending. The researchers also conducted finite element analysis of the beams. Four layers of unidirectional carbon fibers were used to retrofit aluminum square hollow sections, as presented in Figure 2.18. Both aluminum and CFRP were subjected to nonlinear elasto-plasticity and developed progressive damage. The cohesive zone model was used to model debonding and delamination. The stress increase was mostly at the edges under the loading nose, as observed in finite element analysis. When the bending load is reduced, the failure of CFRP was only on a small area directly under the loading nose. Under increased loading, aluminum buckling and bending rupturing were observed. The finite element analysis showed good similarity to the experiment results (Shin et al., 2014).

A research project was undertaken by Chen et al. (2017) to examine the flexural behavior of aluminum hallo beams with circular sections filled with concrete and externally jacked with CFRP as shown in Figure 2.18 and Figure 2.19. The total number of specimens tested was 30, which

included 20 specimens filled with concrete. In addition to the maximum strength and failure modes, other parameters such as flexural stiffness, and ductility were examined. It was observed that strengthening with CFRP provided significant improvement to carbon-filled aluminum alloy tubes (CFAT) in terms of the ultimate strength attained. However, the ductility was mostly weakened.

Lambiase et al. (2021) examined the bond characteristics of aluminum alloy AA7075 with CFRP. The interlocking between the aluminum surface and the CFRP was enhanced by laser texturing the aluminum surface. Other parameters were determined such as the texturing strategy of the joints, the plunging force, and the plunging speed. The mechanism of the bond depended on the mechanical interlocking between the two surfaces. The researchers also reported the role of the CFRP on the shear resistance of the aluminum as being about 10% (Lambiase et al., 2021).

Ge et al. (2022) examined the axial crushing properties of aluminum tubes retrofitted with carbon fiber-reinforced polymer CFRP and aluminum/CFRP/aluminum tubes. It was observed that the direction of CFRP fibers had a significant effect on the energy absorption of the specimens. Both the geometry and the fiber lay-up order influenced the axial crushing energy-absorption behavior as well as the failure modes. The results proved that for both types of hybrid tubes, the energy absorption of the aluminum specimens with (45◦/−45◦) lay-up order was less efficient than the specimens with (0◦/90◦).

2.5 Review of Previous Research on Blast-Resistant Windows

2.5.1 Alameer, A. (2020), Alameer et al. (2023), Alameer and Saatcioglu (2023)

Alameer et al. (2023) conducted extensive tests of windows subjected to simulated blast loads using a Shock Tube. They investigated the effect of blast loads on punched windows attached to building façades. Windows are one of the most vulnerable elements in a building when subjected to blast shock waves. Breakage of glass results in projectiles in the form of broken glass shards that fly into the building, potentially injuring the occupants. Therefore, the windows of critical infrastructure are protected by security films or by using blast-resistant laminated glass.

The researcher conducted extensive experiments on windows using a shock tube, testing windows with different arrangements of protective film and different methods of glazing. One of the main parameters investigated was the strength of window retention anchors. The authors focused on developing a design procedure for blast-resistant retention anchors. This was done by implementing three stages of research: experimental, involving shock tube tests; numerical, involving finite element analysis, and analytical, involving single degree of freedom dynamic analysis (SDOF). The total number of window samples tested was 23 on various substrates such as steel, reinforced concrete, block masonry, and stone masonry walls as illustrated in Figure 2.20. Different parameters, such as the pattern and number of retention anchors, the thickness of protective film, substrate type, window size, window aspect ratio, and type of glazing (wet or mechanical glazing), were investigated. The tests were conducted either under 4 psi (28 Kpa) or 10 psi (69 Kpa) pressures as per the General Services Administration (GSA) of the US Government recommendations. Three different sizes of windows with three aspect ratios ($ℓy/ℓx$) were tested. This is shown in Figure 2.21. Some of the windows were glazed with wet glazing as shown in Figure 2.22 before attaching them to the substrates. This was done by using "structural silicone" that was applied along the edge of the film with a thickness of at least 13 mm around the perimeter of the glass. The majority of the window glazing was done by mechanical glazing, as shown in Figure 2.23. This was done by securing 25 mm square aluminum HSS with a 5 mm wall thickness along the perimeter of the windows. These HSS elements were anchored to the window by using 38 mm long, 6.3 mm diameter self-tapping screws. The retention anchors consisted of high-strength bolts with a diameter of 9.5 mm and a length of 76 mm or 127 mm. Strain gauges were positioned on the first eight windows on the tension side of the frame elements as illustrated in Figure 2.24. The deflection of the anchors was estimated by providing four (LVDT) as illustrated in Figure 2.25. The rest were instrumented by placing strain gauges on the anchors. Typical instrumentation of anchors is shown in Figure 2.26.

After applying the blast loads, it was observed that the unprotected side of the glass pane (facing the interior part of the shock-tube) was destroyed as depicted in Figure 2.27, while the other side of the glass (the side glazed with film layer) stayed in place as illustrated in Figure 2.28.

Subsequent analytical studies resulted in an anchor design procedure that has been adopted by the CSA S853 Standard (Alameer and Saatcioglu, 2023).

2.5.2 Norville, S. and Conrath, E. J. (2001)

This study dealt with factors that affect blast-resistant glazing and the attachment methods of the glazing to window frames. The authors created a design chart for specific explosions, corresponding to TNT equivalent weights and standoff distances. An equivalent 60-s duration static design load was generated. The researchers used the design procedure given in the ASTM E1300 standard in combination with the 60-s duration static design loads to design blast-resistant laminated glass. A glass design chart was constructed by considering the results from the blast tests, air blast pressure, and reflected positive phase impulse. The authors concluded that the use of this chart for blast-resistant glazing designs reduces the need for blast testing for the validation of windows.

2.5.3 Vallabhan C.V. et al. (1997)

The researchers investigated the properties of wet glazing for blast-resistant windows. They found that the most critical glazing occurs when all four sides of the glass are supported. Generally, the glass panels are fabricated to resist lateral forces, such as wind pressures. Once the lateral deflection under lateral pressure increases and exceeds the thickness of the panel, a complicated stress distribution is generated, and the glass plates start acting in the nonlinear mode of deformations. It was further reported that the edges of the sealant are affected by shear and moment forces, for which they developed a mathematical model to calculate the stresses created in the sealant. This model is convenient to calculate displacements and forces in the sealant as it is very difficult to compute them in practice. Progress was made to estimate the slop of the window plate along all the edges for comparison with theoretical results (Vallabban et al., 1997).

2.5.4 Vallabhan C. V. et al. (1990)

The researchers developed an analytical model that focused on the connections between the two glass plates in insulated glass units (IGU), and between the glass plate and the mullion.

The model consists of continuous springs provided along the boundaries of the IGU, with Karman plate equations employed in the mathematical model. When an IGU is exposed to lateral pressure, the forces generated along the IGU seal, structural seal and the stresses generated in glass plates can be computed by the model. The researchers pointed out that the reactions computed along the boundaries show different distribution patterns depending on whether the glass plates behave linearly or nonlinearly. The reaction patterns are one of the most important parameters in the design of IG unit seals (Vallabhan et al., 1990).

2.5.5 Wei, J. and Dharani, L.R (2006)

The researchers conducted a numerical investigation to present solutions for rectangular laminated architectural glazing as affected by simulated blast loading depending on whether small or large deflection plate theories are used. A comparison was made between the results produced by analytical models and a three-dimensional nonlinear dynamic finite element analysis. Most recent studies dealt with the effect of the positive phase of blast loading on window performance. However, this study proved that the dynamic response can be significantly affected by the negative phase of blast loading for a specific laminated glass panel configuration. The deflection of mid-span panel and the maximum tensile stress generated from negative pressure were found to be twice the values generated by positive phase blast loading. In this study, the interlayer considered was viscoelastic PVB, which is a linear elastic material. The nonlinear stress analysis showed that the behavior of a laminated plate exposed to blast loading was primarily controlled by bending stresses although the membrane action can be developed. As summary, the researchers argued that higher dynamic tensile stresses within the negative loading phase may damage the glass panel. Moreover, the results showed that the blast resistance of square panels was less than that of rectangular panels (Wei & Dharani, 2006).

2.5.6 Lusk, B. (2011)

Lusk (2011) investigated the performance of full-scale window systems numerically by implementing dynamic modeling, and experimentally through shock-tube testing. The objective of the research program was to improve the prediction of the dynamic response of windows under blast loading and to develop design recommendations. Numerical simulations were done

by using LS-DYNA software. The results for mid-span deflections and dynamic reactions were compared with those obtained experimentally. Both positive and negative phases of loading on window systems were examined. The dynamic reactions generated were reported to have components in parallel and perpendicular directions of the plane of glazing. These reactions were transferred to the mullions and then to the frame. The specimens used in this research consisted of three laminated window systems and were tested by using a shock-tube facility as illustrated in Figure 2.29. Each laminated window consisted of three layers of glazing in addition to the aluminum frame with dimensions of 1.22m width and 1.68m height. Figure 2.30 shows a window specimen allocated in the test frame before and after the test. Additionally, Figure 2.31 presented sample gauge readings recorded in one of the specimens tested by the shock tube. The dynamic response and reactions were predicted by performing LS-DYNA numerical simulations (Lusk et al., 2011).

2.6 Effect of Blast Load on Curtain Walls and Structural Response

2.6.1 Introduction to Curtain Walls and Mullions

A big transition was observed in the construction industry for building facade design from heavy load-bearing walls to lightweight non-load-bearing curtain walls. The walls generally included multi-wythes of masonry before the transition started (Schwartz, 2001). Currently, curtain walls with aluminum frames are considered the lightest weight of all other external wall systems. The aluminum framing enhances the design of wall systems that could be supported on the edges of the slab due to the benefit of having a high strength-to-weight ratio. Furthermore, the aluminum frames can be attached to steel or concrete easily and can be formed in several complex shapes such as interlocking framing members that perform well under both dynamic and thermal movements. There are several curtain wall systems such as the stick system and the unitized system. In the stick system, vertical mullions span between two floors while the horizontal mullions (transoms) end at the vertical mullions. The connection to concrete slabs is made by casting a steel insert into the concrete, mostly on the top of the slab, with a clip that acts as an erection "shoe" when the mullion is installed. It is common to provide the inserts at the face of the slab as the reduction of the exterior wall thickness is preferable to provide more

floor space. The mullion is anchored to the insert, which is cast in concrete by using an attachment clip that can act as a gravity anchor and tieback (Horowitz, 1991).

2.6.2 Curtain Wall System Formation

The history of curtain walls belongs to the Crystal Palace. However, this history is linked to the skyscrapers in terms of lightweight walling and the use of glass walls. Earlier, the term curtain walls could be defined as “a continuous curtain of masonry penetrated by windows”. Currently, the curtain wall is a grouping of ideas and mainly the separation of the wall from the structure (Yeomans, 1998). Curtain wall systems include two basic types, stick and unitized. Unitized systems are prefabricated and comprise the frame, infill, gaskets, and accessories. Unitised systems are not tubular same as stick systems. However, it is mostly split into two joining halves as shown in Figure 2.32, which improve several functions such as installation and weatherproof sealing of units noted that the unsymmetric sections lead to lateral torsional buckling (Buljan et al., 2016).

The vertical and horizontal mullions support the glass panes of a curtain wall. Usually, the wind forces can be transferred to the frame of the building mostly by the vertical mullion. The main role of the glazing is mainly to transfer the load to the frame and control the lateral-torsional motion of the framing. Moreover, lateral-torsional buckling of the mullions can be controlled by the transoms (Clift, 1989). Aluminum is lighter than steel by 65%. Commonly, aluminum framing members are made of aluminum alloy 6061-T6. Mullions are the vertical component of the framing that can resist the wind forces through the bending effect (Kesawan & Mahendran, 2019). Several curtain wall systems are not only barrier walls, but they act to drain water from the outer plane of a wall (Brown & Klein, 1998).

2.6.3 Mechanism of Blast Resistance in Curtain Wall System

The membrane capacity of the glass attached to the mullions within Blast-resistant curtainwall systems can be improved by the laminated glass in addition to the mullions that transfer the applied forces to the slabs. The response of curtain walls under impulsive blast loading can be evaluated by applying dynamic inelastic analyses. When the glass can be deformed

larger prior to fragmentation the hazard of explosion could be reduced. Single degree of freedom analysis (SDOF) evaluates curtainwall behavior under blast loading. The reaction forces can be calculated when the glass is treated as a SDOF. This reaction can be applied after SDOF analyses for the mullion. In summary, the response of curtainwall can be predicted by applying SDOF methods. Finite element methods (FEM) can verify accurately the interaction between the mullion and the glass. Furthermore, FEM could evaluate accurately the potential failure mechanisms and provide an economical design for blast-resistant curtainwall systems. Besides, FEM analyses evaluate geometric stiffening which leads to generating more precise anchorage forces to be improved at the slabs (Dawson & Smilowitz, 2007).

2.6.4 Previous Research on Curtain Wall Mullions at the University of Ottawa

The Blast Research Laboratory of the University of Ottawa is provided with a facility known as a shock tube to simulate blast application on different types of samples representing different sections of the building. One of these sections is curtain walls. A broad research program was performed at this blast research laboratory to develop and investigate curtain wall performance.

2.6.4.1 Saatcioglu, Alameer and Elnabelsy (2017a)

Many large-scale curtain wall specimens that were supported by two vertical mullions on either side, two horizontal mullions at the top and bottom, and two double-pane glass panels on either side were examined using the University of Ottawa Shock Tube. The main objective of this program was to investigate the performance of curtain walls used by Global Affairs Canada (GAC) to reduce blast risk. Figure 2.33 and Figure 2.34 show the geometry of the tested curtain wall parts and the cross-sections of both vertical and horizontal mullions respectively. Moreover, the glass was a double-pane insulated glass unit (IGU) connected to vertical and horizontal mullions. The formation of the glass panels comprises of laminated blast-resistant tempered glass panes and other glass panes with an insulating air gap in between. The outer pane of the IGU (exposed to the blast waves) includes 4.7 mm thick tempered glass. The inner pane is composed of two 4 mm tempered glass which is laminated by 3 mm lamination located on the protected side of the curtain wall. The typical test specimen is shown in Figure 2.35. This study is considered Phase I and mainly dealt with testing two full-size curtain walls. The two specimens were tested to clarify

the significance of using a catchment system known as “Guardian Coil” to protect the occupants in a building. The “Guardian Coil” catchment systems were used with both specimens, and it was located 300 mm from each specimen as shown in Figure 2.36.

Without any retrofitting, Curtain Wall 1 was evaluated using the test specimen to replicate the conditions that would exist on-site at the building. A ply of 7 mils protective film was mechanically anchored to the second specimen. The protected film was used on the two inner panes. To promote one-way action, the protective film was mechanically anchored to the top and bottom horizontal mullions (rather than to the vertical mullions). The bottom internal pane was secured to the horizontal and vertical mullions along four corners, allowing for two-way movement. The middle horizontal mullion of the second curtain wall was further adapted by being anchored to the two vertical mullions by using drill-through bolts and aluminum angles as shown in Figure 2.37. Both curtain walls received the same reflected pressure-impulse combination of 85.5 kPa and 1334 kPa-MS (1 and 2). The horizontal mullion of curtain wall 1 failed, and glass shards entered the witness panel as a result. According to the standard GSA Rating System, the unprotected outside glass fragments spread for 3 meters away from the curtain wall by piercing the witness panel, scoring a score of 5 (High Hazard-No protection). Also, the curtain wall's glass windows collapsed into the shock-tube.

The Guardian Coil likewise retained its integrity when the coils at the top and bottom where it was linked to the tracks yielded. Several of the hooks attaching the Guardian Coil to the tracks became disconnected, but the device remained in place capturing huge curtain wall components but not the full glass fragments. Following the test, the coil was discovered to be half open. Figure 2.38 and Figure 2.39 show the damage that occurred during and at the end of the test respectively.

The performance of curtain wall 2 was better and damage to the vertical mullions was observed. In the middle areas where the horizontal mullion was bolted both vertical mullions fractured. The glass windowpanes remained in place, secured to the mullions. The external glass panes that were not protected broke and the glass shards flew in through the side openings of the shattered curtain wall where the blast pressure vented and transported glass fragments as

pieces fell into the Shock Tube. The test specimen after the test is illustrated in Figure 2.40 (Saatcioglu et al., 2017)

2.6.4.2 Saatcioglu, Alameer, and Elnabelsy (2017b)

This study (Phase II) dealt with testing two curtain walls that had similar properties of the curtain walls used in (Phase I). It was done without having a catchment system as Phase I. However, the specimens were retrofitted to improve behaviors against blast loads. The first test (labeled Test 3) involved a companion curtain wall with enhanced connections of the mullions utilizing the aluminum angles, glued on the mullions using a marine epoxy adhesive known as "cold weld," as opposed to mechanical connections that were bolted as shown in Figure 2.41. This resulted in a companion curtain wall with enhanced mullion connections. An extra 7-mil protective layer that was mechanically glazed was also put onto the internal glass pane. Only the vertical mullions were used to anchor the film, encouraging one-way motion with 25 mm square aluminum HSS elements that were bolted to the mullions with 6.35 mm diameter, 100 mm long, drill-through bolts. Contrary to the curtain wall examined in Test 2, the connection improvement in the curtain wall of Test 3 was carried out without the use of through bolts, which was thought to have reduced the vertical mullion flexural capacity in the crucial positive moment region. Moreover, Test 3 was performed in a low-hazard environment with a maximum reflected pressure of 80 kPa and a maximum impulse of 448 kPa-msec. This curtain wall behaved admirably. As expected, the exposed top and bottom exterior panes failed. The glazed inner panes performed well and resisted the blast loads without cracking. The horizontal mullion stayed connected to the vertical mullions, and the chemically bonded (epoxy-glued) angles employed to strengthen the connections behaved well with no evidence of detachment. The vertical mullions deflected 25 mm at mid-heights (where the horizontal mullion was attached), while the horizontal mullion deflected by 35 mm at its mid-length. Figure 2.42 illustrates the performance of the curtain wall during Test 3. The curtain wall remained intact, with none of the internal components detached. On one side, the horizontal aluminum component on the unprotected blast side was separated but remained attached to the vertical mullion on the other. Using the standard GSA Rating System, the curtain wall was rated "1," indicating "safe" performance with no blast hazard to the curtain

wall. It should be emphasized, however, that the test specimen consisted of two double pane IGUs stacked one on top of the other, with no side IGUs on either side of the vertical mullions. As a result, the vertical mullions were subjected to loads resulting from pressures acting on one side, implying that they may be subjected to approximately 50% of the blast loads projected.

The second curtain wall specimen was labeled (Test 4) with an additional ply of mechanically anchored 7-mil protective film. The curtain wall was strengthened further by epoxy bonding two 3.18 mm aluminum plates on both sides of each vertical mullion and the central horizontal mullion as shown in Figure 2.43. The goal of this hardening approach was to strengthen the vertical mullions by a factor of 1.5 (assuming a perfect bond between the plates and the existing mullions). This curtain wall and the hardening technique are illustrated Figure 2.44. The technique included two aluminum angles that were added at each end of the horizontal mullion (transom) as shown in Figure 2.45. These angles were attached using epoxy glue and three 9.5 mm self-taping screws. The reflected pressure of 84 kPa and a reflected impulse of 1630 kPa-msec were applied to the curtain wall. In comparison to Test 3, this amount of pressure-impulse combination resulted in a very noticeable increase in the threat level. The performance of the curtain wall (Test 4) was poor due to the detachment of the horizontal mullion and glass panels. The angles detached from the vertical mullion ends. The epoxy glue and the screws were disconnected. Based on the Standard GSA Test Rating, the curtain wall's performance was assessed as "5 - high hazard - no protection." As a result, the retrofitting techniques used in Test 4 were not sufficient to resist 80 kPa - 448 kPa-msec reflected pressure-impulse combination. However, the techniques used in Test 3 were enough to provide adequate protection against the same threat level.

2.6.4.3 Saatcioglu, M. (2020)

Phase III tests were conducted to extend the investigations reported above as Phase I and Phase II. The evaluation of the threat level on curtain walls was performed by using pressure impulse (P-I) diagrams. A comparison was made by using a manual single degree of freedom (SDOF) charted solution using the US Unified Facilities Criteria (UFC) of the US Department of Defence (UFC 3-340-02) and the software that was developed at the University of Ottawa (RC Blast). Comparisons were performed between Curtain Wall 3, without the vertical mullion

retrofit, and Curtain Wall 4 with the strengthened mullions. P-I diagrams were generated and displacement time histories were plotted for different boundary conditions involving simply supported and fully fixed vertical mullions for each case. Figure 2.46 shows the mechanical glazing and mullion connection strengthening. This phase of investigation concluded that the retrofitting techniques that were used previously were not sufficient to provide resistance if the glass panels also existed on either side of the vertical mullions because of the increased tributary area. Therefore, it was decided to add two L-shaped aluminum angles overlapping over the mullion flange instead of the aluminum plates. The connection secured between the horizontal and vertical mullions was used and protective films were mechanically anchored to create an adequate risk mitigation strategy for the chosen threat level.

Additional investigation was done by generating analyses for a first-story mullion using the actual height of a building (3.1 m). These analyses were conducted for a threat level of 100 kg charge weight at 17.8m, generating reflected pressure of 176.5 kPa and impulse of 627.2 kPa-ms with a duration of 7.1 ms. Additional hardening was required because the threat level and the story height were increased. Therefore, an increased HSS size of 63 x 63 x 6.3 mm (2.5 x 2.5 x ¼ in) and additional two steel plates with a thickness of 6.3 mm were considered. The resulting behavior showed significant improvements based on which design recommendations were made (Saatcioglu, 2020).

2.6.4.4 Chavan H. (2021)

Chavan tested hardened curtain wall mullions as a continuation of the previous tests reported above as part of his MASc research. He investigated new strengthening techniques on Aluminum mullions of curtain walls to enhance mullion resistance against blast loads. This study included experimental and analytical investigations of aluminum mullions hardened by steel plates to resist blast loads. The hardening was classified into three main techniques: L-shaped angles as shown in Figure 2.47, steel plates depicted in Figure 2.48, and finally a set of HSS sections made of steel as illustrated in Figure 2.49. Three different sizes of mullions were tested. The first size was 152 mm x 51 mm x 3 mm and was labelled as (Mullion 1). The applied retrofitting technique was to use two steel plates. Each of them had a thickness of 3mm. These plates were

attached to the aluminum mullion using 32 mm long 5.5 mm diameter steel bolts. These bolts were placed with a spacing of 100 mm center to center on both sides of the web. Figure 2.50 shows Mullion 1. The second size was 152 mm x 51 mm x 4.8 mm and was labelled as Mullion 2. The hardening method involved two rectangular steel plates one on each side of the aluminum mullion. The dimensions and properties of the two plates were the same as the plates used to manufacture the L-shaped steel plates. Moreover, the pattern and sizes of the bolts were also the same. Figure 2.51 shows the indicated pattern of bolts. The third mullion size was 127 mm x 51 mm x 3 mm, labelled as Mullion 3. This mullion was hardened with a steel HSS with a size of 51 mm x 51 mm square section and a wall thickness of 3 mm as shown in Figure 2.52. This HSS was attached to the web of the mullion (tension web) and then fixed by using the same screws and bolts used in the first and the second size of mullions used previously. Two companion specimens were tested, one as built and the other as hardened. Different pressure levels were applied for each mullion to investigate mullion behavior within the elastic, and post-yield regions. The load application device used and placed on the shock-tube opening represented the same effect of a glass pane in a curtain wall for transferring the blast loads. The load application device is shown in Figure 2.53. The tests were carried out with simple supports as illustrated in Figure 2.54.

The results proved that the load-carrying capacity of mullions raised to a factor of 2.2 and the reduction in mid-height displacements was up to 30%. This improvement is shown clearly in Table *2.1*. A comprehensive comparison was made between the as-built and hardened mullions. The first set included (Mullion 1 and Mullion 1H) and showed a reduction in deflection of up to one-half under the same applied load. In addition, the blast load capacity of the hardened mullion (Mullion 1H) was increased by a factor of 2.2. Moreover, it was observed that Mullion 1 buckled at mid-height while Mullion 1H deformed slightly, without buckling. This is shown in Figure 2.55. Figure 2.56 illustrates the comparison between the as-built and hardened mullions. Similar improvements were recorded for the second set (Mullion 2 and Mullion 2H). The deformability enhancement in this set was significant. Reducing the spacing of bolts in (Mullion 2H) showed significant improvement in performance as shown in Figure 2.57. Figure 2.58 illustrates the comparison of the behaviors of Mullion 2 and Mullion 2H.

Table 2.1: Experimental test results

Test Specimen	Blast Shot Sequence	Blast Shot Details		Recorded Mid-height Displacement (mm)	Final Residual Displacement (mm)	Failure Description
		Reflected Pressure (kPa)	Reflected Impulse (kPa-msec)			
Mullion 1	Shot 1	27	191	45.7	24	Web buckling at mid-height along compression fibers.
Mullion 1H	Shot 1	27	210	28	60	Composite section web buckling at mid-height along compression fibers.
	Shot 2	59	411	91		
Mullion 2	Shot 1	30	225	37	30	Inelastic bending of the section along the mid span.
	Shot 2	38	270	54		
	Shot 3	44	337	61		
Mullion 2H	Shot 1	41	332	53.5	78	Steel plates suffered web buckling and rupture of the compression flange of aluminum section.
	Shot 2	65	487	88		
	Shot 3	82	645	149		
Mullion 3	Shot 1	25	208	71	42	Inelastic bending of the section along the mid span.
Mullion 3H	Shot 1	26	207	26	70	Steel plates suffered web buckling and rupture of the compression flange of aluminum section.
	Shot 2	51	428	98		

The third set was Mullion 3 and Mullion 3H and the hardening techniques used were attaching a steel HSS to the tension side and also by bolting two steel plates on both sides of the web as shown in Figure 2.59. This led to reduced deformation and increased strength. The strength of Mullion 3H was up to 2.6 times the strength of Mullion 3 without the hardening. Figure 2.60 demonstrates the correlation between Mullion 3 and Mullion 3H.

In addition to the mullion tests, analytical research was conducted to validate the experimental results. The correlation of experimental and SDOF analysis results was very good. The researcher also developed PI diagrams for hardened mullions (Chavan, 2021).

2.6.4.5 Nasseralshariati, Ehsan (2022)

The author underwent a comprehensive research project to investigate curtain wall behavior and their connection to the structural members. A series of phases were performed including the experimental work, numerical analysis by using LS-DYNA software, and non-linear dynamic analysis which were implemented based on single-degree-of-freedom (SDOF). Nine

single mullions attached to one or two concrete beams by steel brackets were investigated in addition to three full-size curtain walls within the first phase of the research. The expected damage between the load application device and the other steel sections and the aluminum mullions was reduced using XRD rubber and spring as energy-absorbing tools, Figure 2.61. The second phase was conducted by applying FEM analysis to generate different models which contribute to establishing a specific validation of the actual test results. Moreover, six various parametric study were generated to accomplish a comprehensive validation and clarify blast effects on support reaction, connections, and curtain wall response. The final phase included the examination of the retrofitting effect and fixity level by performing a SDOF analysis. As a result, the retrofitting and strengthening techniques used for the connections and mullions showed a significant improvement in specimens' resistance and stiffness (Nasseralshariati, 2023)

2.6.5 Previous Research on Curtain Walls Reported by Other Researchers

2.6.5.1 Weggel, D. C., Zapata, B. J., and Keifer, M. J. (2007)

The author examined the dynamic performance of glass curtain walls with split screw spline mullions as shown in Figure 2.62. Laminated glass was used with silicone sealant instead of compression gaskets. An airbag and pluck tests were used to apply static and free vibration tests. The horizontal mullions showed a low rotational stiffness for out-of-plane rotations compared to the vertical centerline of the mullion within the pluck tests. The damping was evaluated for each mode of vibration using the half-power point approach. Modeling was performed by using the ANSYS structural analysis tool and the results showed that there was a 8% disparity between the calculated static and experimental deflections. Ultimately, it was determined that it was feasible to use split screw spline mullions in the curtain wall assembly. The system demonstrated fewer differences when compared to static finite element analysis in predicting the mullion flexural rigidity (Weggel et al., 2007).

2.6.5.2 Behr et al. (1995)

The researchers investigated several different types of glass elements of dry-glazed curtain walls in terms of the breakage and fallout behavior under dynamic movement. It was found from

previous studies that glass breakage can be intensive when out-of-plane motions are added. Mainly, it was observed that higher fallout rates can be obtained from the 6mm annealed monolithic glass. The same type of glass with 0-10mm PET film without anchorage to the mullions, as well as 11mm fully tempered laminated glass tests, were conducted. It was concluded that the post-breakage glass fallout under dynamic racking motions cannot be resisted when the window film is not anchored to the mullions. It was also stated that curtain wall systems with narrower mullions do not have sufficiently large glass-to-aluminum clearances. Therefore, the fallout glass could be critical (Behr et al., 1995).

2.6.5.3 Deng, Rong-Bing and Jin, Xiang-Long (2010)

This study consisted of analytical investigations involving the use of FEM in LS-DYNA and the arbitrary Lagrangian-Eulerian (ALE) approach. This approach is a combination of the purely Lagrangian and fully Eulerian approaches. A fluid parallel method for the contact interface between the ALE and Lagrangian elements was carried out. TNT of 50kg was used against a curtain wall element at a level of 0.5 m above the ground and a standoff distance of 12.5 m. The supporting aluminum frame was modelled as a plastic kinematic model while the glass unit was modelled as a linear elastic entity. The exponential function provided by the Friedlander equation and the Henrych equation, respectively, were used to calculate the pressure time history and the peak overpressure. The shockwave propagation demonstrated the effectiveness of the ALE approach. Figure 2.63 shows the behavior of the curtain wall under blast load where the inner glass layer of each glass pair was found to be cracked. The aluminum frame, however, showed no obvious damage. The outcomes of this numerical analysis were in good agreement with the findings of earlier experiments, indicating that the ALE-implemented FE model behaved as predicted (Deng & Jin, 2010).

2.6.5.4 Norville, H.S. and Conrath, E. J. (2006)

The authors investigated two ways of enhancing the blast-resistance of glazing. One of these two methods was applied specifically to government amenities while the other one was performed for public facilities. A simplified method was used when the threat is unknown and

with minimum blast resistance using the UFC DoD 2003 approach, which is significant for fenestrations design for buildings. The lateral deflections of frame members were limited to L/6 in UFC DoD 2003, which was applied to window frame members in curtain walls, ribbon windows mullions as well as ribbon windows. An equivalent 3-s duration design loading provided by ASTM F 2248-03 ASTM 2003 when used with ASTM E 1300-04 ASTM (2004a) facilitated a selection of a laminated glass thickness which provided blast resistance for a specific threat level.

2.6.5.5 Kennedy, B.T., Weggel D.C., and Keanini, R.G. (2013)

This study carried out several tests on curtain wall specimens. A conventional curtain wall was examined in addition to curtain walls with annealed glass panes with conventional compression gaskets. Moreover, a curtain wall with annealed glass panes glazed with structural silicone sealant was tested. The nonlinear behavior was examined for all specimens in addition to their failure modes and global energy absorption capacities. Figure 2.64 demonstrates the test of a wet-glazed specimen. This study focused on implementing SDOF and MDOF models. Interpolation functions were used to obtain the resistance function for each curtain wall based on the recorded deformations in different positions. The experimental results showed that the ultimate energy absorbed in wet glazing is much higher than that in dry glazing, especially in end rotations and mid-span deflection. The maximum energy absorption capacity was generated by a wet-glazed curtain wall. Therefore, the bilinear resistance function parameters were observed by evaluating the linear elastic region slope as well as the maximum elastic resistance and the deflection at maximum failure. It was found that the numerical investigation and analytical resistance functions produced 6.8% higher energy than the resistance functions obtained from experimental work. Furthermore, the structural silicone sealant caused the separation of the glass pane from the mullion. However, the in-plane tensile stresses associated with membrane action were transferred by the laminated glass although the structural silicone sealant caused the separation of the glass pane from the mullions (Kennedy et al., 2013).

2.6.5.6 Weggle, D. and Zapata, B. (2008)

The authors dealt with conventional laminated glass curtain walls with split screw spline mullions and investigated the linear elastic and nonlinear elastic analyses under low-level blast loading. A comparison based on accelerations, deflections, and dynamic stresses was established between the rectangular glass lites and the identical glass lites, which had one simple support and two supports on the silicon sealant along the four edges. Various parameters were examined such as the connection stiffnesses, moments of inertia, and system damping ratios. FEM analyses were conducted under a uniform blast pressure with a triangular pulse. Comparisons were made to explain the reasons for the principal stress decrease in glass lites. Two main reasons were put forward, the flexibility of the structural silicone bead and the curtain wall system flexibility. Furthermore, the difference in frequencies and mode changes due to the change in boundary conditions were observed. As a result, the transient and modal analyses reflected the true behavior of the curtain wall system. Lower principal stresses were noticed for the glass lites of curtain walls as compared with others that were tightly supported. Typically, the range of the first principal stresses in the silicone-supported lite was noted to be 60 to 102% of those in the simply supported lite while the curtain wall-supported lite was observed to have the first principal stresses within the range of 29–58% of those in the simply supported lite. The final comparison based on linear and nonlinear transient analyses proved that once the influences of geometric nonlinearities are considered, stresses decreased further (Weggel & Zapata, 2008).

2.6.5.7 Gussen, R. and Van Eepoel, P. (2008)

This study demonstrated the use of single degree of freedom (SDOF) analytical methods in blast analysis of glazed façade assembly. It was reported that advanced analysis software assisted by engineers to obtain accurate performance resulted in more economical designs. The study focused on investigating windows and curtain walls under blast loading. The designs performed by using SDOF and analytical approaches were compared. The use of FEM can decrease the cross-sectional size, which also provides the clients with specified blast performance needs. This reduction of cross-section led to savings in materials and weight of the system which reduced the

transportation and erection costs. It was concluded that the use of advanced analysis requires higher engineering costs as compared to the SDOF analysis (Cussen & Van Eepoel, 2008).

2.6.5.8 Edel, M and Kumar, D. (2010)

These researchers focused on several analytical approaches for a suggested curtain wall of a federal government building, which may be exposed to high explosion effects. The building consisted of precast concrete wall panels attached to a reinforced concrete frame in addition to a glass curtain wall which included glass units supported by mullions attached to pretensioned steel cables bridging the foundation to the roof. Mainly, SDOF was used to design the glazing by applying GSA's WINGARD code. Afterward, the results were compared with those obtained from another SDOF glazing analysis program developed by Baker Risk. It was concluded that support rotations greater than 2 degrees may be of concern. However, in this study, the entire wet glazing to mullions created a secure connection including those with large displacements. SDOF and FEM analyses were employed to obtain non-linear models. FEM included ADINA and LS-DYNA codes, using shell elements representing glazing and truss elements representing steel cables. Both programs, ISADS and WINGARD, were used to generate SDOF models. In summary, the results showed that the glazing did not prevent cracking, but no free breakage was observed. Moreover, the results showed that the curtain wall had no failures, and the design provided the level of protection designed for. The reactions obtained at the end of the cables and glazing could be used to design both the supporting reinforced concrete foundation and the superstructure. Figure 2.65 illustrates the comparison of the glazing analyses (Edel & Kumar, 2010).

2.6.5.9 Nawar, M. et al. (2014)

The researchers investigated the behavior of curtain walls with conventional and retrofitted mullions with annealed glass assembly under blast loads as illustrated in Figure 2.66 and Figure 2.67. The conventional curtain wall assembly consisted of an additional laminated glass pane supported by an additional mullion. The specimens were subjected to 42 kPa-320 kPa-msec and 45 kPa-284 kPa-msec pressure impulse combinations by using a shock tube facility. The results presented indicated damage in the annealed and laminated glass. However, no damage was

observed for the supporting mullions. The connection angles between the header and the sill suffered enormous deformations. Good performance was observed in retrofitted curtain walls, especially in the outer part of the curtain wall, while with annealed glass developed failure. However, no damage was observed for the inner assembly with the laminated glass supported by the additional mullion. Analyses of the test specimens were also conducted using LS-DYNA. Shell elements were used to model the glass panes with an assumption of the interlayer polymer material behaving plastically till failure. It was observed that the numerical simulation produced similar results as those attained experimentally. However, although rarely, the numerical evaluation showed failure whereas no failure was observed during the real physical testing. As summary, the retrofitted mullions showed enhanced performance in resisting blast loads (Nawar et al., 2014).

2.6.5.10 Ralston, A. et al (2015)

The main goal of this study was to improve finite element models that were developed for curtain wall analysis and afterward validate them against experiments. Conventional curtain walls were tested under blast loading to examine their effectiveness. Tests were conducted on three specimens with silicone sealant rather than the conventional compression gaskets. The tests were carried out in an open area in the ISERRT facility in Gastonia, NC. Furthermore, a simple nonlinear single degree of freedom expression (NSDOF) was used to investigate the blast resistance of the curtain walls tested. Figure 2.68 illustrates the failure of the curtain walls which were subjected to incremental loading. The combined action of shear and torsion applied on the silicone bead caused the tearing of the glass under the ultimate maximum load. LS-DYNA was used to generate a finite element model. Shell elements were used to model the laminated glass. The corresponding finite element model is illustrated in Figure 2.69. All the parameters obtained and recorded by the transducer during actual tests were used in the FE modeling as idealized blast waveforms based on the effect of fluid-structure interaction (FSI). An identical response was observed from the program simulation related to the FE analyses about deflection time histories of glass and mullions. It was observed from FE analysis that the main cause of failure for most specimens was the large mid-height deflection of the vertical mullions. The researchers

concluded that the accuracy of analysis is controlled by damping of the system and the high strain rates of glass (Ralston et al., 2015).

2.6.5.11 Kennedy, B. and Weggel C. (2009)

The authors investigated a group of five full-scale conventional curtain wall samples. Laminated glass was used instead of monolithic glass and structural silicone sealant instead of compression gaskets which were used to attach the glass to the frame. The way of attaching the laminated glass to the mullions allowed the creation of membrane behavior once they were subjected to quasi-static, uniform blast load and cracked. The resistance curve was created based on the data obtained from experiments. There were three states of energy absorption which were computed by the global resistance curve, the first one is glass first cracking, the second one is mullions first yield, and then the fracture of the system. Furthermore, the ultimate rotations at the end of mullions were calculated as well based on experiment results. It was observed that the ultimate absorbed energy of the wet-glazed curtain wall was 300% greater than the dry-glazed system due to only some of the dry-glazed glasses being cracked and generate the membrane action. The membrane action could occur with the dry glazing when the energy absorption exceeds 50% at the failure mode. Besides, in the case of wet glazing, the maximum rotation at the ends could reach up to 7.5° as shown in Figure 2.70 while the maximum end rotation for the dry-glazed mullion was 4.1°. Once the curtain wall experiences extra damage, both energy absorption and mullion end rotation could be greater noting that the wet glazing still resisted after mullion breakage. As a result, various curtain wall patterns could have various limit states as well as maximum mullion end rotations. Resistance function construction is preferable for curtain wall systems based on simplified nonlinear SDOF or energy-based analyses and designs (Kennedy & Weggel, 2009).

2.6.5.12 Brewer, T. et al. (2015)

The researchers improved various configurations of curtain walls used for US Government overseas infrastructure. This infrastructure comprises steel tubes instead of aluminum mullions which were anchored as steel stud curtain walls (SSCW) between two slabs. The experiments

were conducted on a curtain wall three stories high with a blast load impulse of 2000 KPa-msec. First, the hollow steel sections were installed for the test reaction. Afterward, they were attached to the second floor. Both the first and ground floors consisted of granite cladding and FE/BR windows. For the rest of the floors, the thickness of glazing was reduced from 65 mm to 51 mm. The transmission of blast load was reported to be from the panels to the vertical mullions, and then to the beams and the frames. A typical test of curtain walls is illustrated in Figure 2.71. The fragmentation was noticed for the granite cladding after applying the blast load. Furthermore, it was noticed that the windows were cracked, and the spandrel beam was damaged. The failure of the FE/BR wall caused laminations to break inside the building. The validation of experimental results against analytical modelling based on CFD software was done and a small difference was noticed between the two. In summary, the curtain wall was very strong enough to resist the applied blast loads with minimum destruction (Brewer et al., 2015).

2.6.5.13 Marchand, K. et al. (2017)

Marchand et al. (2017) investigated the performance of conventional curtain walls, which were designed for gravity and wind loads, under blast loads. They performed tests by using a shock tube facility. Test results were compared with finite element analysis using LS-DYNA software. Two shots were applied on eight specimens for five tests to investigate the behavior of mullions and IGU till the failure point. Two IGU glasses were anchored to the frame by silicon sealant. Timoshenko-type beam element represented the aluminum mullions in the FE modelling while connections were considered as pinned supports. Shell elements were used for the IGU panels and the interlayer material while single-point kinematic constraints were used to model the connections to curtain walls. The captured deflections were used to explain the change in behavior from elastic to plastic behavior under increasing blast pressures. Figure 2.72 shows the specimen's behavior before and after the tests. Figure 2.73 shows the FE model used in the analyses.

2.6.5.14 Bedon, C. and Amadio, C. (2017)

Bedon and Amadio (2007) performed a FEA study on blast performance improvements in curtain walls using energy dissipation devices. Figure 2.74 depicts the model used. The devices included visco-elastic (VE) dampers and elasto-plastic dampers (ADAS), shown in Figure 2.75 and Figure 2.76, respectively. VE devices reduced stresses in glass panes silicon joints and mullions. The brittle failure was restricted because of the capability of devices to increase deformations. Once the structure was able to obtain additional dynamic loads besides the blast loading, the finite element modeling demonstrated increased effectiveness. The VE dampers were found to be less stable than ADAS devices. It was suggested that both shear resistance and elastic stiffness must be well-designed to generate reliable stiffness and strength near the supports. The devices behaved as rigid supports until the blast loading resulted in elasto-plastic shear behavior. As a result, it was observed that both VE and ADAS devices can generate the required strength and stiffness in curtain wall frames if they were designed well (Bedon & Amadio, 2017).

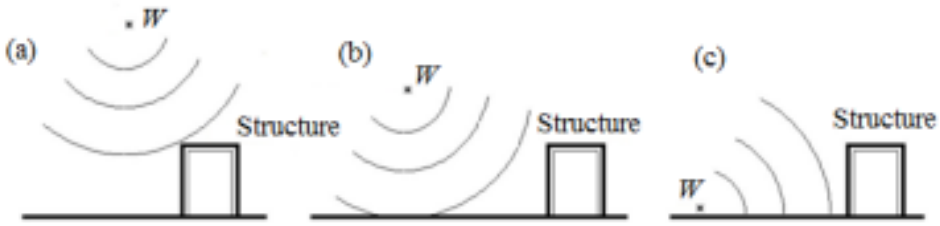

Figure 2.1: Types of explosions (a) Free-air bursts (b) Air bursts (c) Surface bursts (Karlos et al., 2013)

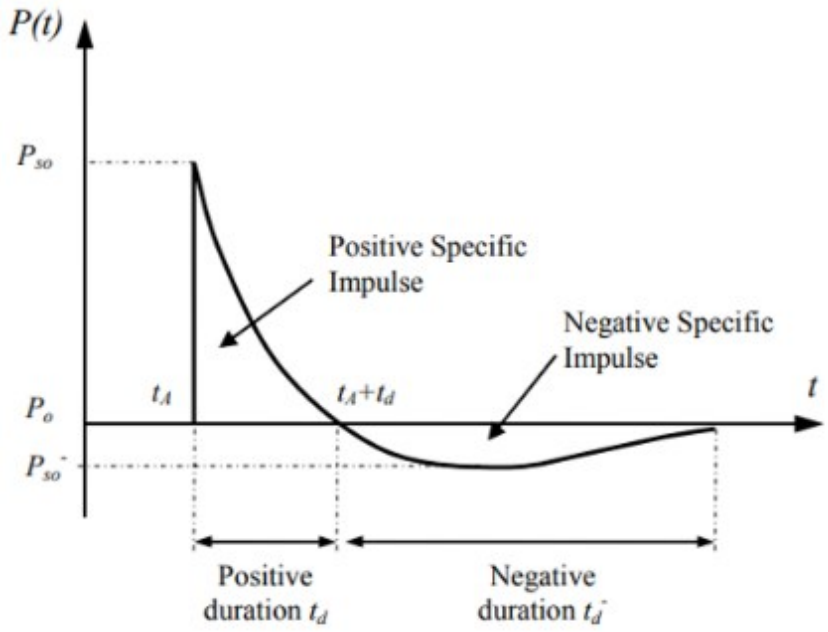

Figure 2.2: Blast wave pressure-time history (Nego, 2007)

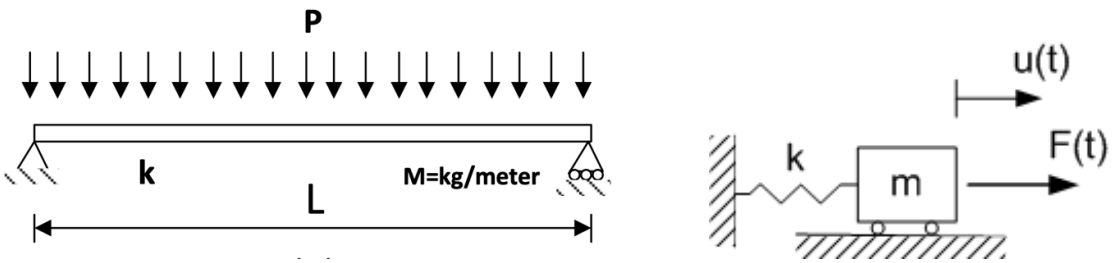

Figure 2.3: Beam with uniformly distributed mass and uniformly distributed pressure (left) represented by an idealized SDOF system (right) having a concentrated mass and a concentrated force

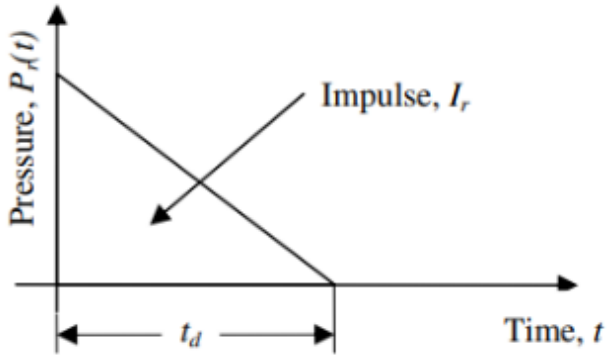

Figure 2.4: Idealized pressure-time history

Figure 2.5: Experimental set up for three-point bending tests (left) and four-point bending tests (Right) (Su et al., 2014)

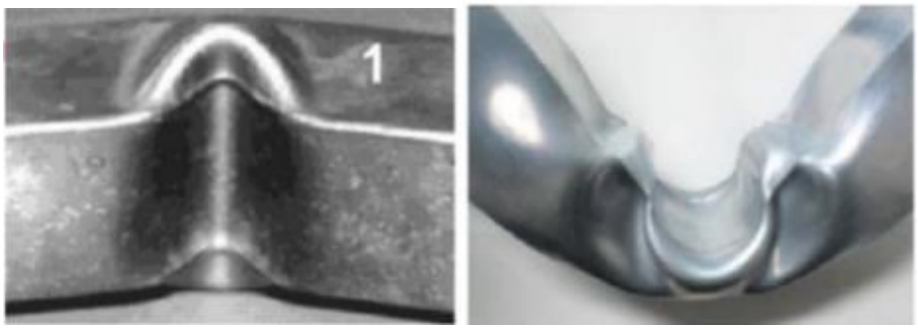

Figure 2.6: Deformation modes of thin-walled tubes under three-point bending. Bending collapse (left) and bending with indentation (right) (Huang & Zhang, 2018)

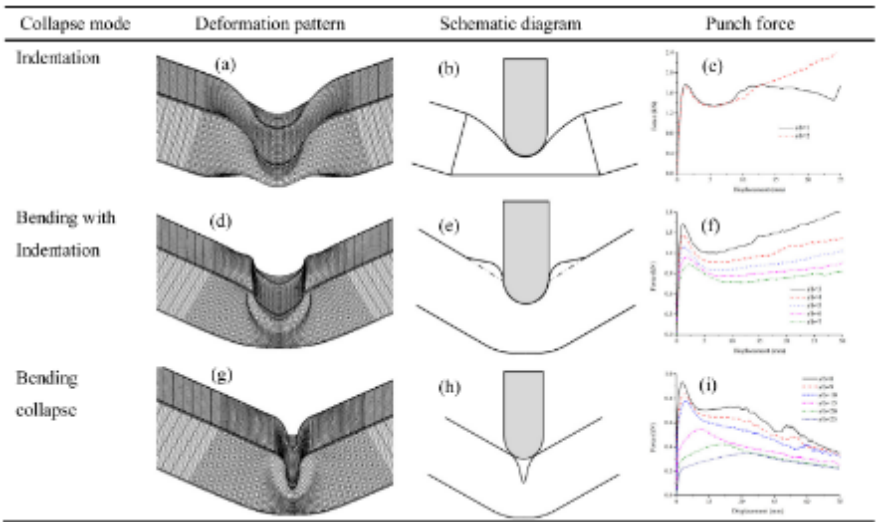

Figure 2.7: Deformation modes of tubes and punch force for different s/b ratio (a/t=30) (Huang & Zhang, 2018)

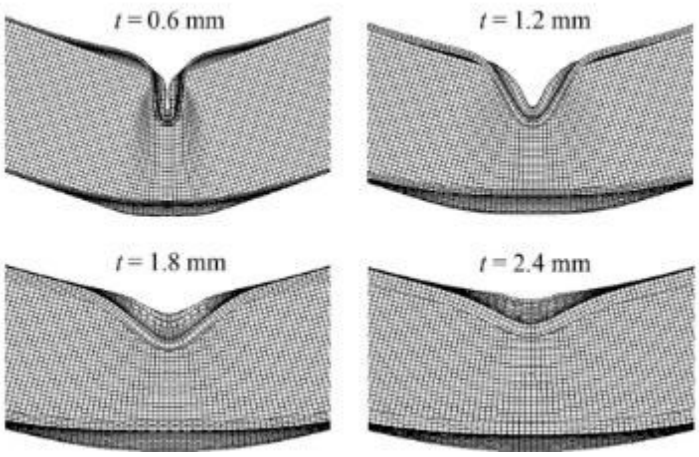

Figure 2.8: Deformed shapes of tubes with different thickness (a=30 mm) (Huang & Zhang, 2018)

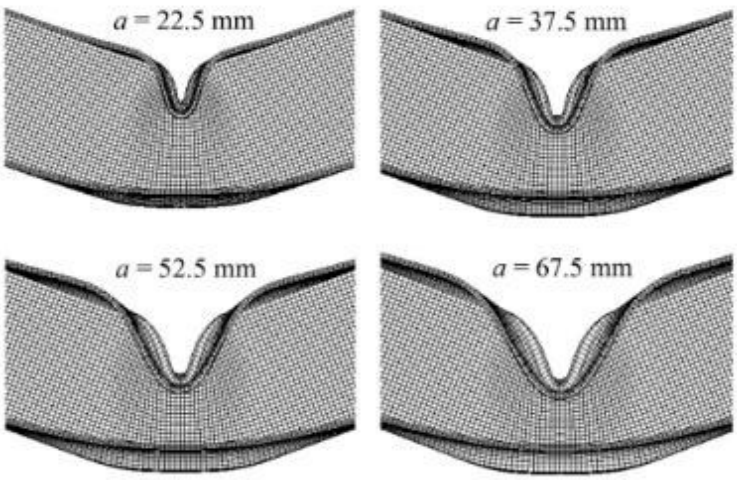

Figure 2.9: Deformed shapes of tubes with different section width (s/b=15) (Huang & Zhang, 2018)

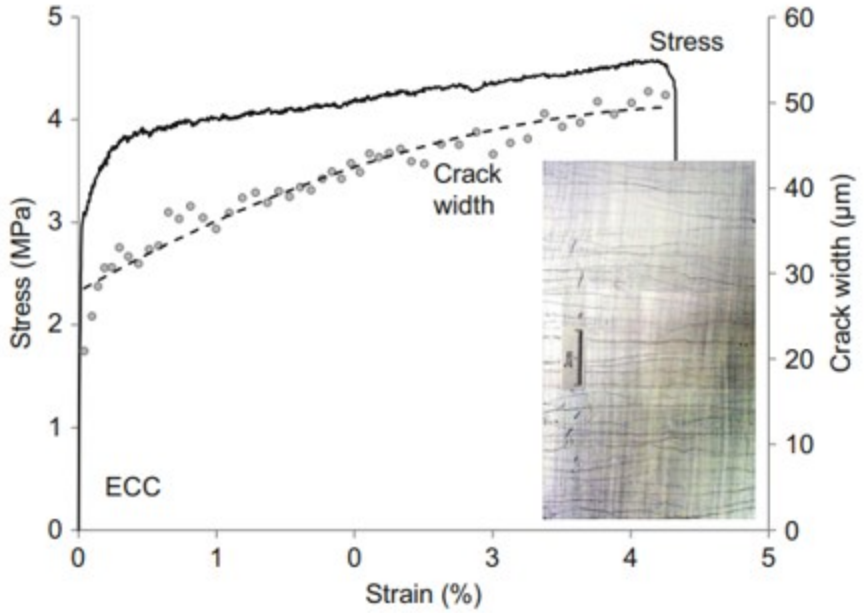

Figure 2.10: Tensile strain hardening of a ECC (containing 2% volume fraction of PVA fibers) maintained load-bearing capacity even under high strain of several percent, with width of multiple cracks limited to below 60 μm (Bentur, 2007)

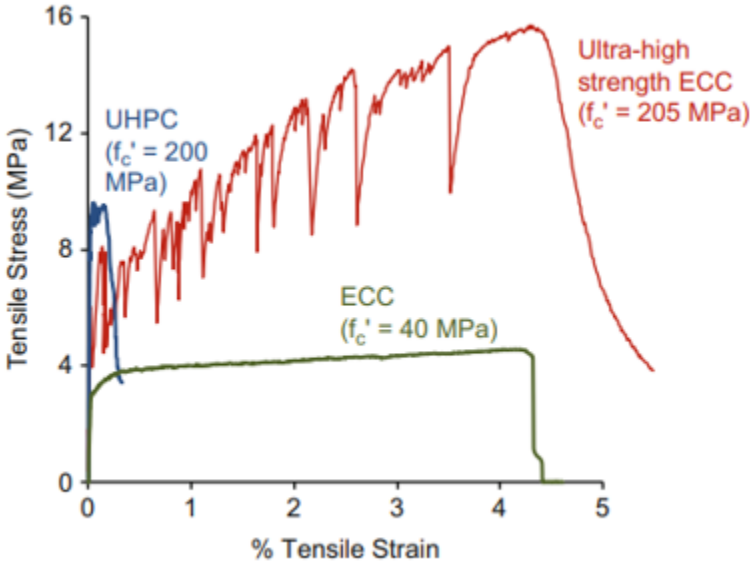

Figure 2.11: The performance of ECC emphasizes tensile ductility, with a wide range of compressive strength feasible. The strain capacity of ECC is typically over 2% or 200 times that of normal concrete or FRC. The compressive strength of ECC ranges from a few MPa to over 200 MPa, designed to meet different demands of different application (Li, 2019)

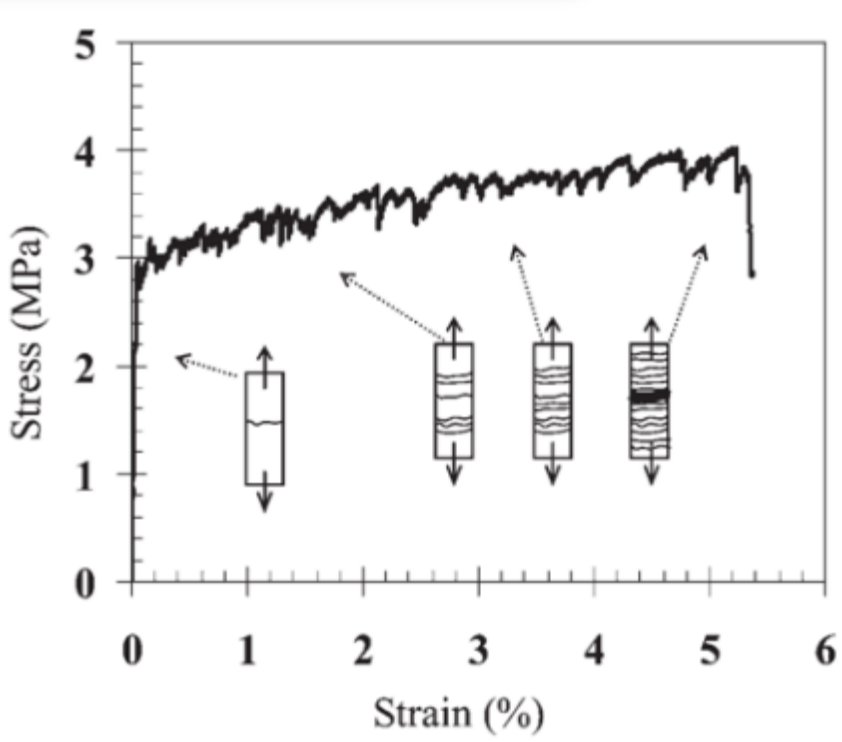

Figure 2.12: Typical ECC tensile stress-strain curve (Yu and Day, 2009)

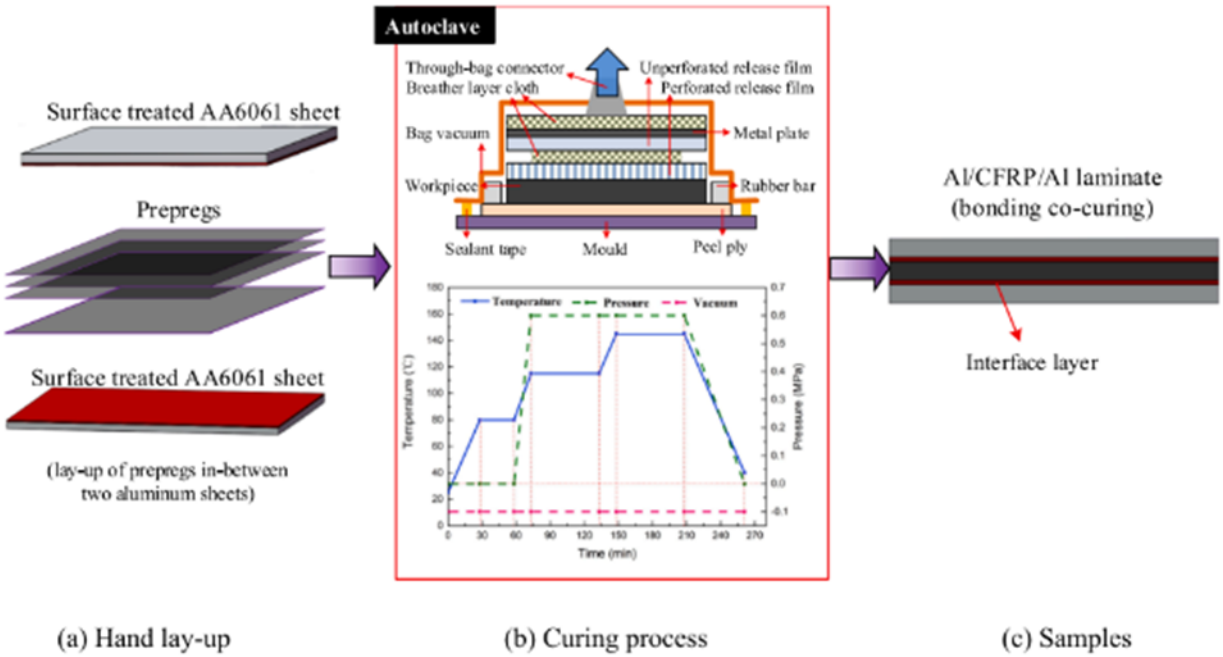

Figure 2.13: Fabrication flow process of workpiece (Zhu et al., 2019)

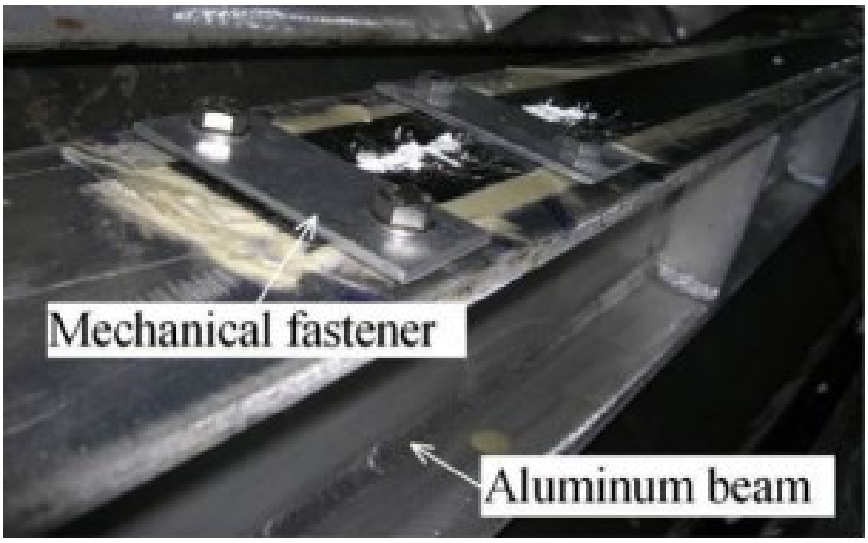

Figure 2.14: Hybrid bonded aluminum beam (Zhou et al., 2014)

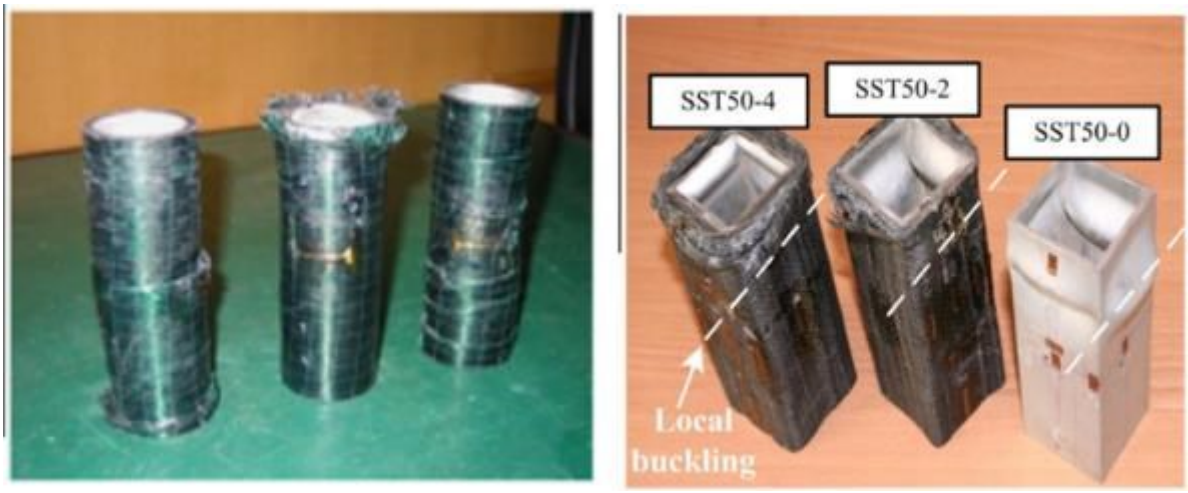

Figure 2.15: Failure modes of the SST series (Feng et al., 2016)

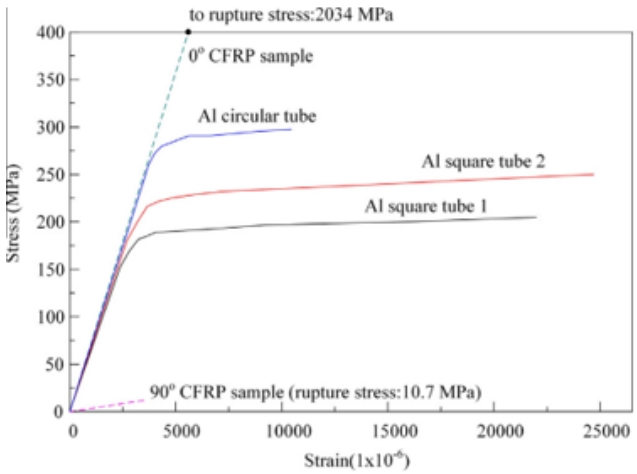

Figure 2.16: Stress-strain curves of AL tubes and CFRP samples (Feng et al., 2016)

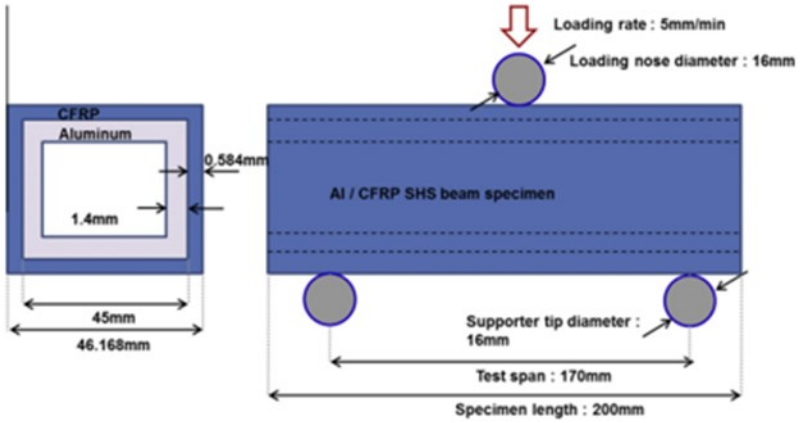

Figure 2.17: Schematic of aluminum-CFRP hybrid beam specimen (Shin et al., 2014)

Figure 2.18: Concrete-filled aluminum alloy CHS tubes with one layer of CFRP

(Chen et al., 2017)

Figure 2.19: Concrete-filled aluminum alloy CHS tubes with one layer of CFRP (Chen et al., 2017)

Figure 2.20: Windows samples with different substrates (Alameer, A., 2020)

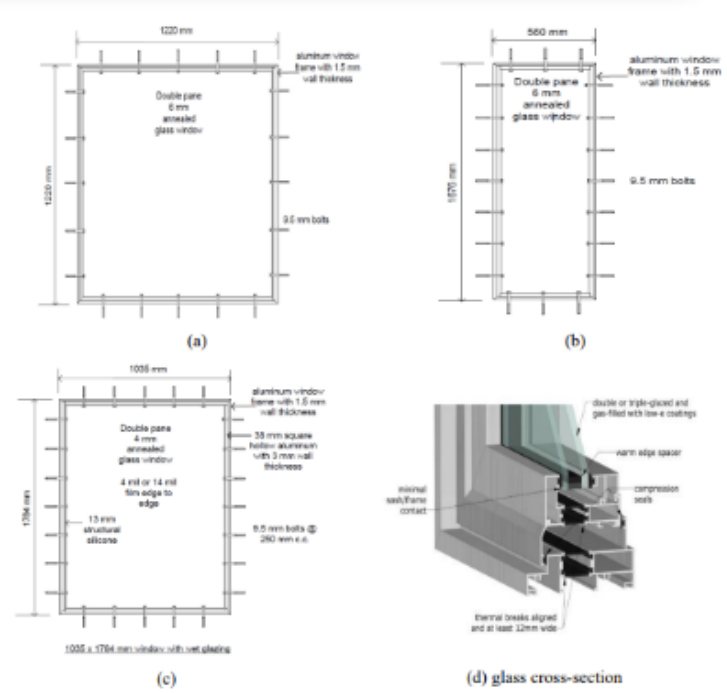

Figure 2.21: Dimension of window test (Alameer, A., 2020)

Figure 2.22: Wet glazing (Alameer, A., 2020)

Figure 2.23: Mechanical glazing (Alameer, A., 2020)

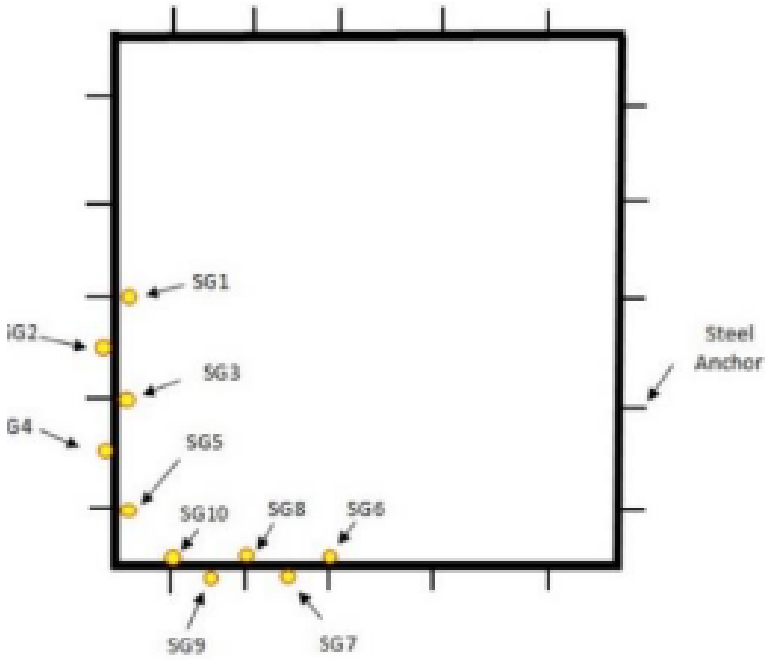

Figure 2.24: Strain gages distribution (Alameer, A., 2020)

Figure 2.25: LVDT connection (Alameer, A., 2020)

Figure 2.26: The instrumentation of anchors (Alameer, A., 2020)

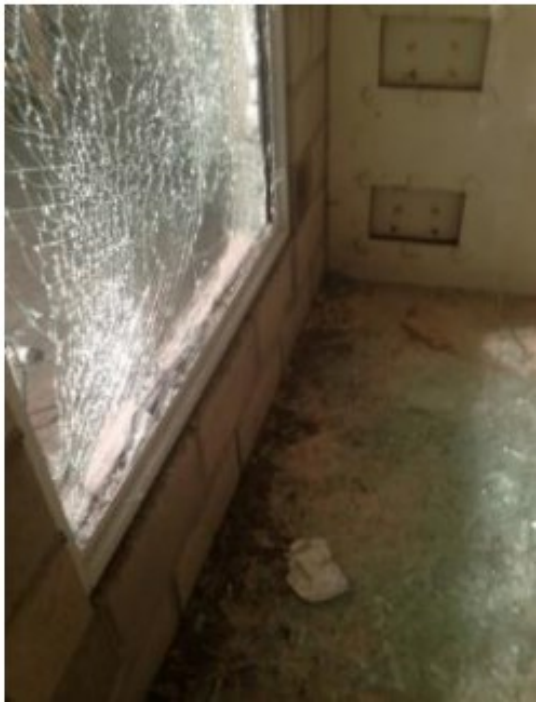

Figure 2.27: Failure of glass pane (without protected film) (Alameer, A., 2020)

Figure 2.28: Failure of glass pane (with protected film) (Alameer, A., 2020)

Figure 2.29: Shock tube (Lusk, 2011)

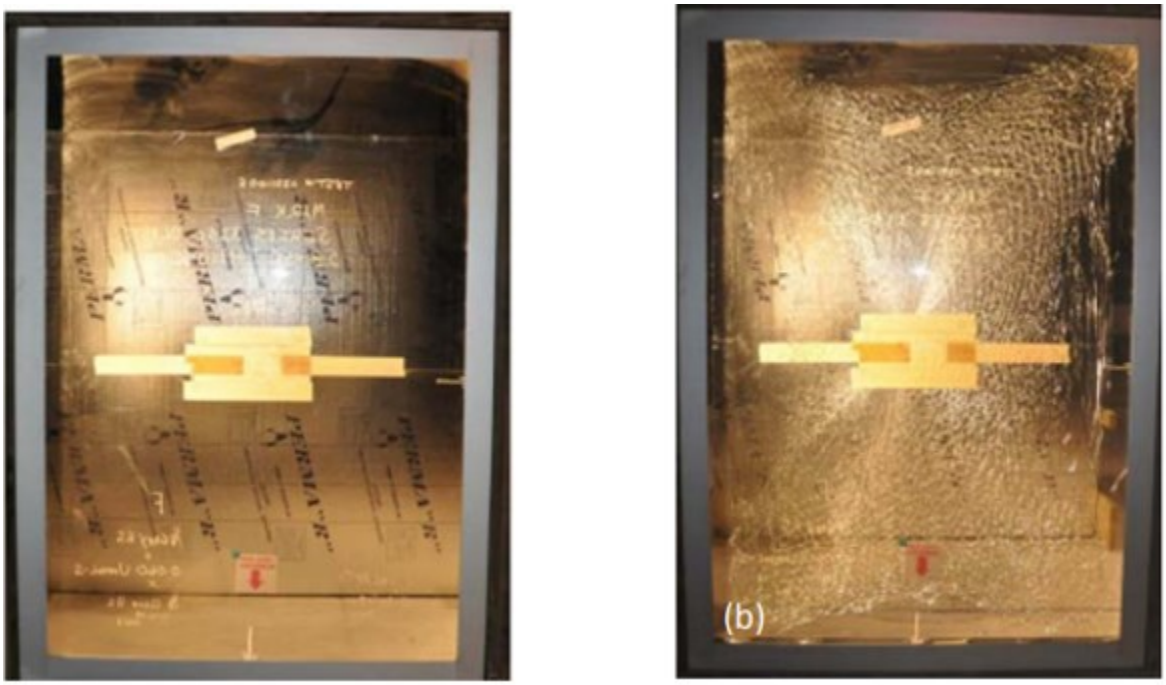

Figure 2.30: Window sample before test (left) and after test (right) (Lusk, 2011)

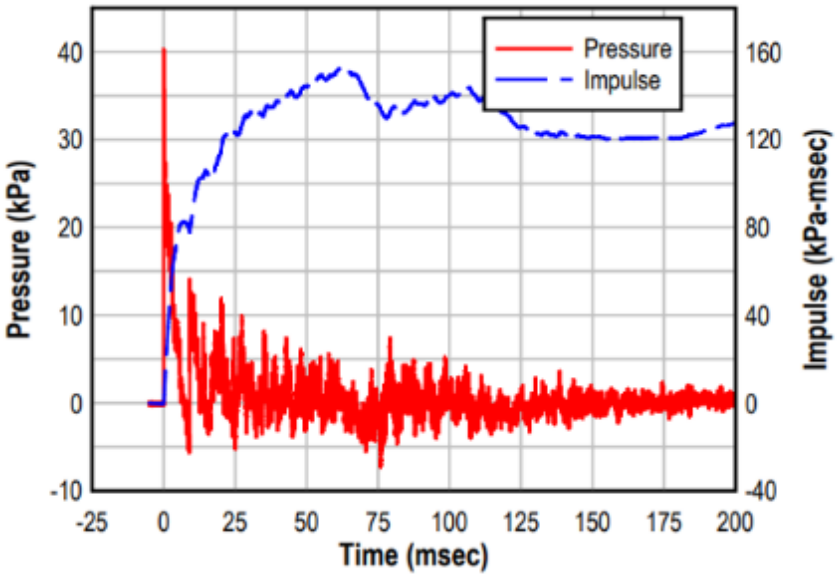

Figure 2.31: Sample pressure-time history (Lusk, 2011)

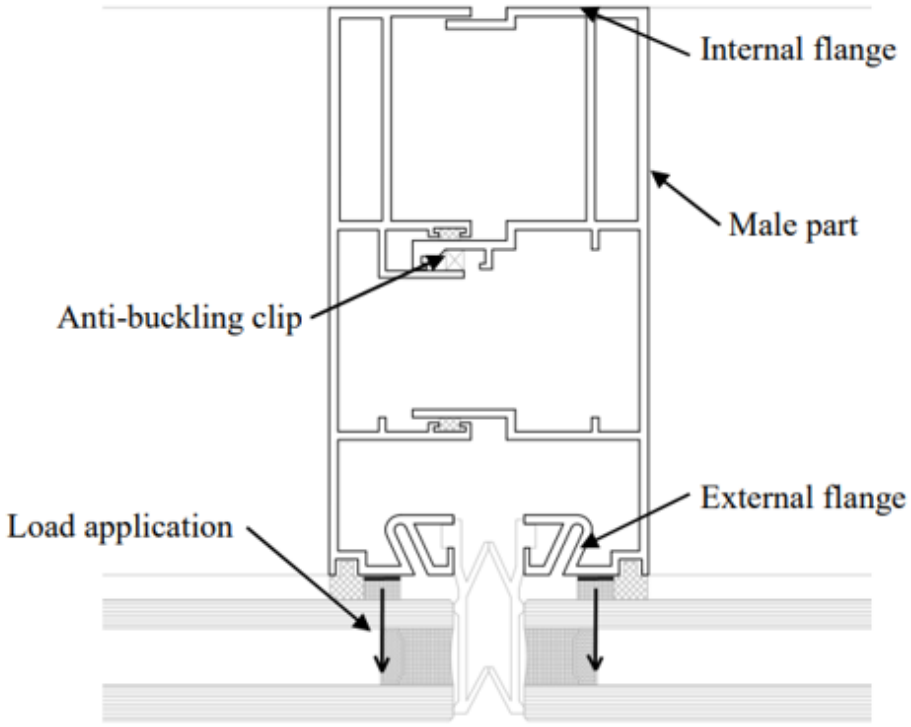

Figure 2.32: Ordinary curtain wall specimen (Buljan et al., 2016)

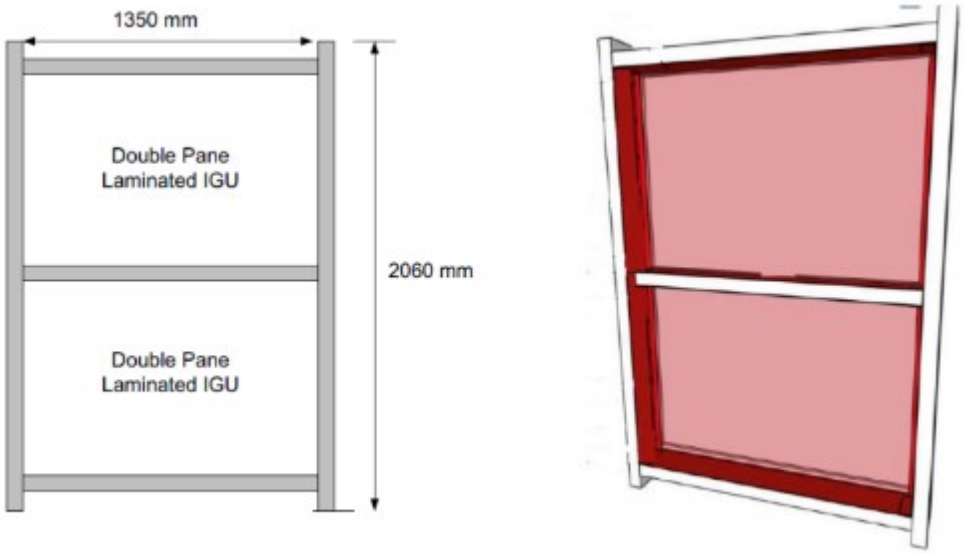

Figure 2.33: Curtain wall front view (left) and curtain wall three dimension (right) (Saatcioglu et al., 2017a)

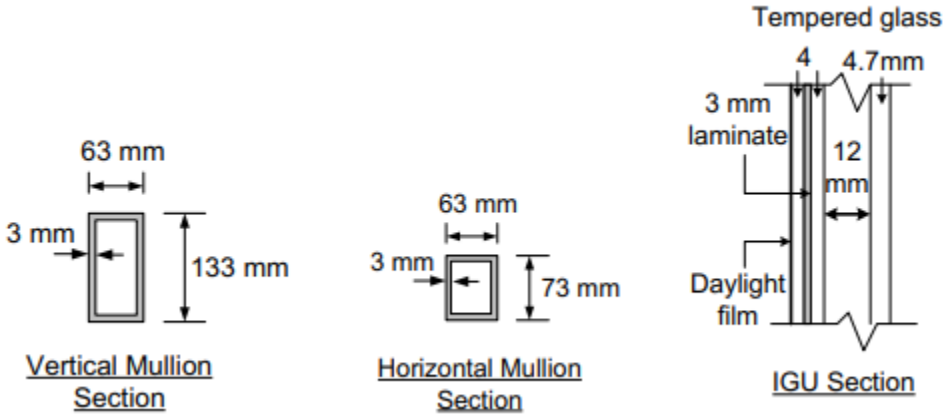

Figure 2.34: Curtain wall components (Saatcioglu et al., 2017a)

Figure 2.35: Installation of curtain wall specimen (Saatcioglu et al., 2017a)

Figure 2.36: Curtain wall 1 prior testing (Saatcioglu et al., 2017a)

Figure 2.37: Curtain wall 2 prior retrofitting (left) and Curtain wall 2 after retrofitting (right) (Saatcioglu et al., 2017a)

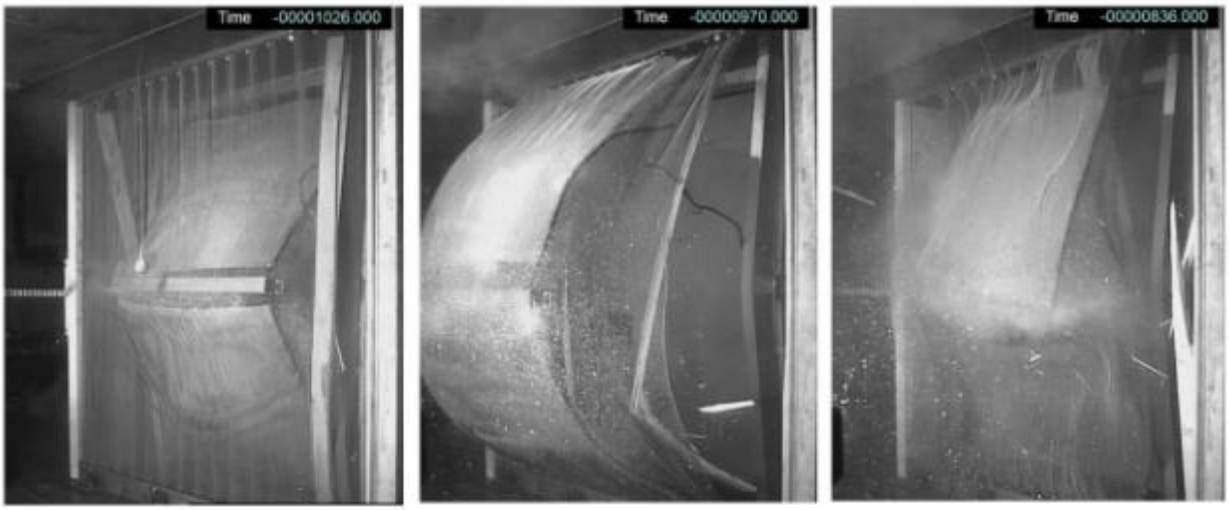

Figure 2.38: Curtain wall 1 test: a. Horizontal mullion Detachment

b. Catchment by guardian coil c. Debris fall back in shock-tube (Saatcioglu et al., 2017a)

Figure 2.39: Curtain wall 1 after testing (Saatcioglu et al., 2017a)

Figure 2.40: Curtain wall 2 with retrofitting after testing (Saatcioglu et al., 2017a)

(a) Mechanical glazing (b) Strengthening mullion

Figure 2.41: Retrofitting of Test 3 (Saatcioglu et al., 2017b)

Figure 2.42: performance of the curtain wall during Test 3

Figure 2.43: Performance of curtain wall during Test 3 (Saatcioglu et al., 2017b)

Figure 2.44: Application of aluminum plates and angles with epoxy adhesive for strength enhancement (Saatcioglu et al., 2017b)

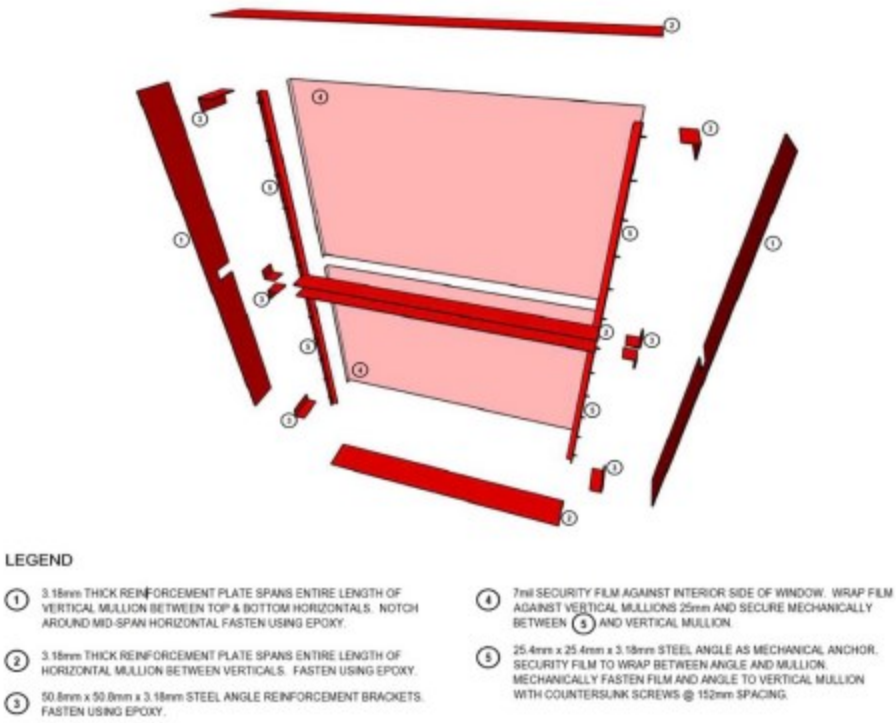

Figure 2.45: Retrofit components for possible field application (Saatcioglu et al., 2017b)

Figure 2.46: Mechanical glazing and mullion connection strengthening (Saatcioglu, 2020)

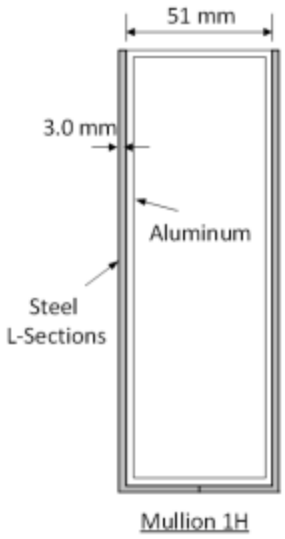

Figure 2.47: Mullion 1H (152 mm x 51 mm x 3 mm) (Chavan, 2021)

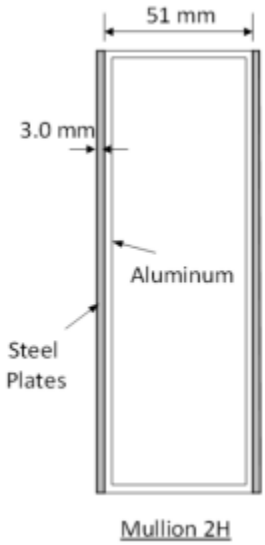

Figure 2.48: Mullion 2H (152 mm x 51 mm x 4.8 mm) (Chavan, 2021)

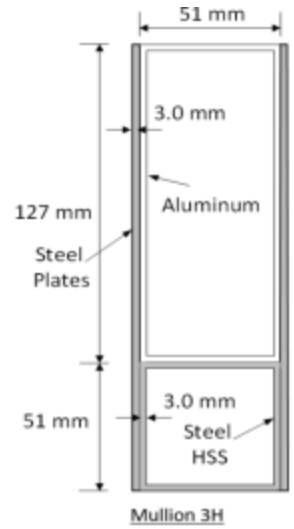

Figure 2.49: Mullion 3H (127 mm x 51 mm x 3 mm) (Chavan, 2021)

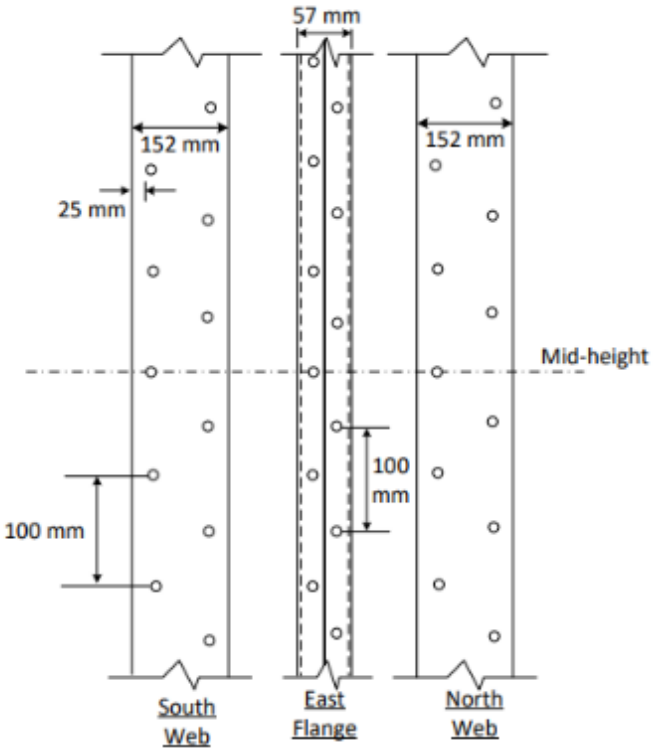

Figure 2.50: L shaped steel plates and Bolted screw pattern for mullion hardening (Chavan, 2021)

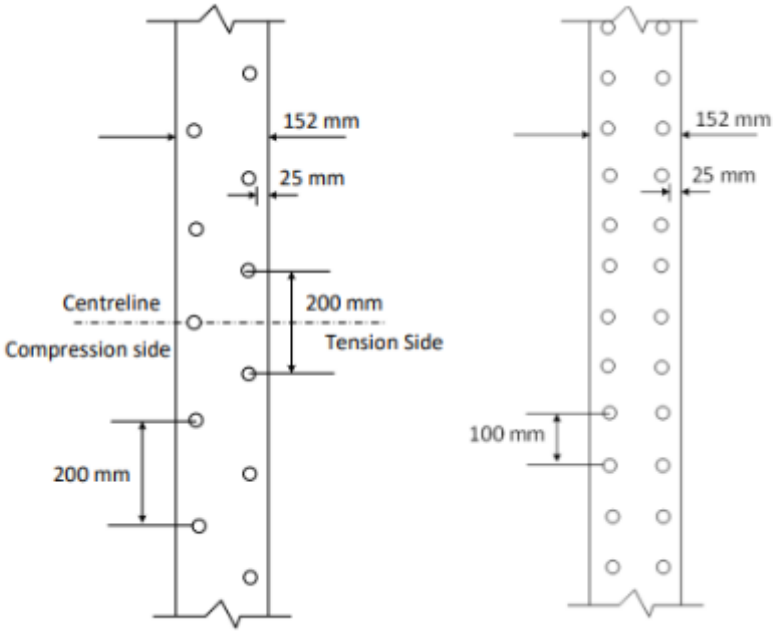

Figure 2.51: Mullion hardening using steel plates with bolted screw pattern (Chavan, 2021)

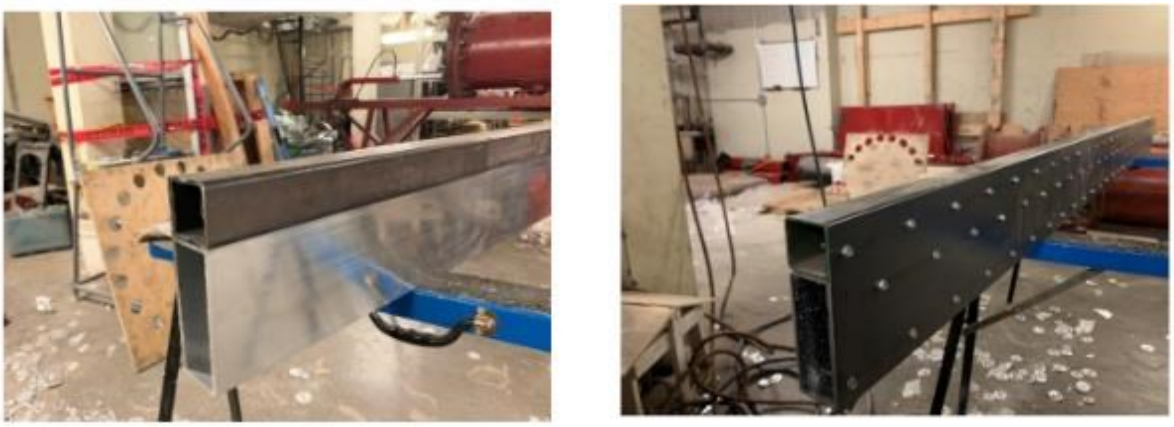

Figure 2.52: Tension flange hardened with HSS (left) and steel plats attached both sides (right) (Chavan, 2021)

Figure 2.53: Load application devise generated the distributed load (Chavan, 2021)

Figure 2.54: The assembly of simple support (Chavan, 2021)

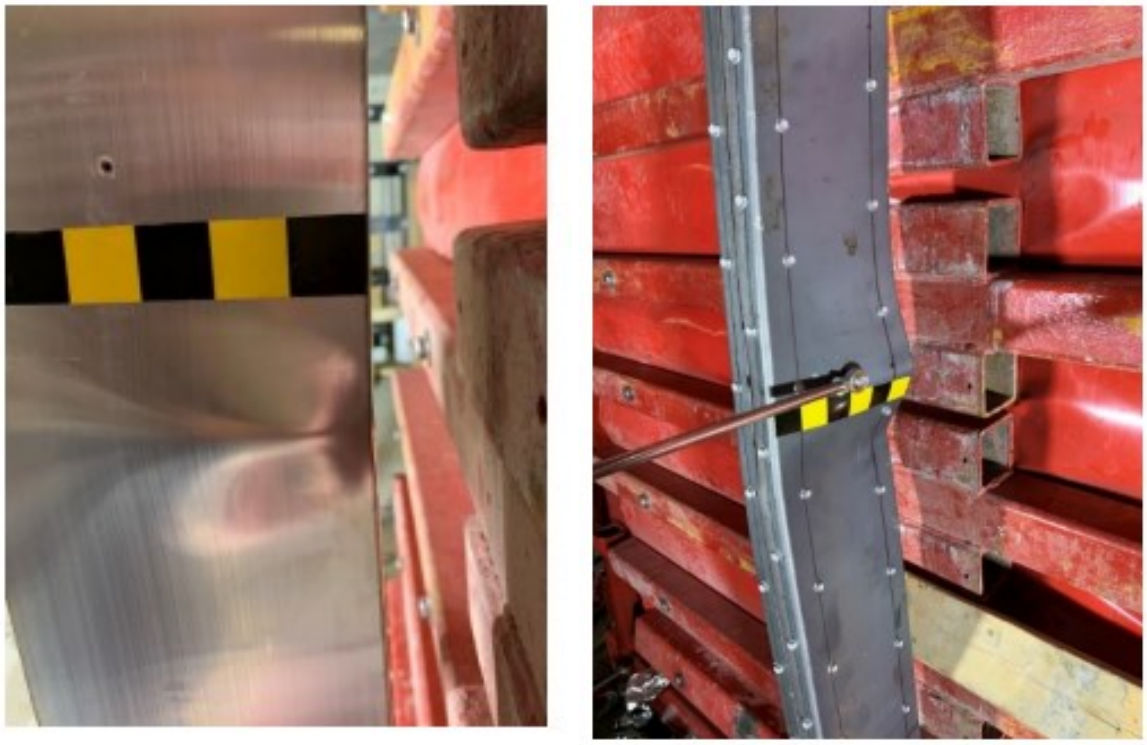

(a) (b)

Figure 2.55: Experimental tests results (a) Mullion 1 and (b) Mullion 1H (Chavan, 2021)

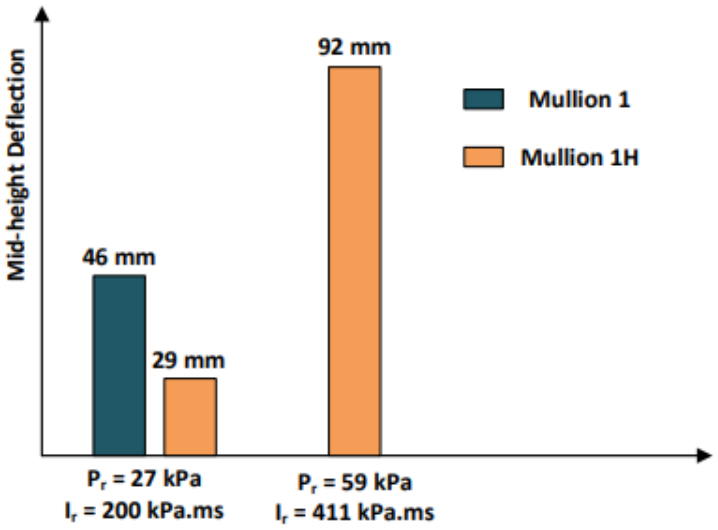

Figure 2.56: Comparison of test results of Mullion1 and Mullion 1H (Chavan, 2021)

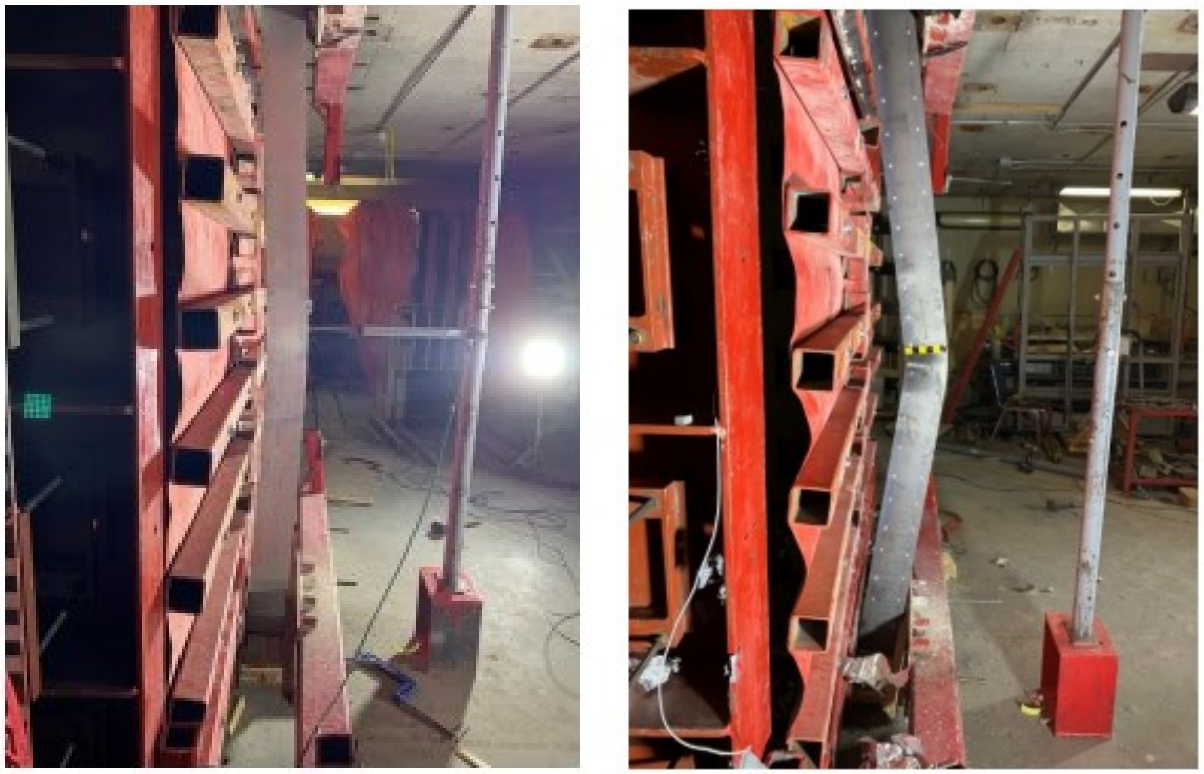

(a) (b)

Figure 2.57: Experimental tests results (a) Mullion 2 and (b) Mullion 2H (Chavan, 2021)

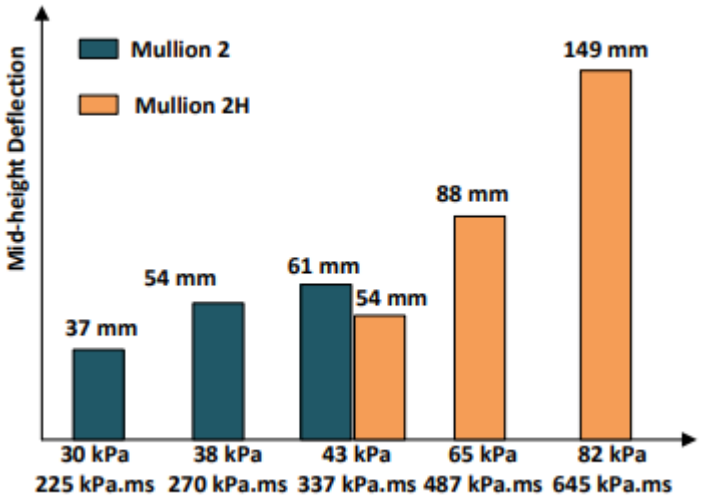

Figure 2.58: Comparison of test results of Mullion2 and Mullion 2H (Chavan, 2021)

Figure 2.59: Mullion 3H with retrofitting (Chavan, 2021)

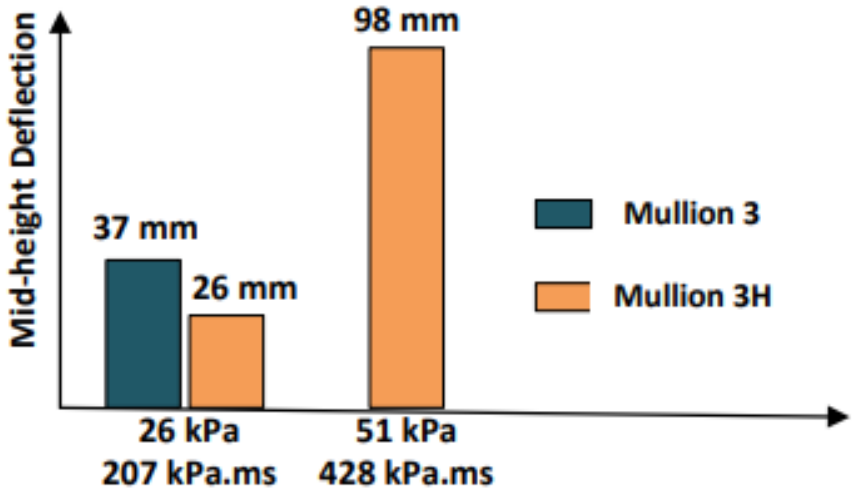

Figure 2.60: Comparison of test results of Mullion3 and Mullion 3H (Chavan, 2021)

Figure 2.61: Testing mullions with different substrates

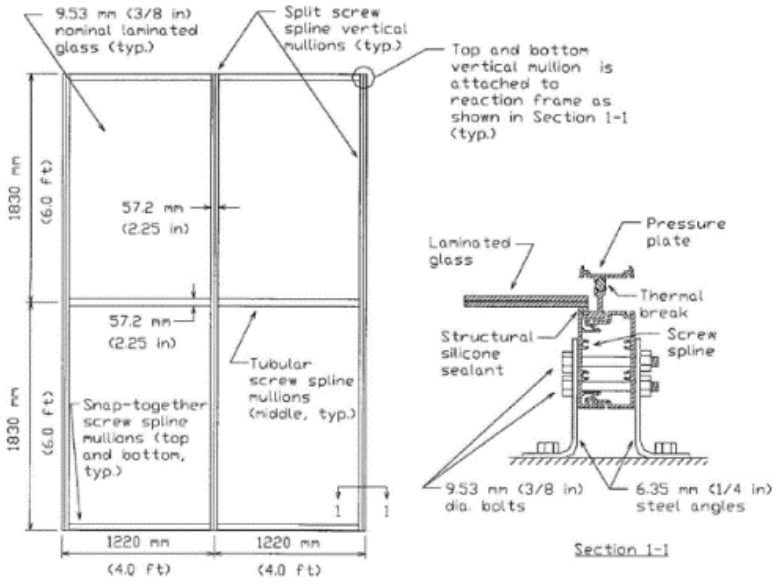

Figure 2.62: Split screw spline curtain wall specimen (Elevation and Section) (Weggel et al., 2007)

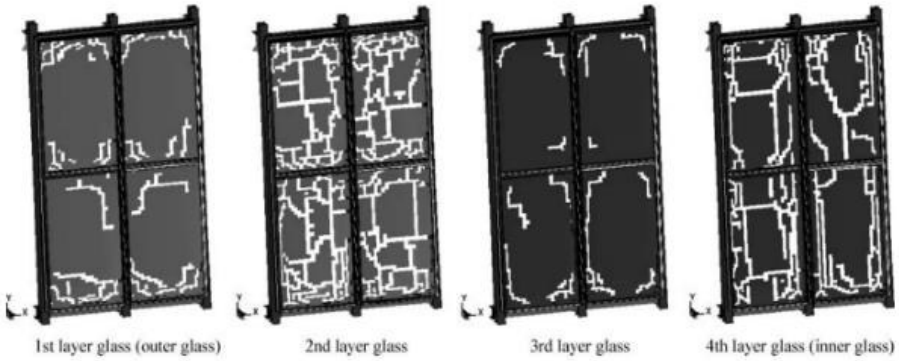

Figure 2.63: Comparison of damage between outer glass and inner glass (Deng & Jin, 2010)

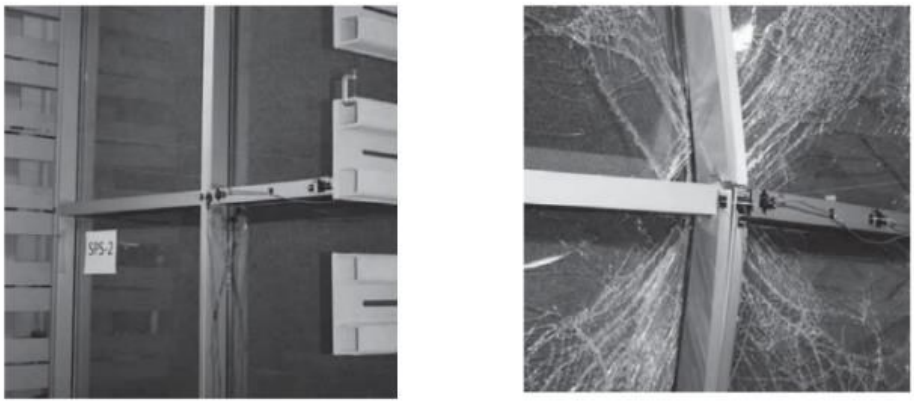

Figure 2.64: Wet glazed specimen before loading (left) and Wet glazed specimen after loading (right) (Kennedy et al., 2013)

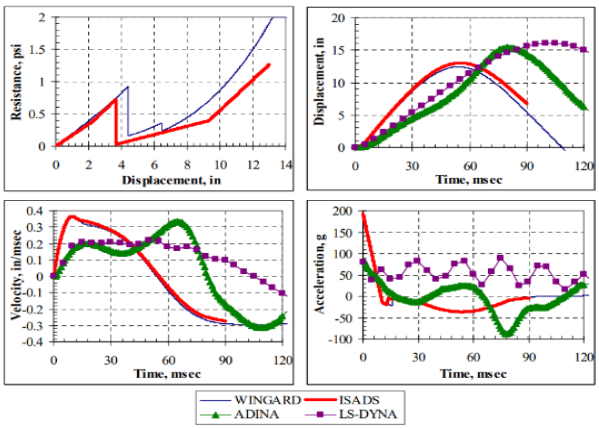

Figure 2.65: Comparison of Glazing Analyses (Edel & Kumar, 2010)

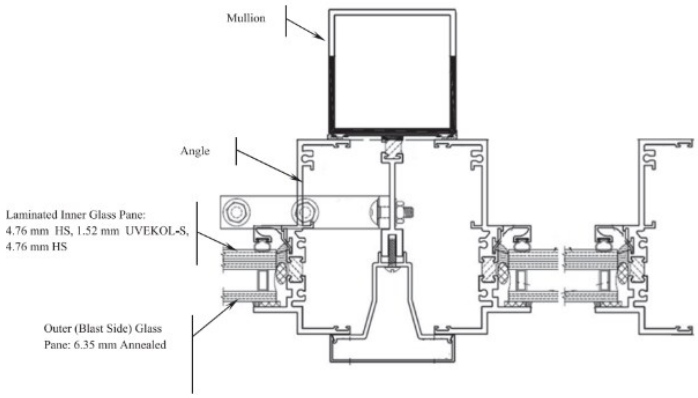

Figure 2.66: Ordinary curtain wall specimen (Nawa et al., 2014)

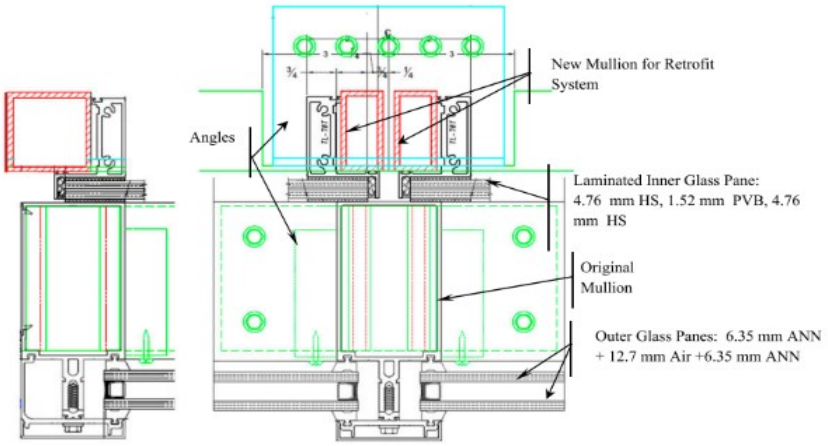

Figure 2.67: Blast-retrofitted CW2 details (Nawar et al., 2014)

Figure 2.68: Specimen before (left) and after (right) the shot (Ralston et al. 2015)

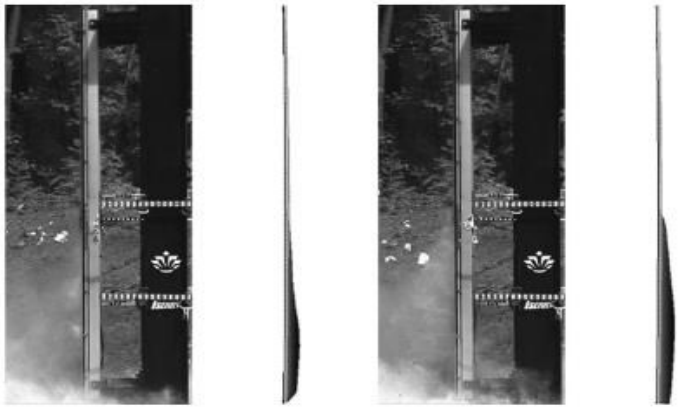

Figure 2.69: Comparison of the FE model to the high-speed video at 18 ms (left) and 30 ms (right) after the blast wave reaches the curtain wall (Ralston et al. 2015)

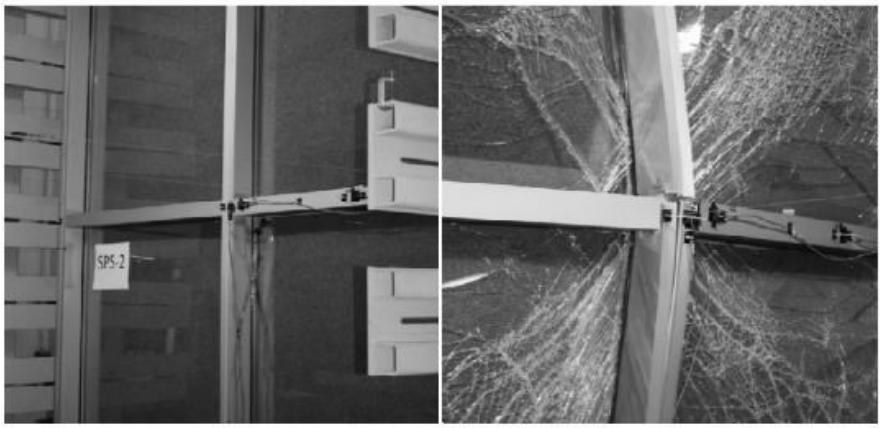

Figure 2.70: Curtain wall specimen in the reaction frame (inside looking out): a) Un loaded specimen b) Loaded specimen just after mullion fracture (Kennedy and Weggel, 2009)

Figure 2.71: Pretest External View (left) and Post-test External View (right) (Brewer et al., 2015)

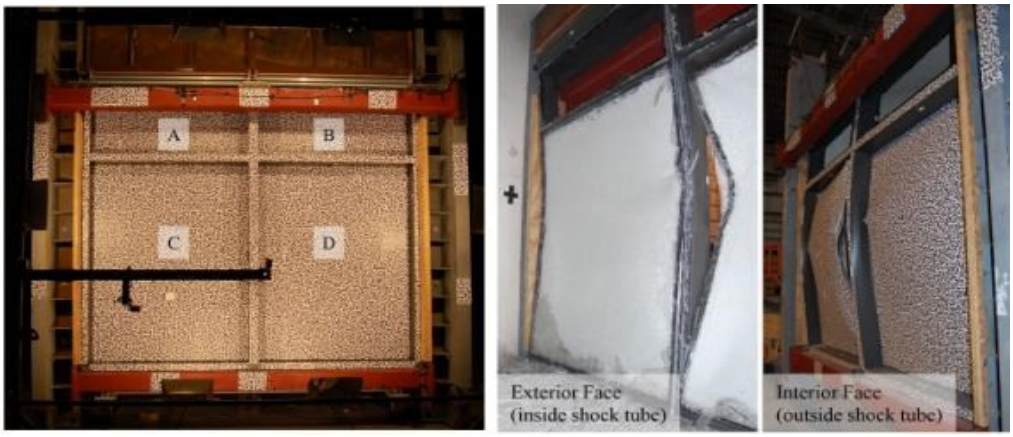

Figure 2.72: Curtain wall a) before test (left) and b) after test (right) (Marchand et al., 2017)

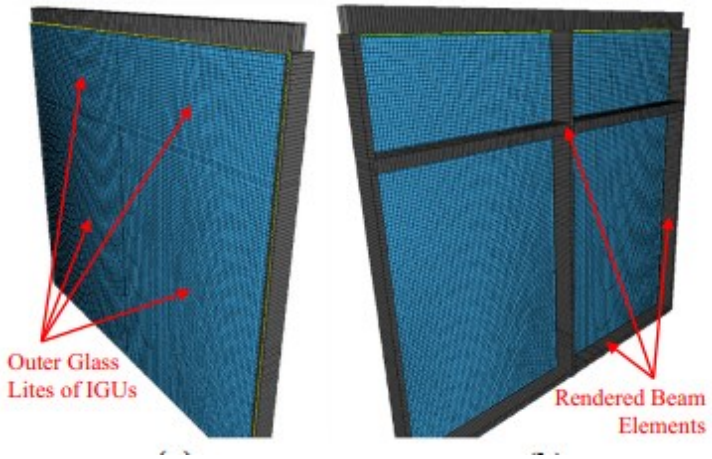

Figure 2.73: Finite element representation of curtain wall specimen: blast-loaded face (left) and protected face (right) (Marchand et al., 2015)

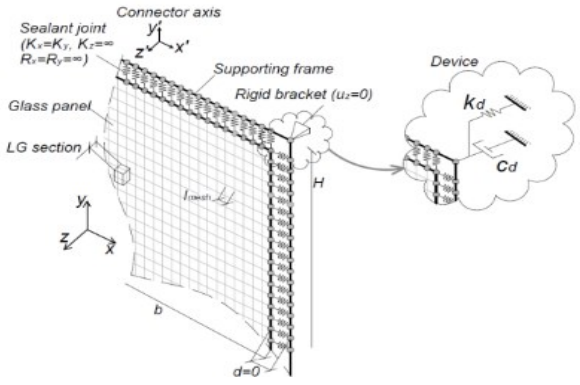

Figure 2.74: Schematic assembly view of the M01 Finite-Element numerical model (ABAQUS/Explicit) (Bedon et al., 2017)

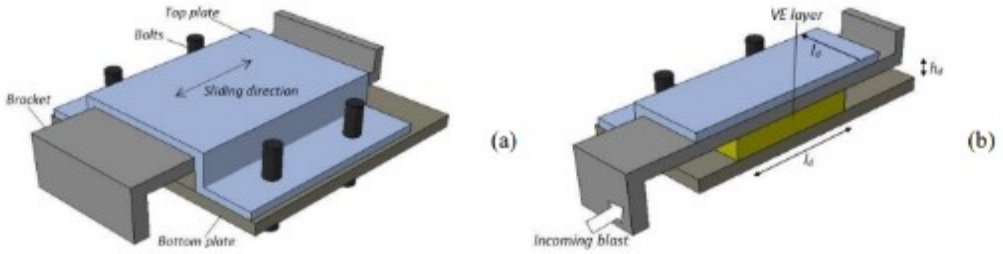

Figure 2.75: Example of VE device for a CW modular unit. (a) Assembly and (b) mid-span transversal cross-section (ABAQUS/Explicit) (Bedon et al., 2017)

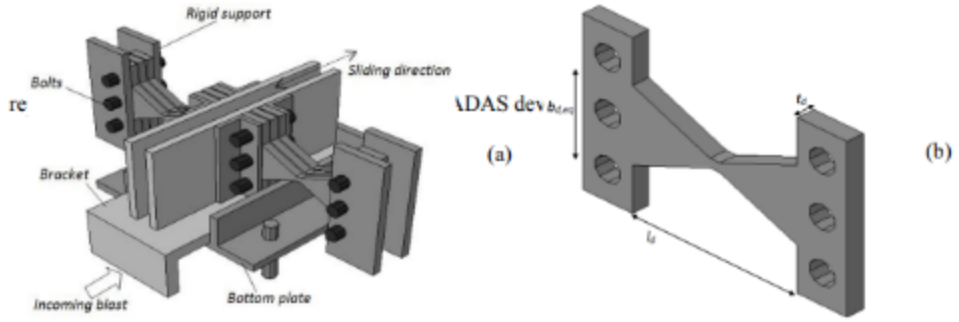

Figure 2.76: Schematic (a) overview of a possible ADAS device for application in glazed curtain walls and (b) typical geometrical properties of the X-shaped steel components (ABAQUS/Explicit) (Bedon et al., 2017)

CHAPTER 3. EXPERIMENTAL INVESTIGATION AND RESULTS

3.1 Introduction

The experimental research consists of tests of curtain wall mullions hardened with different techniques, which involved the use of cementitious infill materials. A total of sixteen aluminum mullions were prepared and tested under simulated blast loading using the University of Ottawa Shock Tube. Different techniques of hardening and strengthening were applied to enhance mullion strength and ductility. The techniques involved filling the mullions with either high-strength mortar (HSM) or engineered cement composites (ECC), with or without internal steel reinforcement or external CFRP sheets. Two control mullions were previously tested under blast loads using the same shock tube by Chavan (2021) as part of the same overall research program and were used as reference mullions.

This chapter presents a summary of the experimental program and shows the main tasks involved in the test program. Also included are material properties, specimen description (preparation and construction) as well as the hardening techniques employed, instrumentation, test setup, and test procedure.

3.2 Construction of Test Specimen

A total of sixteen full-scale aluminum mullions were constructed. These specimens were filled with different cementitious materials to examine the mullion behavior against blast loads. Different hardening techniques were implemented to verify the mullion capacity under blast loads. The control specimens consisted of two different sizes, 51mm x 127mm x 3mm, and 51mm x 152mm x 4.8mm, and were tested previously by Chavan (2021). The sixteen hardened aluminum mullions included eight mullions of size 51mm x 127mm x 3mm thickness. The remaining eight aluminum mullions consisted of size 51mm x 152mm x 4.8mm. Two materials were used to fill the sixteen mullions, i) ECC (Engineering Cementitious composites) and ii) HSM (High Strength Mortar).

The as-built mullions (control mullions) are labeled as Mullion 1 and 2 while hardened mullions are labelled as Mullion F for the mullions filled only with cementitious materials, Mullion H for the mullions hardened with internally placed wires or chains, and Mullion R for the mullions strengthened with externally placed CFRP sheets. Some specimens consisted of a combination of two materials such as Mullion FH and Mullion FR which represent mullions filled with cementitious materials and reinforced with wires or chains, and mullions filled with cementitious materials and strengthened with external CFRP, respectively. A summary of all test specimens is provided in Table 3.1.

Table 3.1: Test specimens considered in the experimental program

No. of mullion	Mullion Classification	Size (mm)	Type of Infill Material	Type of Reinforcement	Type of Support	Application
1	Mullion 1F	51mm x 127mm x 3mm	ECC	Without reinforcement	Simply Supported	
2	Mullion 2FR	51mm x 127mm x 3mm	ECC	CFRP	Fix Supported	CFRP-U-Shape
3	Mullion 3F	51mm x 152mm x 4.8mm	ECC	Without reinforcement	Simply Supported	
4	Mullion 4FR	51mm x 152mm x 4.8mm	ECC	CFRP	Fix Supported	CFRP-U-Shape
5	Mullion 5F	51mm x 127mm x 3mm	HS Mortar	Without reinforcement	Simply Supported	
6	Mullion 6F	51mm x 127mm x 3mm	HS Mortar	Without reinforcement	Fix Supported	
7	Mullion 7F	51mm x 152mm x 4.8mm	HS Mortar	Without reinforcement	Simply supported	
8	Mullion 8F	51mm x 152mm x 4.8mm	HS Mortar	Without reinforcement	Fix Supported	
9	Mullion 9FH	51mm x 127mm x 3mm	HS Mortar	HS Cable	Simply Supported	Two Wires located on the tension side
10	Mullion 10FH	51mm x 127mm x 3mm	HS Mortar	HS Cable	Fix Supported	Four Wires located, two on each side
11	Mullion 11FH	51mm x 152mm x 4.8mm	HS Mortar	HS Cable	Simply Supported	Two Wires located on the tension side
12	Mullion 12FH	51mm x 152mm x 4.8mm	HS Mortar	HS Cable	Fix Supported	Four Wires located, two on each side
13	Mullion 13FH	51mm x 127mm x 3mm	HS Mortar	HS Chain	Simply Supported	One Chain located on the tension side
14	Mullion 14FH	51mm x 152mm x 4.8mm	HS Mortar	HS Chain	Simply Supported	One Chain located on the tension side
15	Mullion 15FR	51mm x 127mm x 3mm	HS Mortar	CFRP	Simply Supported	CFRP-U-Shape
16	Mullion 16FR	51mm x 152mm x 4.8mm	HS Mortar	CFRP	Fix Supported	CFRP-U-Shape

3.2.1 Mullions without reinforcement

Six aluminum mullions were hardened by filling them either with ECC or HSM, without the use of additional reinforcement. Two of the specimens were filled with ECC and four of the specimens were filled with HSM. One of the mullions filled with ECC had 51mm x 127mm x 3mm dimensions (Mullion 1F) and the other had 51mm x 152mm x 4.8mm in dimensions (Mullion 3F). Both mullions had simple supports during testing. Table *3.2* provides the details of these mullions.

The remaining four specimens, filled with HSM, had two different mullion sizes and were tested in pairs. One mullion in each pair was tested with simple supports whereas the other mullion in the same pair was tested with fixed support conditions. Table 3.3 summarizes the details of these four mullions.

Each rectangular mullion was first closed from one end by means of a wooded plug, which was screwed to the aluminum to prevent the filler material from leaking out during casting. Figure 3.1 and Figure *3.2* show this process. The mullions were filled with either ECC or HSM. Each specimen was filled with three sequential batches. The mullions were tapped on the floor 10 times to ensure proper placement of the filler material as illustrated in Figure 3.3. Once ECC and HSM mixes were poured into designated mullions, the other ends were closed with other wooden pieces before the mullions were left for the curing of the filler materials.

3.2.2 Mullions strengthened with high-strength wires

One mullion of each size with HSM filler material was reinforced with two 6.0 mm diameter high-strength wires and placed on the tension side (protected side) during blast loading (Mullion 9FH and Mullion 11FH). These two mullions were tested with simple supports. Table 3.4 provides the details of these test specimens.

The remaining two specimens in this group also included one mullion of each size, filled with HSM (Mullions 10FH and 12FH). However, this time four 6.0 mm diameter steel wires were placed, two on each side (threat and protected sides). These mullions were tested with fixed supports and were expected to develop tension at mid-height on one side and tension on the other side near the supports. Table 3.5 provides the details of these mullions.

Table 3.2: Detailed specimens (Mullion1F and Mullion 3F)

Specimen Label	Cross-Section Measurement	Hardening	Cross-Section Measurement
Mullion 1F	51mm x 127mm x 3mm (2in x 5in x 1/8in)	Filled with ECC only (simply supported)	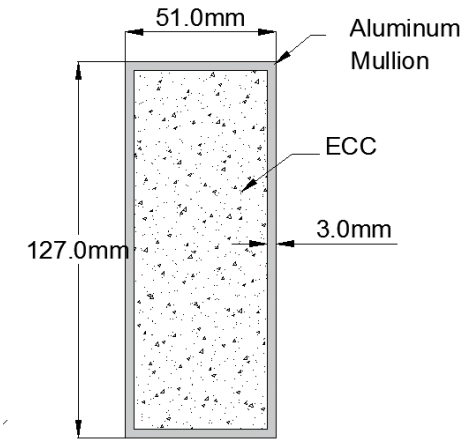
Mullion 3F	51mm x 152mm x 4.8mm (2in x 6in x 3/16in)	Filled with ECC only (simply supported)	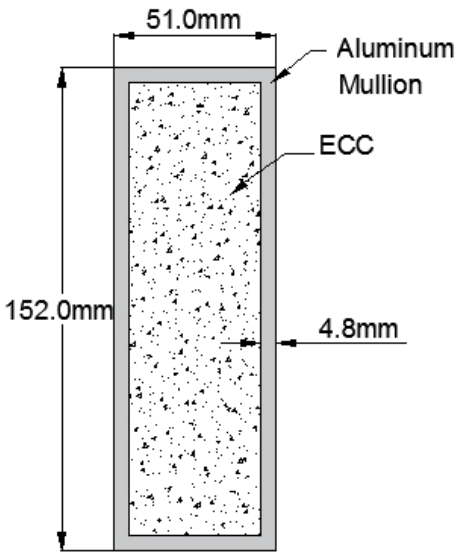

Table 3.3: Detailed specimens (Mullion5F, Mullion 6F, Mullion 7F and Mullion 8F)

Specimen Label	Cross-Section Measurement	Strengthening	Cross-Section Measurement
Mullion 5F and Mullion 6F	51mm x 127mm x 3mm (2in x 5in x 1/8in)	Filled with HSM only (simply and fix supported)	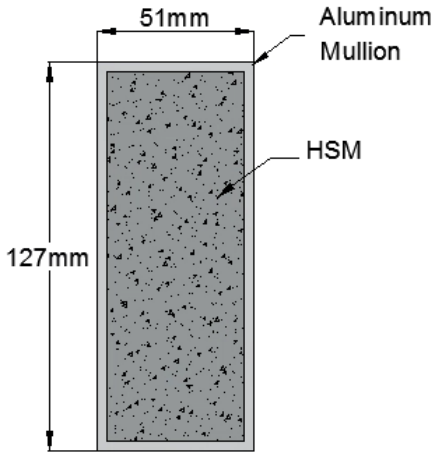
Mullion 7F and Mullion 8F	51mm x 152mm x 4.8mm (2in x 6in x 3/16in)	Filled with HSM only (simply and fix supported)	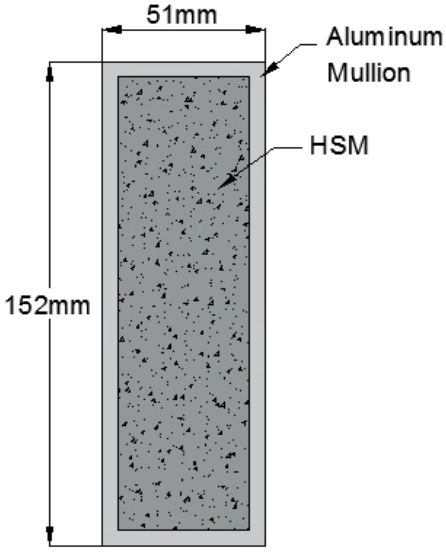

Table 3.4: Detailed specimens (Mullion 9FH and Mullion 11FH)

Specimen Label	Cross-Section Measurement	Strengthening	Cross-Section Measurement
Mullion 9FH	51mm x 127mm x 3mm (2in x 5in x 1/8in)	Filled with HSM and two wires strengthen the tension side (simply supported)	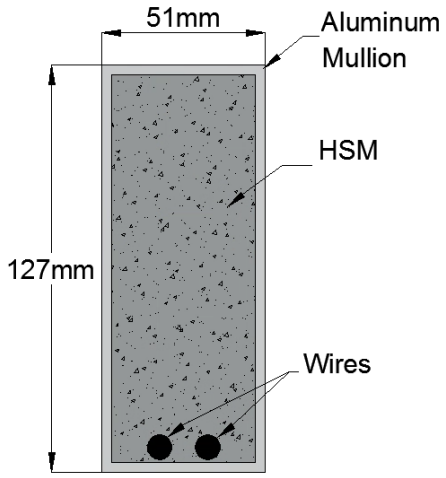
Mullion 11FH	51mm x 152mm x 4.8mm (2in x 6in x 3/16in)	Filled with HSM and two wires strengthen the tension side (simply supported)	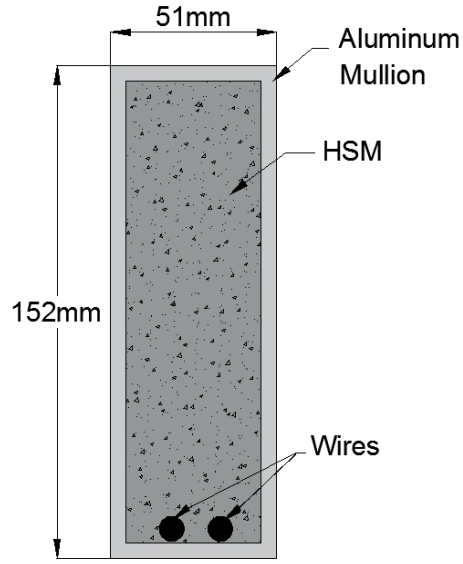

Table 3.5: Detailed specimens (Mullion 10FH and Mullion 12FH)

Specimen Label	Cross-Section Measurement	Strengthening	Cross-Section Measurement
Mullion 10FH	51mm x 127mm x 3mm (2in x 5in x 1/8in)	Filled with HSM and four wires strengthen the tension and compression side (fix supported)	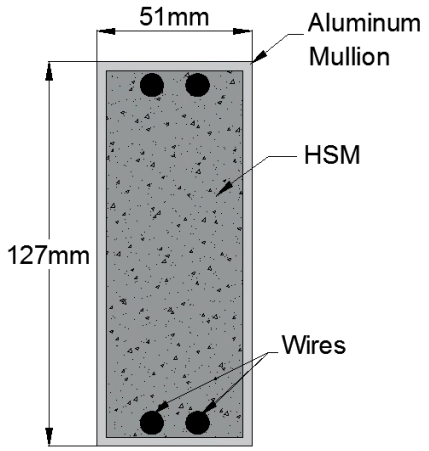
Mullion 12FH	51mm x 152mm x 4.8mm (2in x 6in x 3/16in)	Filled with HSM and four wires strengthen the tension and compression side (fix supported)	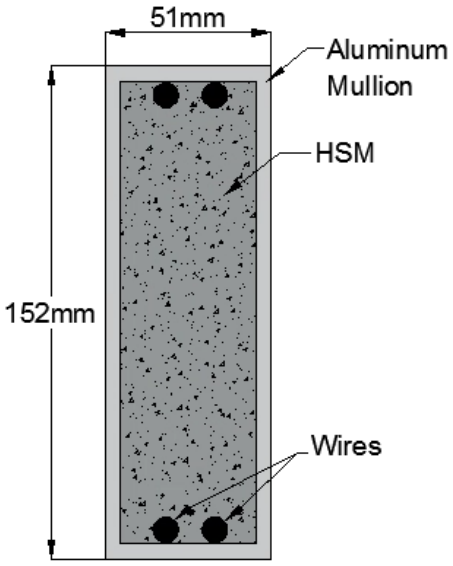

Specific techniques were used to insert and fix the high-strength wires in the mullions. Two holes were drilled through the wooden piece located at the bottom of Mullion 11FH. One wire was inserted through each hole and fixed with a 1/4-inch Zinc-Plated Wire Rope Clip as shown in Figure 3.4. The other ends of the wires were tightened by temporary thin steel wires to ensure the locations of the wires to be in the required tension zones before pouring the mix of HSM as illustrated in Figure 3.5. The top ends of the mullions were closed with another wooden piece and the specimen was left for curing for 28 days.

A different technique was used in Mullion 9FH to illustrate how this type of mullion strengthening can be implemented in practice for existing curtain wall mullions without access from the mullion end. Accordingly, one end of the mullion was first closed with a wooden block as was done in the previous cases. Two holes were then drilled on the tension side near the opposite end of the mullion 40 mm from the end. This is presented in Figure 3.6. Two high-strength wires were inserted and anchored with two 1/4-inch Zinc-Plated Wire Rope Clip. The other ends of the two wires were inserted through two other holes which were made at 70 mm from the far end of the mullion. The two ends of the specimen were closed with two pieces of wood before pouring the HSM mix. Another larger size hole of 15 mm diameter was opened at a distance of 50 mm from the top for filling the HSM mix. A funnel was used to pour the mix as illustrated in Figure 3.7 and left for 28 days for curing.

The steel placement techniques for Mullions 10FH and 12FH were similar to that for Mullion 11FH. Each specimen was closed with a thick wooden piece which was screwed properly to the mullion from one end to fill with the required cementitious material. Four holes were drilled through the wood. Four wires were inserted through these holes to extend two wires per side. All wires were anchored with four 1/4-inch Zinc-Plated Wire Rope Clip on the bottom side of the specimens as presented in Figure *3.8*. The other ends were tensioned and hooked temporarily to the mullion to keep them attached to both mullion webs during the pouring of HSM. The specimens were tapped on the ground during the filling process, more times than the specimens without reinforcement to ensure proper placement around the inserted reinforcement.

3.2.3 Mullions Strengthened with High-Strength Chains

Two specimens were constructed and strengthened with high-strength chains. This was done with a view that the placement of a chain as reinforcement, with its weight pulling it down, would be more convenient than inserting small diameter wires. The specimens were filled with HSM. The same two mullion sizes used were also used for reinforcement with chains, one in each size, labelled as Mullion 13FH and Mullion 14FH as shown in Table 3.6 and Figure 3.9. Both specimens were strengthened by placing the high-strength chain on the tension side of the aluminum mullions. The specimens were supported at the ends by simple supports. Therefore, no tension strengthening was needed on the opposite side near the supports. The same steps as those followed in placing steel cables were also used for providing the chains as reinforcement. This is illustrated in Figure 3.10. Furthermore, the chains were fixed properly on the tension side by using straps as illustrated in Figure 3.11.

Each specimen was filled with HSM. Three batches were required to completely fill each mullion. They were tapped on the ground to consolidate the mortar and ensure that all the voids inside were removed. Table 3.6 provides sections dimensions and properties for each specimen.

3.2.4 Mullions Retrofitted with CFRP

Four aluminum mullions were retrofitted with two layers of Carbon Fiber-Reinforced Polymer (CFRP) sheets, two filled with ECC and the other two with HSM. The retrofitting process was performed after the curing period of the filler material. Each layer of CFRP composite had a 0.9 mm thickness. The same two sizes of mullions used in the test program were used, one size for each pair of specimens, and labelled as Mullions 2FR and 4FR for ECC-filled specimens and Mullions 15FR and 16FR for HSM-filled specimens except mullion 15FR which is supported with simple supports. This is illustrated in Table 3.7 and Table 3.8. All the specimens in this category were tested using fixed supports. The CFRP was applied as U-shaped surface-bonded elements along the entire height, covering the tension side (the side subjected to tension in the mid-height region) and the sides of the web. The CFRP application in this way ensures an improved bond between the aluminum and the CFRP sheets.

Table 3.6: Detailed specimens (Mullion 13FH and Mullion 14FH)

Specimen Label	Cross-Section Measurement	Strengthening	Cross-Section Measurement
Mullion 13FH	51mm x 127mm x 3mm (2in x 5in x 1/8in)	Filled with HSM and **one** chain strengthen the tension side (simply supported)	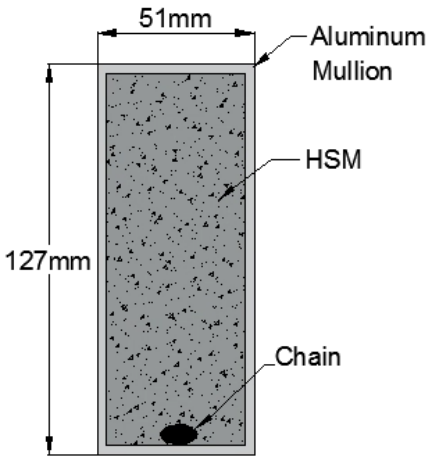
Mullion 14FH	51mm x 152mm x 4.8mm (2in x 6in x 3/16in)	Filled with HSM and **one** chain strengthen the tension side (simply supported)	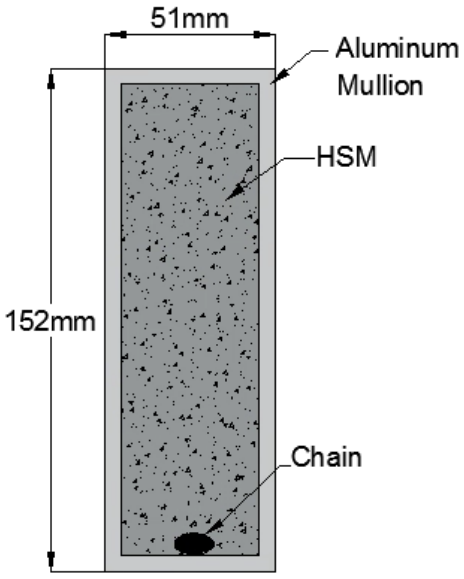

Table 3.7: Detailed specimens (Mullion 2FR and Mullion 4FR)

Specimen Label	Cross-Section Measurement	Strengthening	Cross-Section Measurement
Mullion 2FR	51mm x 127mm x 3mm (2in x 5in x 1/8in)	Filled with ECC and U-shape CFRP strengthen the tension side (fix supported)	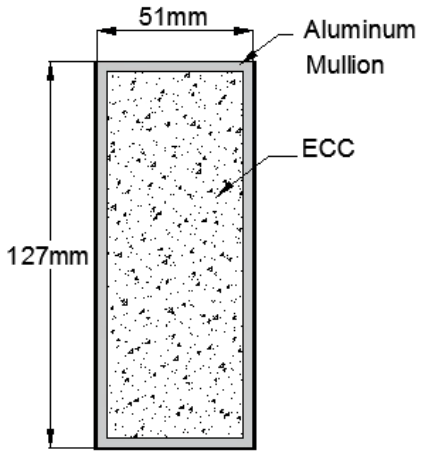
Mullion 4FR	51mm x 152mm x 4.8mm (2in x 6in x 3/16in)	Filled with ECC and U-shape CFRP strengthen the tension side (fix supported)	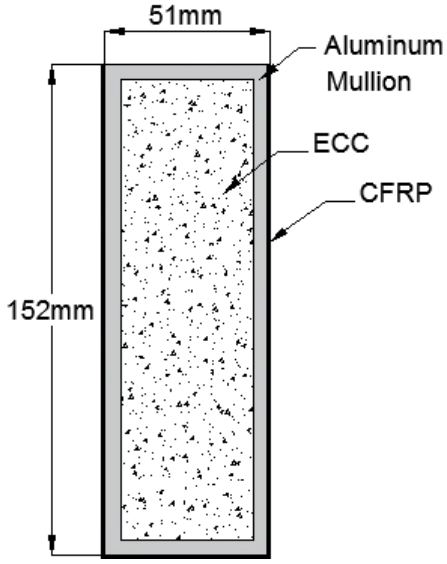

Table 3.8: Detailed specimens (Mullion 15FR and 16FR)

Specimen Label	Cross-Section Measurement	Strengthening	Cross-Section Measurement
Mullion 15FR	51mm x 127mm x 3mm (2in x 5in x 1/8in)	Filled with HSM and U-shape CFRP strengthen the tension side (simply supported)	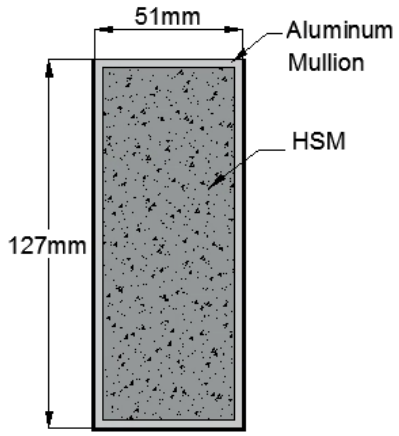
Mullion 16FR	51mm x 152mm x 4.8mm (2in x 6in x 3/16in)	Filled with HSM and U-shape CFRP strengthen the tension side (fix supported)	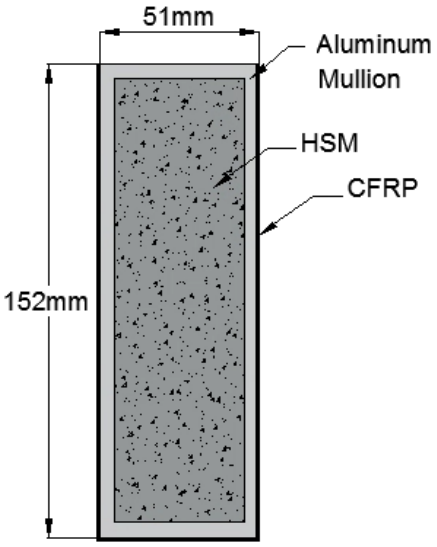

The following procedure was used in the preparation of CFRP-strengthened mullions:

1. The mullion surfaces were cleaned from any dust or materials accumulated on the surface during the ECC and HSM filling process, which could lead to debonding. This is shown in Figure 3.12.

2. The mullion surfaces were sanded using a grinder with a steel brush, specifically intended for aluminum use, as shown in Figure 3.13. After the sanding process, the aluminum surfaces were wiped with cloth and acetone as illustrated in Figure 3.14. The purpose of sanding was to produce a rough surface for improved bond.

3. A layer of epoxy was applied to the specimens using a paint roller as shown in Figure 3.15 to provide proper adhesion between the CFRP and the aluminum surface. Epoxy resin was mixed following the manufacturer instructions using the tools shown in Figure 3.16. Two-component epoxy, consisting of primer and saturant (A and B) was mixed as illustrated in Figure 3.17. The two components were mixed by using a hand mixer as illustrated in Figure 3.18

4. The first layer of CFRP was applied on the epoxy directly and saturated well with more epoxy. A ribbed steel roller was used to remove the air bubbles between the CFRP sheet and the aluminum surface as illustrated in Figure 3.19.

5. The second layer of CFRP was applied to the previous one after adding a layer of epoxy mix using the paint roller. The ribbed steel roller was used to remove any air bubbles between the two layers.

6. Specimens were cured for more than one week before shock-tube testing as shown in Figure *3.20*.

3.3 Material Properties

Material testing was conducted for each material to establish its mechanical properties. The following sections provide the details of material testing.

3.3.1 Aluminum Mullion

The main local supplier of the aluminum mullions in Ottawa is Loucon. The aluminum mullions were ordered from the supplier. The length of each mullion supplied was 2.5 meters for all sixteen mullions tested. Eight mullions had a cross-sectional size of 51 mm length by 127 mm width with a wall thickness of 3 mm. The remaining eight mullions had a size of 51mm length by 152 mm width with a wall thickness of 4.8 mm. The type of aluminum used for the mullions was of 6061-T6, with the mechanical properties shown in Table 3.9 as obtained from the manufacture. Figure 3.21 illustrates a typical stress-strain relationship for the Aluminum used.

Table 3.9: Aluminum properties

Material	Aluminum
Yield Stress (MPa)	270
Density of Material (kg/m^3)	2700
Modulus of Elasticity (N/mm^2)	70000
Shear Modulus (N/mm^2)	25800
Poisson's ratio	0.33

3.3.2 Materials Used to Strengthen Aluminum Mullions

3.3.2.1 ECC (Engineering Cementitious Composites)

3.3.2.1.1 Mix Design

Different mix designs are available for different applications of ECC depending on the required flowability and ductility. The ECC blend and fibers were purchased from the producers (Boddy Rhods) located in Toronto. The ECC mix includes the ECC blend, fibers, water, and superplasticizer. The ECC blend obtained was an improved product for use in earthquake-prone areas for higher ductility. The ECC mix had the required particle gradation for a specific amount of fiber. The workability of ECC was provided by the dry polymer included in the mix, which resulted in ideal physical properties. The material was strong, durable, and naturally cured. High-performance ingredients were included to help cure the ECC mix. The required reinforcement can be added to obtain higher capacity.

Various fiber lengths were considered for adding to the mix. PVA fibers (Polyvinyl Alcohol) are known to provide high performance in concrete and mortar. It resists cracks 300% greater than other fibers, provides a high modulus of elasticity, and generates high tensile strength and molecular bond strength. Furthermore, the ECC selected can fight chemicals, including alkali, while providing fatigue resistance. Table 3.10 shows different lengths and diameters of PVA fibers available.

Table 3.10: Properties of PVA fibers (Polyvinyl Alcohol)

Length	Fiber	Filament Diameter
PVA RECS 7	0.25 in (6 mm)	5 Denier (24 Microns)
PVA RECS 15	0.375 in (8mm)	8 Denier (38 Microns)
PVA RECS 100	0.5 in (13 mm)	20 Denier (100 Microns)

The fibers included in the ECC mix are very small in size, with 100 microns being the most visible. Although the PVA 100 fibers are preferred to get flowable and workable mixes, PVA 15

fibers were used in this research as they provide higher strain hardening and ductility than the other types of fibers. Table 3.11 shows the mix design used in current research.

Table 3.11: ECC mix design

Material	Amount (Kg)
ECC blend	136.2
PVA RECS 15	2.16
Water	24
Superplasticizer	5

3.3.2.1.2 Mixing Process and Curing

Mixing of ECC was performed in the Structures Laboratory of the University of Ottawa. The big mixer, which is a 420-volt multi-flow pan mixer with three stationary paddle blades attached to the cover of the mixer, was used for this purpose. This is shown in Figure 3.22. The pan of the mixer allows high-velocity rotation to provide the required mixing force. The mixer consists of additional two paddles that help scrape the inner sides of the mixer during mixing. The mixer allows 0.108 m^3 of mixture at once. Therefore, the mix of ECC for the four specimens was done at once as one batch.

All the ingredients were prepared and weighed before mixing. The fibers were bundled; therefore, they were placed in a clean bucket with a lid that had a small hole, and an air blow gun was applied to the hole to apply pressured air into the bucket and disperse the fiber bundles into a separate single fiber throughout the mix. This also created a multi-direction fiber network as illustrated in Figure 3.23 and Figure 3.24. Clean potable water was first added into the mixer, followed by the superplasticizer for first mixing. Gradually, the dry ingredients were added while the mixer was in operation as illustrated in Figure 3.25. PVA RECS 15 fibers were added slowly until a homogeneous mix was attained. This is depicted in Figure 3.26. The duration of mixing was approximately 10-15 minutes. As soon as the mixture was blended properly, the filling operation of the specimens started. A large size funnel was used and placed on the open end of

the aluminum mullion to facilitate the filling process. Figure 3.27 shows the pouring process through the funnel. The mullions were filled to 1/3 of the entire volume at a time in each stage the specimen was shaken and taped to consolidate the mix. The specimen end was then closed by a wood plug and left for 28 days for curing in a vertical position.

3.3.2.1.3 Compressive Strength

The compressive strength of ECC was established mainly by testing cube and cylinder specimens similar to normal concrete and fiber-reinforced concrete (FRC). The procedures followed for materials testing conformed to the ASTM C39 and C109 standards (C39/C39M – 21), (C109/C109M-23). The results provided the compressive strength, as well as the stress-strain relationships. A series of ECC cylinders and cubes were cast during filling the full-scale aluminum mullions as illustrated in Figure 3.28. Three cylinders with standard sizes of 100 mm diameter and 200 mm height and six cubes with a standard size of 50 mm side length were tested from each batch. All the samples were vibrated on the shaking table and left to cure for 24 hours. The samples were then de-molded and soaked in a big bucket to cure for 28 days. Figure 3.29 shows the preparation of cylinders, including the grinding process before testing.

A compression testing machine was used to test the cylinders and cubes as presented in Figure 3.30 and stress-strain relationship in compression was obtained as illustrated in Figure 3.31. Table 3.12 includes average compressive strength for both cylinders and cubes.

Table 3.12: ECC average compressive strength

Mullion	Filling Type	Cylinder	Compressive Strength (MPa)	Average Compressive Strength (MPa)	Cube	Compressive Strength (MPa)	Average Compressive Strength (MPa)
1F 2FR 3F 4FR	ECC	1	56.55	60.95	1	70.72	63.56
					2	63.56	
		2	62.45		3	45.8	
					4	68.24	
		3	60.87		5	66.16	
					6	66.88	

3.3.2.1.4 Modulus of Elasticity

The modulus of elasticity of ECC was calculated from compression tests. Four coupons were cast from the same batch used to fill the full-scale aluminum mullions, as shown in Figure 3.32. The samples were cured for 24 days. A universal testing machine was used to perform the tests following the procedure outlined in the ASTM Standards. Figure 3.33 illustrates a typical tensile strength test using a coupon specimen with specific dimensions. Figure 3.34 presents the tensile stress-strain relationship. The modulus of elasticity of ECC was calculated to be approximately 23,000 MPa.

3.3.2.2 HSM (High Strength Mortar)

3.3.2.2.1 Mix Design

Various mix designs were examined for HSM to select the highest strength for use in blast-resistant aluminum mullions. Four main stages were performed for this selection process. In each stage, more than one batch was cast using different amounts of superplasticizer to reach the highest strength. Table 3.13 provides the stages followed and the mix designs used to evaluate the strength gain. The label C in this Table refers to high-strength cement with 8% silica fume, purchased from the Lafarge supplier, while S refers to sand which was available in the Laboratory.

The final selection of the mix design was 50%C + 50%S with 3.33% superplasticizer, which provided the highest strength value of 72 MPa. This mix was the most economical in terms of cement consumption. The final mix design that was used to fill the full-scale mullions as presented in Table 3.14.

3.3.2.2.2 Mixing Process and Curing

The constituent materials were prepared and weighed before mixing. Each mix was sufficient to fill four full-scale aluminum mullions. Therefore, three batches were used to fill twelve mullions with HSM. The mixing process started by pouring dry ingredients into the mixer. The SF cement and the sand were mixed properly for 15 minutes. The superplasticizer was added to the water and mixed before adding it to the mixture of the dry ingredients. The mixer was operated for 15-20 minutes until a homogeneous mix with proper consistency was obtained. The rest of the batch was used to fill the cylinders and the cube molds, which were placed using the vibrator available in the Laboratory. All the small and full-scale specimens were left to harden for 24 hours, and the small specimens were soaked in big buckets for curing for 28 days before testing.

Table 3.13: HSM mix designs trials

Stage I	**Stress (MPa)**	**Super plasticizer%**
50%C+50%S	39	1.5%
60%C+40%S	36.34	1.7%
70%C+30%S	25.8	1.9%
Stage II	**Stress (MPa)**	**Super plasticizer%**
50%C+50%S	33.7	1.2%
40%C+60%S	26.5	2%
60%C+40%S	32.8	1.5%
Stage III	**Stress (MPa)**	**Super plasticizer%**
50%C+50%S	47	2.2%
50%C+50%S	72	3.33%
Stage IIII	**Stress (MPa)**	**Super plasticizer%**
60%C+40%S	75	2.6%
60%C+40%S Normal Cement	41	3.9%

Table 3.14: Final mix design of HSM

Material	Amount (Kg)
SF cement	60
Sand	60
Water	15
Superplasticizer	4

3.3.2.2.3 Compressive Strength

The compressive strength obtained from cylinders and cubes is tabulated in Table *3.15* through Table 3.17 for the three batches mixed.

Table 3.15: HSM average compressive strength - batch 1

Mullion	Filling Type	Number of Mixes	Cube Label	Compressive Strength (MPa)	Average Compressive Strength (MPa)
5F 6F	HSM	Mix 1	1	62	66
			2	60	
7F 8F			3	73	
			4	67	

Table 3.16: HSM average compressive strength - batch 2

Mullion	Filling Type	Number of Mixes	Cylinder Label	Compressive Strength (MPa)	Average Compressive Strength (MPa)
9FH 10FH	HSM	Mix 1	1	72	73
			2	75	
			3	72	
11FH 12FH		Mix 2	1	83	75
			2	73	
			3	70	

Table 3.17: HSM average compressive strength - batch 3

Mullion	Filling Type	Number of Mixes	Cylinder Label	Compressive Strength (MPa)	Average Compressive Strength (MPa)
13FH 14FH	HSM	Mix 1	1	52	63
			2	76	
			3	61	
15FR 16FR		Mix 2	1	96	84
			2	91	
			3	63	

3.3.2.2.4 Modulus of Elasticity

The modulus of elasticity of HSM was calculated during some of the compressive strength tests. Some of the cylinders were equipped with two LVDTs positioned vertically to obtain a full stress-strain relationship as illustrated in Figure *3.35*. The cylinders were selected from different batches used to fill the full-scale aluminum mullions. The cylinders were tested after curing for 28 days. Figure *3.36* shows the stress-strain relationship. The modulus of elasticity was established to be approximately 27,000 MPa.

3.3.2.3 High Strength Wires

The high-strength wires used to strengthen the mullions were selected among different types of wires available in the market. This was done by preparing and testing prisms reinforced by wires under a three-point load as shown in Figure *3.37*. The wire-reinforced specimens showed the required improvement when compared with a companion control specimen. This is shown in Figure *3.38*. The maximum stress in the extreme tension fibre of the control specimen resulted in 3.08 MPa while the wire-strengthened specimen showed 10.84 MPa. The wire used was galvanized and had a 6 mm diameter wire (Area 28.26 mm^2), capable of resisting an average tensile force of 6,300 N.

3.3.2.3.1 Mechanical Properties

The stress-strain curve for high-strength wire used is illustrated in Figure *3.39*. The results were obtained by testing several wire coupons using a universal testing machine. This is shown in

Figure 3.40. Each coupon was 730 mm long. The test was applied following the ASTM specification A931 – 18. The modulus of elasticity was obtained to be 60,000 MPa.

3.3.2.4 High Strength Chain

The high-strength chain used in the mullions was selected among different types available in the market. The high-strength chain selected was a Grade 70 (Chorate Gold) chain with a steel diameter of 6.4 mm per side, with a maximum tensile strength of 13,975 N.

3.3.2.4.1 Mechanical Properties

Tension tests were performed on chains using a 730 mm chain length. The samples were tested using a universal testing machine, as shown in Figure 3.41 The stress-strain relationship recorded is presented in Figure 3.42. The modulus of elasticity was considered to be 55,000 MPa.

3.3.2.5 CFRP

Carbon fiber reinforced polymer (CFRP) composite material was selected to strengthen aluminum mullions externally. The thickness of each layer of the fabric was 0.8 mm, which resulted in a thickness of 0.9 mm after it was embedded in epoxy to form a composite material. The CFRP composite layers were applied longitudinally on the mullions to develop tension resistance.

3.3.2.6 Mechanical Properties

The properties of CFRP were established through coupon tests following the procedure outlined in the ASTM D3039-76 standard. The tests provided tensile strength and the modulus of elasticity. The stress-strain relationship showed linear elastic behavior until failure in tension as shown in Figure 3.43. The graph shows that the coupon failed at a tensile strain of 1.2% and the corresponding tensile strength of 780 MPa (Elnabelsya, 2013) .

3.4 Shock Tube Testing Facility

3.4.1 General

The blast tests were conducted in the Blast Research Facility of the University of Ottawa which is equipped with a blast simulator in the form of a Shock Tube. This equipment simulates the effects of blast loading without detonating explosives and hence provides a convenient and safe testing environment. It was used in the past to test large-scale specimens, such as columns, beams, joists, walls, slabs, windows, and curtain wall components. It can simulate the effects of far-range explosions. The created shock waves simulate blast load waves which are generated by hemispherical free-air surface bursts (Lloyed et al., 2010). The shock tube, illustrated in Figure *3.44* was designed by Baker Engineering and Risk Consultants.

The shock-tube is mainly divided into four components as presented below:

i. *Variable Length Driver*

The driver section comprises six parts of steel pipe. The sections can be connected with twelve 32.7 mm bolts. The driver length varies and consists of different length segments (305 mm, 610 mm, 915 mm, and 1525 mm). Each segment has a thickness of 6.35 mm. The inner diameter is 597 mm. These parts can be adjusted depending on the required applied pressure and impulse. These segments are sealed during the operation by gaskets. Figure *3.45* illustrates the connected driver segments which is located on an inverted curved base. A 38 mm thick steel plate closes the far end of the driver section while the other end is connected to the spool section.

ii. *Spool Section*

The driver and expansion sections are connected together with a spool section in between. The spool section is measured to be 90 mm and it holds a combination of disk holders (Lloyed, 2015). Mainly, the connections between the spool section with the driver and the spool section with the expansion chamber include aluminum diaphragms (Grade 1100) with appropriate capacity. The aluminum diaphragms (foils) are replaced every time the shock tube is used depending on the required applied

pressure. Figure *3.46* shows an aluminum foil after use. Figure *3.47* shows the spool section clamped with the required foils in place.

iii. *Expansion Chamber*

The expansion section comprises two openings, a circle opening with a diameter measurement of 597 mm at one end, which is clamped to the spool section, and a square opening at the other end where the test set-up and the specimen are located. This opening is square and has the dimensions of 2023 mm x 2023 mm. The total length of the expansion chamber is 6096 mm as illustrated in Figure *3.48* This section is responsible for delivering the blast shock wave generated in the spool section, which is applied to the test specimen attached to the shock-tube opening. Twelve pressure relief vents are placed at the end of the expansion section near the test frame. The vents, shown in Figure *3.49*, serve two purposes: to decrease the number of peaks caused by the shock wave reflection passing through the shock-tube, and to improve the negative pressure. As a result, the pressure generated in the driver section ruptures both diaphragms, rushing towards the test specimen at supersonic velocities impacting the test specimen clamped to the frame of the shock-tube.

iv. *Rigid End Frame*

A rigid steel frame is attached to the end of the expansion section where the test specimens are attached for testing. The frame elements are 203 mm wide and 12.5 mm thick. Twenty holes of 19 mm diameter are drilled on the frame to facilitate the attachment of test specimens.

3.4.2 Shock-tube Mechanism

During the detonation of an explosive charge, the chemical reaction that takes place results in hot gases, which causes a pressure differential with the surrounding air. This difference in pressure creates a shock front that moves toward the target object at supersonic velocities. The interaction of the shock wave with the object and the secondary dynamic wind pressure that follows result in blast loads. The same mechanism happens in a shock-tube. The driver section is charged with high air pressure through a compressor, controlled remotely. The spool section is also charged with the required level of air pressure to balance the pressure in the driver section

until the spool pressure is released to create the shock front. This is done by the control station of the shock-tube placed on the main floor of the University of Ottawa Structures Laboratory. The pressure through the driver and spool sections is measured and controlled by pressure gauges. The differential pressure across both components, i.e., the driver and the spool sections are monitored and increased gradually to ensure that the pressure differential in both sections is continuously less than the diaphragm rupturing capacity until the required pressure is attained. At this point, the firing of the shock-tube is triggered. The firing is initiated when the pressure is vented through the spool section towards the expansion section and the pressure in the driver section exceeds the capacity of the diaphragm.

The reflected pressure and impulse are functions of the combined driver length and driver pressure as shown in Figure *3.50*. There is a unique relation between the driver pressure, reflected pressure, and different driver lengths as illustrated in Table *3.18*. The relationships for different combinations are explained by Lloyd (2010) and Lloyd et al. (2010).

The period of the first positive phase represents the time of the initial rise in the impulse-time history graph. The shock-tube is not equipped to verify the negative pressure phase resulting from intensive explosions. Secondary peaks are observed after testing because of variable venting that occurs through the vents, driver length, and the initial driver pressure. These peaks are generated once the shock front moves back and forth inside the shock tube.

Lloyd et al. (2010) provides general information about the shock-tube mechanism. Accordingly, there is an 8% deviation in the shock front arrival time. Moreover, the shock-tube was designed to sustain a maximum value of 100 KPa with sufficient safety margin. The positive phase duration becomes longer as the driver length is increased.

Table 3.18: The relationship between driver length, reflected pressure and reflected impulse.

				Approximate Equivalent TNT (Hemispherical - Reflected)	
Driver Length (mm)	Reflected Pressure (kPa)	Reflected Impulse (kPa-ms)	Mass (Kg)	Standoff (m)	Scaled Distance (m/$Kg^{1/3}$)
305	78	217	8	12	6.0
915	92	410	42	18	5.2
1830	100	840	290	33	5.0
3355	103	1760	2500	67	4.9
4880	104	2690	10000	106	4.9

3.5 Instrumentation

The instrumentation setup is important as it generates the entire data obtained from the experiments. Instrumentation used in a typical shock tube test consists of a data acquisition system (DAS), linear variable displacement transducers (LVDTs), pressure sensors, high-speed cameras, and camera tracking software. The activation sequence of these instruments is such that the shock wave is generated first, which activates the pressure sensors located on the expansion chamber sides. This wave triggers the DAS. DAS sends a signal to the camera which starts capturing video recordings, which is then saved in the dedicated laptop. DAS receives data from the LVDTs and pressure sensors. These data are saved to generate pressure and displacement time histories. Further details of the instrumentation are given below in respective sub-sections.

3.5.1 Data Acquisition System

The required data is obtained by using the Yokogawa SL1000 High-Speed Data Acquisition Unit with the ability to record about 100 samples per second, leading to a record of each sample every 10 μs. Samples comprise of strains, displacements, and pressure values. Triggering is mainly a process of starting a unit loop towards recording the data until the blast load is applied and the pressure sensors are activated. The data is recorded with a period of 3 seconds. Finally, the data

is transferred to a specific format (csv) through XViewer. Figure *3.51* shows the Data Acquisition System which is located on the main floor of the laboratory.

3.5.2 High Speed Camera

Once the blast load is applied to a specific specimen, the behavior is recorded by a high-speed camera. The camera brand is AOS Technology X-PRI, and it is shown in Figure *3.52*. This type of camera is very accurate and can record images in full color and 800 x 600 pixels with 1000 frames per second. During the test, usually, two cameras are placed in different positions. One is located in front of the specimen while the other one is placed in a specific distance on the side of the shock-tube to record the deflected shape. Once the pressure sensors are triggered, the video starts recording with a 10% pre-trigger stage. Two 1000W lights are located with each camera to obtain clear video recording. The cameras are monitored by a laptop that uses MS Windows operation system.

3.5.3 Pressure Gauges

Two pressure sensors are placed, one on the side and the other at the bottom of the shock-tube opening, near the test specimen to capture reflected pressure. The sensors are of PCB Piezotronics Model #112A22 brand. The sensors trigger a signal to record the data. Furthermore, pressure-time histories can be obtained.

3.5.4 Strain Measurements

During the current experimental research, six strain gages were placed on each specimen in the same locations as shown in Figure 3.53. The strain gages have a length of 10 mm with 350 ± 1.0 ohms resistance. The readings of the strain gages are recorded in the DAS. The strain gauge readings are plotted in Appendix A. Six strain gages were applied on each specimen and labelled as follows: M-T and M-C denote strain gauges positioned at the mid-span of the specimen on the tension and compression sides, respectively. Similarly, T-T and T-C refer to strain gauges installed on the top surface of the specimen, also on the tension and compression sides, but located half a meter away from the mid-span. Likewise, B-T and B-C represent strain gauges placed on the

bottom surface of the specimen on the tension and compression sides, also positioned half a meter from the mid-span.

3.5.5 Linear Variable Displacement Transducers (LVDT)

In this research, one Celesco CLWG-300 linear variable displacement transducer was used and connected to the mid-span of the specimen to record the maximum displacement for each sample. A nut-bolt assembly was used to secure the connection between the LVDT and the specimen. The lateral displacements of specimens were recorded through DAS. The LVDT range for the stoke was 300 mm as illustrated in Figure *3.54*.

3.5.6 Test Setup

The test setup used during testing is illustrated in Figure *3.55*. Each aluminum mullion with or without a strengthening technique, was tested using a “load transfer device’” which collected the pressure acting on the 2.0 m by 2.0 m test area and transferred it to the test mullion as uniformly distributed load. The load transfer device (LTD) was observed to move together with the test specimens until they reached maximum deflection, beyond which the LTD was separated from the mullions as the mullions vibrated in free-vibration mode.

3.5.6.1 Load Transfer Device (LTD)

The LTD is needed to transfer the shockwave pressure to the specimen as a uniformly distributed blast load. The LTD was designed such that it would not provide resistance to applied load, while transferring the load. It consists of a very flexible steel sheet that would not provide any appreciable resistance to the applied load and a set of horizontal HSS beams that facilitate the application of the load on the test specimen. The flexible portion was made of 0.67 mm 22 Gauge steel sheets covering the entire shock-tube opening with dimensions of 2m by 2m. Eight HSS with a 76 mm square section with steel side walls of 4.8 mm thickness are secured on the steel sheets. They are attached horizontally to the steel sheet with four screws. The LTD was secured at the top of the shock-tube, hanging down, allowing free movement as illustrated in Figure *3.56*. It was free from both sides to simulate and apply the distributed load on each

specimen without providing any resistance. The total mass of the LTD was 107 kg which was equivalent to a double-glazed IGU unit mass and a curtain wall assembly.

3.5.6.2 Supports

Two different supports were used during the experiments. Simple support was used for nine specimens, and fixed support was used for seven specimens. The simple support allowed the specimen to rotate at the ends. This type of support simulates the curtain wall assembly connected to slabs in the actual prototype building. Figure *3.57* shows the simple support condition. For fixed supports, both ends of the aluminum mullion were restrained laterally in an effort to avoid rotations at the ends as shown in Figure *3.58*. Based on previous studies conducted by Jacques et al. (2012) at the University of Ottawa, the fixed support generated by clamping the ends created partial fixity with a rotational stiffness of approximately 903000 N*m/rad. Therefore, in assessing the effects of support fixity, especially when compared with analytical results that were based on fully fixed condition, this factor was considered. The supports were built by a welded steel plate on a 6-in hollow steel section. Rods with a diameter of 6 mm were used to fix the HSS to the end frame of the shock tube. The clear span of the mullion between the supports was measured to be 2200 mm for simple supports and 2100 mm for fixed supports.

3.6 Testing and Test Procedure

Each specimen was tested under incrementally increasing pressure up to failure. The failure was represented by tension or compression failure in flexure. Internal wire rupture was only observed at mid-span and steel rupture near the supports was rarely observed. The number of shots needed to reach to failure point was 2 to 3 shots for each sample. The driver pressures applied corresponded to 30 psi (207 KPa), 40 psi (276 KPa), and 60 psi (414 KPa). The required driver length selected for this pressure range was 9ft (2743 mm). The foil sheet thickness varied for each shot. Two foils with a thickness of 0.006 mm and 0.01 mm were placed on the expansion side and the driver side of the spool, respectively to achieve 30 psi (207 KPa) driver pressure. The foil thickness was increased to (0.006+0.01) mm and (0.01+0.01) mm on the expansion and the driver sides, respectively for 40 psi (276 KPa) pressure, and two foils with a thickness of

(0.01+0.01) mm and three foils with a thickness of (0.01+0.01+0.01) mm for 60 psi (414 KPa) pressure. All the specimens were examined under each intensity of blast load to assess behavior until failure. The residual displacements were also recorded. The instrumentation explained previously recorded all mid-span deflections and reflected pressures.

Table 3.19: Summary of recorded test data

Specimen Label	Applied Blast Load Psi/ (Kpa)	Reflected Pressure (kPa)	Reflected Impulse (kPa-msec)	Duration (msec)	Mid-height Displacement (Incremental) (mm)	Residual Displacement (Incremental) (mm)	δ_{max} (Total) (mm)	δ_{res} (Total) (mm)	θ_{max} (^{0})	θ_{res} (^{0})	Response Limit
M – 1F	30 (207)	27.5	269.3	19.5	89.5	82.4	89.5	82.4	4.7	4.3	Heavy damage
	40 (276)	42.0	414.9	19.8	184	184	266.4	266.4	13.6	13.6	Blowout
	60 (414)	---	---	---	---	---	---	---	---	---	---
M – 2FR	30 (207)	34.4	330.2	19.6	60	38	60	38	3.3	2.1	Moderate damage
	40 (276)	43.6	413.2	18.0	85	60	123	98	6.7	5.3	Heavy damage
	60 (414)	54.1	561.3	21	120	Failed	180	NA	9.7	NA	Blowout
M – 3F	30 (207)	35.3	359.5	20.0	59.6	15.8	59.6	15.8	3.1	0.8	Superficial damage
	40 (276)	46.6	478.7	19.8	93.8	34.6	109.6	50.4	5.7	2.6	Moderate damage
	60 (414)	65.1	542.7	18.4	115.4	28.6	150	63.2	7.8	3.3	Heavy damage
M – 4FR	30 (207)	28.6	343.0	20.0	36.9	32	36.9	32	1.9	1.7	Moderate damage
	40 (276)	39.1	417.4	18.0	26	12	58	44	3.2	2.4	Moderate damage
	60 (414)	52.6	549.0	20.0	81.6	27.6	93.6	39.6	5.1	2.2	Moderate damage
M – 5F	30 (207)	46.0	331.9	17.6	183	140	183	140	9.4	7.3	Hazardous failure
	40 (276)	39.3	396.3	19.8	168	129	308	269	16	13.7	Blowout
	60 (414)	---	---	---	---	---	---	---	---	---	
M – 6F	30 (207)	32.9	330.5	17.6	93.5	65.7	93.5	65.7	5.1	3.6	Heavy damage
	40 (276)	45.1	449.3	18.0	92.3	82.7	158	148.4	8.6	8	Hazardous failure
	60 (414)	---	---	---	---	---	---	---	---	---	---

Specimen Label	Applied Blast Load Psi/ (Kpa)	Reflected Pressure (kPa)	Reflected Impulse (kPa-msec)	Duration (msec)	Mid-height Displacement (Incremental) (mm)	Residual Displacement (Incremental) (mm)	δ_{max} (Total) (mm)	δ_{res} (Total) (mm)	θ_{max} (^{0})	θ_{res} (^{0})	Response Limit
M – 7F	30 (207)	33.7	340.0	18.0	59	17.5	59	17.5	3.1	0.9	Superficial damage
	40 (276)	46.0	493.0	20.8	202	86	219.5	103.5	11.3	5.4	Heavy damage
	60 (414)	---	---	---	---	---	---	---	---	---	---
M –8F	30 (207)	37.5	341.0	18.4	46.4	13	46.4	13	2.5	0.7	Superficial damage
	40 (276)	42.8	438.5	20.6	47.4	7	60.4	20	3.3	1.1	Moderate damage
	60 (414)	55.5	579.7	19.2	121.5	37	128.5	44	7	2.4	Moderate damage
M – 9FH	30 (207)	37.2	347.7	18.6	126.3	77	126.3	77	6.5	4	Heavy damage
	40 (276)	40.1	416.0	19.2	160(Failed)	Failed	237	NA	12.2	NA	Blowout
	60 (414)	---	---	---	---	---	---	---	---	---	---
M – 10FH	30 (207)	37.4	347.7	20.8	65.4	22	65.4	22	3.6	1.2	Moderate damage
	40 (276)	41.5	452.0	20.2	65	30.9	87	52.9	4.7	2.9	Moderate damage
	60 (414)	62.8	621.3	19.8	223	Failed	253	NA	13.6	NA	Blowout
M – 11FH	30 (207)	34.8	334.0	18.0	61	17	61	17	3.2	0.9	Superficial damage
	40 (276)	52.9	516.0	19.7	147	138	164	155	8.5	8	Hazardous failure
M – 12FH	30 (207)	38.3	352.9	21.0	35	3	35	3	1.9	0.2	Superficial damage
	40 (276)	41.9	447.2	19.8	54	10	57	13	3.1	0.7	Superficial damage
	60 (414)	56.5	616.4	21.4	68	17	78	27	4.2	1.5	Moderate damage

Specimen Label	Applied Blast Load (Psi/ (Kpa)	Reflected Pressure (kPa)	Reflected Impulse (kPa-msec)	Duration (msec)	Mid-height Displacement (Incremental) (mm)	Residual Displacement (Incremental) (mm)	δ_{max} (Total) (mm)	δ_{res} (Total) (mm)	θ_{max} (^{0})	θ_{res} (^{0})	Response Limit
M – 13FH	30 (207)	28.7	307.4	16.4	122	67	122	67	6.3	3.5	Heavy damage
	40 (276)	40.2	417.4	19	111	16	178	83	9.2	4.3	Heavy damage
	60 (414)	---	---	---	---	---	---	---	---	---	---
M – 14FH	30 (207)	34.6	345.3	17.6	56.9	12.6	56.9	12.6	3	0.7	Superficial damage
	40 (276)	41.2	453.0	16.8	69.8	15	82.4	27.6	4.3	1.4	Moderate damage
	60 (414)	55.0	575.0	17.8	129	73	144	88	7.5	4.6	Heavy damage
M – 15FR	30 (207)	30.4	312.8	17.6	116	32	116	32	6	1.7	Moderate damage
	40 (276)	33.2	310.8	18.2	125	103	157	135	8.1	7	Hazardous failure
	60 (414)	---	---	---	---	---	---	---	---	---	---
M – 16FR	30 (207)	34.2	367.6	20.2	35.7	4	35.7	4	1.9	0.2	Superficial damage
	40 (276)	40.7	450.9	24.4	45	2	49	6	2.7	0.3	Superficial damage
	60 (414)	57.0	606.0	21.0	74	13	76	15	4	0.8	Superficial damage
	80 (551)	78.7	683.0	19.6	81.6	Fail	94.6	NA	5.1	NA	Blowout

*Total displacement: the displacement from the location of the undeformed specimen to the maximum point.

**Incremental displacement: the displacement from the previous residual point to the maximum point.

3.7 Description of Experimental Results and Failure Modes

Sixteen aluminum mullions were subjected to shockwave loading with each mullion filled with ECC or HSM. Many mullions were also reinforced using various techniques, including internally placed high-strength wires or chains; or externally placed CFRP sheets. The experimental results were analyzed in terms of the characteristics of shockwaves, such as reflected pressure, impulse, and positive wave duration, as well as maximum and residual displacements. The driver length used was 2743 mm. Two to three shots were applied to reach the point of failure. The shots were taken at different driver pressures; specifically, 30 psi (207 KPa), 40 psi (276 KPa) and 60 psi (414 KPa). This section presents the test results in terms of pressure-time, impulse-time, and displacement-time histories.

3.7.1 M-1F

M-1F had a specimen size of 51 mm x 127 mm x 3 mm and it was filled with ECC only, without any reinforcement. It was subjected to two shots. The first shot was performed by applying a driver pressure of 30 psi (207 KPa) with a resulting reflected pressure-impulse combination of 27.5 kPa – 269.3 kPa-ms. The positive phase duration was 19.5 ms, as shown in Figure 3.59.

The mid-span deflection was recorded by an LVDT. During the test, the LVDT moved and provided an inaccurate reading. Therefore, the deflection readings were measured accurately from the video camera recordings. The specimen experienced a maximum deflection of 89.5 mm which occurred at 28 ms. The residual displacement was measured as 82.4 mm. No damage was observed on the specimen, and it remained elastic during this first shot.

The second shot was applied with an increased driver pressure of 40 psi (276 KPa). The reflected pressure was recorded as 42 kPa with an impulse of 415.9 kPa-ms and a positive duration of 19.8 ms, which resulted in a maximum deflection of 184 mm. The residual displacement was 184 mm. The recorded data is shown in Figure 3.60. The performance of specimen M-1F during testing and the extent of damage at the final stage of testing are illustrated in Figure 3.61.

3.7.2 M-2FR

Mullion M-2FR had dimensions 51 mm x 127 mm x 3 mm and it was filled with ECC. It was tested with fix-fix support conditions. Three shots were applied to the specimen to observe the behavior under blast loading starting from the elastic to the inelastic stages of loading. The first shot had a driver pressure of 30 psi (207 KPa). This resulted in a reflected pressure-impulse combination of 34.4 kPa – 330.2 kPa-ms with a positive phase duration of 19.6 ms. The specimen was retrofitted externally with two layers of CFRP sheets forming a U-shape along the tension side. The LVDT readings were unreliable since the drilling of the mullion near the critical section to secure the tip of the LVDT was not advisable and the slippage of LVDT was observed. Consequently, the video recording was used to obtain accurate readings for the maximum and residual deflections. The maximum deflection at mid-height was 60 mm and the residual deflection was 38mm at the same location. This is illustrated in Figure 3.62. The specimen remained elastic during this first shot. However, there were signs of debonding of CFRP near the mid-height region.

The second shot was applied using an increased driver pressure of 40 psi (276 KPa). This resulted in a reflected pressure of 43.6 kPa and a reflected impulse of 413.2 kPa-ms. The positive phase duration was 18 ms. The second shot generated a maximum deflection of 85 mm at mullion mid-span and residual displacement of 60 mm. These readings were obtained from the video recording and are shown in Figure 3.63. There was a significant debonding observed between the CFRP sheets and the aluminum surface, with some local rupturing of the CFRP.

The specimen was subjected to a third shot with a driver pressure of 60 psi (414 KPa). This resulted in reflected pressure and impulse of 54 kPa and 561.3 kPa-ms within a positive phase duration of 21 ms. The maximum deflection at the mid-span was measured using the video recording as 120 mm as indicated in Figure 3.64. The specimen suffered rupturing of the aluminum at three locations: near the supports and at mid-height, forming three plastic hinges as the failure mode. This is illustrated in Figure 3.65.

3.7.3 M-3F

Specimen M-3F had a mullion size of 51 mm x 152 mm x 4.8 mm, filled with ECC without any additional reinforcement. The test was performed with pin–pin (simple) supports at the ends. The specimen was subjected to three shots until it reached failure. The first level of driver pressure was 30 psi (207 KPa), which generated a reflected pressure impulse combination of 35.3 kPa and 359.5 kPa-ms, respectively. The positive phase duration was 20 ms as depicted in Figure 3.66. The LVDT for this specimen was connected properly and captured the displacement readings clearly. These readings were verified against the video recording with excellent agreement. No damage was observed after the first shot. The maximum deflection was 59.6 mm and residual deflection was 15.8 mm.

The second shot was applied with a driver pressure of 40 psi (276 KPa). The recorded combination of reflected pressure and impulse was 46.6 kPa – 478.7 kPa-ms. The duration of pressure was 19.8 ms as shown in Figure 3.67. This specimen, with infilled ECC showed ductile behavior and no damage was observed at mid-span or close to the supports. The maximum deflection generated at mid-span was 93.8 mm with a residual displacement 34.6 mm.

The third shot was applied with a driver pressure of 60 psi (414 KPa), which resulted in a reflected pressure-impulse combination of 65. kPa – 542.7 kPa-ms. The equivalent positive duration was 18.4 ms as illustrated in Figure 3.68. The LVDT at this stage was disconnected as the specimen fractured. Therefore, the maximum deflection was obtained from the video recording with a value of 115.4 mm. Furthermore, the residual displacement was measured from the video recording as 28.6 mm. The specimen fractured at the mid-height of the specimen, and no damage was observed near the supports as depicted in Figure 3.69.

3.7.4 M-4FR

The specimen had a mullion size of 51 mm x 152 mm x 4.8 mm and was infilled with ECC. It was also externally reinforced with CFRP sheets having a U-shape coverage placed on the tension side of the aluminum mullion in the mid-span positive moment region. The specimen had fixed supports at both ends. The first shot was applied with a driver pressure of 30 psi (207 KPa). The

resulting reflected pressure and impulse combination was 28.6 kPa – 343 kPa-ms with a positive phase duration of 20 ms. The maximum deflection was recorded by the LVDT as 36.9 mm. It was observed that the residual deflection was almost the same as the maximum displacement with a recorded value of 32 mm. Figure 3.70 shows the reflected pressure, impulse, and deflection-time relationships.

The second shot was applied with a driver pressure of 40 psi (276 KPa), resulting in a reflected pressure–impulse combination of 39.1 kPa – 417.4 kPa-ms. The positive duration was 18 ms. CFRP layers showed preliminary debonding at this stage of loading, specifically in the middle area of the span. The maximum displacement was 26 mm and the residual displacement was approximately 12 mm as illustrated in Figure 3.71. The specimen showed very significant ductility similar to the smaller size companion mullion (M-2FR) with a lower deflection because of the size increase.

The third shot was applied with a driver pressure of 60 psi (414 KPa), which produced a reflected pressure-impulse combination of 52.6 kPa – 549 kPa-ms. The duration of the positive phase was 20 ms as illustrated in Figure 3.72. The CFRP reinforcement lost its bond, especially around the mid-span region. The specimen was cracked but no wide fracture was observed. The maximum displacement was 81.6 mm and the residual displacement was 27.6 mm. Figure 3.73 presents the behavior of the specimen under three shots as well as the failure at 60 psi (414 KPa) driver pressure.

3.7.5 M-5F

The specimen had a mullion size of 51 mm x 127 mm x 3 mm. It was filled with HSM. The supports were simple, and no reinforcement was used in this specimen. It was subjected to two shots. The first shot was at a driver pressure of 30 psi (207 KPa), and the observed deflection was 183 mm with a residual deflection of 140 mm. Furthermore, the recorded reflected pressure was approximately 46 kPa and the reflected impulse was 331.9 kPa – ms with a positive phase duration of 17.6 ms. These recordings are shown in Figure 3.74. The LVDT was properly secured to the mullion and the readings were reliable, hence no additional deflection readings were taken from

the video recording. The specimen showed higher deflection compared to the previous specimens under the first shot of 30 psi (207 KPa) driver pressure.

The second and last shot for this sample was 40 psi (276 KPa) driver pressure, which generated a combination of reflected pressure and impulse of 39.3 kPa – 396.3 kPa – ms. The positive phase duration of blast load was 19.8 ms. The recorded maximum displacement was 168 mm as captured from the video recording with a residual displacement of 129 mm. Figure 3.75 shows the pressure and displacement time histories. The specimen failed at this shot and developed about a 10 mm crack width with no damage at the supports. Figure 3.76 shows the behavior and failure mode of the specimen.

3.7.6 M-6F

The size of the mullion for this specimen was 51 mm x 127 mm x 3 mm. It was infilled with HSM, without any additional reinforcement. This specimen was able to sustain two shots at driver pressures of 30 psi (207 KPa) and 40 psi (276 KPa). It was tested with two fixed supports. The reflected pressure and impulse observed from the first shot were 32.9 kPa and 330.5 kPa-ms, respectively. The duration of blast wave during the positive phase was 17.6 ms. The maximum deflection at this stage of loading was 93.5 mm at the mid-span with a residual displacement of 65.7 mm. These readings were based on the LVDT readings. Figure 3.77 illustrates pressure-time history in addition to the reflected impulse and maximum displacement.

The specimen was subsequently subjected to second shot, which resulted in failure. The reflected pressure impulse combination was 45.1 kPa - 449.3 kPa-ms with a positive phase duration of 18 ms. Figure 3.78 shows the reflected pressure and impulse–time histories in addition to the maximum and residual deflections of 92.3 mm 82.7 mm. This shot resulted in the rupturing of the aluminum and the formation of a plastic hinge at mid-height. This is shown in Figure 3.79.

3.7.7 M-7F

Specimen M-7F was of 51mm x 152 mm x 4.8 mm size. It was infilled with HSM without any additional reinforcement. The supports were simply supported. Two shots were applied. The first shot had a driver pressure of 30 psi (207 KPa), which resulted in a pressure-impulse combination

of 33.7 kPa – 340 kPa-ms. The LVDT readings indicated a maximum and a residual deflection of 59 mm, and 17.5 mm. Pressure, impulse, and displacement – time histories are shown in Figure 3.80. The total positive phase blast wave duration was 18 ms.

The second shot was applied with a driver pressure of 40 psi (276 KPa), which generated a reflected pressure of 46 kPa and impulse of 493 kPa-ms. The positive phase duration of the shock wave was 20.8 ms. The maximum and residual deflections were 202 mm and 86 mm as recorded by the video camera. Figure 3.81 depicts the recorded data. The failure of the specimen occurred at mid-height due to the fracture of the aluminum on the tension side with a local buckling on the compression side. Figure 3.82 illustrates the specimen behavior and failure.

3.7.8 M-8F

Specimen M-8F was companion to M-6F with infilled HSM, without additional reinforcement, except for the increased mullion size of 51 mm x 152 mm x 4.8 mm. It was subjected to three shots with fixed supports. The first shot was applied with a driver pressure of 30 psi (207 KPa), which generated a combination of 37.5 kPa-341 kPa-ms reflected pressure and impulse. The positive phase duration was 18.4 ms. The LVDT readings indicated a maximum deflection of 46.4 mm with a residual value of 13 mm as shown in Figure 3.83. It was noticeable that the displacement at mid-span was small compared to specimen M-7F which was identical except for simple supports.

The second shot was 40 psi (276 KPa) driver pressure and resulted in 42.8 kPa as reflected pressure and 438.5 as reflected impulse. Furthermore, the maximum displacement was 47.4 mm and the residual displacement was 7 mm. These readings were observed based on LVDT recorded data. The positive phase duration of the shock wave was 20.6 ms. Figure 3.84 shows the recorded time histories. The specimen showed minor ductility behavior at this stage.

The applied third shot was 60 psi (414 KPa) driver pressure. This shot led to the failure of the specimen with a fracture at mid-height without any damage near the support region. Figure 3.85 presents the pressure-time history of the specimen under the reflected pressure of 55.5 kPa and reflected impulse of 579.7 kPa – ms. The positive phase duration for this shot was 19.2 ms. The

highest deflection was measured at mid-span with a value of 121.5 mm while the residual displacement at the same location was 37 mm. These readings were taken from LVDT recordings. The specimen experienced severe fracture at mid-span as illustrated in Figure 3.86.

3.7.9 M-9FH

The specimen M-9FH had a mullion size of 51 mm x 127 mm x 3 mm and it was filled with HSM. This specimen was reinforced internally with two high-strength wires on the tension side. The wires were located to resist the positive moment at mid-span by developing tension under blast loads. This specimen was prepared to simulate the process of strengthening mullions in practice. In other words, an opening was created at the top, through which the wires were inserted, prior to filling the mullion with HSM. It was tested with pin-ended supports and hence the entire mullion was subjected to positive bending. The recorded reflected pressure due to the application of 30 psi (207 KPa) driver pressure as first shot, was 37.2 kPa and the reflected impulse was 347.7 kPa-ms. Figure 3.87 depicts the time histories of recorded test data. The positive phase duration of shock wave was 18.6 ms and the recorded maximum displacement was 126.3 mm. Furthermore, the residual displacement at the end of the first shot was 77 mm.

The specimen resisted two shots only. The second shot was 40 psi (276 KPa) driver pressure, resulting in a reflected pressure-impulse combination of 40.1 kPa and 416 kPa-ms. The duration of the positive phase shock wave was 19.2 ms. The test data are plotted in Figure 3.88, indicating a maximum deflection of 160 mm. The residual displacement could not be obtained due to the LVDT disconnection and the loss of camera recording. The failure occurred due to the fracture of the aluminum mullion at the top one-third height of the specimen. This was attributed to the additional holes in the mullion created at this location to guide the wires in the mullions to ensure that they were placed on the tension side. Therefore, the aluminum area around these holes was lost, weakening the section. As a result, the first fracture occurred at this weak section as illustrated in Figure 3.89.

3.7.10 M-10FH

The size of this specimen was 51 mm x 127 mm x 3 mm and the infill material was HSM. The mullion was internally reinforced with four high-strength wires running along the height. Two wires were placed on the tension side of the mullion to resist positive moment at mid-span and the other two wires were placed on the compression side to resist the negative moment at the supports, which were fixed against rotation. The specimen was subjected to three shots. The first shot was 30 psi (207 KPa) driver pressure, which resulted in a reflected pressure and impulse combination as 37.4 kPa and 347.7 kPa-ms. The maximum displacement at mid-span was 65.4 mm and the residual deflection was 22 mm as depicted in Figure 3.90. The total equivalent positive phase duration of the shock wave was 20.8 ms.

The second shot was 40 psi (276 KPa) driver pressure with a generated reflected pressure-impulse combination of 41.5 kPa- 452 kPa-ms. The duration of blast in the positive phase was 20.2 ms. The maximum deflection at mid-span was 65 mm with a residual displacement of 30.9 mm as shown in Figure 3.91.

The third shot had 60 psi (414 KPa) driver pressure, generating 62.8 kPa reflected pressure and 621.3 kPa-ms reflected impulse. The positive phase duration was 19.8 ms. Figure 3.92 presents pressure, impulse, and deflection time histories. The maximum deflection was limited to 223 mm, which was obtained from the video camera recording. The specimen suffered failure at this load stage, rupturing at three locations: near the supports and at the mid-height. Figure 3.93 illustrates the behaviour of the mullion at different levels of blast shots.

3.7.11 M-11FH

M-11FH was companion to M-9FH with HSM infill and two high-strength wires on the tension (positive moment) side of bending with simple supports except for the size, which was increased to 51 mm x 152 mm x 4.8 mm. The specimen sustained three shots. The first shot had 30 psi (207 KPa) driver pressure resulting in a reflected pressure-impulse combination of 34.8 kPa-334 kPa-ms. The positive phase of duration of the shock wave was 18 ms. Maximum deflection was measured by the LVDT to be 61 mm. The residual deflection of 17 mm was obtained from the

video recordings. Figure 3.94 shows pressure-time history, as well as impulse and displacement time history relationships.

The second shot was applied at 45 psi (310 KPa) driver pressure. This level of pressure was slightly higher than the 40 psi (276 KPa) applied to other specimens for the second shot. This resulted in a pressure-impulse combination of 52.9 kPa – 516 kPa-ms with a positive phase duration of 19.7 ms. The reflected pressure time relationship is shown in Figure 3.95. The maximum displacement was recorded as 147 mm based on the LVDT readings. The residual displacement was 138 mm. The mullion failed at this load stage by a fracture along the specimen at mid-height section as illustrated in Figure 3.96.

3.7.12 M-12FH

The specimen M-2FH was companion to M-11FH, except for the support conditions and hence the reinforcement layout inside. The mullion size was 51 mm x 152 mm x 4.8 mm with fixed supports. It was also infilled with HSM. Because of the negative bending generated in the support regions 4 wires were placed continuously along the mullion height internally, 2 on the tension side at mid-height and the remaining 2 on the tension side at the supports. The first shot had 30 psi (207 KPa) driver pressure resulting in reflected pressure and impulse of 38.3 kPa and 352.9 kPa – ms with a positive phase duration of 21 ms. The maximum displacement recorded at mid-span was 35 mm and the residual displacement was 3mm as illustrated in Figure *3.97*.

The second shot was applied with 40 psi (276 KPa) driver pressure and generated a reflected pressure of 41.9 kPa and an impulse of 447.2 kPa – ms. The positive phase duration of the shock wave was 19.8 ms. The maximum deflection was 54 mm and the residual displacement was 10 mm. These values are less than those recorded in the companion specimen with simple supports, as expected. Figure 3.98 shows the deflection readings.

The third shot had 60 psi (414 KPa) driver pressure and 56.5 kPa reflected pressure. The impulse was 616.4 kPa -ms within a duration of 21.4 ms. Based on the LVDT reading, the maximum deflection was 68 mm and the residual deflection was 17 mm as presented in Figure 3.99. The failure occurred at this stage of loading. The failure mode was a fracture along the specimen mid-

height section in the positive moment region. There was no visible damage observed at the supports. Figure 3.100 shows the mullion performance at the end of each shot.

3.7.13 M-13FH

This mullion consisted of an aluminum section with dimensions of 51 mm x 127 mm x 3 mm. It was filled with HSM. It was internally reinforced with a high-strength chain placed inside the aluminum section prior to casting the mortar along the height on the tension side of the specimen (under positive bending). The reason for using a chain as an alternate reinforcement was for convenience during placement as the weight of the chain would keep it straight upon placement in the mullion. The specimen was tested with simple supports. The first applied shot had a driver pressure of 30 psi (207 KPa). This resulted in a reflected pressure impulse combination of 28.7 kPa and 307.4 kPa-ms with a positive phase duration of 16.4 ms. The maximum deflection at mid mid-height was 122 mm based on the LVDT recordings. The residual deflection was 67 mm as presented in Figure 3.101.

The second shot had 40 psi (276 KPa) driver pressure, causing a reflected pressure of 40.2 kPa and a reflected impulse of 417.4 kPa-ms. The positive phase duration of the shock wave duration was 19 ms. The maximum deflection recorded at mid-height was 111 mm and the residual deflection was 16 mm based on the LVDT readings. Figure 3.102 presents the time histories of recorded data. This shot resulted in the failure of the mullion. Unlike most failure modes observed in other mullions this specimen failed due to local web buckling without any tension rupturing. This is attributed to the increased tension steel area provided through the internal chain in comparison with smaller percentage of steel when high-strength wires were used. Figure 3.103 shows the behaviour of the mullion under the two shots applied.

3.7.14 M-14FH

This specimen was companion to M-13FH except for a larger size aluminum mullion used with dimensions of 51 mm x 152 mm x 4.8 mm, also filled with HSM and internal reinforcement as high-strength chain. It was subjected to three shots. The first shot was performed by applying a driver pressure of 30 psi (207 KPa) , which resulted in a reflected pressure-impulse combination

of 34.6 kPa – 345.3 kPa-ms and a positive phase duration of 17.6 ms as shown in Figure 3.104. Mid-span maximum deflection was recorded by the LVDT connected to the mid-height of the specimen. The specimen experienced a maximum deflection of 56.9 mm and a residual deflection of 12.6 mm. No damage was observed on the specimen, and it remained elastic after the first shot.

The second shot had an increased driver pressure of 40 psi (276 KPa). The reflected pressure was 41.2 kPa and the reflected impulse was 453 kPa-ms. The positive phase duration of the shock wave was 16.8 ms. This shot resulted in a maximum deflection of 69.8 mm at mullion mid-span and a residual deflection of 15 mm as recorded by the attached LVDT. This is shown in Figure 3.105.

The specimen was subjected to a third shot at 60 psi (414 KPa) driver pressure, which produced a reflected pressure impulse combination of 55 kPa – 575 kPa-ms with a positive phase duration of 17.8 ms. The deflection at the mid-height was measured by the LVDT as 129 mm with a residual deflection of 73 mm as depicted in Figure 3.106. This shot caused the failure of the specimen with the failure mode as local web buckling on the compression side, without rupturing of aluminum on the tension side. This is the same failure mode observed in the companion M-13FH, except M-14FH sustained one more shot because of the larger cross-section of the aluminum mullion. The test performance is illustrated in Figure 3.107.

3.7.15 M-15FR

Specimen M-15FR was companion to M2-FR having the same size of aluminum section 51mm x 127mm x 3mm with externally placed U-shaped CFRP sheets except for the infill material being HSM rather than the ECC used in the previous specimen, as well as having simple supports as opposed to having fixed supports of M-2FR. It was subjected to two shots until it reached failure. The first shot had a driver pressure of 30 psi (207 KPa), which generated a reflected pressure-impulse combination of 30.4 kPa-312.8 kPa-ms. The positive phase duration of the shock wave was 17.6 ms. The recorded time histories of test data are depicted in Figure 3.108. The LVDT was disconnected during this blast shot and hence the deflection measurements were

taken from the recorded video. No damage was observed after this shot. The recorded maximum and residual displacements were 116 mm and 32 mm, respectively.

The second shot was applied with a driver pressure of 40 psi (276 KPa). The recorded combination of reflected pressure and impulse was 33.2 kPa – 310.8 kPa-ms with a positive phase duration of 18.2 ms. This is shown in Figure 3.109. No damage to aluminum was observed to aluminum, but the CFRP sheets ruptured and deboned as s illustrated in Figure 3.110. The maximum deflection generated at the mid-span was 125 mm with residual displacement 103 mm.

3.7.16 M-16FR

Specimen M-16FR was exactly the same as M-4FR with the same size aluminum section 51mm x 152mm x 4.8mm and external U-shaped CFRP sheets except for the use of HSM as infill material as opposed to using ECC. The support conditions were also the same as fixed supports. The specimen was subjected to four shots. The first shot was applied with a driver pressure of 30 psi (207 KPa). The resulting reflected pressure impulse combination was 34.2 kPa – 367.6 kPa-ms and the duration of the shock wave was 20.2 ms. The maximum deflection as provided by the attached LVDT was 35.7 mm. The residual deflection was 4 mm, indicating mostly elastic response. Figure 3.111 shows the pressure, impulse, and deflection-time relationships.

The second shot had 40 psi (276 KPa) driver pressure resulting in a reflected pressure–impulse combination of 40.7 kPa – 450.9 kPa-ms. The positive duration was 24.4 ms. CFRP layers showed debonding at the middle area of the span. The maximum displacement was 45 and the residual displacement was approximately 2mm as illustrated in Figure 3.112. The specimen showed very significant ductility with a lower deflection value compared to the smaller specimens due to the effect of size increase and fixed supports at the ends of the specimens and CFRP retrofitting.

The third shot had 60 psi (414 KPa) driver pressure, and the resulting reflected pressure-impulse combination was 57 kPa – 606 kPa-ms. The duration of the positive phase was 21 ms as illustrated in Figure 3.113. During this level of loading, CFRP deboned at mid-height. The specimen developed hairline cracks, but no wide crack was observed as in some of the previously tested

mullions. The recorded deflection at the mid-span location was not large as the fixed support restrained the specimen and CFRP layers contributed towards the strengthening of the specimen. The maximum displacement was 74 mm and the residual displacement was 13 mm.

Specimen M-16FR which was retrofitted with CFRP suffered failure after applying a fourth shot. The failure was represented by a thin crack at the mid-span of the specimen with no fracture and this showed the contribution of CFRP retrofitting compared with specimens without retrofitting. The obtained reflected pressure-impulse combination was 78.7 kPa – 683 kPa-ms. The duration of the positive phase was 19.6 ms. Additionally, the maximum displacement was 81.6 mm as illustrated in Figure 3.114. Figure 3.115 presents the behavior of the specimen under four shots and the failure mode at 80 psi (551 KPa).

3.8 Effects of Test Parameters

3.8.1 Effect of Filler Material (ECC vs HS Mortar)

3.8.1.1 M-1F-ECC and M-5F-HSM (SS – 5" mullions -no reinforcement)

Figure 3.116 illustrates the performance of two different specimens with the same size mullions (51 mm x 127 mm x 3 mm) both simply supported: M-1F was infilled with ECC and M-5F was infilled with HSM. Though the first shots show a difference in deflection readings, this is attributed to the unequal blast loads applied. The reflected pressure on M-5F was applied at a significantly higher magnitude accidentally during the test, hence resulting in a larger deflection. The comparison of Shot 2 deflections for the two specimens indicates similar behaviour, with slightly reduced deflection (by 9%) in the ECC filled mullion because of the high tensile capacity and ductility of ECC as compared to HSM. Maximum support rotation θ_{max} for Specimen M-1F was approximately 13.6^{o} while the maximum support rotation θ_{max} for Specimen M-5F was 9.4^{o} at this stage of loading. Figure 3.116 also indicates that filling the mullions with ECC or HSM increased blast resistance relative to the reference specimen without the infill materials. The reference control specimen was a hollow aluminum mullion, which failed at 26 kPa reflected pressure, whereas infilled mullions could sustain approximately 40 kPa reflected pressures before they suffered failure.

3.8.1.2 M-3F-ECC and M-7F-HSM (SS – 6” mullions -no reinforcement)

The effect of infill material was also investigated by testing companion mullions with a larger size mullion (51 mm x 152 mm x 4.8 mm). The comparison of M-3F and M-7F mid-height deflections is shown in Figure 3.117. The behavior of both specimens under the first blast shot was the same. Both specimens M-3F and M-7F showed a reduction in mid-span deflection compared to the small specimens discussed in the previous section (M-1F and M-5F) due to the increase in section dimensions. Maximum support rotations $\theta_{max}$for Specimen M-3F and M-7F were approximately 3.1^{o} and 3.1^{o}, respectively. The second shot pressures applied on the specimens was approximately the same. Shot 2 resulted in the rupturing of the mullion and complete failure of M-7F with HSM developing a support rotation of 11.3^{o}, whereas M-3F with ECC was able to sustain the shot with a maximum support rotation of 5.7^{o}. Therefore, it was subjected to Shot 3 at 65 kPa reflected pressure before it ruptured at a much lower deflection than the mullion with HSM under Shot 2. This is attributed to the higher tensile capacity of ECC and more ductile behaviour of the material under both tension and compression. Maximum support rotation for M-3F at failure under Shot 3 was 7.8^{o}. The superior performance of ECC filled mullion in this series, with a larger size mullion, relative to M-1F discussed in the previous section when the mullion prematurely ruptured at Shot 2 indicates that the superior performance of ECC is realized when there is sufficient tension capacity in the aluminum mullion over and above that provided by the ECC infill, preventing premature tension failure. Indeed, in this case the rupturing of the aluminum is delayed until Shot 3 at 65 kPa reflected pressure.

3.8.2 Effect of Support Condition (SS versus FS)

3.8.2.1 M-5F-HSM and M-6F-HSM (SS-FS – 5” mullions – no reinforcement)

In this section, the effect of support condition is assessed by comparing the same size mullions 51mm x 127mm x 3mm infilled with HSM having either simple support (M-5F) or fixed support (M-6F) at both ends. The comparison for each shot is shown in Figure 3.118 for Shots 1 and 2. For both shots M-5F with simple supports experienced significantly higher mid-height

deflections, developing about 9.4^{o} support rotation than the fixed end companion specimen which developed maximum support rotations of about 5.1^{o} as expected.

3.8.2.2 M-7F-HSM and M-8F-HSM (SS-FS – 6" mullions – no reinforcement)

The effect of support conditions was also investigated by testing larger size mullions with 51 mm x 152 mm x 4.8 mm dimensions filled with HSM, one having simple supports (M-7F) and the other having fixed supports (M-8F). The results are compared in Figure 3.119. For all the shots the simply supported mullion developed larger displacements, showing 3.1^{o} and 11.3^{o} support rotations during Shots 1 and 2, respectively, relative to the specimen with fixed supports, which developed 2.5^{o} and 3.3^{o} at Shots 1 and 2 respectively. The simply supported mullion failed after Shot 2 whereas the mullion with fixed supports was able sustain an increased blast load during Shot 3 with a maximum reflected pressure of 55.5 kPa and a support rotation of 7^{o}.

3.8.3 Effect of internal cable as reinforcement

3.8.3.1 M-5F-HSM versus M-9FH-HSM (SS- 5" mullions) and M-7F versus M-11F (SS-6" mullions)

The mullion hardening strategy included reinforced infill materials. This section discusses the behavior of two specimens having the same size 51mm x 127mm x 3mm with simple supports. Specimen M-5F was infilled with HSM without any internal reinforcement and the companion specimen M-9FH was internally reinforced with two high-strength steel wires, each having a nominal diameter of 6.0 mm (area of 28.3 mm^2). This corresponds to 1.0 % steel reinforcement placed on the tension side of the mullion. The results are compared in Figure 3.120. and indicate that the mullion with internal reinforcement developed lower deflection as compared to the companion specimen without the steel, though during the first shot the specimen without the steel reinforcement was subjected to higher pressure and hence developed higher than expected deflection.

A similar comparison is made on two other mullions with a larger section size (51 mm x 152 mm x 4.8 mm), also having simple supports and two cables in HSM on the tension side (0.96%

steel). The results are compared in Figure 3.121, indicating the contribution of steel being negligible under low levels of blast loads as the tension capacity provided by the aluminum tube would dominate the behavior. However, when the level of reflected blast pressure is increased to a level where the rupturing of aluminum was initiated, the contribution of internal steel became more significant. Indeed, under Shot 2, Specimen M-11F with two steel wires showed increased capacity and reduced deflection when compared with M-7F without the internal reinforcement.

3.8.3.2 M-6F-HSM versus M-10FH-HSM (FS- 5" mullions) and M-8F versus M-12FH (FS- 6" mullions)

The effect of internal reinforcement in the form of high-strength steel wires was also investigated in mullions infilled with HSM and tested with fixed support conditions. This time, because of the fixity at the support three critical regions were created, two (negative moment) regions near the supports and the mid-height (positive moment) region. Because there would be tension created on both sides of the mullions, 4 wires were used, two on each side. The results of the mullions with smaller size (51 mm x 127 mm x 3 mm) are compared in Figure 3.122. The effect of steel was observed to be higher in this case, in comparison with simply supported mullions. Specimen M-10FH with four cables, showed higher resistance and developed lower displacements under comparable blast loads than the companion specimen without the steel reinforcement (M-6F). At shot 2 the maximum support rotation of M-6F was 8.6^{o} whereas it was 4.7^{o} for M-10FH. Specimen without the reinforcement developed failure during Shot 2 by rupturing of the aluminum tube, whereas the specimen reinforced with steel cables survived this load stage without failure and sustained higher blast loads at Shot 3 before it experienced tension failure at maximum support rotation of 13.6^{o}.

The same comparison was made by testing two companion mullions with a larger cross-section (51 mm x 152 mm x 4.8 mm) under the same fixed-fixed support conditions, also infilled with HSM. The comparison is shown in Figure 3.123. This time because of the increased area of aluminum tube on the tension faces, both mullions (with and without internal cables) sustained Shot 3 but specimen M-12FH with the internal reinforcement showed higher resistance and lower

displacement at failure. At Shot 3 the maximum rotation θ_{max} for M-8F was 7^o and for M-12FH it was 4.2^o.

3.8.4 Effect of internal chain as reinforcement

3.8.4.1 M-5F-HSM and M-13FH-HSM (SS- 5" mullions – with and without Chain)

In addition to providing internal steel cables as reinforcement, as discussed in the previous sections, the use of chains internally placed as reinforcement was implemented in two mullions infilled with HSM. The rationale for using chains would be the ease in construction as chains dropped into the empty mullion prior to casting HSM would align itself in the correct position, i.e., near tension side, by its weight (rather than having to guide the steel cables in the previous application). Grade 70 chain with a steel diameter of 6.4 mm was used, hence providing two legs of a chain in each section. This resulted in 2 times the individual area of 32.2 mm^2 for each leg (2 x 32.2 mm^2 = 64.4 mm^2), producing 1.2% steel area in a 51 mm x 127 mm x 3 mm in size mullion. Two mullions of the same size, one with and the other without internally placed chain reinforcement were subjected to similar blast loads and compared. The comparison of results between M-5F without any reinforcement and M-13F with a steel chain as reinforcement on the tension side of the mullion is illustrated in Figure 3.124. The results indicated that the mullions reinforced with steel chain showed reduced displacement at each shot. The maximum support rotations measured during Shot 1 was 9.4^o for M-5F and 6.3^o for M-13FH. Both specimens were subjected to second shot, and both failed at this stage of blast loading. However, the failure mode of the specimens was different. Specimen M-5F failed with a partial fracture of the aluminum at mid-span, whereas the specimen M-13FH failed through local compression buckling of the aluminum without tension rupturing. This is attributed to higher tension resistance provided by the additional internal reinforcement provided by the chain. The maximum support rotation θ_{max} was around 16^o for M-5F and 9.2^o for M-13FH.

3.8.4.2 M-7F-HSM and M-14FH-HSM (SS- 6" mullions – with and without Chain)

The effect of internally placed chain on mullion performance was also investigated using a larger size mullion having the dimensions of 51 mm x 152 mm x 4.8 mm. The mullions were

tested with simple supports with a critical section at mid-height. The same size chain as before was provided on the tension side. Figure 3.125 depicts the effect of reinforcement on improving blast strength capacity and stiffness against blast loading. Specimen M-7F was filled with HSM without any internal reinforcement whereas specimen M-14FH had a single chain providing 1.1% reinforcement. They were subjected to 34 kPa reflected pressure as Shot 1. At this stage of low blast pressure, both specimens performed elastically, and the presence of additional reinforcement did not result in an appreciable reduction in displacement. However, when the second shot was applied at 41.2 kPa to M-14FH and 46 kPa to M-7F, the contribution of the additional steel chain reinforcement was substantial, resulting in maximum support rotations of 11.3^{o} for unreinforced M-7F and 4.3^{o} for reinforced mullion M-14FH. Furthermore, M-7F experienced tensile rupturing of the aluminum and failed at this load stage, whereas M-14FH did not fail. Subsequently, M-14FH was subjected to a higher blast load as the Third Shot. It sustained 55 kPa of reflected pressure and still did not experience tension rupture, which was attributed to the extra reinforcement provided in the form of steel chain, but experienced compression buckling of the aluminum at a maximum support rotation of 7.5^{o}. These comparisons clearly illustrate the beneficial effects of providing additional steel reinforcement in the form of internally placed chain.

3.8.5 Effect of externally bonded CFRP sheets

3.8.5.1 M-5F-HSM and M-15FR-HSM (SS- 5” mullions – with and without CFRP)

The effect of providing externally bonded U-shaped CFRP sheets was investigated as another means of providing additional reinforcement to the mullions in addition to filling them with HSM. Specimens M-5F and M-15FR both had 51 mm x 127 mm x 3 mm section size with the former without CFRP reinforcement whereas the latter had two sheets of CFRP with 0.9 mm thickness per layer resulting in 1.8 mm thick U-shaped CFRP on the tension side of the mullion, while also covering the web for improved bond, with fibres running in the longitudinal direction. The results are compared in Figure 3.126. M-15FR with the CFRP showed increased strength and stiffness, developing lower displacements than the companion specimen without the additional reinforcement. The maximum support rotations recorded were 9.4^{o} for M-5F and 6^{o} for M-15FR

although part of the additional deflection recorded for M-5F can be attributed to the slightly higher blast pressure applied on this specimen. The second shot resulted in a wide flexural crack in M-5F without the CFRP, almost splitting the mullion into two, whereas M-15FR survived the shot with only a hairline crack in spite of the surface bond failure between the aluminum and the CFRP. The maximum support rotation θ_{max} for M-5F was 16^o and 8^o for M-15FH.

3.8.5.2 M-8F-HSM and M-16FR-HSM (FS- 6" mullions – with and without CFRP)

A second set of specimens were tested to investigate the effectiveness of external CFRP on mullion performance. This time the mullions were fixed at their supports and a larger size of aluminum tubes were used as mullions (51 mm x 152 mm x 4.8 mm). Figure 3.127 illustrates the difference in performance between two specimens infilled with HSM and having all other parameters the same except for the presence of CFRP as external reinforcement on M-16FR. Both specimens performed about the same during the first two shots when the mullions essentially remained elastic. However, when the blast pressure was increased for Shot 3, Specimen M-8F without the CFRP failed through a wide tensile crack in the aluminum, whereas M-16FR with the CFRP survived the shot while partially debonding from the aluminum. At this stage of loading the maximum support rotations were measured to be 7^o and 4^o for M-8F and M-16FR, respectively. The blast pressure was increased to 88 kPa and applied as Shot 4 on M-16FR producing a maximum support rotation of 5.1^o. The test was discontinued at this stage as the CFRP completely de-bonded.

The above observations clearly show the beneficial effects of surface bonded CFRP as blast hardening technique until the surface bond failure of CFRP is reached.

3.8.6 Effects of Mullion Size (5" vs 6")

The effect of mullion section size was investigated by comparing 6 pairs of specimens where each mullion in a pair either had a 51 mm x 127 mm x 3 mm or a 51 mm x 152 mm x 4.8 mm cross-section. The mullions in each pair otherwise had the same properties. The mullions either had ECC or HSM infill, with or without additional reinforcement. The test results are compared in Figure 3.128 through Figure 3.133. In all cases larger mullions showed stronger and

more stiff response at comparable blast loads. The majority of smaller size mullions suffered from failure at Shot 2, while the larger mullions were able to sustain Shot 3 at higher blast pressures. Furthermore, the mullion size, especially the increased wall thickness of the aluminum sections changed the failure mode from tension rupturing to compression buckling at Shot 3. Further details of each specimen are discussed in the preceding sections in terms maximum displacements, support rotations and failure patterns.

3.9 Response limits

The CSA S850-23 standard sets out specific guidelines for both the structural design of new buildings and the assessment of existing ones to withstand blast effects. Its primary aim is to minimize injuries and reduce damage to property resulting from explosive air blasts. The standard also recognizes that it's not possible to precisely predict the magnitude or impact of an explosion. The building's response and occupant safety depend on the intended level of protection and the defined design basis threat (DBT). Table 3.20 and Table 3.21 illustrates various levels of building damage and response limits according to CSA performance benchmarks. Glazing system framing was considered to assess the level of damage for all specimens tested in this research as shown in Table 3.19.

Table 3.20: Component damage versus response limits

Component damage level	Component damage level descriptions	Response limits
Blowout	Component is overwhelmed by blast load causing debris with significant velocities.	Response greater than B4
Hazardous failure	Component has failed with no significant velocities.	Response between B3 and B4
Heavy damage	Component has not failed, but it has significant permanent deflections causing it to be unrepairable.	Response between B2 and B3
Moderate damage	Component has some permanent deflection. It is generally repairable, if necessary, although replacement might be more economical and aesthetic.	Response between B1 and B2
Superficial damage	Component has no visible permanent damage.	Response less than B1

Table 3.21: Response limit for steel glazing system framing in flexure

Element type			B1		B2		B3		B4	
			μ_{max}	θ_{max}	μ_{max}	θ_{max}	μ_{max}	θ_{max}	μ_{max}	θ_{max}
Flexure	**Open web steel joist**	Downward loading†	1	—	—	3°	—	6°	—	10°
		Upward loading‡	1	—	1.5	—	2	—	3	—
		Shear response§	0.7	—	0.8	—	0.9	—	1	—
	Cold-formed steel	Girt or purlin	1	—	—	3°	—	10°	—	20°
		Stud with sliding connection at top	0.5	—	0.8	—	0.9	—	1	—
		Stud connected at top and bottom**	0.5	—	1	—	2	—	3	—
		Stud with tension membrane††	0.5	—	1	0.5°	2	2°	5	5°
		Corrugated panel (1-way) with full tension membrane‡‡	1	—	3	3°	6	6°	10	12°
		Corrugated panel (1-way) with some tension membrane§§	1	—	—	1°	—	4°	—	8°
		Corrugated panel (1-way) with limited tension membrane***	1	—	1.8	1.3°	3	2°	6	4°
	Glazing system framing	Steel	1	—	—	3°	—	6°	—	10°

* *Where a dash (—) is shown, the corresponding parameter is not applicable as a response limit.*

† *Values assume tension yielding of bottom chord with adequate bracing of top chord to prevent lateral buckling.*

Figure 3.1: Hole drilling at mullion ends

Figure 3.2: Closing mullion end by a wooden block

Figure 3.3: Specimens after the taping process

Figure 3.4: Wires anchored to the mullion (bottom of the mullion)

Figure 3.5: Wires anchored to the mullion (top of the mullion)

Figure 3.6: Wire inserting technique for use in practice

Figure 3.7: Material pouring into the mullion by using a plastic funnel

Figure 3.8: 1/4-inch Zinc-Plated Wire Rope Clip used to fix wires

Figure 3.9: High strength chain located on the tension side of the mullion

Figure 3.10: Epoxy paste for gap sealing

Figure 3.11: High strength chain tensioning by straps

Figure 3.12: Mullion surface cleaning from the excess materials

Figure 3.13: Sanding mullion surface by a metal brush specific for aluminum surfaces

Figure 3.14: Mullion surface cleaning prior to CFRP application

Figure 3.15: Epoxy application by a paint roller

Figure 3.16: Tools used for epoxy application

Figure 3.17: Two components (A and B) of epoxy mixture

Figure 3.18: Epoxy mixing process using a hand mixer

Figure 3.19: Ribbed steel roller

Figure 3.20: Specimen curing

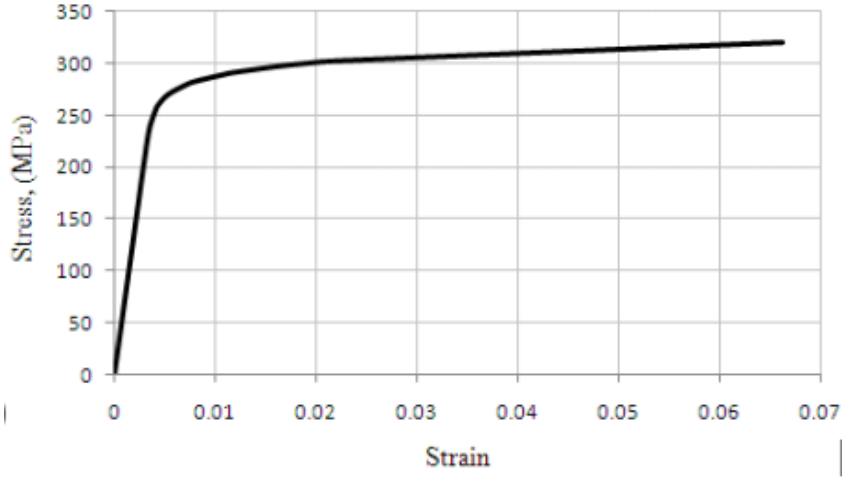

Figure 3.21: Typical stress-strain relationship of aluminum

Figure 3.22: The large size mixer at the University of Ottawa

Figure 3.23: Pressure air application to disperse the fiber bundles

Figure 3.24: PVA fibers after air pressure application

Figure 3.25: ECC powder addition to the water and superplasticizer mixture

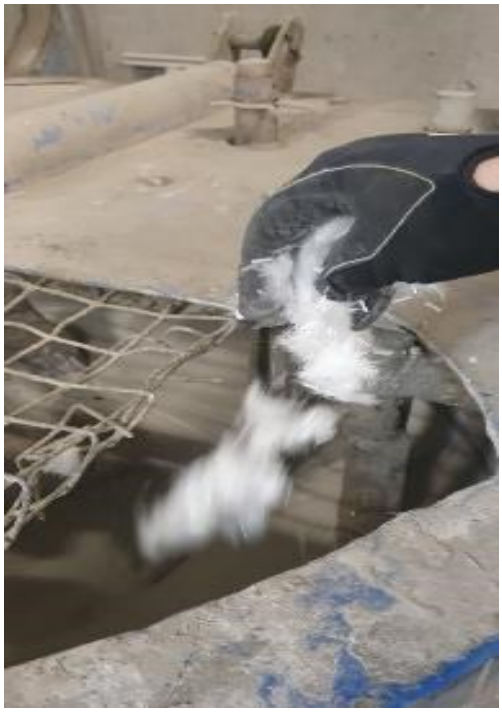

Figure 3.26: PVA fibers gradually added to ECC mix

Figure 3.27: Pouring material into the mullion using a plastic funnel

Figure 3.28: Material casting as small specimens

Figure 3.29: Samples grinding

Figure 3.30: Compressive testing machine

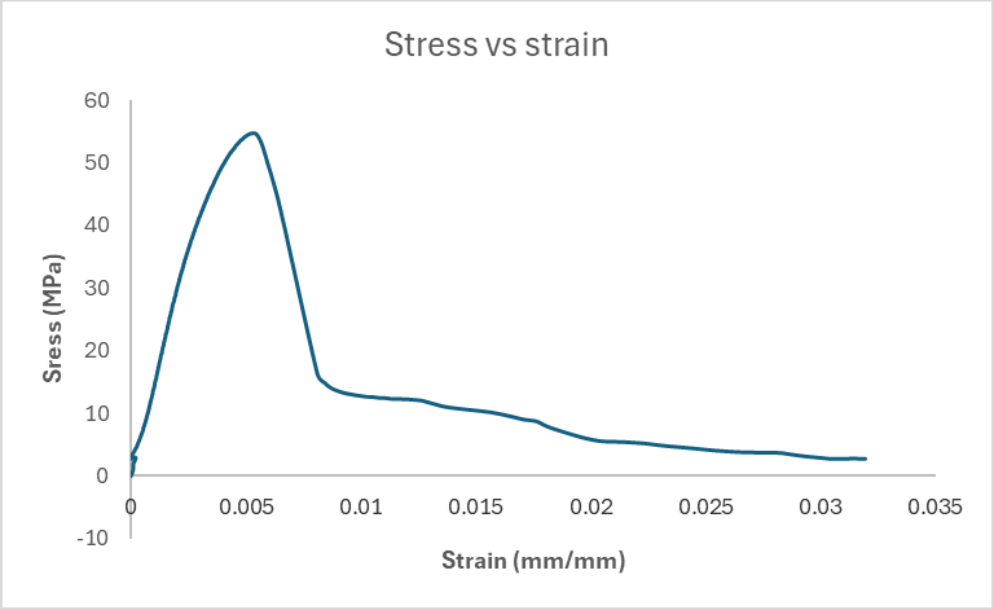

Figure 3.31: Stress-strain relationship of ECC in compression

Figure 3.32: Coupon test specimens

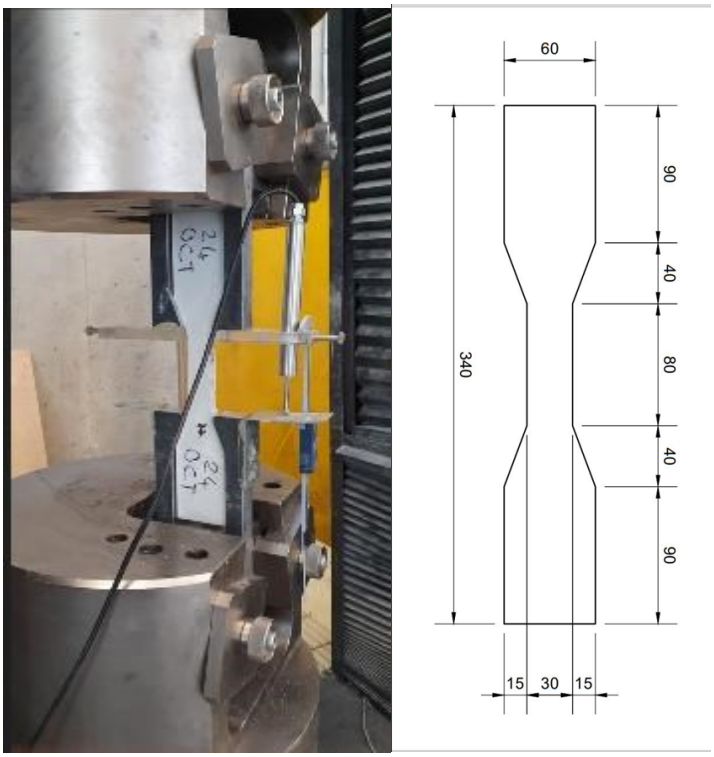

Figure 3.33: Coupon tensile test

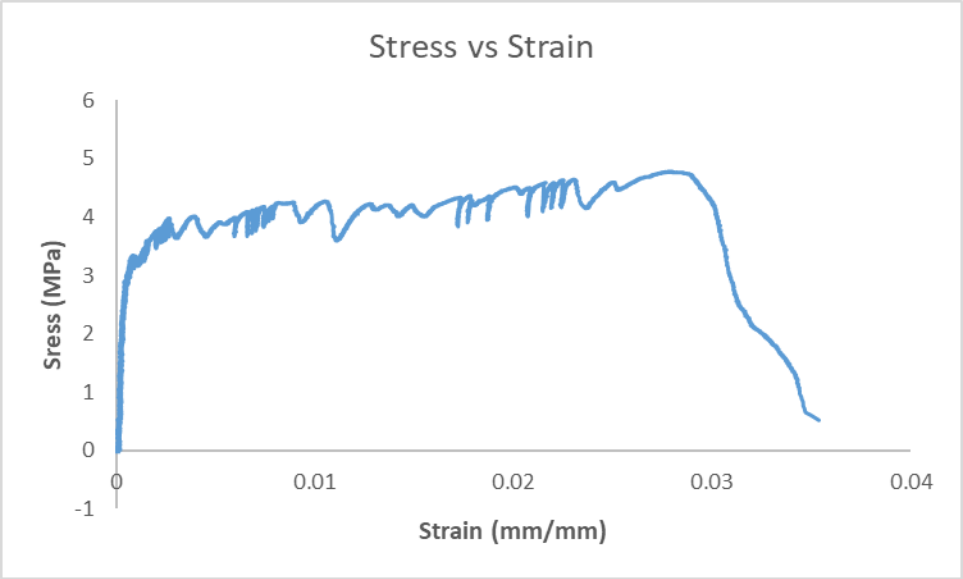

Figure 3.34: Stress-strain relationship of ECC in tension

Figure 3.35: Compressive strength of HSM samples attached with LVDT

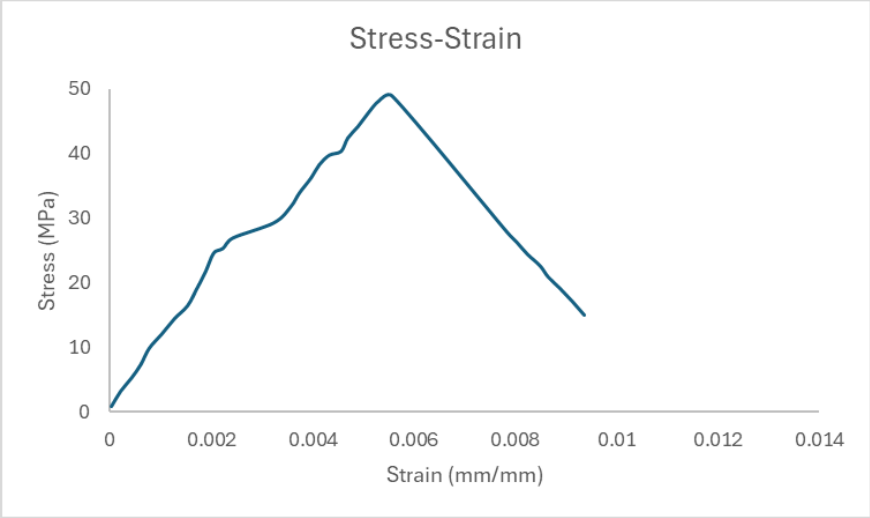

Figure 3.36: Stress-strain relationship for HSM

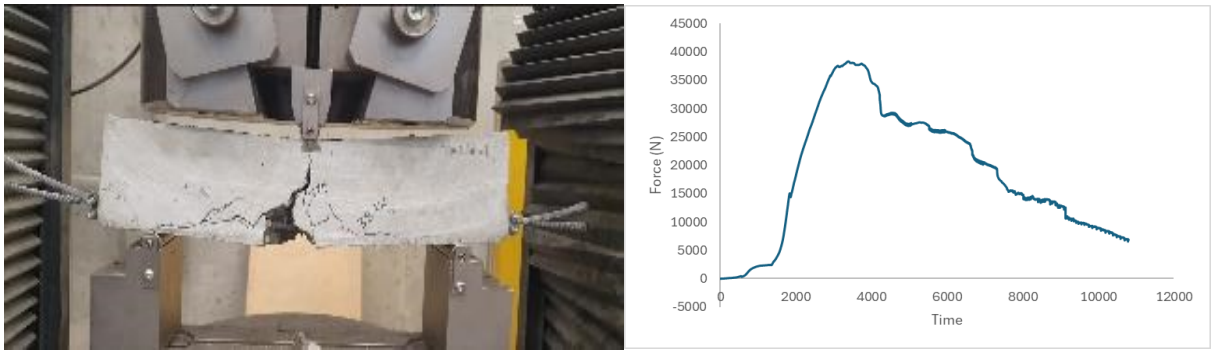

Figure 3.37: Flexural strength text for prism specimen with high strength wires

Figure 3.38: Flexural strength text for prism specimen without high strength wires

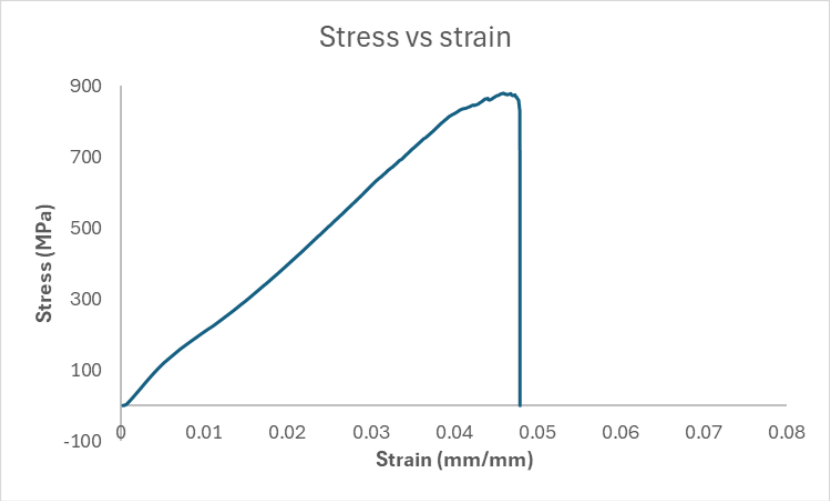

Figure 3.39: Stress-strain relationship for high strength wires

Figure 3.40: Tensile strength test for high strength wire

Figure 3.41: Tensile strength test for high strength chain

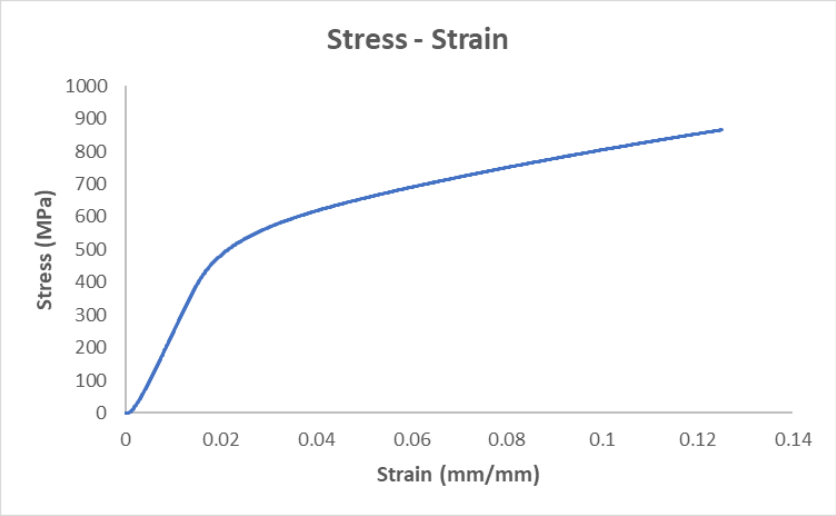

Figure 3.42: Stress-strain relationship for high strength chain

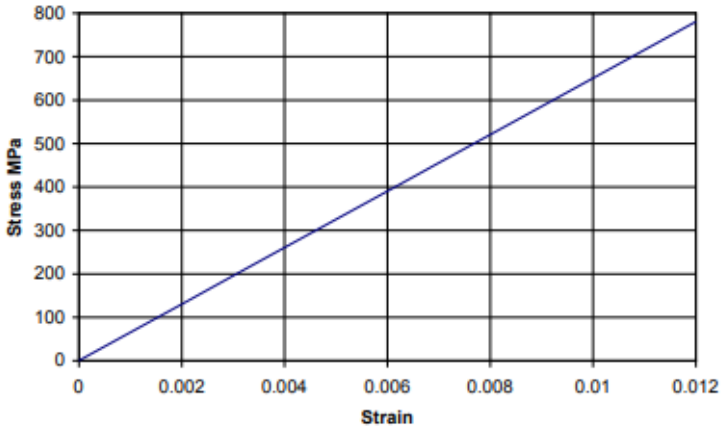

Figure 3.43: Stress-strain relationship for CFRP (Alnabelsy, 2013)

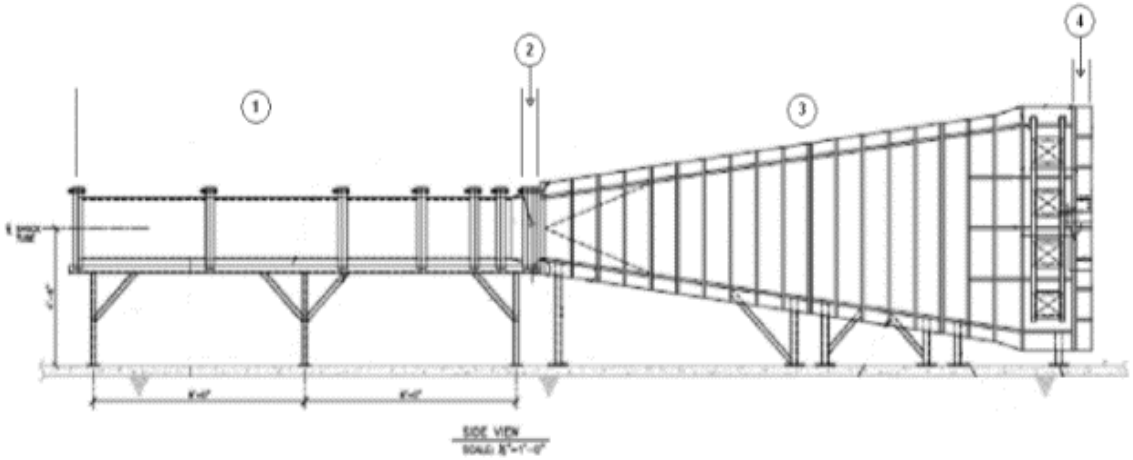

Figure 3.44: Shock-tube facility (Lloyd, 2010)

Figure 3.45: Variable length driver

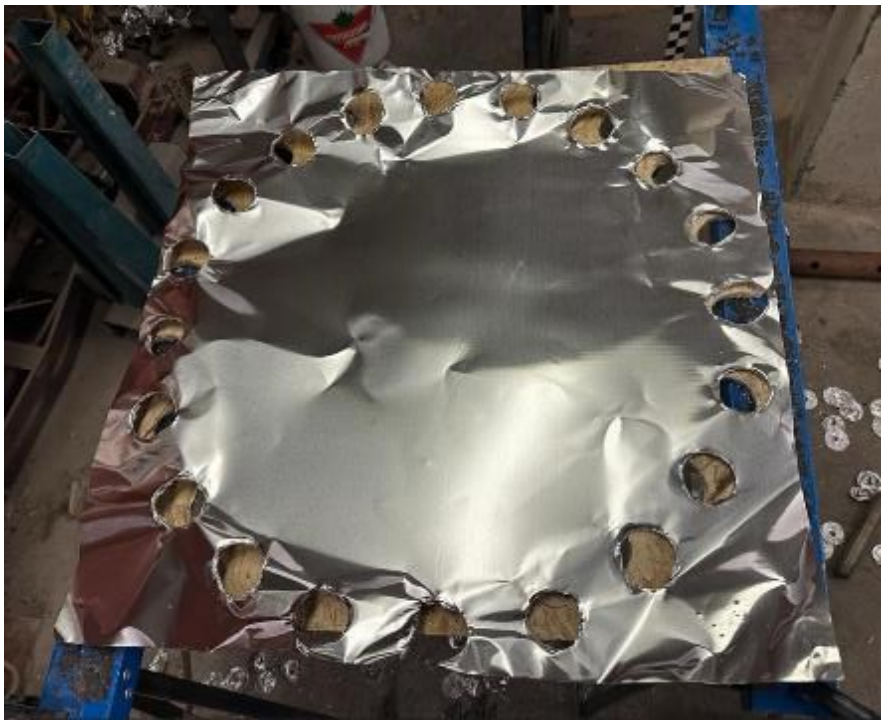

Figure 3.46: Aluminum diaphragms preparation prior to be inserted into the shock-tube

Figure 3.47: Spool section

Figure 3.48: Expansion section

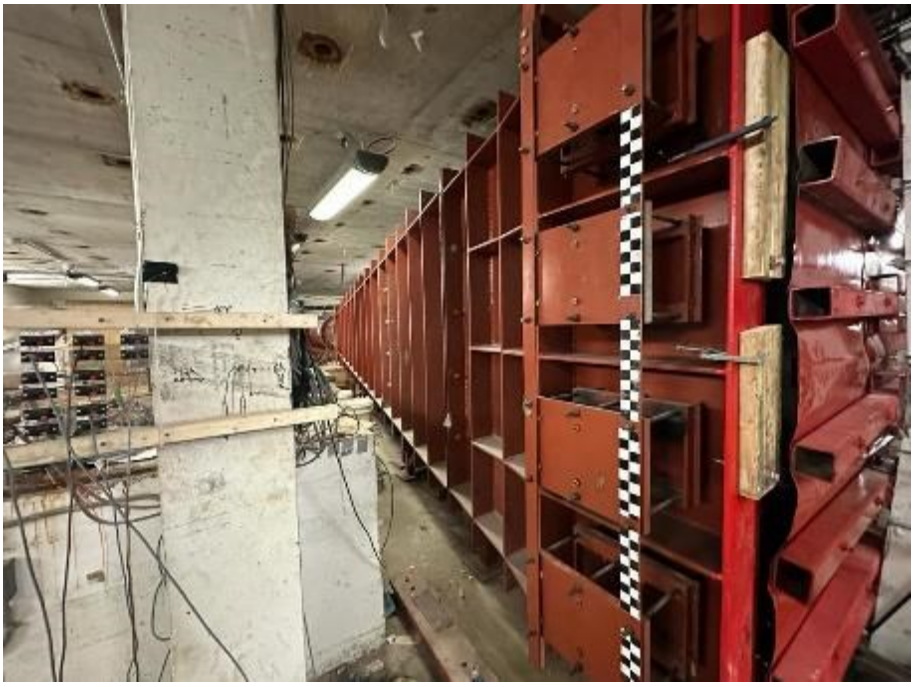

Figure 3.49: Square vents close to shock-tube opening

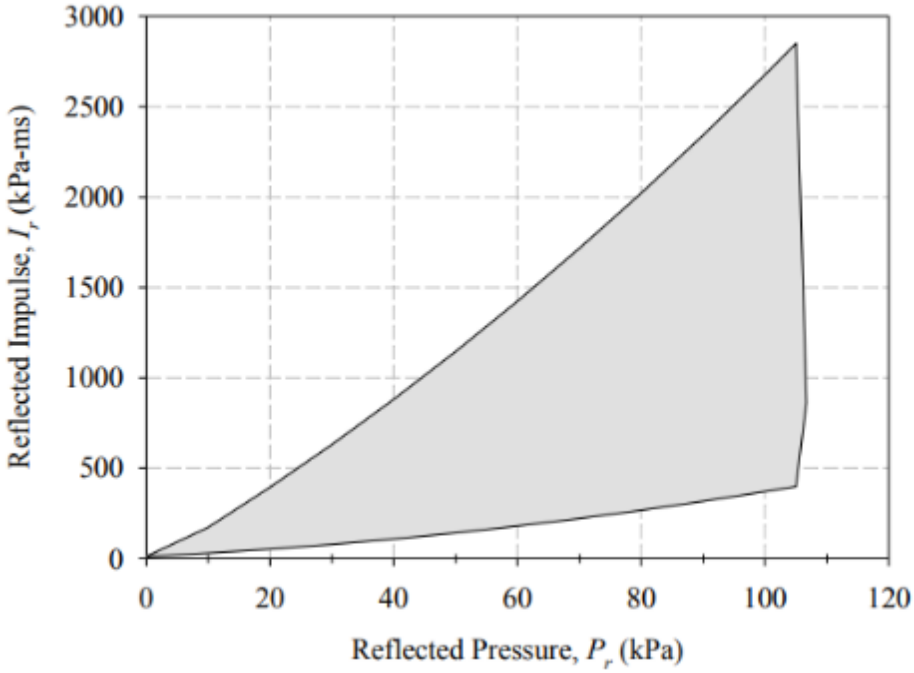

Figure 3.50: Range shock-tube capacities (Lloyd, 2015)

Figure 3.51: Data Acquisition system

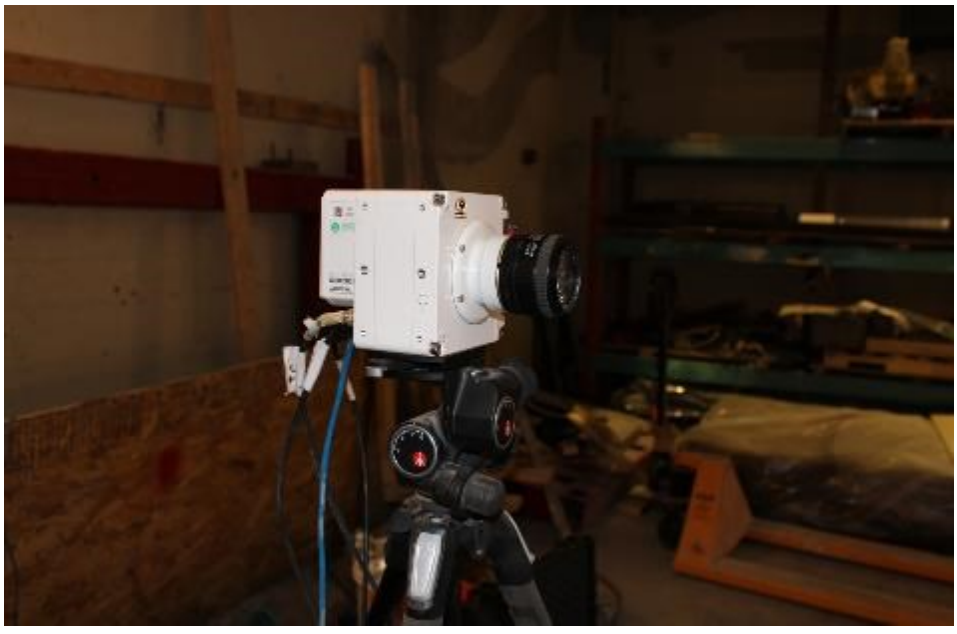

Figure 3.52: High-speed camera

Figure 3.53: Strain gage distribution

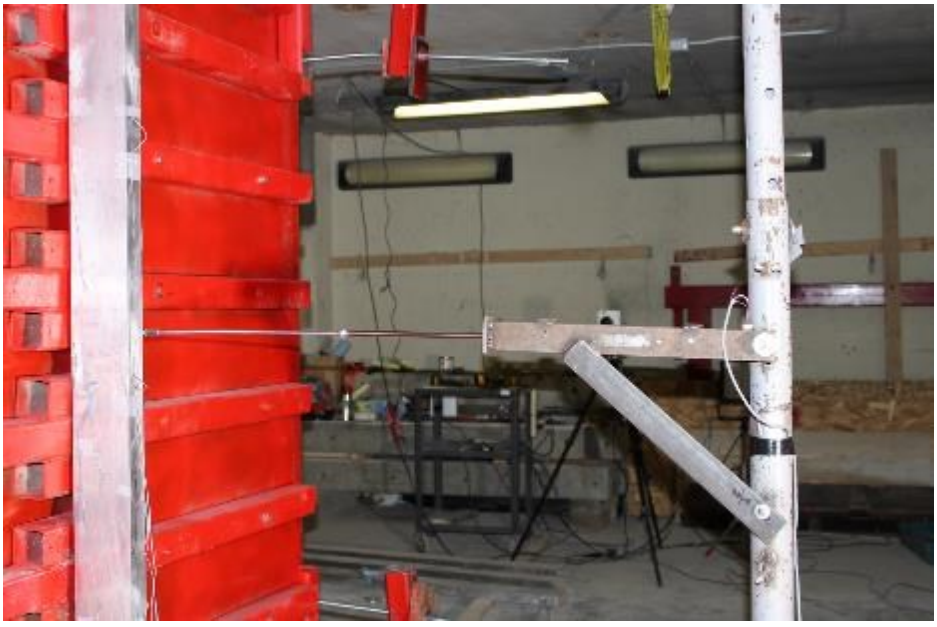

Figure 3.54: LVDT (Linear Variable Displacement Transducers)

Figure 3.55: Test setup

Figure 3.56: LTD attached to shock-tube opening by bolts

Figure 3.57: Simple support

Figure 3.58: Fixed support

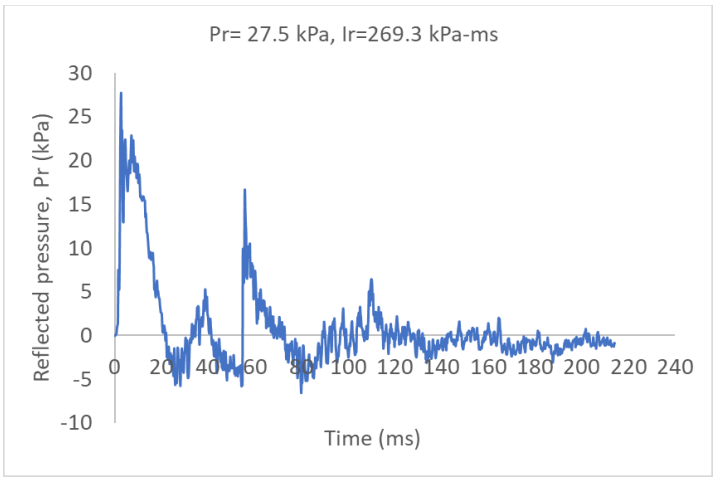

(a)

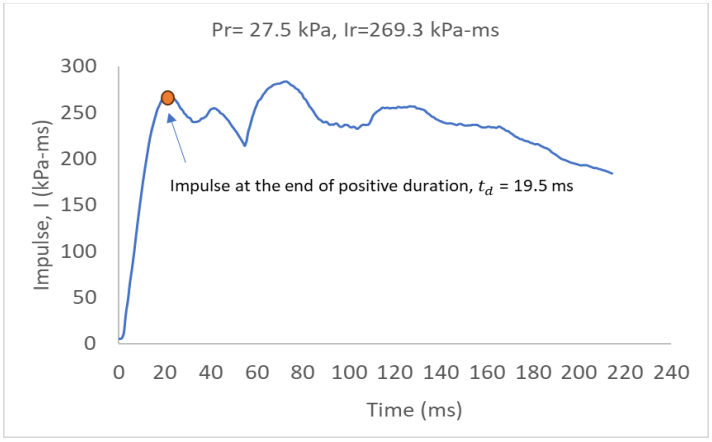

(b)

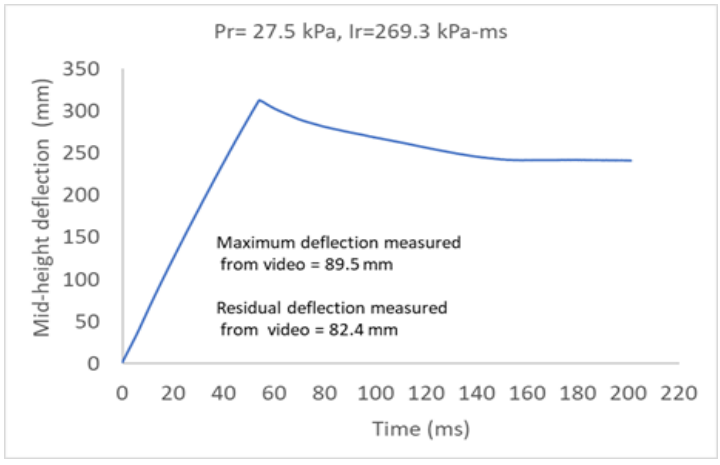

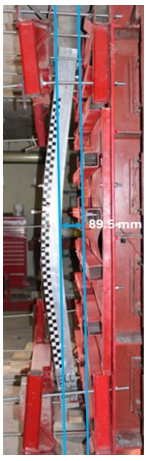

(c)

Figure 3.59: Tests results - Mullion 1F - shot 1 (a)Pressure-time history (b)Impulse-time history (c) Mid-height mullion deflection-time history

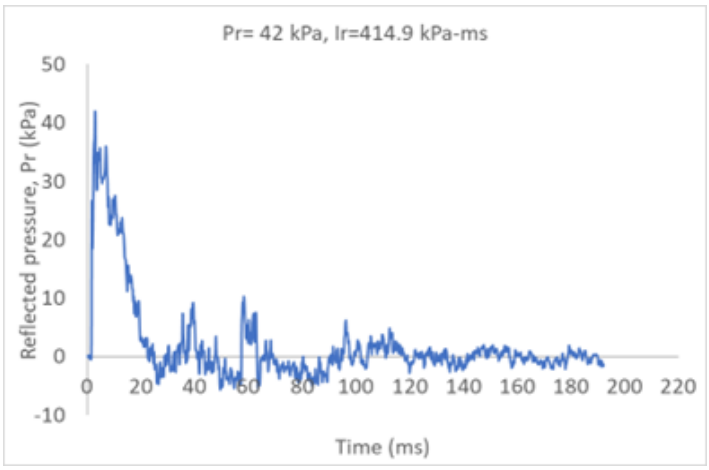

(a)

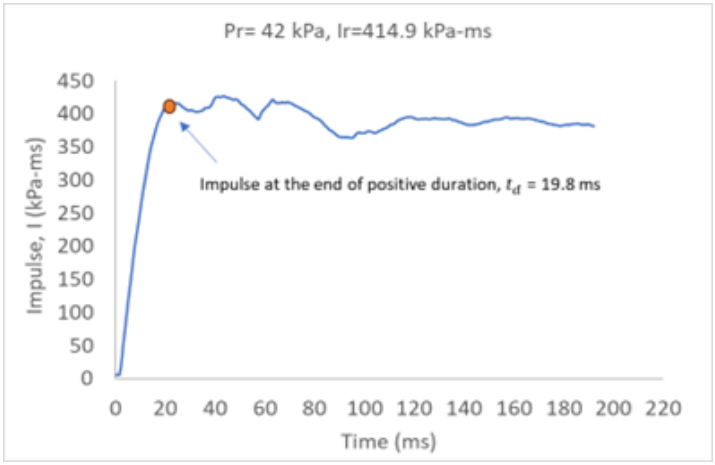

(b)

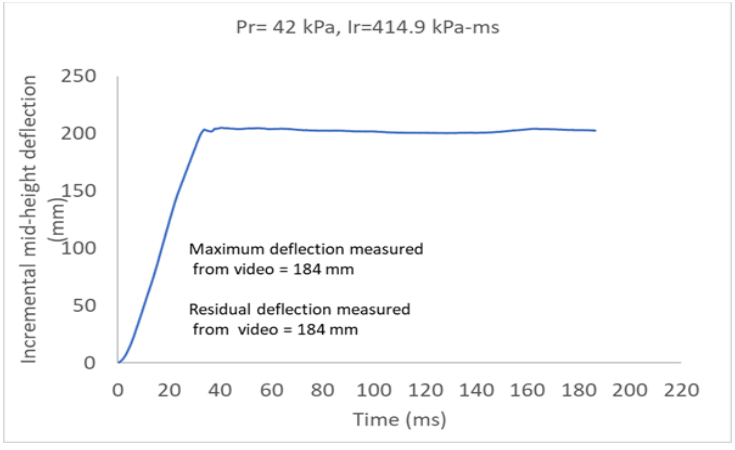

(c)

Figure 3.60: Tests results - Mullion 1F - Shot 2 (a)Pressure-time history (b)Impulse-time history (c) Incremental mid-height mullion deflection-time history

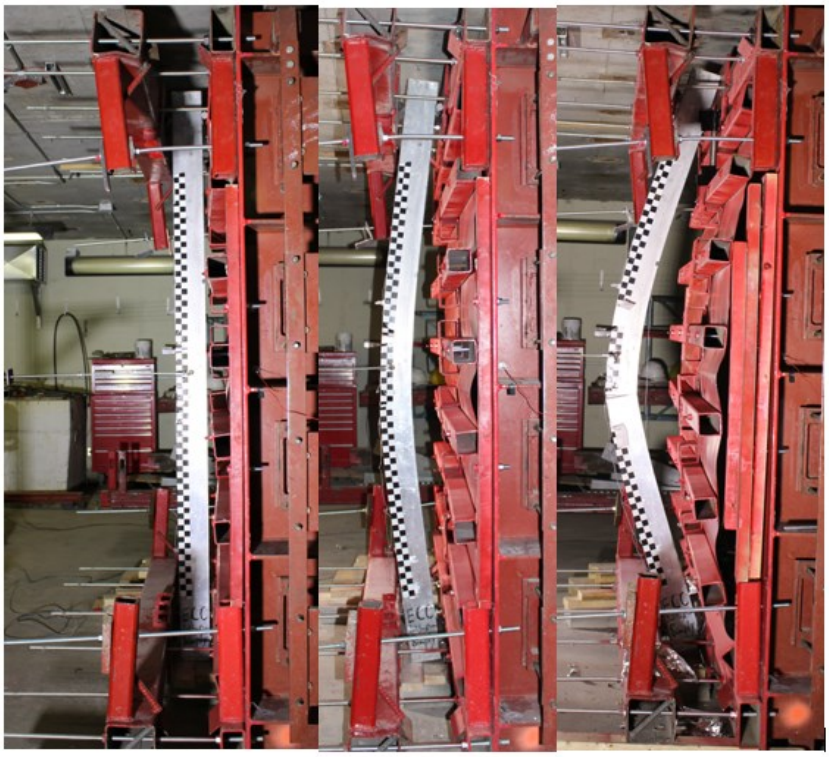

Before Testing Shot 1 Shot 2

Top Support Bottom Support

Sample Failure at 40 psi (276 KPa)

Figure 3.61: Mullion performance after blast load application-Mullion 1F

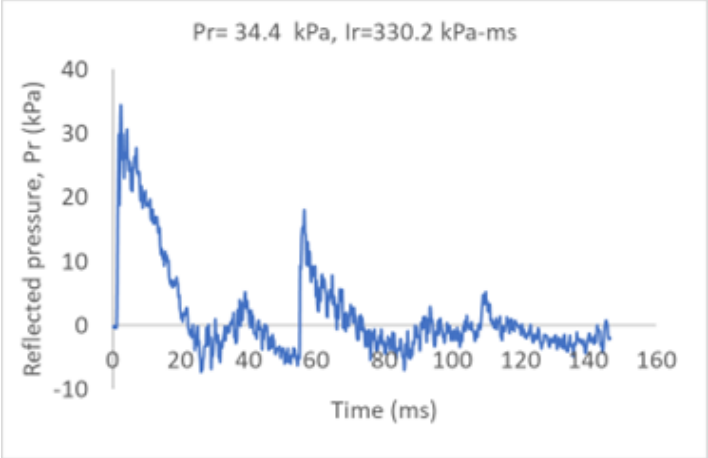

(a)

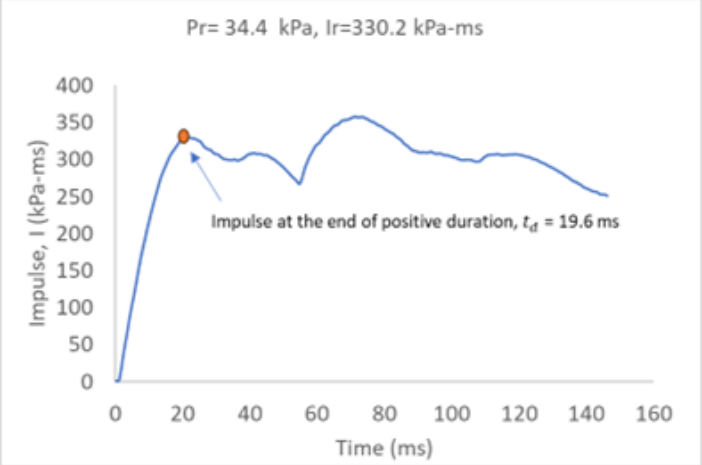

(b)

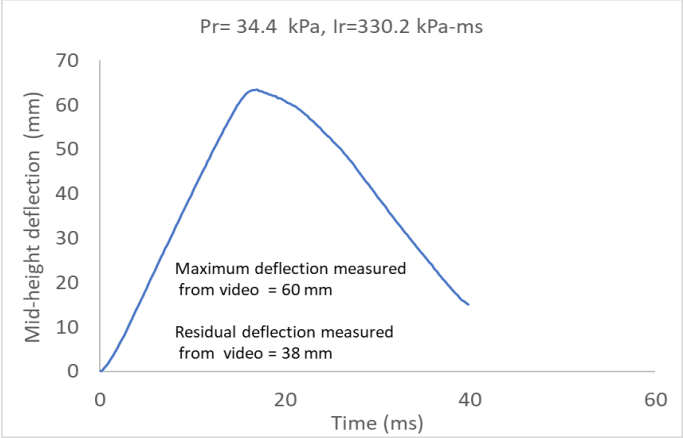

(c)

Figure 3.62: Tests results - Mullion 2FR - Shot 1 (a)Pressure-time history (b)Impulse-time history (c) Mid-height mullion deflection-time history

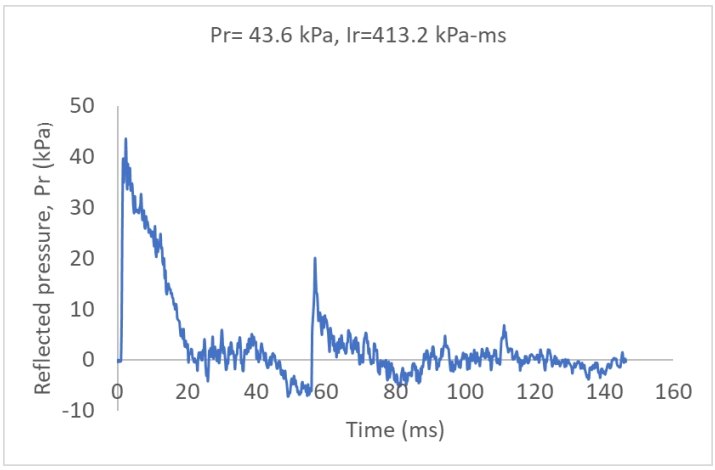

(a)

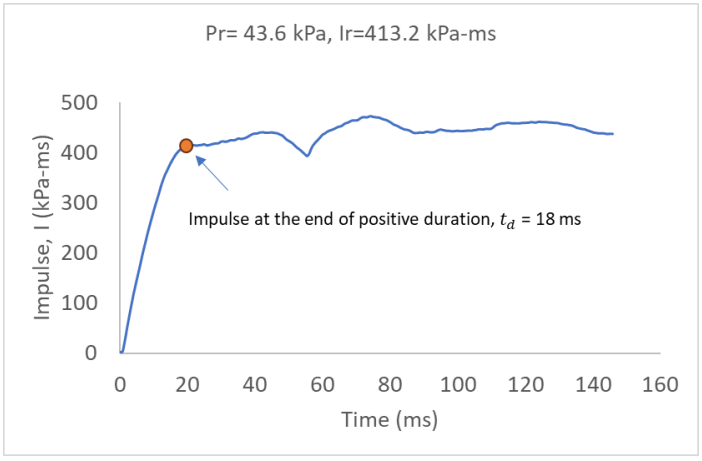

(b)

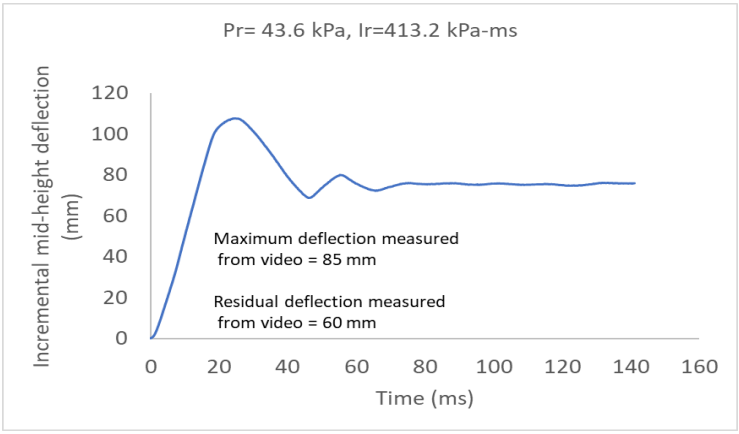

(c)

Figure 3.63: Tests results - Mullion 2FR - Shot 2 (a)Pressure-time history (b)Impulse-time history (c) Incremental mid-height mullion deflection-time history

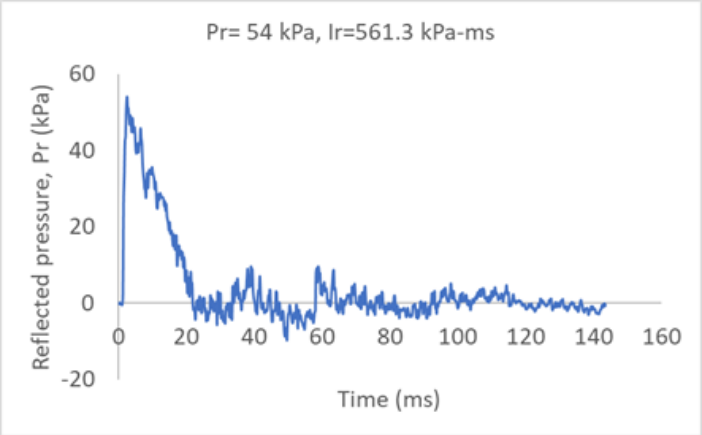

(a)

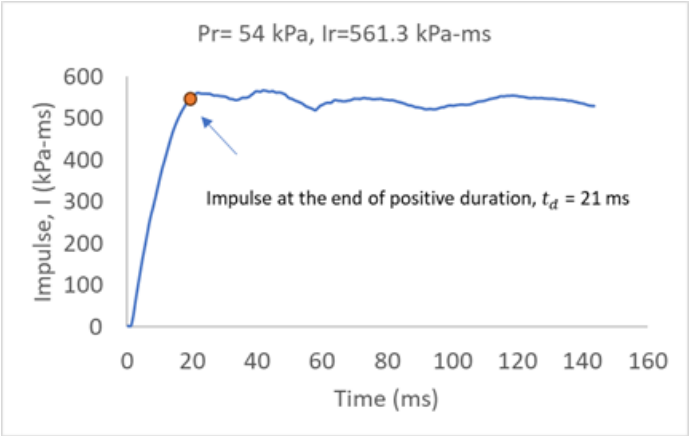

(b)

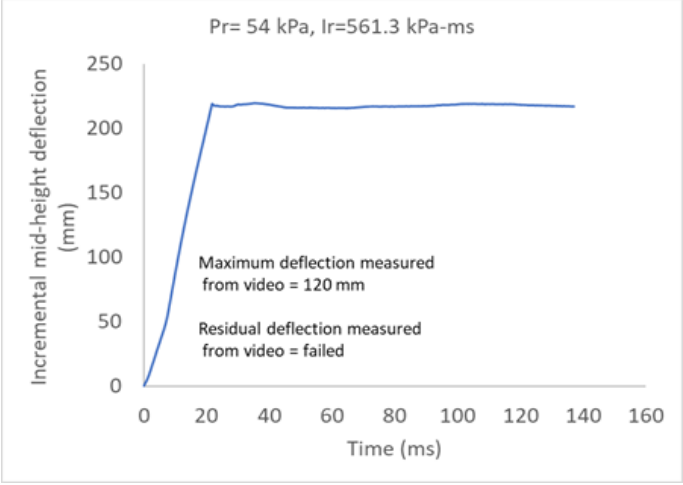

(c)

Figure 3.64: Tests results - Mullion 2FR - Shot 3 (a)Pressure-time history (b)Impulse-time history (c) Incremental mid-height mullion deflection-time history

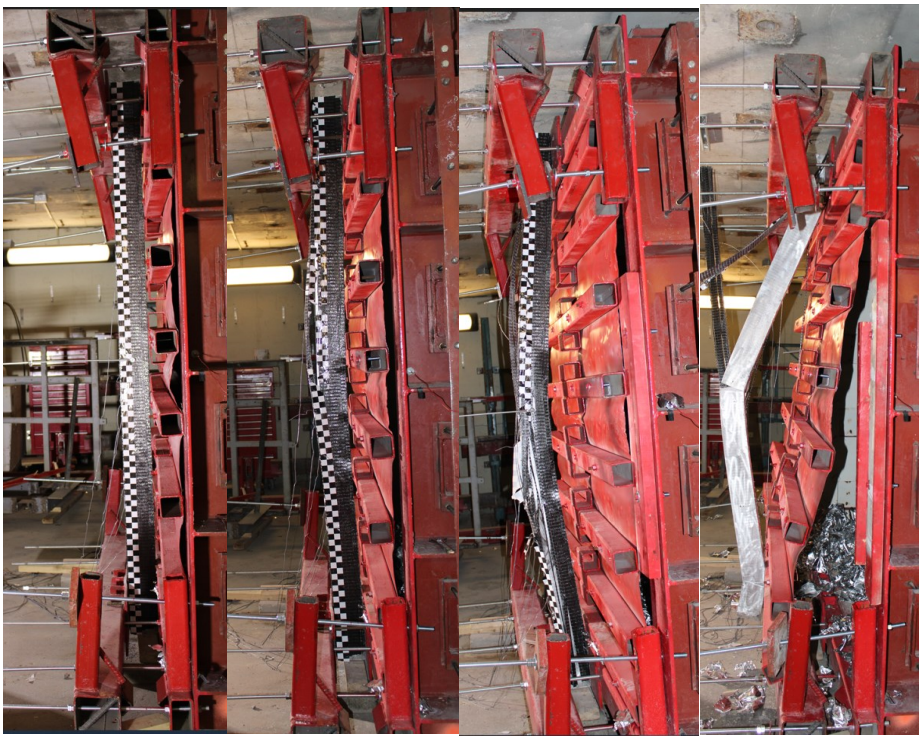

Before Testing Shot 1 Shot 2 Shot 3

Top Support Bottom Support

Sample Failure at 60 psi (414 KPa) (Plastic hinge failure)

Figure 3.65: Mullion performance after blast load application-Mullion 2FR

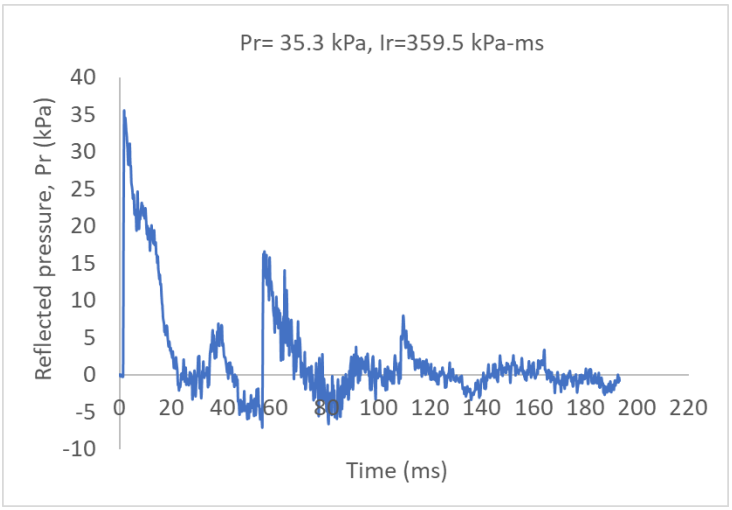

(a)

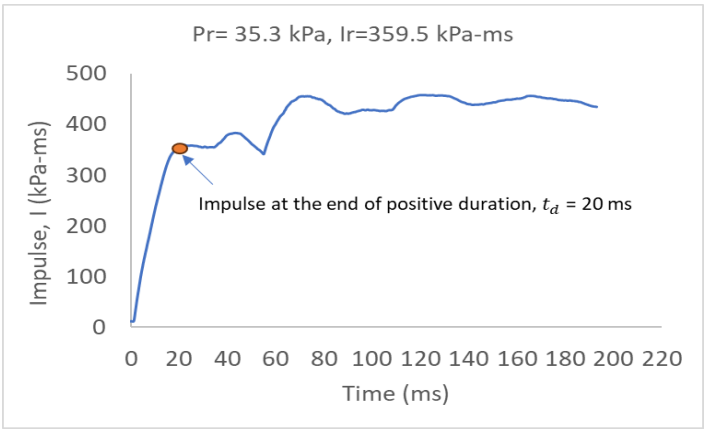

(b)

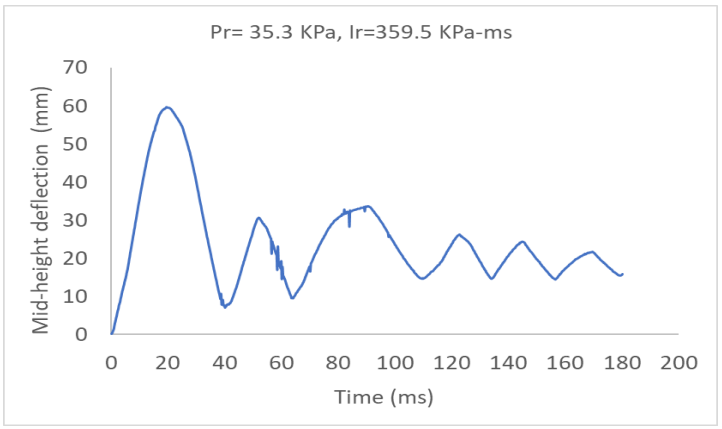

(c)

Figure 3.66: Tests results - Mullion 3F- Shot 1 (a)Pressure-time history (b)Impulse-time history (c) Mid-height mullion deflection-time history as recorded by LVDT

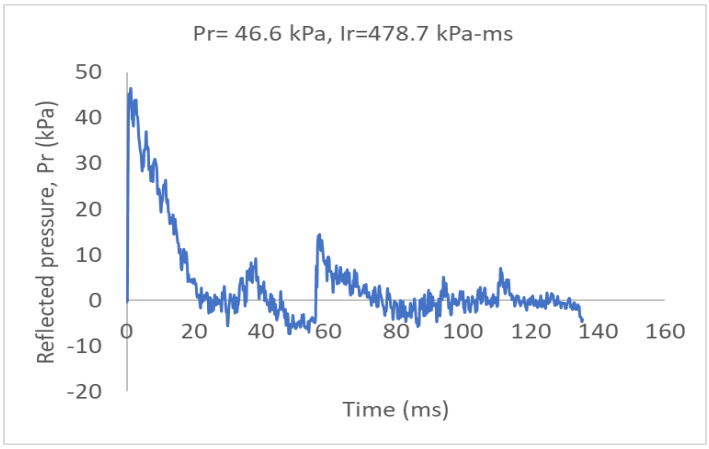

(a)

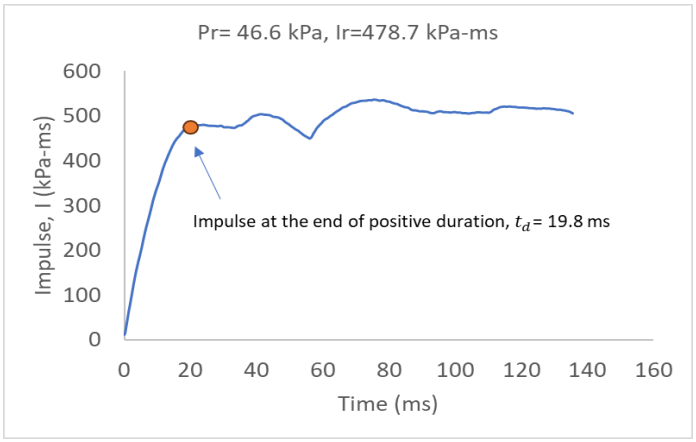

(b)

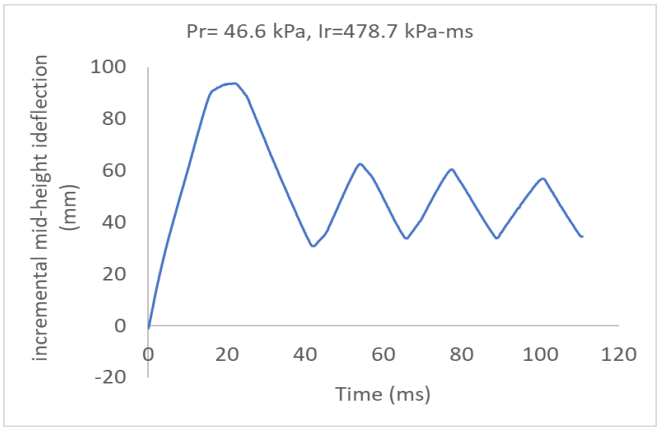

(c)

Figure 3.67: Tests results - Mullion 3F - Shot 2 (a)Pressure-time history (b)Impulse-time history (c) Incremental mid-height mullion deflection-time history as recorded by LVDT

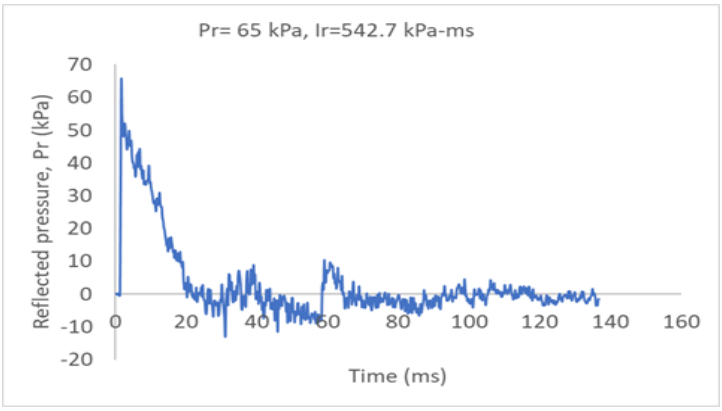

(a)

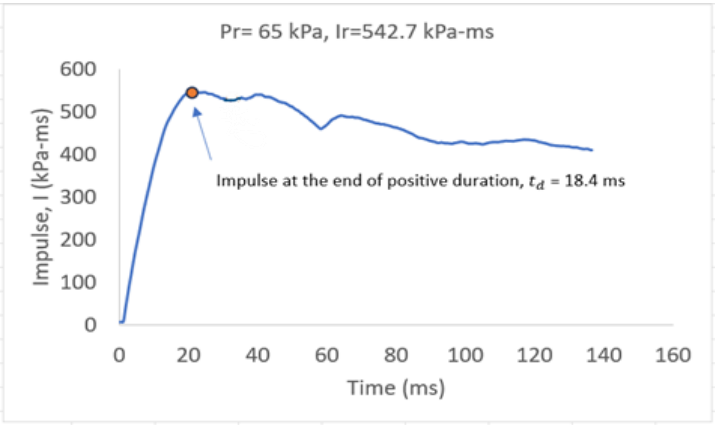

(b)

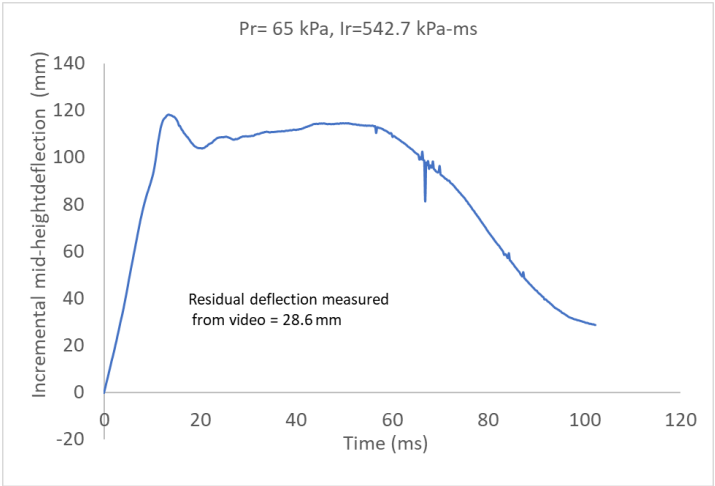

(c)

Figure 3.68: Tests results - Mullion 3F - Shot 3 (a)Pressure-time history (b)Impulse-time history (c) Incremental mid-height mullion deflection-time history as recorded by LVDT

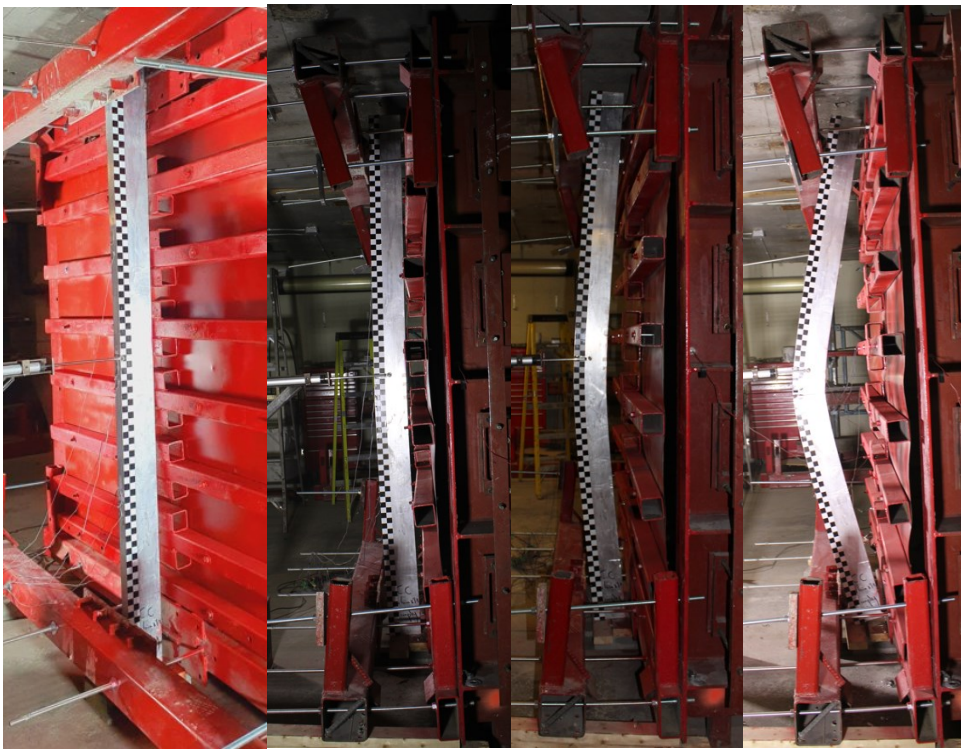

Before Testing Shot 1 Shot 2 Shot 3

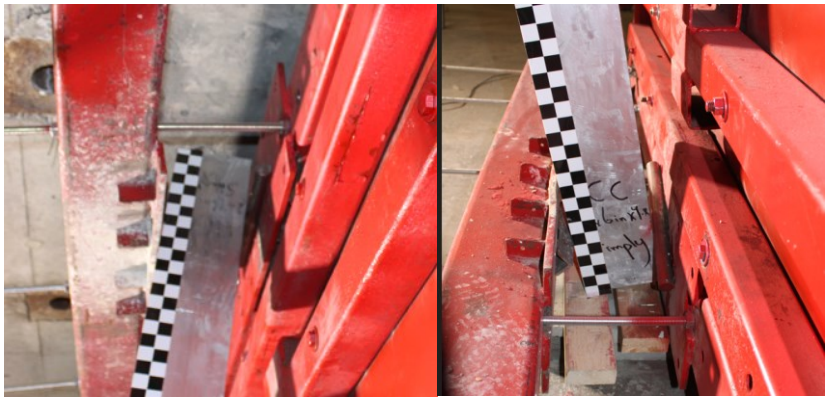

Top Support Bottom Support

Sample Failure at 60 psi (414 KPa)

Figure 3.69: Mullion performance after blast load application-Mullion 3F

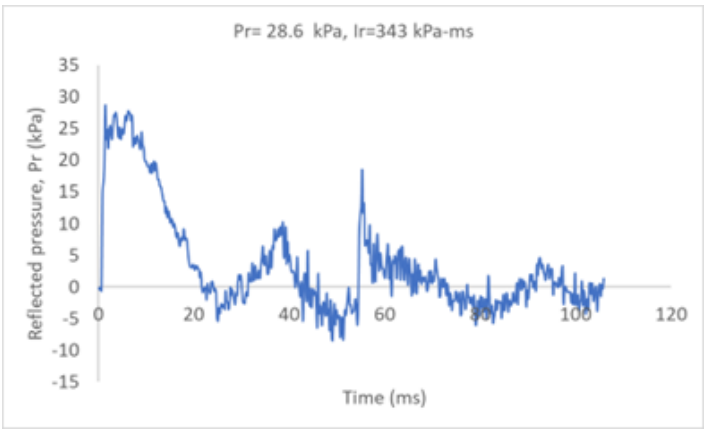

(a)

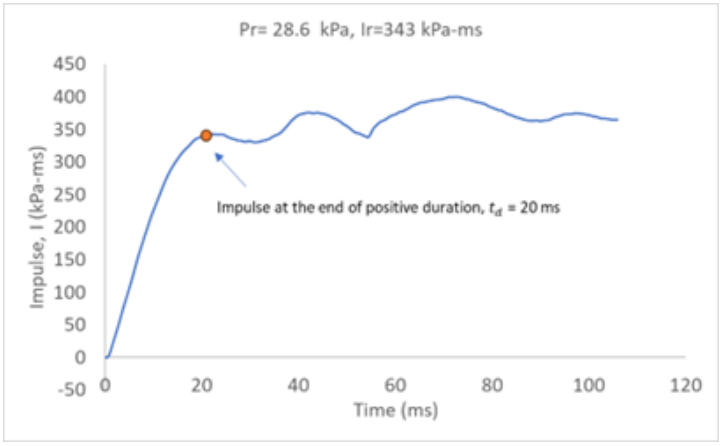

(b)

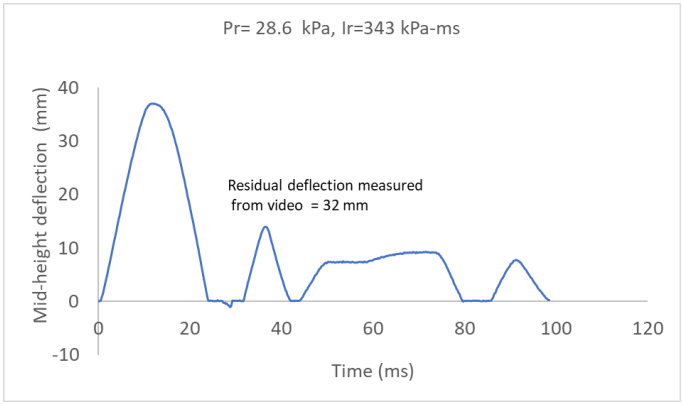

(c)

Figure 3.70: Tests results - Mullion 4FR - Shot 1 (a)Pressure-time history (b)Impulse-time history (c) Mid-height mullion deflection-time history as recorded by LVDT

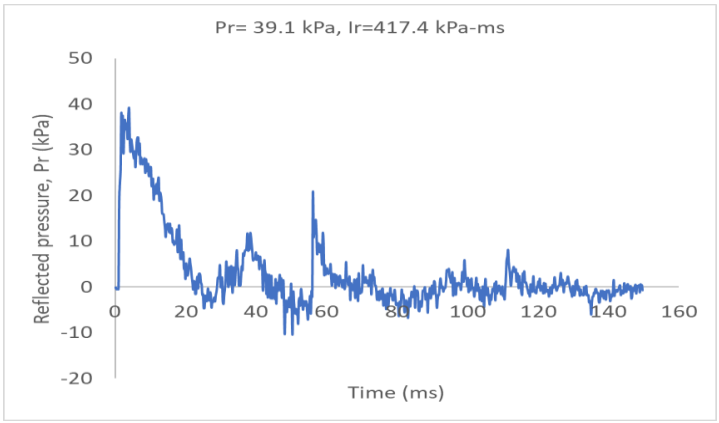

(a)

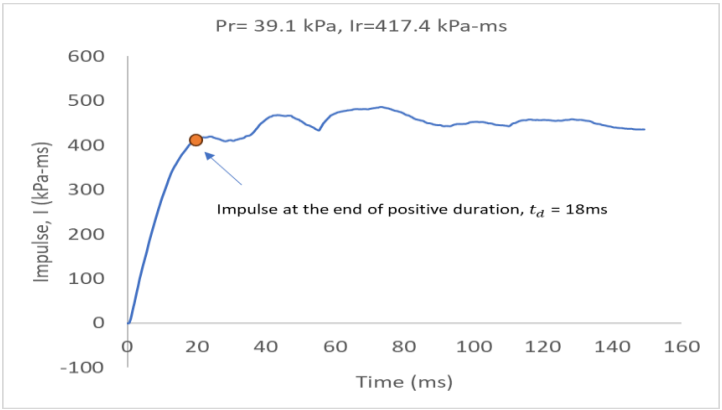

(b)

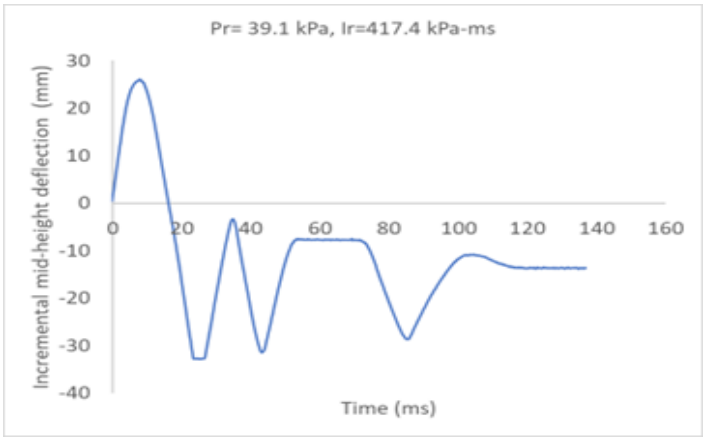

(c)

Figure 3.71: Tests results - Mullion 4FR - Shot 2 (a)Pressure-time history (b)Impulse-time history (c) Incremental mid-height mullion deflection-time history as recorded by LVDT

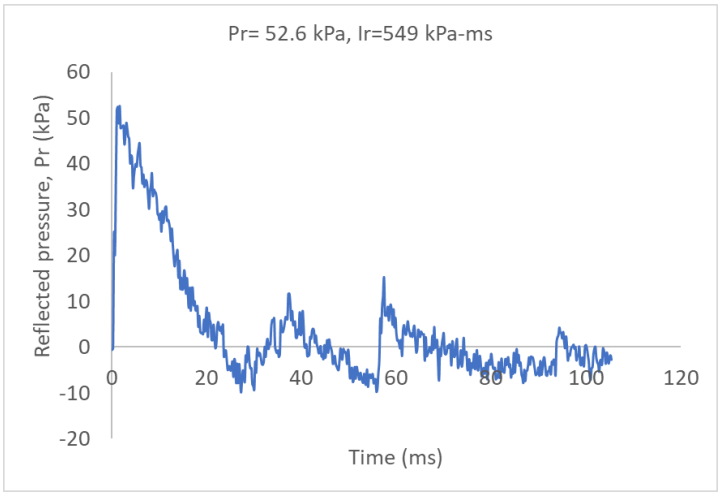

(a)

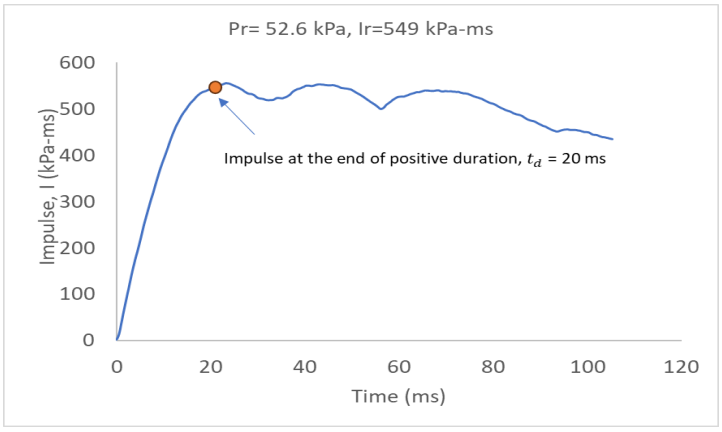

(b)

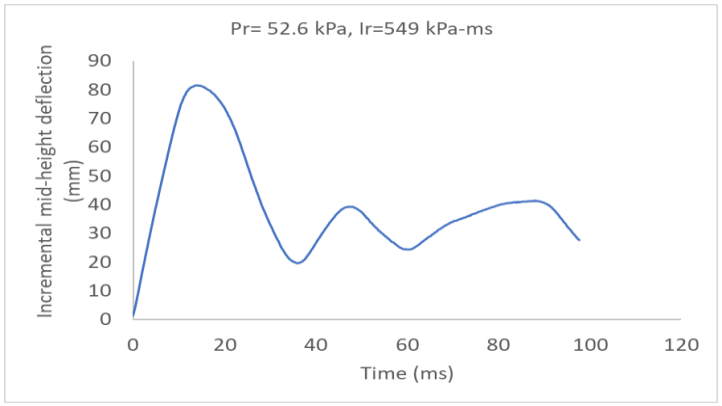

(c)

Figure 3.72: Tests results - Mullion 4FR - Shot 3 (a)Pressure-time history (b)Impulse-time history (c) Incremental mid-height mullion deflection-time history as recorded by LVDT

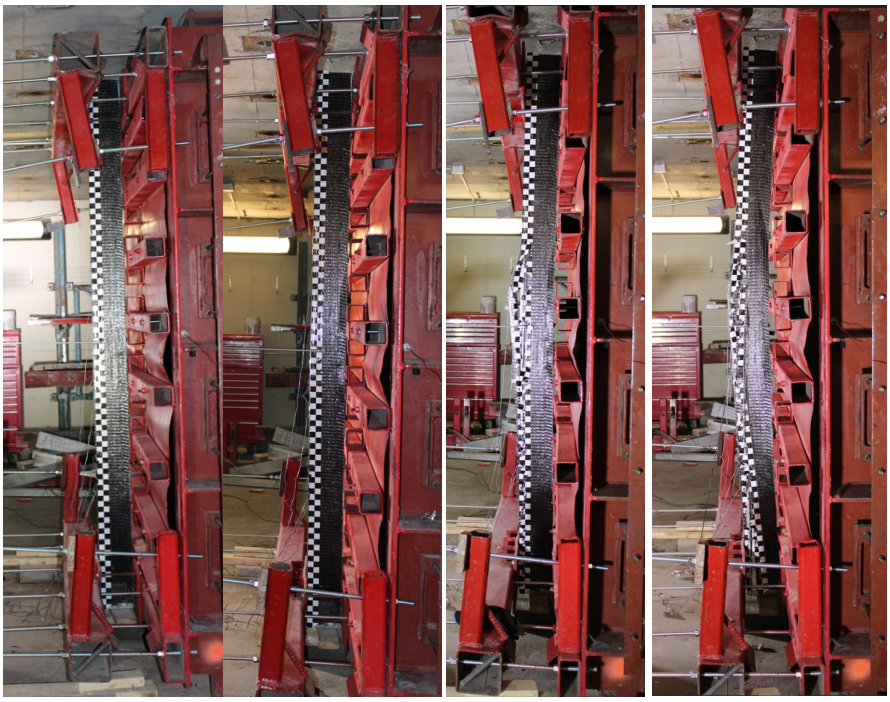

Before Testing Shot 1 Shot 2 Shot 3

Top Support Bottom Support

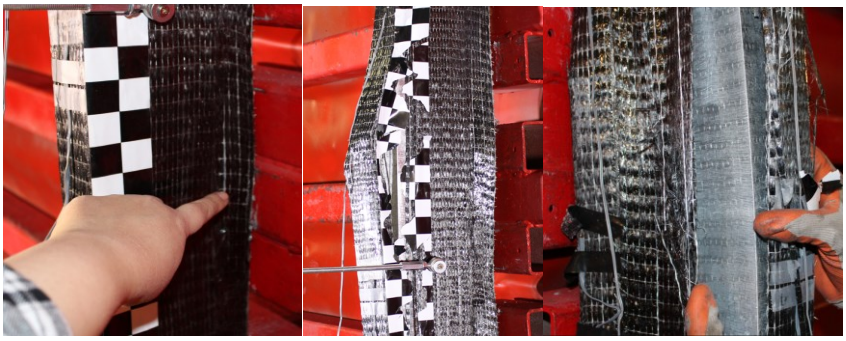

Stages of CFRP debonding

Figure 3.73: Mullion performance after blast load application-Mullion 4FR

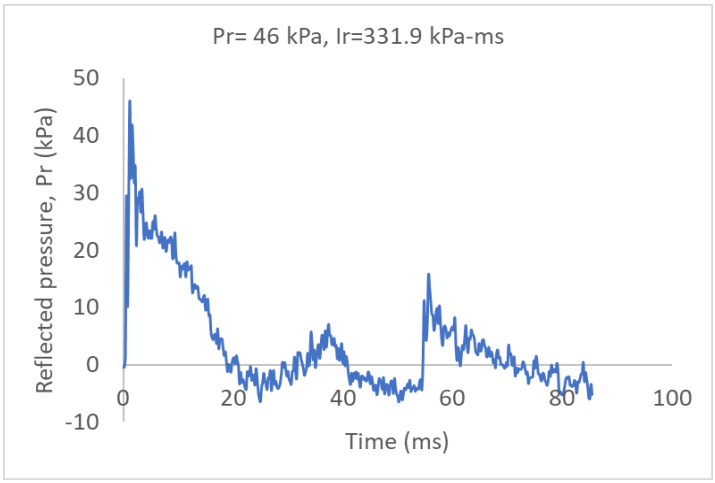

(a)

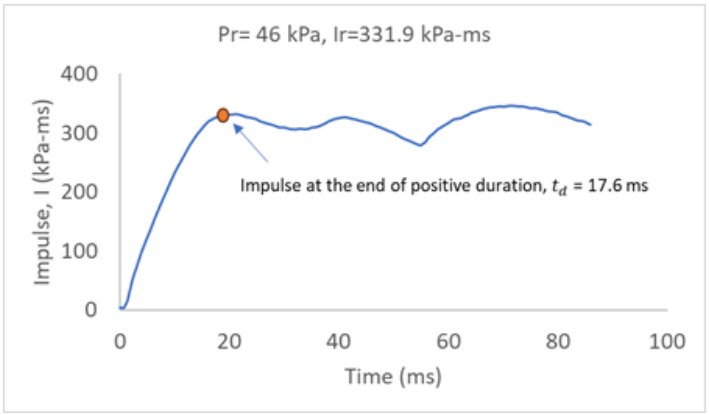

(b)

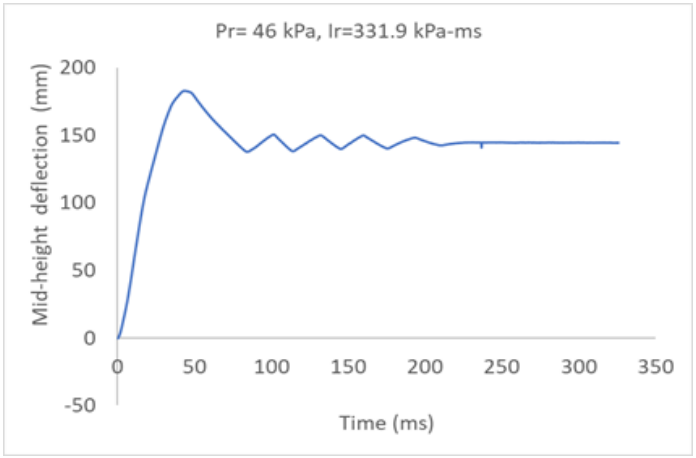

(c)

Figure 3.74: Tests results - Mullion 5F- Shot 1 (a)Pressure-time history (b)Impulse-time history (c) Mid-height mullion deflection-time history as recorded by LVDT

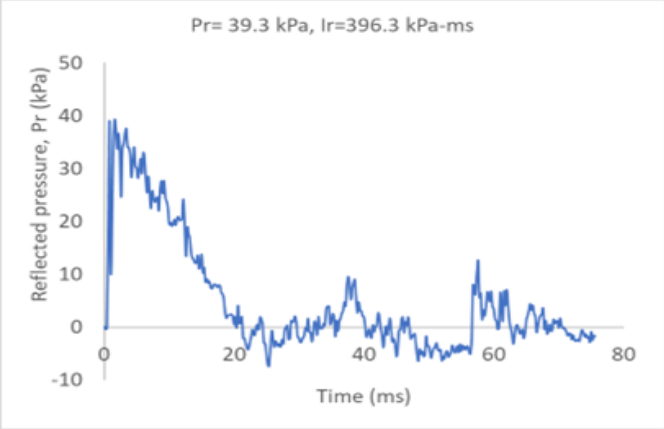

(a)

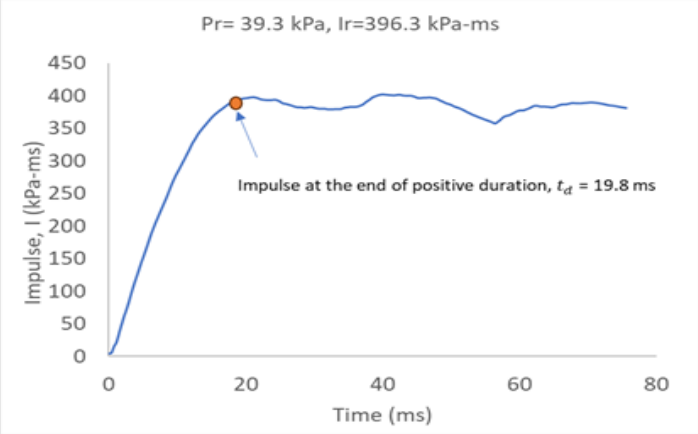

(b)

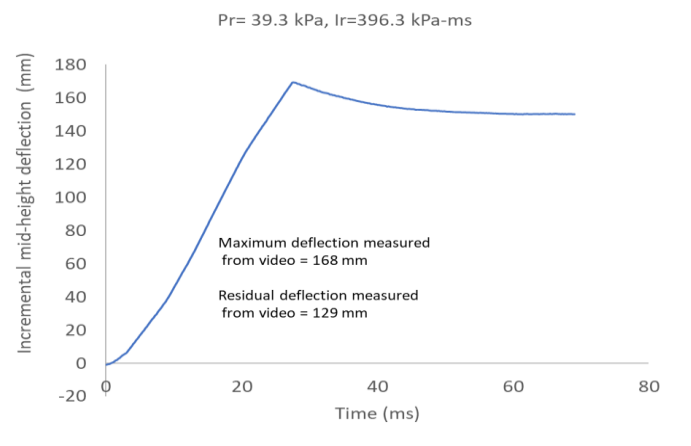

(c)

Figure 3.75: Tests results - Mullion 5F - Shot 2 (a)Pressure-time history (b)Impulse-time history (c) Incremental mid-height mullion deflection-time history

Before Testing Shot 1 Shot 2

Top Support Bottom Support

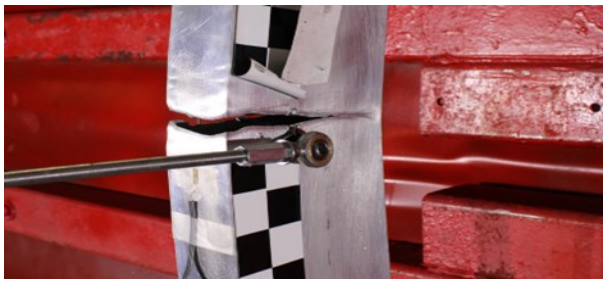

Sample Failure at 40 psi (276 KPa)

Figure 3.76: Mullion performance after blast load application-Mullion 5F

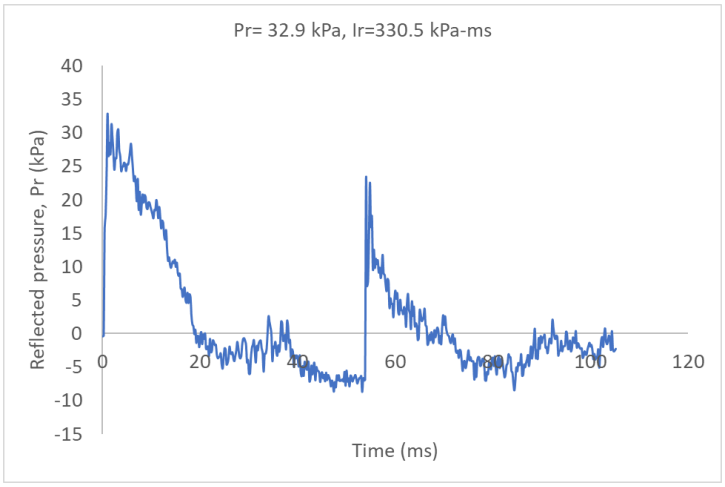

(a)

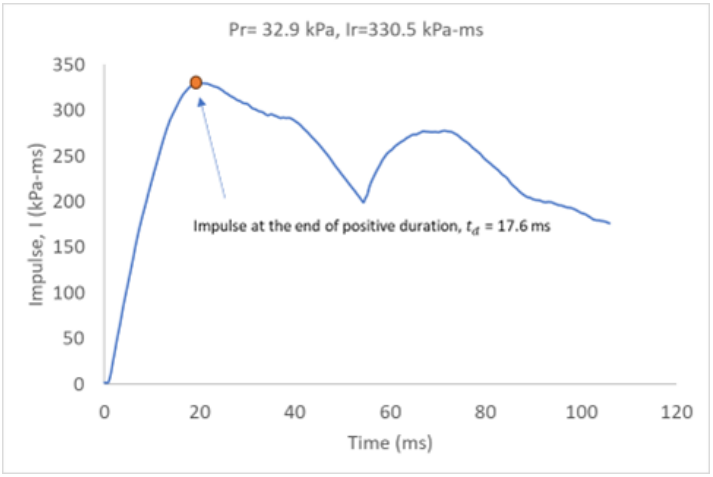

(b)

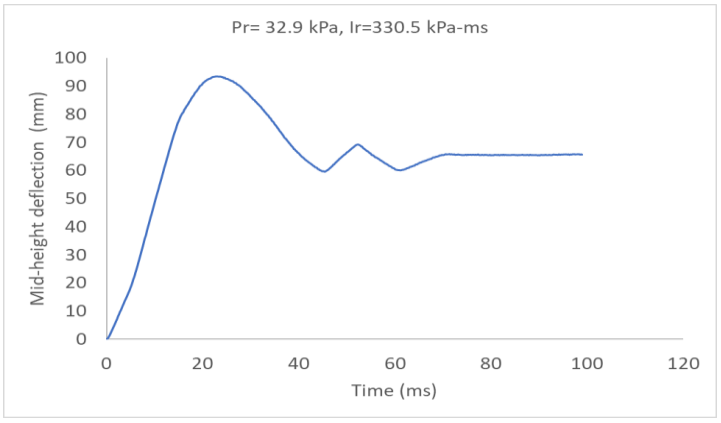

(c)

Figure 3.77: Tests results - Mullion 6F - Shot 1 (a)Pressure-time history (b)Impulse-time history (c) Mid-height mullion deflection-time history as recorded by LVDT

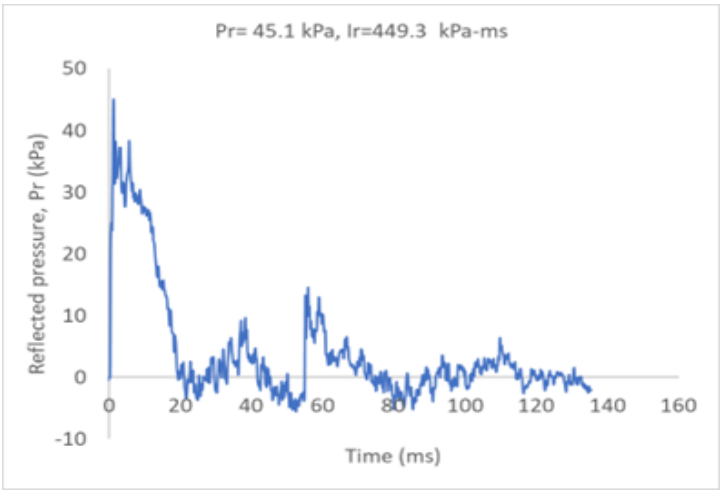

(a)

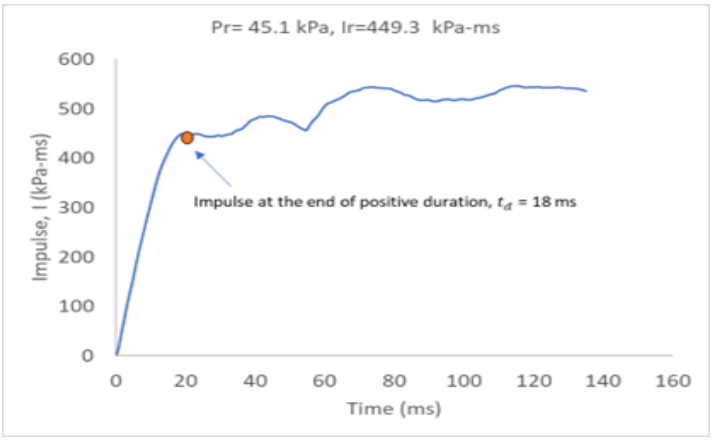

(b)

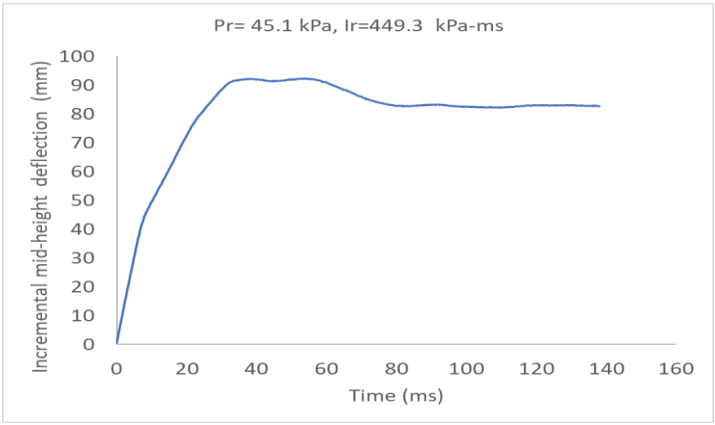

(c)

Figure 3.78: Tests results - Mullion 6F - Shot 2 (a)Pressure-time history (b)Impulse-time history (c) Incremental mid-height mullion deflection-time history as recorded by LVDT

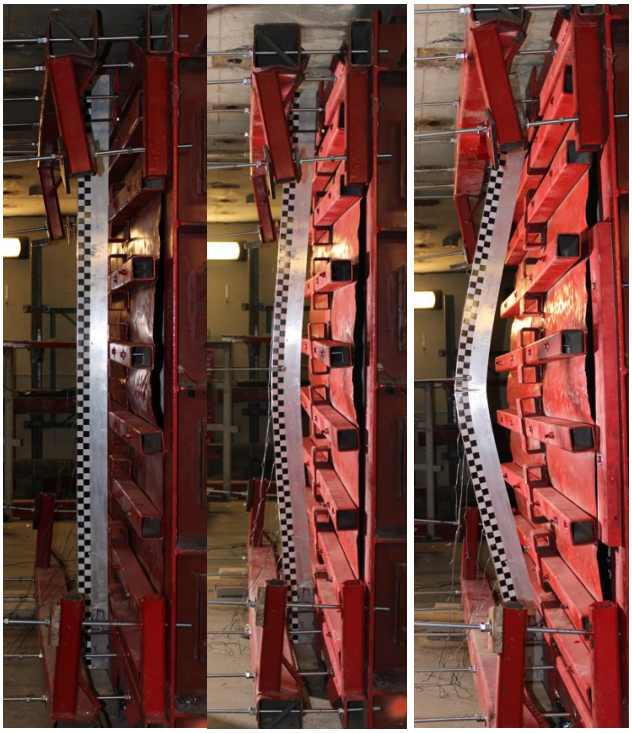

Before Testing Shot 1 Shot 2

Top Support Bottom Support

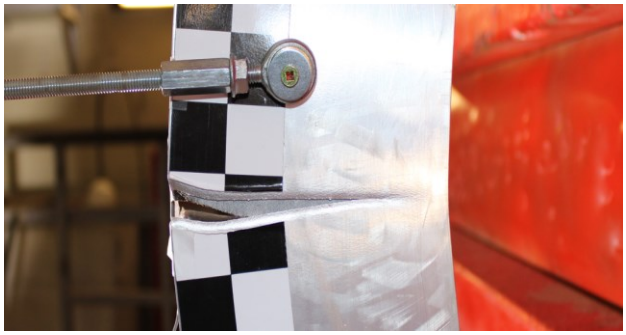

Sample Failure at 40 psi (276 KPa)

Figure 3.79: Mullion performance after blast load application-Mullion 6F

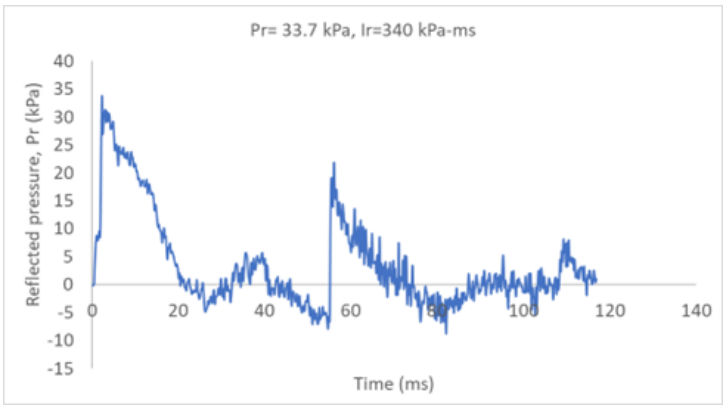

(a)

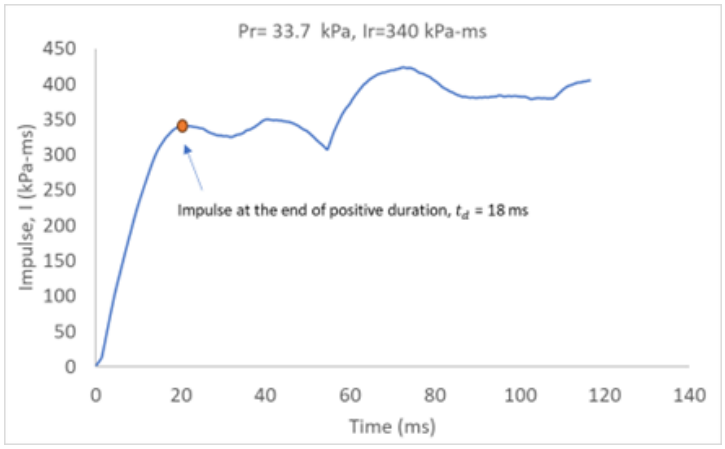

(b)

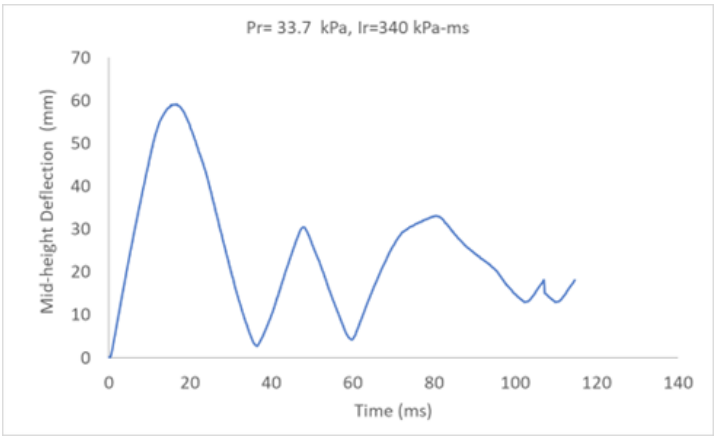

(c)

Figure 3.80: Tests results - Mullion 7F - Shot 1 (a)Pressure-time history (b)Impulse-time history (c) Mid-height mullion deflection-time history as recorded by LVDT

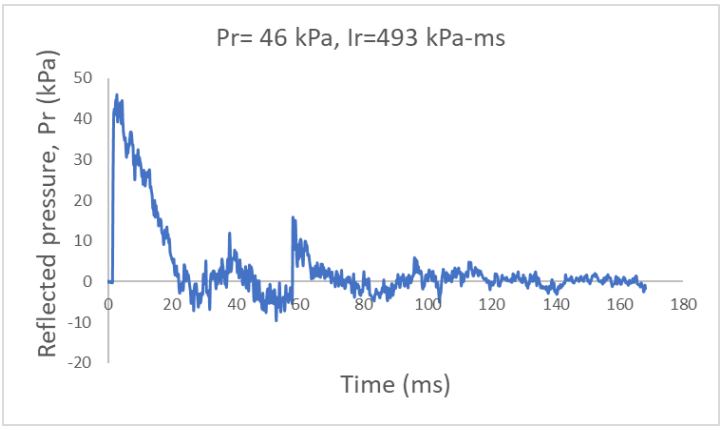

(a)

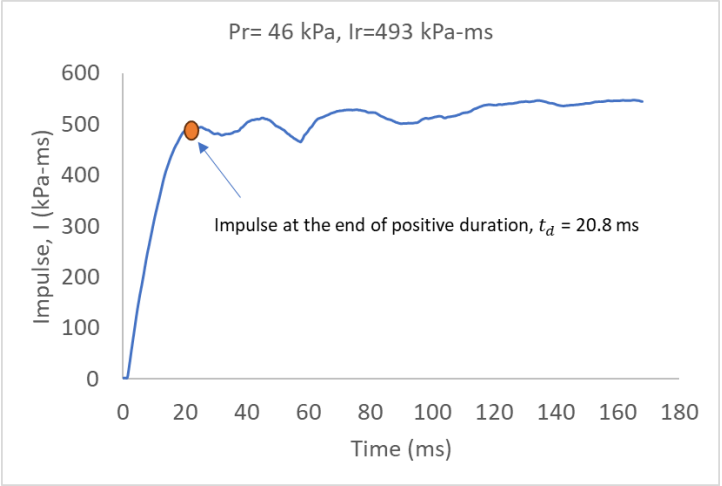

(b)

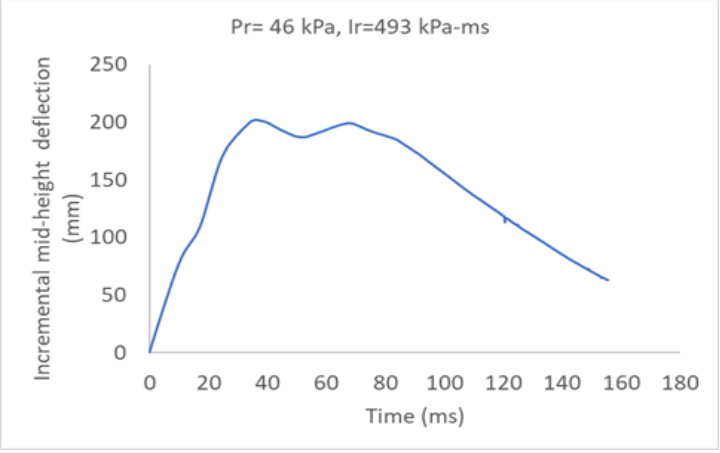

(c)

Figure 3.81: Tests results - Mullion 7F - Shot 2 (a)Pressure-time history (b)Impulse-time history (c) Incremental mid-height mullion deflection-time history as recorded by LVDT

Before Testing Shot 1 Shot 2

Top Support Bottom Support

Sample Failure at 40 psi (276 KPa)

Figure 3.82: Mullion performance after blast load application-Mullion 7F

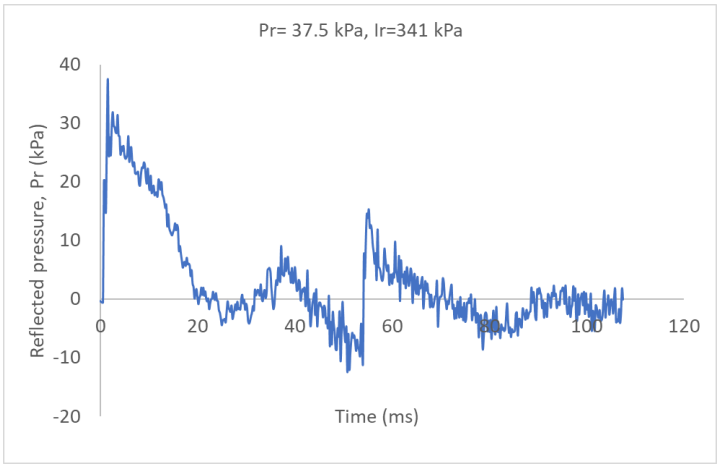

(a)

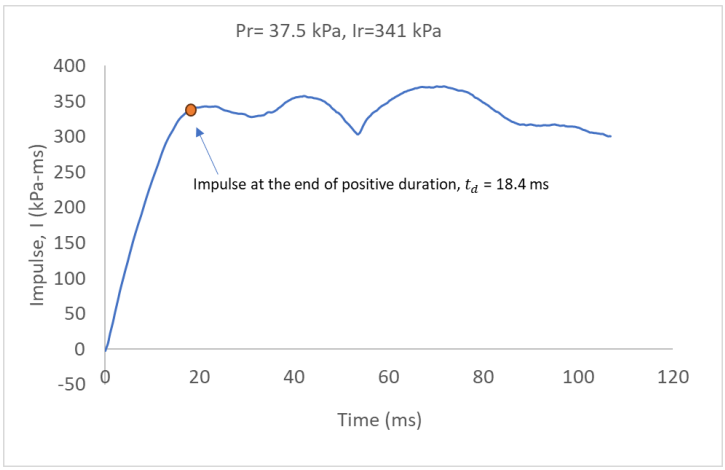

(b)

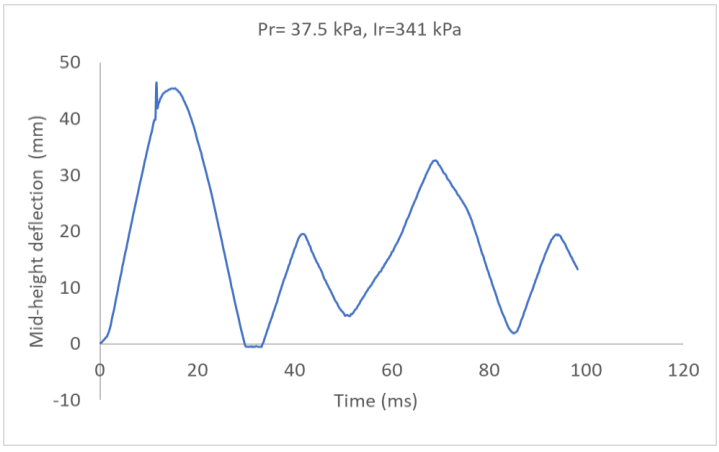

(c)

Figure 3.83: Tests results - Mullion 8F - Shot 1 (a)Pressure-time history (b)Impulse-time history (c) Mid-height mullion deflection-time history as recorded by LVDT

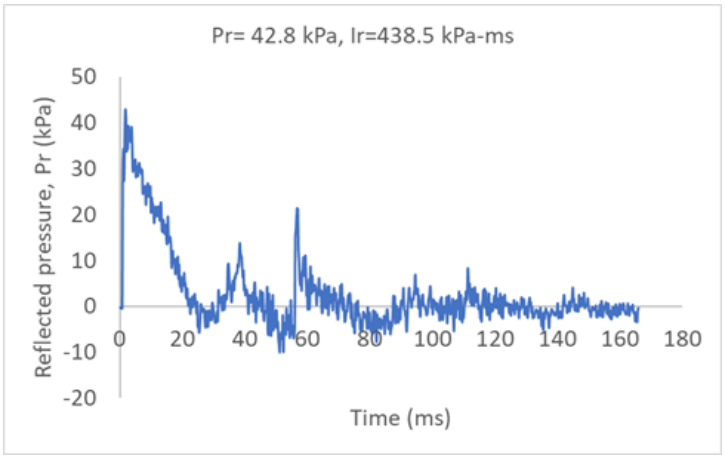

(a)

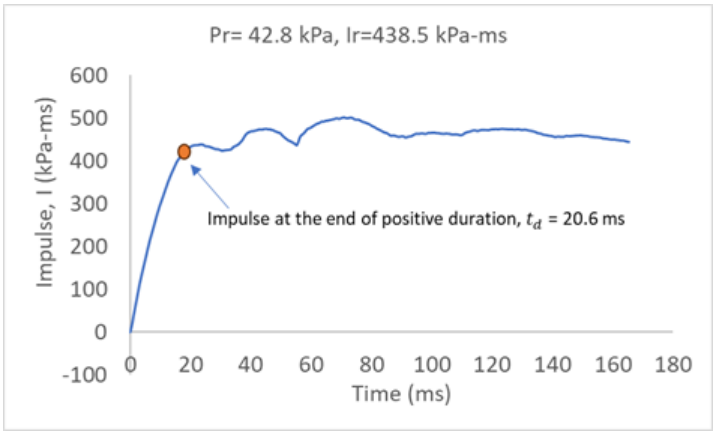

(b)

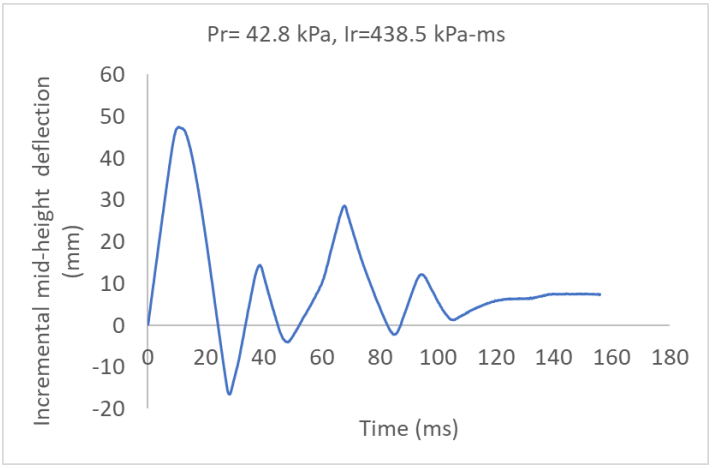

(c)

Figure 3.84: Tests results - Mullion 8F - Shot 2 (a)Pressure-time history (b)Impulse-time history (c) Incremental mid-height mullion deflection-time history as recorded by LVDT

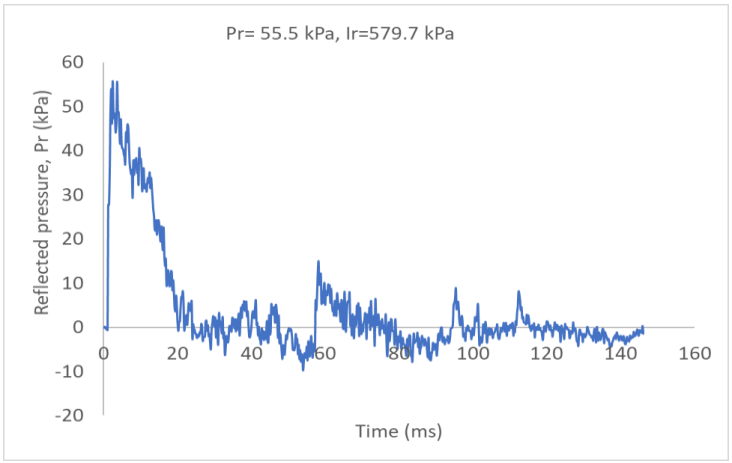

(a)

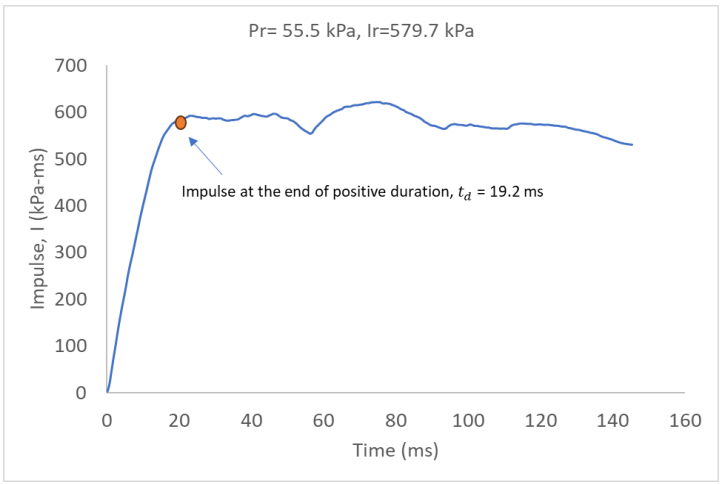

(b)

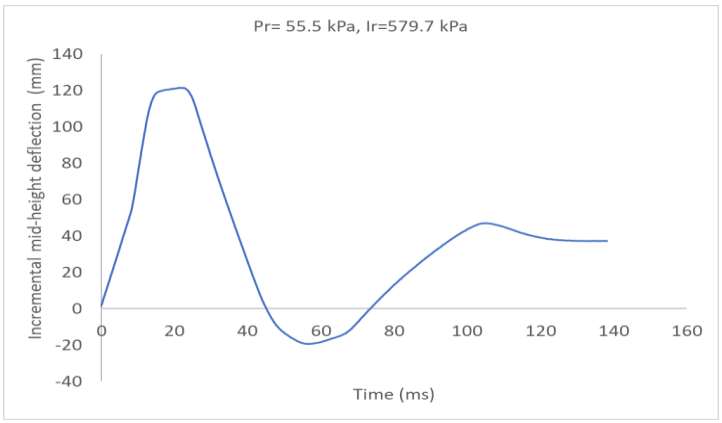

(c)

Figure 3.85: Tests results - Mullion 8F - Shot 3 (a)Pressure-time history (b)Impulse-time history (c) Incremental mid-height mullion deflection-time history as recorded by LVDT

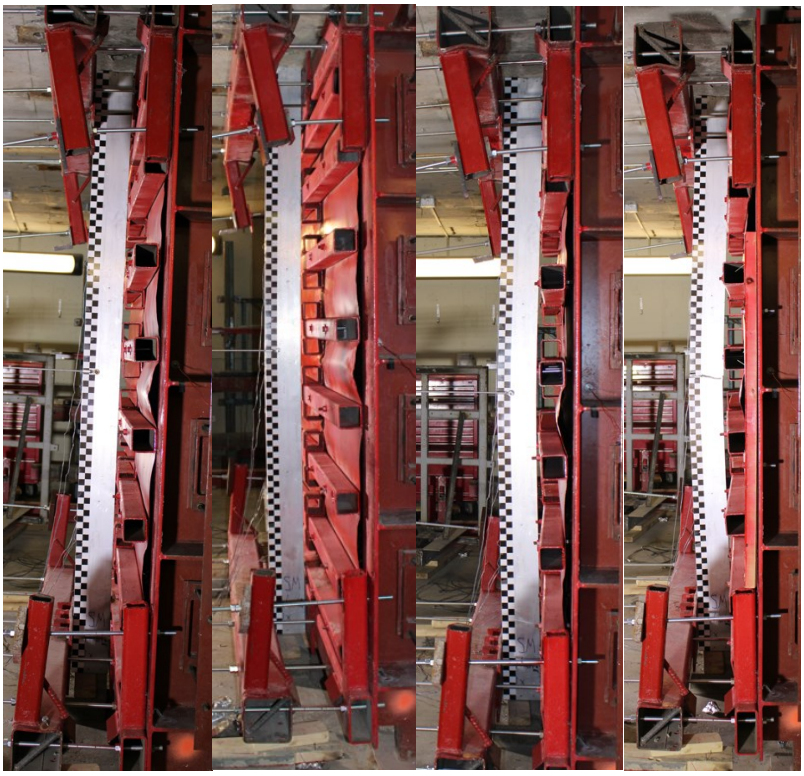

Before Testing Shot 1 Shot 2 Shot 3

Top Support Bottom Support

Sample Failure at 60 psi (414 KPa)

Figure 3.86: Mullion performance after blast load application-Mullion 8F

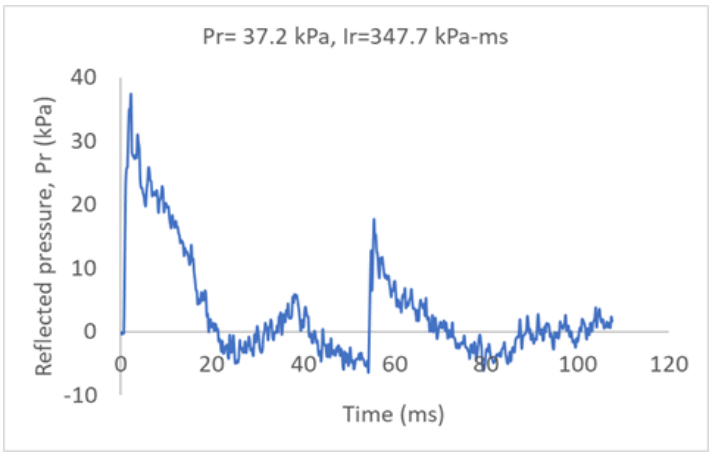

(a)

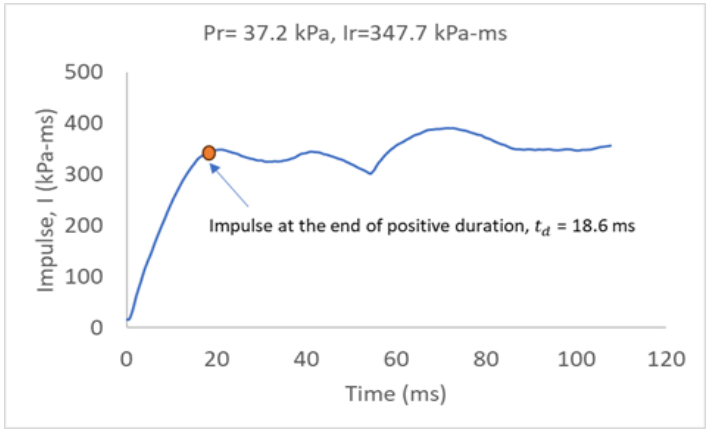

(b)

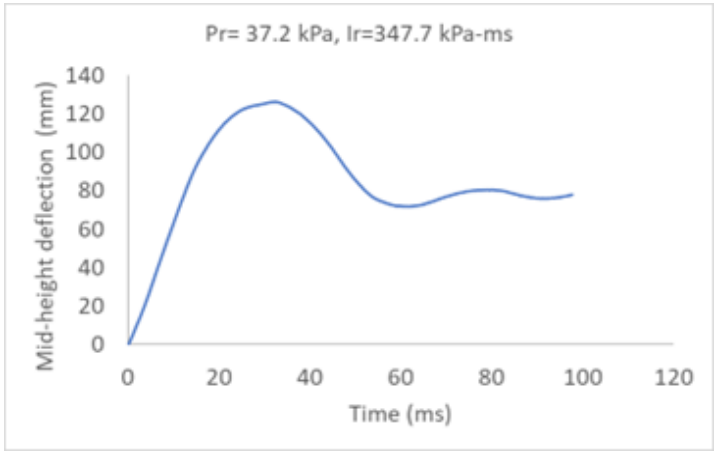

(c)

Figure 3.87: Tests results - Mullion 9FH- Shot 1 (a)Pressure-time history (b)Impulse-time history (c) Mid-height mullion deflection-time history as recorded by LVDT

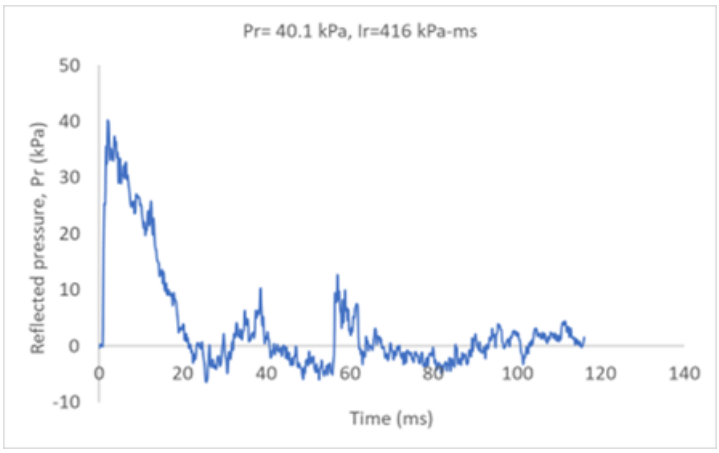

(a)

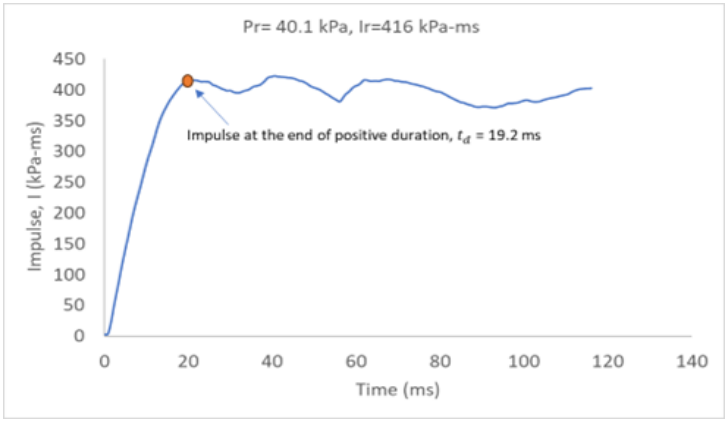

(b)

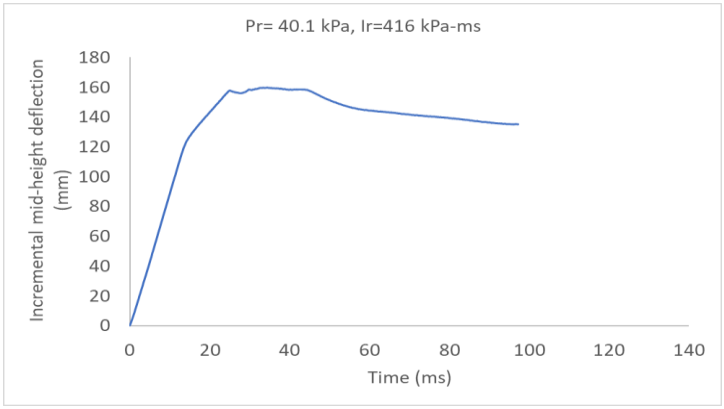

(c)

Figure 3.88: Tests results - Mullion 9FH- Shot 2 (a)Pressure-time history (b)Impulse-time history (c) Incremental mid-height mullion deflection-time history as recorded by LVDT

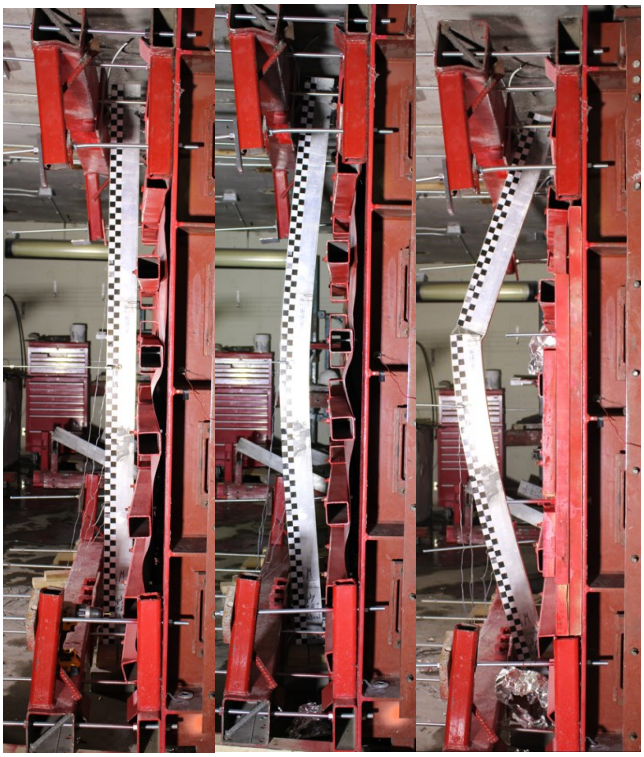

Before Testing Shot 1 Shot 2

Top Support Bottom Support

Sample Failure at 40 psi (276 KPa)

Figure 3.89: Mullion performance after blast load application-Mullion 9FH

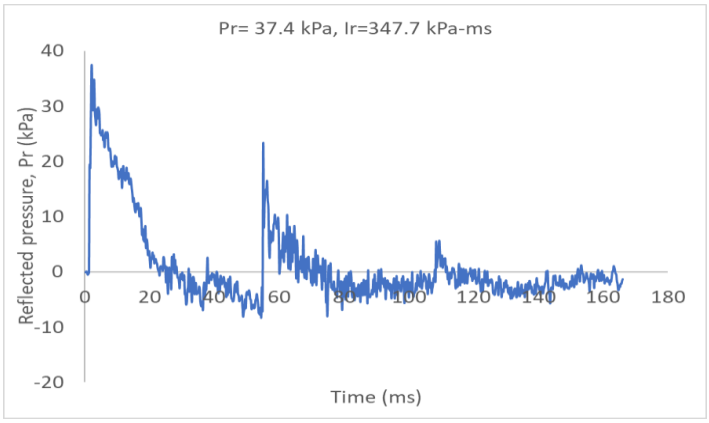

(a)

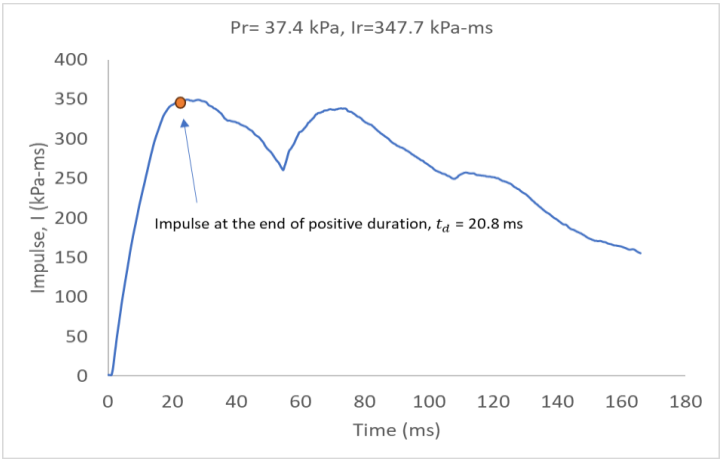

(b)

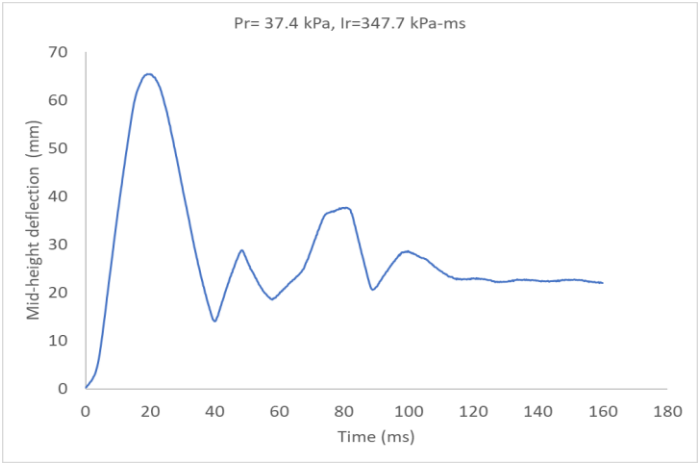

(c)

Figure 3.90: Tests results - Mullion 10FH- Shot 1(a)Pressure-time history (b)Impulse-time history (c) Mid-height mullion deflection-time history as recorded by LVDT

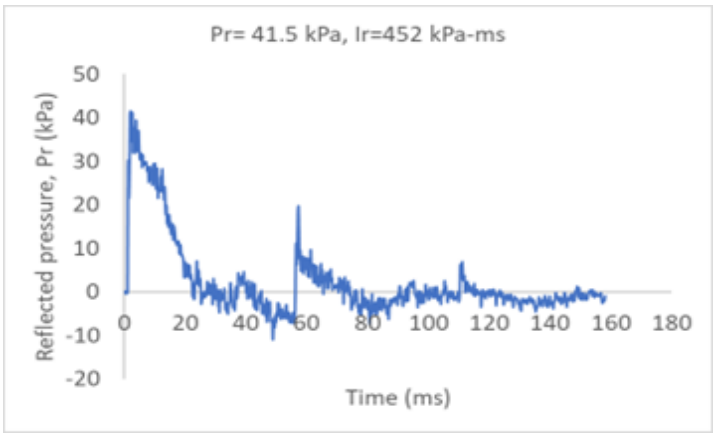

(a)

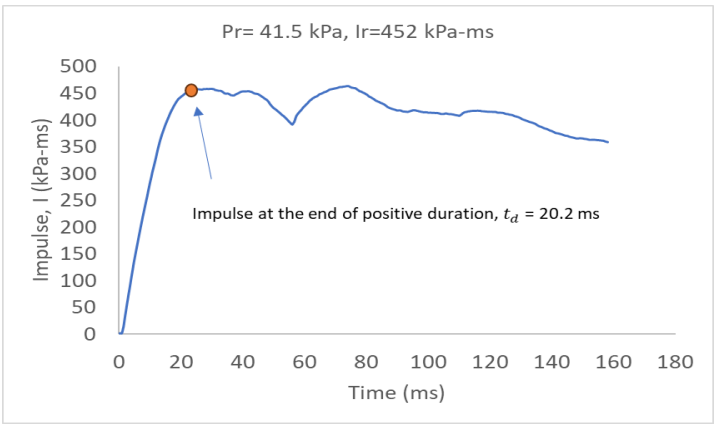

(b)

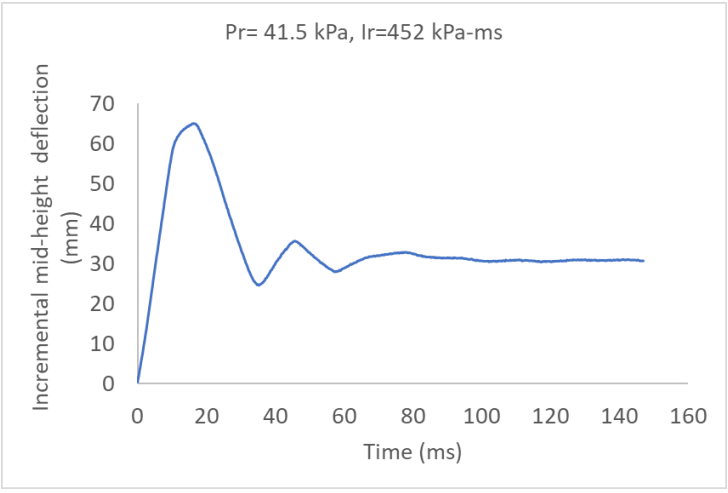

(c)

Figure 3.91: Tests results - Mullion 10FH- Shot 2(a)Pressure-time history (b)Impulse-time history (c) Incremental mid-height mullion deflection-time history as recorded by LVDT

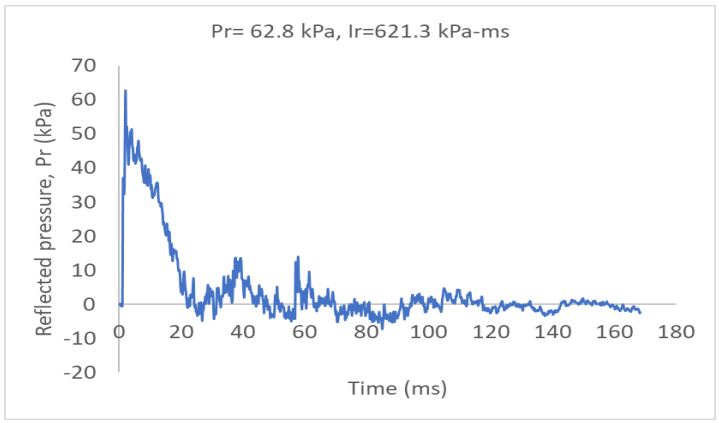

(a)

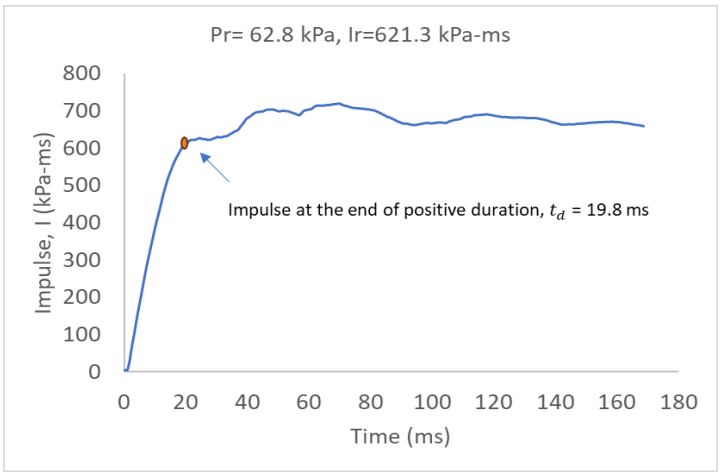

(b)

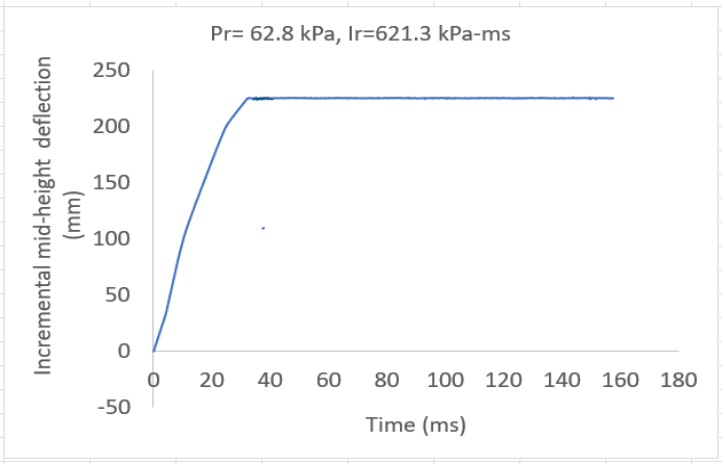

(c)

Figure 3.92: Tests results - Mullion 10FH- Shot 3(a)Pressure-time history (b)Impulse-time history (c) Incremental mid-height mullion deflection-time history as recorded by LVDT

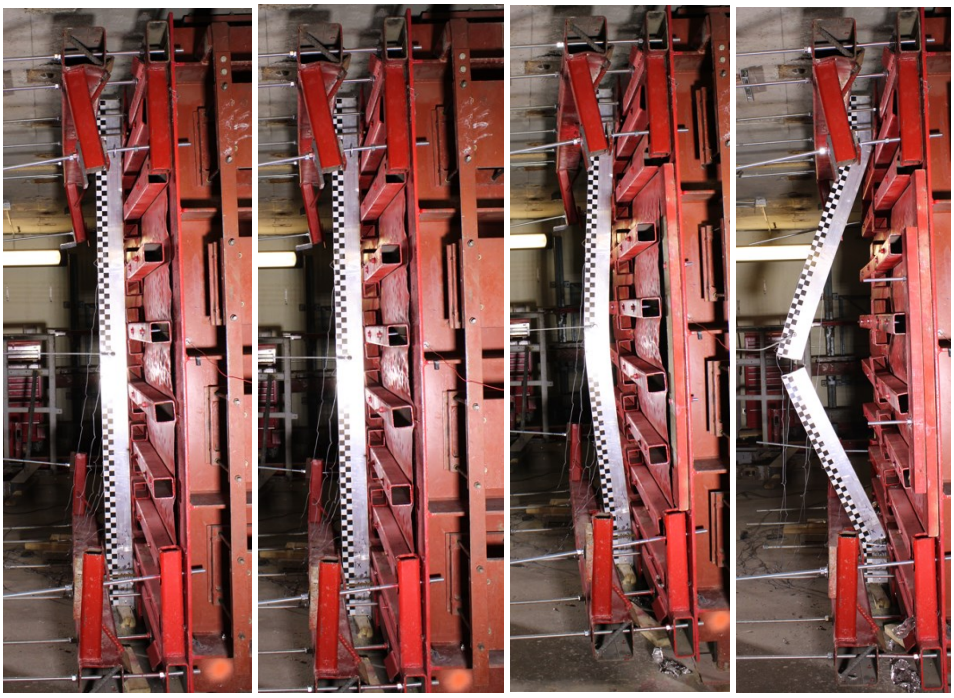

Before Testing Shot 1 Shot 2 Shot 3

Top Support Bottom Support

Sample Failure at 60 psi (414 KPa)

Figure 3.93: Mullion performance after blast load application-Mullion 10FH

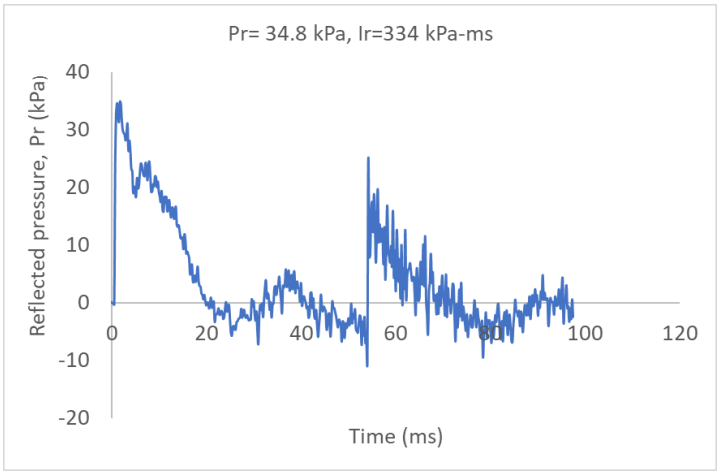

(a)

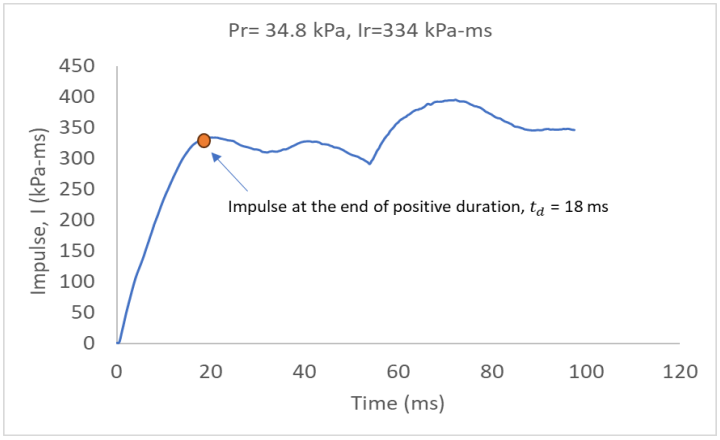

(b)

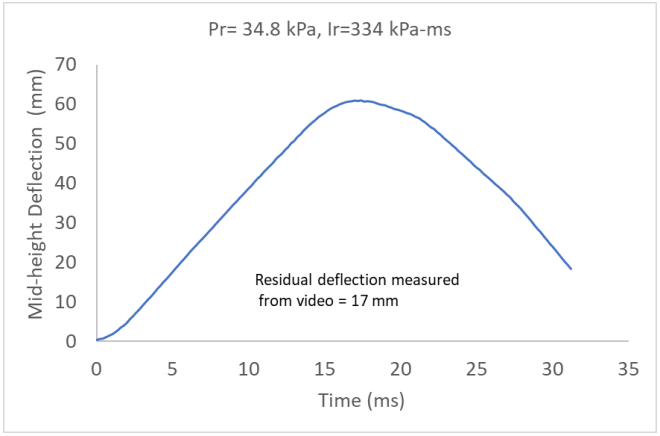

(c)

Figure 3.94: Tests results - Mullion 11FH- Shot 1(a)Pressure-time history (b)Impulse-time history (c) Mid-height mullion deflection-time history as recorded by LVDT

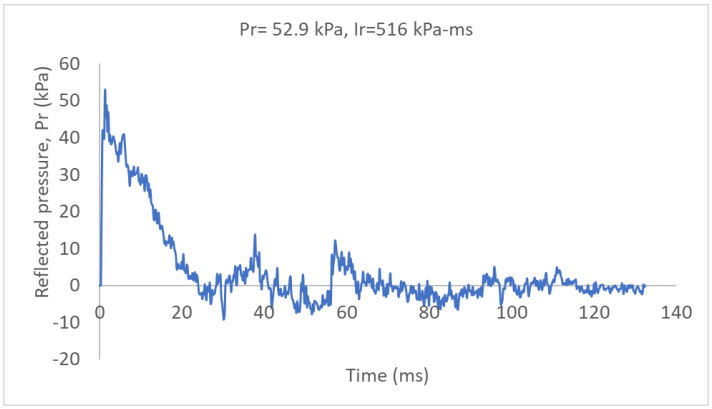

(a)

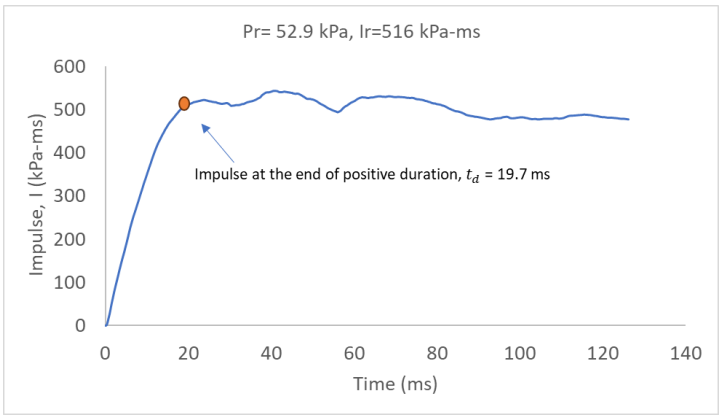

(b)

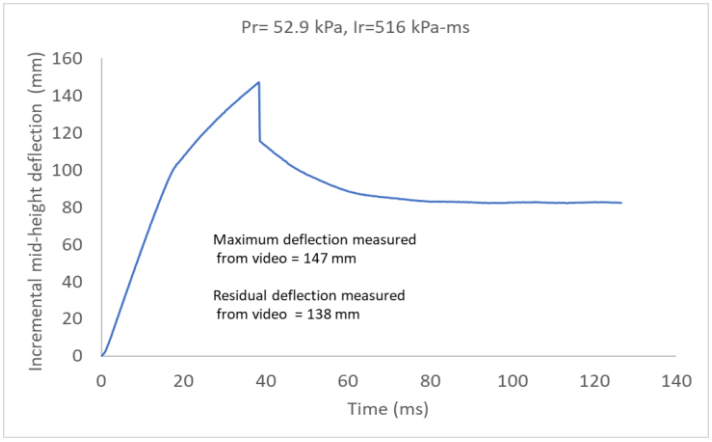

(c)

Figure 3.95: Tests results - Mullion 11FH- Shot 2 (a)Pressure-time history (b)Impulse-time history (c) Incremental mid-height mullion deflection-time history

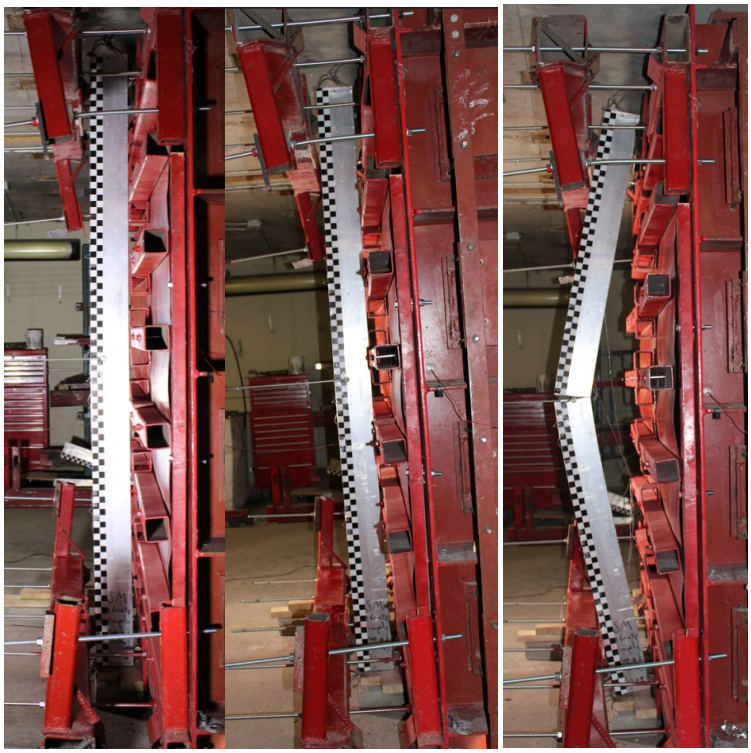

Before Testing Shot 1 Shot 2

Top Support Bottom Support

Sample Failure at 40 psi (276 KPa)

Figure 3.96: Mullion performance after blast load application-Mullion 11FH

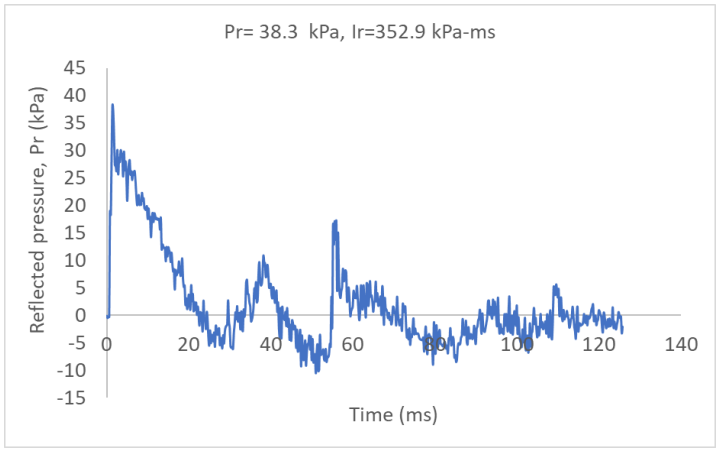

(a)

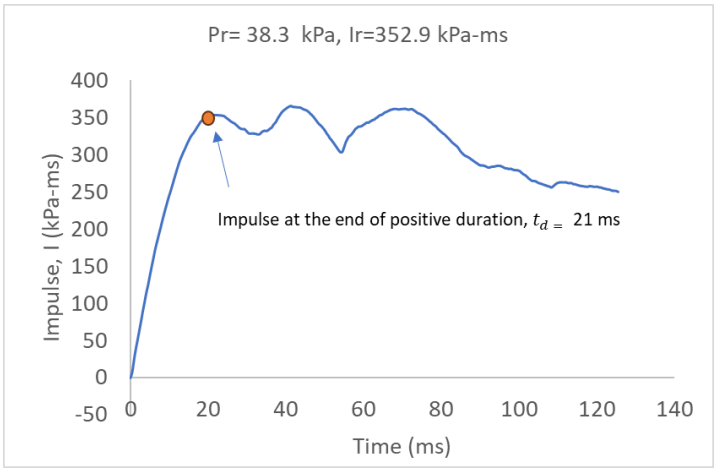

(b)

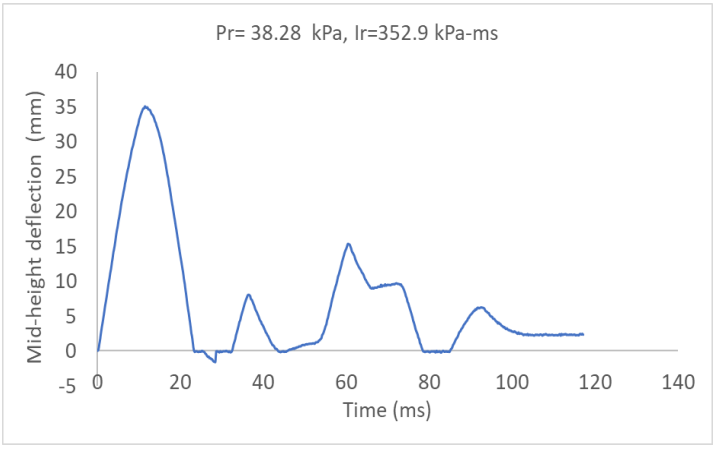

(c)

Figure 3.97: Tests results - Mullion 12FH- Shot 1(a)Pressure-time history (b)Impulse-time history (c) Mid-height mullion deflection-time history as recorded by LVDT

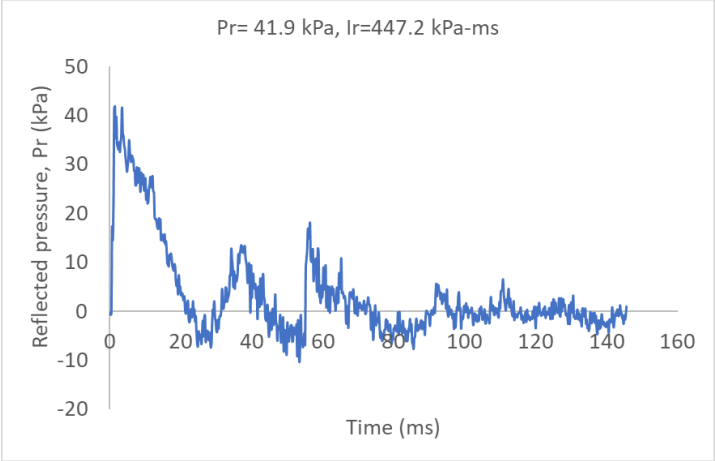

(a)

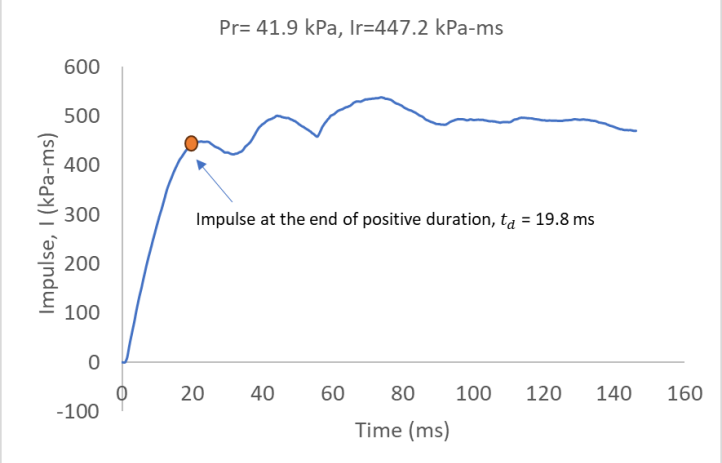

(b)

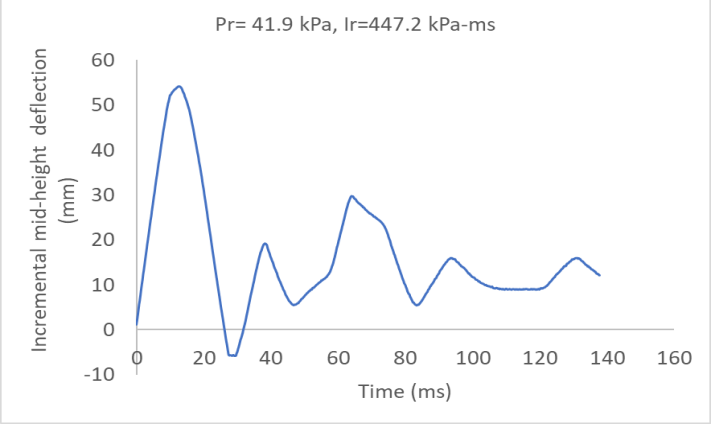

(c)

Figure 3.98: Tests results - Mullion 12FH- Shot 2(a)Pressure-time history (b)Impulse-time history (c) Incremental mid-height mullion deflection-time history as recorded by LVDT

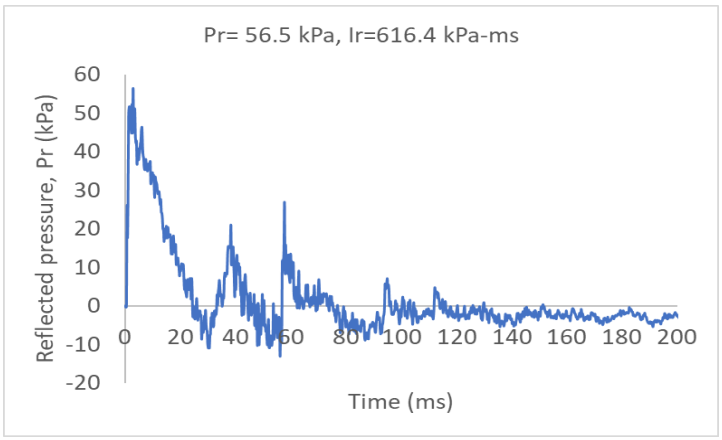

(a)

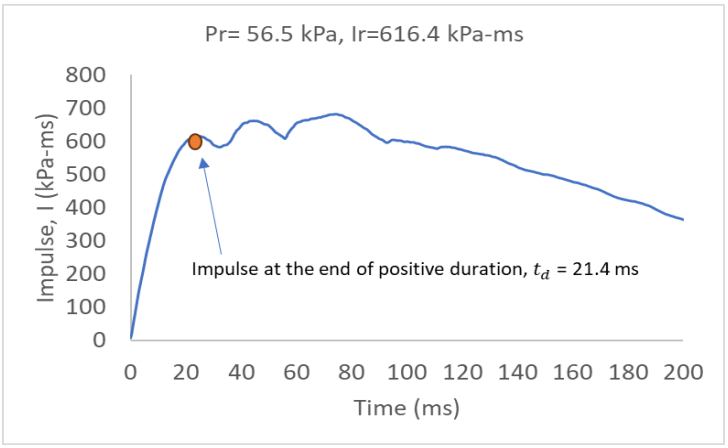

(b)

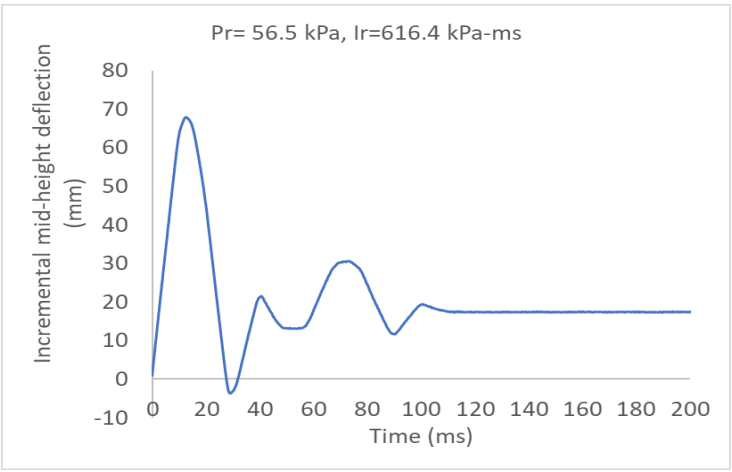

(c)

Figure 3.99:Tests results - Mullion 12FH- Shot 3(a)Pressure-time history (b)Impulse-time history (c) Incremental mid-height mullion deflection-time history as recorded by LVDT

Before Testing Shot 1 Shot 2 Shot 3

Top Support Bottom Support

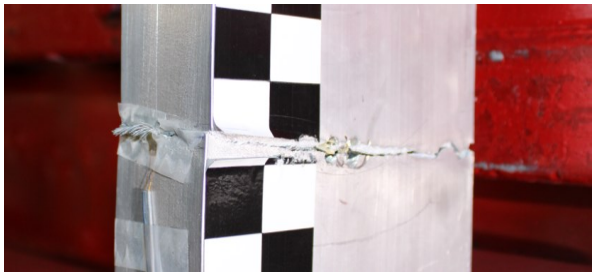

Sample Failure at 60 psi (414 KPa)

Figure 3.100: Mullion performance after blast load application-Mullion 12FH

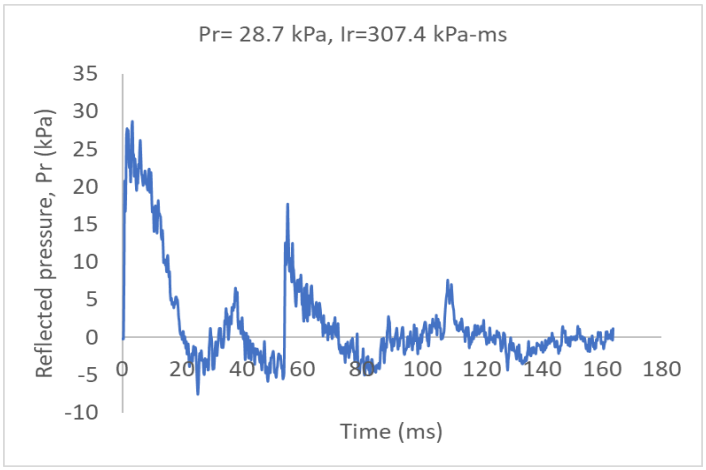

(a)

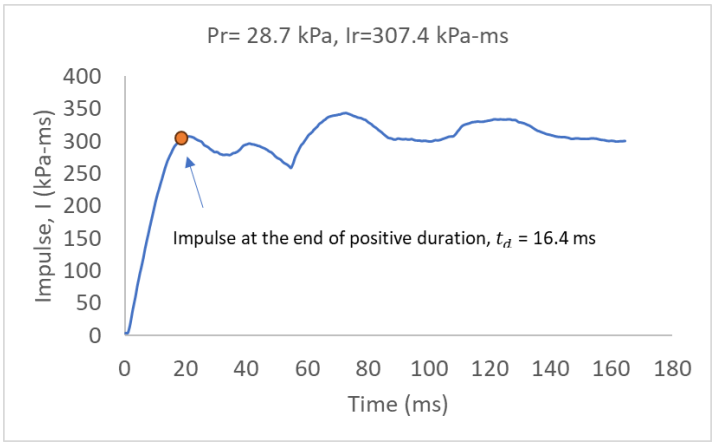

(b)

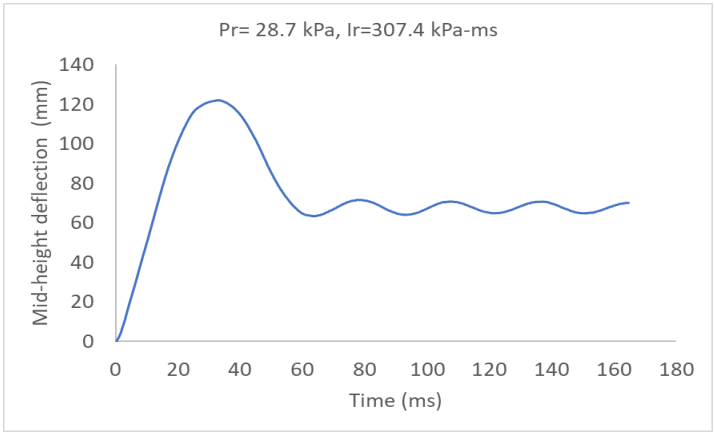

(c)

Figure 3.101: Tests results - Mullion 13FH- Shot 1(a)Pressure-time history (b)Impulse-time history (c) Mid-height mullion deflection-time history as recorded by LVDT

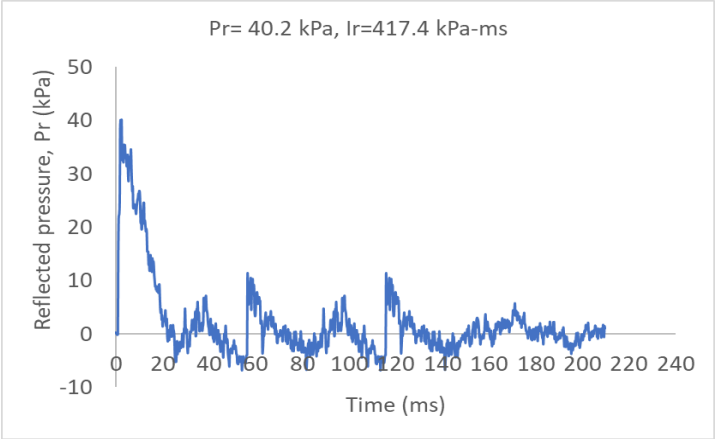

(a)

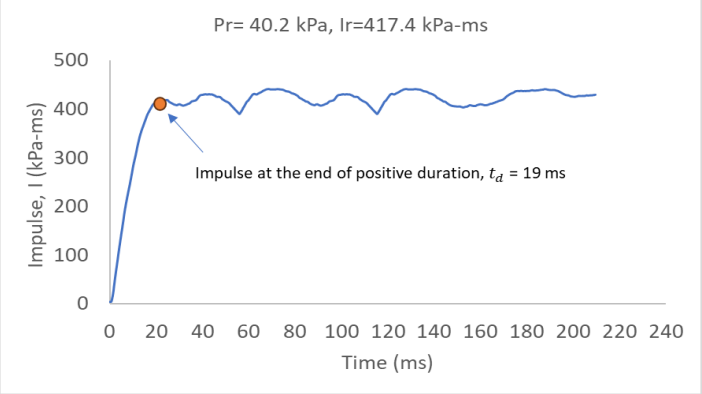

(b)

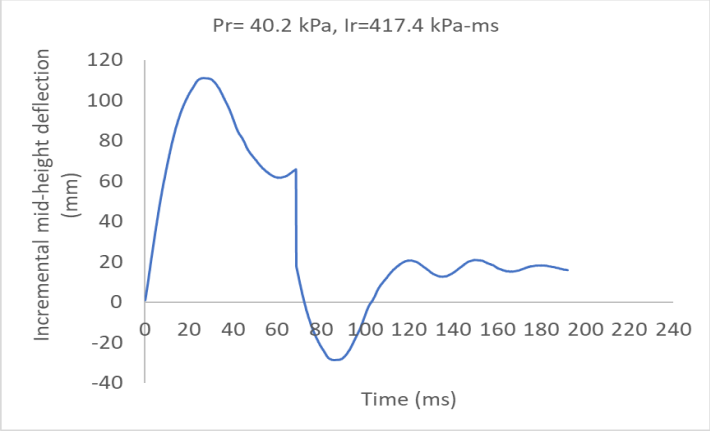

(c)

Figure 3.102: Tests results - Mullion 13FH- Shot 2(a)Pressure-time history (b)Impulse-time history (c) Incremental mid-height mullion deflection-time history as recorded by LVDT

Before Testing Shot 1 Shot 2

Top Support Bottom Support

Sample Failure at 60 psi (414 KPa)

Figure 3.103: Mullion performance after blast load application-Mullion 13FH

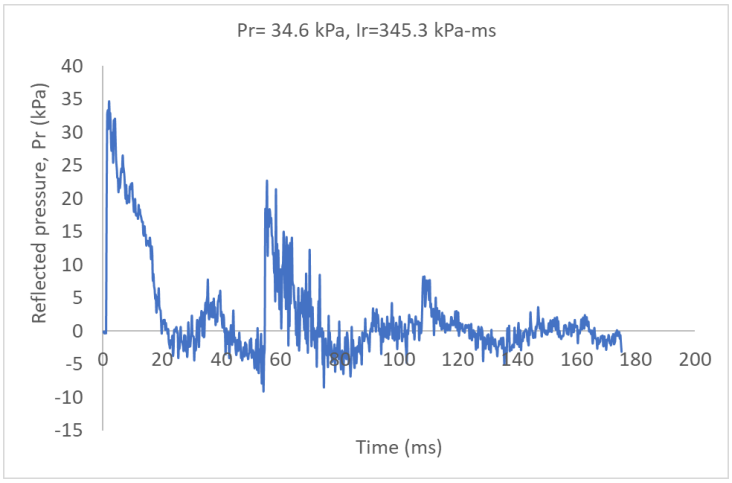

(a)

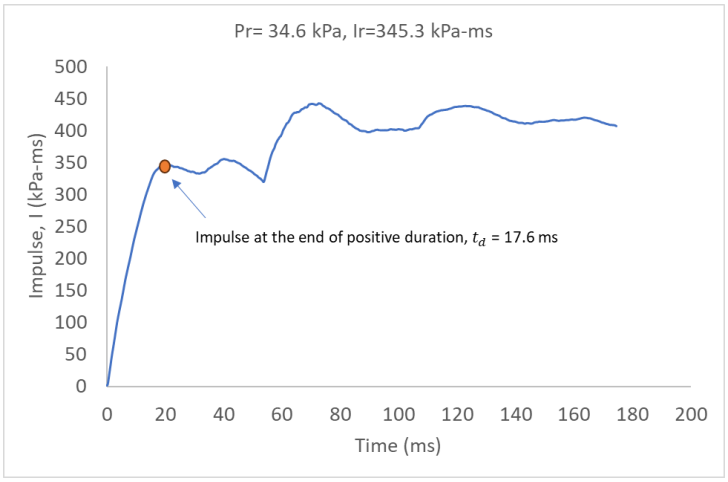

(b)

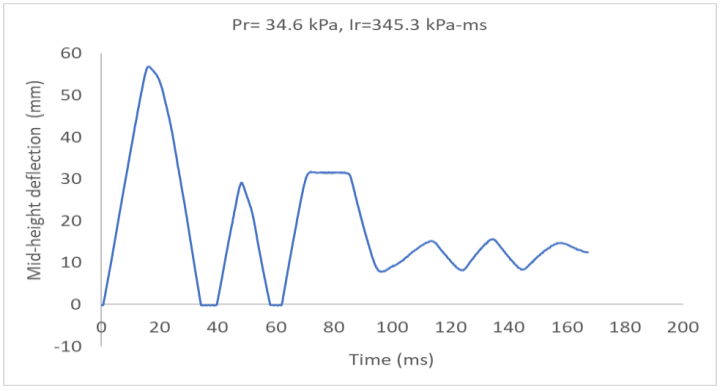

(c)

Figure 3.104: Tests results - Mullion 14FH- Shot 1(a)Pressure-time history (b)Impulse-time history (c) Mid-height mullion deflection-time history as recorded by LVDT

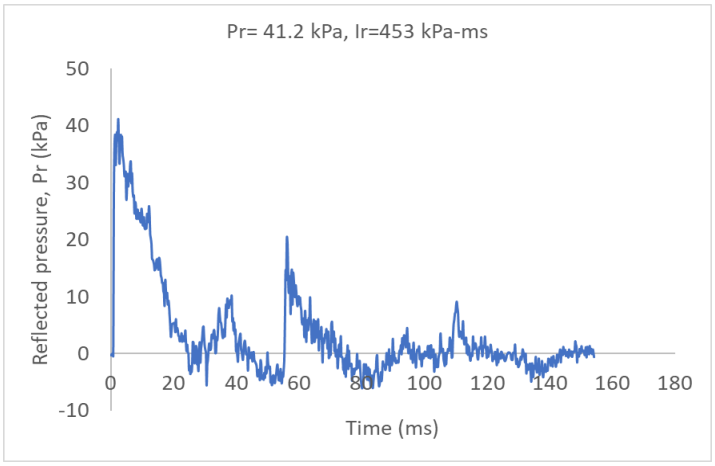

(a)

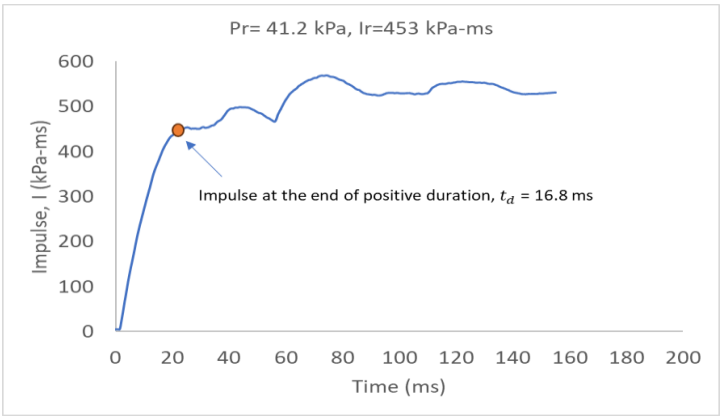

(b)

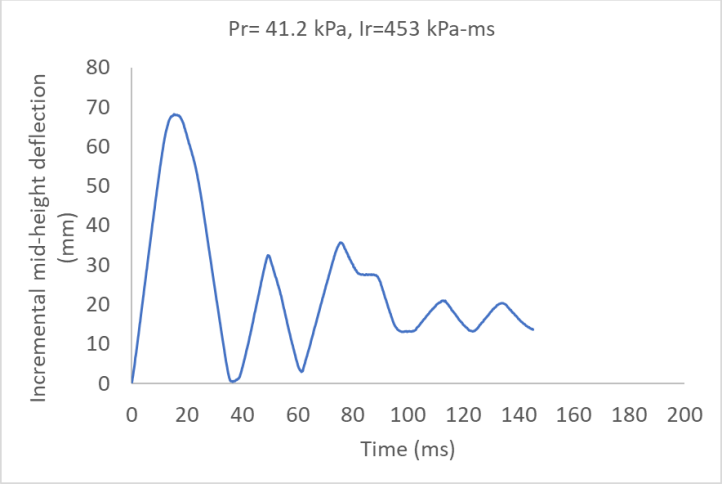

(c)

Figure 3.105:Tests results - Mullion 14FH- Shot 2 (a)Pressure-time history (b)Impulse-time history (c) Incremental mid-height mullion deflection-time history as recorded by LVDT

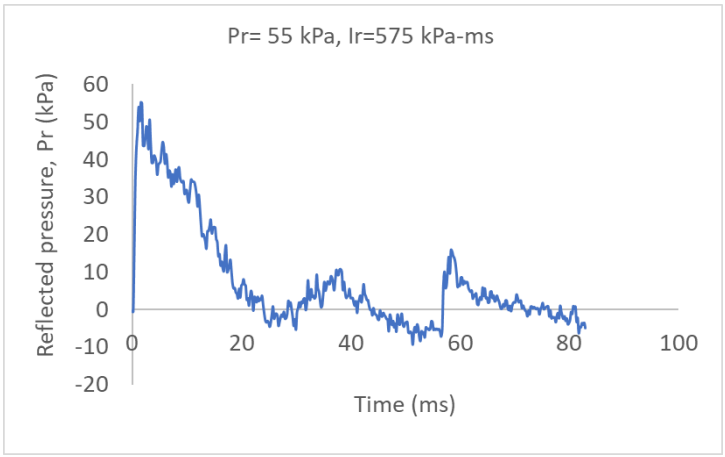

(a)

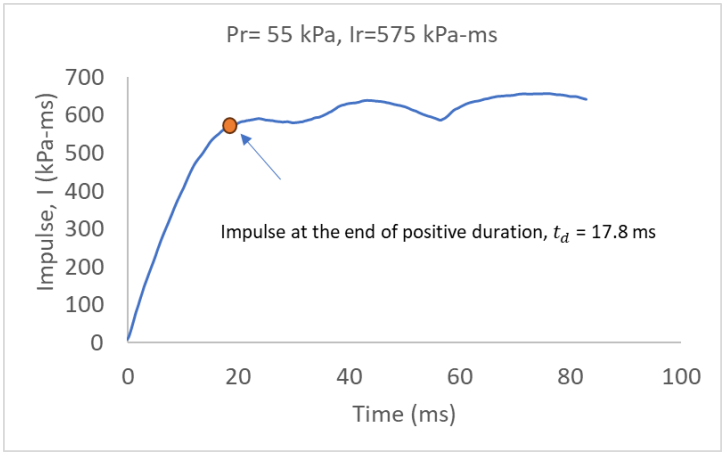

(b)

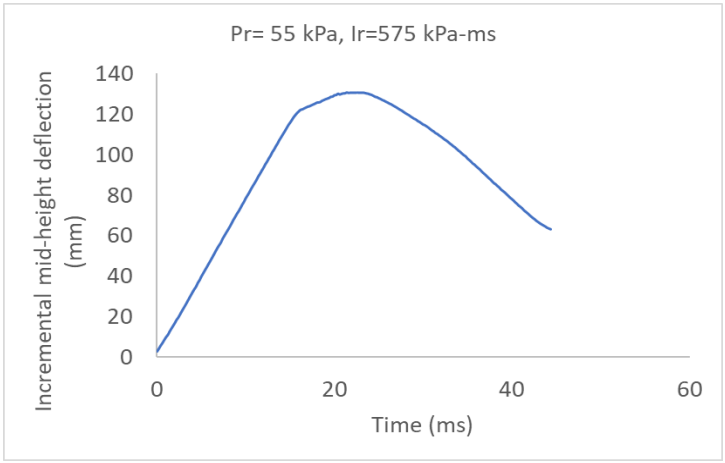

(c)

Figure 3.106: Tests results - Mullion 14FH- Shot 3 (a)Pressure-time history (b)Impulse-time history (c) Incremental mid-height mullion deflection-time history as recorded by LVDT

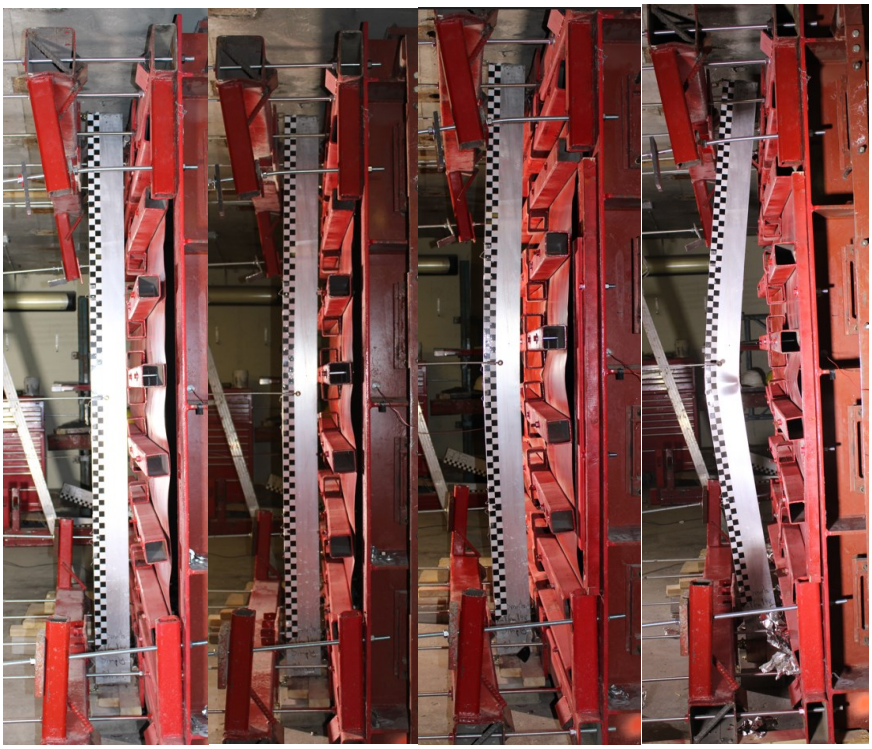

Before Testing Shot 1 Shot 2 Shot 3

Top Support Bottom Support

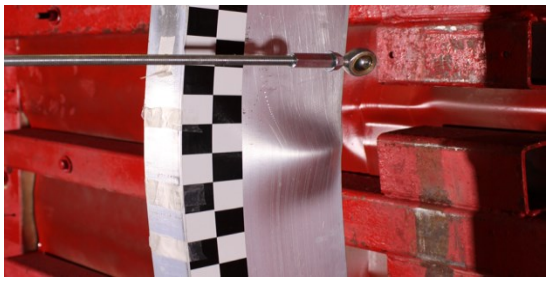

Sample Failure at 60 psi 60 psi (414 KPa)

Figure 3.107: Mullion performance after blast load application-Mullion 14FH

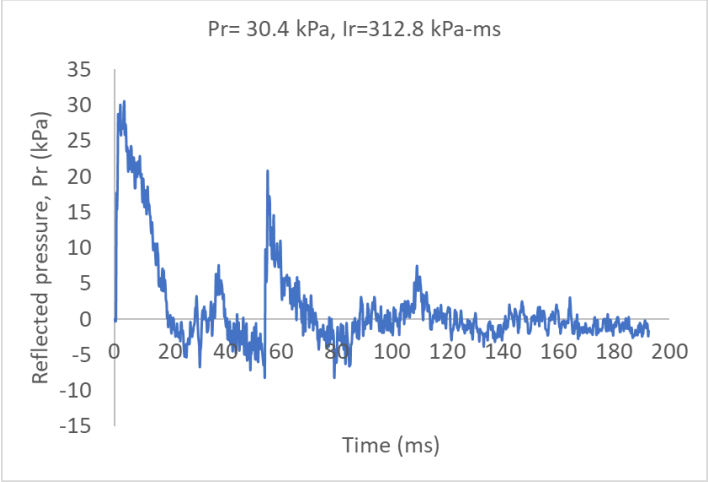

(a)

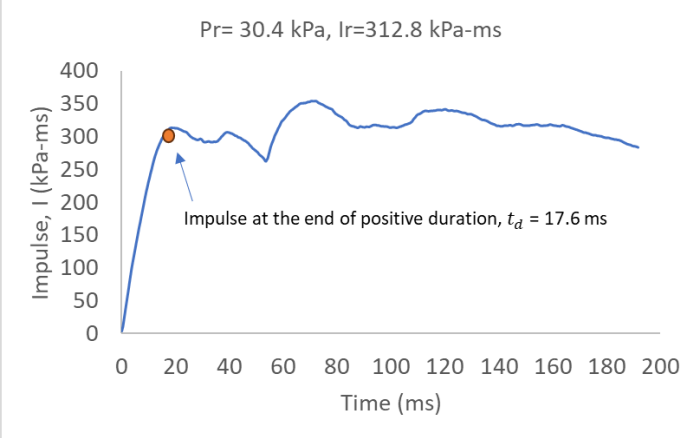

(b)

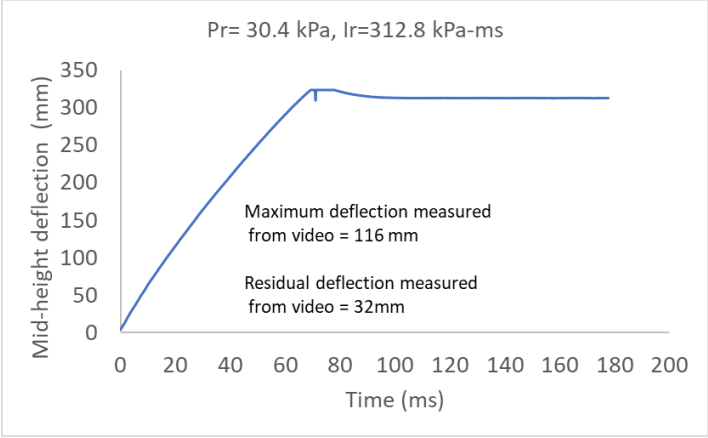

(c)

Figure 3.108: Tests results - Mullion 15FR- Shot 1 (a)Pressure-time history (b)Impulse-time history (c) Mid-height mullion deflection-time history

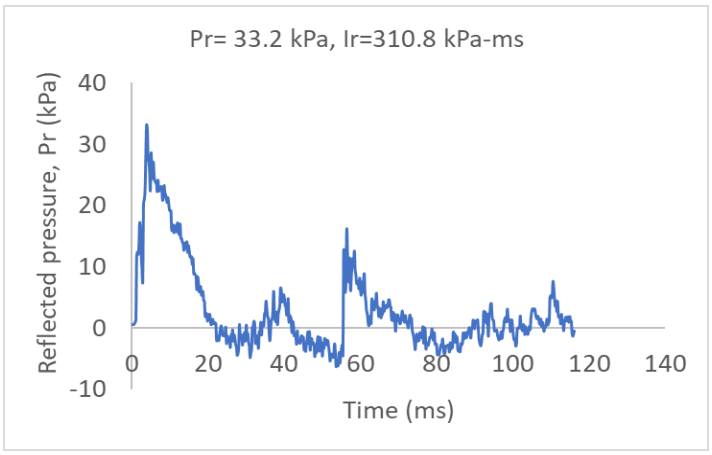

(a)

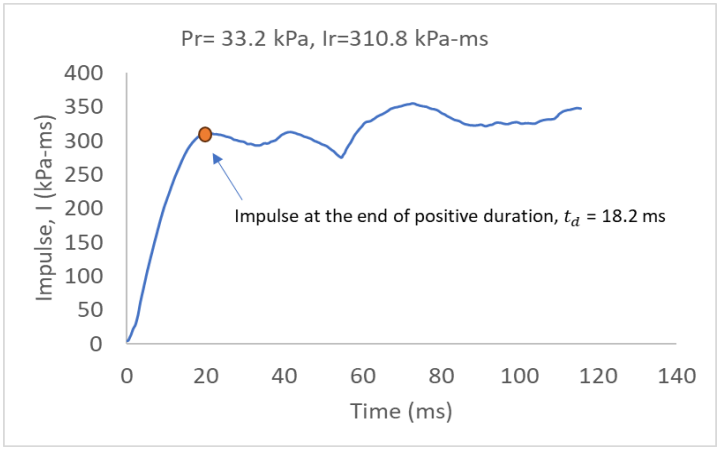

(b)

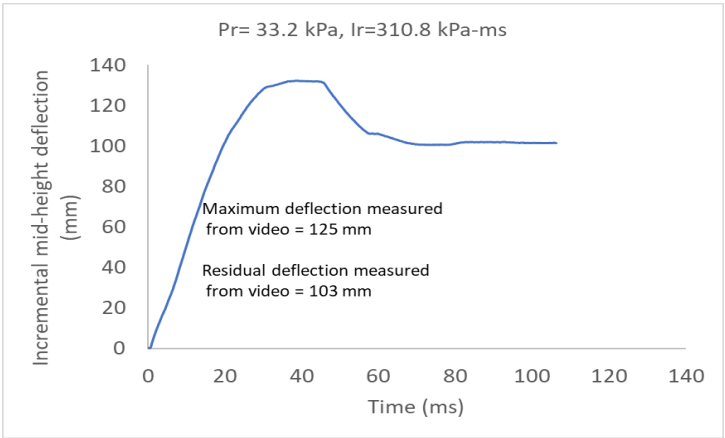

(c)

Figure 3.109: Tests results - Mullion 15FR- Shot 2 (a)Pressure-time history (b)Impulse-time history (c) Incremental mid-height mullion deflection-time history

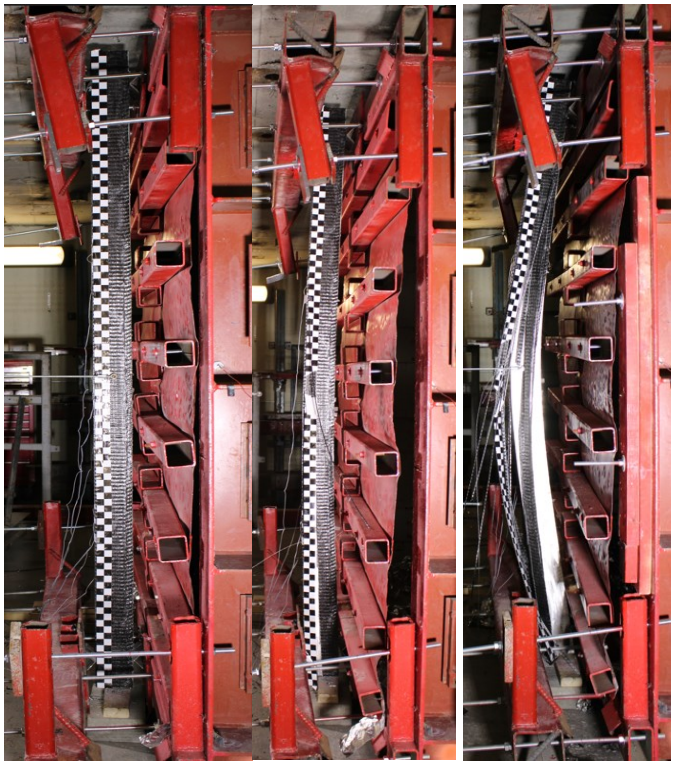

Before Testing Shot 1 Shot 2

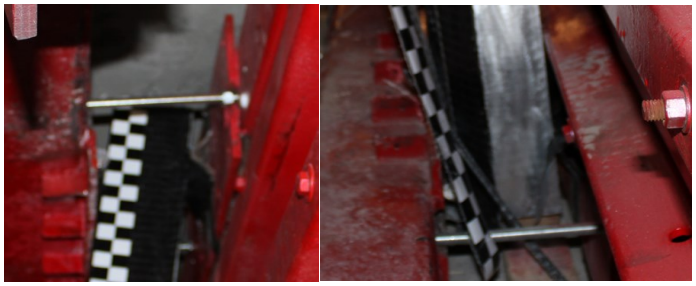

Top Support Bottom Support

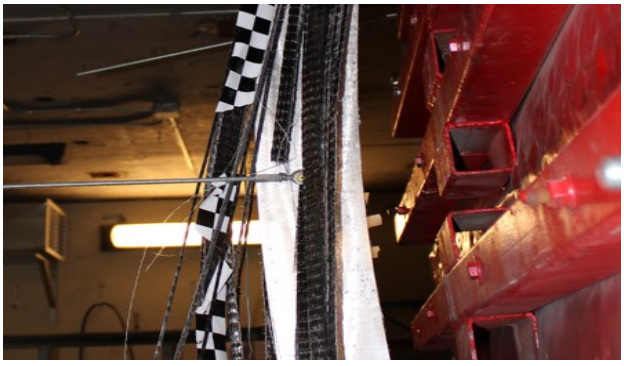

Sample Failure at 40 psi 40 psi (276 KPa)

Figure 3.110: Mullion performance after blast load application-Mullion 15FR

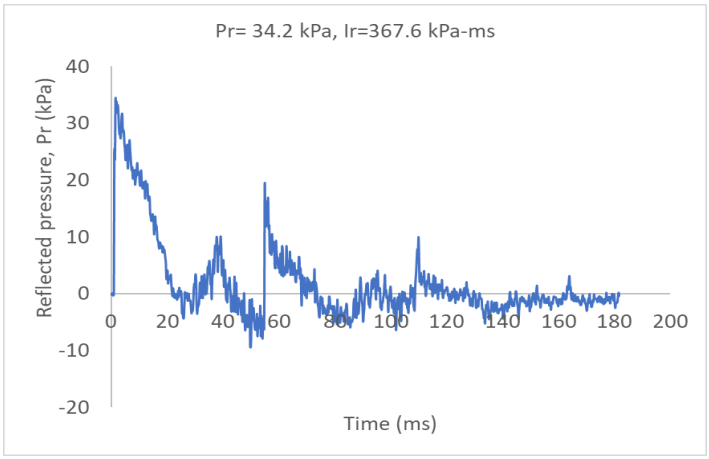

(a)

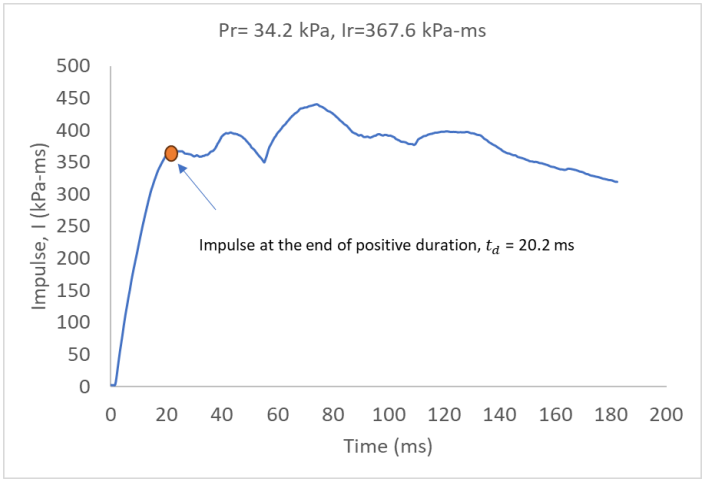

(b)

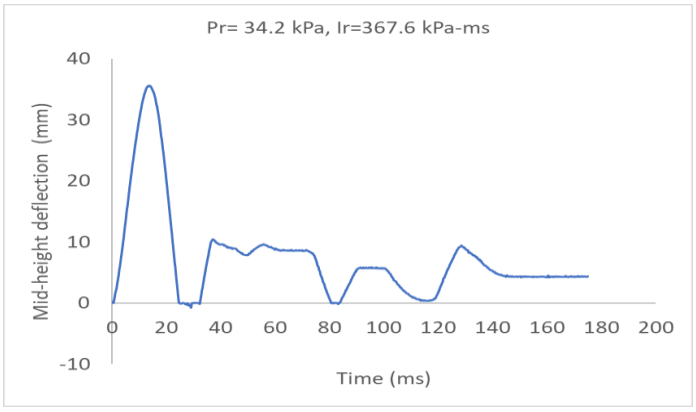

(c)

Figure 3.111: Tests results - Mullion 16FR- Shot 1 (a)Pressure-time history (b)Impulse-time history (c) Mid-height mullion deflection-time history as recorded by LVDT

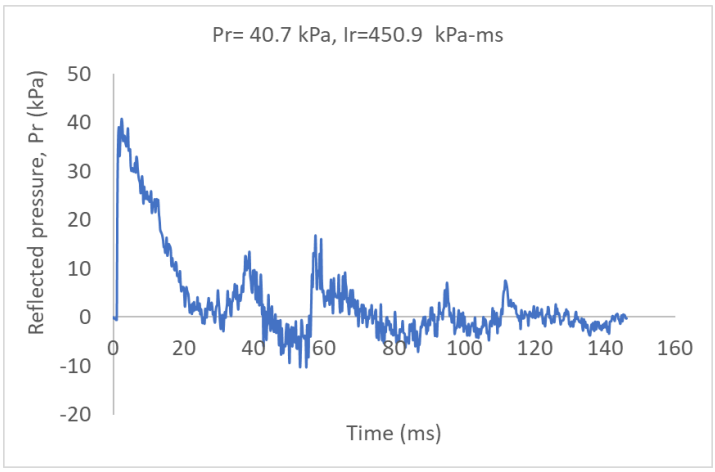

(a)

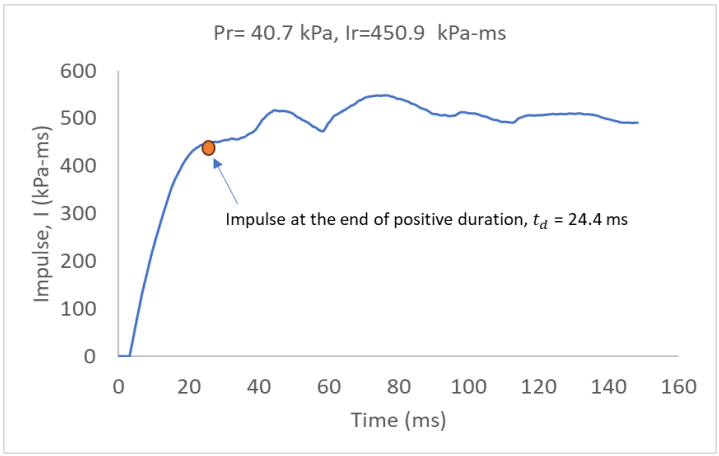

(b)

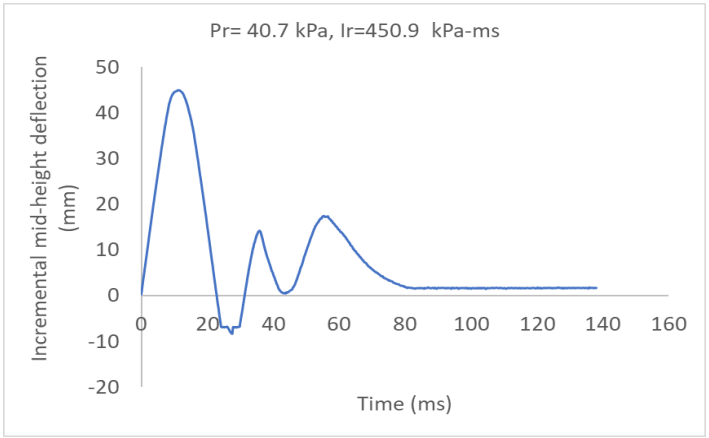

(c)

Figure 3.112: Tests results - Mullion 16FR- Shot 2 (a)Pressure-time history (b)Impulse-time history (c) Incremental mid-height mullion deflection-time history as recorded by LVDT

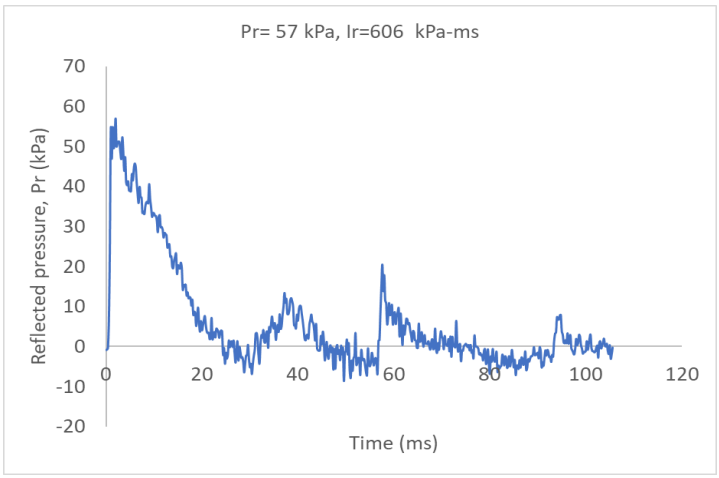

(a)

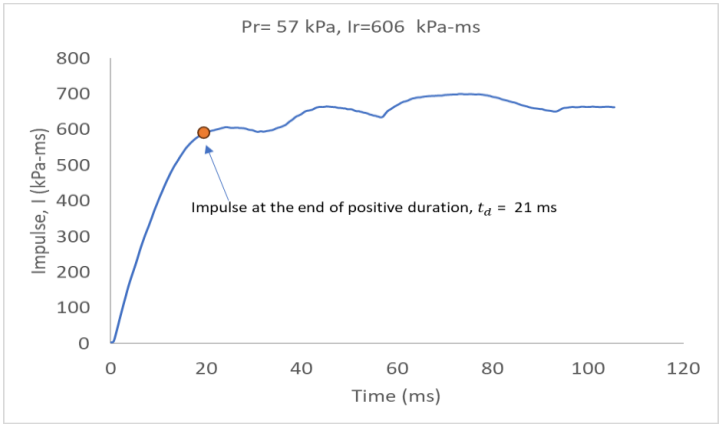

(b)

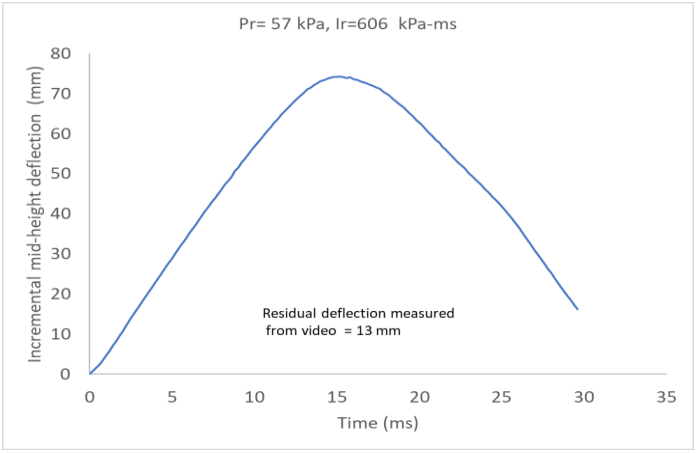

(c)

Figure 3.113: Tests results - Mullion 16FR- Shot 3 (a)Pressure-time history (b)Impulse-time history (c) Incremental mid-height mullion deflection-time history as recorded by LVDT

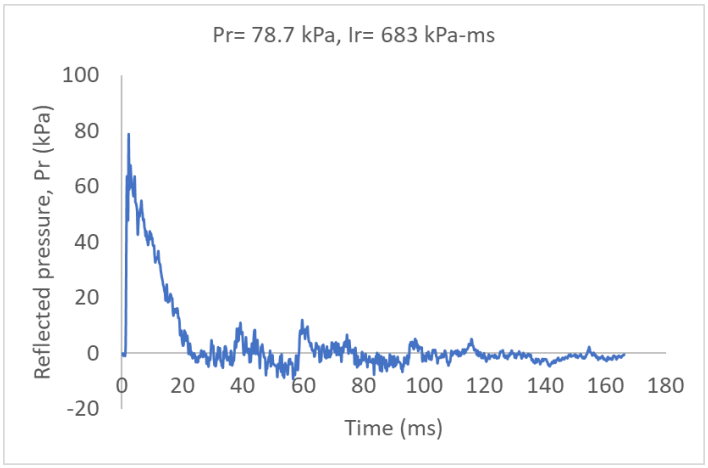

(a)

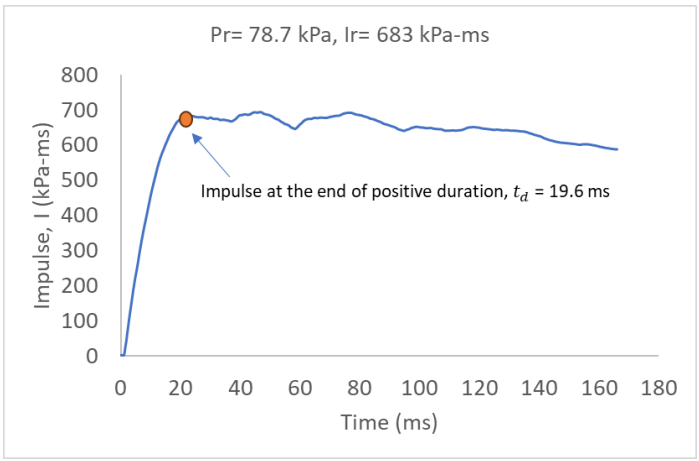

(b)

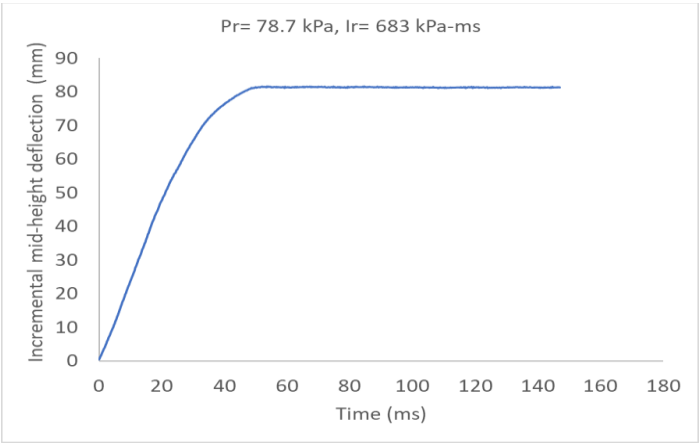

(c)

Figure 3.114: Tests results - Mullion 16FR- Shot 4 (a)Pressure-time history (b)Impulse-time history (c) Mid-height mullion deflection-time history

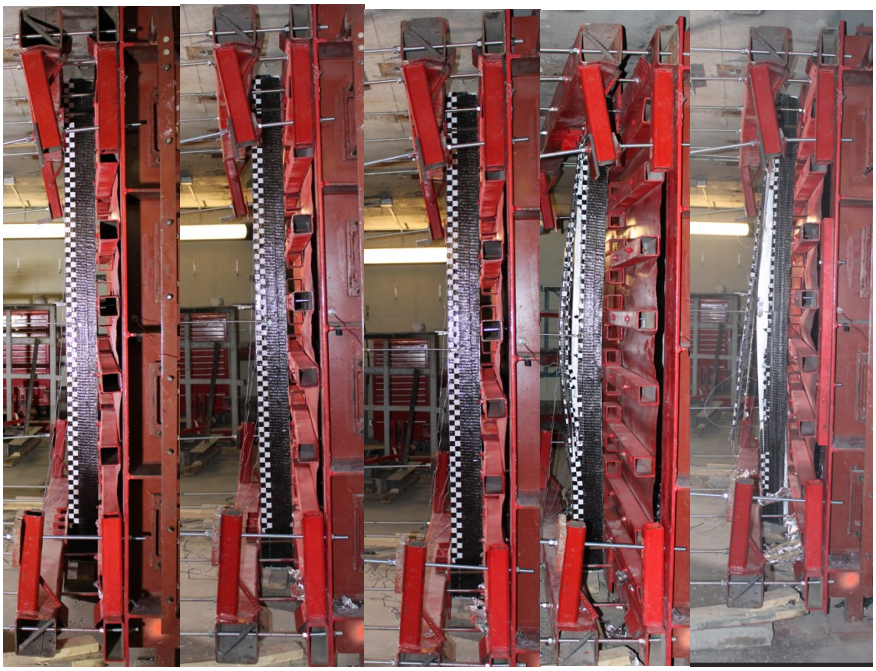

Before Testing Shot 1 Shot 2 Shot 3 Shot 4

Top Support Bottom Support

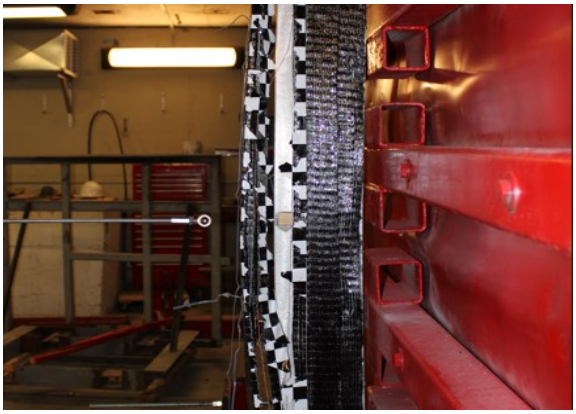

Sample Failure at 80 psi (551 KPa)

Figure 3.115: Mullion performance after blast load application-Mullion 16FR

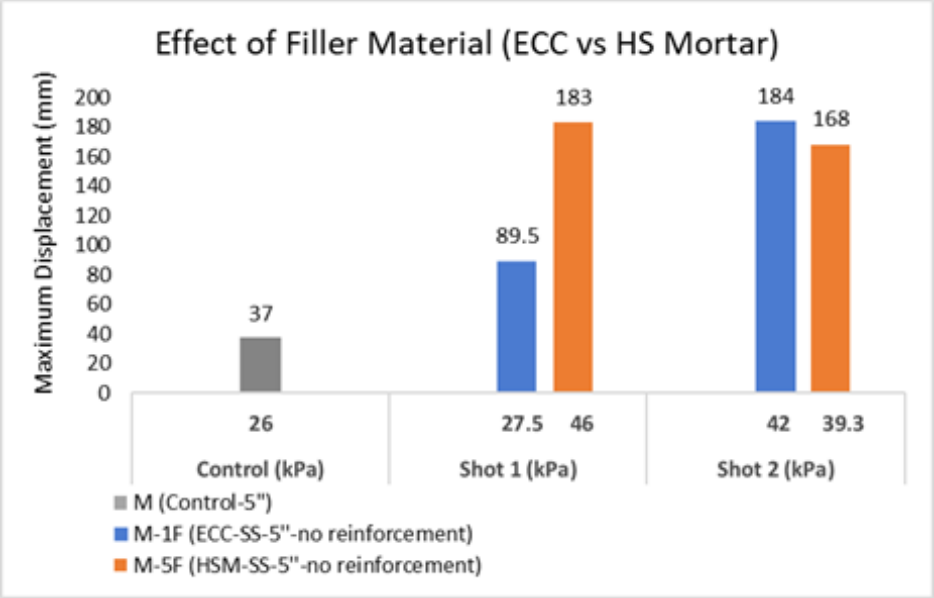

Figure 3.116: Comparison of Mullion 1F and Mullion 5F based on filler material

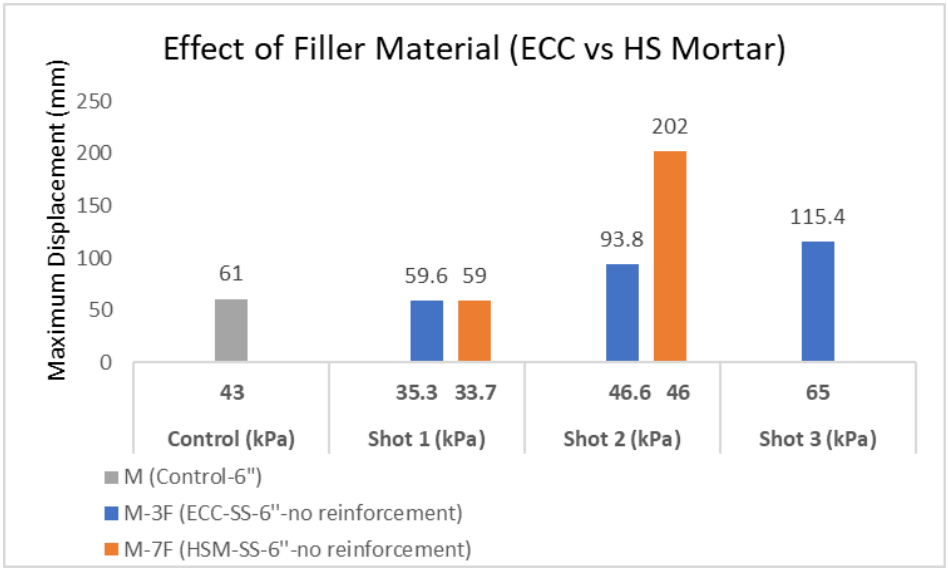

Figure 3.117: Comparison of Mullion 3F and Mullion 7F based on filler material

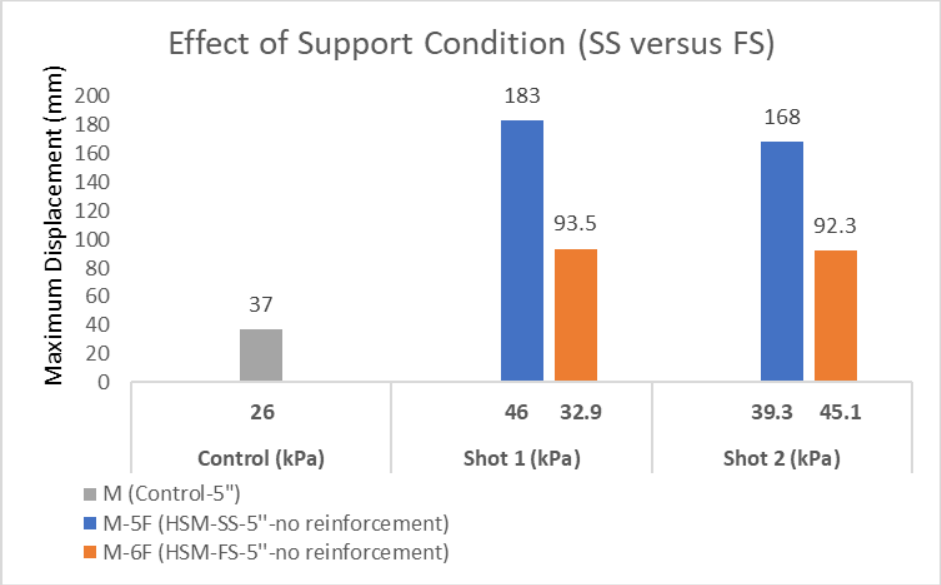

Figure 3.118: Comparison of Mullion 5F and Mullion 6F based on support conditions

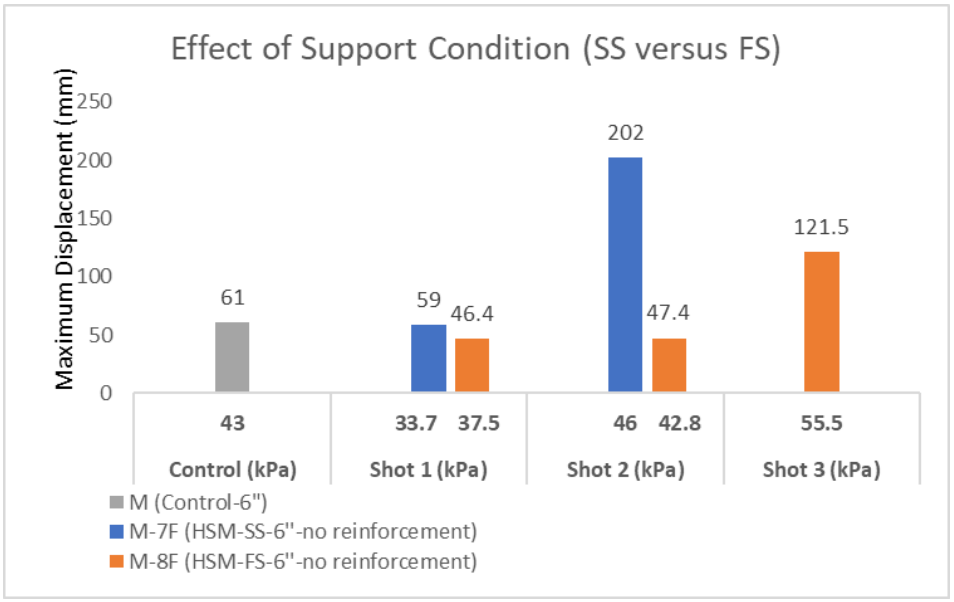

Figure 3.119: Comparison of Mullion 7F and Mullion 8F based on support conditions

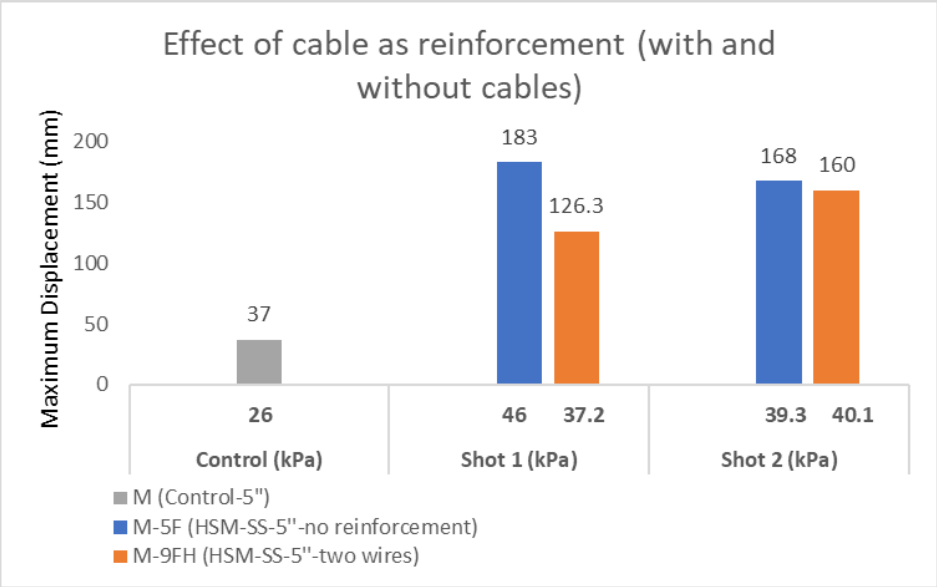

Figure 3.120: Comparison of Mullion 5F and Mullion 9FH based on reinforcement-Wires

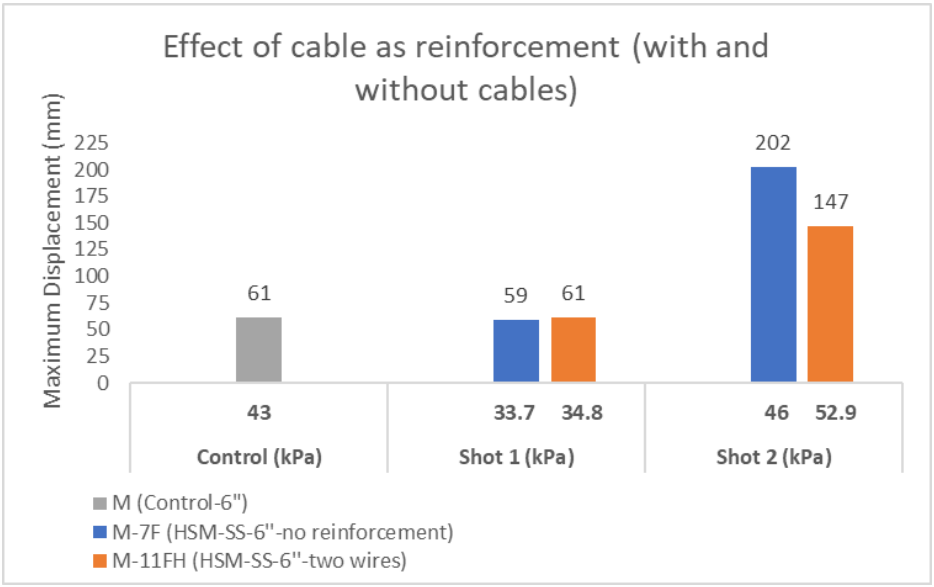

Figure 3.121: Comparison of Mullion 7F and Mullion 11FH based on reinforcement-Wires

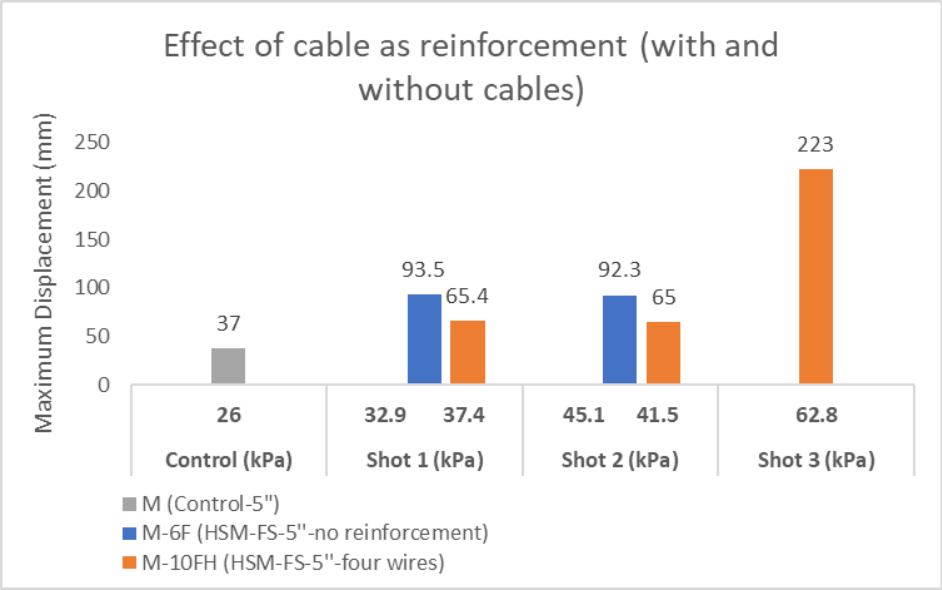

Figure 3.122: Comparison of Mullion 6F and Mullion 10FH based on reinforcement-Wires

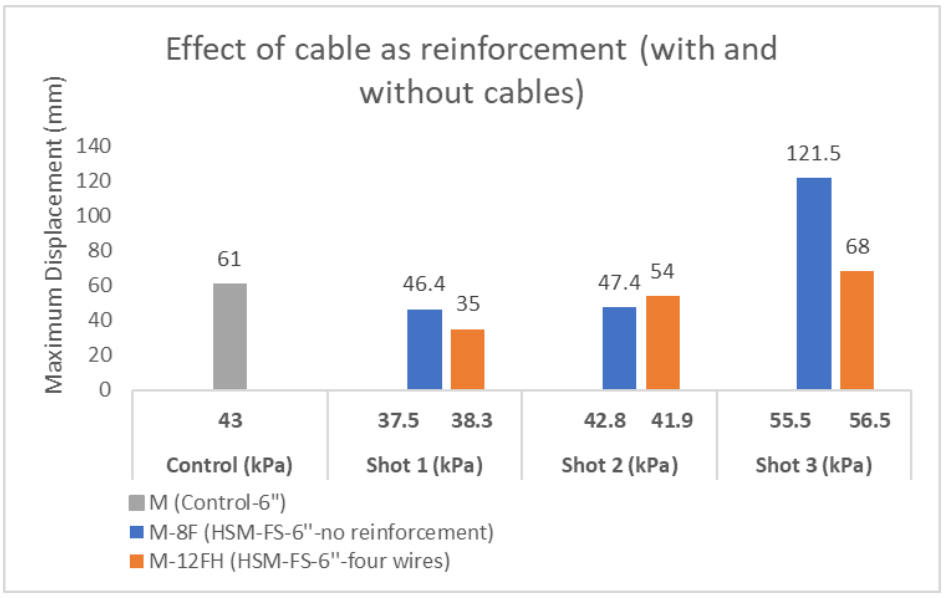

Figure 3.123: Comparison of Mullion 8F and Mullion 12FH based on reinforcement-Wires

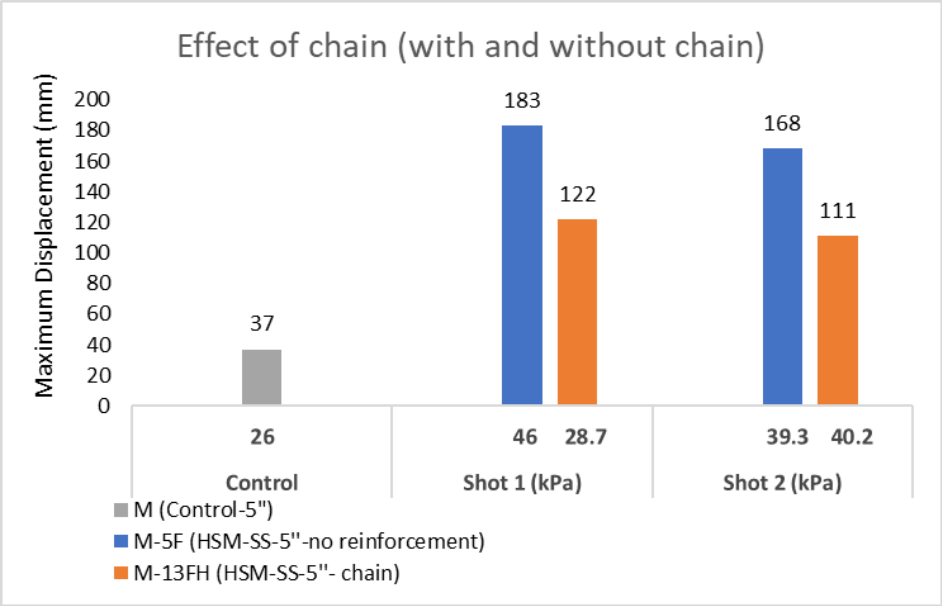

Figure 3.124: Comparison of Mullion 5F and Mullion 13FH based on reinforcement-chain

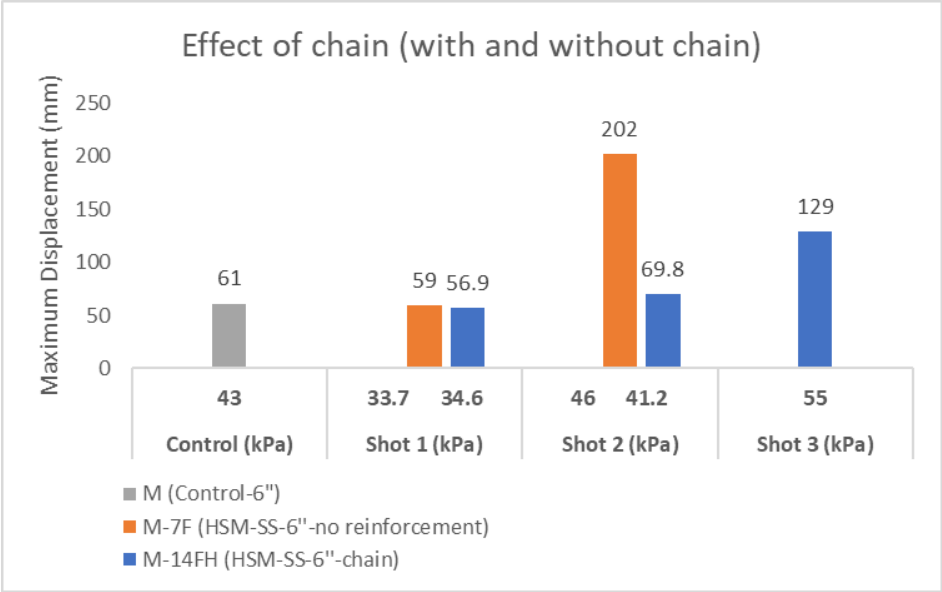

Figure 3.125: Comparison of Mullion 7F and Mullion 14FH based on reinforcement-chain

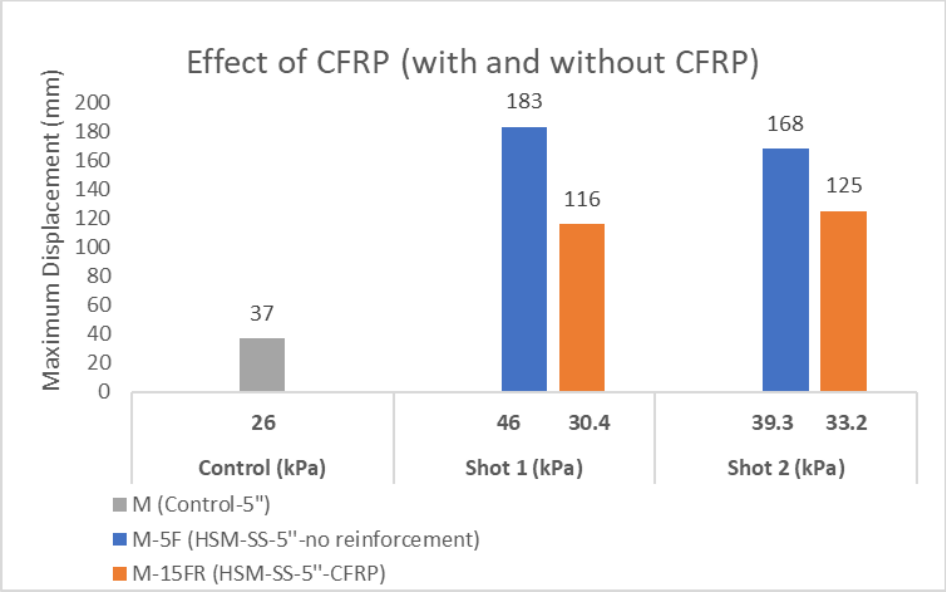

Figure 3.126: Comparison of Mullion 5F and Mullion 15FH based on retrofitting-CFRP

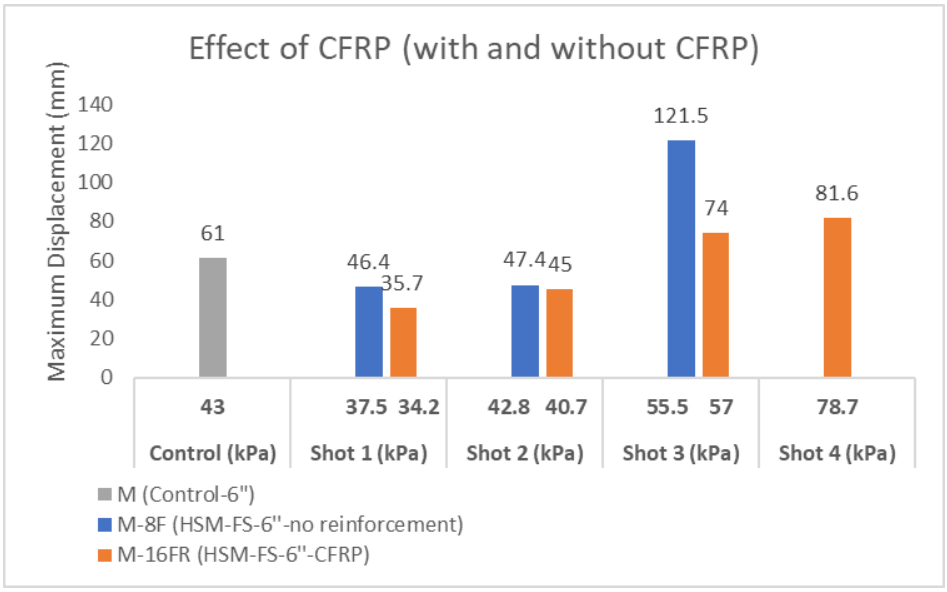

Figure 3.127: Comparison of Mullion 8F and Mullion 16FH based on retrofitting-CFRP

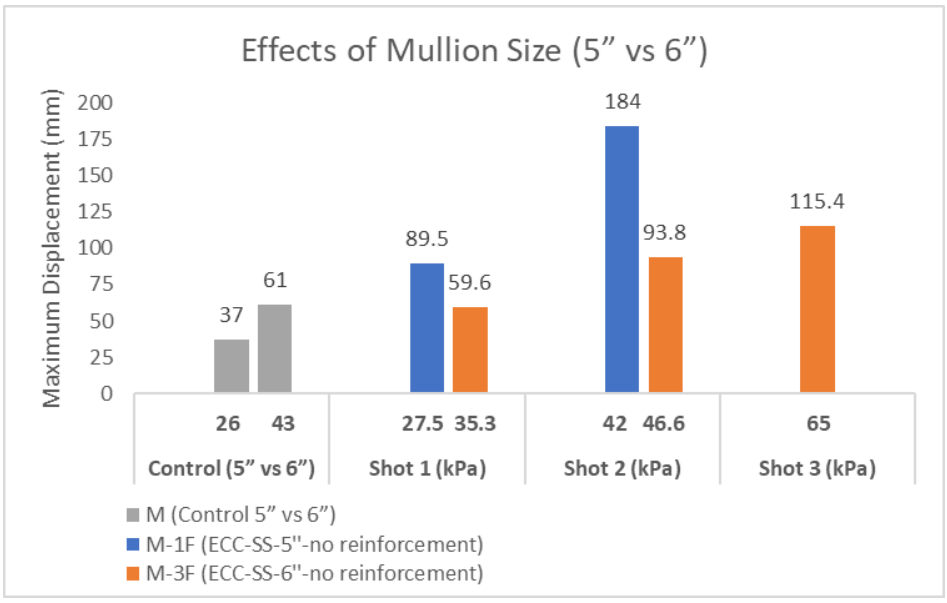

Figure 3.128: Comparison of Mullion 1F and Mullion 3FH based on specimen size

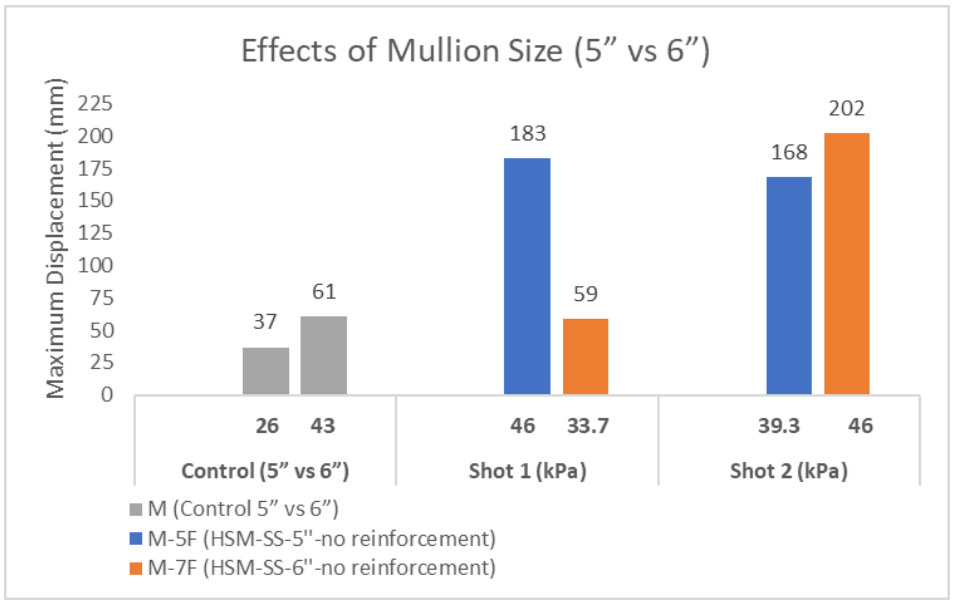

Figure 3.129: Comparison of Mullion 5F and Mullion 7FH based on specimen size

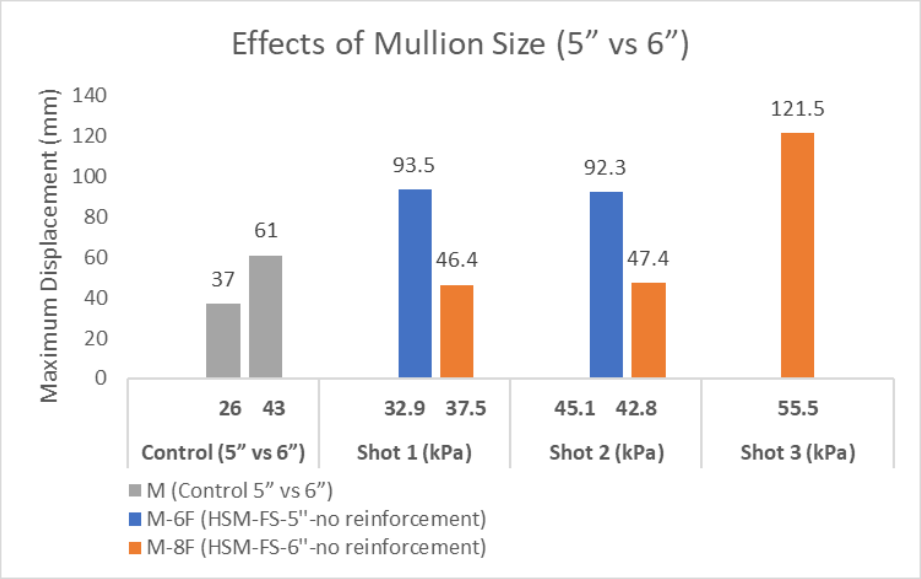

Figure 3.130: Comparison of Mullion 6F and Mullion 8F based on specimen size

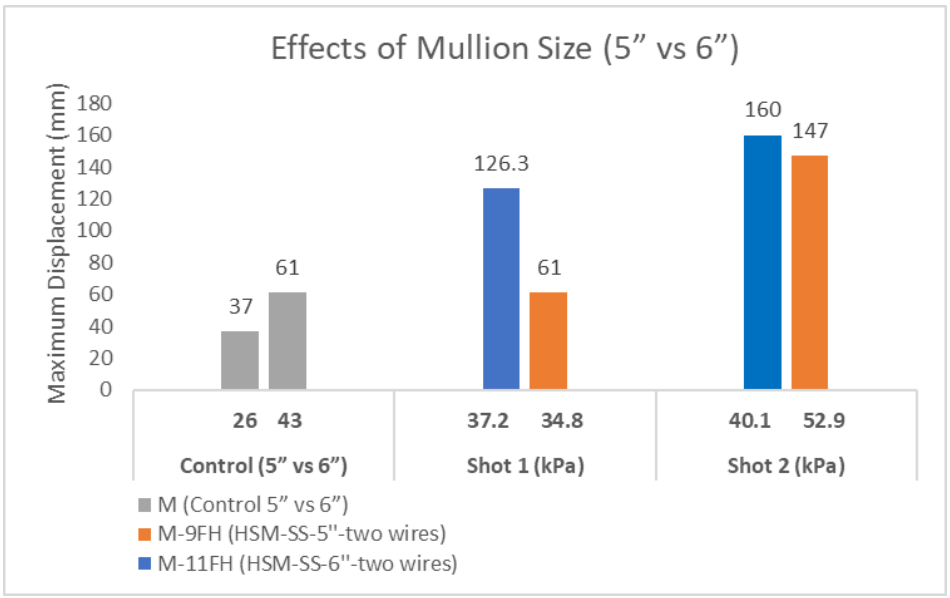

Figure 3.131: Comparison of Mullion 9FH and Mullion 11FH based on specimen size

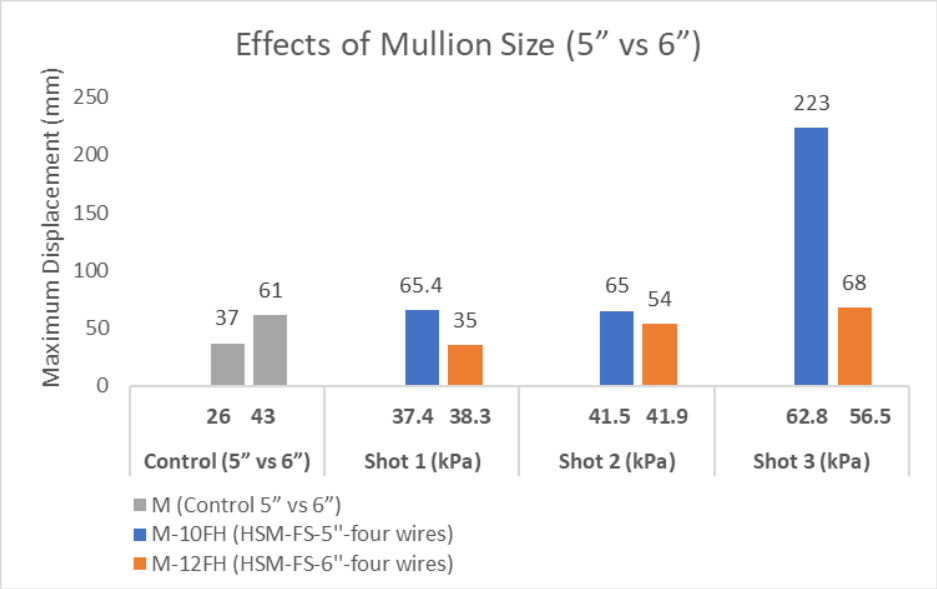

Figure 3.132: Comparison of Mullion 10FH and Mullion 12FH based on specimen size

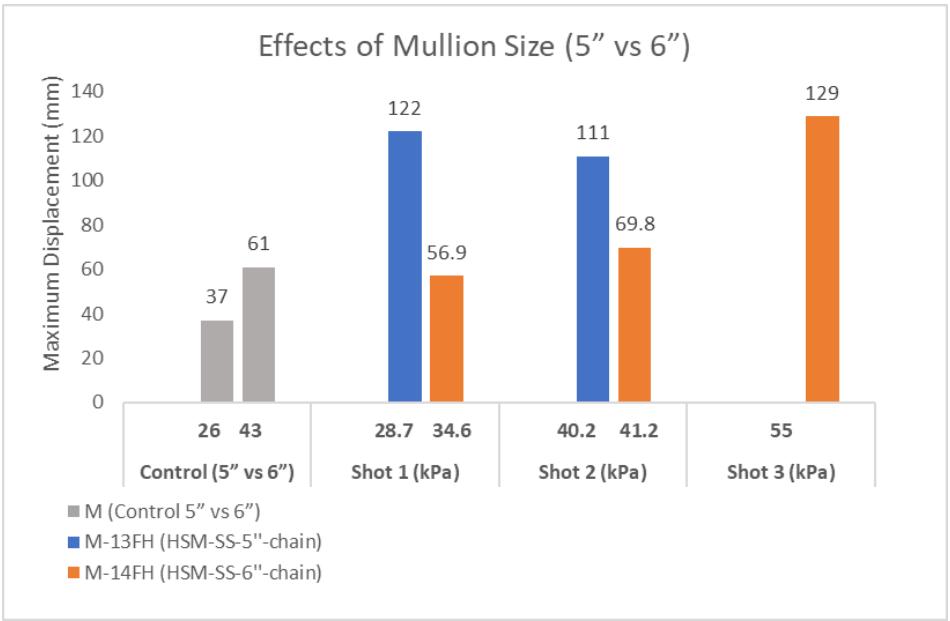

Figure 3.133: Comparison of Mullion 13FH and Mullion 14FH based on specimen size

CHAPTER 4. NUMERICAL INVESTIGATION

4.1 Introduction

The numerical investigation consists of non-linear dynamic analysis of mullions hardened with the technique developed in the current investigation. The test mullions were analyzed as single-degree-of-freedom (SDOF) models as typically done for member analysis under blast loads. This was done by employing the software RC-Blast, developed (Jacques et al., 2013)at the University of Ottawa. The analysis results were validated against the test data generated in the experimental phase of research for all the hardened mullions infilled by two infill materials (ECC and HSM), with and without internal and external reinforcement of different types (steel cables, chain and CFRP). The validation of the analytical model was essential for two reasons. First to expand the findings through an analytical parametric investigation as discussed in Chapter 5 by considering design parameters beyond those considered in the experimental phase of research; and second, for developing a design procedure using SDOF analysis as a design tool for obtaining maximum design quantities as discussed in Chapter 6. An important aspect of the nonlinear SDOF analysis was to generate resistance functions to trace the variation in member stiffness through various stages of non-linear analysis. A significant effort was devoted to the generation of resistance functions with appropriate material constitutive models representing ECC and HSM with due considerations given to the effects of confinement by the enclosing aluminum tube as well as the properties of the reinforcing materials in the form of high-strength steel cables, steel chains, aluminum enclosure and externally bonded CFRP sheets. The resistance functions also offer an option of conducting SDOF manually using the US Army UFC charts developed for blast analysis in the inelastic range of materials under impulsive blast loads. This approach was also validated against both the test data and the analysis results obtained from the RC-Blast software and may be a preferred design tool for manual calculations with sufficient degree of accuracy. The details of the analytical investigation are discussed in this chapter.

4.2 RC-Blast Software

4.2.1 SDOF Analysis

RC-Blast was developed for blast analysis of reinforced concrete elements using a numerical approach for SDOF analysis under a specified pressure-time forcing function. It solves the dynamic equation of motion by employing "constant-acceleration numerical integration technique". The elements of the SDOF model, i.e., lumped mass (m), spring stiffness (k), and the applied force (F) are computed from the actual distributed mass, element flexural stiffness, and uniformly distributed blast load by employing transformation factors. The resulting equivalent mass (M_e), equivalent stiffness (k_e), and equivalent force (F_e) are used to express the equation of motion for a SDOF system.

$$M_e\ddot{u} + k_e u = F_e \quad 4.1$$

$$M_e = K_M M_t \quad 4.2$$

$$k_e = K_R k \quad 4.3$$

$$F_e = K_L F \quad 4.4$$

Where K_M, K_R and K_L are the transformations factors for mass, stiffness, and load.

$$K_M M_t\ddot{u} + K_R k u = K_L F \quad 4.5$$

Dividing all the terms by KL and substituting $\mathrm{k_R}$= $\mathrm{k_L}$ because the deflection caused by the load is directly proportional to stiffness, the equation motion becomes:

$$K_{LM} M_t\ddot{u} + k u = F \quad 4.6$$

Where $\mathrm{k_{LM}}$=$\mathrm{k_M}$/$\mathrm{k_L}$ is the load-mass factor.

The load-mass factor is an input item for RC-Blast when manual entry of resistance function is selected. These factors have been developed by (Biggs, 1964) for elastic and inelastic response using the principle of the conservation of energy based on an assumed shape function (deflected shape). They are also included the US Army document UFC 340 (2008). Table: *4.1* contains the load-mass factors, as well as the stiffness values for elements subjected to uniform blast pressures under different support conditions.

Element stiffness is computed as the slope of the resistance function (force-displacement relationship). The details of constructing resistance function are given in the next section. The spring constant k given in Table: *4.1* can be used if an idealized bilinear or a trilinear resistance function is employed and input in RC-Blast by the user. A typical element subjected to uniform lateral blast pressure develops a resistance function that can be idealized as a bi-linear relationship when simply supported with a plastic hinge forming at mid-height, and a trilinear relationship when plastic hinges form at mid-height as well as at the supports. Figure 4.1 illustrates these two scenarios. A more accurate way of constructing the resistance function is employed by the analysis module built in software RC-Blast, the details of which are explained in the next section.

Table: 4.1 Load-mass factors and stiffness constants for use in SDOF analysis

k: Spring constant I: Moment of inertia E: Elastic modulus		F = pL p: Peak uniform blast pressure per length R: Resistance			M_s :Negative moment at support R_m: Maximum resistance For members with uniform mass	
Loading diagram	Strain range	Load factor, K_L	Mass factor, K_M	Load-mass factor, K_{LM}	Spring constant k	Dynamic Reaction V
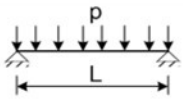	Elastic	0.64	0.50	0.78	$384EI/5L^3$	$0.39R+0.11F$
	Plastic	0.50	0.33	0.66	0	$0.38R_m+0.12F$
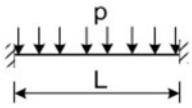	Elastic	0.53	0.41	0.77	$384EI/L^3$	$0.36R+0.14F$
	Elastic-plastic	0.64	0.50	0.78	$384EI/5L^3$	$0.39R+0.11F$
	Plastic	0.50	0.33	0.66	0	$0.38R_m+0.12F$
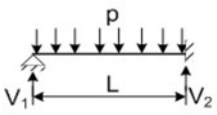	Elastic	0.58	0.45	0.78	$185EI/L^3$	$V_1=0.26R+0.12F$ $V_2=0.43R+0.19F$
	Elastic-plastic	0.64	0.50	0.78	$384EI/5L^3$	$V=0.39R+0.11F\pm M_s/L$
	Plastic	0.50	0.33	0.66	0	$V=0.39R_m+0.12F\pm M_s/L$

Adopted from Biggs (1964)

4.2.2 Computation of Resistance Function

The SDOF analysis in RC-Blast is conducted either by following a user-specified resistance function or by internally generating the resistance function through the built-in member analysis module. If internal generation of resistance function is selected, the analysis module constructs

it from given geometry, support conditions and material constitutive models while also accounting for the presence of axial load. The software is intended to conduct flexural analysis. It is also equipped with a hysteretic model to compute the rebound stiffnesses.

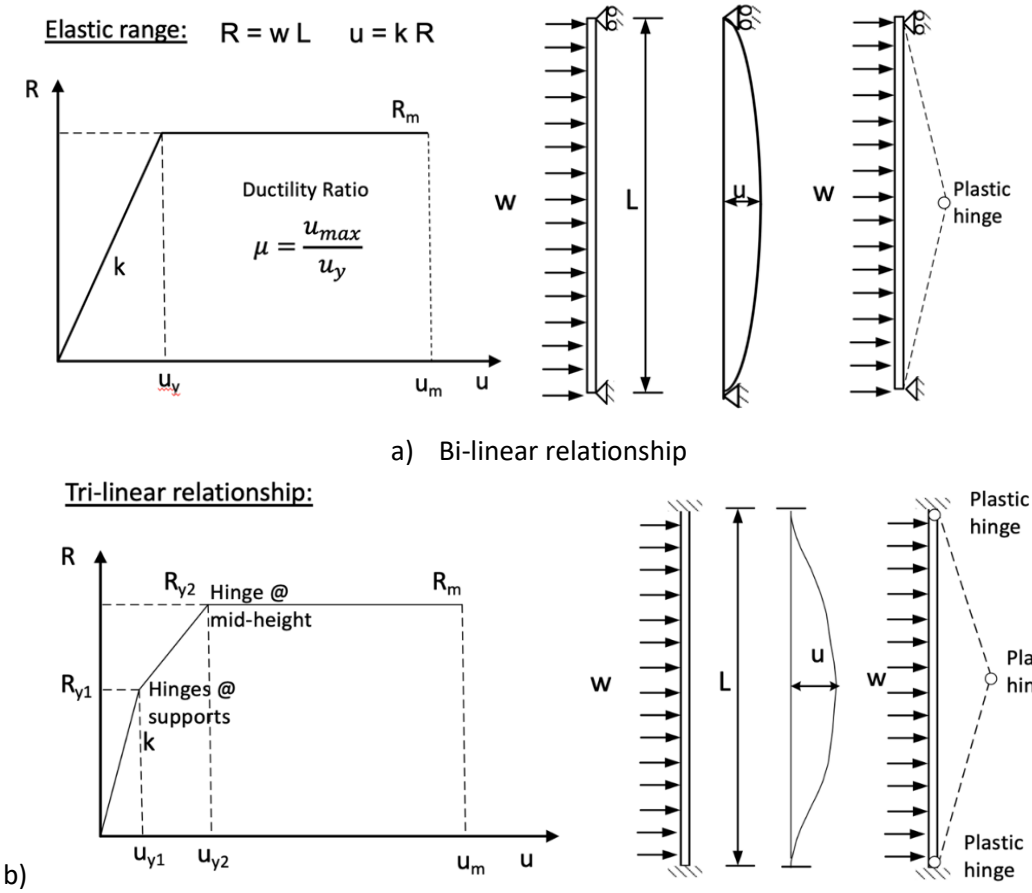

a) Bi-linear relationship

b)

b) Tri-linear relationship

Figure 4.1: Idealized resistance functions defining stiffness k

The first step executed by the built-in module is the computation of sectional moment curvature relationship. This is done through a strain compatibility analysis based on standard assumptions of flexural analysis. The assumptions include Bernoulli's principle (plane sections before bending remaining plane after bending), perfect bond between concrete and reinforcement, and the use of known material models. The sectional analysis is conducted by dividing the cross-section into horizontal strips and integrating strains, stresses and strip forces. The strain profile for a section is generated by selecting the extreme compressive fiber strain and initial depth of the neutral axis. Through an iterative procedure, the neutral axis location is

established when the internal forces generated on concrete and steel achieve force and moment equilibrium. The moment-curvature relationship is established under incrementally increasing moment. Integration of curvatures along the member length up to the yield curvature provides elastic and cracked rotations, from which deflections are computed up to the yield point. Post-yield deformations are computed by considering plastic hinge rotations and displacements based on the assumption of forming ultimate rotation with a constant curvature distribution within the plastic hinge length, which is a user-defined input quantity. The member rotation at ultimate is specified below.

$$\theta_u = (\phi_u - \phi_y)\, x\, L_{pl} + \frac{M_y}{k_{rot}} \qquad 4.7$$

Yield moment M_y represents the moment of a member at the stage of yielding while θ_u, ϕ_u and L_{pl} correspond to maximum rotation, maximum curvature, and plastic hinge length, respectively. L_{pl} can be specified either as being equal to member dimension or the effective section depth. There are different models in the literature for defining plastic hinge length (Corley, 1966), (Mattock, 1964) and (Sawyer, 1964). The software can manage numerical errors by following the secant stiffness formula which represents the slope of the linear curve of the moment rotation relationship starting from the origin to the point where moment and rotation are incremented as shown in the equation below:

$$k_{sp,i} = \frac{M_i}{\theta_i} \qquad 4.8$$

The rotational spring stiffness of the hinge is represented by the term $k_{sp,i}$. Furthermore, the incremental moment corresponding to M_i represents rotation θ_i. The resistance function and load-mass transformation factors are calculated in the pre-yield stage based on an increasing lateral load and the resulting displaced shape. Following yielding, the hinge reacts in line with its moment-rotation connection, increasing the inelastic rotation correspondingly until a new rotational spring stiffness is achieved. After all plastic hinges are produced, RC-Blast proceeds iteratively along the moment rotation curve. From the inelastic rotations at the critical sections, all specimen displacements are then determined. The sectional and member analyses described

above are highly dependent on the material constitutive models discussed in the next sub-section.

4.2.3 Material Constitutive Models

An important set of input parameters specified by the user is material constitutive models in the form of stress-strain relationships for concrete and reinforcement. Two different types of concrete stress-strain relationships can be specified in RC-Blast, one for confined core concrete and the other for unconfined cover concrete. In the current investigation the cover concrete option was not utilized as it does not exist. Both ECC and HSM are confined by the enclosing aluminum section. Wong et al. (2020) reported that the confined behaviour of high-strength ECC is similar to that of high-strength of concrete. Similarly, the behaviour of confined HSM was established by Feng et al. (2021) to be similar to that of high-strength concrete. Therefore, it was decided to use the confined concrete model proposed by (Saatcioglu & Razvi, 1992). Accordingly, the confinement effect on concrete is to increase strength and deformability of concrete in compression. The level of confinement provided by transverse reinforcement is dependent on the volumetric ratio, the spacing, and the arrangement of transverse reinforcement. In a cementitious material like ECC or HSM confined by an enclosing tube, as in the case of the aluminum mullion, it is reasonable to assume maximum effectiveness of confinement reinforcement in terms of the spacing and arrangement of discrete steel reinforcement provided in typical columns with longitudinal and transverse reinforcement for which the confinement model was developed. The passive confinement pressure provided by the aluminum tube can be computed by considering the yield strength of the aluminum and assuming that the lateral pressure would be uniformly distributed as in the case of closely spaced spiral reinforcement where the confining pressure (f_ℓ) is dependent on hoop tension with maximum effectiveness of confinement, leading to uniform pressure.

$$f'_{cc} = f'_{co} + k_1 f_\ell \qquad 4.9$$

$$k_1 = 6.7(f_\ell)^{-0.17} \qquad 4.10$$

$$f_\ell = \frac{2t_a f_{ya}}{b_a} \quad 4.11$$

$$K = \frac{k_1 f_\ell}{f'_{co}} \quad 4.12$$

Where, f'_{cc} and f'_{co} are confined and unconfined compressive strengths of the cementitious infill material (ECC or HSM). Coefficient k_1 relates lateral confinement pressure (f_ℓ) to the incremental increase in strength (K) and was obtained from empirical data on triaxial tests. Yield strength of aluminum is denoted by f_{ya}, and the thickness of the aluminum tube and the short side dimension (parallel to the bending axis) are designated as t_a and b_a, respectively. The stress strain relationship can then be expressed using Hognestad's parabola for the ascending branch up to the peak stress (f'_{cc}) and corresponding strain (ε_1) as follows, followed by a linear descending branch to pass through 85% of confined strength at a strain of ε_{85}.

$$f_c = f'_{cc}\left[2\left(\frac{\varepsilon_c}{\varepsilon_1}\right) - \left(\frac{\varepsilon_c}{\varepsilon_1}\right)^2\right]^{\frac{1}{(1+2K)}} \leq f'_{cc} \quad 4.13$$

$$\varepsilon_1 = \varepsilon_{01}(1 + 5K) \quad 4.14$$

$$\varepsilon_{85} = 260\rho\varepsilon_1 + \varepsilon_{085} \quad 4.15$$

$$\rho = 2t_a b_a \quad 4.16$$

Where, ρ is the transverse reinforcement ratio, ε_{01} and ε_{085} are the strain values for unconfined material at unconfined peak and 85% of the unconfined strength on the descending branch. Figure 4.2 shows the confinement model and the resulting unconfined and confined materials. Confined ECC and HSM stress-strain relationships obtained in 5'' (127 mm) and 6" (152 mm) mullions with 1/8 in (3.2 mm) and 3/16 " (4.8 mm) wall thicknesses are illustrated in Figure 4.3 and Figure 4.4.

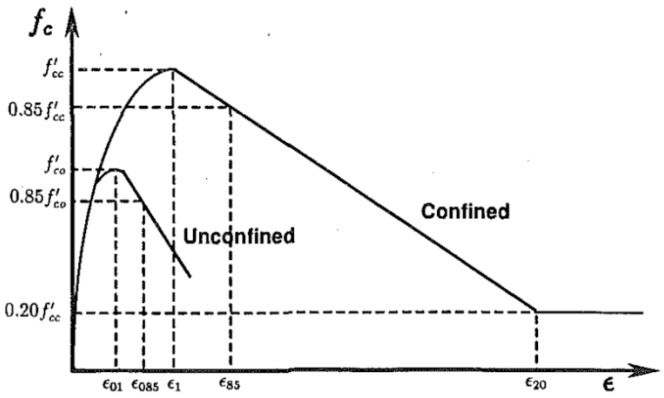

Figure 4.2: Confined concrete model by Saatcioglu and Razvi (1992)

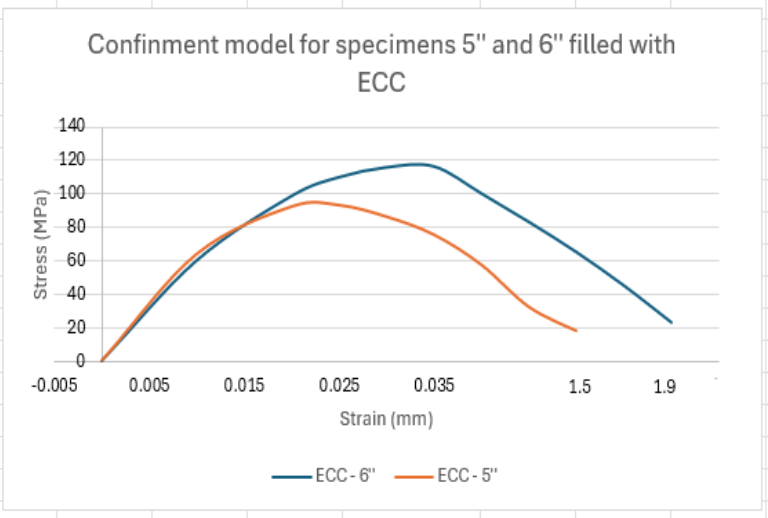

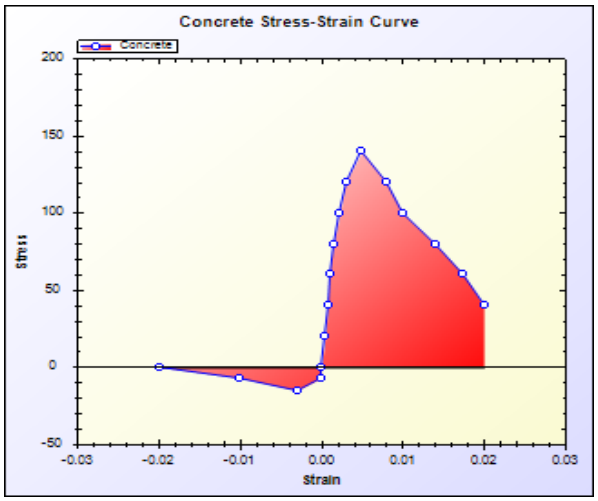

Figure 4.3: Un confined and confined ECC stress-strain relationships for 5” and 6” aluminum mullions

The stress-strain relationships used for aluminum tubes, internal steel cables, and the chain, as well as externally bonded CFRP sheets are given in Chapter 3 as obtained from material testing.

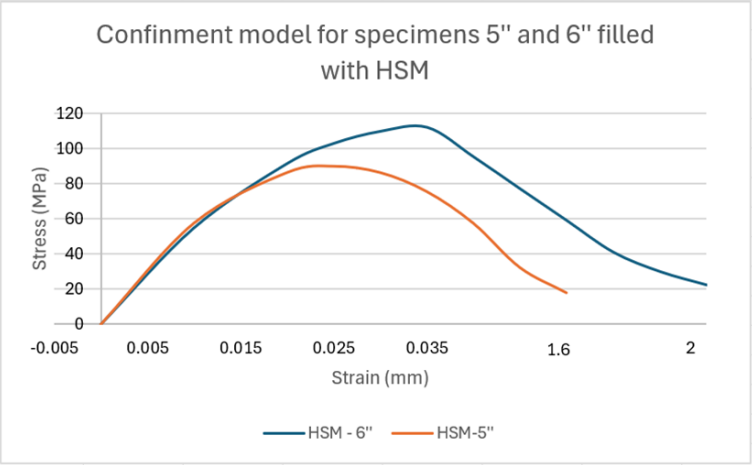

Figure 4.4: Confined HSM stress-strain relationships for 5” and 6” aluminum mullions

4.2.4 Resistance Functions and SDOF Analysis for Test Mullions by RC-Blast

The procedure for establishing resistance functions discussed in the preceding sections was applied to each of the 16 mullions tested in the experimental phase. The geometry, material constitutive models, and support conditions were specified for each mullion. Each specimen model consisted of an external aluminum tube and either ECC or HSM material filling either core dimensions of 45 mm x 121 mm (for specimens 1F, 2FR, 5F, 6F, 9FH, 10FH, 13FH and 15FR) or 41.4 mm x 142.4 mm (for specimens 3F, 4FR, 7F, 8F, 11FH, 14FH, and 16FR). The software was developed for reinforced concrete sections and therefore the reinforcement is specified in terms of re-bars positioned in the section with a specific area. The aluminum tube with either 1032 mm^2 (for 5’’ mullions) or 1857 mm^2 (for 6’’ mullions) area was specified in terms of closely spaced re-bars around the perimeter of the section with the aluminum stress-strain relationship. This is shown in Figure *4.5*. The aluminum properties used for all specimens were yield strength of 270 MPa, modulus of elasticity of 70000 MPa, and density of 2700 kg/m^3.

The software also has the capability of specifying externally bonded FRP reinforcement along the tension face. When U-shaped FRP was used the two sides of the FRP was introduced as

additional reinforcement concentrated at the centroid of the side lengths. Figure 4.5 illustrates the cross-sectional geometry and the reinforcement locations. Fully composite behaviour was assumed between the infill material and the aluminum tubes. This was verified during the tests as there was no separation of the materials observed. The software was equipped with elasto-plastic hysteretic model. This model facilitates member stiffness during unloading and reloading (rebound) branches of the force-displacement relationship under cyclic loading.

The majority of the mullions suffered from tension rupturing of the aluminum during testing. Some suffered from local compression buckling of the critical region, especially if they were reinforced with higher percentage of reinforcement. The resistance functions computed by RC-Blast are shown in Figure 4.6. It is noteworthy that the mullions with fixed supports developed elastic-plastic regions (tri-linear behaviour) because of the sequential hinging of the mid-height region and the support regions. The plastic hinge length for each hinge was taken to be equal to the length of the aluminum tube in the direction of loading, i.e., 127 mm and 152 mm for 5” and 6” mullions, respectively.

RC-Blast requires mass to be input for the SDOF analysis. The mullion mass for each specimen was calculated as the combined mass of the aluminum mullion, the infill material and the internal reinforcement, if any. The mass of the load application device used during testing, consisting of steel sheets and horizontal HSS elements was 107 kg and it was also included in the analysis. This was necessary as the load application device, described in Chapter 3, initially responded together with the specimen during the test as they together moved toward the maximum displacement in the positive direction. After reaching the maximum displacement the load application device separated from the specimen as observed in all the recorded high-speed videos. The load application device was designed to transfer the reflected pressure at the end of the Shock Tube to the test specimen as linearly distributed blast load without providing resistance. Hence, its function was limited to applying the load. The thin steel sheet was free to follow the specimen without providing any resistance to applied load. The resistance to blast load was only provided by the specimen. In the RC-Blast analysis the mass remained constant until the end of the blast response. Therefore, the analysis results beyond the peak were not reliable and hence were not used. Obtaining maximum mullion deflection was sufficient for the purpose of

the current investigation and the use of SDOF as a design tool through which the maximum design displacement could be obtained.

The blast load is specified in the form of reflected pressure-time history. For the reflected pressure under which the specimens were tested, it is usually sufficient to idealize the forcing function as a linear pressure-time relationship.

The blast load is specified in the form of reflected pressure-time history. For the reflected pressure under which the specimens were tested, it is usually sufficient to idealize the forcing function as a linear pressure-time relationship. The RC-Blast SDOF analysis results are shown in Appendix B in terms of displacement response time histories for all 16 test specimens under all the shots applied during the tests. Maximum displacements obtained the analyses are tabulated in Table 4.2. The analyses for mullions with fixed supports were conducted twice, first with fixed supports and the second time with simple supports. This was done because the support fixity during the tests was provided by clamping the ends with HSS sections to prevent rotations. However, the test videos indicated that the supports were not always fully fixed with zero support rotation. The specimens were not instrumented for support rotations and the degree of fixity could not be established exactly. Comparisons of computed deflections with experimental data discussed in the next section indicates that when 80% support fixity was considered for specimens with fixed supports (M-2FR, M-4FR, M-6F, M-8F, M-10FH, M-12FH, M-16FR) the correlation with test data improved significantly. For comparison with experimental data, which is given later in this chapter, the results shown in Table 4.2 include simply supported analysis for these specimens.

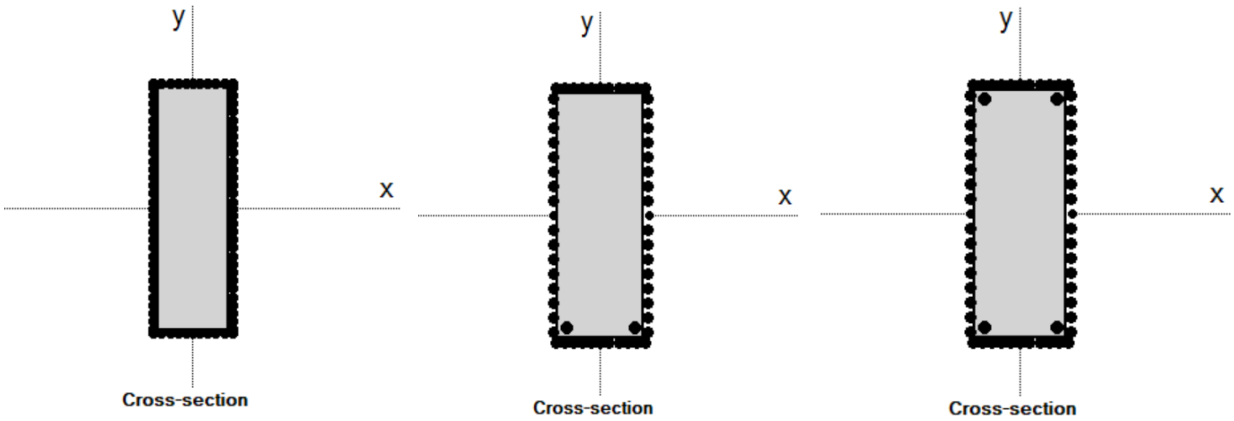

a) Mullion with infill material b) Section with two cables c) Section with four cables

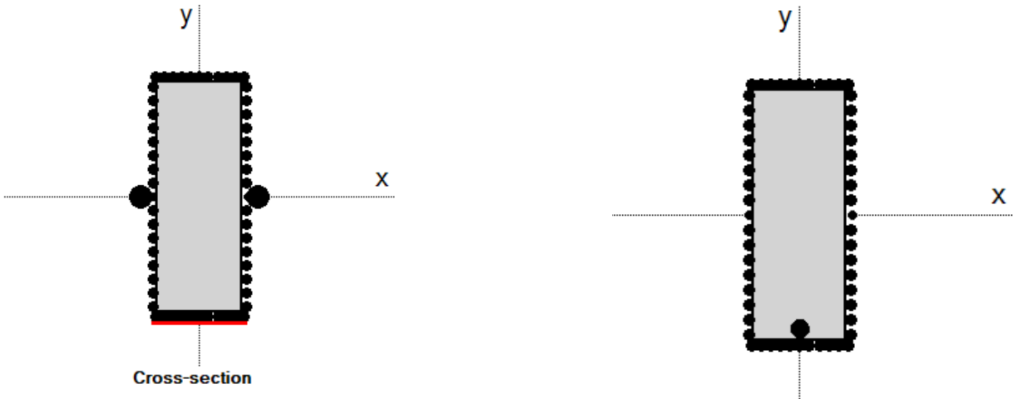

d) Mullion with external CFRP e) Section with steel chain

Figure 4.5: Cross-sectional geometry and reinforcement arrangement

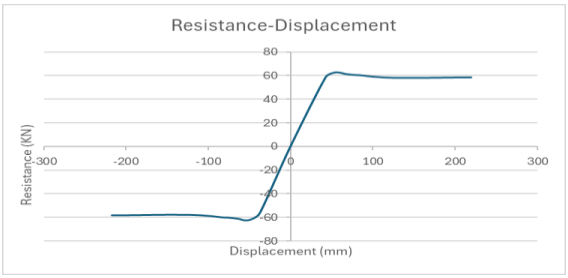

(a) M-1F

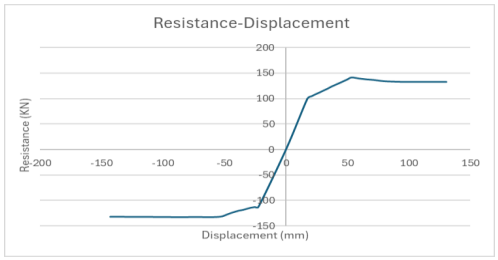

(b) M-2FR

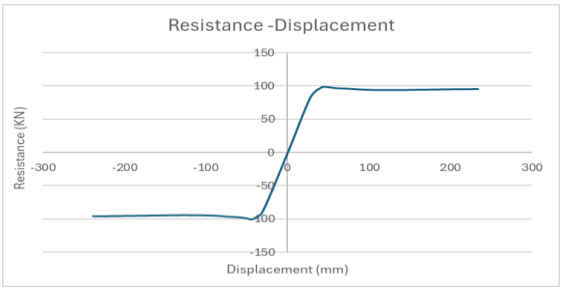

(c) M-3F

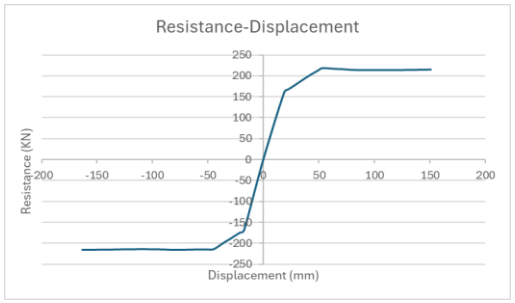

(d) M-4FR

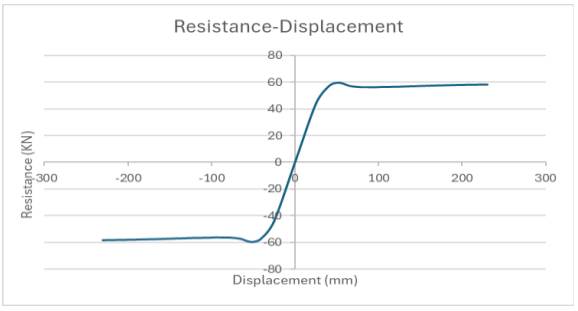

(e) M-5F

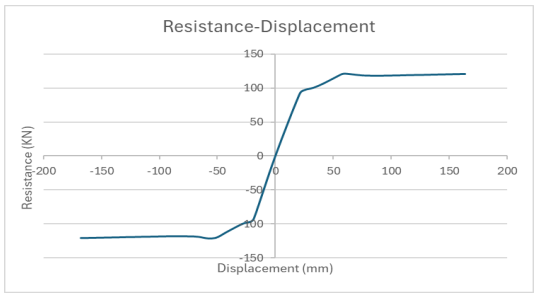

(f) M-6F

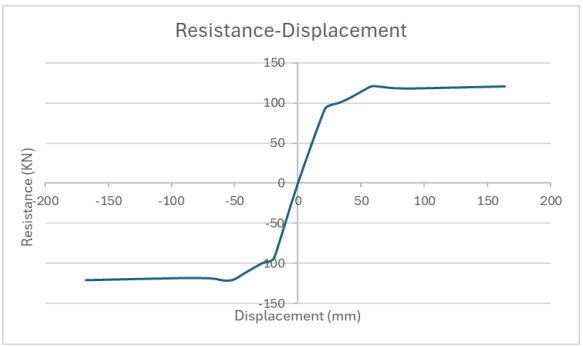

(g) M-7F

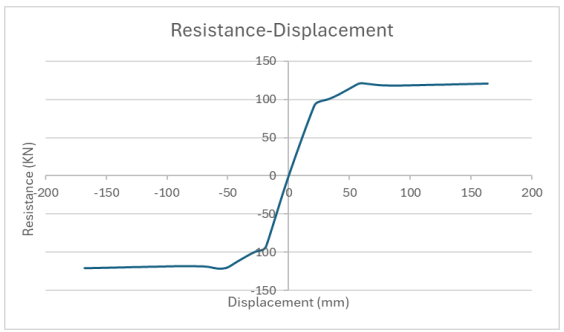

(h) M-8F

Figure 4.6: (Cont'd)

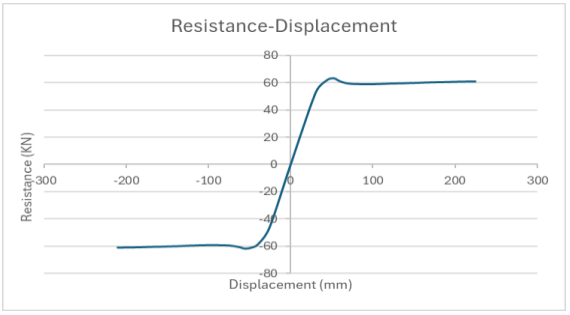

(i) M-9-FH

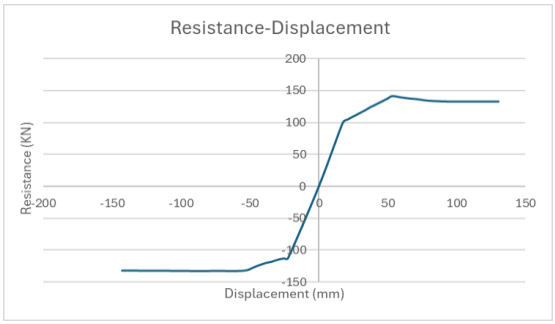

(j) M-10FH

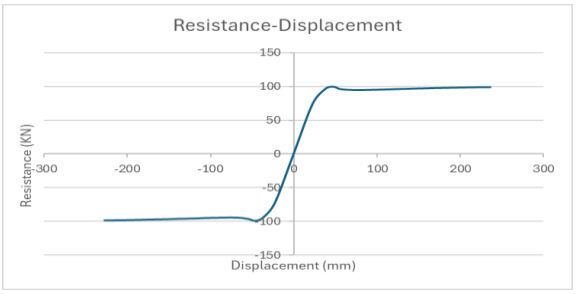

(k) M-11FH

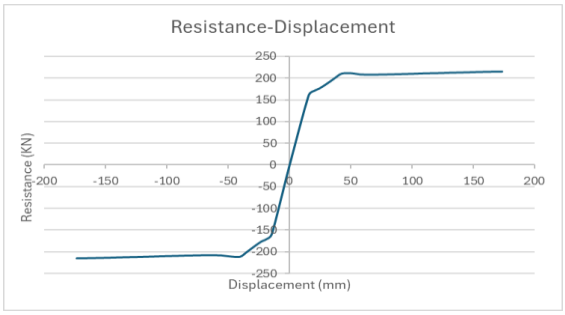

(l) M-12FH

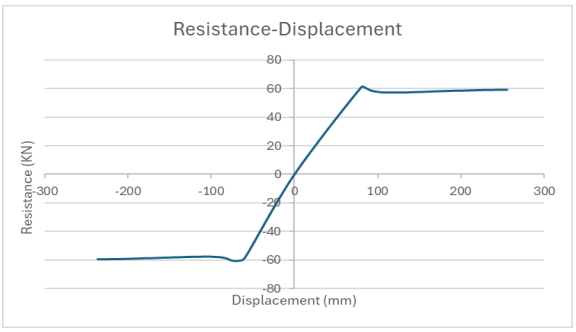

(m) M-13FH

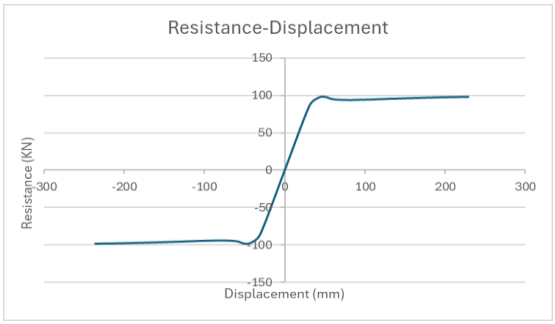

(n) M-14FH

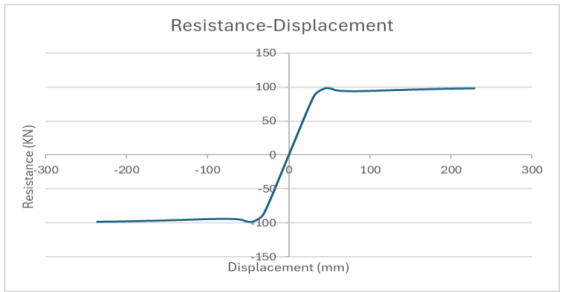

(o) M-15FR

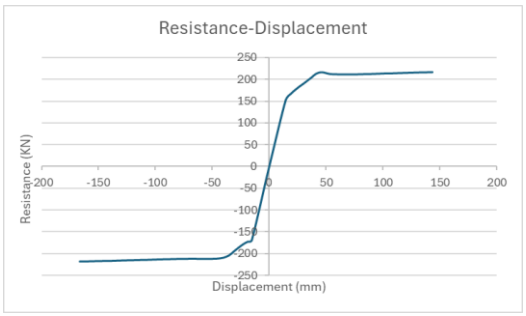

(p) M-16FR

Figure 4.6: Resistance functions of test mullions as computed by RC-Blast

4.3 SDOF Analysis using UFC Charted Solution

The US Army document UFC 3-340-02 (2008) includes empirical charts that permits SDOF analysis for inelastic analysis to facilitate manual calculations. The charts are provided for different forcing functions and bi-linear resistance curves. Figure 4.7 shows the UFC chart for a triangular forcing function, representative of the positive phase loading under reflected blast shock wave and an idealized bi-linear resistance function. For mullions that have fixed supports, the resistance function can be tri-linear as shown in Figure 4.1 (b). In this case the resistance function can be idealized as a bi-linear relationship having equal area under the curve. This is shown in Figure 4.8. The horizontal axis is for "t_d/T" ratio, where "t_d" is the positive phase duration of load. "T" is the fundamental period of the SDOF system based on the effective elastic stiffness. The vertical axis gives expected displacement ductility factor as the ratio of maximum to yield displacement. The curves in the chart are for the ratio of maximum resistance to maximum blast load (R_m/F_1). The following is the UFC charted solution for Specimen M-1F under Shot 1, provided as an example. The calculations for all specimens are included in Appendix B. The maximum deflections computed by this charted solution manually are also included in Appendix C.

R_m= 58.5, U_y=42.6, $K_s = \frac{R_m}{U_y} = \frac{58.5}{42.6}$ =1.37 KN/mm

$T_s = 2\pi\sqrt{\frac{K_{LM}\,X\,M}{K_s}} = 2\pi\sqrt{\frac{0.78\ x\ 140.64}{1.37\ x\ 10^6}}$ = 56ms $\rightarrow T_d = \frac{2\ x\ I_r}{P_r} = \frac{2\ x\ 269.3}{27.5}$ = 19.6 ms, $\frac{T_d}{T_s}$ = 0.35, when μ =1

From the UFC Chart $\frac{R_m}{F_1}$ =1.1, Tributary Area (A_T) = 2.032 x 2.032 = 4.129 m^2,

$F_1 = P_1$ x A_T= 27.5 x 4.129= 113.6 KN

R_m (demand) = 113.6 x 1.1 = 125 KN > R_m (capacity) = 59KN (The specimen is in inelastic zone), Therefore, use K_{LM} = 0.70 (closer to K_{LM} = 0.66)

$T_s = 2\pi\sqrt{\frac{0.7\ x\ 140.64}{1.37\ x\ 10^6}} = 53\text{ms} \rightarrow \frac{T_d}{T_s} = 0.37 \rightarrow \frac{R_m}{F_1}$ =0.52 →read μ = 2.3, Um = 42.6 x 2.3 = 97 mm

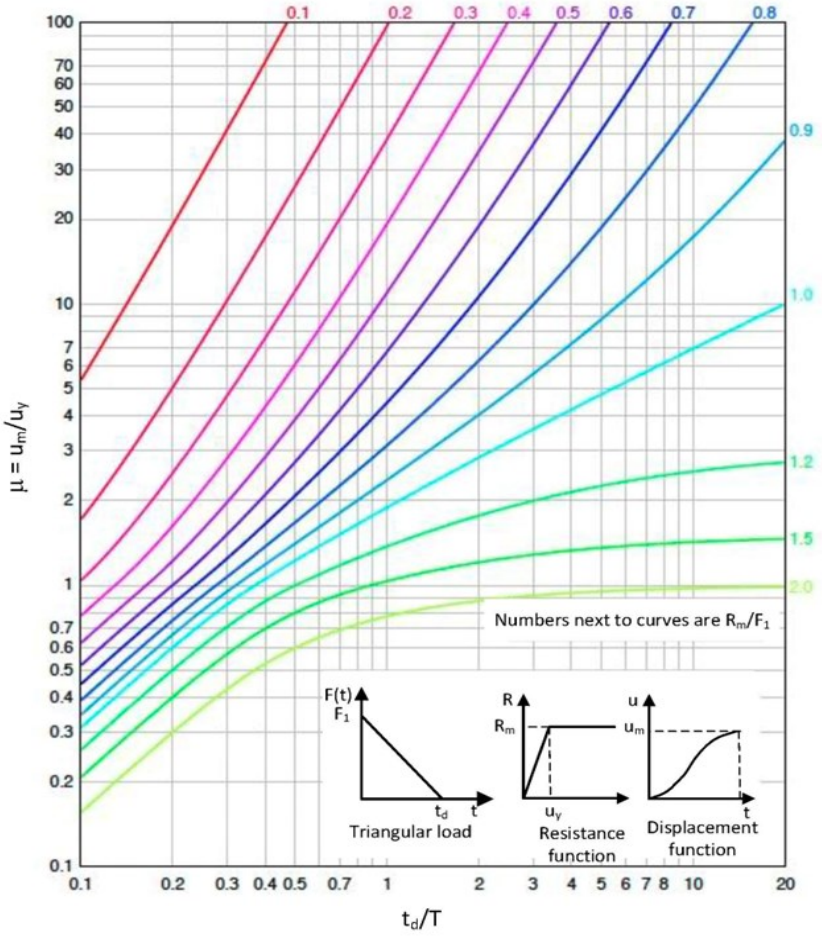

Figure 4.7: UFC Chart for nonlinear SDOF analysis

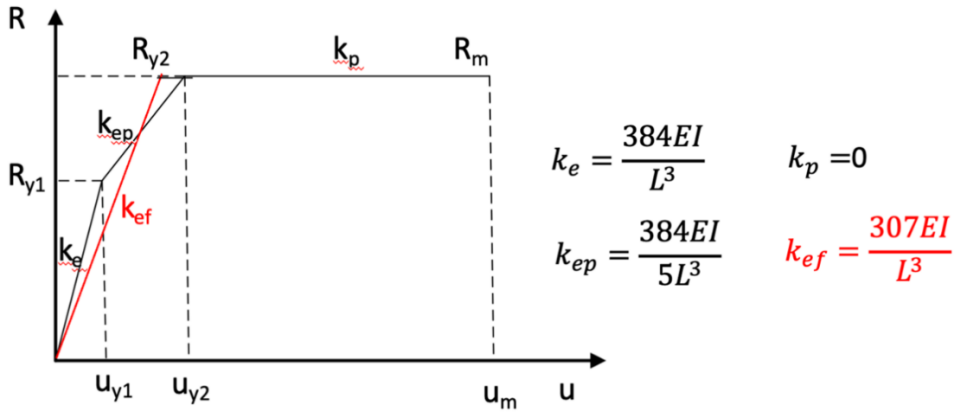

Figure 4.8: Bi-linear idealization of a tri-linear resistance function

4.4 Comparisons of Experimental and Analytical Results

The maximum deflection response quantities, experimentally measured by the shock tube tests are compared with those computed by SDOF analyses either using software RC-Blast or UFC manual charted solution in Table 4.2. The results are also plotted in Figure 4.10 to Figure 4.17 as bar charts for the first two shots applied to all the specimens in groups of 4 for clarity in the plots. These two shots represent limited inelasticity, where the correlations between the analysis and experimental results are expected to be good prior to rupturing or buckling of the aluminum beyond which the analysis is not intended to represent the behaviour. Exception to this observation is M-7F which failed during the second shot. Figure 4.18 and Figure 4.19 shows the comparisons of results for the third shot. The comparisons of the recorded and computed mid-height deflections show very good correlations, indicating that the RC-Blast SDOF analysis can be used for design purposes, as discussed in Chapter 6. The statistical analysis of data was also conducted. This was conducted for all mid-heigh deflections, including those with simple supports as well as fixed supports. Table 4.2 shows the ratio of SDOF analysis to experimentally recorded deflection values with a mean value of 0.94 and the coefficient of variation of 24%. The experimental versus computed deflections are plotted in Figure 4.9(a) with the regression analysis indicating the coefficient of determination (R-square value) of 0.90. When the degree of fixity for fixed support conditions was relaxed as observed during the tests, the correlation improved. The same data was re-analyzed by assuming 80% fixity at the supports. This is shown in Table 4.2 and the experimental values are plotted against the computed values in Figure 4.9(b). This time the regression analysis indicated the coefficient of determination (R-square value) of 0.92 with a mean value of 1.06 for the ratio of SDOF analysis to experimental deflections and a coefficient of variation of 19%.

The discrepancies between the experimental and analytical values, however small they may be, can be explained by several factors. Shock tube testing for blast loading involves inherently a challenging procedure. In addition to the support conditions, especially for fixed supports mentioned above, some difficulties were encountered with LVDT readings. The LVDTs sometimes moved during testing and sometimes malfunctioned. For these cases the backup system of

readings from high-speed cameras were used. This may have introduced some inaccuracies. The shock tube also moved during the firing of shots. These movements were measured and monitored, and it was found to vary, depending on the test, between 2.0 mm and 6.0, for which the correction was not introduced to the reported values because of the relatively small effects. Furthermore, the use of the load application device may not have transferred the load as perfectly as anticipated, especially in shots 2 and shot 3, if the specimen survived the previous shots, as each time the shots were applied on specimens that have already experience residual displacements. Although this was accounted for in the displacement plots, this procedure may also be a source of error. The contact between the load transfer device and the specimen was assumed to be uniform and perfect up until the maximum displacement, providing the reason for including the mass of the load application device in analytical calculations, this may not be the case during testing, also resulting in small errors. Furthermore, the pressure time history recorded during testing was idealized as a linear relationship for the analysis, which may be an additional error in the analysis results. The transformation factors used in the software to transform distributed specimen mass to a lumped mass and the uniform blast pressure to a concentrated load for SDOF analysis were internally generated based on Table: *4.1* (Biggs, 1964)for elastic, elastic-plastic and plastic regions of response. Even though the results are not very sensitive to minor changes is transformation factors, this could account for some of the analytical inaccuracies. Similarly, the input item for plastic hinge length was assumed to be the cross-sectional dimension in the direction of loading. This could vary in actual response and contribute to sources of error. Although the correlation of experimental data with analysis results as indicated by their ratios resulted in R-square value of 0.90 for the regression analysis with a mean value of 0.94, indicating very good agreement, the aforementioned sources of errors are recognized as potential contributions to some of the discrepancies observed.

As was mentioned in Section 4.3, the SDOF analysis was also conducted manually by following the UFC charted solution, using the charts provided by the US Army document UFC 3-340-02 (2008). The results are tabulated in Table 4.2 with the details given in Appendix C. It is noteworthy that the resistance function used in the UFC analysis was obtained from that computed by RC-Blast. However, the UFC charts are given for bi-axial resistance functions and the specimens with

fixed supports developed tri-linear resistance functions. For these cases an idealized bi-linear resistance function was obtained as illustrated in Figure *4.8*. The results are compared with the SDOF analysis conducted by RC-Blast in Figure 4.9 (c) and show very good correlations with the ratio of RC-Blast deflections to UFC deflections showing a mean value of 1.04 and a coefficient of variation of 13%. The minor discrepancy observed between these two sets of results is attributed to the inaccuracies that result from visually reading values from the charts, idealization of the resistance function as a bi-linear relationship, as well as the sources of errors discussed earlier related to the use of RC-Blast software for SDOF analysis. The comparisons discussed in this section demonstrate that SDOF analysis for design purposes can be conducted either by using a numerical approach, as in the case of software RC-Blast, or a charted manual procedure as in the case of the UFC procedure.

4.5 Pressure-Impulse Diagrams

Elements experience different combinations of pressure and impulse when exposed to blast loads. The level of damage, particularly the development of inelastic displacement, can be studied by analyzing pressure-impulse (P-I) diagrams, also known as iso-damage curves. These diagrams are commonly used for design purposes. The impact of blast load can be correlated with the peak response of the structural system through the utilization of P-I curves. The evaluation of structural safety involves demonstrating the extent of damage caused by blast loading effects. The levels can be evaluated by analyzing P-I diagrams, which depict the extent of damage to each component caused by the blast loading impact. Figure 4.20 displays a standard P-I curve that is primarily categorized into three sections, varying along two axes. The vertical axis shows the pressure exerted, while the horizontal asymptote reflects the impulse applied. The initial region corresponds to the impulse zone, known as the impulsive region, where the damage is not considered susceptible to the degree of applied pressure. In this region, the damage increases proportionally with the impulse while the pressure remains constant. Meanwhile, the dynamic region signifies the alterations in damage that occur because of variations in both pressure and impulse. Moreover, in the quasi-static area, the level of damage escalates in direct proportion to the pressure applied for a given impulse.

The level of maximum deflection for a member subjected to a specific pressure and impulse combination can be specified by the user of RC-Blast program and the P-I diagram can be easily generated. An iterative approach is used by the software to implement P-I plots for a specified maximum displacement, which may reflect the required level of ductility.

The P-I diagram clarifies the blast threat range for each element comprising the damage level of different levels of blast load applications noted that pressure-impulse combinations related to various combinations of charge weight and standoff distance. Pressure-impulse diagrams were generated for the 16 hardened mullions tested and analyzed with and without the hardening techniques implemented. These P-I diagrams can be used as quick design aids for given design basis threats (DBTs) for the specific mullions for which they were developed. RC-Blast (or similar SDOF software) can be used to expand the mullions considered for commonly used mullions if a set of design aids are to be generated for common applications. Figure 4.21 illustrates a sample P-I diagram generated for Mullion M-1F at the first blast shot. Appendix B contains all the P-I diagrams generated.

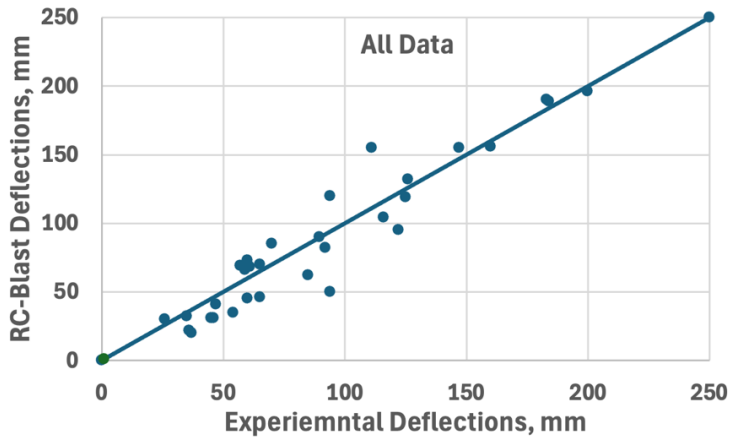

(a)

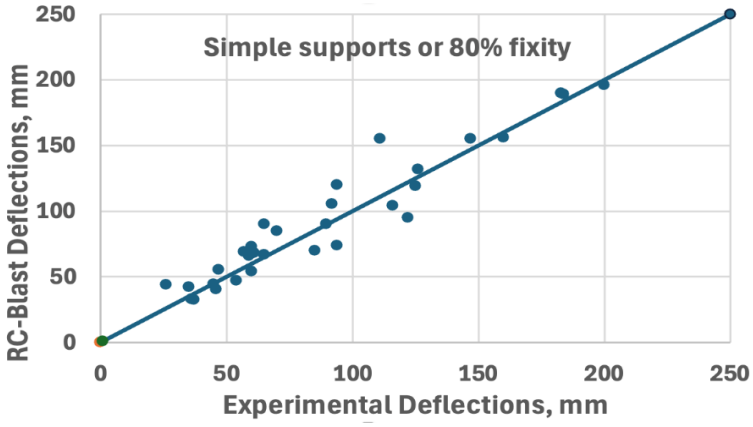

(b)

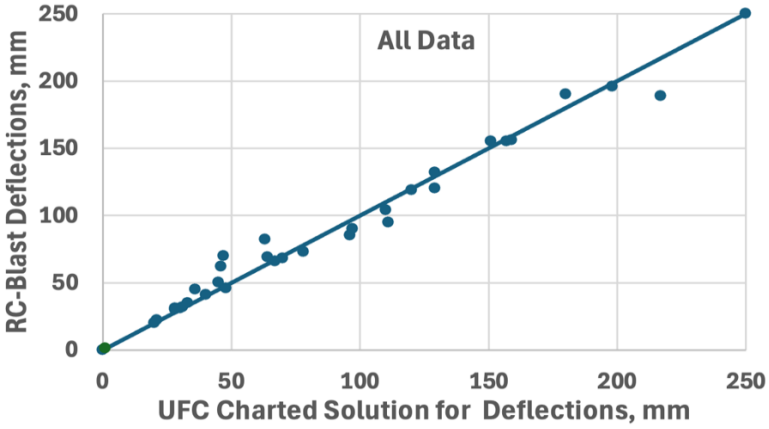

(c)

Figure 4.9: Comparisons of mid-height maximum deflections for the first 2 shots, excluding shots that resulted in the failure of specimens

Table 4.2: Mid-height deflections obtained by tests and SDOF analysis

Specimen Label	Target Driver pressure *Psi/KPa*	Shock Wave Properties			Mid-Span Displacement Comparison				
		Reflected Pressure P_r *kPa*	*Reflected Impulse* I_r *kPa - ms*	*Duration* t_d *ms*	Experimental Deflection δ_{exp} mm	RC-Blast (SDOF) $\delta_{RC-Blast}$ *mm*			UFC-3-340-02 δ_{UFC} *mm*
						Simple Supports	Fixed Supports	80% fixity	
M – 1F Simply Supported	30 (207)	27.5	269.3	19.5	89.5	90			97
	40 (276)	42.0	414.9	19.8	184	189			217
	60 (414)	---	---	---	---	---	---	---	---
M – 2FR Fixed Supports	30 (207)	34.4	330.2	19.6	60		45	54	36
	40 (276)	43.6	413.2	18.0	85		62	70	46
	60 (414)	54.1	561.3	21.0	120		115		77
M – 3F Simply Supported	30 (207)	35.3	359.5	20.0	59.6	73			78
	40 (276)	46.6	478.7	19.8	93.8	120			129
	60 (414)	65.1	542.7	18.4	115.4	200			196
M – 4FR Fixed Supports	30 (207)	28.6	343.0	20.0	36.9		20	32	20
	40 (276)	39.1	417.4	18.0	26		30	44	28
	60 (414)	52.6	549.0	20.0	81.6		48		44
M – 5F Simply Supported	30 (207)	46.0	331.9	17.6	183	190			180
	40 (276)	39.3	396.3	19.8	168	196			198
	60 (414)	---	---	---	---	---	---	---	---
M – 6F Fixed Supports	30 (207)	32.9	330.5	17.6	93.5		50	74	48
	40 (276)	45.1	449.3	18.0	92.3		82	105	63
	60 (414)	---	---	---	---	---	---	---	---
M – 7F Simply Supported	30 (207)	33.7	340.0	18.0	59	66			67
	40 (276)	46.0	493.0	20.8	202	120			123
	60 (414)	---	---	---	---	---	---	---	---
M –8F Fixed Supports	30 (207)	37.5	341.0	18.4	46.4		31	40	30
	40 (276)	42.8	436.5	20.6	47.4		41	56	41
	60 (414)	55.5	579.7	19.2	121.5		62		60
M – 9FH Simply Supported	30 (207)	37.2	347.7	18.6	126.3	132			129
	40 (276)	40.1	416.0	19.2	160(Failed)	156			159
	60 (414)	---	---	---	---	---	---	---	---
M – 10FH Fixed Supports	30 (207)	37.4	347.7	20.8	65.4		46	67	48
	40 (276)	41.5	452.0	20.2	65		70	90	47
	60 (414)	62.8	621.3	19.8	223		153		100
M – 11FH Simply Supported	30 (207)	34.8	334.0	18.0	61	68			70
	40 (276)	52.9	516.0	19.7	147	155			151
	60 (414)	---	---	---	---	---	---	---	---
M – 12FH Fixed Supports	30 (207)	38.3	352.9	21.0	35		32	42	31
	40 (276)	41.9	447.2	19.8	54		35	47	32
	60 (414)	56.5	616.4	21.4	68		62		50
M – 13FH Simply Supported	30 (207)	28.7	307.4	16.4	122	95			111
	40 (276)	40.2	417.4	19.0	111	155			155
	60 (414)	---	---	---	---	---			---
M – 14FH Simply Supported	30 (207)	34.6	345.3	17.6	56.9	69			64
	40 (276)	41.2	453.0	16.8	69.8	85			96
	60 (414)	55.0	575.0	17.8	129	150			176
M – 15FR Simply Supported	30 (207)	30.4	312.8	17.6	116	104			110
	40 (276)	33.2	310.8	18.2	125	119			124
	60 (414)	---	---	---	---	---	---	---	---
M – 16FR Fixed Supports	30 (207)	34.2	367.6	20.2	35.7		22	39	21
	40 (276)	40.7	450.9	24.4	45		31	51	29
	60 (414)	57.0	606.0	21.0	74		54		39
	80 (551)	78.7	683.0	19.6	81.6		100		84

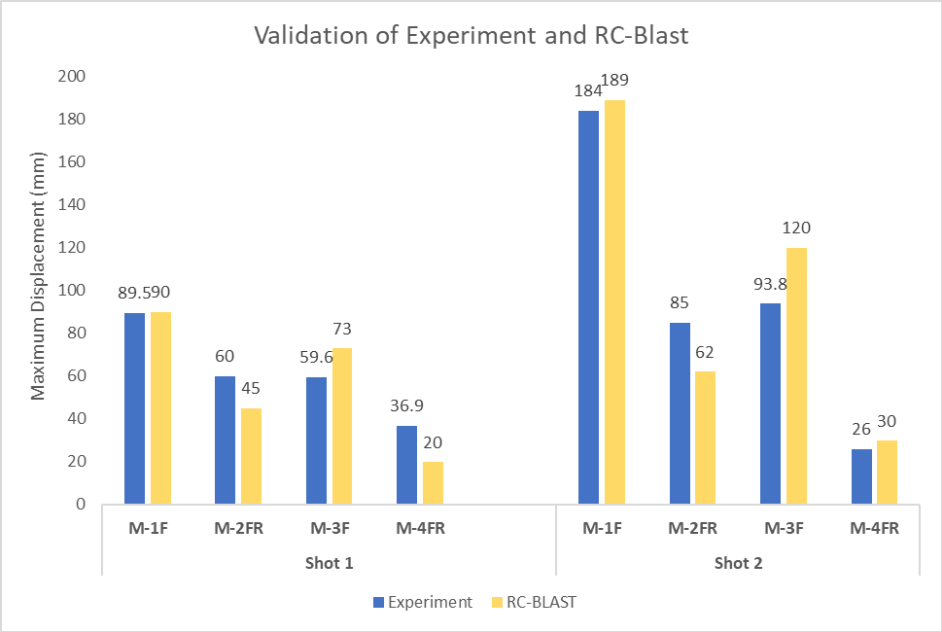

Figure 4.10: Validation of experiment vs SDOF (M-1F, M-2FR, 3F and 4FR)

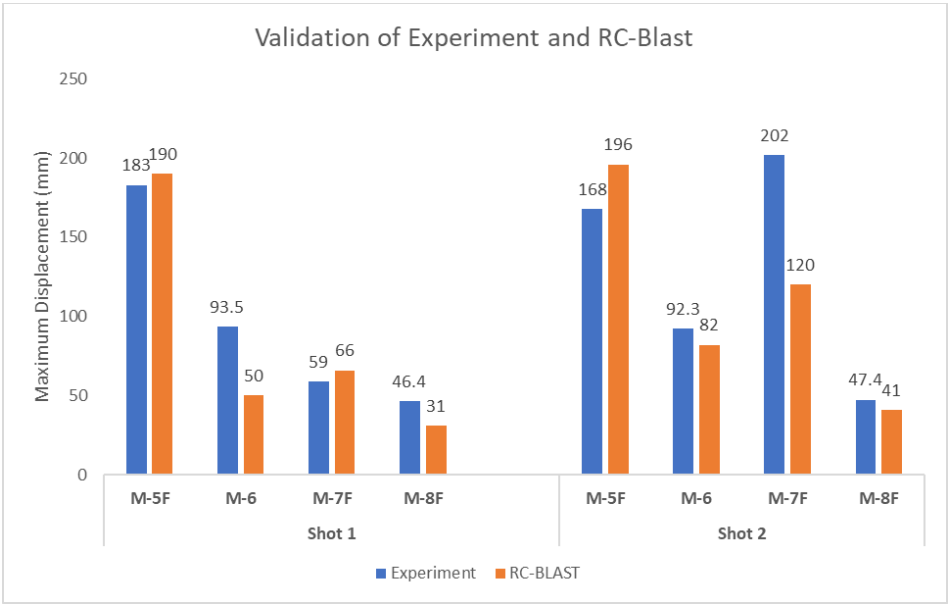

Figure 4.11: Validation of experiment vs SDOF (M-5F, M-6F, M-7F and M-8F)

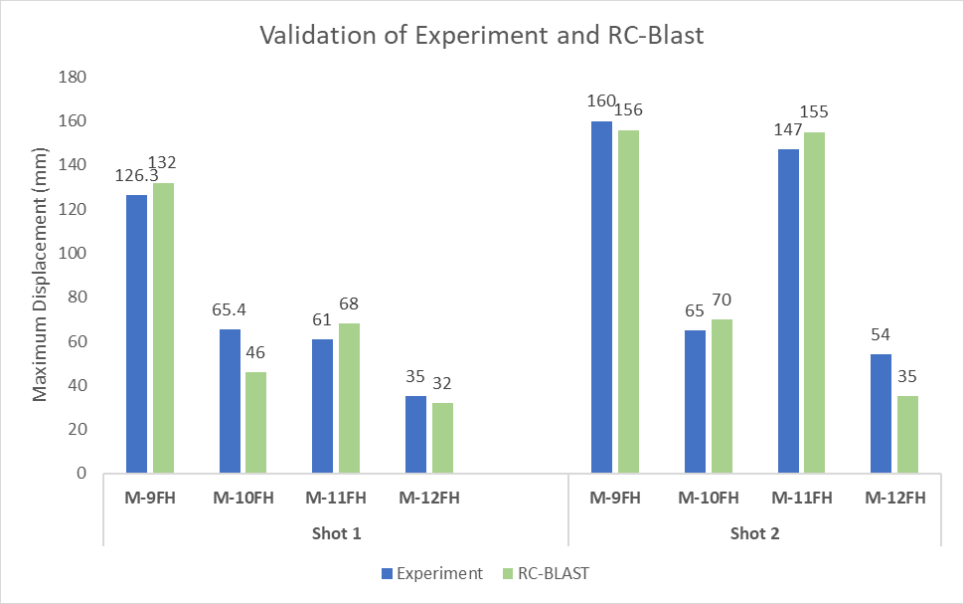

Figure 4.12: Validation of experiment vs SDOF (M-9FH, M-10FH, M-11FH and 12FH)

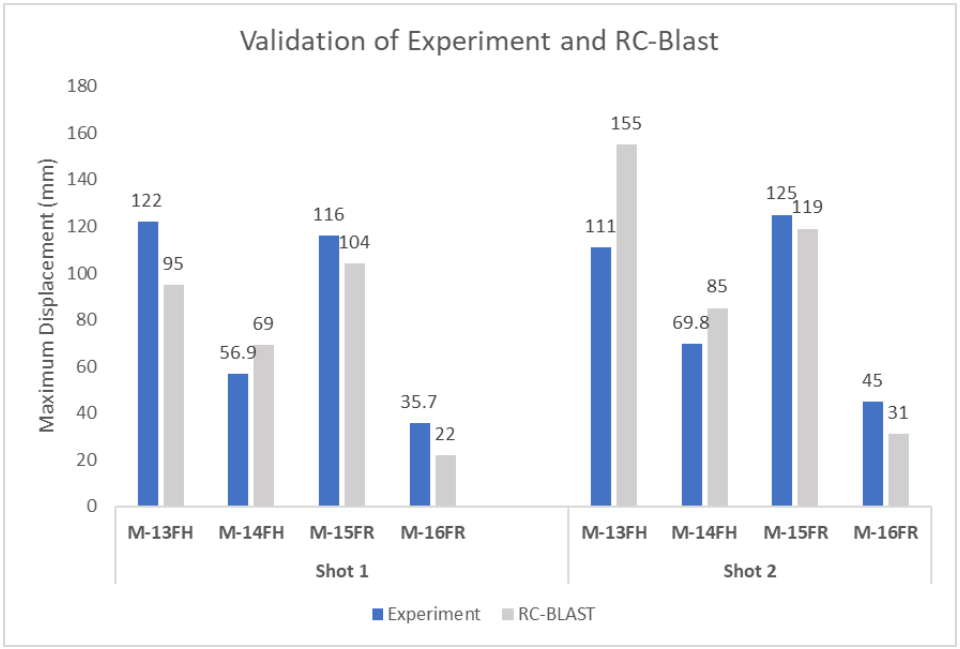

Figure 4.13: Validation of experiment vs SDOF (M-13FH, M-14FH, M-15FR and 16FR)

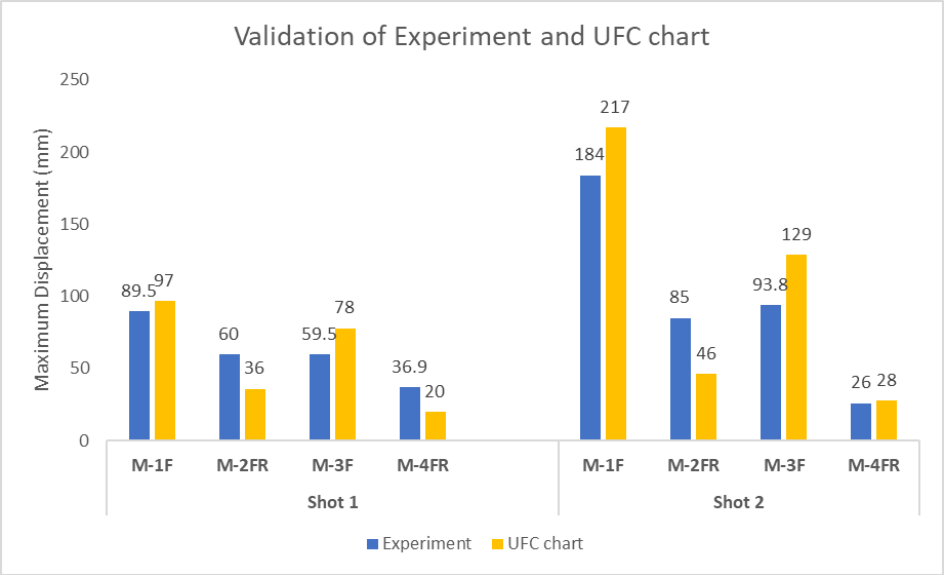

Figure 4.14: Validation of experiment vs UFC chart (M-1F, M-2FR, 3F and 4FR)

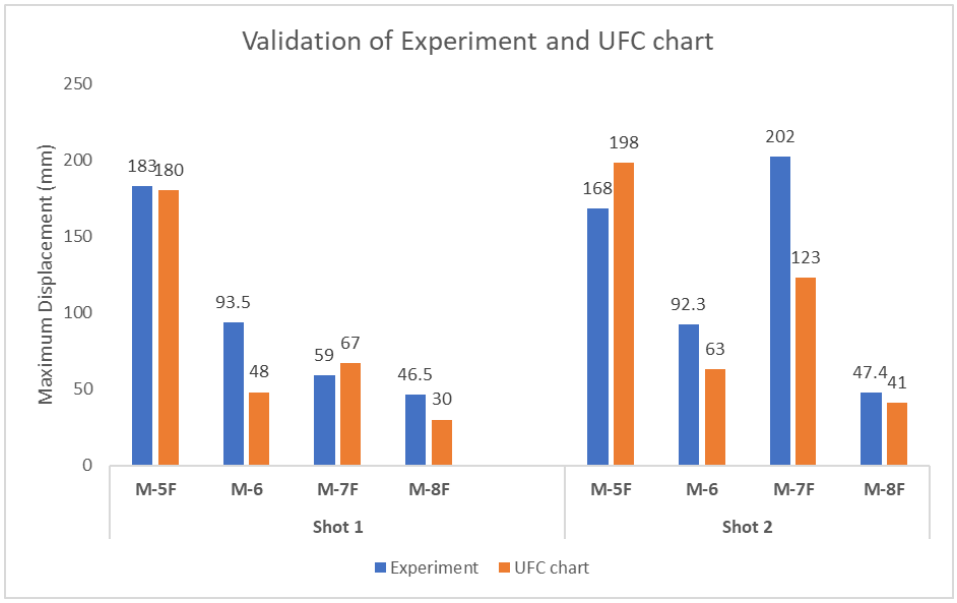

Figure 4.15: Validation of experiment vs UFC chart (M-5F, M-6F, M-7F and M-8F)

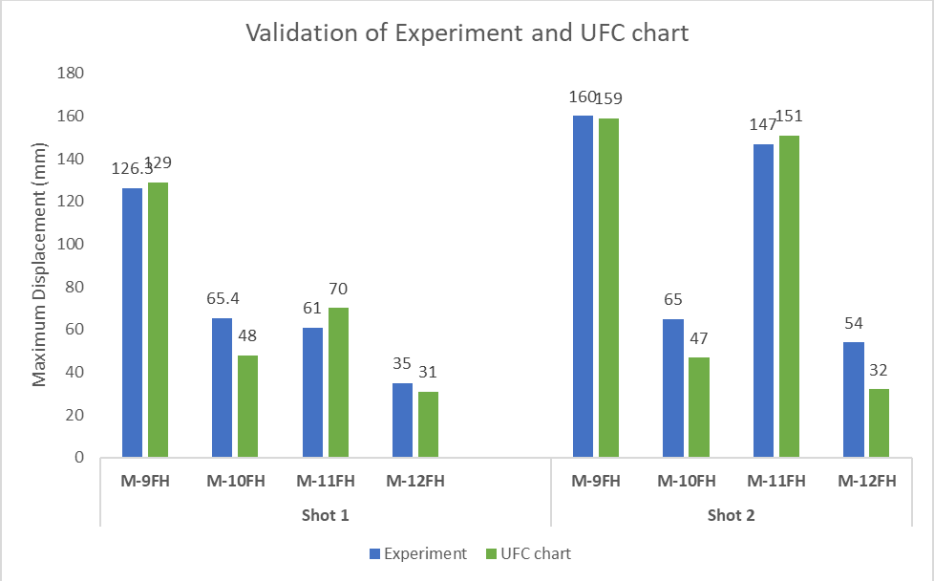

Figure 4.16: Validation of experiment vs UFC chart (M-9FH, M-10FH, M-11FH and 12FH)

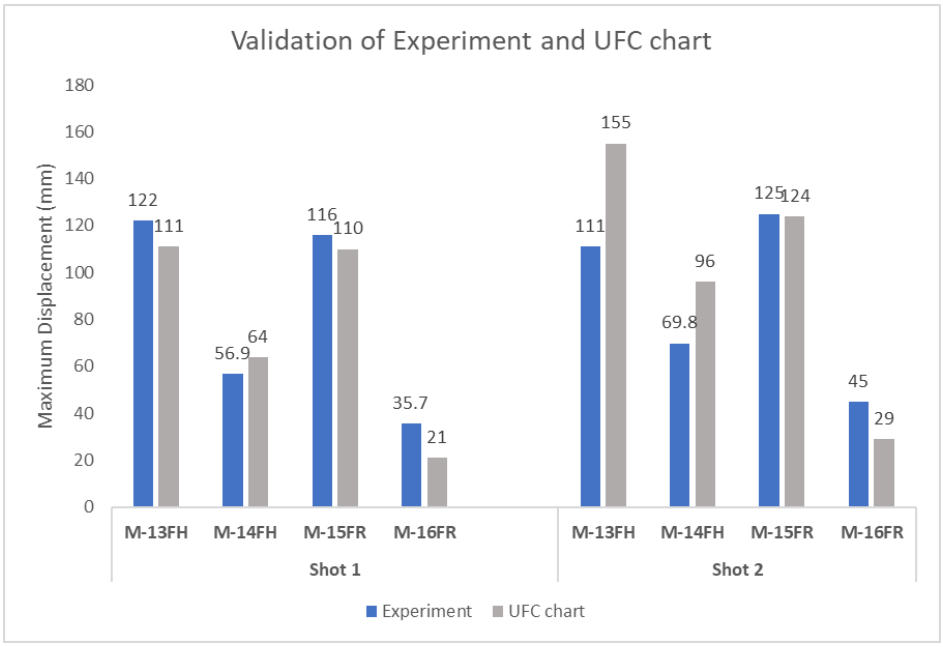

Figure 4.17: Validation of experiment vs UFC chart (M-13FH, M-14FH, M-15FR and 16FR)

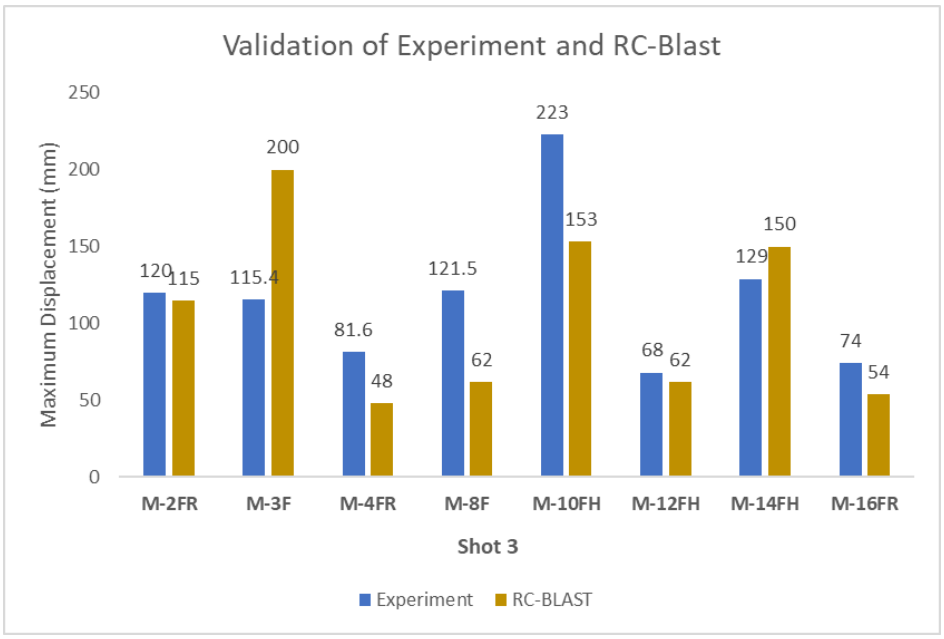

Figure 4.18: Validation of experiment vs SDOF (RC-Blast) (M-2FR, M-3F, M-4FR, M-8F, M-10FH, 12FH, 14FH, 16FR)

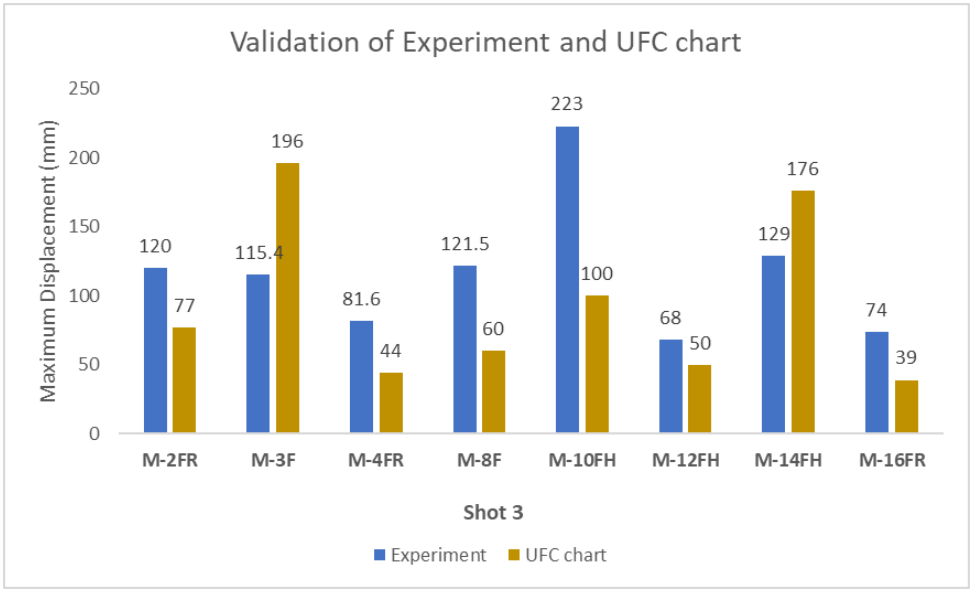

Figure 4.19: Validation of experiment vs SDOF (UFC Chart) (M-2FR, M-3F, M-4FR, M-8F, M-10FH, 12FH, 14FH, 16FR)

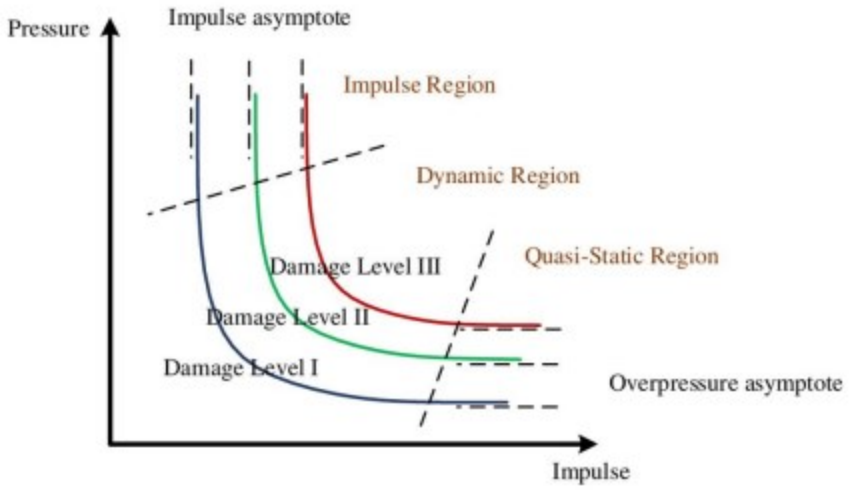

Figure 4.20: Pressure-Impulse (P-I) Diagram (Parisi et al. 2016)

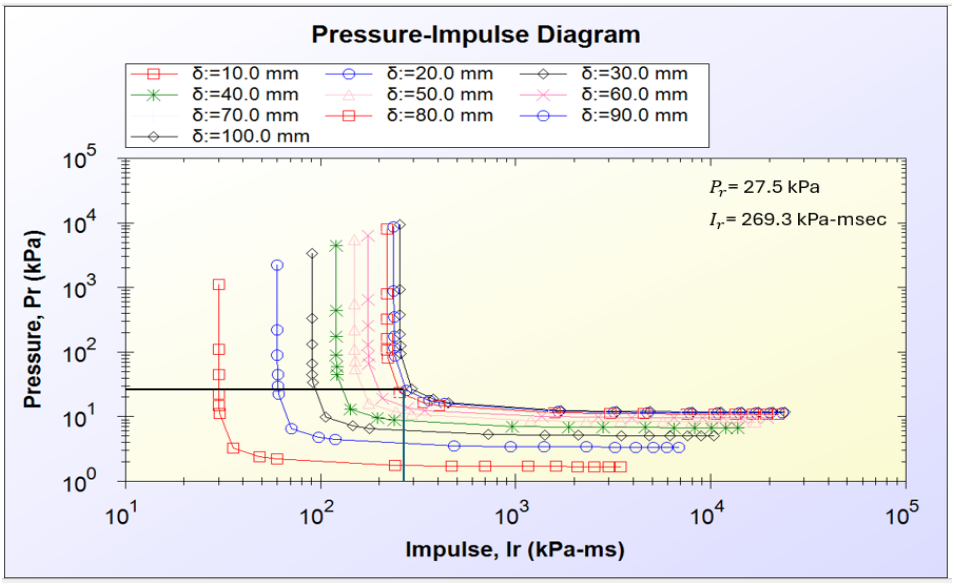

Figure 4.21 : Pressure-Impulse (P-I) Diagram -M-1F – Blast 1

CHAPTER 5. ANALYTICAL PARAMETRIC STUDY

The analytical investigation discussed in Chapter 4 was expanded to conduct analytical parametric study under selected threat scenarios. The aim of the study was to assess the effects of design parameters for curtain wall mullions under actual threat scenarios while extending the results of Chapters 3 (experimental research) and 4 (analytical research). The threat scenarios considered include incrementally increasing charge weights ranging between 10 kg TNT and 90 kg until the mullion failure is observed when the standoff distance is kept constant at 20 m. Table 5.1 shows the threat scenarios considered with reflected pressure, positive phase duration and the reflected impulse indicated. The blast load parameters were obtained by Software ''Overpressure" (Jacques 2013). Figure 5.1 illustrates the output of the software for 50 kg TNT at 20 m standoff distance as an example, displaying positive and negative phase pressure distributions under incident and reflected pressure conditions.

The design variables considered include aluminum mullions without any infill material and additional reinforcement as control mullions, infill material, internal steel reinforcement (cable and chain) and surface-bonded CFRP sheets. In this set of analyses two percentages of steel wire were considered, one having the same percentage of steel used in the tests, and the other 4 times the steel wire area used earlier to investigate the effectiveness of increasing the steel percentage. Also, in both the earlier experimental and analytical investigations, the chain as internal reinforcement was used with high-strength mortar (HSM) as the infill material. In the current set of analyses the chain reinforcement was used in ECC to see its effectiveness when combined with an infill material that has tensile capacity and deformability. Furthermore, a new high-strength infill material in the form of ultra-high performance fiber reinforced concrete (UHPFRC) was considered to assess strength and stiffness enhancements in mullions. Additional analyses were also conducted using externally bonded CFRP sheets as a mullion hardening technique with twice the CFRP thickness of the thickness used in the experimental phase and the earlier analytical investigation. The analyses conducted in this chapter included two sizes of aluminum mullions for each case (51 mm x 127 mm x 3 mm and 51 mm x 152 mm x 4.8 mm) and two support conditions as simple supports and fixed supports, resulting in a total of 28 analyses, including 4 control

mullions without any hardening, i.e., without any infill material and additional reinforcement. The mullions had a 2.5 m height, but the centre-to-centre distance between the supports was 2.2 m for simply supported mullions and 2.1 m for fixed-fixed supports. Table 5.2 shows the cases considered in the parametric study reported in Chapter 5. In all cases the RC-Blast software discussed in Chapter 4 was used to conduct non-linear SDOF analysis with resistance functions computed by the member analysis module incorporated in the software, similar to those illustrated in Figure 4.6. The results of the parametric study shed further light on the effectiveness of the new hardening techniques developed in the current research project.

5.1 Analysis of Control Mullions without Infill Material and Reinforcement

Four aluminum mullions, with dimensions of either 51 mm x 127 mm x 3 mm or 51 mm x 152 mm x 4.8 mm were analyzed using either simple or fixed supports as control mullions. The analysis results are then compared with hardened mullions. The stress-strain relationship in tension used for aluminum was the relationship provided by the supplier (f_y = 270 MPa; E = 70,000 MPa), as shown in Figure 5.2 (a). The stress-strain relationship in compression accounted for local buckling, as this was the common failure mode observed for mullions without infill material by Chavan (2021)as depicted in Figure 5.2 (b). The local buckling model that was suggested for aluminum members by Faella et al. (2000) was employed. Figure 5.2 shows the stress-strain relationships used for the aluminum mullions in tension and in compression.

5.2 Use of High-Strength Wires as Reinforcement with ECC Infill Material

The effect of using ECC infill material with and without internal steel cables as additional reinforcement was investigated through series of analysis. Four different percentages of internal steel wire reinforcement were used in each of the two sizes of mullions considered (5” and 6”) to assess the significance of adding steel reinforcement internally in the ECC infill material in addition to the reinforcement provided by the enclosing aluminum mullions. Two amounts of internal steel were provided as part of the parametric investigation. The first amount consisted of two cables on the tension side of simply supported mullions, and four cables along the

perimeter of fixed mullions. This resulted in 1.00% and 2.00% steel in 5” mullions; and 0.96% and 1.92% steel in 6” mullions for simply supported and fixed mullions, respectively. The second amount consisted of 4 times the area of steel used in the first case, resulting in 4.00% and 8.00% steel in 5” mullions; and 3.84% and 7.68% steel in 6” mullions for simply supported and fixed mullions, respectively. The details of the test parameters and the labels assigned to each analysis are shown in Table 5.2.

The analysis results are compared in Figure 5.3 through Figure 5.10 for the case of ECC infill material or ECC reinforced with internal steel wire. In all cases the use of infill material with and without the steel reinforcement increased capacity and reduced deflections. When the 5” mullions were simply supported the behaviour was governed by a single critical section and the use of ECC infill material alone increased the capacity from 10 kg TNT to 25 kg TNT with failure deflection increasing from 45 mm to 151 mm (Figure 5.3). The use of steel wires further increased the capacity to 40 kg TNT with ability to deflect up to 232 mm at failure. When the percentage of steel increased by a factor of 4, the mullion became more rigid and developed smaller deflection relative to the companion mullion with 1% steel (Figure 5.4).

When the mullions were fixed at their supports, three regions contributed to the resistance, two support regions (under negative bending) and the mid-heigh region (under positive bending). Therefore, the capacity of the mullions was higher. When filled with ECC the capacity increased from 10 kg TNT to 40 kg TNT, with the failure deflection of the mid-height region increasing from 29 mm to 133 mm, Figure 5.5. The increase in capacity due to use of internal steel was also observed (from 40 kg TNT to 50 kg TNT). When the percentage of steel increased by a factor of 4, the contribution of steel became more significant. This time the capacity increased up to 70 kg TNT, Figure 5.6 with an increase in the failure deflection from 133 mm to 165 mm. The use of 4 times the area of steel resulted in an increase in capacity of 75% as compared with the use of smaller percentage, which was only 25%.

A similar improvement was obtained when 6” mullions were analyzed. The results are compared in Figure 5.7 through Figure 5.10. This time the effect of internal steel was relatively small because of the predominance of the larger aluminum section and associated higher

percentage of reinforcement provided by the aluminum. It is noteworthy that in this series of mullions even the control mullions without any infill material developed relatively high capacity of 45 kg of TNT because of the increased size of the 6” mullions (as compared to only 10 kg of 5” mullions).

5.3 Use of High-Strength Chain as Reinforcement with ECC Infill Material

The effect of using ECC infill material with and without internal use of high-strength chain as reinforcement was investigated through series of analysis. The chain selected was the same material used in the experimental and analytical phases of research, reported in Chapters 3 and 4 with a steel diameter of 6.4 mm per side of each loop of chain. This resulted in 2 times the individual area of 32.2 mm^2 for each leg (2 x 32.2 mm^2 = 64.4mm^2), producing 1.2% steel area in 51 mm x 127 mm x 3 mm size mullions and 1.1% steel area in 51 mm x 152 mm x 4.8 mm mullions when a single chain is provided on the tension side of simply supported mullions. Each size mullion was analyzed with ECC infill material with and without the chain as internal reinforcement while either with simple or fixed supports. Mullions with fixed supports were reinforced with two chains provided in ECC infill material, one on either side as tension reinforcement, as the mullion is expected to develop positive and negative moment resistances at mid-height and support regions, respectively. Table 5.2 provides the details of this set of analysis. The results are compared in Figure 5.11 and Figure 5.12 for simply supported mullions and indicate higher capacities when the chain reinforcement is used. However, the contribution of chain to member capacity is higher in the case of 5” mullions, increasing resistance from 40 kg TNT to 60 kg TNT, as compared to 6” mullions which experience limited improvement from 50 kg to 55 kg. This is attributed to the higher percentage of aluminum reinforcement provided in the 6” mullion relative to the 5” mullion, while both having approximately the same steel percentage, hence higher contribution by the aluminum to blast resistance in the 6” mullion.

The effect of internal chain to blast resistance followed the same trend as above when the mullions had fixed supports. This is illustrated in Figure 5.13 and Figure 5.14 for 5” and 6” mullions, respectively. The resistances of mullions with fixed supports were higher than those of simply supported mullions with smaller mid-height deflections. Accordingly, the 5” fixed-fixed

mullion capacity increase was from 40 kg to 60 kg TNT (Figure 5.13) and that of 6” mullion was from 70 kg to 85 kg of TNT (Figure 5.14). The results indicate that a similar behaviour in load resistance can be obtained when the same percentage of internal reinforcement is used irrespective of the type of steel (cable or chain) as expected. The selection of the type of steel to be used is dictated by the convenience of the placement of steel into the mullion during construction.

5.4 Use of Surface-Bonded CFRP as External Reinforcement

The effect of using ECC infill material with and without externally provided surface-bonded CFRP reinforcement was investigated through 4 additional analyses, consisting of 5” (51 mm x 127 mm x 3 mm) and 6” (51 mm x 152 mm x 4.8 mm) mullions with either simple or fixed supports. The external CFRP consisted of four layers of CFRP, where each layer of carbon fiber fabric was 0.8 mm thick, which became 0.9 mm when saturated with epoxy to form the composite material. Hence the total thickness of CFRP applied was 4 x 0.9 = 3.6 mm with 780 MPa tensile strength of the composite material, 1.2% rupturing strain and 65,000 MPa elastic modulus. The FRP showed linear behaviour up to tensile rupturing, without any ductility. The CFRP had U-shape covering the tension flange at mid-height and extending over both sides of the web to develop sufficient bond.

The results of the analyses are compared in Figure 5.15 and Figure 5.16 for simply supported mullions and Figure 5.17 and Figure 5.18 for mullions with fixed supports. When 5” mullions were reinforced with CFRP sheets there was an increase in capacity from 25 kg to 35 kg TNT. Furthermore, the CFRP increased the stiffness of the mullion, developing smaller deflections as compared to mullions with ECC infill material only at each stage of loading. When applied on the 6” mullion, the increase in capacity was observed to be less (from 50 kg to 55 kg of TNT). This can be attributed to the relatively smaller role played by the CFRP in the larger aluminum section, which provided higher reinforcement percentage for the additional CFRP reinforcement to make a substantial difference. The mullions with fixed supports exhibited similar trends and similar improvements in capacity as in the case of simply supported mullions reinforced with externally bonded CFRP reinforcement.

5.5 Use of Ultra High-Performance Fibre-Reinforced (UHPFRC) as Infill Material

The effect of using Ultra High-Performance Fiber Reinforced Concrete (UHPFRC) as infill material was investigated to assess the compatibility of the aluminum mullions with this ultra-high strength material and possible improvements in load resistance for use as a hardening methodology for curtain wall mullions. The UHPCFRC that was selected was the same as that produced by (Burrell, 2012)at the University of Ottawa. The concrete mix consisted of 4mm aggregate size with binder consisting of 20% micro-silica and ordinary Portland cement. The mix contained 6% of fibers, where the fiber type was of OL-12/40 and the workability was improved by using a dry powder superplasticizer. The maximum compressive strength of the material was assumed to be 140 MPa with an approximate density of 3000 Kg/m^3. Figure 5.19 shows the unconfined and confined stress-strain relationship for the UHPFRC. The confined UHPCFRC material model was used as the infill material in 4 mullions, two 5" (51 mm x 127 mm x 3 mm) and two 6" (51 mm x 152 mm x 4.8 mm) size with either simple supports or fixed supports. The mullions were then subjected to incrementally increasing blast loads, as was done for all the other cases in this Chapter and compared with companion mullions with ECC infill material. Figure 5.3 includes the mullions analyzed. The results are compared in Figure 5.20 and Figure 5.21 for simply supported mullions and Figure 5.22 and Figure 5.23 for mullions with fixed supports.

Figure 5.20 indicates that the use of UHPFRC as infill material in 5" mullion improved blast resistance from 25 kg TNT capacity for a companion mullion with ECC infill material to 40 kg TNT. At this failure load the 5" aluminum mullion ruptured in tension while trying to balance high internal compressive forces generated in the UHPFRC. When the section size was increased to 6" mullion, the capacity was also increased to 55 kg TNT as can be seen in Figure 5.21.

Figure 5.22 and Figure 5.23 for mullions with fixed supports indicate higher resistance to blast loads with 55 kg TNT capacity in 5" mullion and 85 kg TNT capacity in 6" mullion.

Table 5.1: Blast load parameters considered*

Blast load (kg of TNT)	Reflected pressure (kPa)	Wave duration (msec)	Reflected impulse (kPa-msec)
10	34.71	10	114.6
15	42.49	11	151.55
20	49.35	11.8	183.13
25	55.66	12.4	212.24
30	61.59	12.9	240.34
35	67.22	13.3	267.65
40	72.67	13.7	294.5
45	78.04	14.1	319.19
50	83.47	14.4	340.95
55	88.84	14.7	362.36
60	94.14	14.9	383.47
65	99.4	15.2	404.33
70	104.58	15.4	424.91
75	109.67	15.6	445.19
80	114.8	15.8	465.47
85	119.93	16	485.6
90	124.89	16.2	505.34
95	130.05	16.3	525.4

* Standoff distance was kept constant at 20 m

Table 5.2: Parameters considered in the analytical parametric study

Specimen Label	Size	Support Condition	Infill Material	Reinforcement Type	Parameters
SS	51mm x 127mm x 3mm	Simple Supports	---	---	Control
LS	51mm x 152mm x 4.8mm	Simple Supports	---	---	
SF	51mm x 127mm x 3mm	Fixed Supports	---	---	
LF	51mm x 152mm x 4.8mm	Fixed Supports	---	---	
S-1F	51mm x 127mm x 3mm	Simple Supports	ECC	---	Internal Steel Wire Reinforcement
S-3FH	51mm x 127mm x 3mm	Simple Supports	ECC	1% Steel Wires	
I-3F	51mm x 127mm x 3mm	Simple Supports	ECC	4% Steel Wires	
S-2F	51mm x 127mm x 3mm	Fixed Supports	ECC	---	
S-4FH	51mm x 127mm x 3mm	Fixed Supports	ECC	2% Steel Wires	
I-4FH	51mm x 127mm x 3mm	Fixed Supports	ECC	8% Steel Wires	
S-5F	51mm x 152mm x 4.8mm	Simple Supports	ECC	---	
S-7FH	51mm x 152mm x 4.8mm	Simple Supports	ECC	0.96% Steel Wires	
I-7FH	51mm x 152mm x 4.8mm	Simple Supports	ECC	3.84% Steel Wires	
S-6F	51mm x 152mm x 4.8mm	Fixed Supports	ECC	---	
S-8FH	51mm x 152mm x 4.8mm	Fixed Supports	ECC	1.92% Steel Wires	
I-8FH	51mm x 152mm x 4.8mm	Fixed Supports	ECC	7.68% Steel Wires	
C-1F	51mm x 127mm x 3mm	Simple Supports	ECC	---	Internal Chain Reinforcement
C-3FH	51mm x 127mm x 3mm	Simple Supports	ECC	1.2% Steel Chain	
C-5F	51mm x 152mm x 4.8mm	Simple Supports	ECC	---	
C-7FH	51mm x 152mm x 4.8mm	Simple Supports	ECC	1.1% Steel Chain	
C-2F	51mm x 127mm x 3mm	Fixed Supports	ECC	---	
C-4FH	51mm x 127mm x 3mm	Fixed Supports	ECC	1.2% Steel Chain	
C-6F	51mm x 152mm x 4.8mm	Fixed Supports	ECC	---	
C-8FH	51mm x 152mm x 4.8mm	Fixed Supports	ECC	1.1 Steel Chain	
R-1F	51mm x 127mm x 3mm	Simple Supports	ECC	---	External CFRP Reinforcement
R-3FH	51mm x 127mm x 3mm	Simple Supports	ECC	3.6 mm CFRP	
R-5F	51mm x 152mm x 4.8mm	Simple Supports	ECC	---	
R-7FH	51mm x 152mm x 4.8mm	Simple Supports	ECC	3.6 mm CFRP	
R-2F	51mm x 127mm x 3mm	Fixed Supports	ECC	---	
R-4FH	51mm x 127mm x 3mm	Fixed Supports	ECC	3.6 mm CFRP	
R-6F	51mm x 152mm x 4.8mm	Fixed Supports	ECC	---	
R-8FH	51mm x 152mm x 4.8mm	Fixed Supports	ECC	3.6 mm CFRP	
E-1F	51mm x 127mm x 3mm	Simple Supports	ECC	---	Infill Material
U-3F	51mm x 127mm x 3mm	Simple Supports	UHPFRC	---	
E-5F	51mm x 152mm x 4.8mm	Simple Supports	ECC	---	
U-7F	51mm x 152mm x 4.8mm	Simple Supports	UHPFRC	---	
E-2F	51mm x 127mm x 3mm	Fixed Supports	ECC	---	
U-4F	51mm x 127mm x 3mm	Fixed Supports	UHPFRC	---	
E-6F	51mm x 152mm x 4.8mm	Fixed Supports	ECC	---	
U-8F	51mm x 152mm x 4.8mm	Fixed Supports	UHPFRC	---	

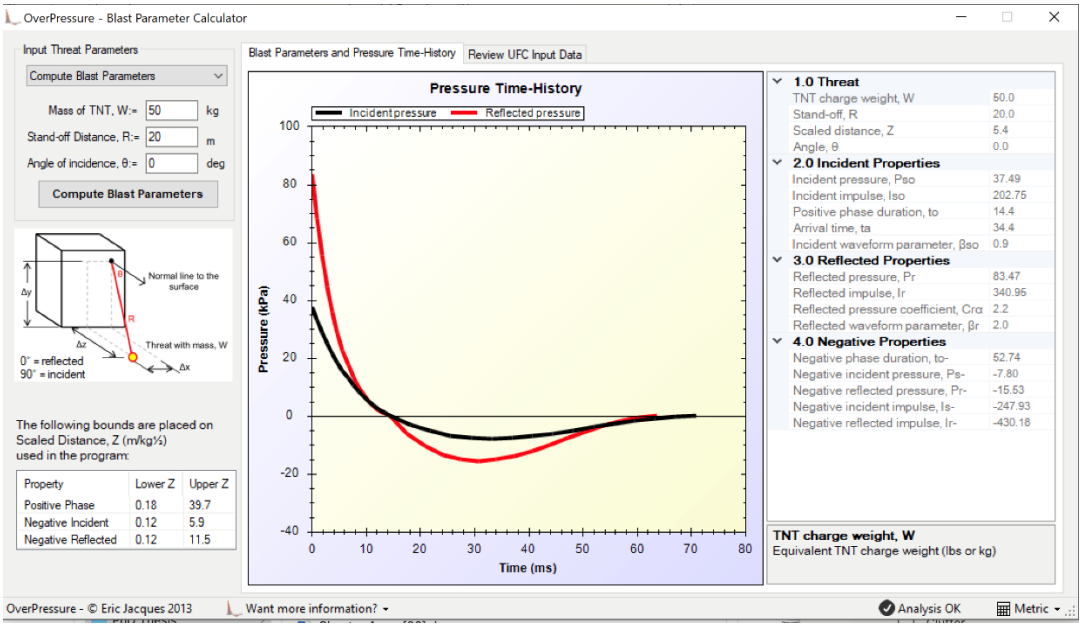

Figure 5.1: Bast load parameters as obtained from Overpressure software

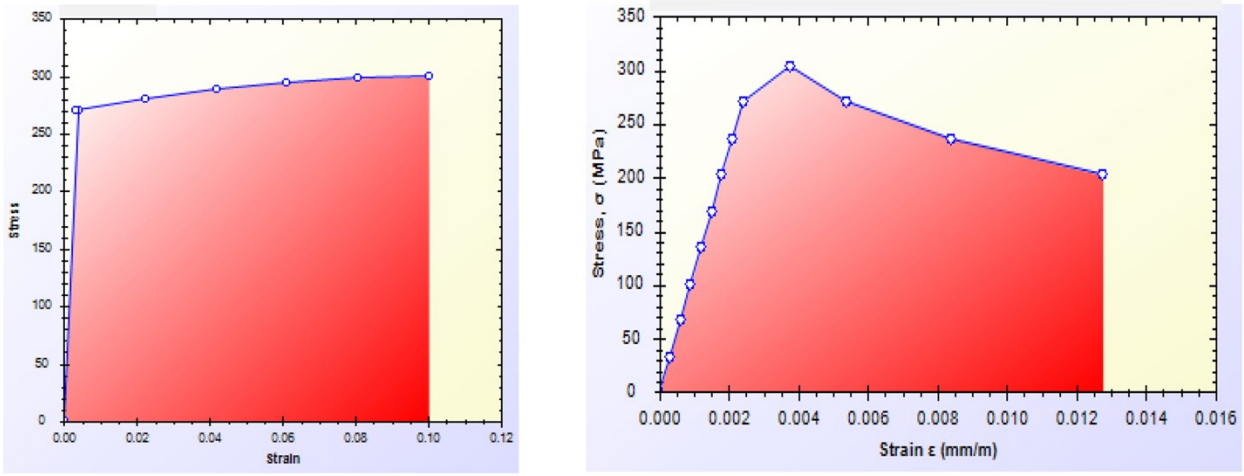

a) Tension b) Compression

Figure 5.2: Stress-strain relationships for aluminum

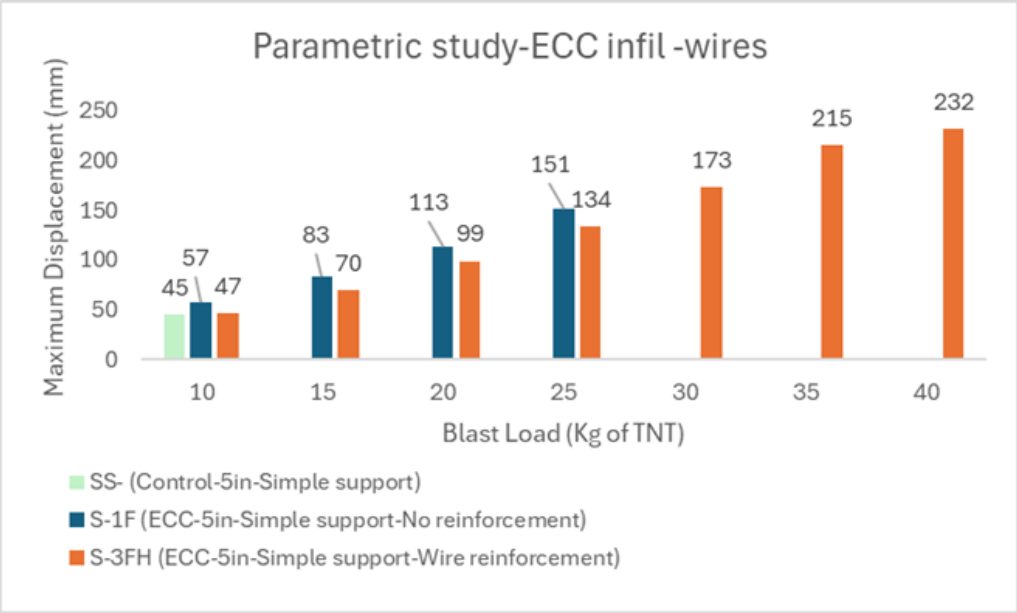

Figure 5.3: Effects of ECC infill material with and without high-strength wire reinforcement

(Use of 1% steel in 5” mullions with simple supports)

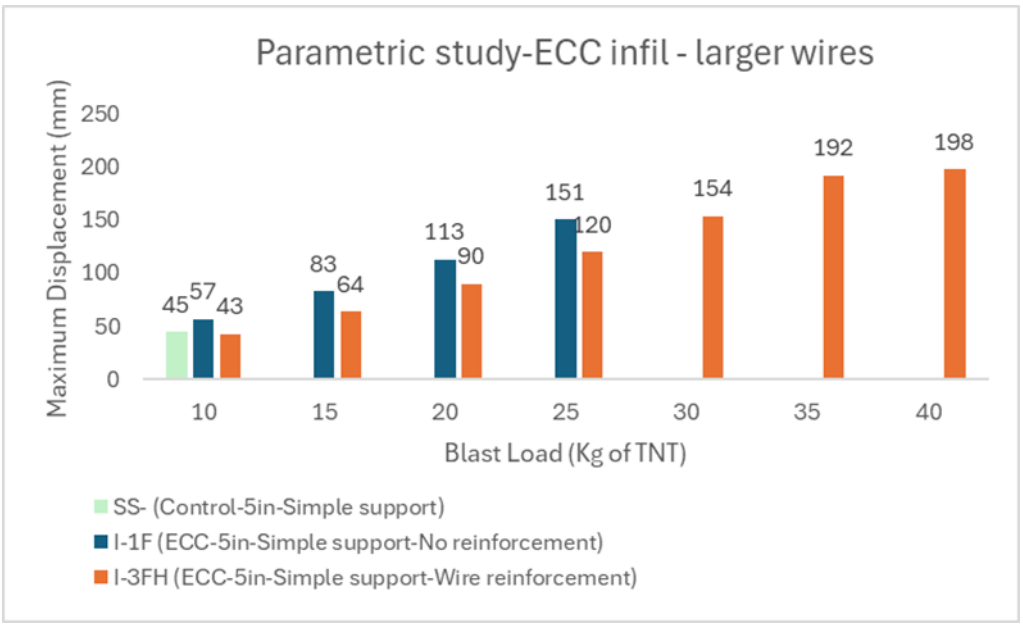

Figure 5.4: Effects of ECC infill material with and without high-strength wire reinforcement

(Use of 4% steel in 5” mullions with simple supports)

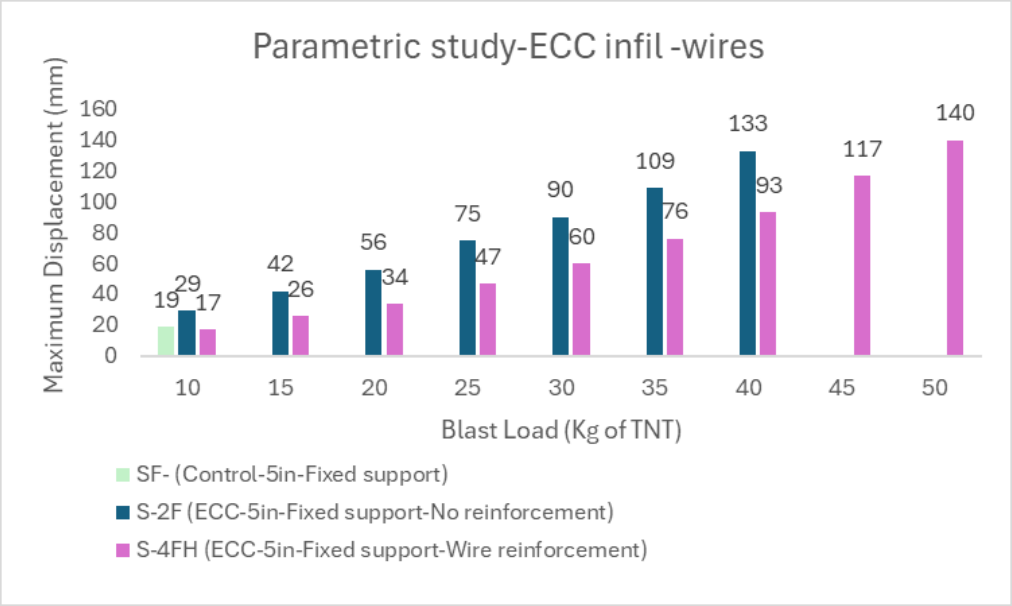

Figure 5.5: Effects of ECC infill material with and without high-strength wire reinforcement

(Use of 2% steel in 5" mullions with fixed supports)

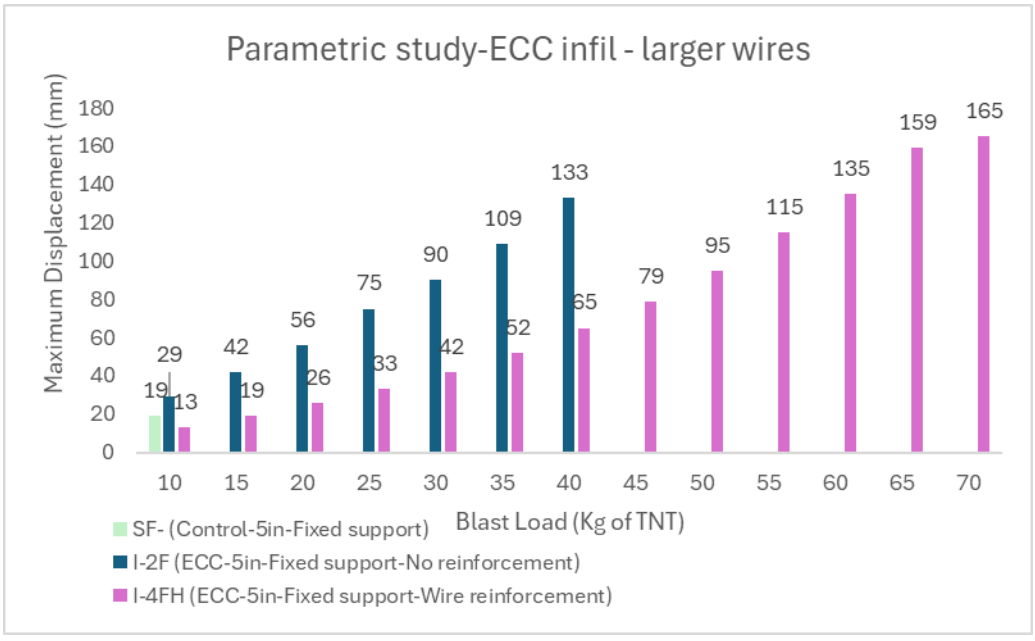

Figure 5.6: Effects of ECC infill material with and without high-strength wire reinforcement

(Use of 8% steel in 5" mullions with fixed supports)

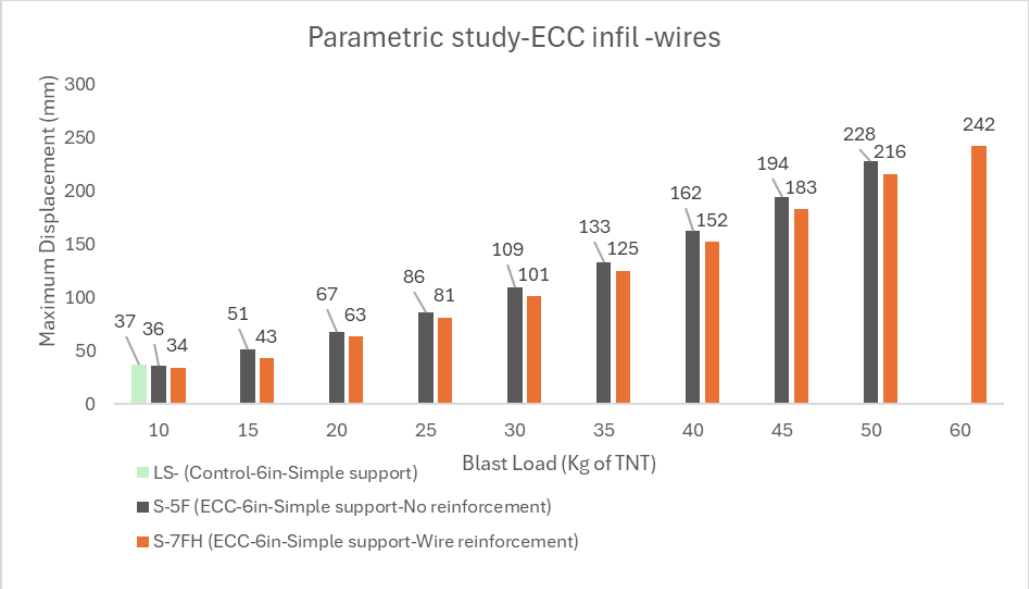

Figure 5.7: Effects of ECC infill material with and without high-strength wire reinforcement

(Use of 0.96% steel in 6” mullions with simple supports)

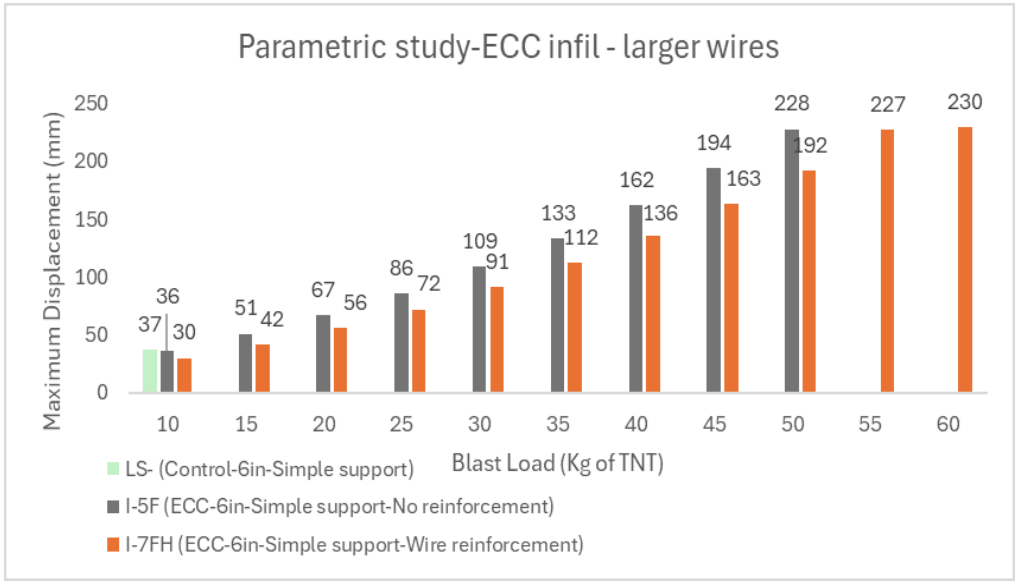

Figure 5.8: Effects of ECC infill material with and without high-strength wire reinforcement

(Use of 3.84% steel in 6” mullions with simple supports)

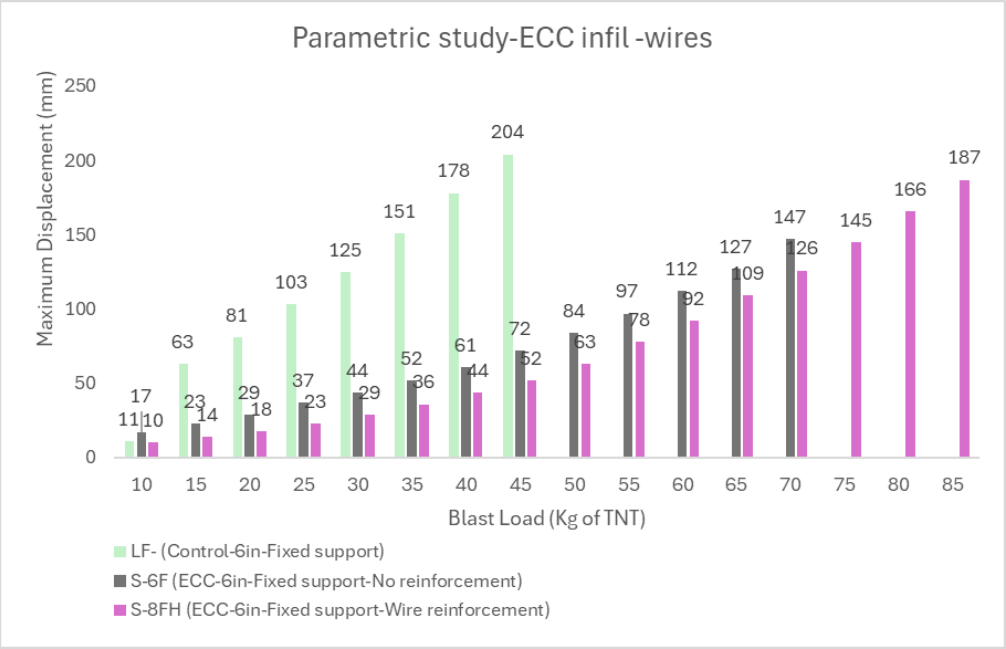

Figure 5.9: Effects of ECC infill material with and without high-strength wire reinforcement (Use of 1.92% steel in 6” mullions with fixed supports)

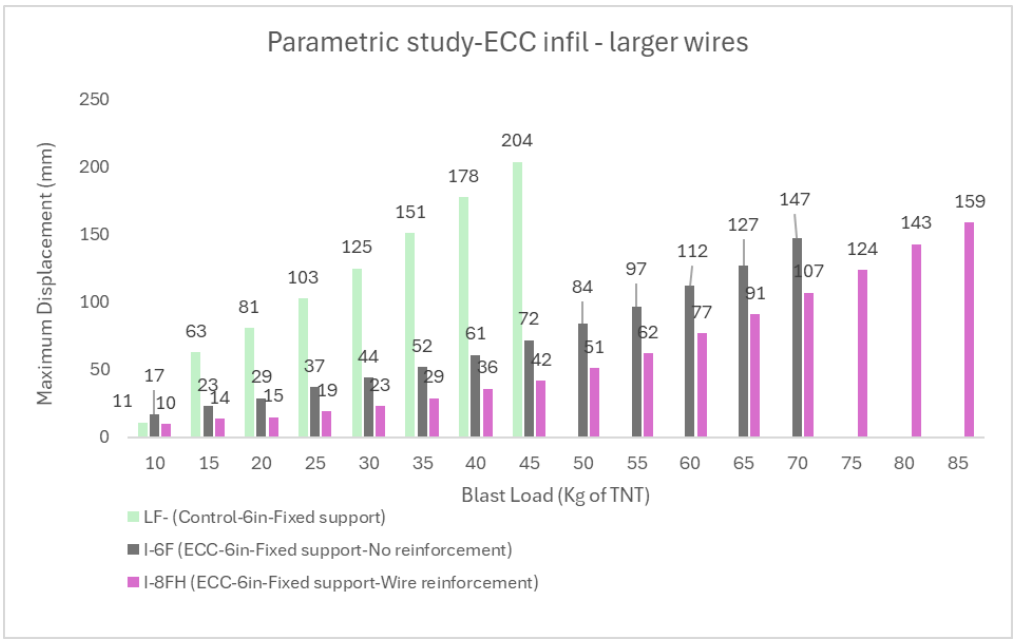

Figure 5.10: Effects of ECC infill material with and without high-strength wire reinforcement (Use of 7.68% steel in 6” mullions with fixed supports)

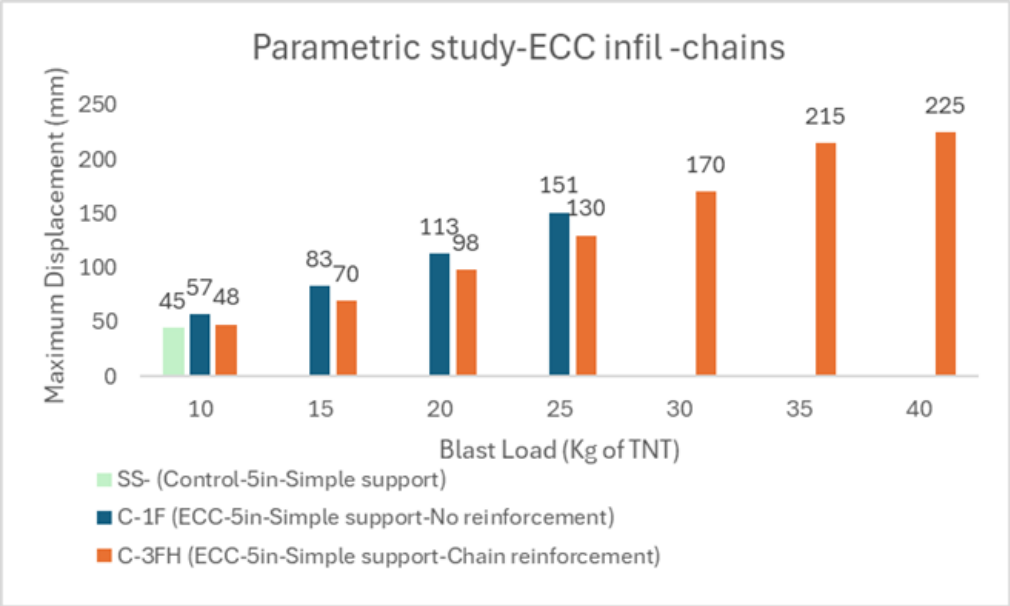

Figure 5.11: Effects of ECC infill material with and without high-strength chain reinforcement (Use of 1.2% steel in 5” mullions with simple supports)

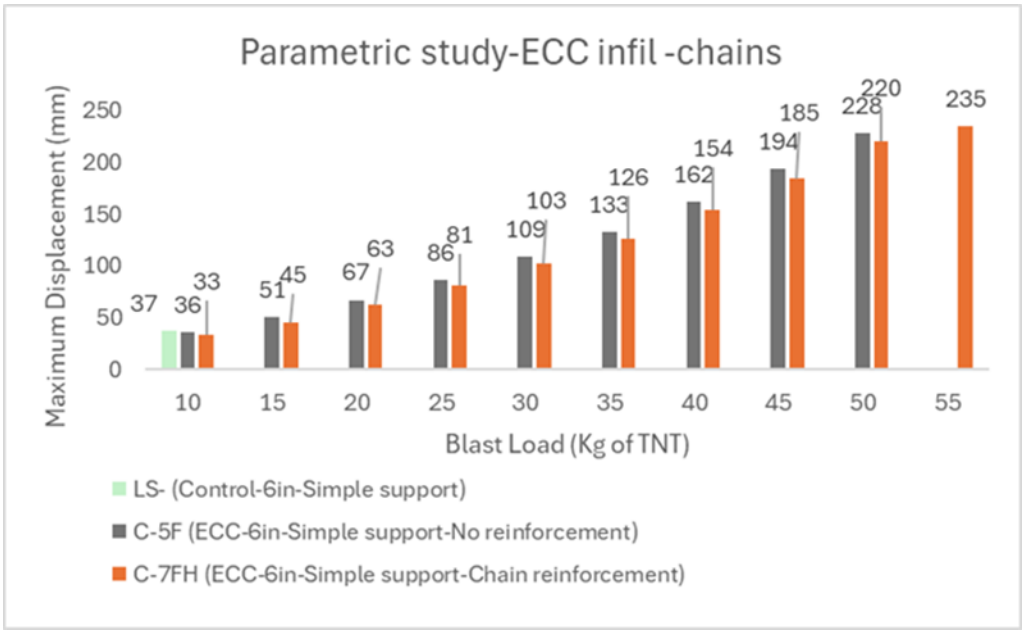

Figure 5.12: Effects of ECC infill material with and without high-strength chain reinforcement (Use of 1.1% steel in 6” mullions with simple supports)

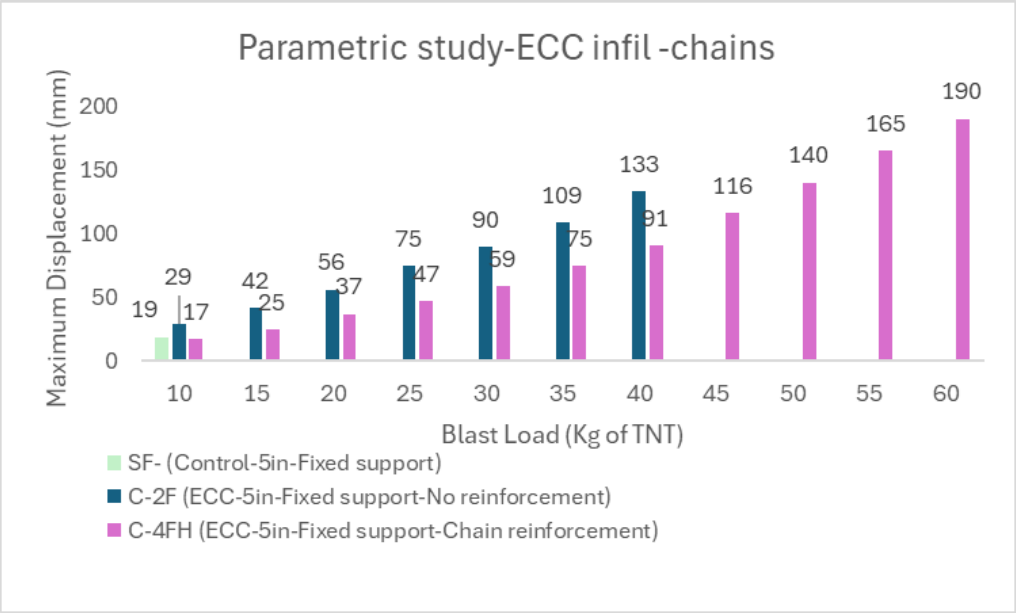

Figure 5.13: Effects of ECC infill material with and without high-strength chain reinforcement

(Use of 1.2% steel in 5” mullions with fixed supports)

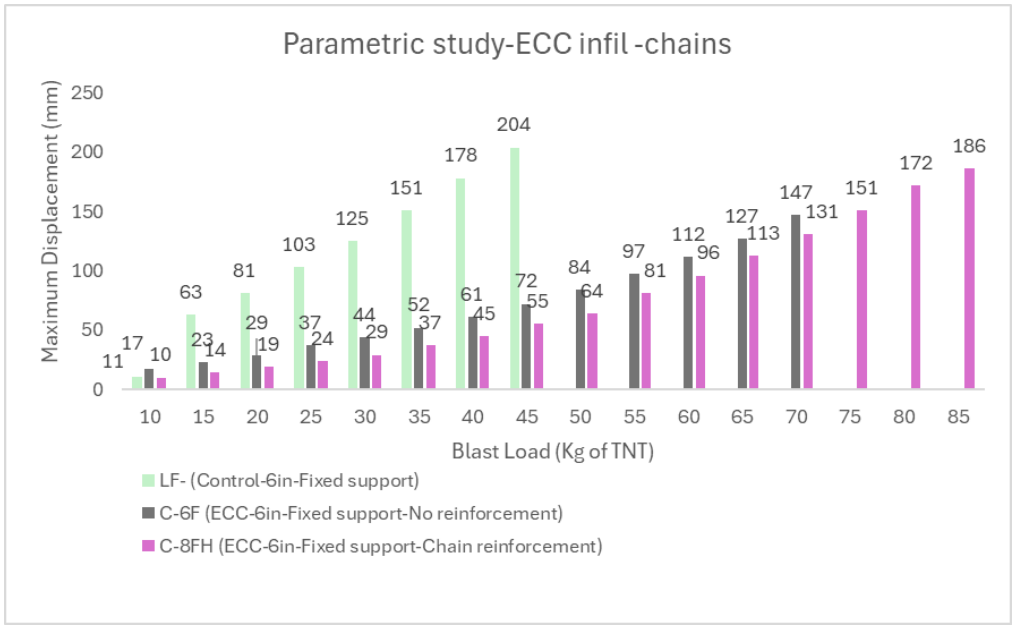

Figure 5.14: Effects of ECC infill material with and without high-strength chain reinforcement

(Use of 1.1% steel in 6” mullions with fixed supports)

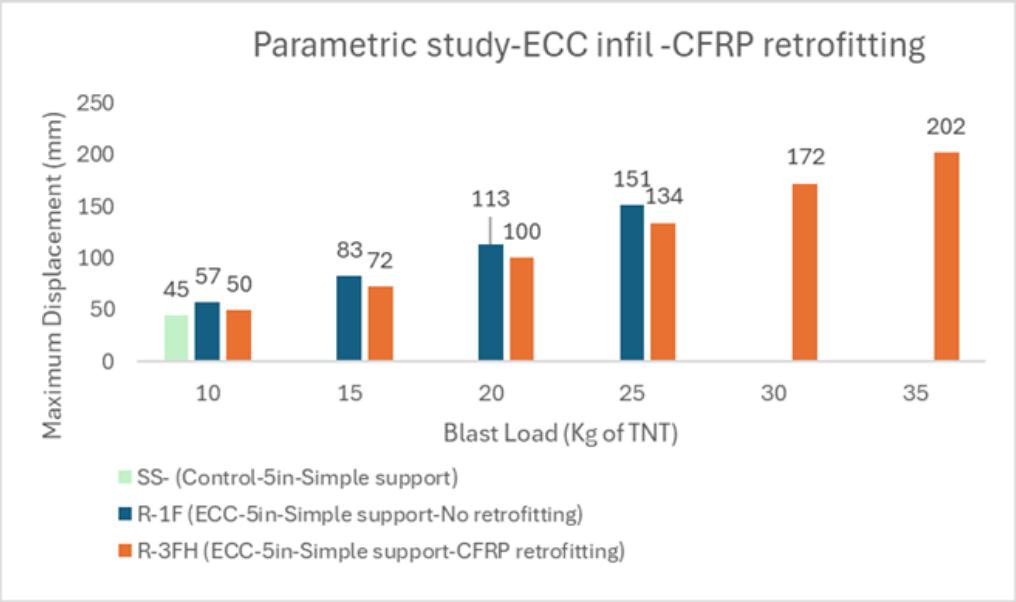

Figure 5.15: Effects of ECC infill material with and without CFRP reinforcement

(Use of 1.8 mm thick CFRP on 5” mullions with simple supports)

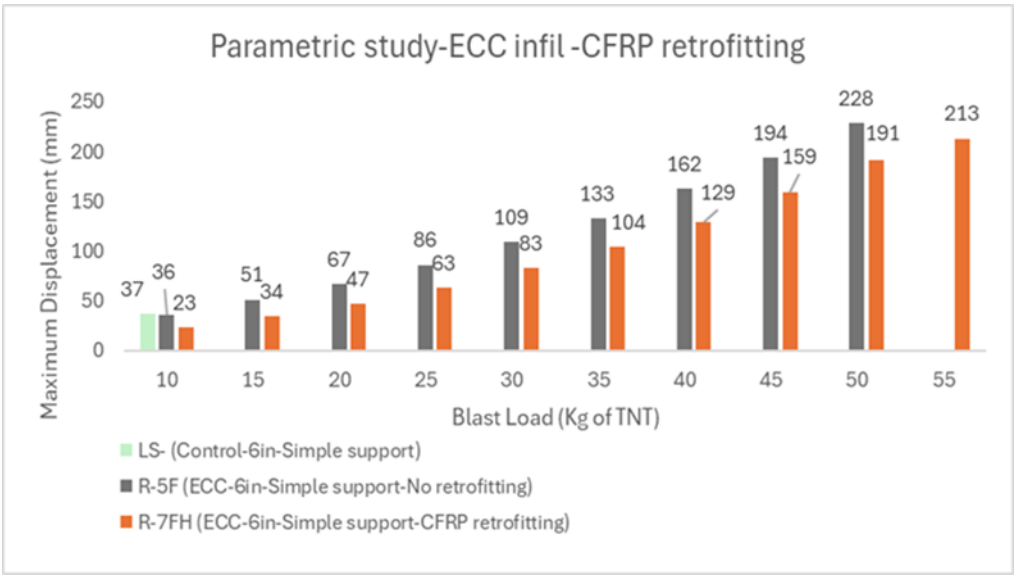

Figure 5.16: Effects of ECC infill material with and without CFRP reinforcement

(Use of 1.8 mm thick CFRP on 6” mullions with simple supports)

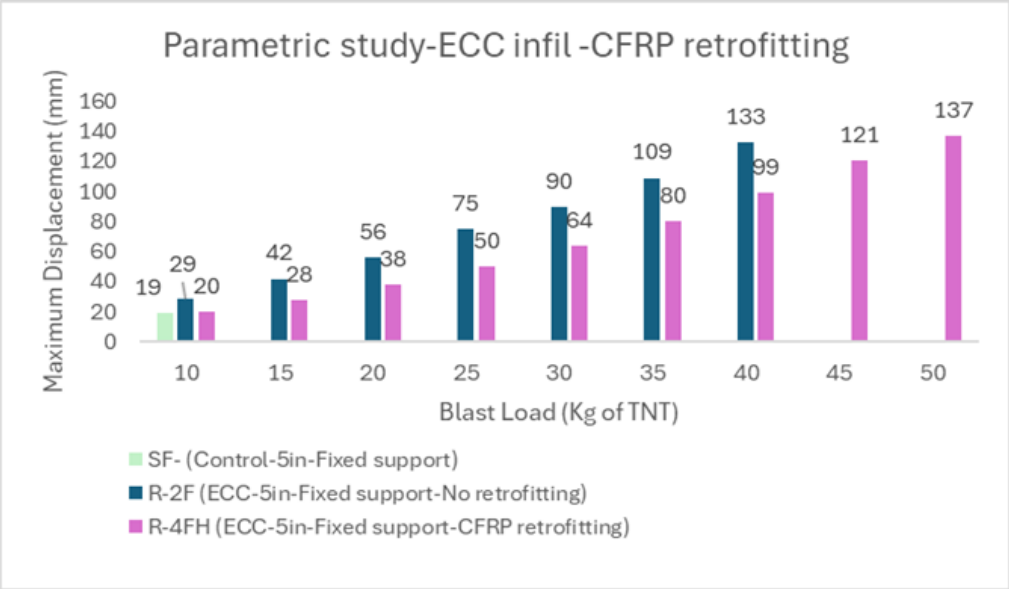

Figure 5.17: Effects of ECC infill material with and without CFRP reinforcement

(Use of 1.8 mm thick CFRP on 5” mullions with fixed supports)

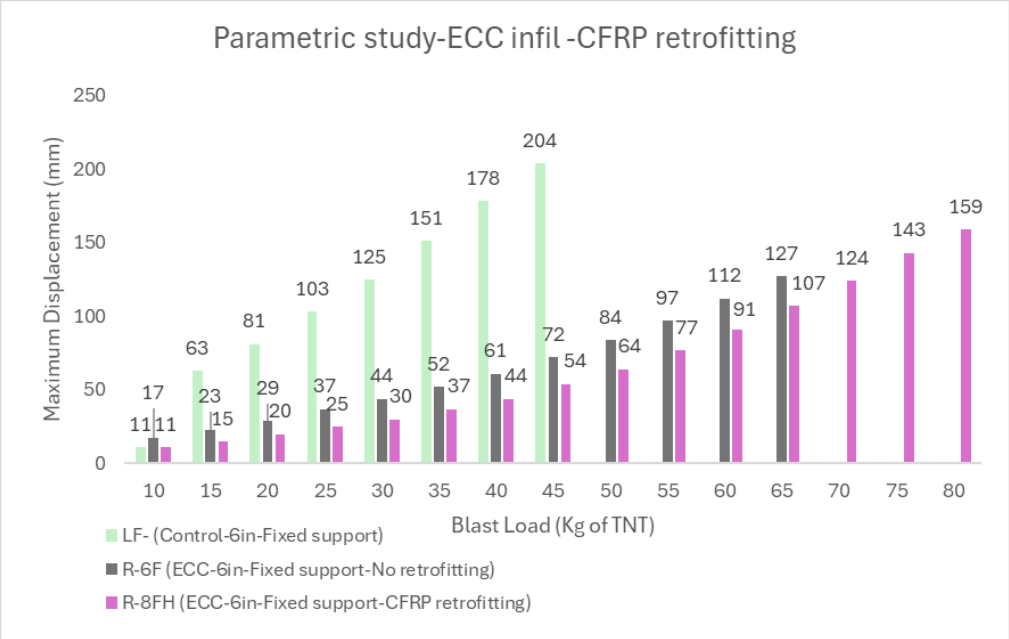

Figure 5.18: Effects of ECC infill material with and without CFRP reinforcement

(Use of 1.8 mm thick CFRP on 6” mullions with fixed supports)

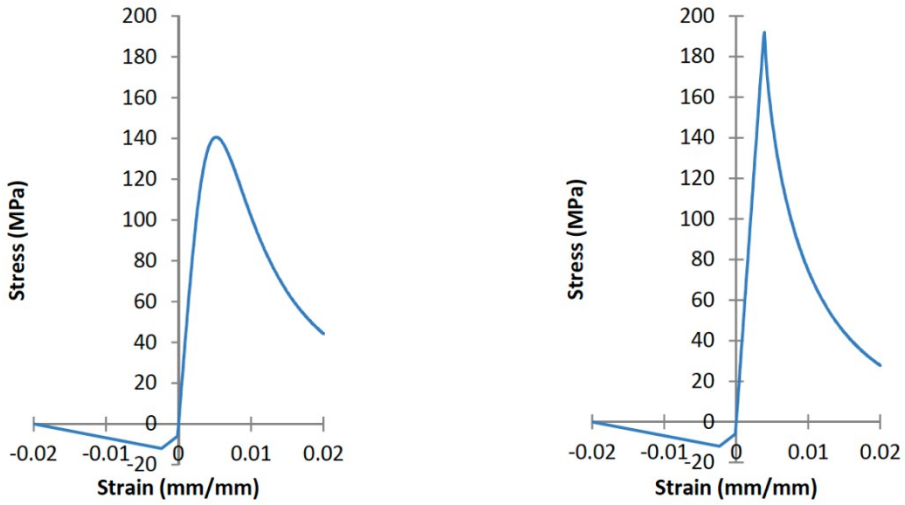

Figure 5.19: Stress-strain relationship for UHPFRC

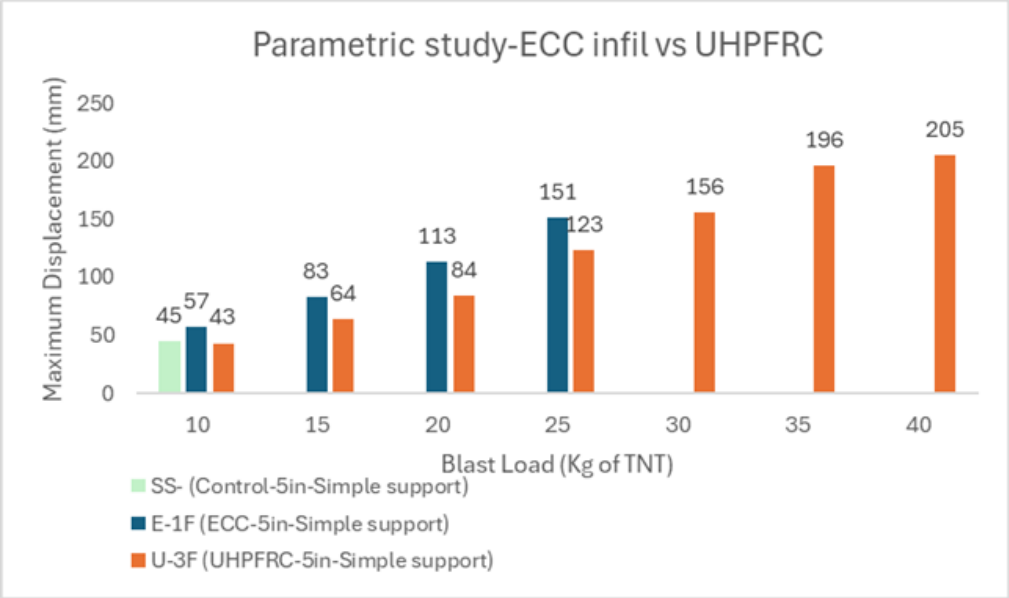

Figure 5.20: Effects of ECC and UHPFRC infill materials

(5” mullions with simple supports)

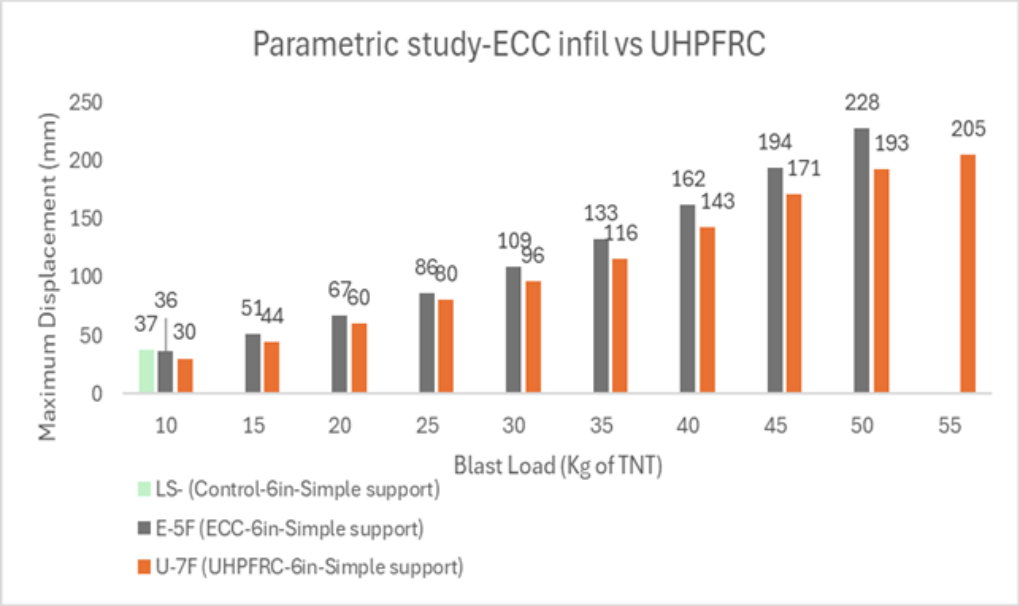

Figure 5.21: Effects of ECC and UHPFRC infill materials

(6” mullions with simple supports)

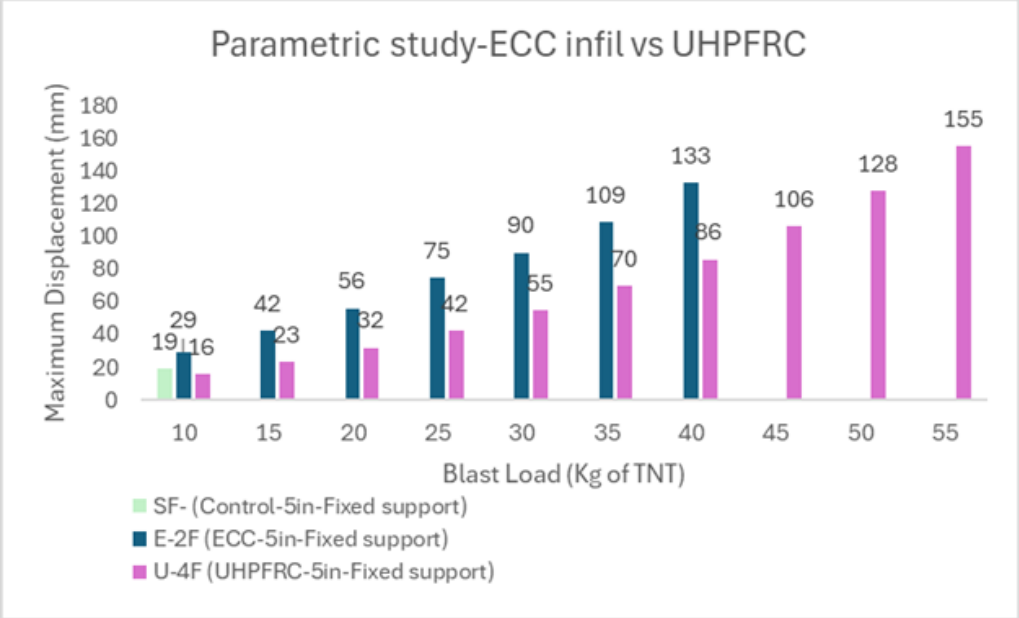

Figure 5.22: Effects of ECC and UHPFRC infill materials

(5” mullions with fixed supports)

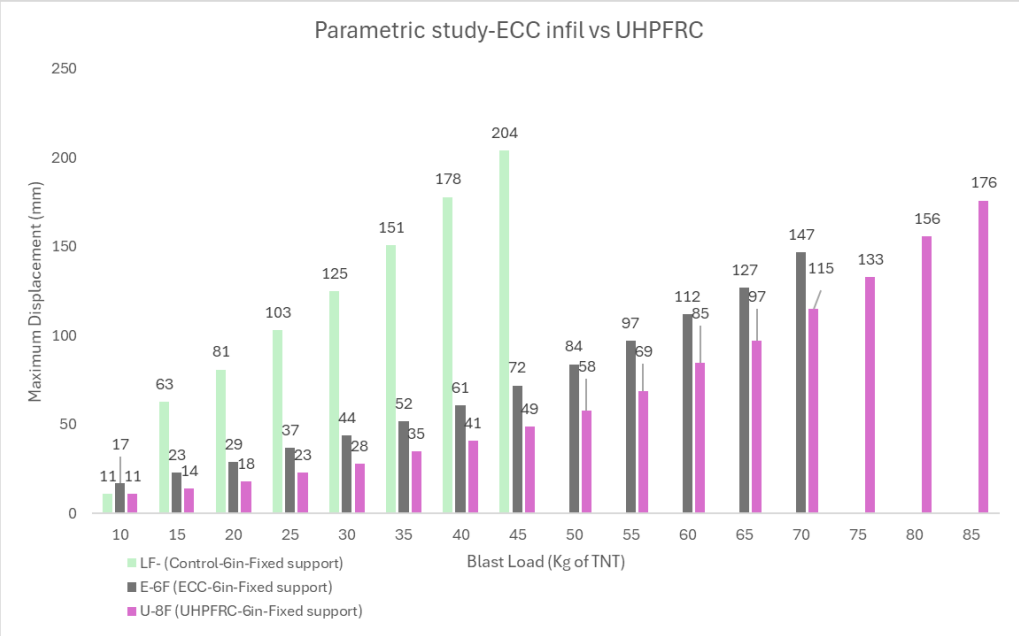

Figure 5.23: Effects of ECC and UHPFRC infill materials

(6” mullions with fixed supports)

CHAPTER 6. DEVELOPMENT OF DESIGN PROCEDURE AND CONCLUSION

6.1 Summary

A comprehensive experimental and analytical investigation was conducted to develop a new and innovative mullion hardening technology for curtain walls in blast-resistant buildings. The technology consists of filling existing mullions with contentious materials to increase strength and deformability of mullions with or without additional reinforcement. The infill materials considered include high-strength mortar (HSM), engineered cementitious composite (ECC), and ultra-high performance fibre reinforced concrete (UHPFRC). The additional tension reinforcement provided consists of internally placed steel wires or steel chains and externally surface bonded carbon fibre reinforced polymer (CFRP) sheets. Two sets of specimen sizes were, (51 mm x 127 mm x 3 mm) and (51 mm x 152 mm x 4.8 mm). The research programs had experimental and analytical phases. The experimental phase was conducted using the University of Ottawa Shock Tube as a blast simulator. The experimental program was conducted in two phases. Nine mullions were tested with simple supports while the other seven mullions were tested with fixed supports. The hardened mullions were subjected to incrementally increasing simulated blast shots and observations were made in terms of strength and stiffness increases obtained by the proposed new technology. The parameters indicated above were all considered in the experimental research except for UHPFRC, which was included in the analytical parametric investigation. The analytical research had two objectives, i) validation of SDOF dynamic inelastic analysis procedure for use in design both through the use of software that utilizes a numerical integration approach and a charted UFC solution that can be implemented manually, ii) analytical parametric investigation to assess the performance of hardened mullions under threat scenarios while also expanding analysis results. The results of the combined experimental and analytical research were used to develop a design and construction procedure for the implementation of the technology in practice for the benefit of engineers and security professionals as explained in the next section.

6.2 Recommendations for Design and Construction

Recommendations for Design:

The following procedure is recommended for the design of hardened mullions using the methodology developed in the current research project.

1. Design basis threat (DBT) will be used to conduct nonlinear dynamic SDOF analysis to assess potential deficiencies in curtain wall mullions. If needed, the mullions will be hardened by using cementitious infill material. The use HSM or ECC is recommended as infill materials based on the findings of the current study. Both materials have resulted in approximately 50% increase in reflected pressure resistance under a constant positive phase duration (of about 20 msec). The use of ECC showed reduced deflections at the same reflected pressure, indicating increased stiffness due to the tensile capacity and enhanced deformability of ECC.

2. Another possibility for infill material is the use of UHPFRC, which has higher compressive capacity (only validate through analytical research, without any tests), preventing local buckling of aluminum until after the rupturing of aluminum occurs on the tension side, thereby increasing resistance to blast loads. The increase in resistance can be higher for larger aluminum sections as the tension-compression internal force couple results in high moment resistance.

3. When the use of infill cementitious material cannot increase the blast resistance, as verified by SDOF analysis to the level required by the DBT, then additional tension reinforcement is provided. The tension reinforcement can be provided either in the form of flexible steel cables that facilitate internal placement in an existing mullion, or steel chains consisting of links that provide the required flexibility for easy placement prior to the casting of the infill material. The resulting assembly becomes a composite section with aluminum encasement and internal reinforced concrete infill. The required area of

internal reinforcement can be established through trial SDOF analyses until the desired resistance is attained within practical limits of construction (discussed in the next section).

4. An alternative to adding internal reinforcement is the externally applied, surface bonded CFRP sheets with carbon fibers running along the length of the mullion. CFRP sheets provide additional resistance, which increases with the number of plies (layers) of CFRP sheets. The choice of additional reinforcement depends on the requirements in the field and the level of protection sought, while paying attention to architectural and esthetic requirements. The resistance of the resulting hardened mullion can be assessed through dynamic inelastic SDOF analysis.

5. The use of infill cementitious material increases the mass of the mullions, which provides additional inertia resistance, the effect of which is accounted for through SDOF dynamic analysis. However, the additional mass may require strengthening of the mullion connections where the vertical mullions are attached to the substrate.

6. It is paramount that appropriate resistance functions be developed for the SDOF analysis with due consideration given to the mullion support conditions. Mullions connected to the substrate through simple supports develop plastic hinges at their mid-height regions, leading to a bi-linear resistance functions, whereas those continuous over supports (ex: slabs) may develop multiple hinges with the additional reinforcement to be placed in tension flanges on both sides of the mullion. The resistance function for such mullions can be tri-linear or may consist of multi-linear segments. It is also essential to use representative material models to simulate the actual behaviour in terms of their stress-strain characteristics, tensile rupturing points, local buckling in compression, the increase in compression capacity and deformability of the infill material due to the confinement provided by the enclosing aluminum tubes, as well as any potential increase in tensile capacity of the ECC infill material. In addition, possible debonding strain limit of surface-bonded CFRP, if not fully jacketed with overlaps, should be monitored during the analysis.

7. The design procedure described above is limited to the use of hardening materials employed in the current project, with observed fully composite behaviour in flexure. It excludes shear-critical mullions while also excluding the connection design.

Recommendations for Construction:

The hardening techniques developed in the current research project has not been researched or implemented in practice before. Therefore, it is important to provide construction guidelines based on the experience gained during the experimental phase of research. The technique is intended to be an alternative to conventional steel jacketing, with steel plates welded and secured on the existing aluminum mullions, for hardening of existing curtain walls. Of primary consideration is the esthetics and architectural requirements for existing mullion in existing buildings, which often dictate the decision for the hardening procedure.

1. Placement of infill material: Infill cementitious material may have to be placed and consolidated in an existing mullion that is forming an existing curtain wall. Therefore, the workability of the material plays a major role, especially when fibres are used as in the case of ECC and UHPFRC. No-slump, pumpable mix is required to be placed either from an opening created near the top connection or pumped from an opening placed near the bottom connection, which requires pressurized material placement but provides improved consolidation in the aluminum tube.

2. Placement of internal steel cables: Steel cables must be placed in the mullions through an opening cut on the exposed surface of the aluminum at one end of the mullion and fished throughout the length of the mullion until the opening cut at the other end where they are guided to make sure they are placed without slack in the intended location. This location is the tension side of simply supported mullions. For mullions with fixed supports, the cables are inserted in both flanges of the mullion to provide tension resistance in double curvature (when subjected to positive and negative bending moments).

3. Placement of internal steel chains: As an alternative to flexible steel cables that can be bent and placed inside the mullions, steel chains with their flexibility associated with chain links, can be dropped into the mullion, taking advantage of the chain weight that helps assume the intended position inside the mullion. The placement procedure, prior to casting the infill material is similar to that described above for the steel cables.

4. Installation of external CFRP reinforcement: External CFRP sheets can be epoxy glued on the face of the aluminum mullions, ensuring that they are placed on the tension side. This can be done either using U-shaped CFRP fabrics, as was done in the experimental program or as a full wrap around the mullions with CFRP overlaps for improved bond.

6.3 Conclusions

The following conclusions can be made based on the combined experimental and analytical research conducted in this project:

- Aluminum mullions used in curtain wall frames, typically design to resist wind loads, can be hardened to resist blast loads by placing cementitious infill material in the form of HSM, ECC or UHPFRC. The infill material provides additional compression resistance delaying or preventing local buckling upon yielding of the aluminum in compression, increasing blast resistance in flexure. The tension resistance provided by the aluminum and the compression resistance provided by the infill material in combination with the aluminum generates enhanced moment resistance until the aluminum in tension fractures. Therefore, larger aluminum sections with thicker section walls provide higher resistance preventing premature rupturing of aluminum, better utilizing the compression resistance of the infill material. An additional factor for improved performance of infilled mullions is the increase in mass, which provides inertia resistance to blast loads.

- Among the infill materials investigated, ECC and UHPFRC materials showed superior performance over HSM because of the enhanced resistance of the material in tension and improved deformability in both tension and compression, increasing strength and stiffness of the mullions with reduced deflections at each load stage.

- The flexural strength of infilled mullions under blast loads can be increased by providing internal reinforcement. The two types of internal reinforcement investigated in the current research project include steel wires and steel chains. The rationale for selecting these two materials was to take advantage of their flexibility during the placement in the mullions of existing curtain walls. The flexural resistance increased with increasing percentage of reinforcement as expected. The reinforcement was more effective in smaller mullion sections as they had a larger percentage of contribution relative to the aluminum in tension when compared with larger aluminum sections. It is recommended to select a reinforcing material that has high ductility to prevent premature tensile rupturing.

- An alternative to internal reinforcement is the use of external CFRP reinforcement in the form of CFRP sheets with carbon fibres providing reinforcement when permitted by architectural requirements from visibility perspective. Surface bonded U-shaped CFRP reinforcement generated increased strength, the level of which depended on the thickness of the CFRP. It was observed that the failure of CFRP initiated by debonding prior to reaching the tensile rupturing capacity of the material. Therefore, when accessible to all sides, it is advisable to wrap the mullions completely by CFRP sheets with overlapping ends for improved bond to aluminum.

- Simply supported mullions with a single critical section at mid-height developed lower resistance and higher deflections than fixed mullions that simulated continuity over the supports because of the multiple potential plastic hinge regions in double curvature. This

observation applies to all cases, with and without hardening as well as with and without additional reinforcement.

- The blast performance of hardened aluminum mullions can be predicted by SDOF dynamic inelastic analysis. An essential component of the analysis is the generation of resistance functions representing force-deformation characteristics and hence the member stiffness under blast loads. The software RC-Blast with an internal solver for computing resistance function starting from material models for moment curvature analysis and the computation of moment rotation and force-displacement relationships with assumed constant curvature over plastic hinge regions provided very good correlations with experimental data having a coefficient of determination (R-square value) of 0.92. UFC Charted solution, also providing manual SDOF computation based on bilinear idealization of resistance function also provided very good correlations. Either approach can be used for hardening design of mullions employing the new technology developed in the current investigation.

- Aluminum mullions infilled with cementitious materials, with and without the additional reinforcement exhibited fully composite behaviour as observed during the tests and as confirmed through the analysis.

- Support fixity that was intended during the mullion tests in this category, by clamping the ends at the supports with steel HSS sections resulted in partial fixity. When assumed 80% fixity in the SDOF analysis, the correlation with test data improved, indicating this level of partial fixity was likely attained during testing.

- The design and construction recommendations developed in the current investigation, utilizing an iterative design procedure employing inelastic SDOF analysis can be used for the implementation of the hardening technology developed in the research project.

6.4 Recommendations for Future Work

This research is designed to develop a new and innovative hardening technique for curtain wall mullions by using cementitious infill materials with and without additional reinforcement. A shock Tube was used as a blast simulator using two selected sizes of available aluminum mullions. Though the proof-of-concept objective has been achieved with the two mullion sizes, it is recommended that large size mullions, both in terms of mullion length and cross-sectional dimensions is recommended as future research, while considering the limitations of the shock tube to be used. The use of thick aluminum walls for the mullion sections is important as the failure modes observed were governed either by the rupturing of aluminum in tension or the buckling of the aluminum in compression, as both capacities will increase with the use of larger sections providing compatibility with the higher strength infill materials used. It is also recommended to extend the experimental testing to field tests to provide further verification of the technique, if possible, while recognizing the challenges involved in live testing with explosives. Further research is also recommended for using different infill materials than ECC and HSM considered in the current investigation. Though analytical research was conducted on mullions infilled with UHPFRC, tests were not conducted, and this is also recommended for future research. The use of other infill materials, especially with those with higher compressive strengths and tensile strengths as in the case of other types of fibre-reinforced cementitious materials or high-performance concrete with silica fume with high compressive strength with improved workability for easy placement is recommended for testing and analysis.

Consideration of other types of internal and external reinforcement as well as other percentages of reinforcement is recommended both for testing and numerical research. Relating to the external reinforcement, increased number and orientation of layers of CFRP can be introduced in a multidirectional fashion, for instance, multi-layers (three-plies) can be oriented in different angles such as [0°/90°/0°] or [0°/+45°/90°]. The use of glass fibre reinforced polymer (GFRP) is also highly recommended as this material is known to be economically more advantageous despite its lower elastic modulus. The application of FRP as complete wrapping of the mullions may prove to have higher contribution to strength and hence is recommended,

though this may be a challenge in existing mullions as the other face of the mullions may not be accessible.

Further numerical analysis is recommended to better understand the level of composite action obtained in both the experiments and the SDOF analyses. FEM analysis is recommended with appropriate models. An important aspect of the infill material is the confinement effect of the enclosing aluminum sections. It is recommended to expand on this aspect in developing resistance functions for analytical research. Further numerical research with different design parameters may need to be pursued to generate additional design data.

REFERENCES

Alameer, A. M. (2020). *Performance and Design of Retention Anchors in Blast Resistant Windows*.

Allana, P. K. , & C. D. (2012). *Curtain walls issues, problems and solutions*. 9–111.

Al-Saidy, A. H., Klaiber, F. W., & Wipf, T. J. (2007). Strengthening of steel–concrete composite girders using carbon fiber reinforced polymer plates [Article]. *Construction & Building Materials*, *21*(2), 295–302. https://doi.org/10.1016/j.conbuildmat.2005.08.018

Aydın, S., Yazıcı, H., & Baradan, B. (2008). High temperature resistance of normal strength and autoclaved high strength mortars incorporated polypropylene and steel fibers [Article]. *Construction & Building Materials*, *22*(4), 504–512. https://doi.org/10.1016/j.conbuildmat.2006.11.003

Bedon, C., & Amadio, C. (2017). Enhancement of the seismic performance of multi-storey buildings by means of dissipative glazing curtain walls [Article]. *Engineering Structures*, *152*, 320–334. https://doi.org/10.1016/j.engstruct.2017.09.028

Behr, R. A., Belarbi, A., & Culp, J. H. (1995). Dynamic racking tests of curtain wall glass elements with in-plane and out-of-plane motions. *Earthquake Engineering & Structural Dynamics*, *24*(1), 1–14. https://doi.org/10.1002/eqe.4290240102

Bentur, Arnon. (2007). *Fibre reinforced cementitious composites* (Sidney. Mindess, Ed.; 2nd ed.) [Book]. Taylor & Francis.

Biggs, J. M. (1964). *Introduction to structural dynamics.* [Book]. McGraw-Hill,.

Brewer, T. R., Morrill, K. B., & Crawford, J. E. (2015). A New Kind of Blast-Resistant Curtain Wall Façade [Article]. *International Journal of Protective Structures*, *6*(4), 671–689. https://doi.org/10.1260/2041-4196.6.4.671

Brown, MA., & Klein, KA. (1998). *Custom Molded Silicone Flashing Shapes for Sealing Curtain Walls* (MA. Brown & KA. Klein, Eds.) [Book]. ASTM International. https://doi.org/10.1520/STP15675S

Buljan, N., Vido, H., Skejić, D., & Lukić, M. (2016). Lateral Torsional Buckling of Split Aluminium Mullion [Article]. *Key Engineering Materials*, *710*, 445–450. https://doi.org/10.4028/www.scientific.net/KEM.710.445

Burrell, R. P. (2012). *Performance of Steel Fibre Reinforced Concrete Columns under Shock Tube Induced Shock Wave Loading* (Ottawa-Carleton Institute for Civil Engineering., Ed.).

Chavan, H. (2021). *Experimental and analytical investigation of steel hardened curtain wall mullions* (M. Saatcioglu, Ed.).

Clift, C. (1989). Lateral Buckling of Structurally Glazed Curtain Wall Framing [Bookitem]. In *Science and Technology of Glazing Systems* (pp. 73–84). ASTM International. https://doi.org/10.1520/STP22991S

Corley, W. G. (1966). Rotational capacity of reinforced concrete beams. . *ASCE Structural Journal*, 121–146.

Cussen, R., & Van Eepoel, P. (2008). Inelastic Dynamic Finite-Element Design of Glazed Facade Systems for Blast Loading [Proceeding]. *Proceedings of the 2008 Structures Congress - Structures Congress 2008: Crossing the Borders*, *314*, 1–11. https://doi.org/10.1061/41016(314)153

Davis, J. R. (1993). *Aluminum and Aluminum Alloys*. https://doi.org/10.1361/autb2001p351

Dawson, H., & Smilowitz, R. (2007). Inelastic Dynamic Response of Curtainwall Systems to Blast Loading [Article]. *Journal of ASTM International*, *4*(5), 1–5. https://doi.org/10.1520/JAI100481

Deng, R., & Jin, X. (2010). Numerical Simulation for Blast Analysis of Insulating Glass in a Curtain Wall [Article]. *International Journal of Computational Methods in Engineering Science and Mechanics*, *11*(3), 162–171. https://doi.org/10.1080/15502281003702302

Edel, M. T., & Kumar, D. (2010). Blast Design Approach Comparisons for Curtain Wall [Bookitem]. In *Structures Congress 2010* (pp. 2076–2089). https://doi.org/10.1061/41130(369)188

EJSE Special Issue: Loading on Structures (2007). (n.d.).

Elnabelsya, G. (2013). *USE OF CARBON FIBER REINFORCED POLYMER SHEETS AS TRANSVERSE REINFORCEMENT IN BRIDGE COLUMNS*.

Faella, C., Mazzolani, F. M., Piluso, V., & Rizzano, G. (2000). Local Buckling of Aluminum Members: Testing and Classification [Article]. *Journal of Structural Engineering (New York, N.Y.)*, *126*(3), 353–360. https://doi.org/10.1061/(ASCE)0733-9445(2000)126:3(353)

Feng, M., Wang, Z., & Wu, L. (2021). Experimental Study on High-Strength Concrete, Ultrahigh-Strength Concrete and Corresponding Mortar Under Triaxial Compression [Article]. *Arabian Journal for Science and Engineering (2011)*, *46*(11), 11179–11194. https://doi.org/10.1007/s13369-021-05663-y

Feng, P., Hu, L., Qian, P., & Ye, L. (2016). Compressive bearing capacity of CFRP–aluminum alloy hybrid tubes [Article]. *Composite Structures*, *140*, 749–757. https://doi.org/10.1016/j.compstruct.2016.01.041

G Vallabban, C. V, Ziilfii, M. A., & KandiQ, K. (1997). *ANALYSIS OF STRUCTURAL GLAZING SYSTEMS* (Vol. 65, Issue 2).

Ge, F., Lin, Y., Zhang, F., Zhang, Z., & Wang, M. (2022). Crushing Characteristics Comparison between Aluminum/CFRP and Aluminum/CFRP/Aluminum Hybrid Tubes [Article]. *Polymers*, *14*(19), 4034. https://doi.org/10.3390/polym14194034

Horowitz, JM. (1991). *The Interrelation of Exterior Wall and Structural Systems in Buildings* (JM. Horowitz, Ed.) [Book]. ASTM International. https://doi.org/10.1520/STP20123S

Huang, Z., & Zhang, X. (2018). Three-point bending collapse of thin-walled rectangular beams [Article]. *International Journal of Mechanical Sciences*, *144*, 461–479. https://doi.org/10.1016/j.ijmecsci.2018.06.001

Jacques, E., Lloyd, A., & Saatcioglu, M. (2013). Predicting reinforced concrete response to blast loads1. *Canadian Journal of Civil Engineering*, *40*(5), 427–444. https://doi.org/10.1139/L2012-014

Karlos, vasilic and C. G. (2013). *Calculation of Blast Loads for Application to Structural Components*. https://doi.org/10.2788/61866

Kennedy, B. T., & Weggel, D. C. (2009). Energy Limit States and Maximum Mullion End Rotations for Nearly-Conventional Curtain Walls Subjected to Extreme Out-of-Plane Loads [Bookitem]. In *Proceedings of the 2009 Structures Congress - Don't Mess with Structural Engineers: Expanding Our Role* (pp. 1–10). https://doi.org/10.1061/41031(341)144

Kennedy, B. T., Weggel, D. C., & Keanini, R. G. (2013). Experimental program and simplified nonlinear design expression for glass curtain walls with low-level blast resistance [Article]. *International Journal of Computational Methods and Experimental Measurements*, *1*(3), 321–343. https://doi.org/10.2495/CMEM-V1-N3-321-343

Kesawan, S., & Mahendran, M. (2019). Buckling behaviour and design of complex-shaped aluminium mullion sections [Article]. *Advances in Structural Engineering*, *22*(2), 547–564. https://doi.org/10.1177/1369433218795118

Khandelwal, S., & Rhee, K. Y. (2020). Recent advances in basalt-fiber-reinforced composites: Tailoring the fiber-matrix interface [Article]. *Composites. Part B, Engineering*, *192*, 108011. https://doi.org/10.1016/j.compositesb.2020.108011

Kissell, J. R. (1995). *Aluminum structures : a guide to their specifications and design* (R. L. Ferry, Ed.) [Book]. Wiley.

Krauthammer, Theodor. (2008). *Modern protective structures* [Book]. CRC Press. https://doi.org/10.1201/9781420015423

Lambiase, F., Paoletti, A., & Durante, M. (2021). Mechanism of bonding of AA7075 aluminum alloy and CFRP during friction assisted joining [Article]. *Composite Structures*, *261*, 113593. https://doi.org/10.1016/j.compstruct.2021.113593

Li, L., Wang, H., Wu, J., Li, S., & Wu, W. (2021). Experimental investigation on dynamic tensile behaviors of engineered cementitious composites reinforced with steel grid and fibers [Article]. *Materials*, *14*(22), 7042. https://doi.org/10.3390/ma14227042

Li, V. (2019). *Engineered cementitious composites (ECC) : bendable concrete for sustainable and resilient infrastructure* [Book]. Springer. https://doi.org/10.1007/978-3-662-58438-5

Lusk, B., Salim, H., Perry, K., Nawar, M., Wedding, W. C., Kiger, S., & Ibrahim, A. (2011). *Modeling and Testing of Laminated Window Systems under Blast Loading*.

Maalej, M., Quek, S. T., Zhang, J., & Lin, V. J. (2012). *BEHAVIOR OF HYBRID FIBER ECC PANELS SUBJECTED TO LOW AND HIGH VELOCITY PROJECTILE IMPACT-A REVIEW*. 1FTR and Woodhead Pub!

Marchand, K., Davis, C., Sammarco, E., Bui, J., & Casper, J. (2017). Coupled glass and structure response of conventional curtain walls subjected to blast loads: validation tests and analysis [Article]. *Glass Structures & Engineering*, *2*(1), 17–43. https://doi.org/10.1007/s40940-016-0037-y

Mattock, A. H. (1964). *Rotational capacity of hinging regions in reinforced concrete beams* [Book]. Proceedings of the International Symposium on Flexural Mechanics of Reinforced Concrete.

Mehta, P. K. (Povindar K. (2014). *Concrete : microstructure, properties, and materials* (P. J. M. Monteiro, Ed.; Fourth edition / ...) [Book]. McGraw-Hill Education.

Moen, L. A., Hopperstad, O. S., & Langseth, M. (1999). Rotational Capacity of Aluminum Beams under Moment Gradient. I: Experiments [Article]. *Journal of Structural Engineering*, *125*(8), 910–920. https://doi.org/10.1061/(ASCE)0733-9445(1999)125:8(910)

Mondolfo, L. F. (Lucio F.). (1976). *Aluminium alloys : structure and properties.* [Book]. Butterworths,.

Nasseralshariati, E. (2023). *Improved Connections for Blast-Resistant Curtain Walls.* (M. Saatcioglu, Ed.).

Nawar, M., Salim, H., Lusk, B., & Kiger, S. (2014). Numerical Simulation and Verification of Curtain Wall Systems under Shock Pressure [Article]. *Practice Periodical on Structural Design and Construction*, *19*(2). https://doi.org/10.1061/(ASCE)SC.1943-5576.0000193

Ngo, T., Mendis, P., Gupta, A., & Ramsay, J. (2007). *Blast Loading and Blast Effects on Structures*.

Ralston, A. D., Weggel, D. C., Whelan, M. J., & Fang, H. (2015). Experimental and numerical investigations of glass curtain walls subjected to low- level blast loads [Article]. *International Journal of Computational Methods and Experimental Measurements*, *3*(2), 121–138. https://doi.org/10.2495/CMEM-V3-N2-121-138

Rolater, G. (2022). *A Proposed Methodology to Analyze Cold-Formed Steel Trusses Subjected to Blast Loading Using Single-Degree-of-Freedom for Design and Assessment*.

Saatcioglu, M., Alameer, A., & Elnabelsy, G. (2017). *"Blast Tests of Curtain Walls – Phase I: Windows Protected by Guardian Coil*.

Saatcioglu, M., & Eng, P. (2020). *Building Envelop Hardening Measures*.

Saatcioglu, M., & Razvi, S. R. (1992). Strength and Ductility of Confined Concrete [Article]. *Journal of Structural Engineering (New York, N.Y.)*, *118*(6), 1590–1607. https://doi.org/10.1061/(ASCE)0733-9445(1992)118:6(1590)

Sawyer, H. A. (1964). Design of Concrete Frames For Two Failure Stages. *Proceedings of the International Symposium on the Flexural Mechanics of Reinforced Concrete, ASCE-ACI, Miami*, 405–437.

Scheffler, C., Zhandarov, S., & Mäder, E. (2017). Alkali resistant glass fiber reinforced concrete: Pull-out investigation of interphase behavior under quasi-static and high rate loading [Article]. *Cement & Concrete Composites*, *84*, 19–27. https://doi.org/10.1016/j.cemconcomp.2017.08.009

Schwartz, T. A. (2001). Glass and Metal Curtain-Wall Fundamentals [Article]. *APT Bulletin (1986)*, *32*(1), 37–45. https://doi.org/10.2307/1504691

Serna, P., Llano-Torre, A., Martí-Vargas, J. R., & Navarro-Gregori, J. (2020a). Bond Between Steel Reinforcement Bars and Fiber Reinforced Cement-Based Composites [Bookitem]. In *Fibre Reinforced Concrete: Improvements and Innovations* (Vol. 30, pp. 313–321). Springer International Publishing AG. https://doi.org/10.1007/978-3-030-58482-5_29

Serna, P., Llano-Torre, A., Martí-Vargas, J. R., & Navarro-Gregori, J. (2020b). Numerical Evaluation the Effect of Specimen Thickness on Fibre Orientation in Self-consolidating Engineered Cementitious

Composites [Bookitem]. In *Fibre Reinforced Concrete: Improvements and Innovations* (Vol. 30, pp. 661–669). Springer International Publishing AG. https://doi.org/10.1007/978-3-030-58482-5_59

Shin, D. K., Kim, H. C., & Lee, J. J. (2014). Numerical analysis of the damage behavior of an aluminum/CFRP hybrid beam under three point bending [Article]. *Composites. Part B, Engineering*, *56*, 397–407. https://doi.org/10.1016/j.compositesb.2013.08.030

Smith, P. D. (1994). *Blast and ballistic loading of structures* (J. G. Hetherington, Ed.) [Book]. Butterworth-Heinemann.

Su, M.-N., Young, B., & Gardner, L. (2014). Deformation-based design of aluminium alloy beams [Article]. *Engineering Structures*, *80*, 339–349. https://doi.org/10.1016/j.engstruct.2014.08.034

Uddin, Nasim. (2010). *Blast protection of civil infrastructures and vehicles using composites* (Nasim. Uddin, Ed.) [Book]. CRC Press.

V Girya Vallabhan, B. C., Chou, G. D., & Minor, J. E. (1990). *SEAL FORCES IN STRUCTURAL GLAZING SYSTEMS*.

Wang, H., Hao, X., Yan, K., Zhou, H., & Hua, L. (2018). Ultrasonic vibration-strengthened adhesive bonding of CFRP-to-aluminum joints [Article]. *Journal of Materials Processing Technology*, *257*, 213–226. https://doi.org/10.1016/j.jmatprotec.2018.03.003

Weggel, D. C., & Zapata, B. J. (2008). Laminated Glass Curtain Walls and Laminated Glass Lites Subjected to Low-Level Blast Loading [Article]. *Journal of Structural Engineering (New York, N.Y.)*, *134*(3), 466–477. https://doi.org/10.1061/(ASCE)0733-9445(2008)134:3(466)

Weggel, D. C., Zapata, B. J., & Kiefer, M. J. (2007). *Properties and Dynamic Behavior of Glass Curtain Walls with Split Screw Spline Mullions*. https://doi.org/10.1061/ASCE0733-94452007133:101415

Wei, J., & Dharani, L. R. (2006). Response of laminated architectural glazing subjected to blast loading. *International Journal of Impact Engineering*, *32*(12), 2032–2047. https://doi.org/10.1016/j.ijimpeng.2005.05.012

Wong, W. M., Cruz-Noguez, C. A., & Tolou-Kian, M. J. (2020). Confinement of rectangular columns made with engineered cementitious composites (ECC) [Article]. *Canadian Journal of Civil Engineering*, *47*(11), 1215–1225. https://doi.org/10.1139/cjce-2019-0313

YEOMANS, D. (1998). The pre-history of the curtain wall [Article]. *Construction History : Journal of the Construction History Group*, *14*, 59–82.

Yu, J. H., & Dai, L. (2009). Strain rate and interfacial property effects of random fibre cementitious composites [Article]. *Journal of Strain Analysis for Engineering Design*, *44*(6), 417–425. https://doi.org/10.1243/03093247JSA513

Zain, M. R. M., Oh, C. L., & Lee, S. W. (2018). Evaluation of the Design Mix Proportion on Mechanical Properties of Engineered Cementitious Composites [Article]. *Key Engineering Materials*, *775*, 589–595. https://doi.org/10.4028/www.scientific.net/KEM.775.589

Zhang, X., Hao, H., & Wang, Z. (2015). Experimental Investigation on Monolithic Tempered Glass Window Responses to Blast Loads. In *International Journal of Protective Structures* (Vol. 6, Issue 2).

Zhou, Y., Fan, H., Jiang, K., Gou, M., Li, N., Zhu, P., & Tu, Y. (2014). Experimental flexural behaviors of CFRP strengthened aluminum beams [Article]. *Composite Structures*, *116*(1), 761–771. https://doi.org/10.1016/j.compstruct.2014.06.012

Zhu, W., Xiao, H., Wang, J., & Fu, C. (2019). Characterization and properties of AA6061-based fiber metal laminates with different aluminum-surface pretreatments [Article]. *Composite Structures*, *227*, 111321. https://doi.org/10.1016/j.compstruct.2019.111321

Appendix A. Strain Gages

A.1. M-1F

A.1.1 Shot 1

T-T

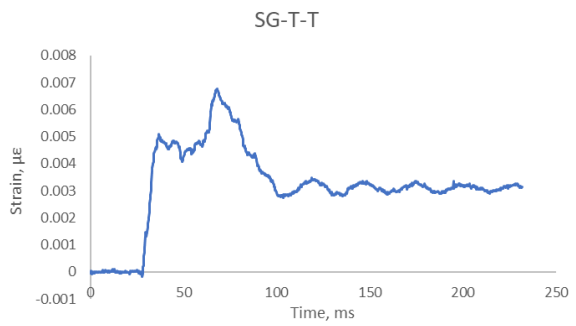

T-C

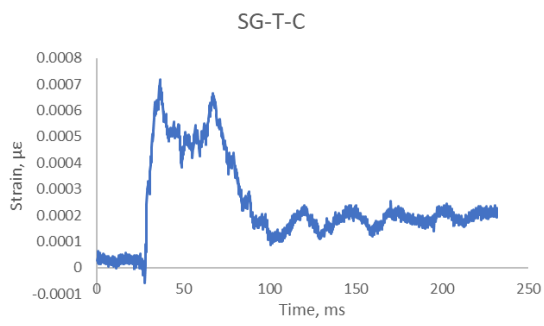

M-T

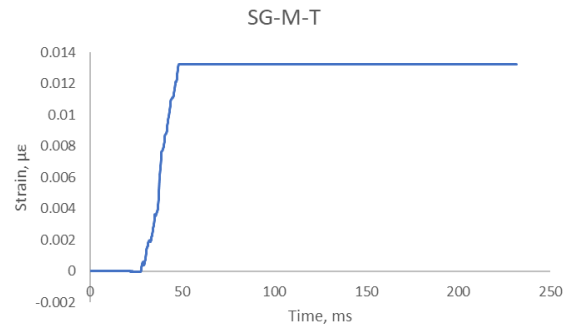

M-C

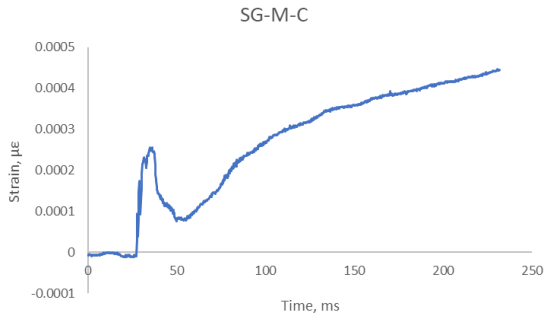

B-T

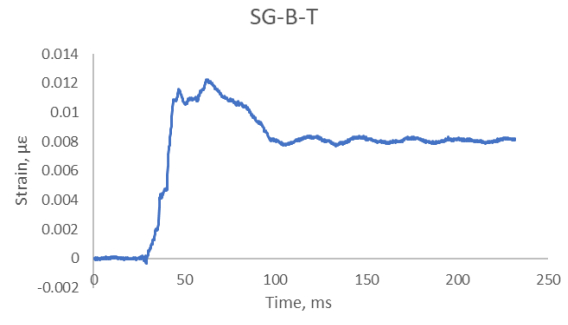

B-C

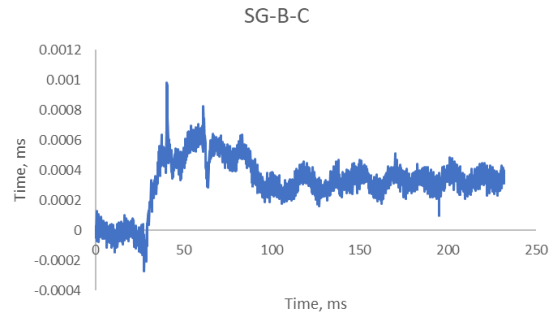

A.1.2 Shot 2

T-T	T-C
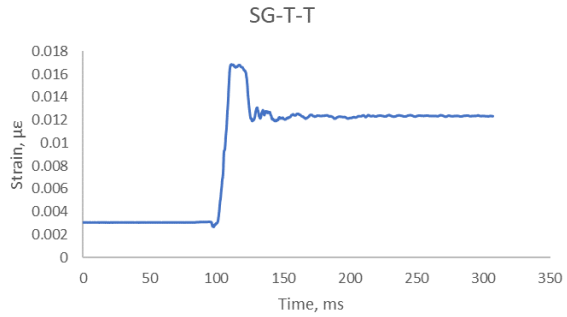	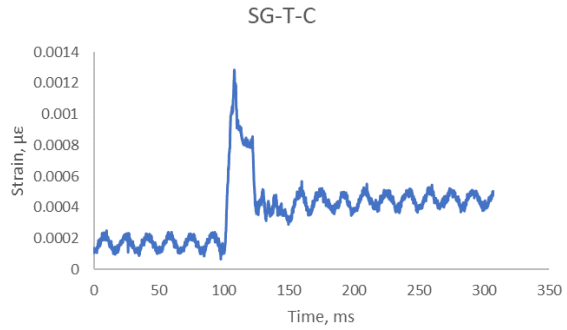
M-T	**M-C**
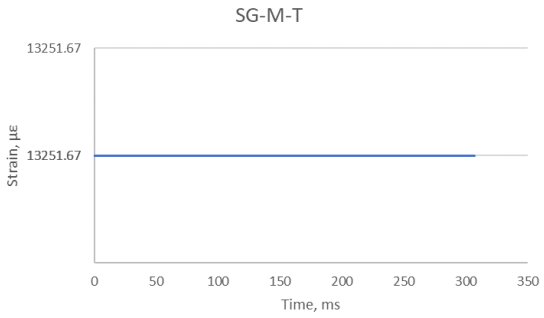	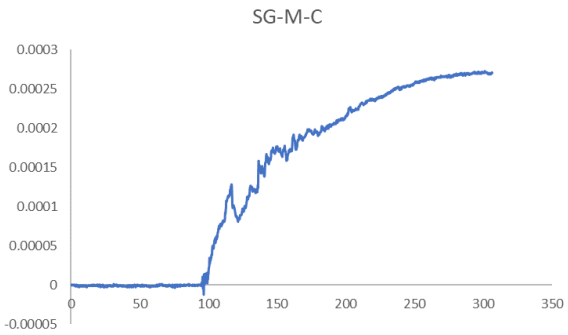
B-T	**B-C**
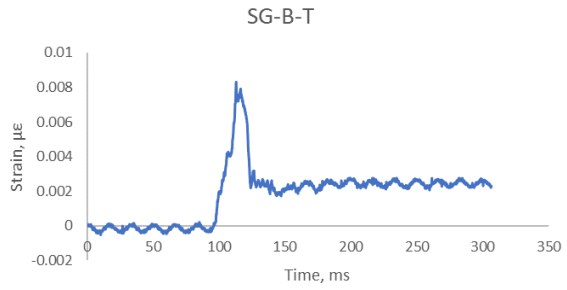	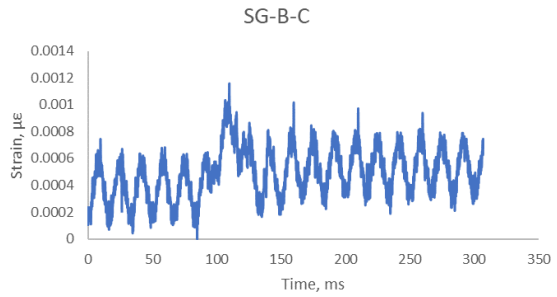

A.2. M-2FR

A.2.1 Shot 1

T-T	T-C
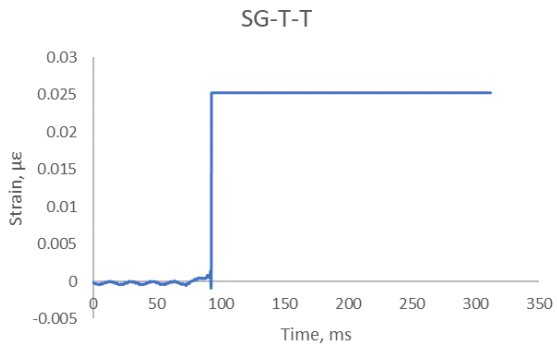	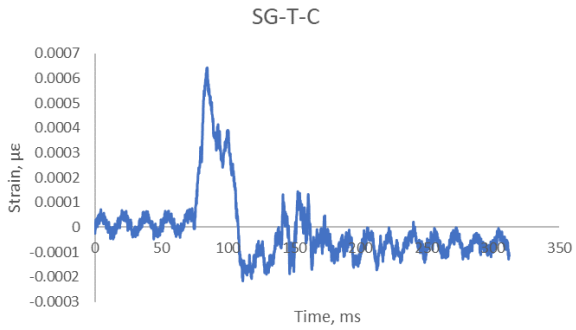
M-T	**M-C**
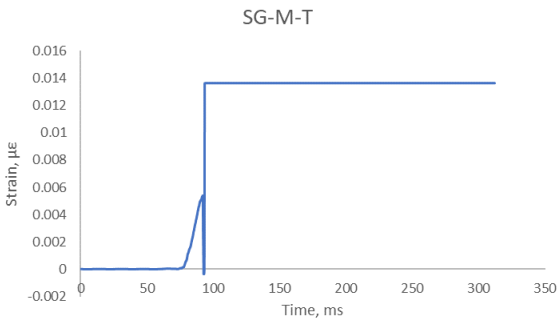	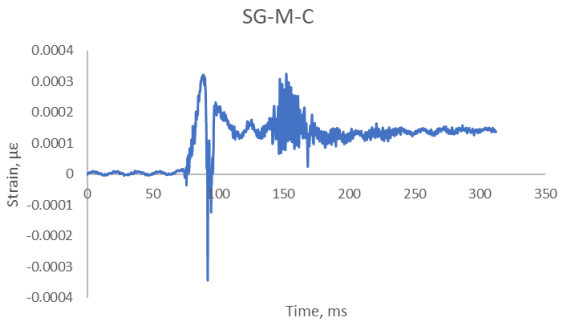
B-T	**B-C**
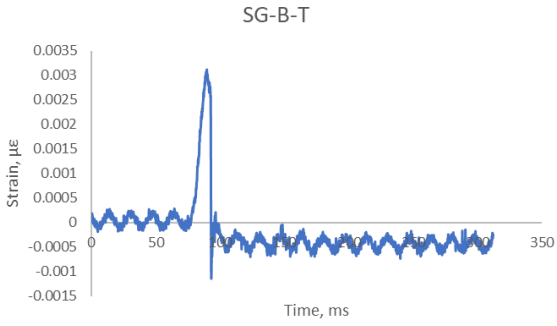	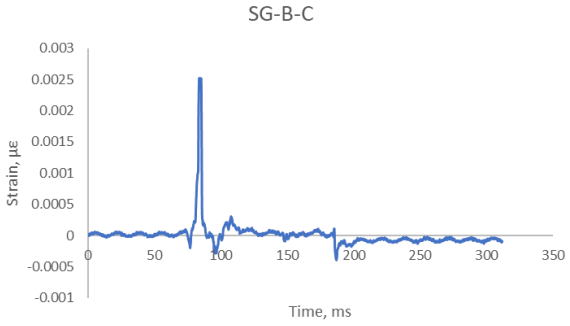

A.2.2 Shot 2

T-T

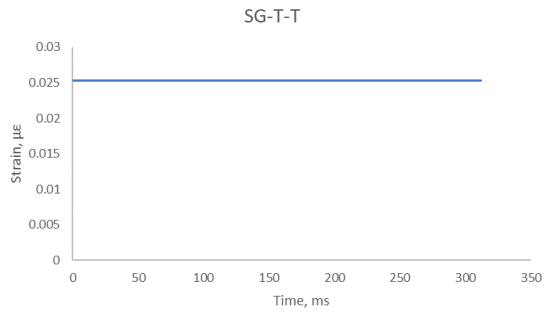

T-C

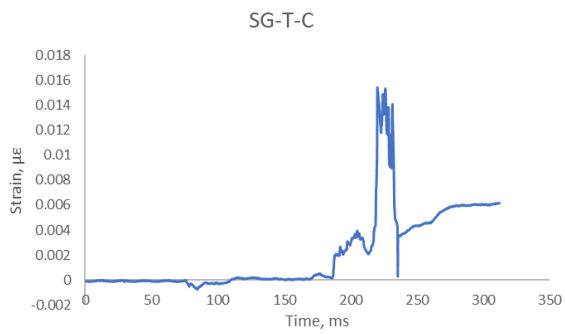

M-T

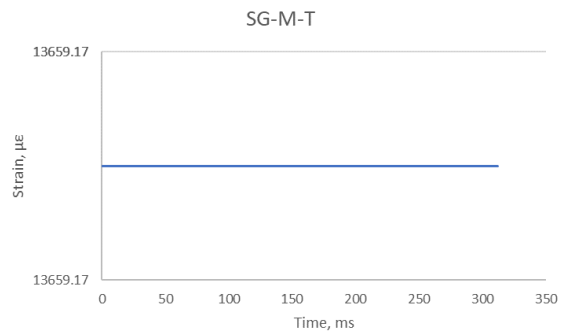

M-C

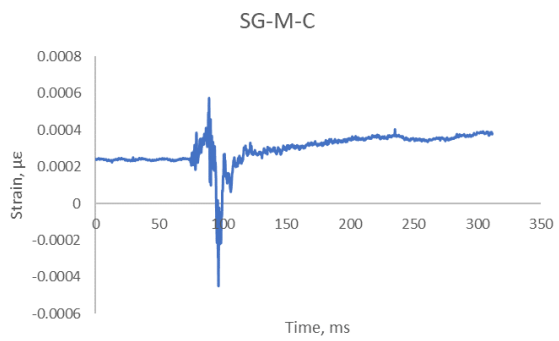

B-T

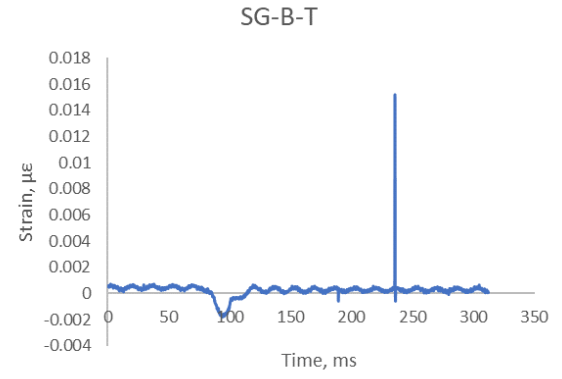

B-C

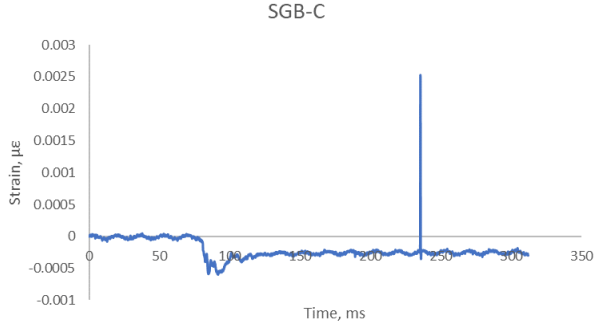

A.2.3 Shot 3

T-T

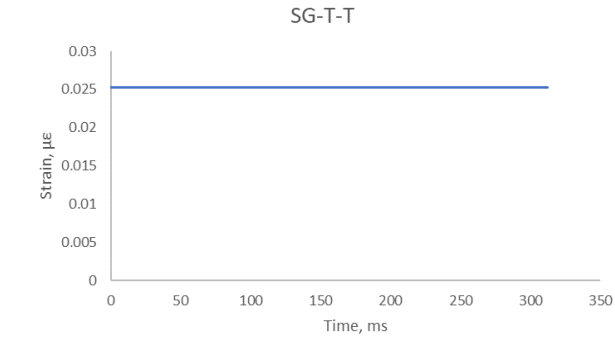

T-C

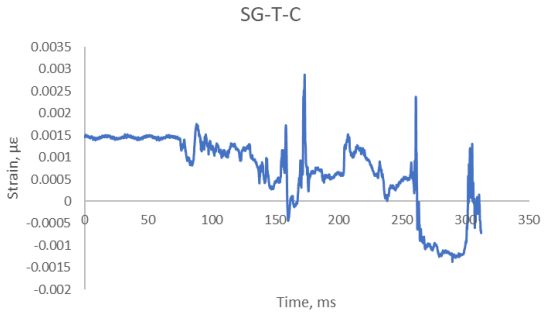

M-T

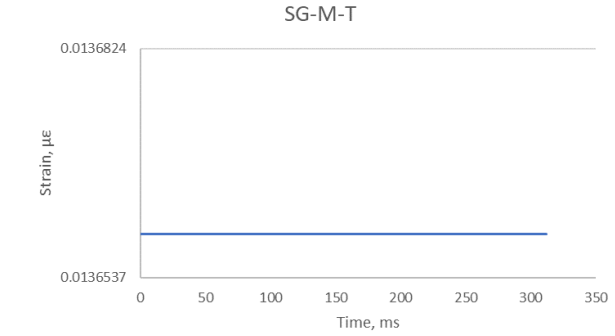

M-C

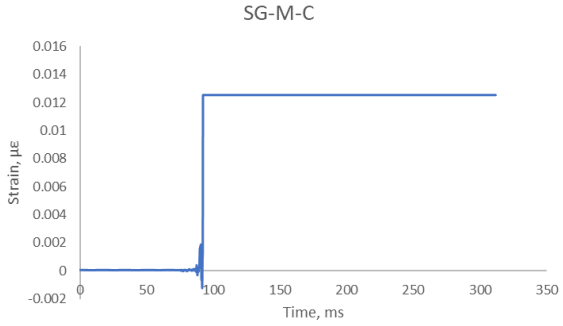

B-T

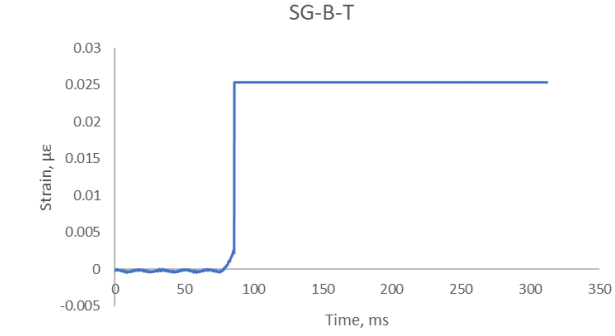

B-C

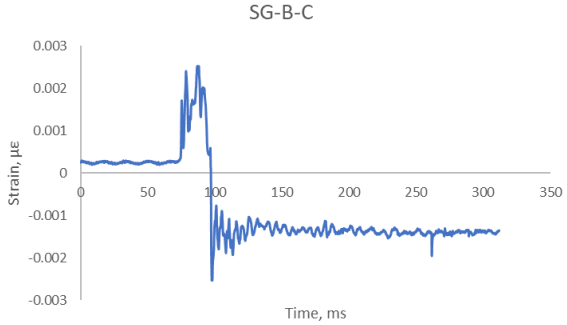

A.3. M-3F

A.3.1 Shot 1

T-T	T-C
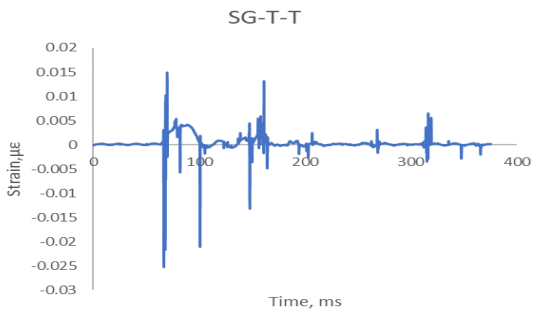	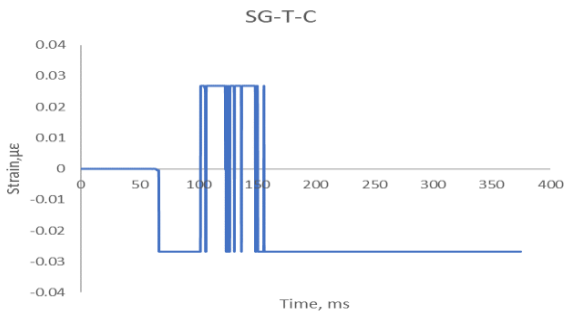
M-T	**M-C**
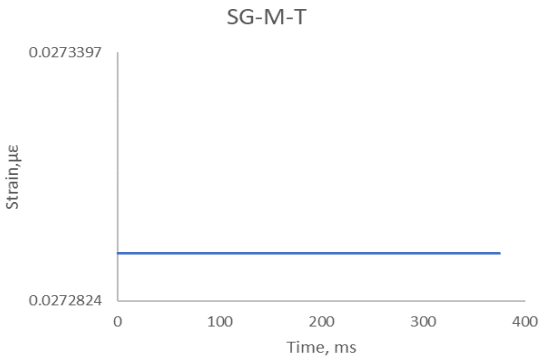	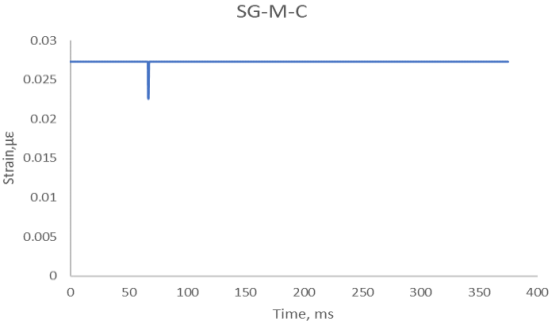
B-T	**B-C**
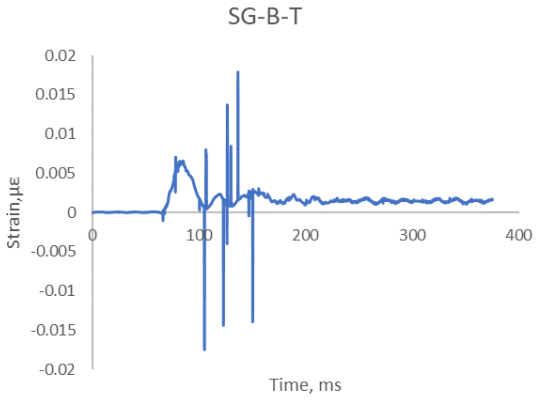	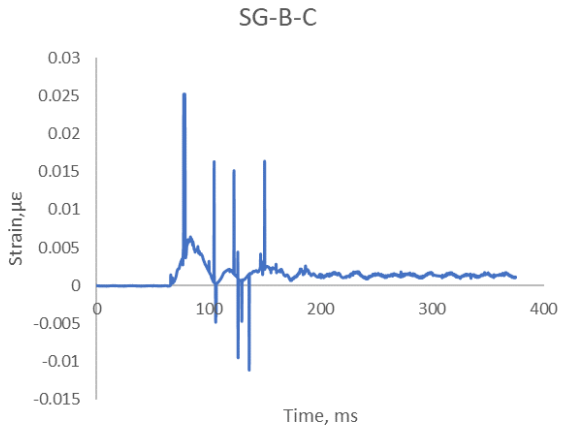

A.3.2 Shot 2

T-T	T-C
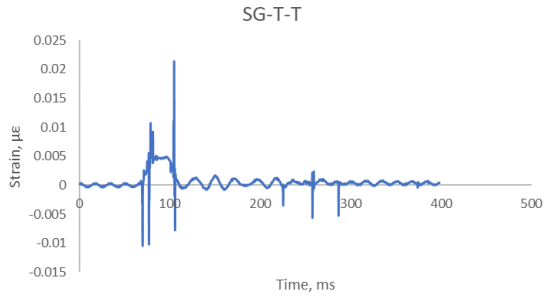	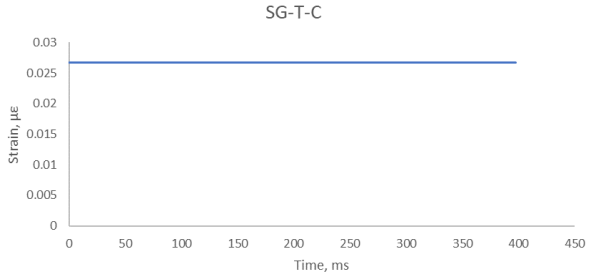
M-T	**M-C**
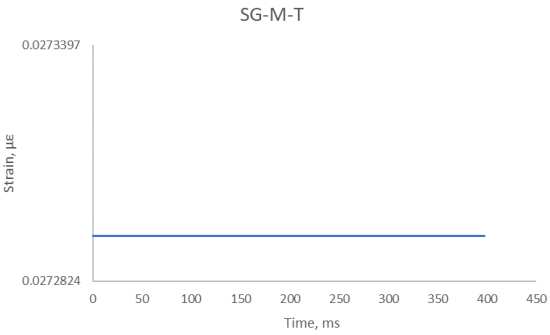	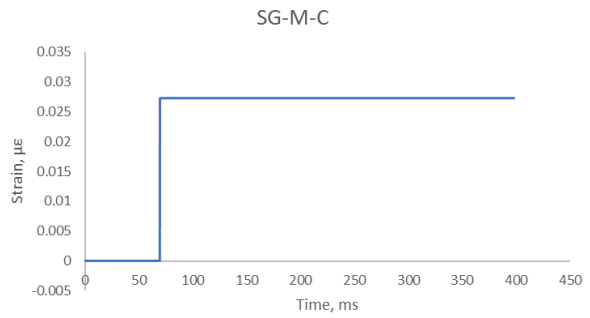
B-T	**B-C**
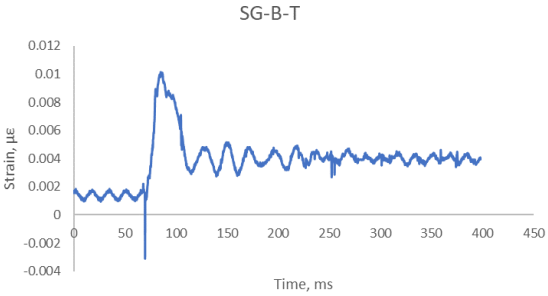	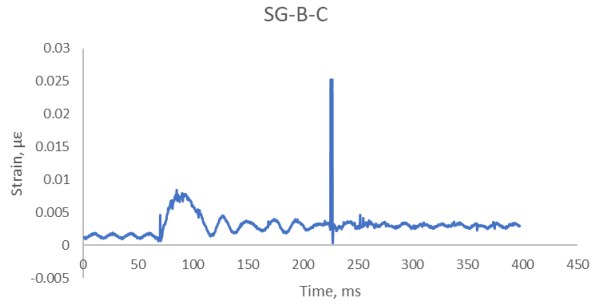

A.3.3 Shot 3

T-T	T-C
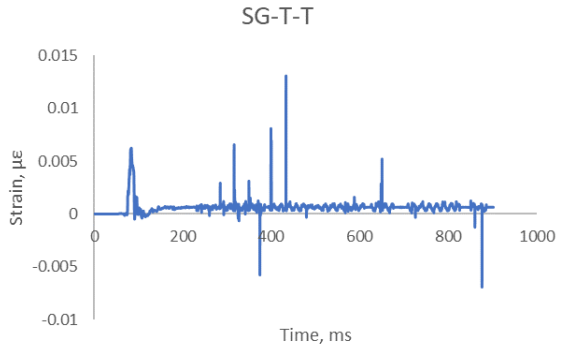	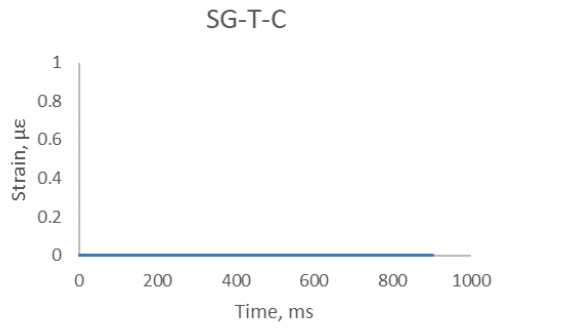
M-T	**M-C**
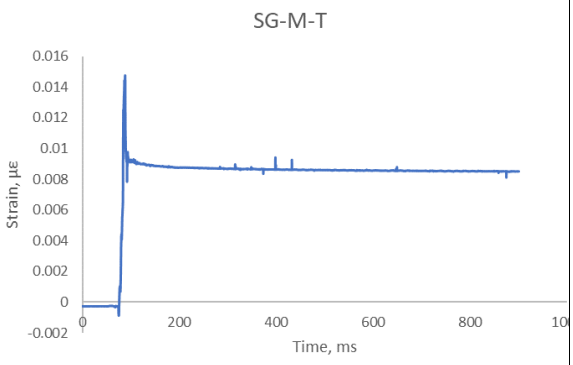	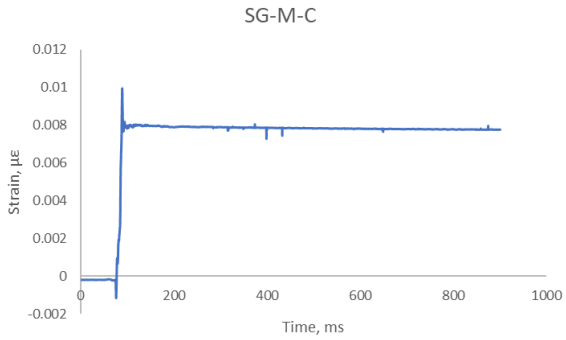
B-T	**B-C**
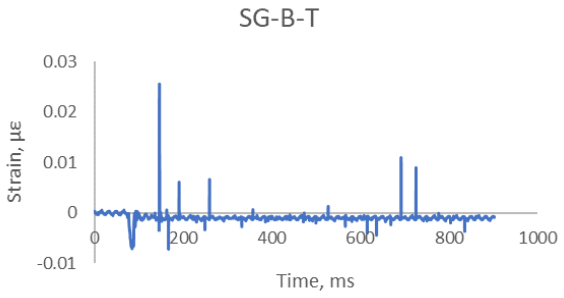	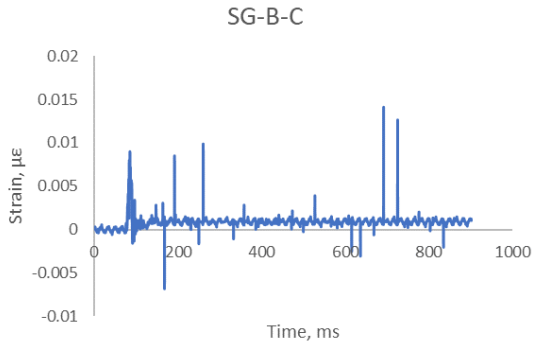

A.4. M-4FR

A.4.1 Shot 1

T-T	T-C
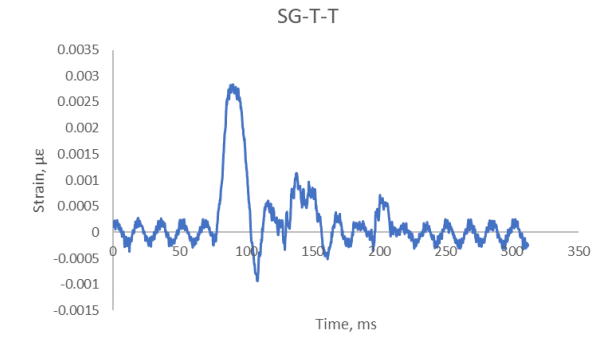	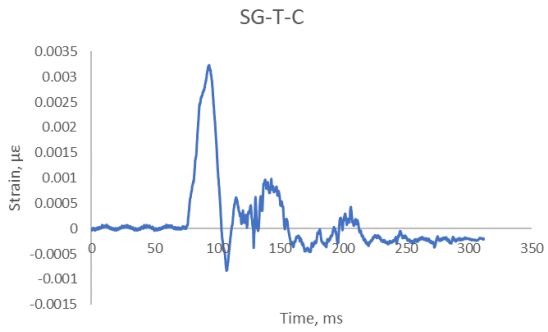
M-T	**M-C**
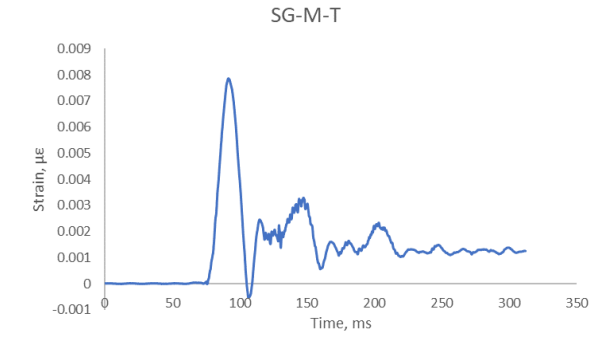	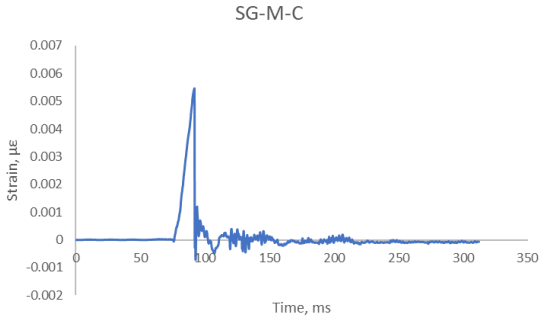
B-T	**B-C**
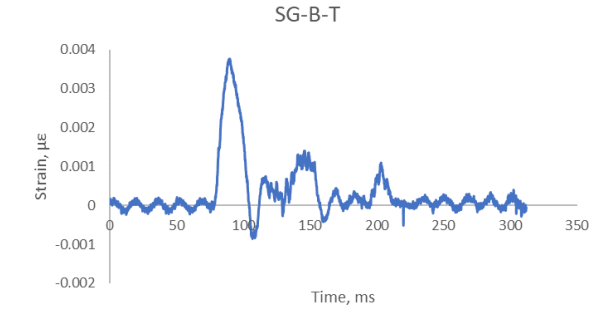	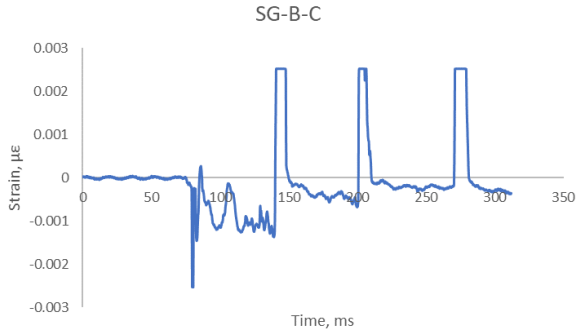

A.4.2 Shot 2

T-T	T-C
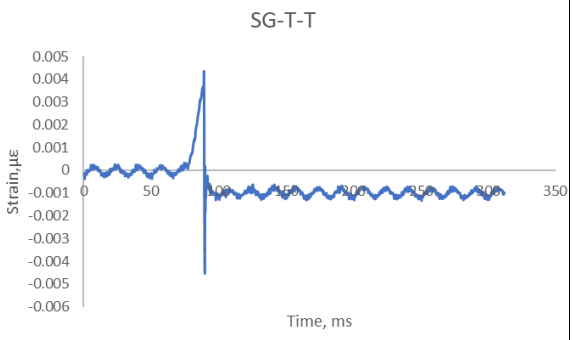	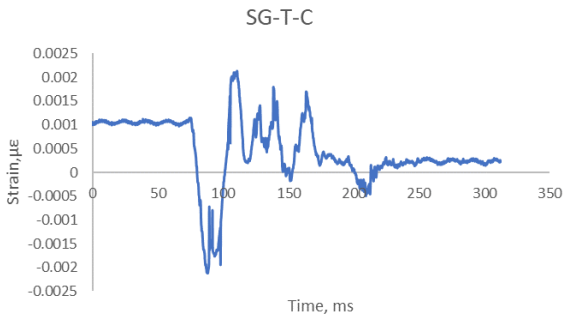
M-T	**M-C**
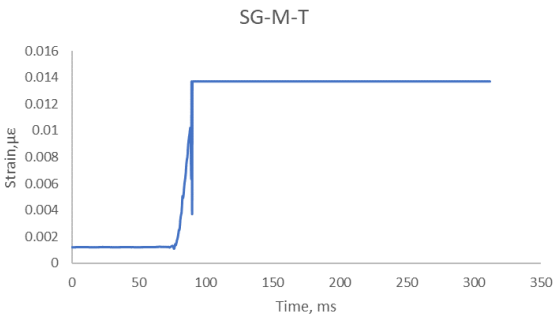	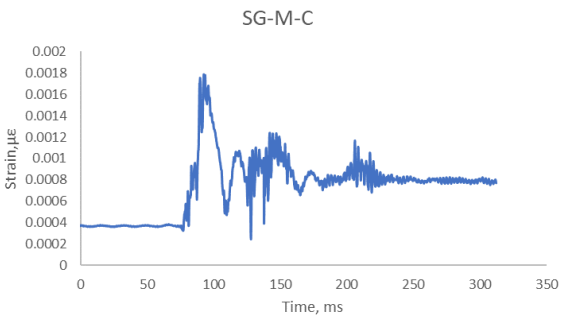
B-T	**B-C**
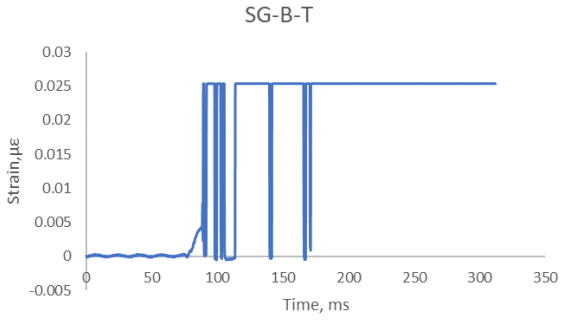	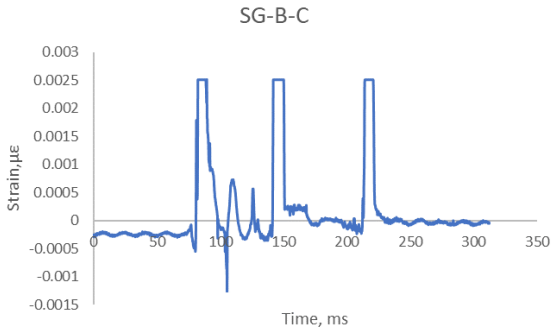

A.4.3 Shot 3

T-T	T-C
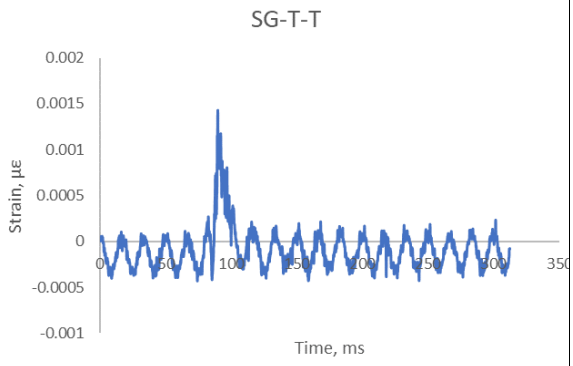	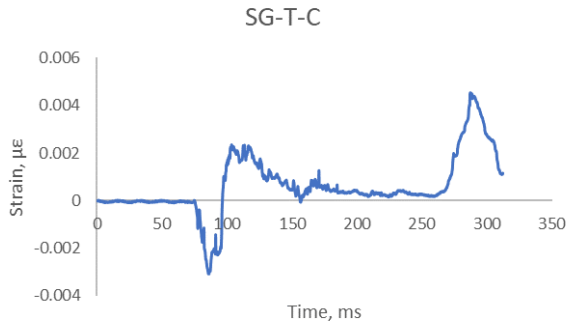
M-T	**M-C**
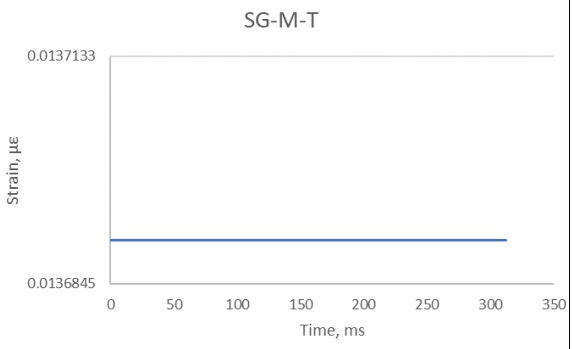	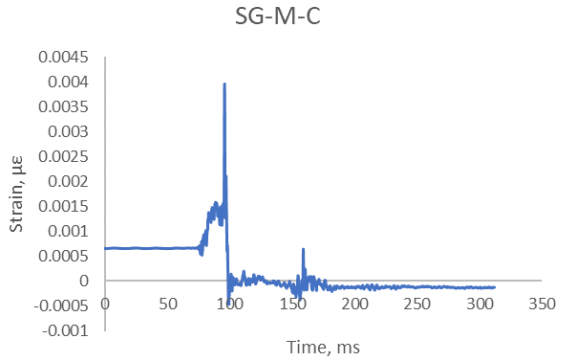
B-T	**B-C**
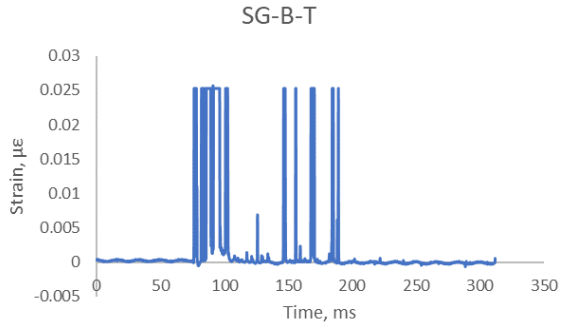	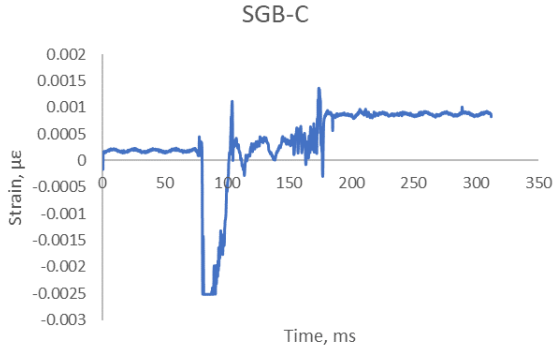

A.5. M-5F

A.5.1 Shot 1

T-T	T-C
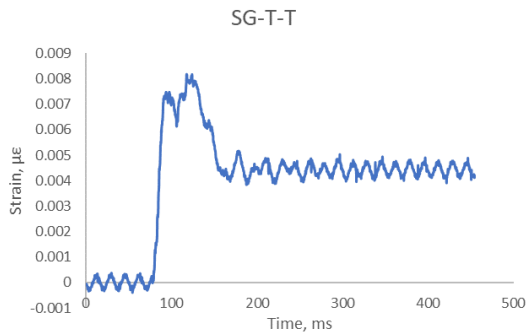	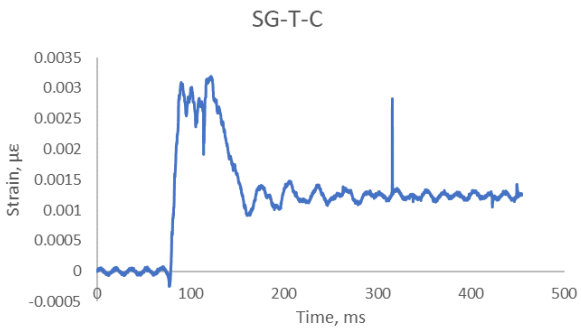
M-T	**M-C**
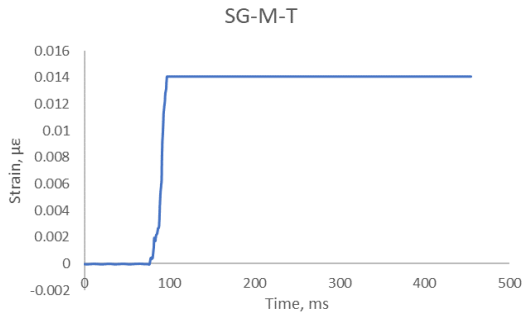	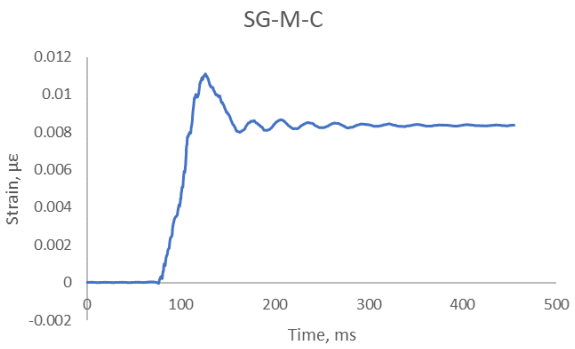
B-T	**B-C**
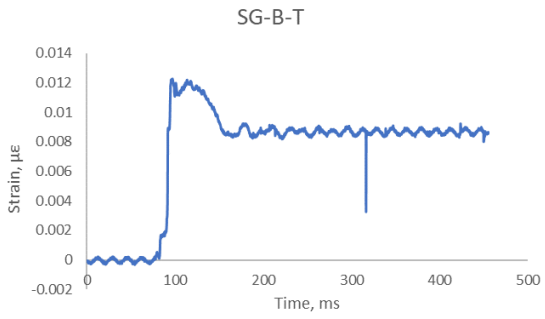	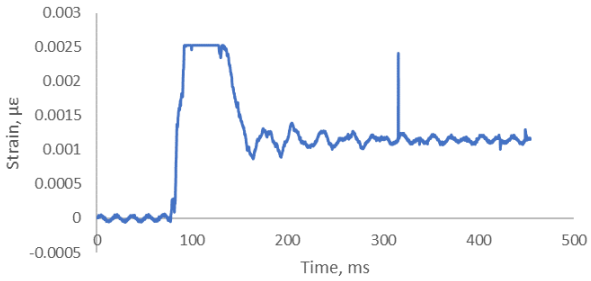

A.5.2 Shot 2

T-T	T-C
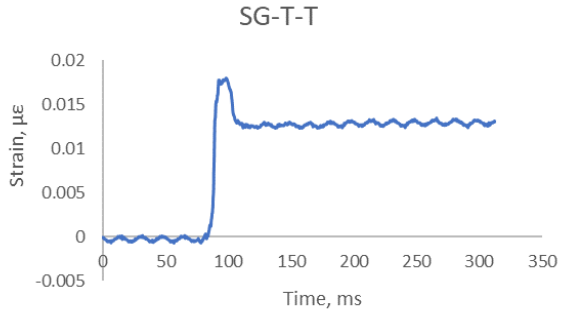	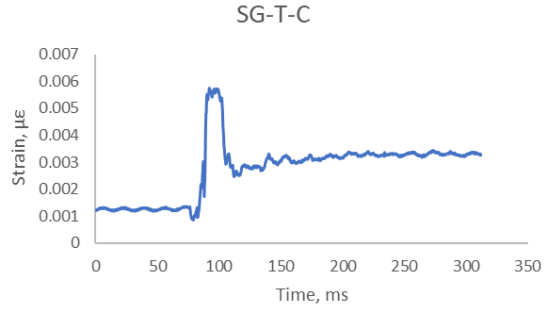
M-T	**M-C**
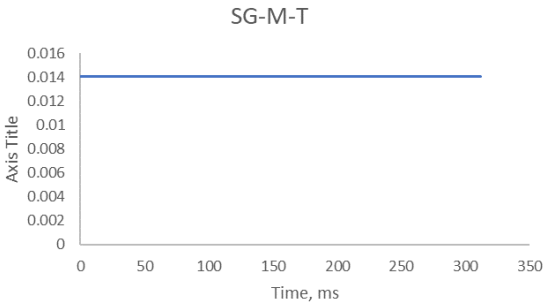	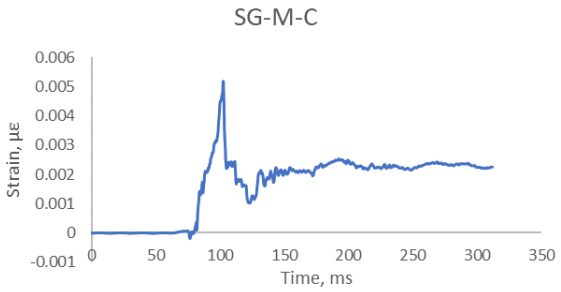
B-T	**B-C**
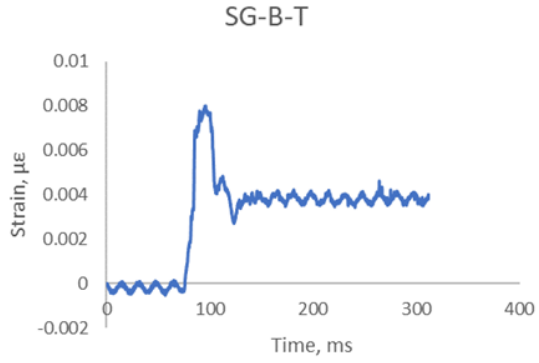	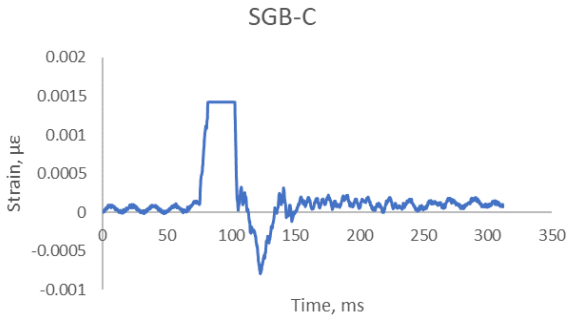

A.6. M-6F

A.6.1 Shot 1

T-T	T-C
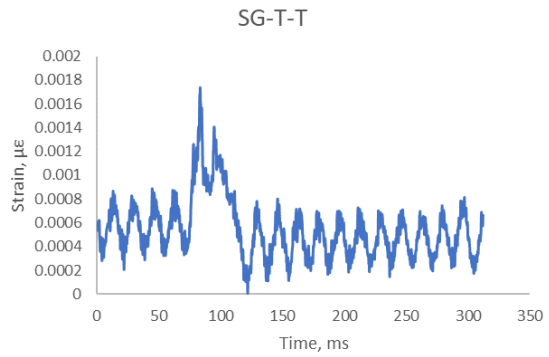	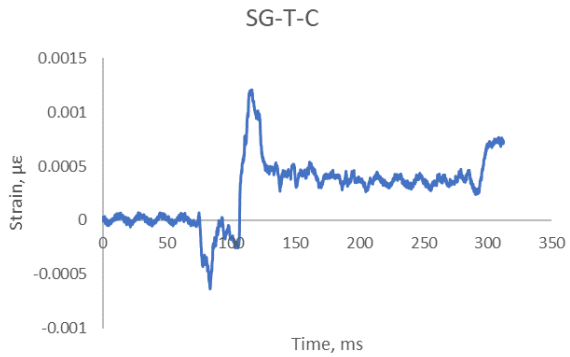
M-T	**M-C**
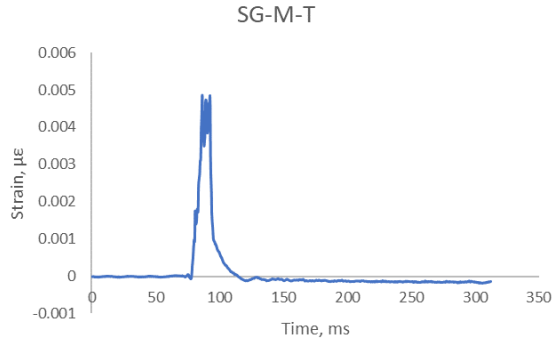	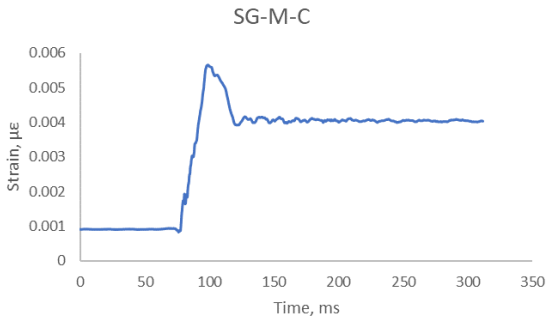
B-T	**B-C**
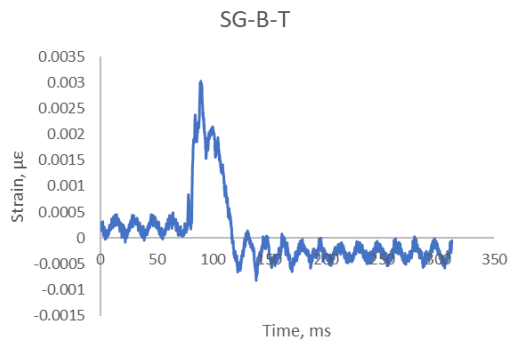	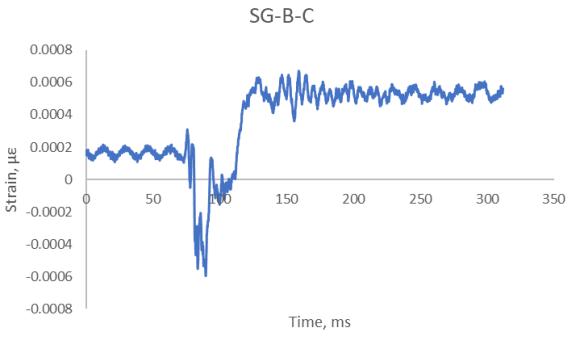

A.6.2 Shot 2

T-T	T-C
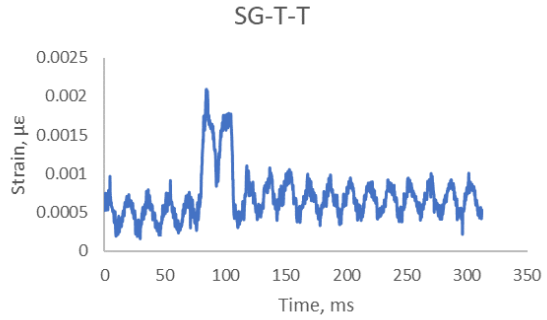	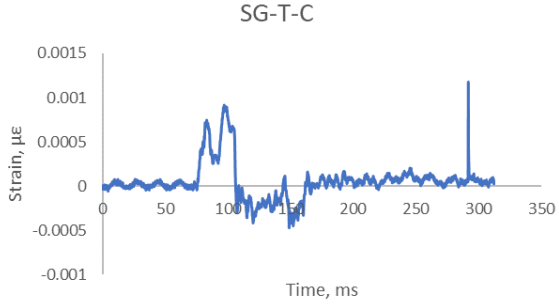
M-T	**M-C**
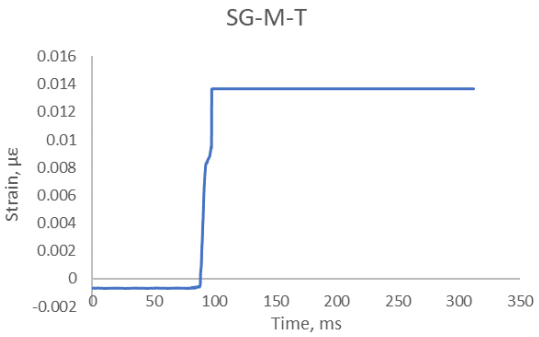	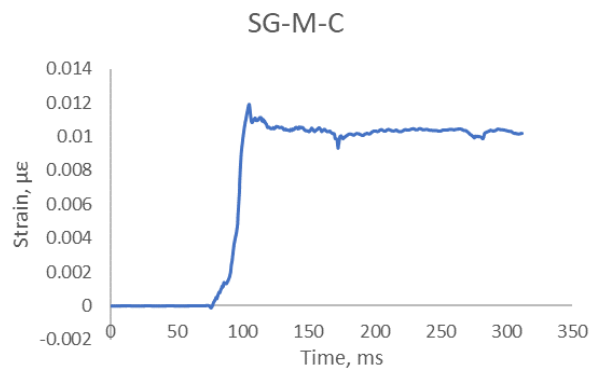
B-T	**B-C**
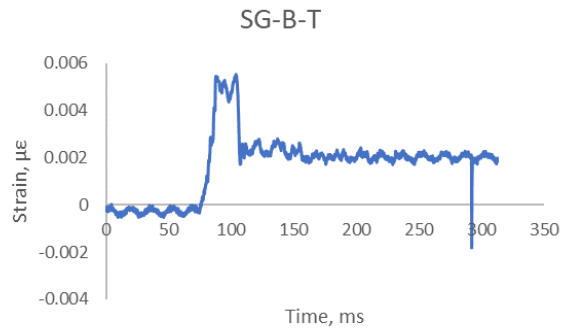	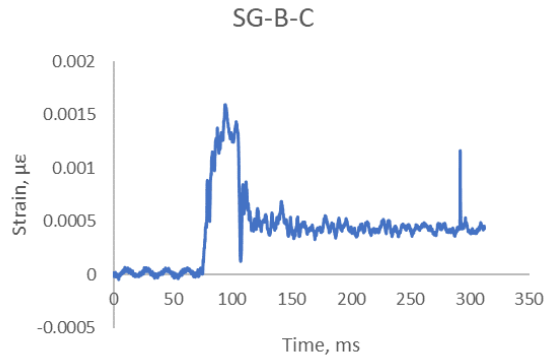

A.7. M-7F

A.7.1 Shot 1

T-T	T-C
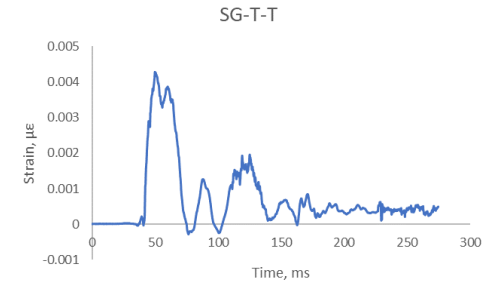	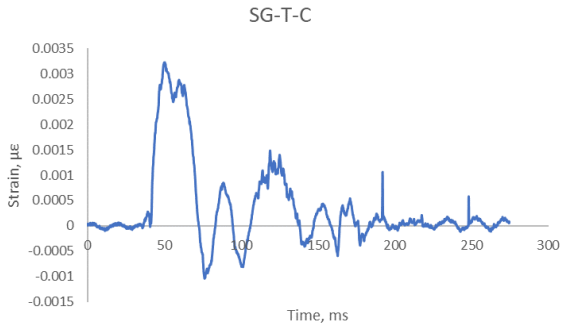
M-T	**M-C**
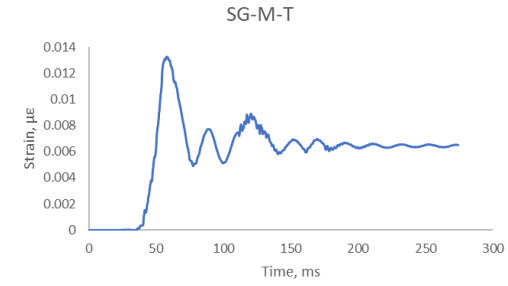	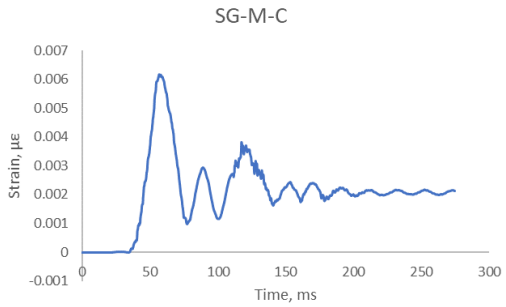
B-T	**B-C**
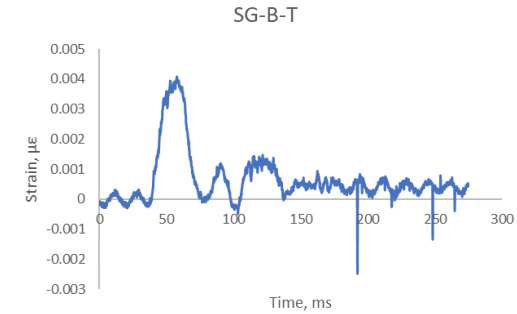	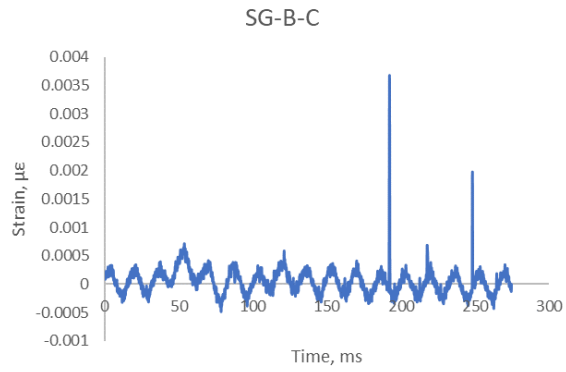

A.7.2 Shot 2

T-T	T-C
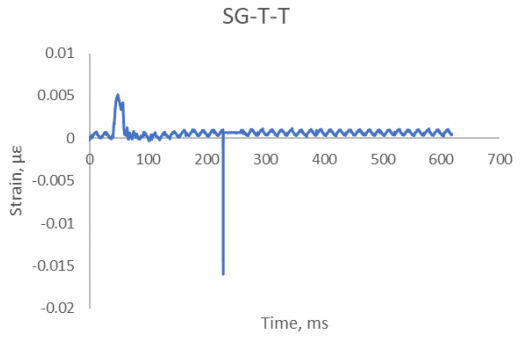	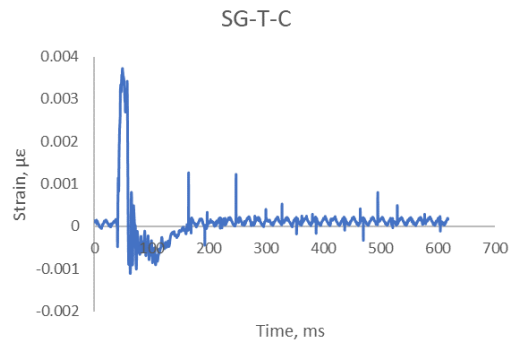
M-T	**M-C**
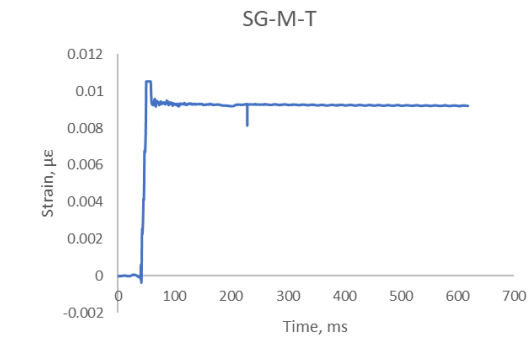	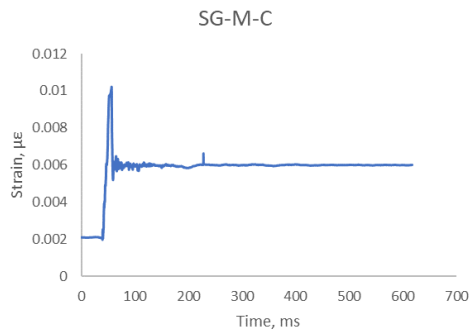
B-T	**B-C**
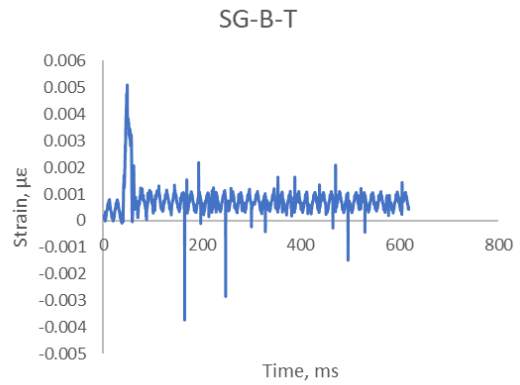	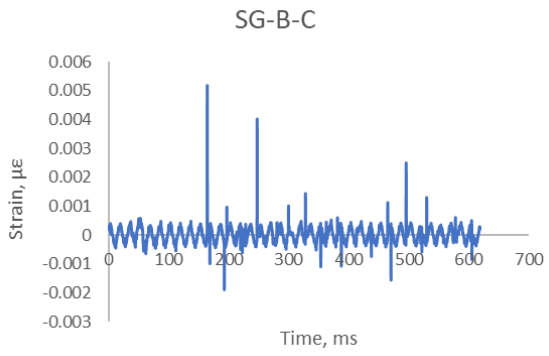

A.8. M-8F

A.8.1 Shot 1

T-T	T-C
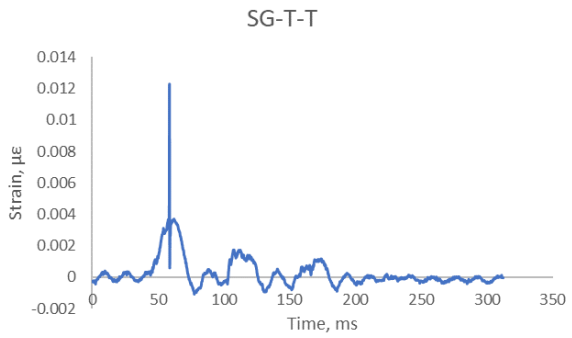	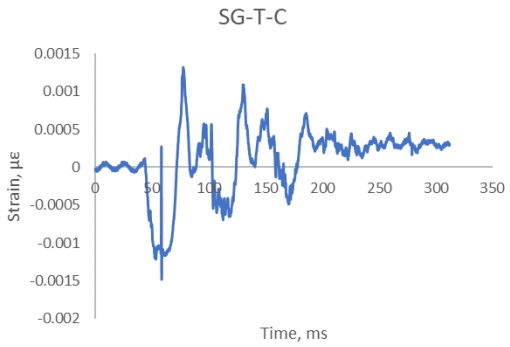
M-T	**M-C**
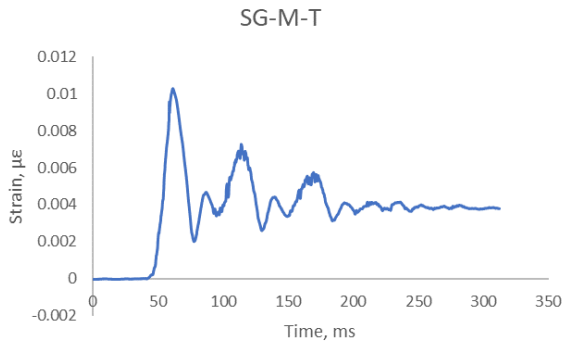	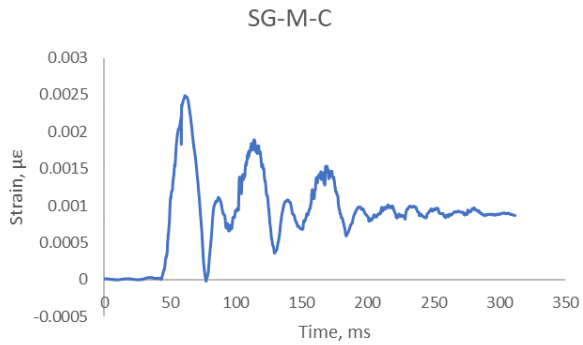
B-T	**B-C**
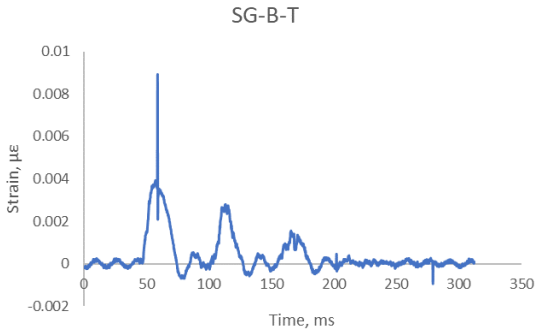	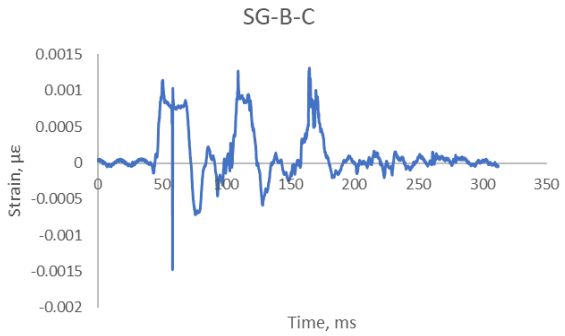

A.8.2 Shot 2

T-T	T-C
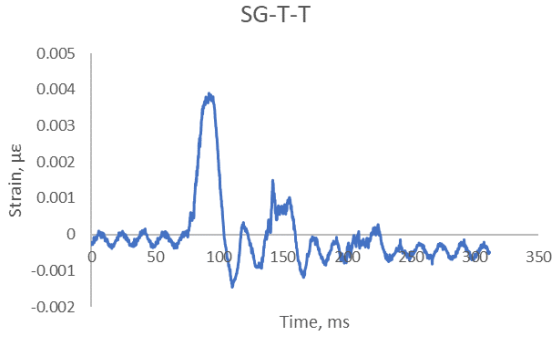	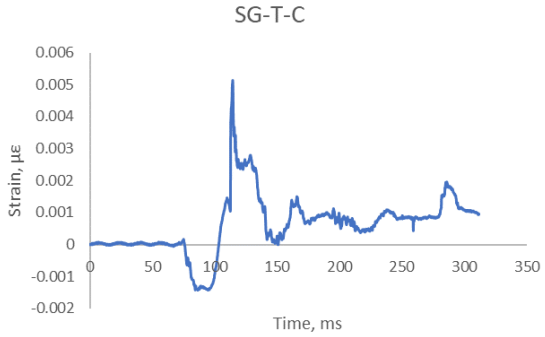
M-T	**M-C**
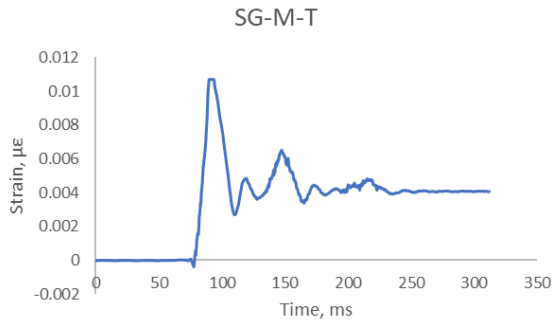	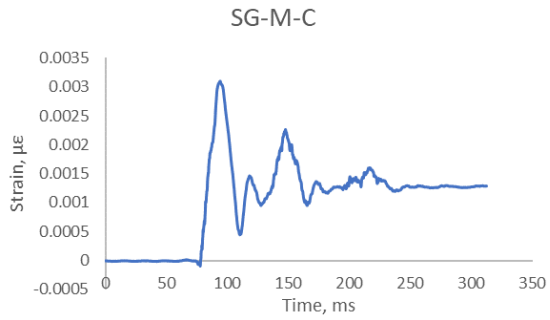
B-T	**B-C**
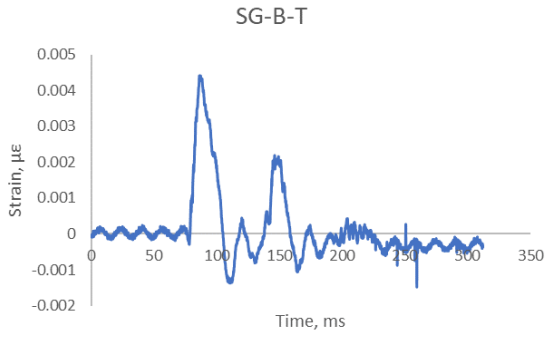	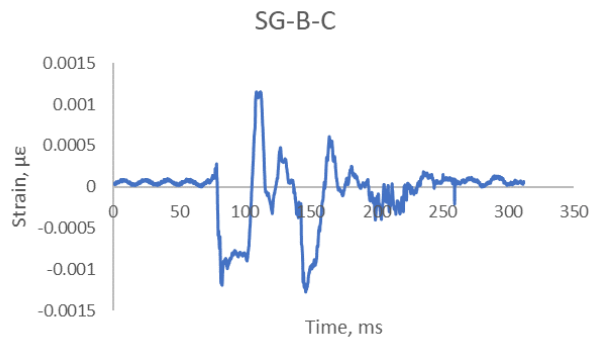

A.8.3 Shot 3

T-T	T-C
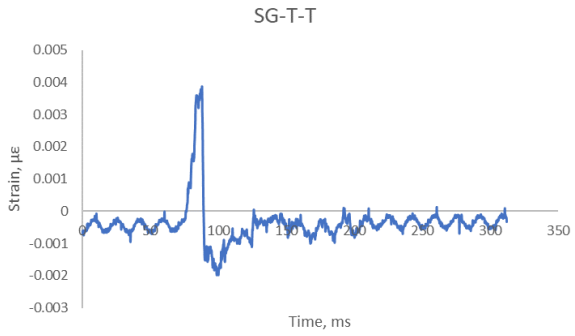	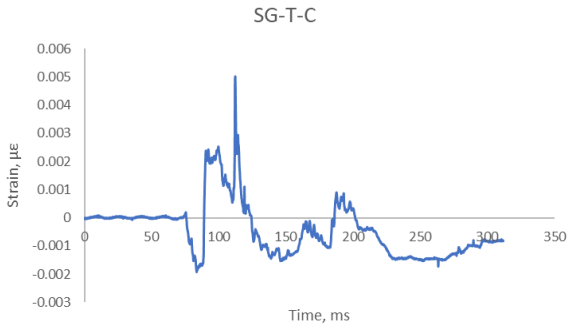
M-T	**M-C**
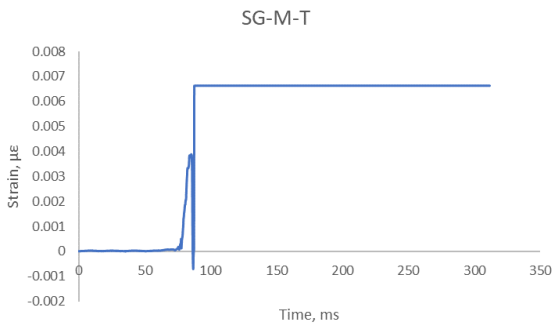	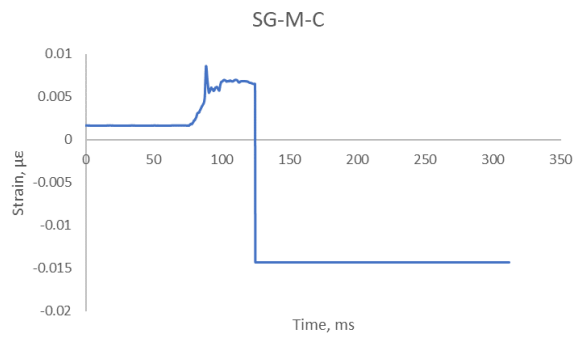
B-T	**B-C**
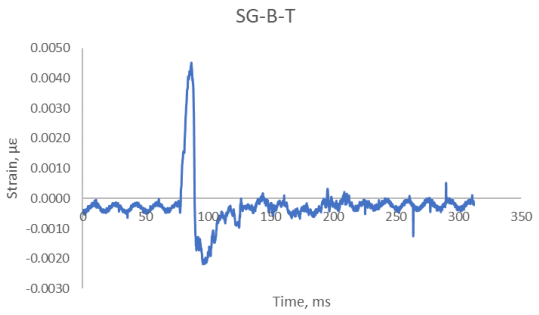	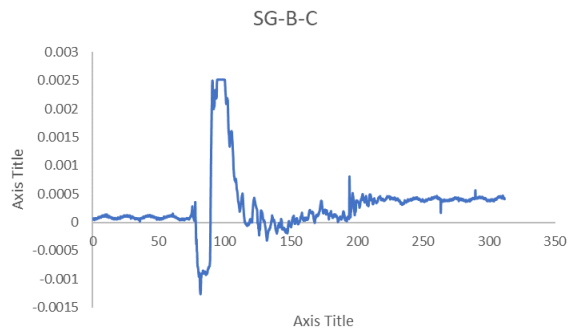

A.9. M-9FH

A.9.1 Shot 1

T-T

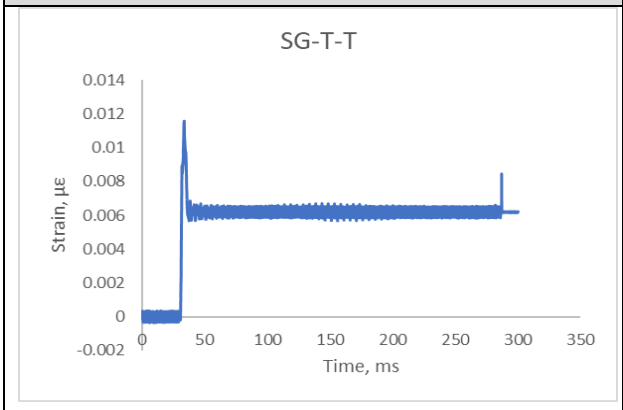

T-C

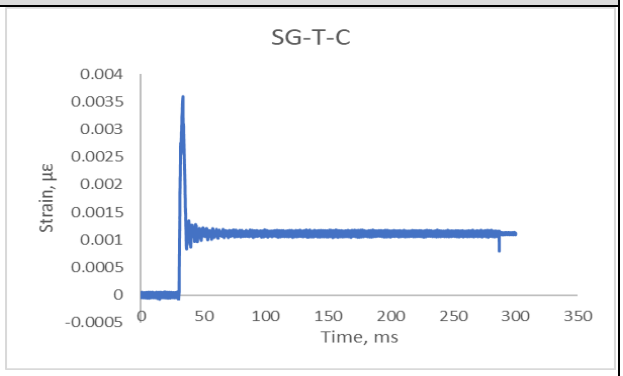

M-T

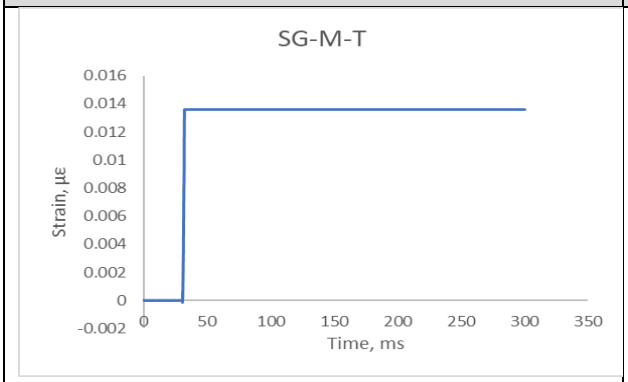

M-C

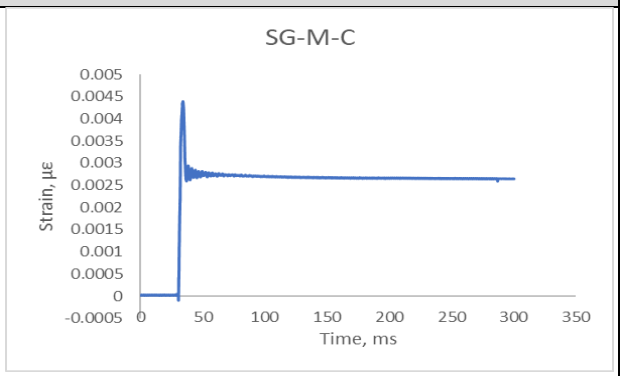

B-T

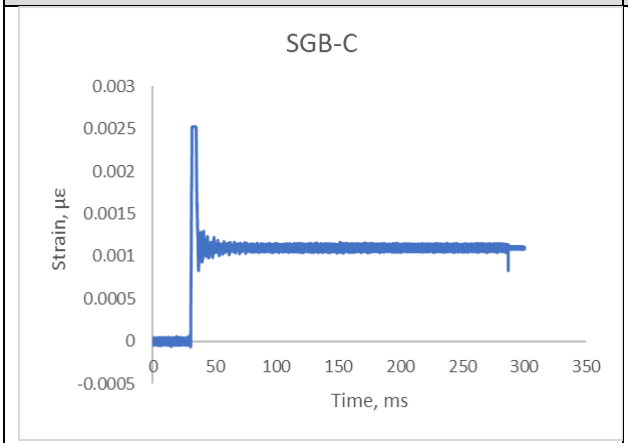

B-C

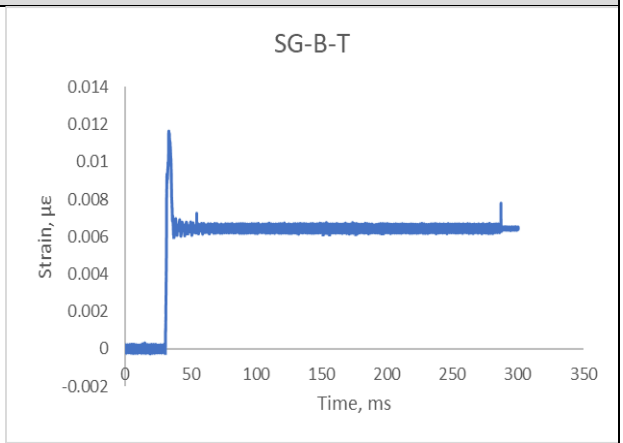

A.9.2 Shot 2

T-T	T-C
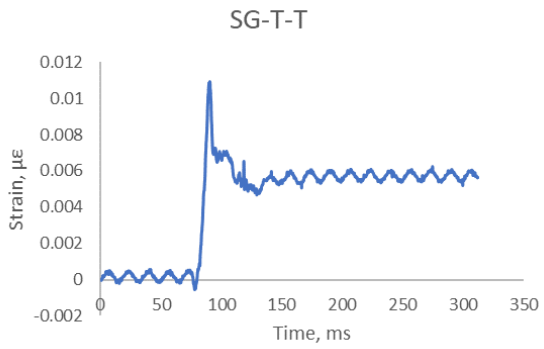	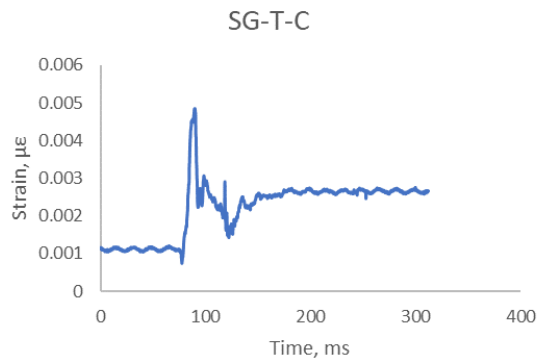
M-T	**M-C**
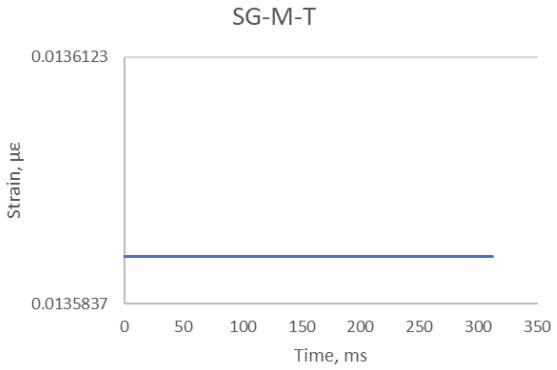	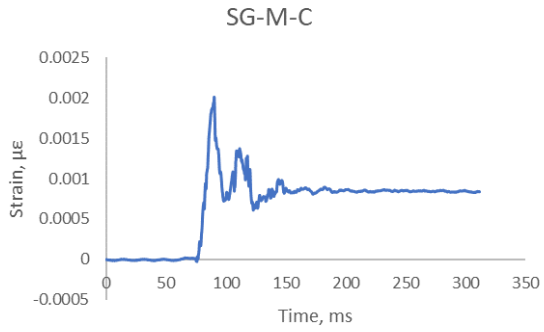
B-T	**B-C**
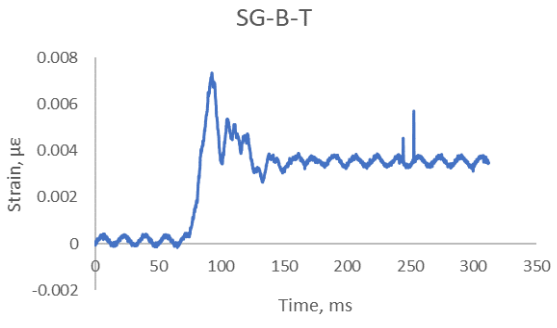	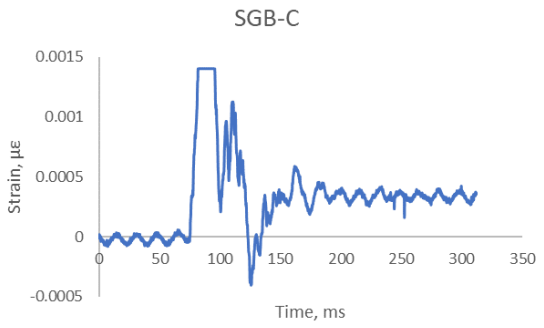

A.10. M-10FH

A.10.1 Shot 1

T-T	T-C
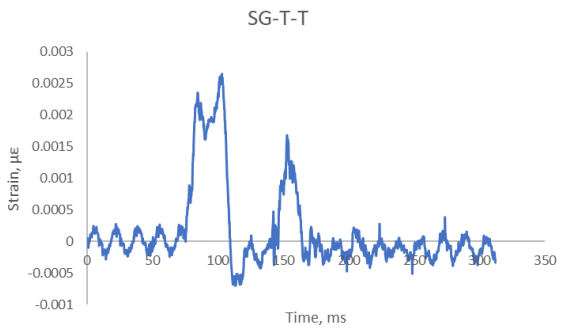	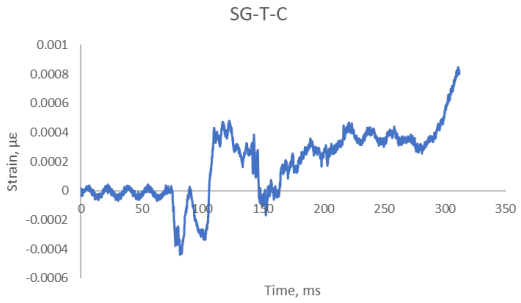
M-T	**M-C**
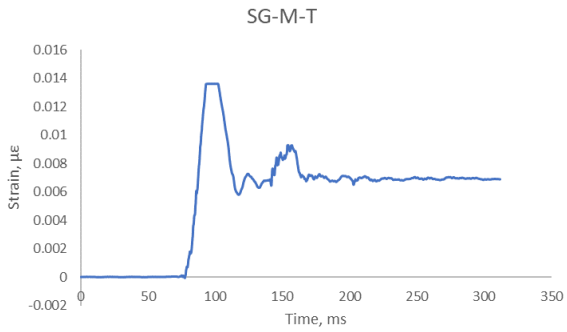	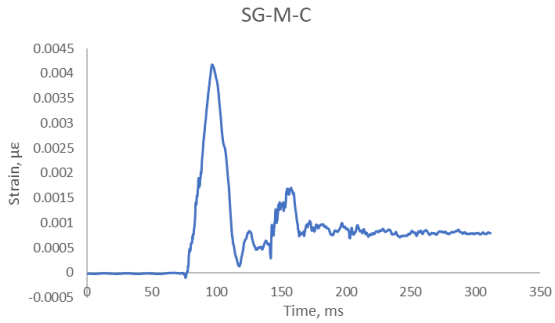
B-T	**B-C**
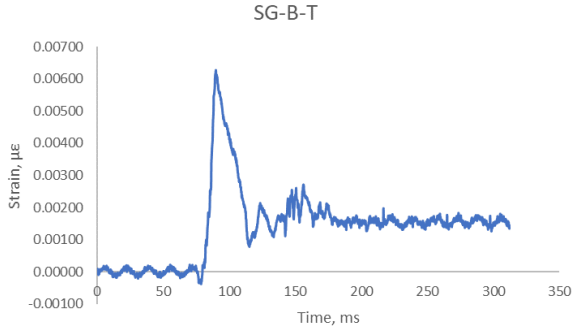	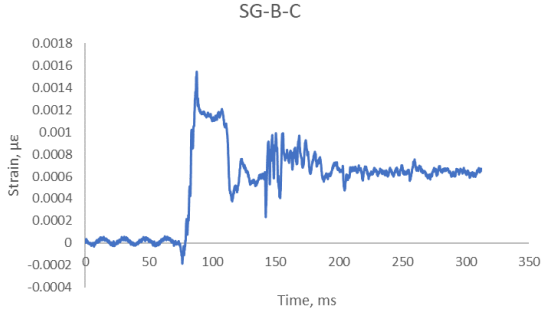

A.10.2 Shot 2

T-T	T-C
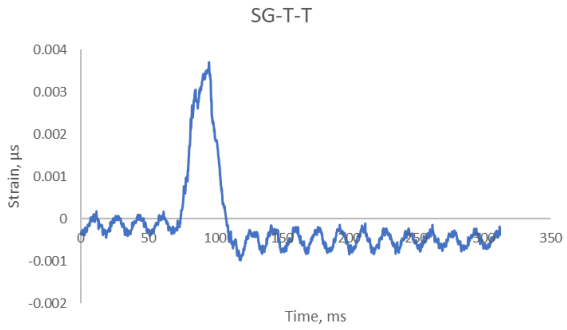	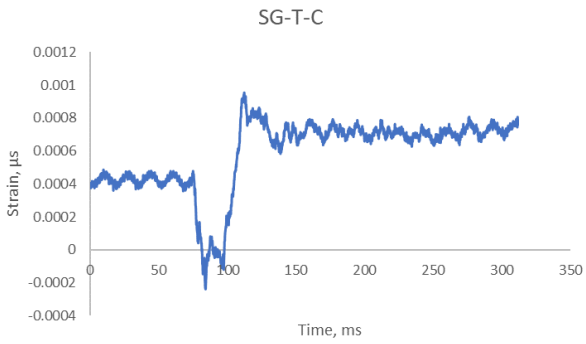
M-T	**M-C**
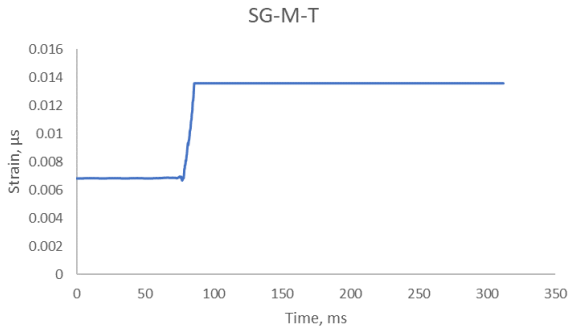	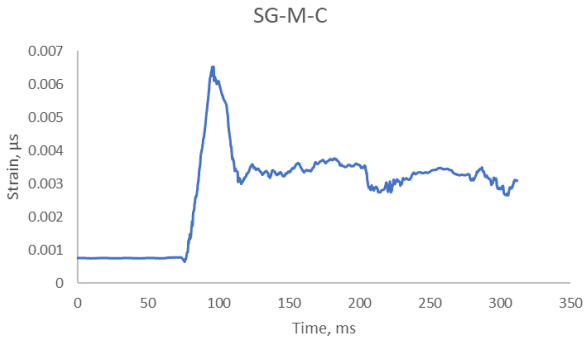
B-T	**B-C**
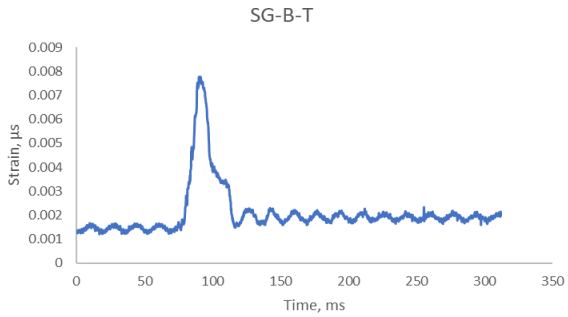	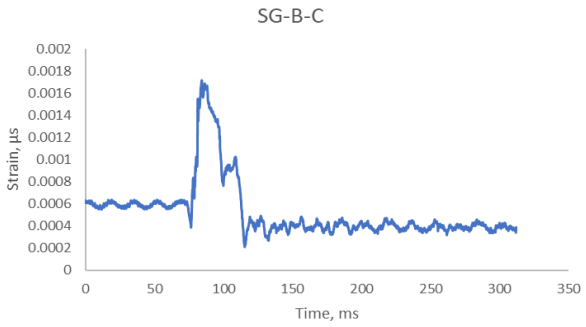

A.10.3 Shot 3

T-T	T-C
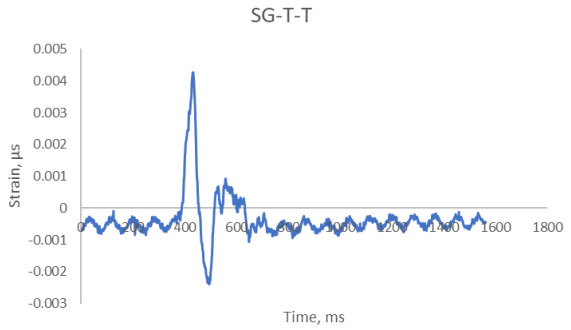	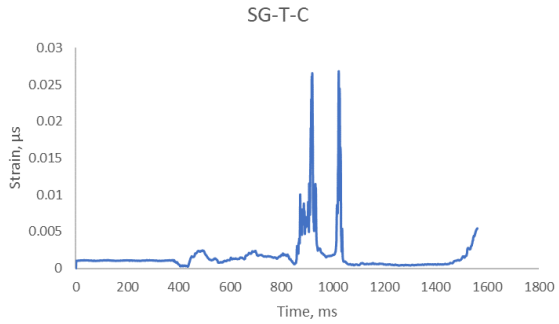
M-T	**M-C**
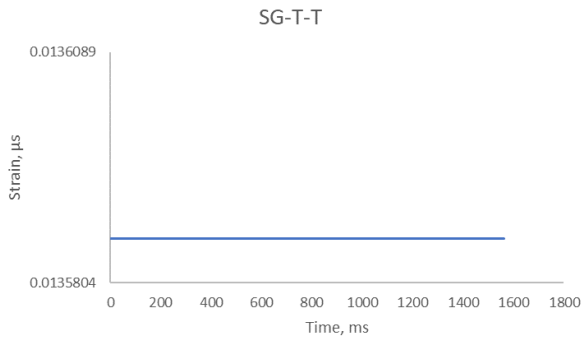	
B-T	**B-C**
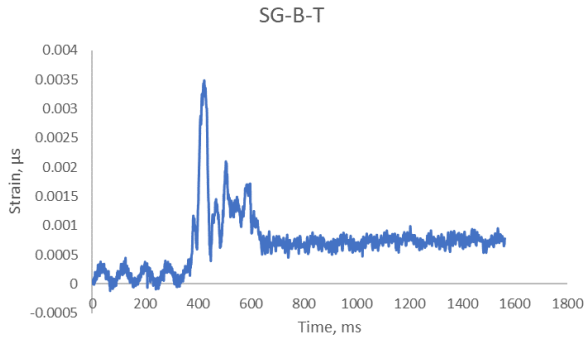	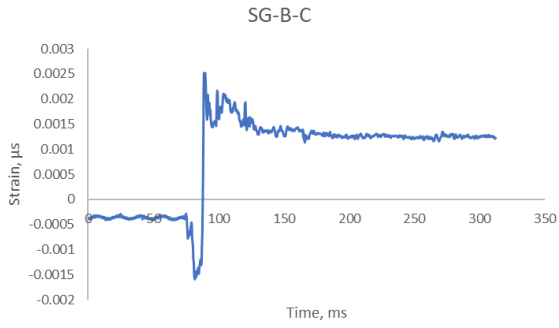

A.11. M-11FH

A.11.1 Shot 1

T-T	T-C
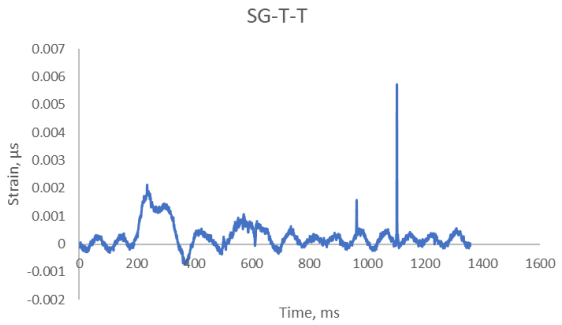	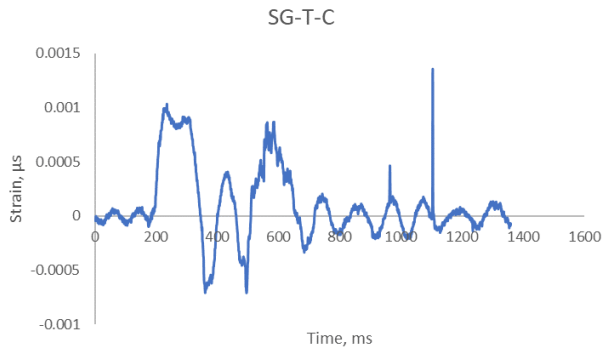
M-T	**M-C**
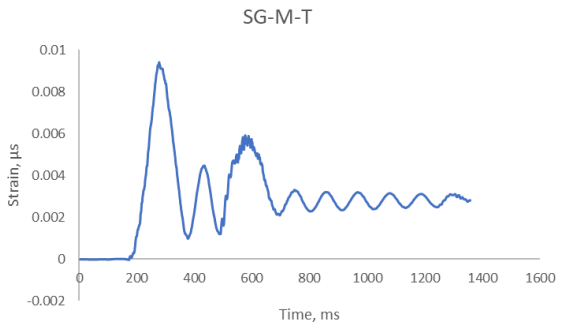	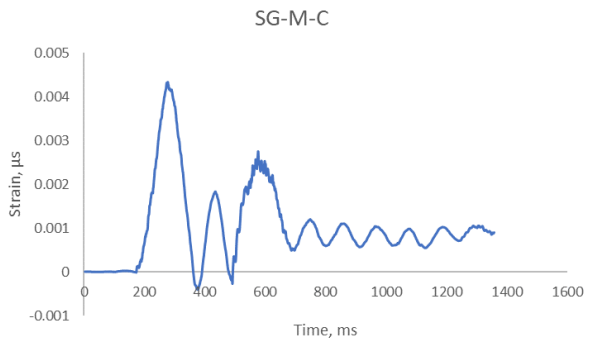
B-T	**B-C**
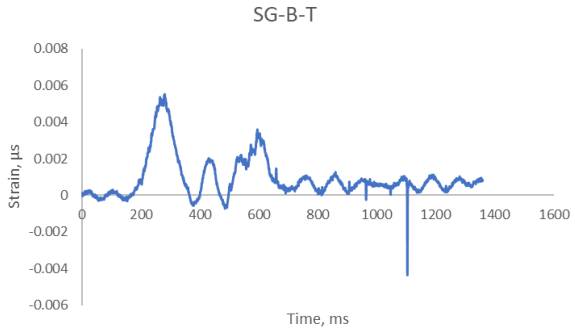	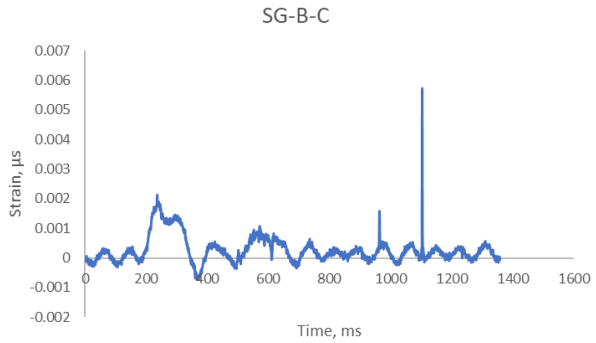

A.11.2 Shot 2

T-T	T-C
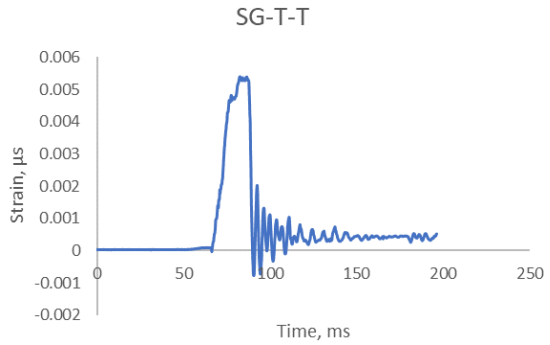	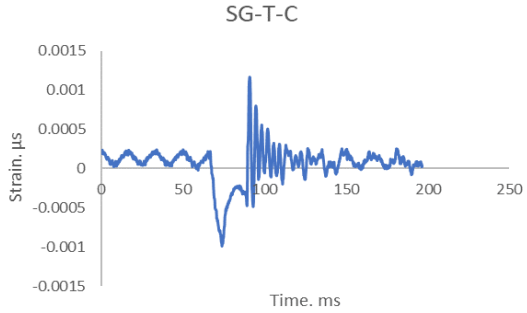
M-T	**M-C**
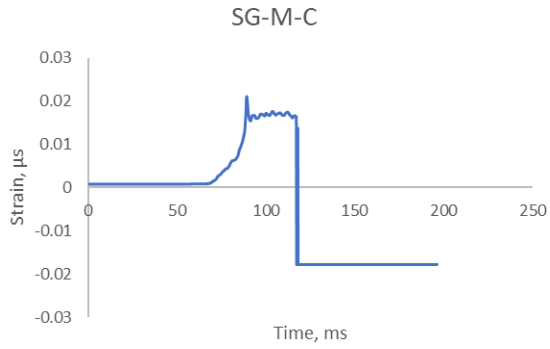	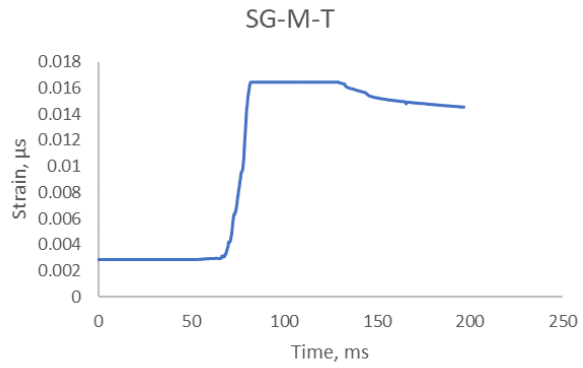
B-T	**B-C**
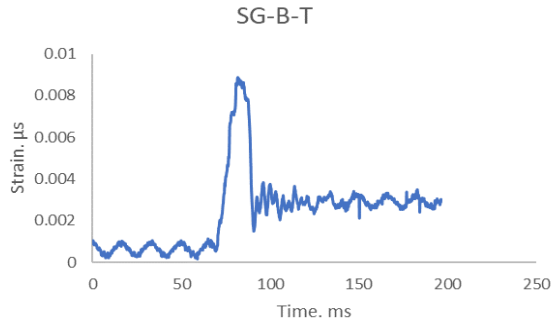	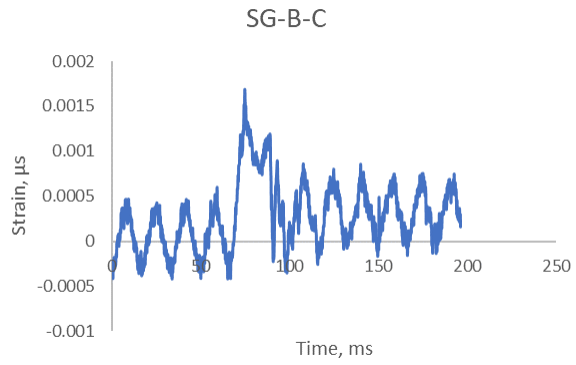

A.12. M-12FH

A.12.1 Shot 1

T-T	T-C
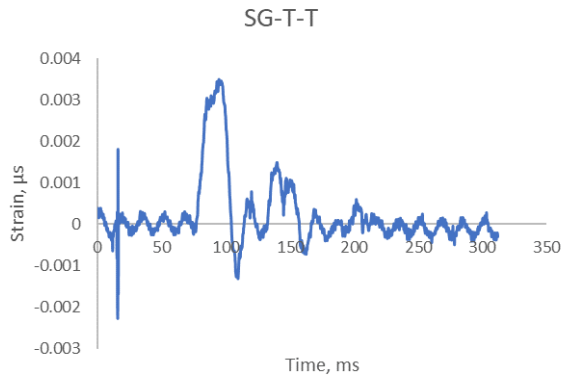	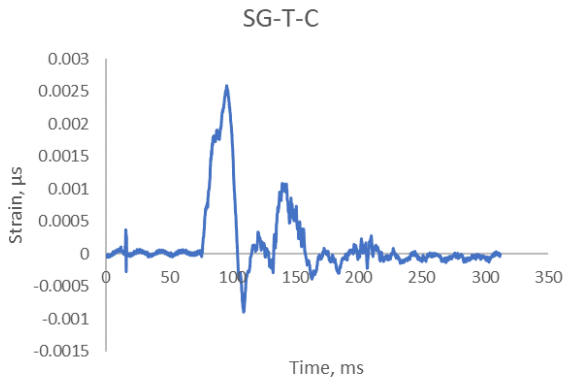
M-T	**M-C**
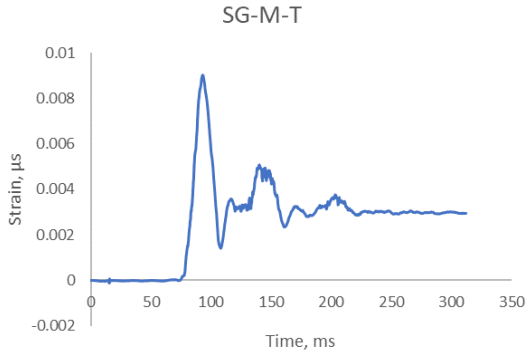	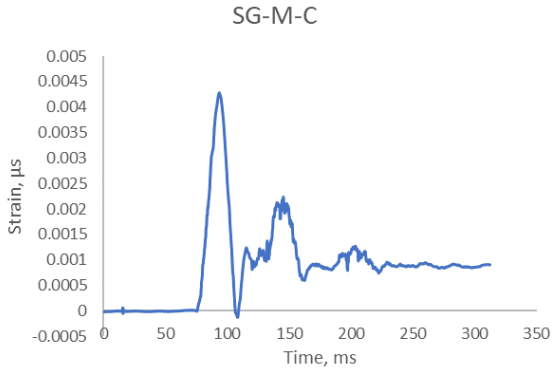
B-T	**B-C**
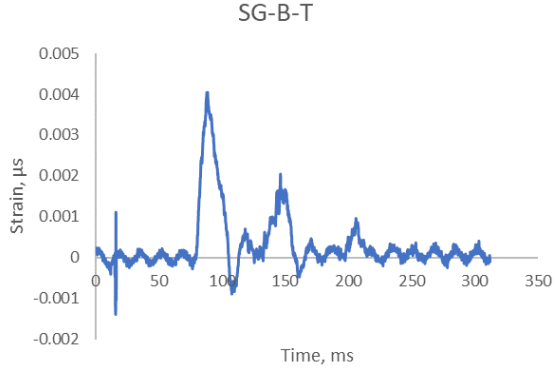	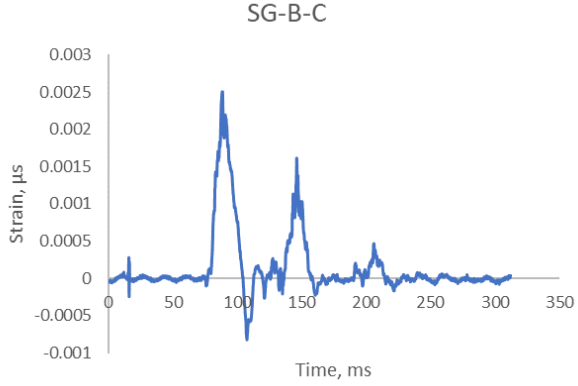

A.12.2 Shot 2

T-T

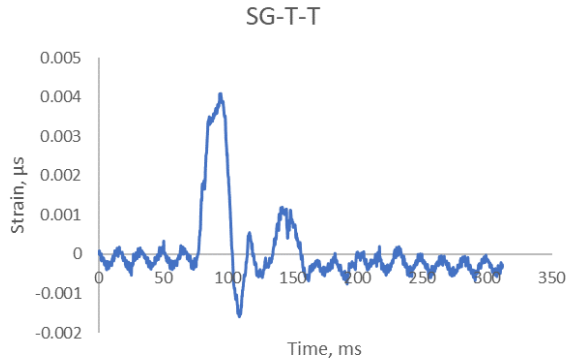

T-C

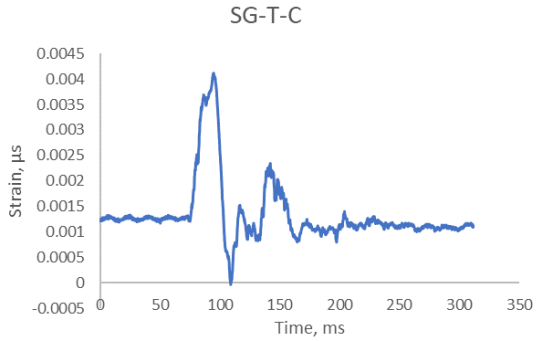

M-T

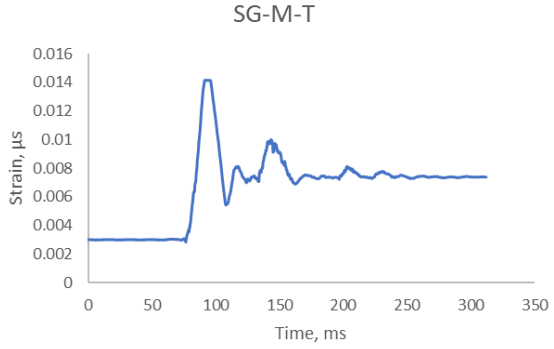

M-C

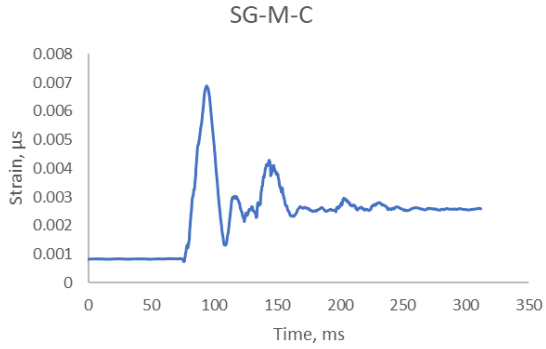

B-T

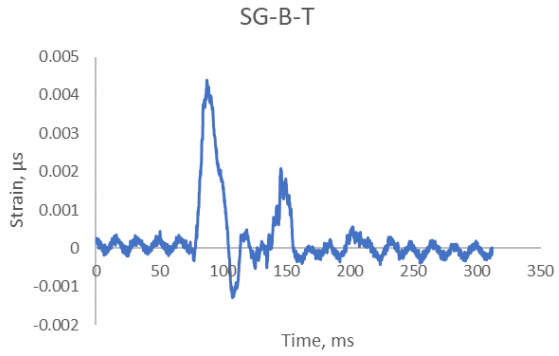

B-C

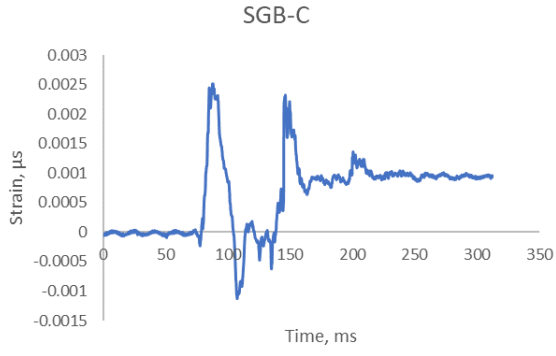

A.12.3 Shot 3

T-T	T-C
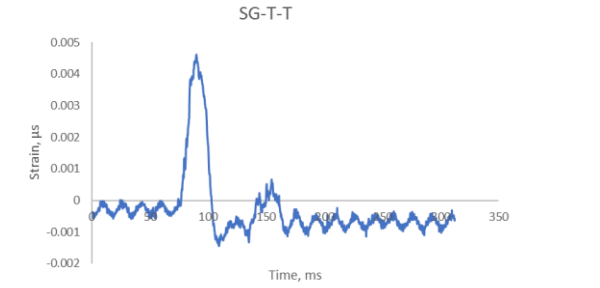	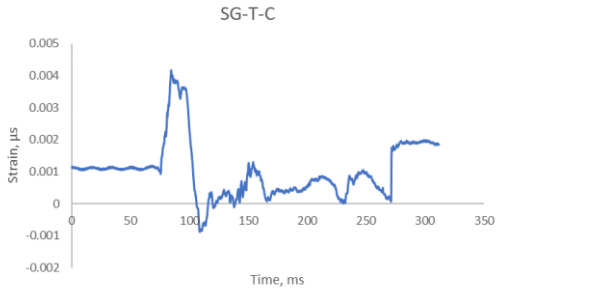
M-T	**M-C**
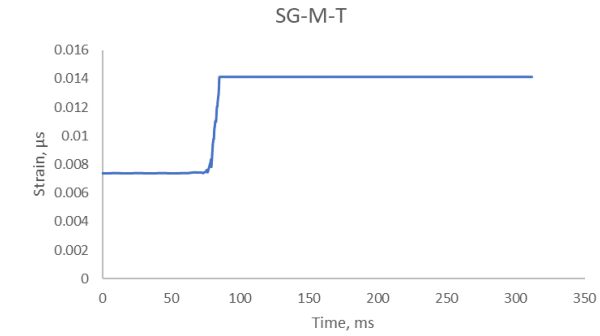	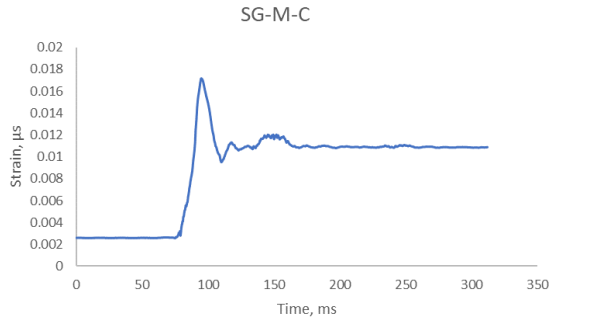
B-T	**B-C**
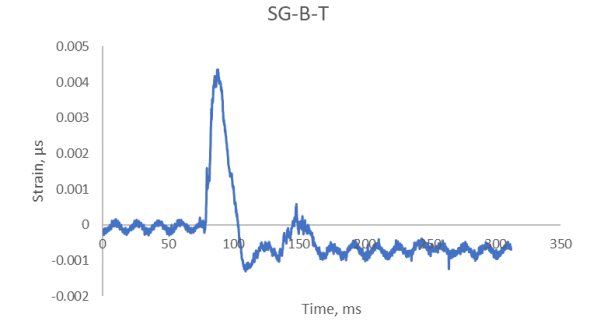	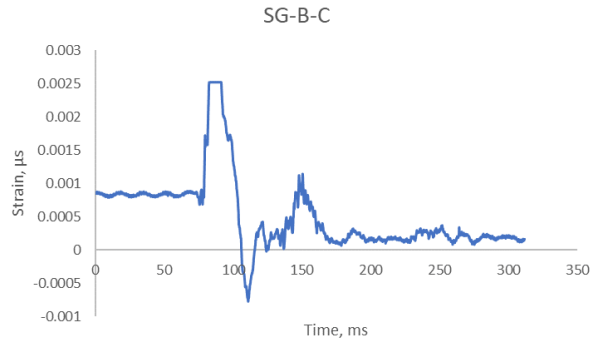

A.13. M-13FH

A.13.1 Shot 1

T-T	T-C
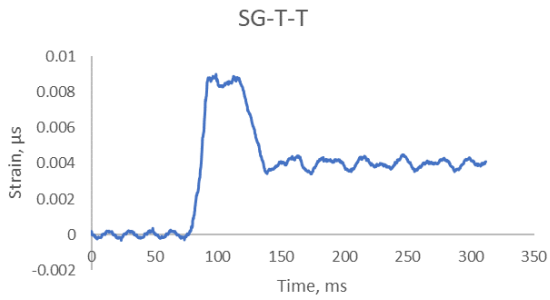	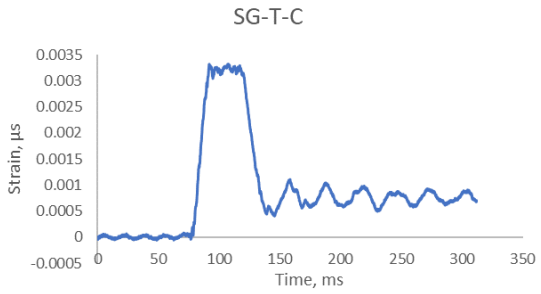
M-T	**M-C**
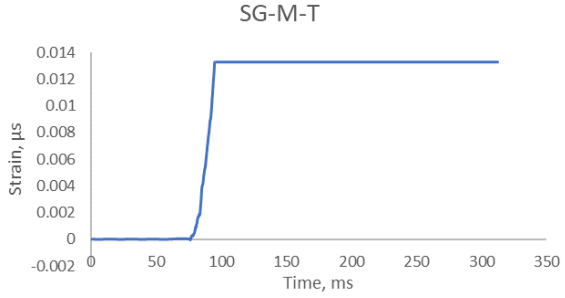	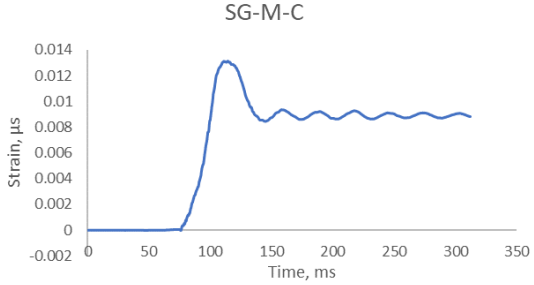
B-T	**B-C**
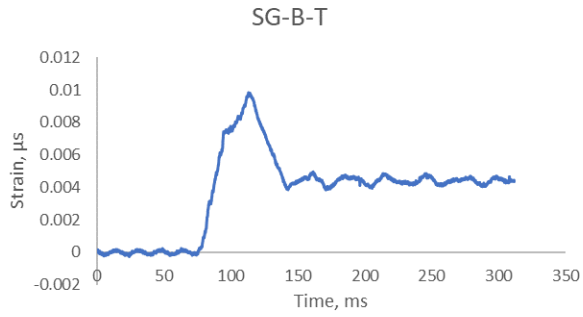	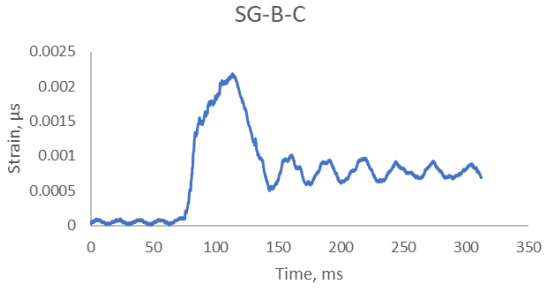

A.13.2 Shot 2

T-T	T-C
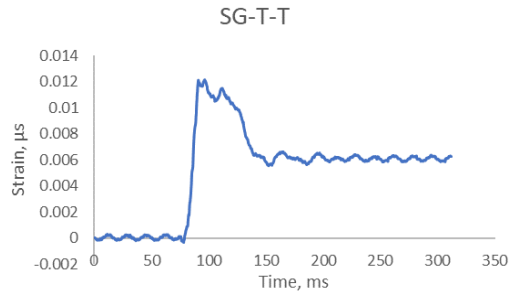	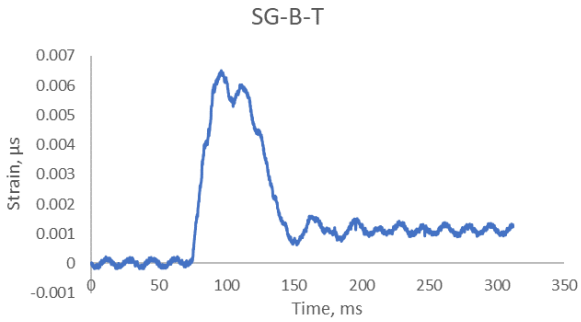
M-T	**M-C**
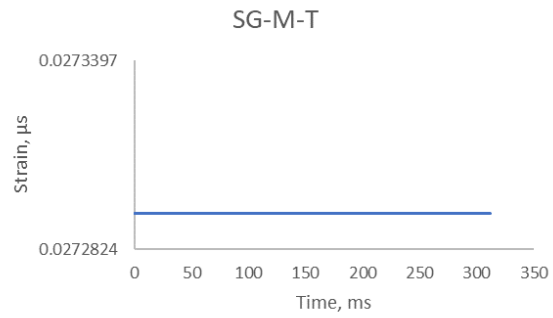	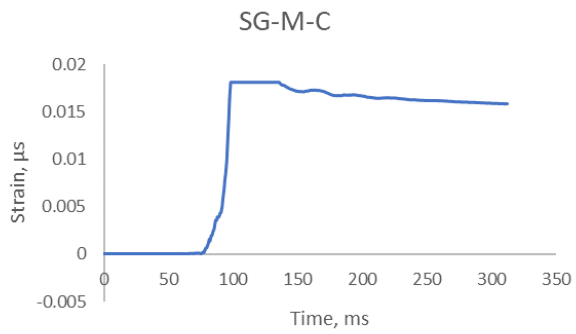
B-T	**B-C**
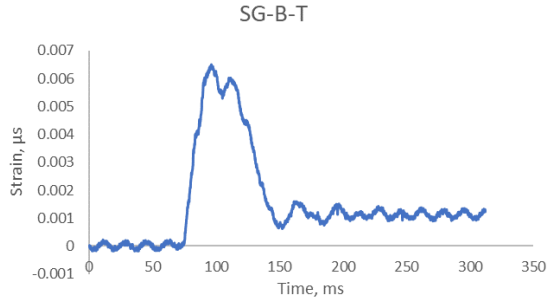	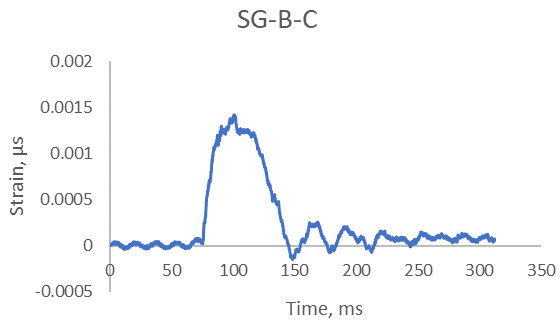

A.14. M-14FH

A.14.1 Shot 1

T-T	T-C
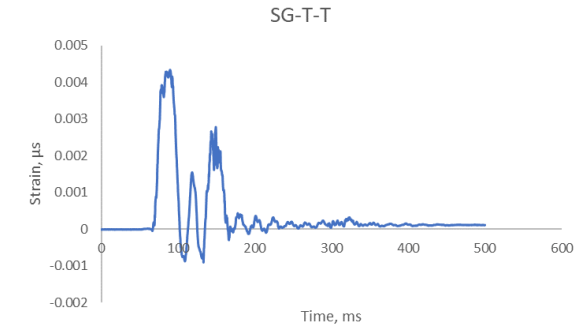	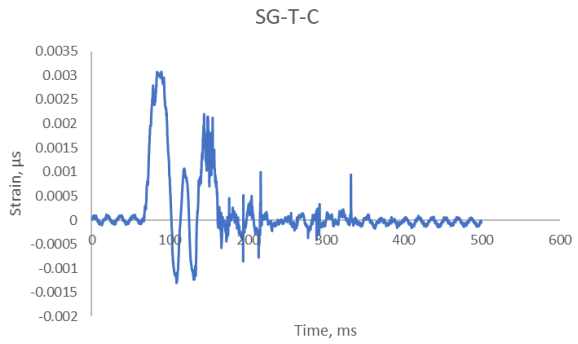
M-T	**M-C**
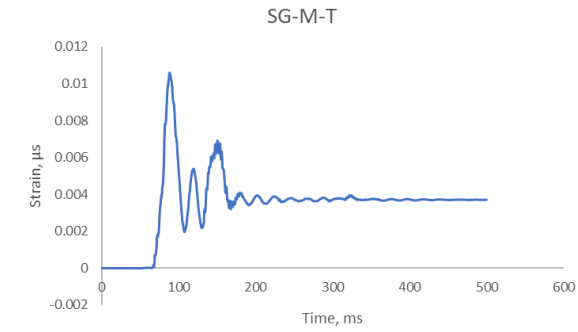	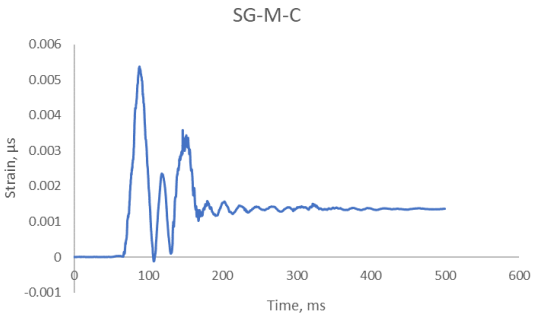
B-T	**B-C**
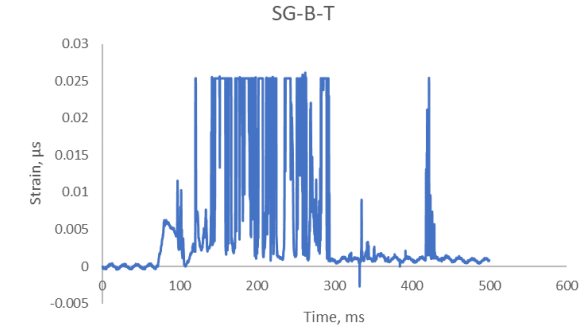	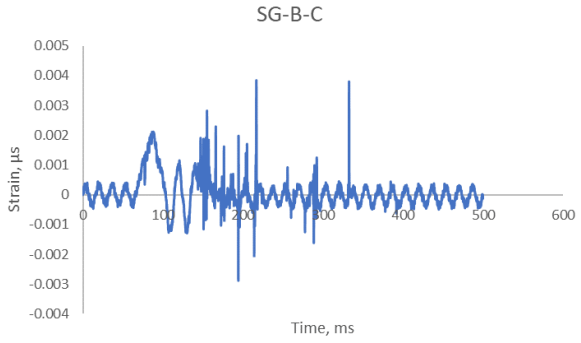

A.14.2 Shot 2

T-T	T-C
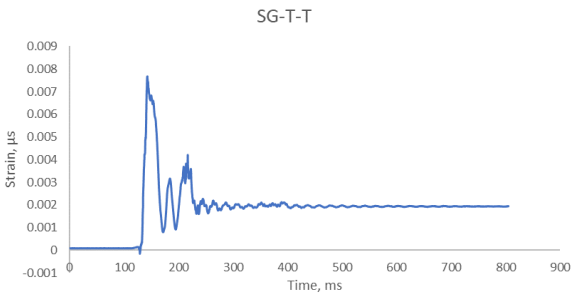	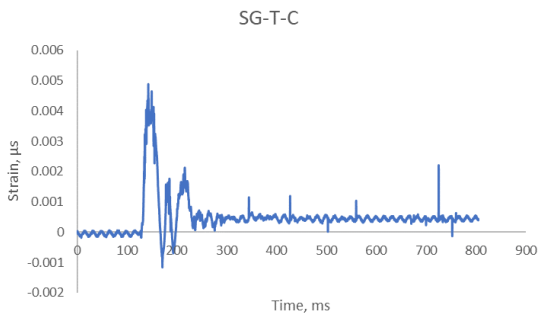
M-T	**M-C**
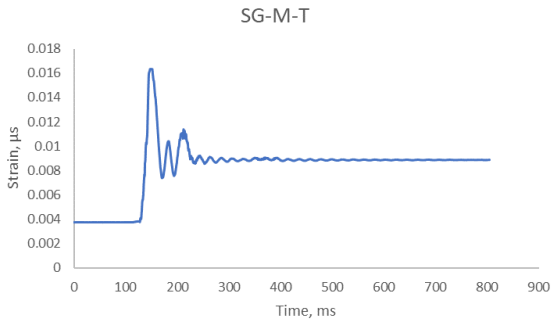	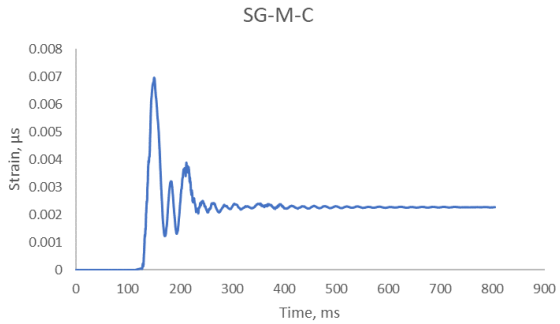
B-T	**B-C**
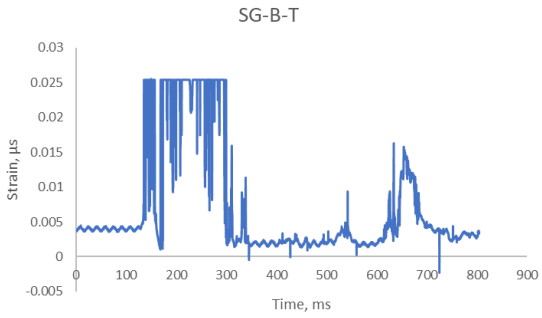	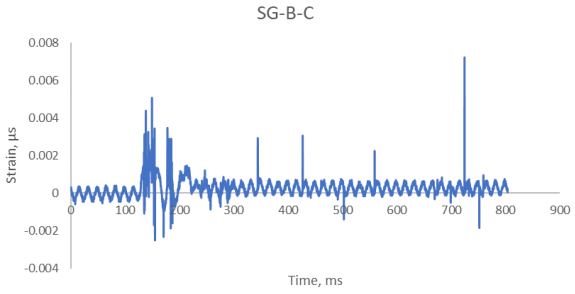

A.14.3 Shot 3

T-T	T-C
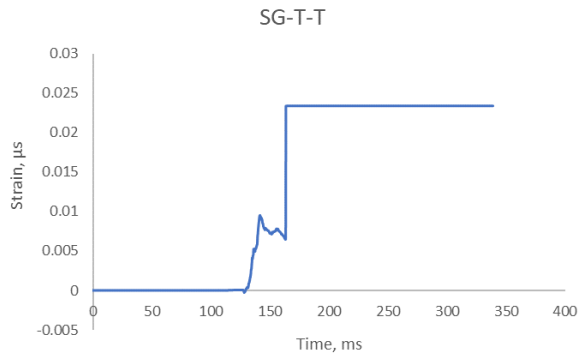	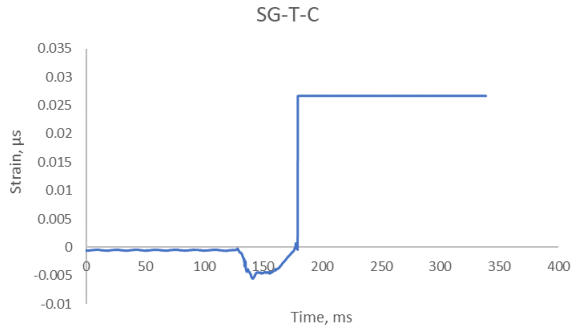
M-T	**M-C**
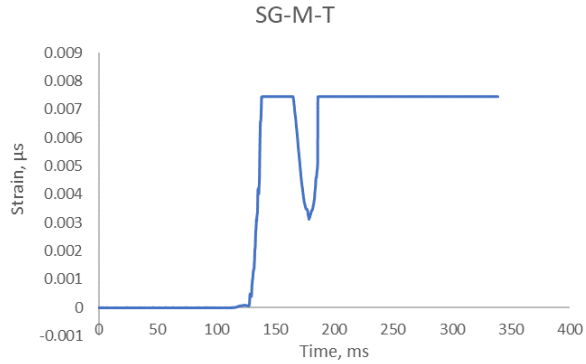	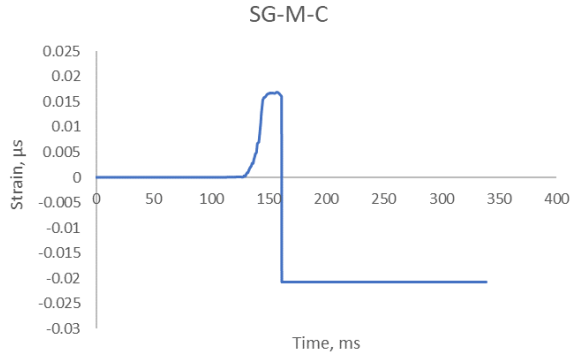
B-T	**B-C**
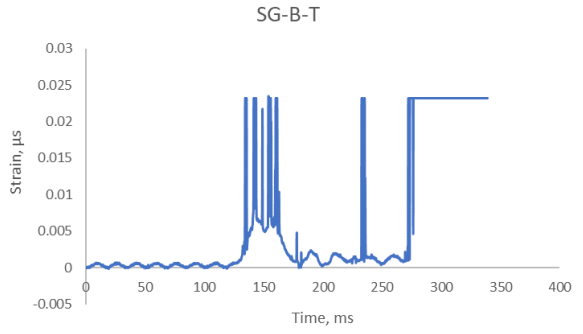	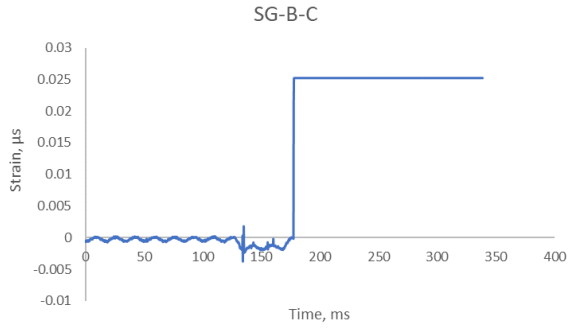

A.15. M-15FR

A.15.1 Shot 1

T-T	T-C
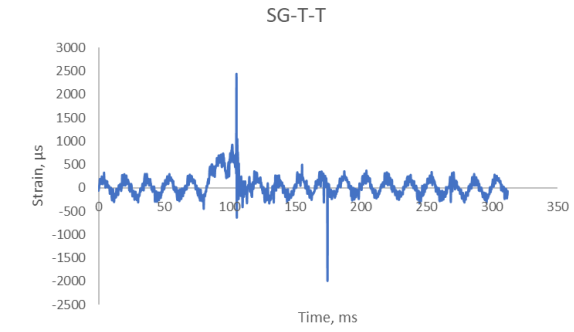	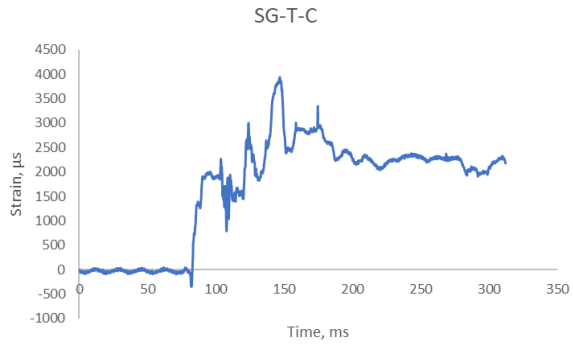
M-T	**M-C**
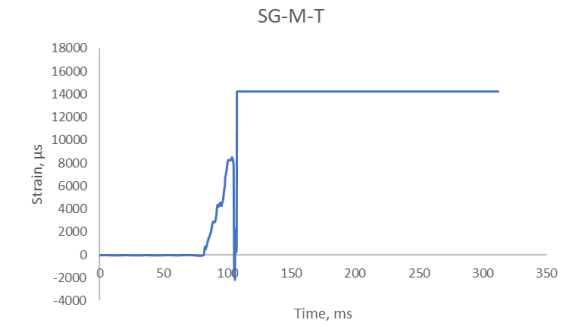	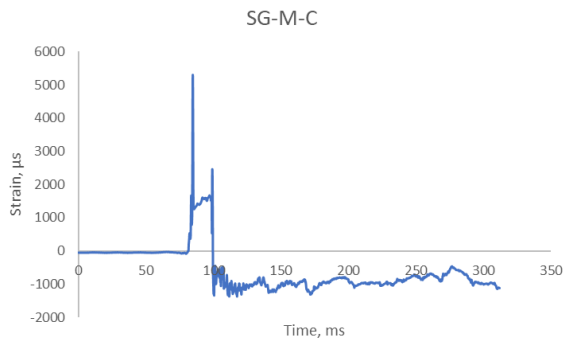
B-T	**B-C**
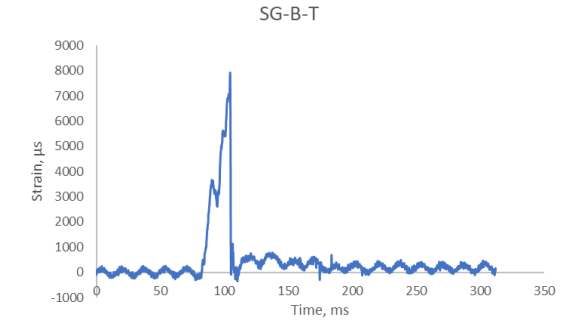	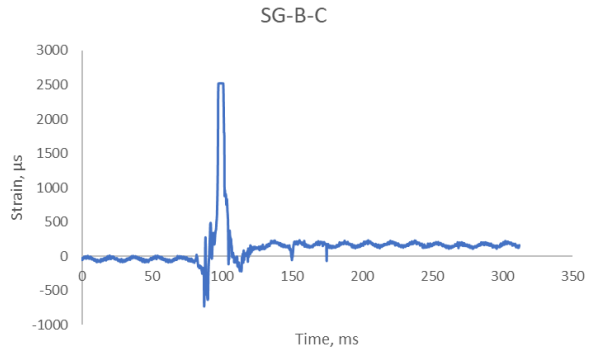

A.15.2 Shot 2

T-T	T-C
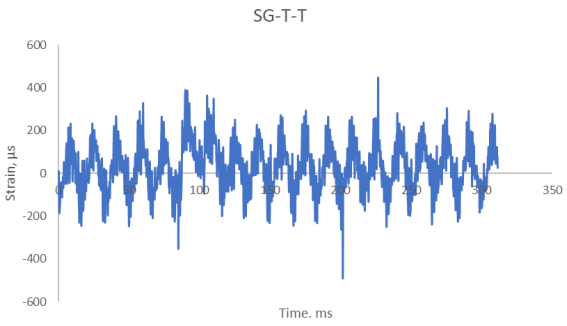	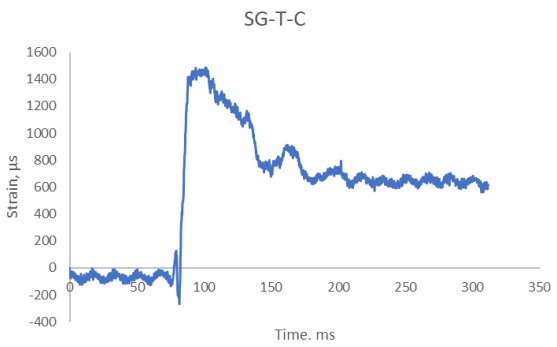
M-T	**M-C**
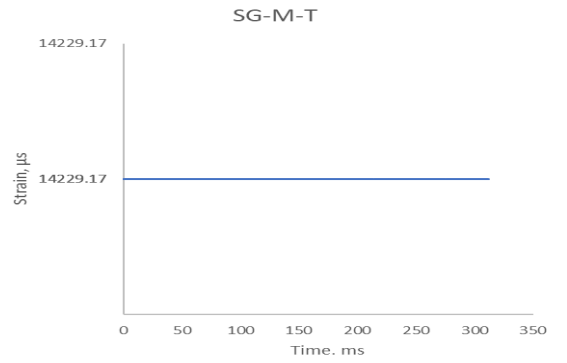	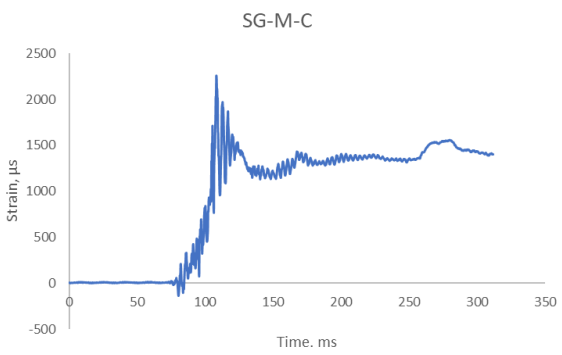
B-T	**B-C**
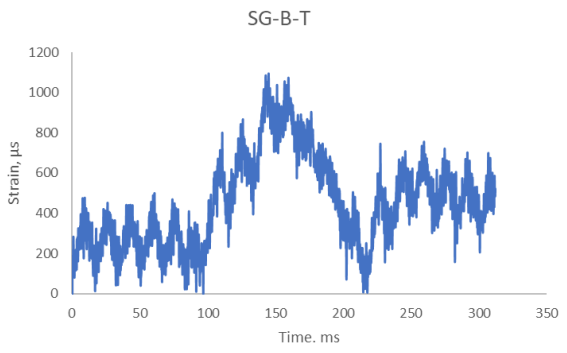	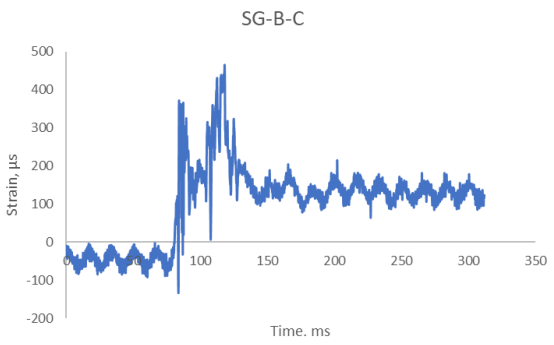

A.16. M-16FR

A.16.1 Shot 1

T-T

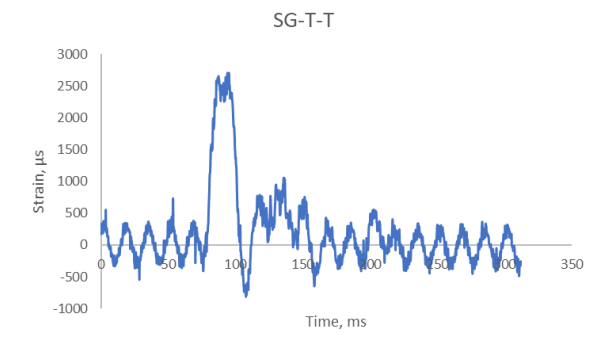

T-C

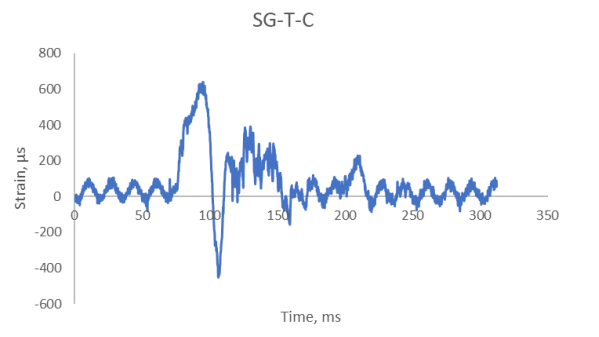

M-T

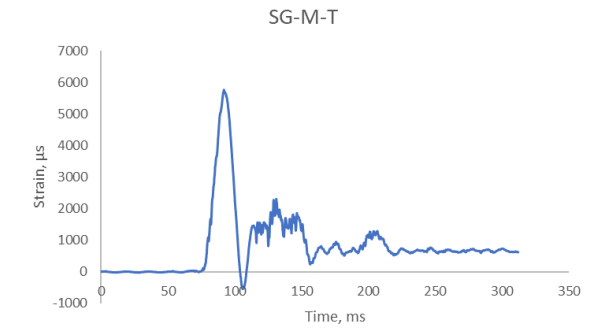

M-C

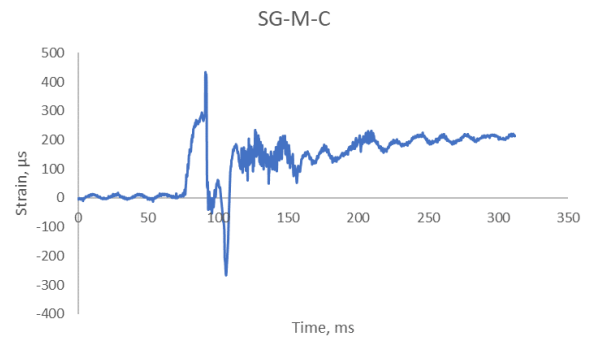

B-T

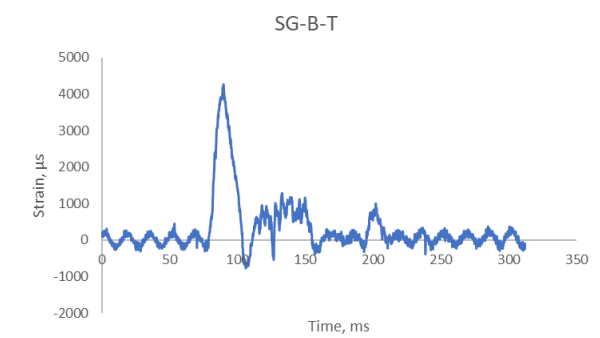

B-C

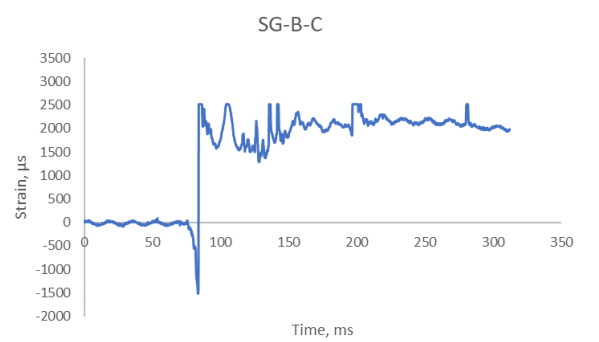

16.2 Shot 2

T-T	T-C
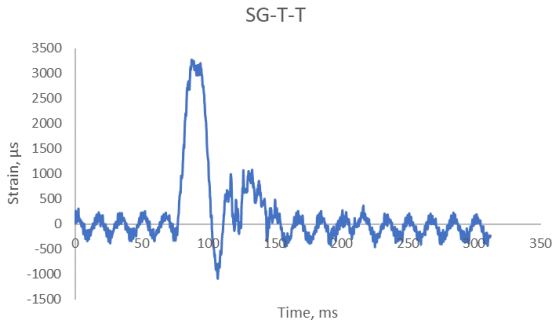	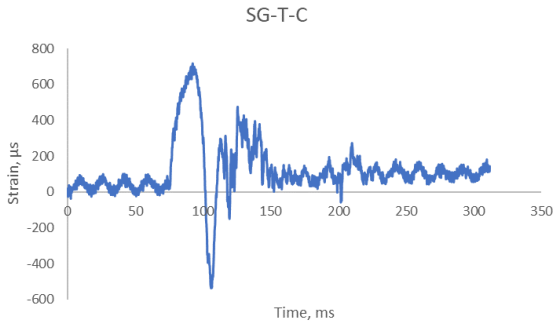
M-T	**M-C**
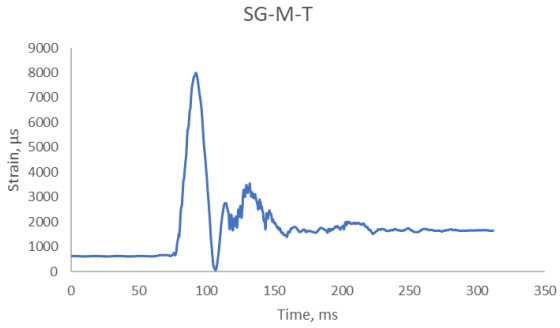	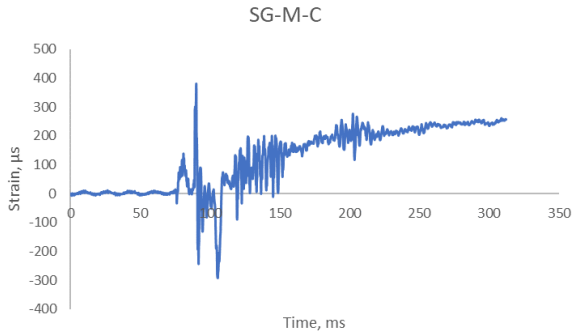
B-T	**B-C**
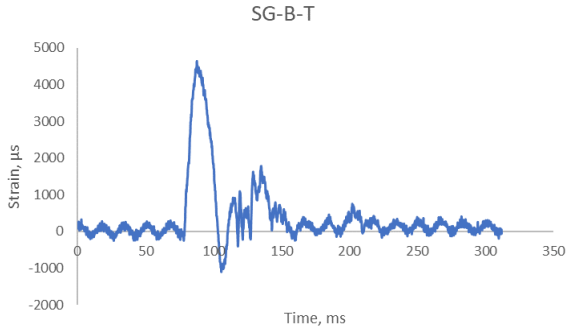	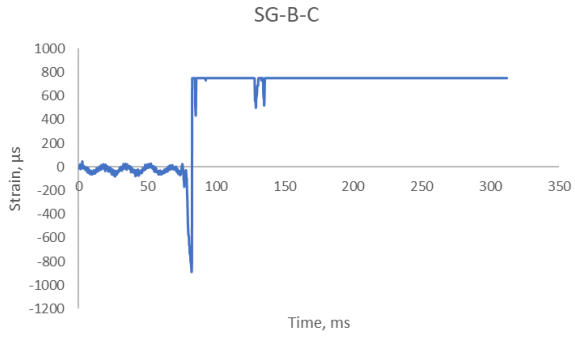

Appendix B. RC- Blast

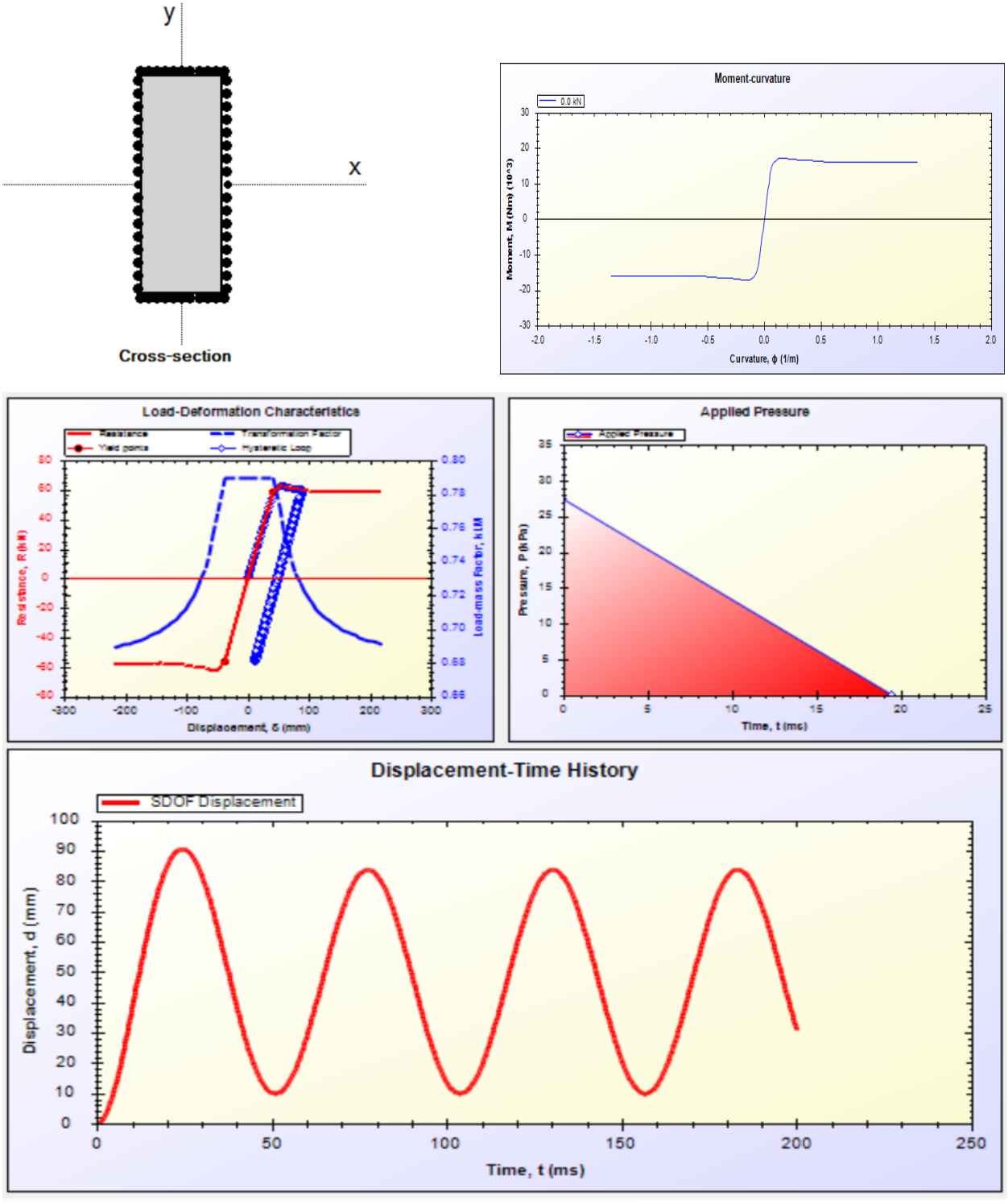

B 1: SDOF for specimen M-1F – Blast 1

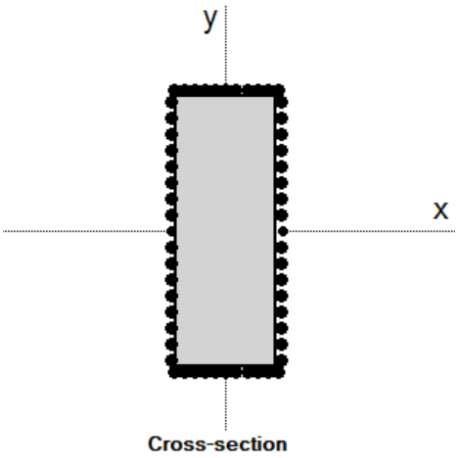

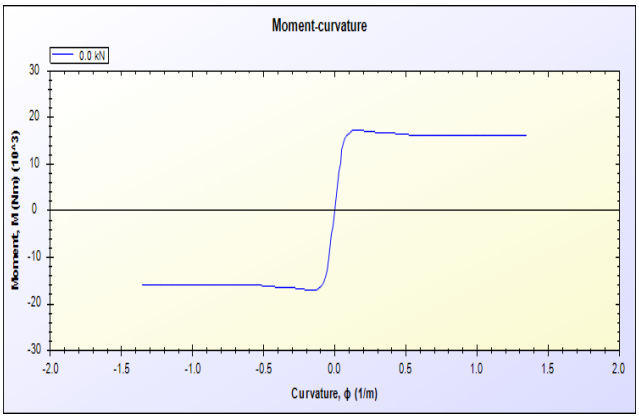

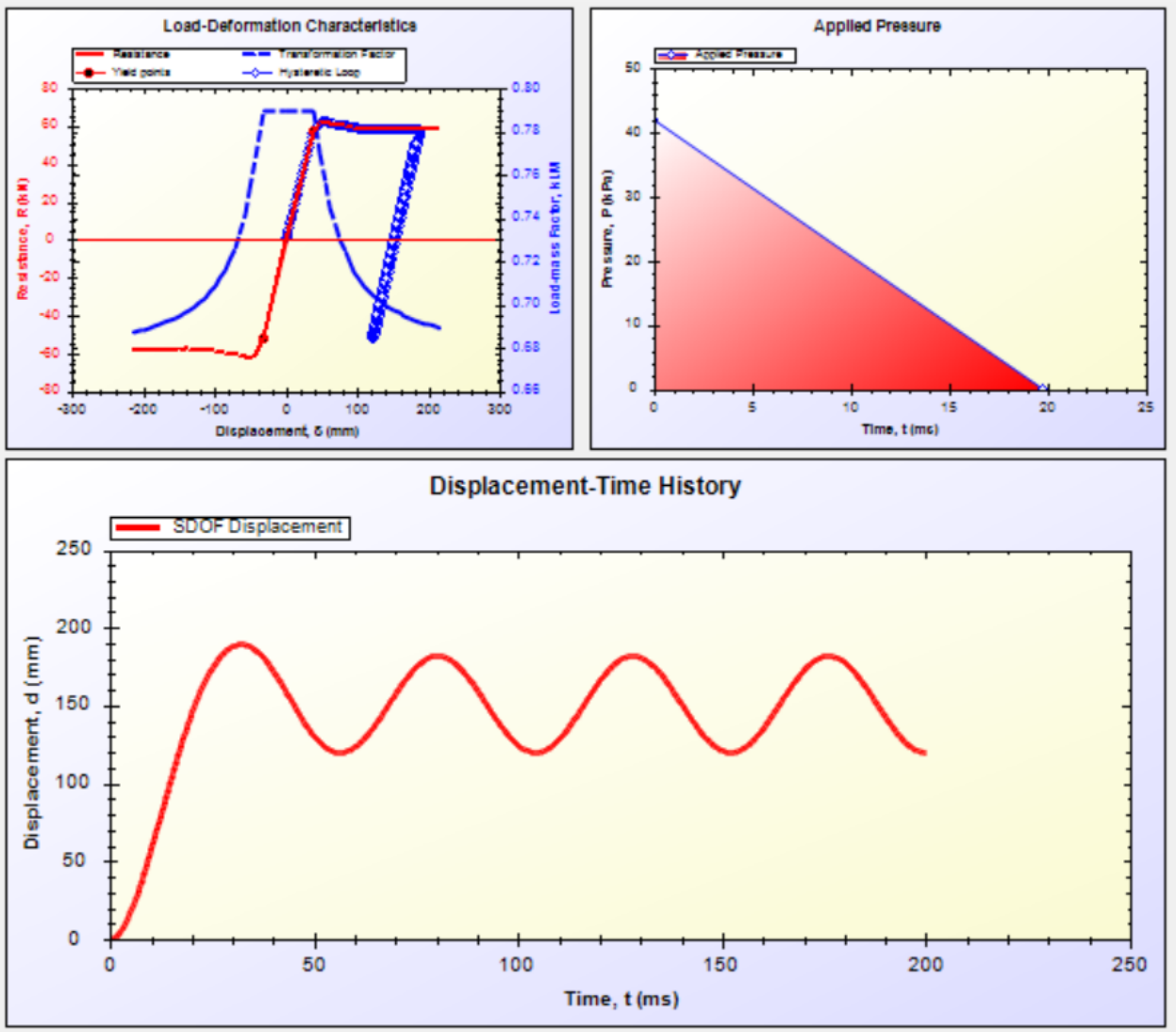

B 2: SDOF for specimen M-1F – Blast 2

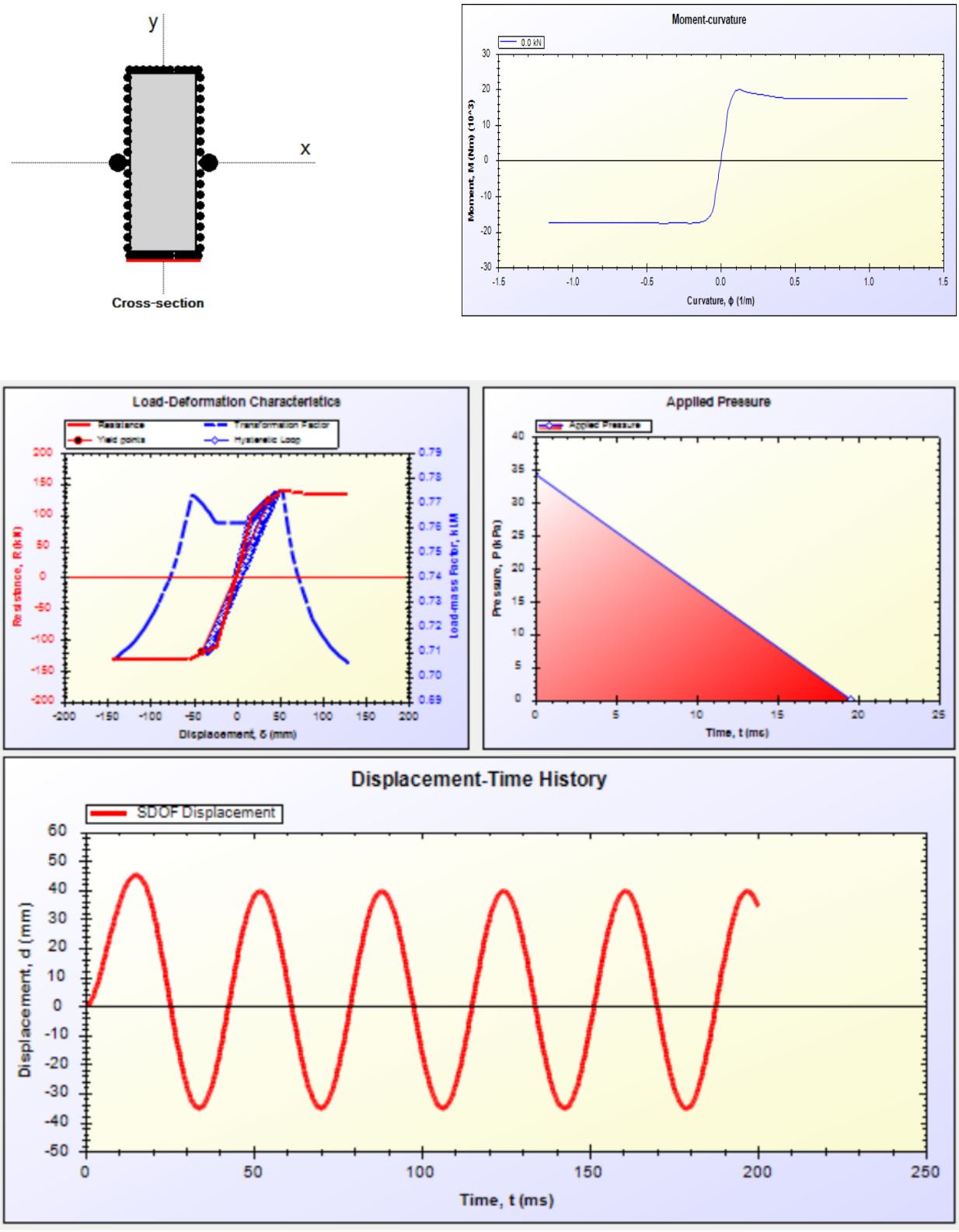

B 3: SDOF for specimen M-2FH – Blast 1

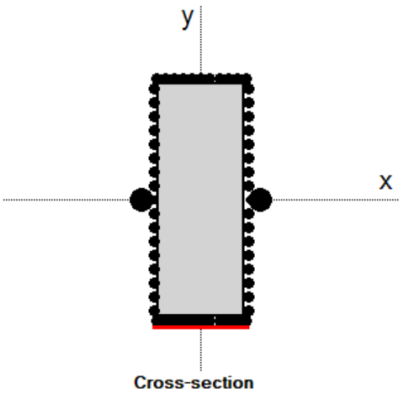

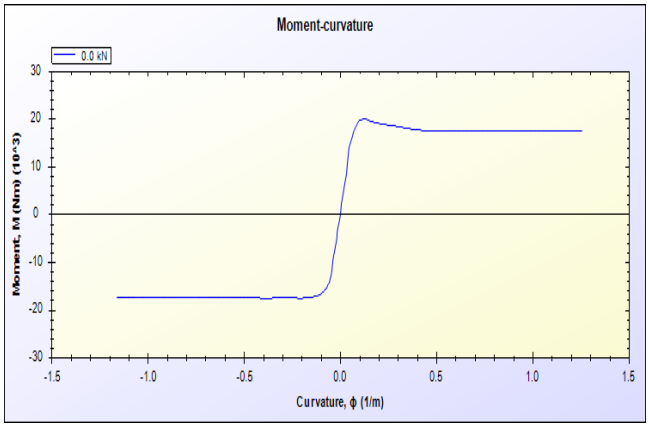

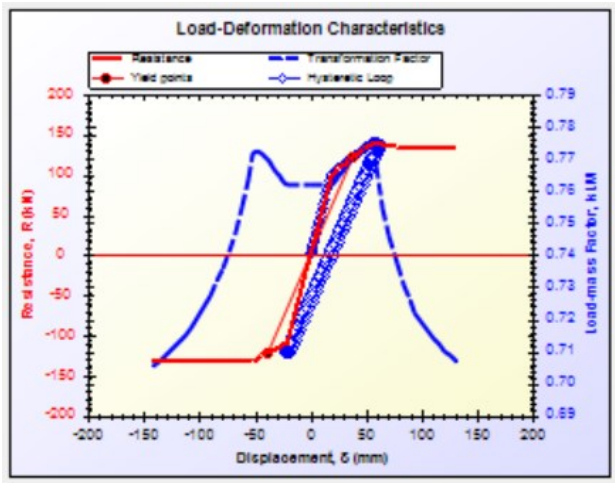

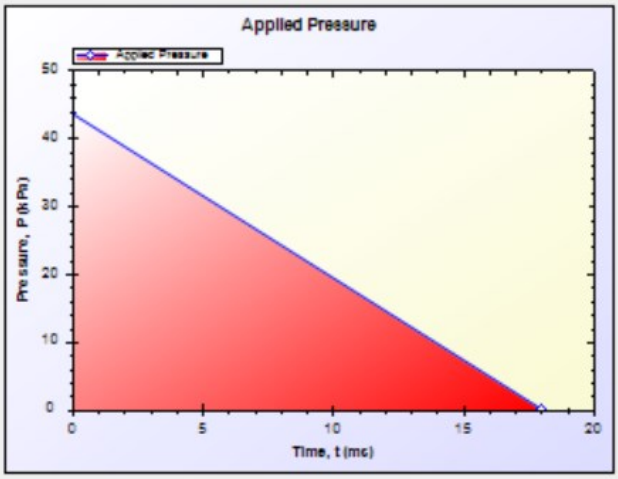

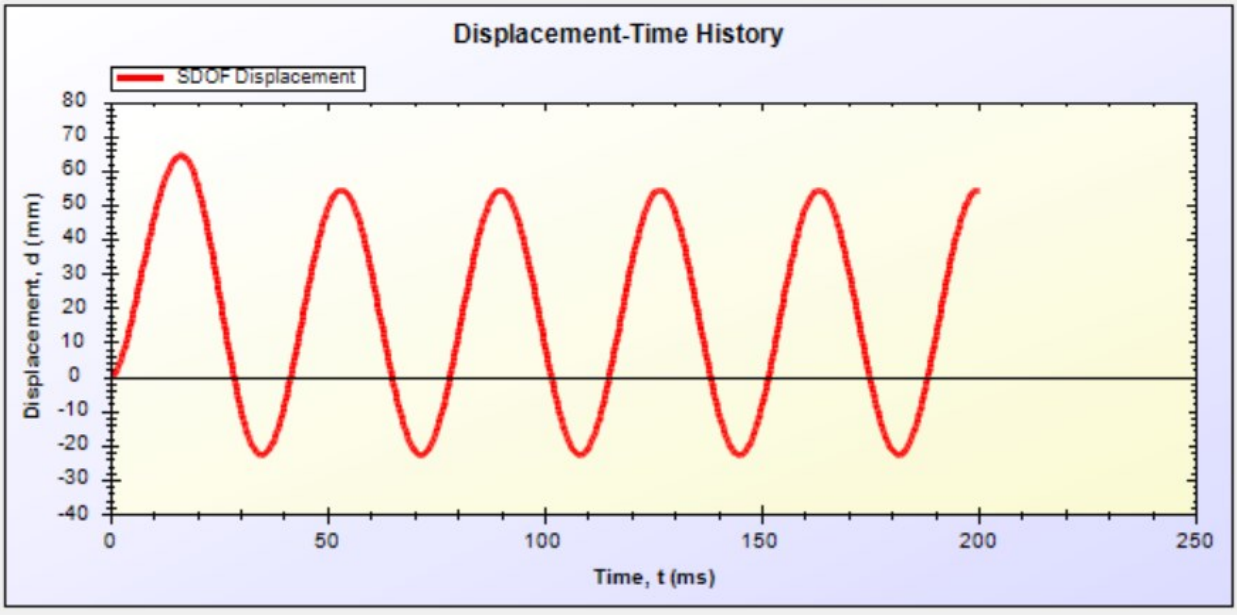

B 4: SDOF for specimen M-2FH – Blast 2

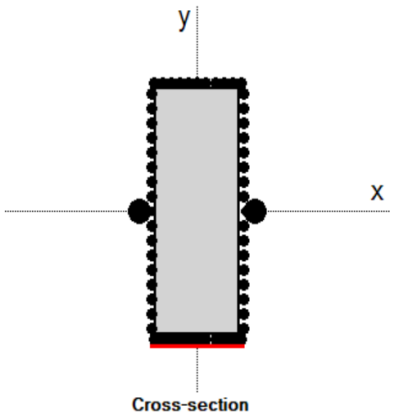

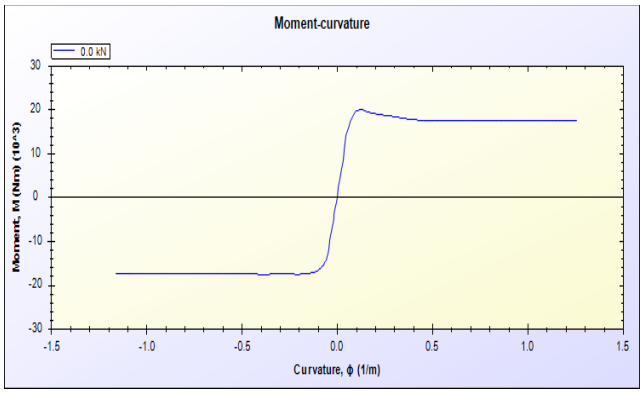

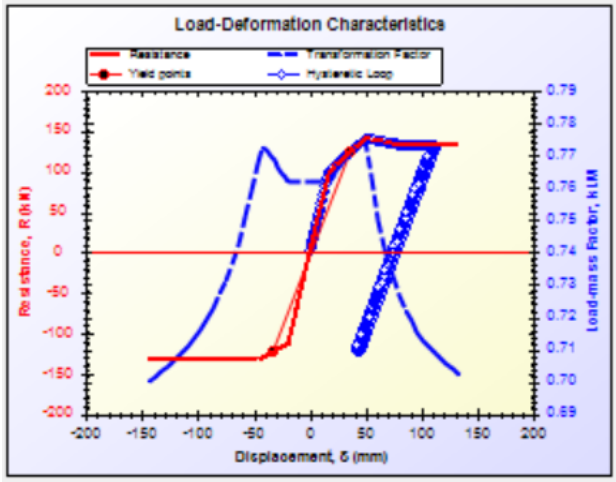

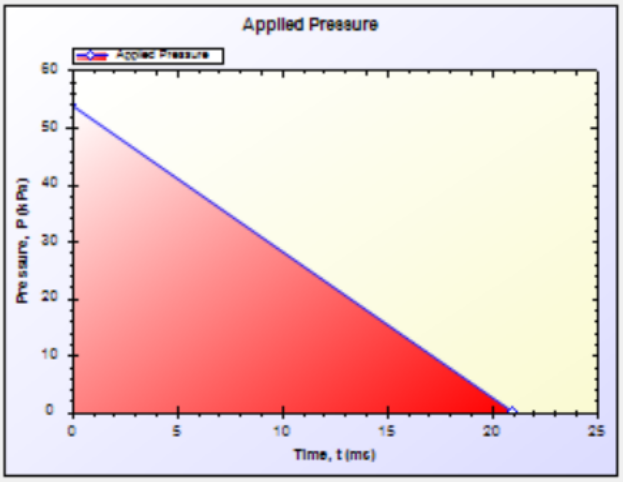

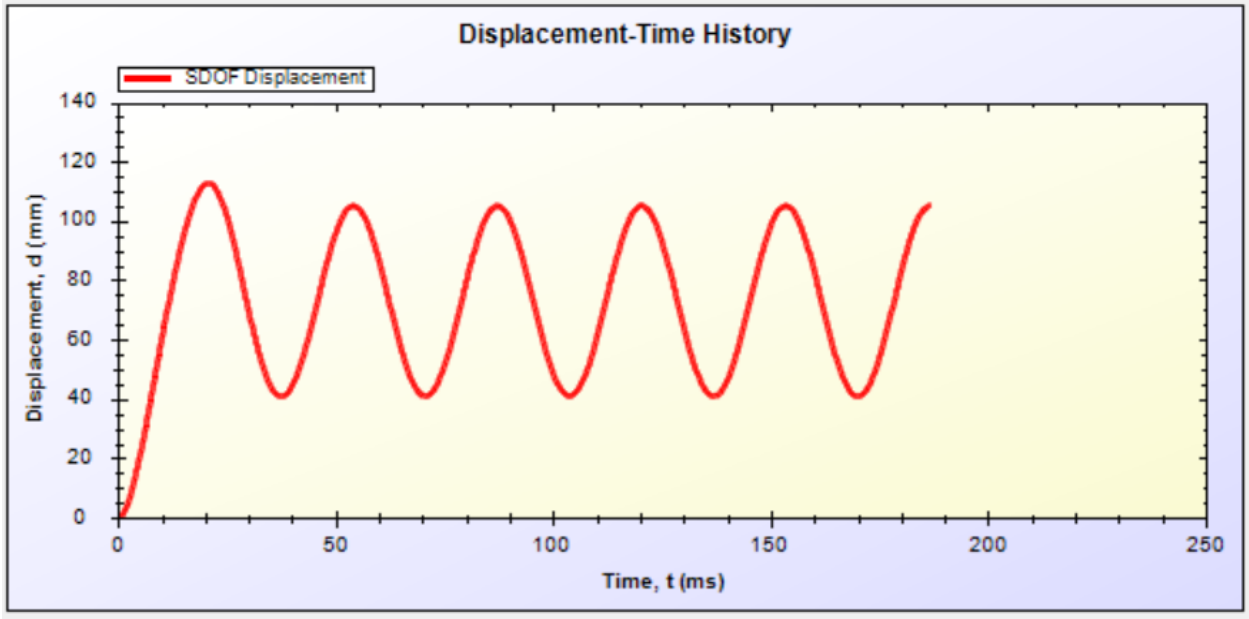

B 5: SDOF for specimen M-2FH – Blast 3

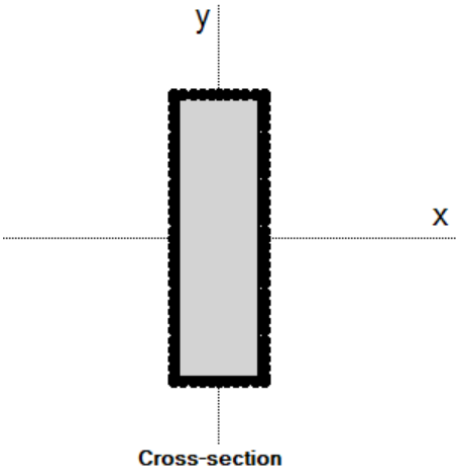

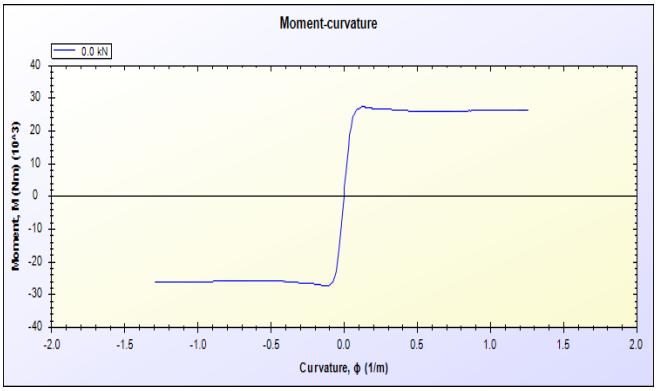

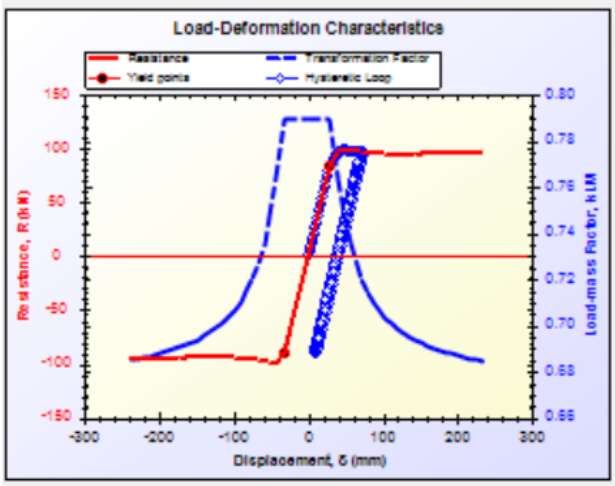

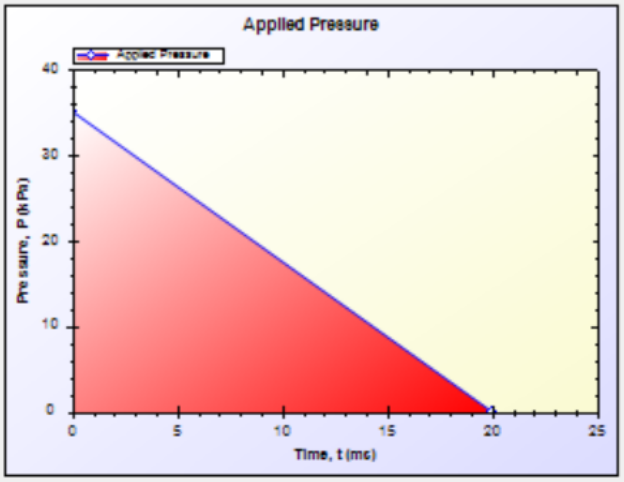

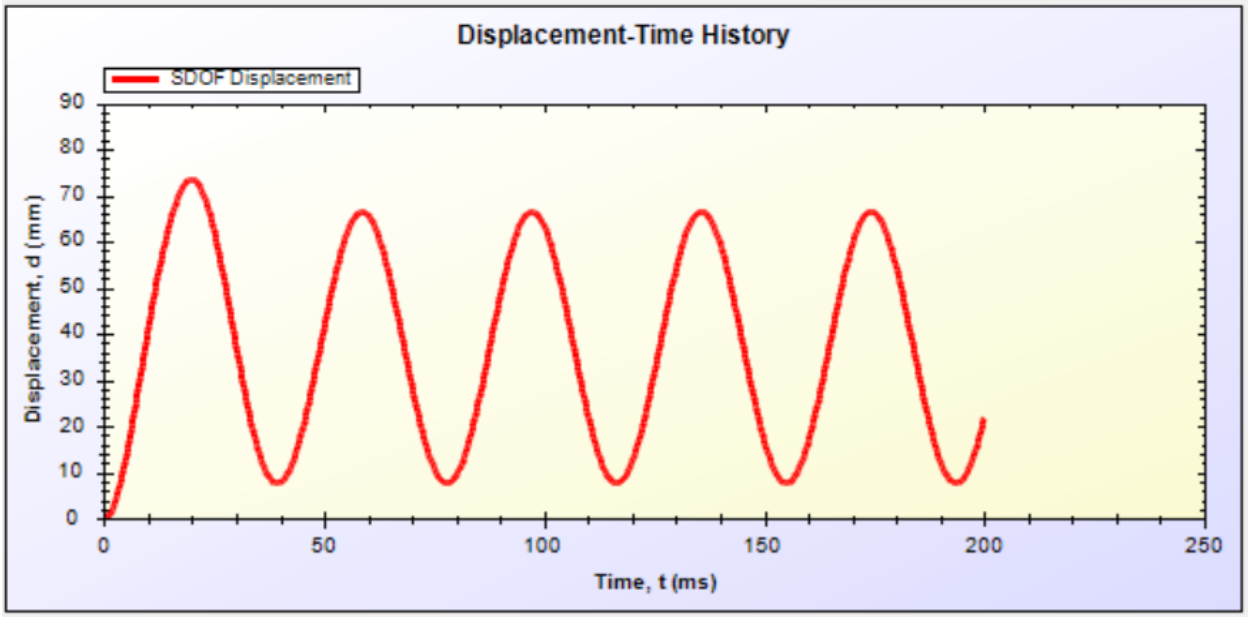

B 6: SDOF for specimen M-3F – Blast 1

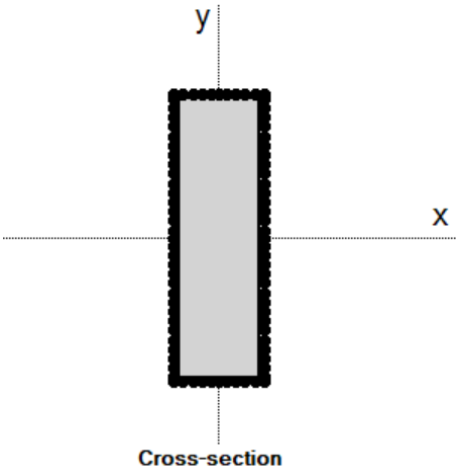

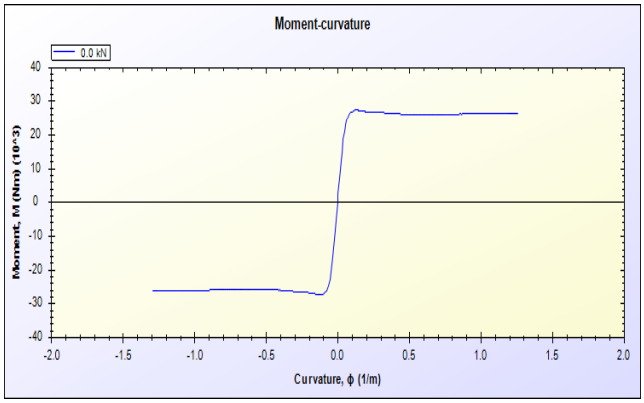

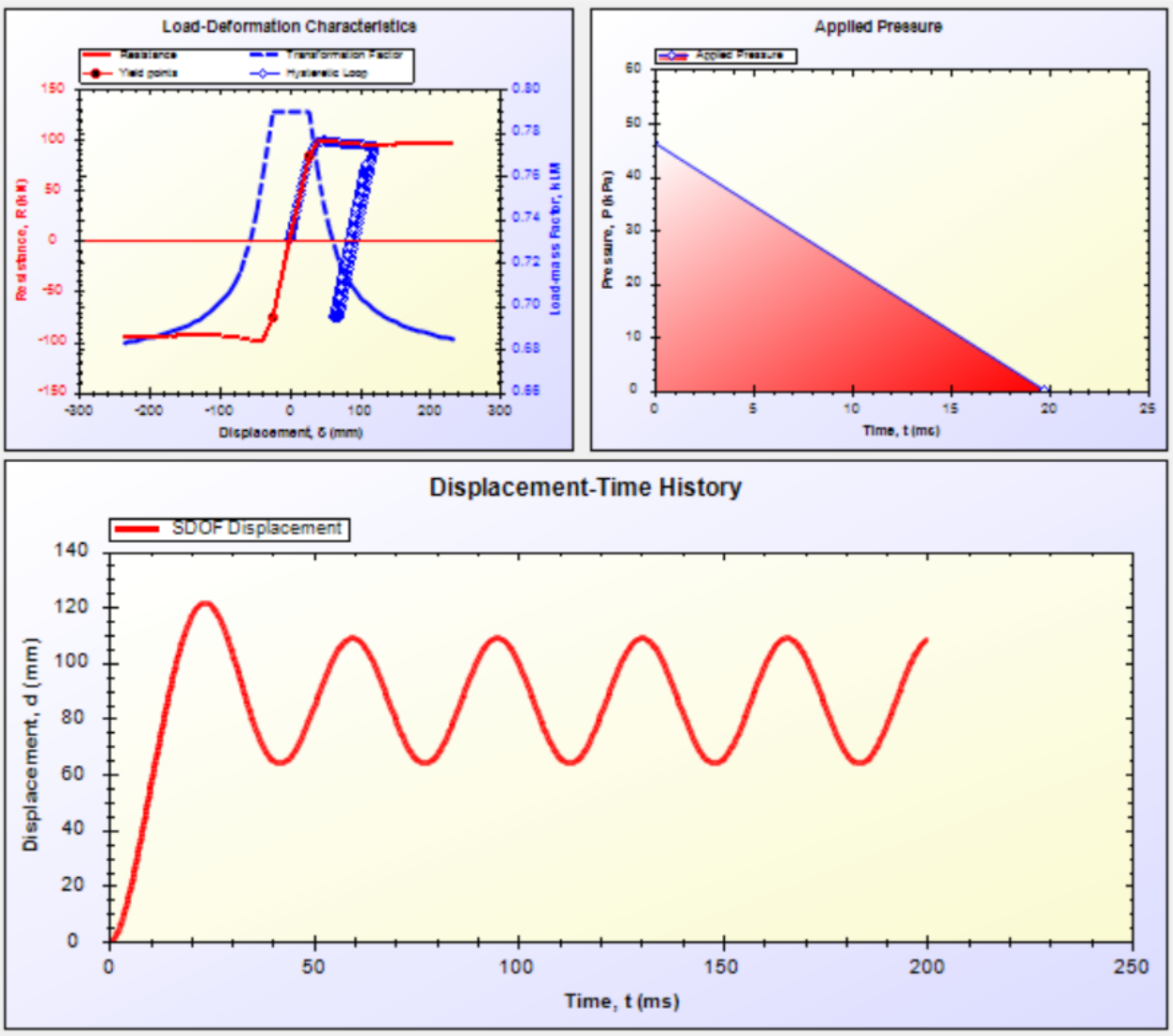

B 7: SDOF for specimen M-3F – Blast 2

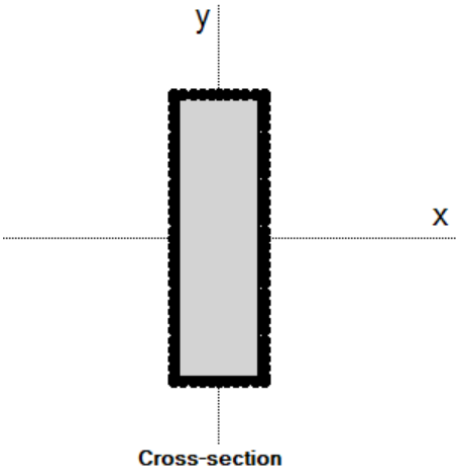

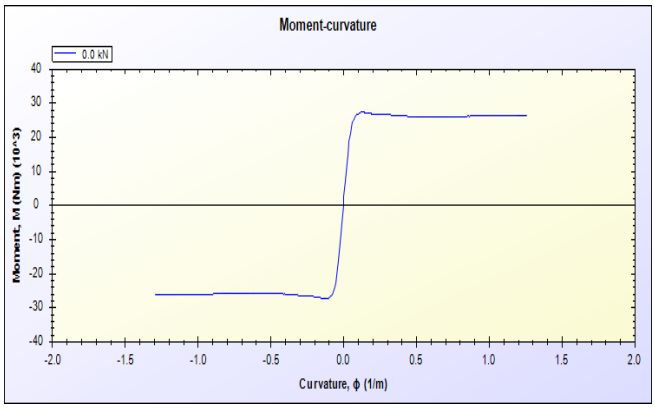

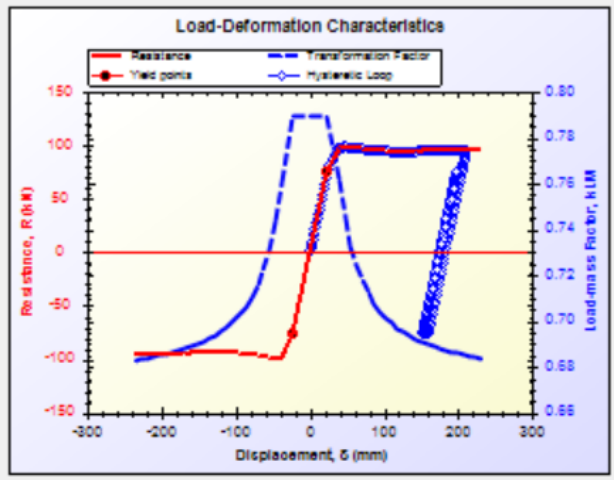

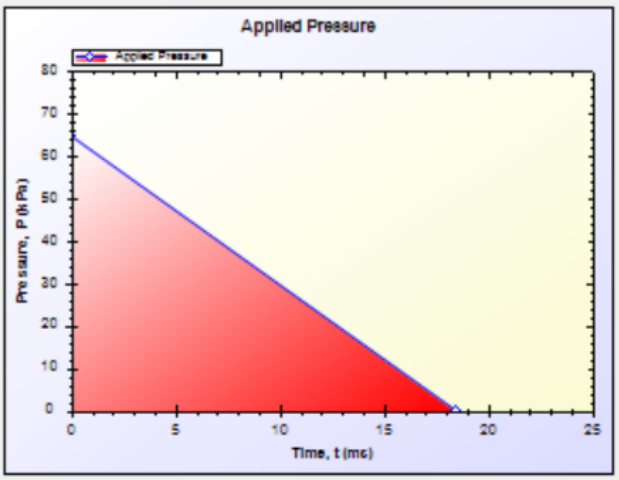

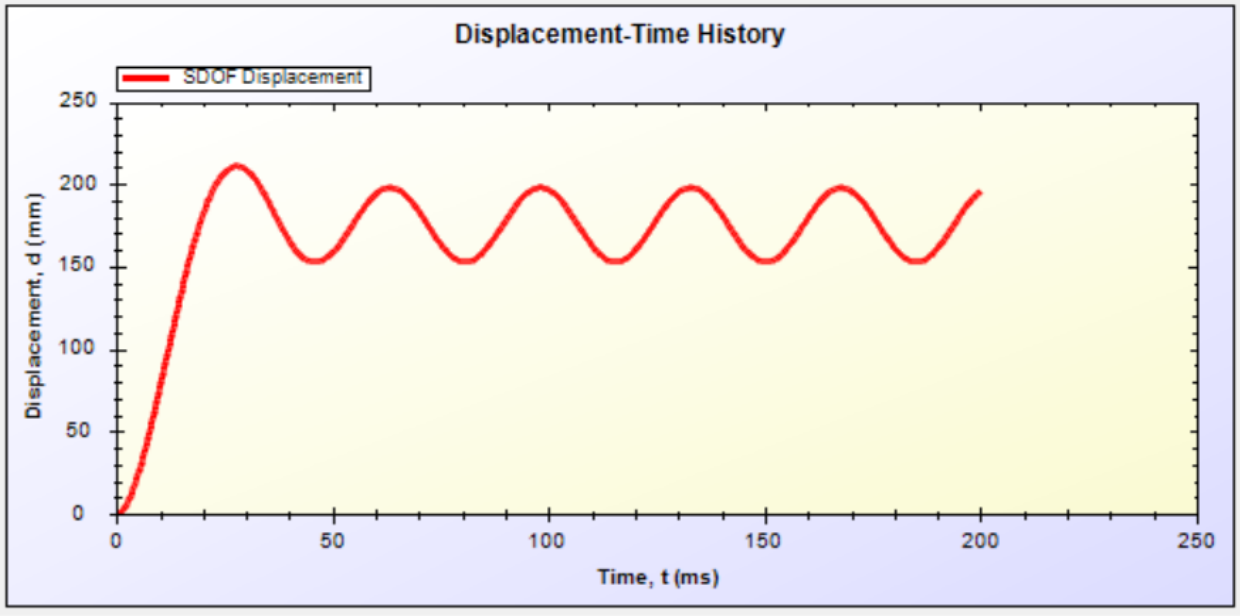

B 8: SDOF for specimen M-3F – Blast 3

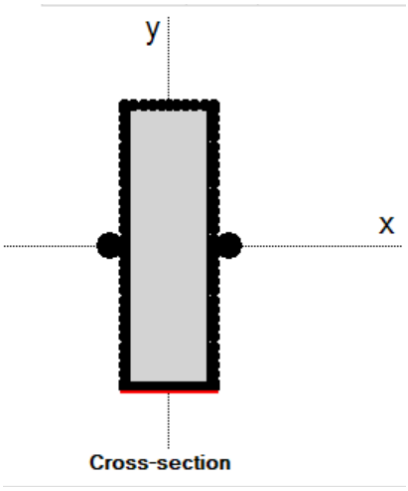

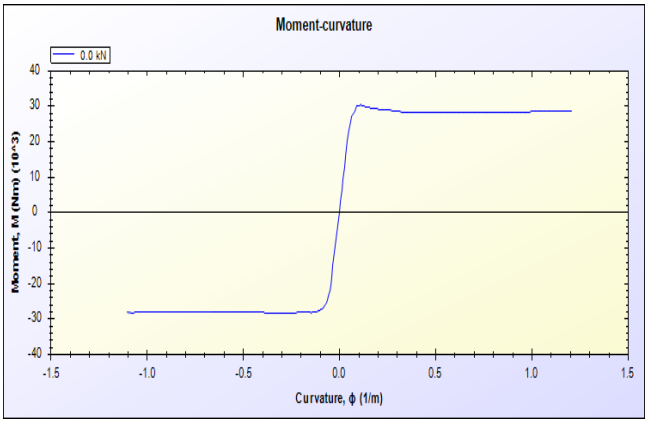

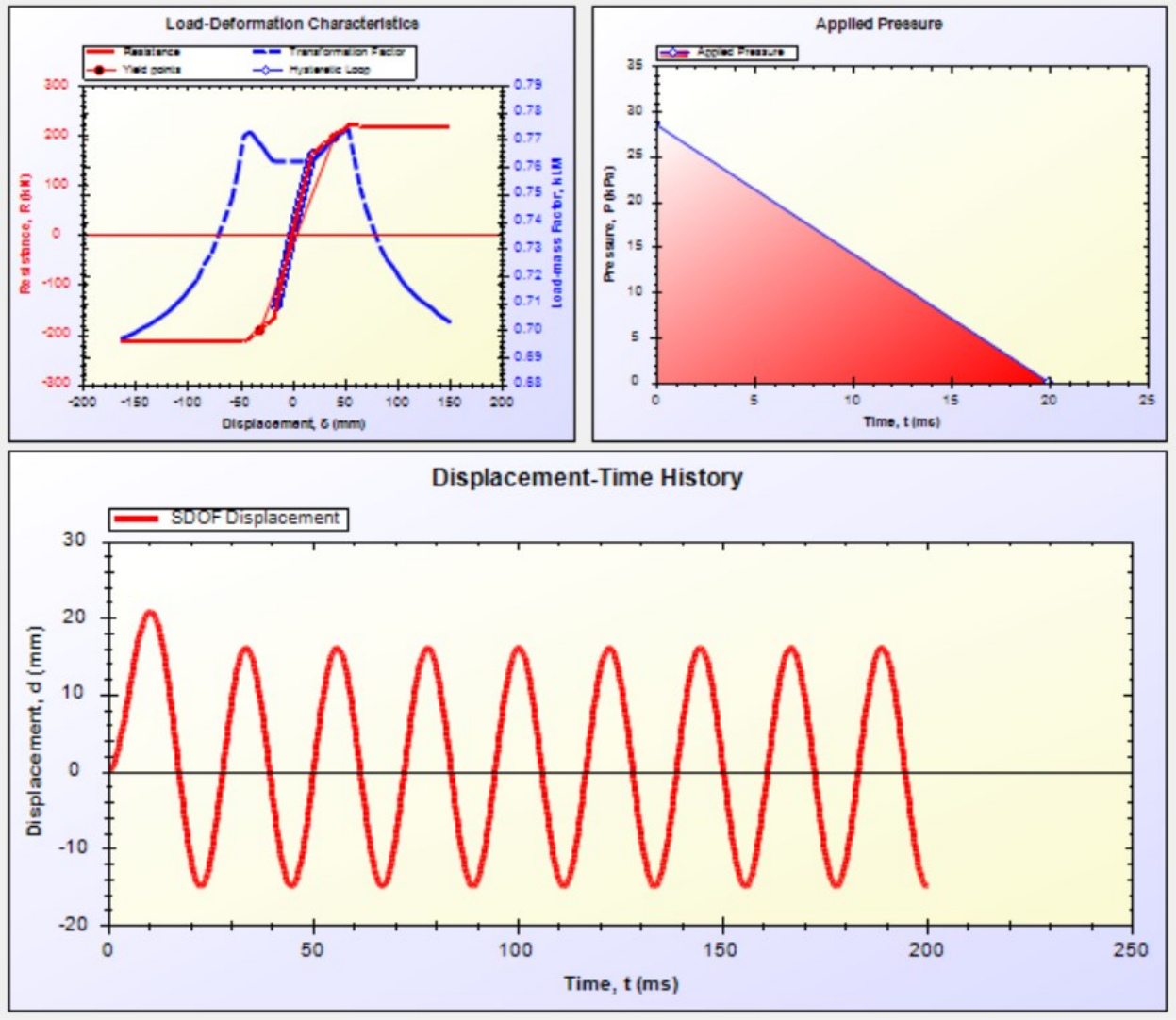

B 9: SDOF for specimen M-4FH – Blast 1

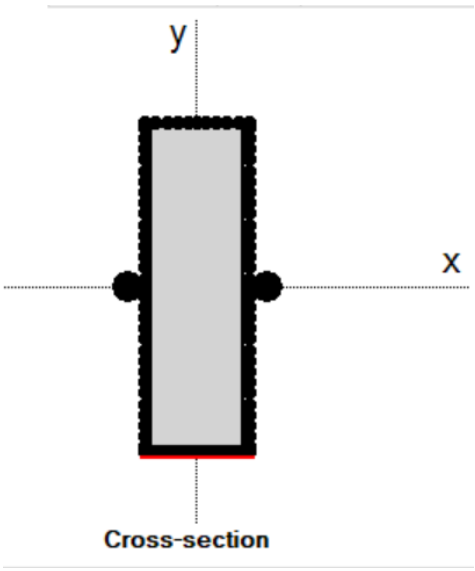

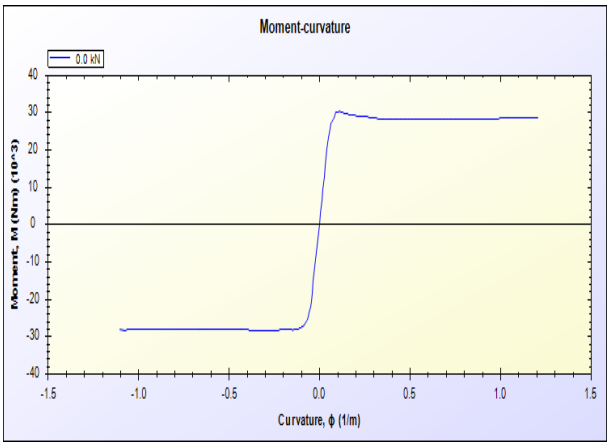

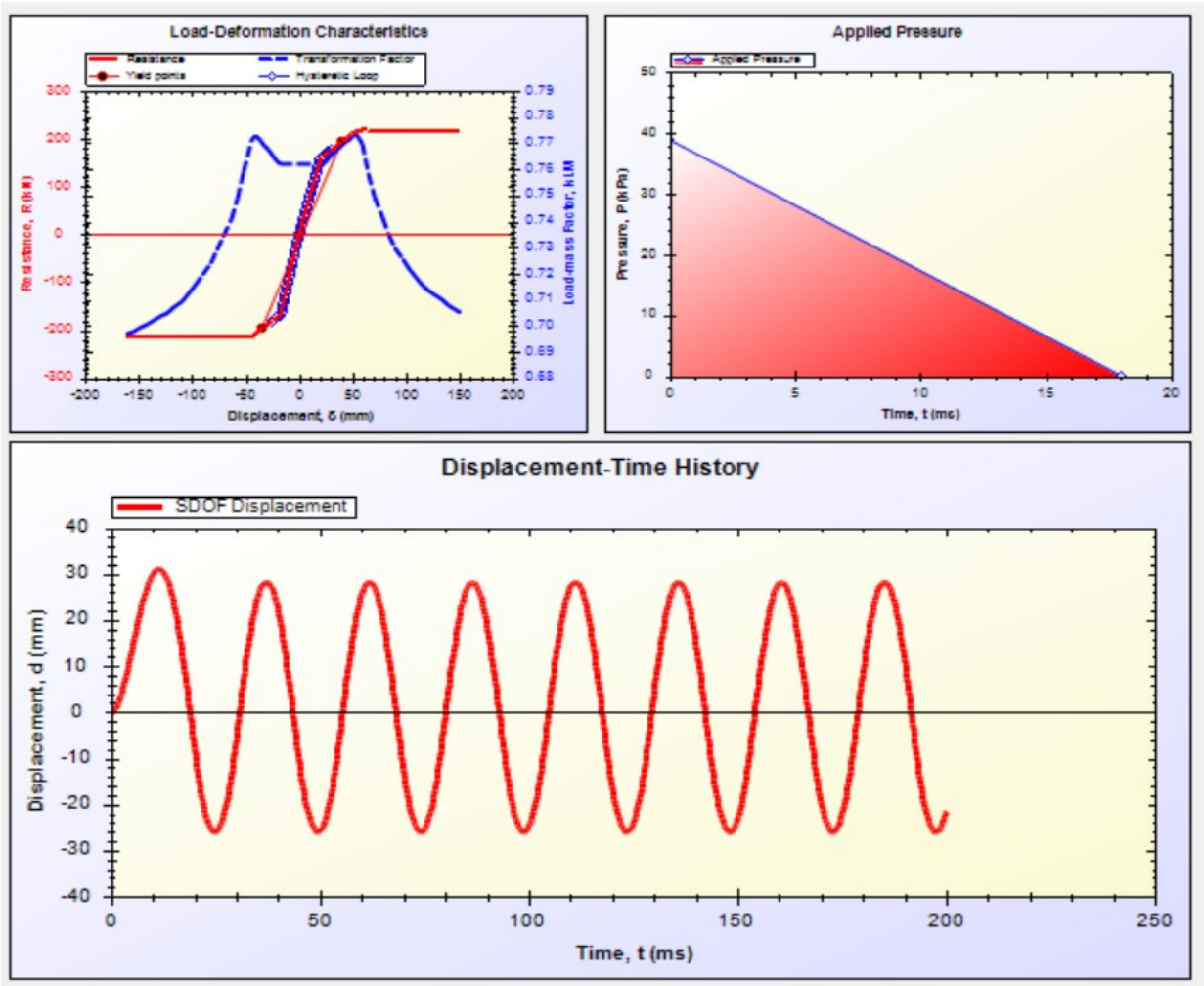

B 10: SDOF for specimen M-4FH – Blast 2

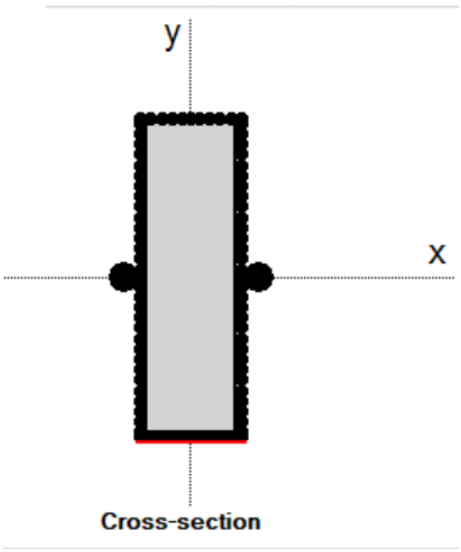

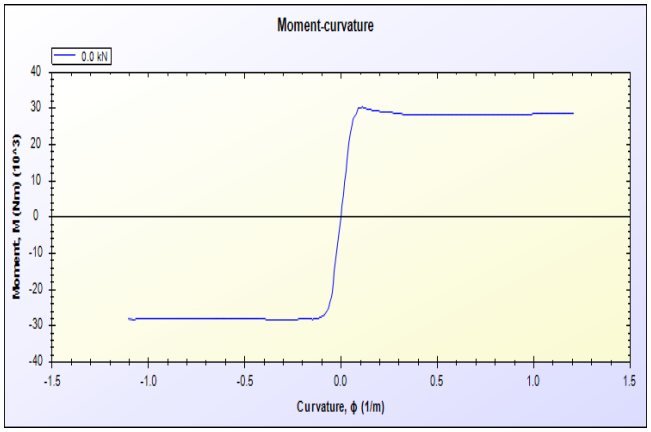

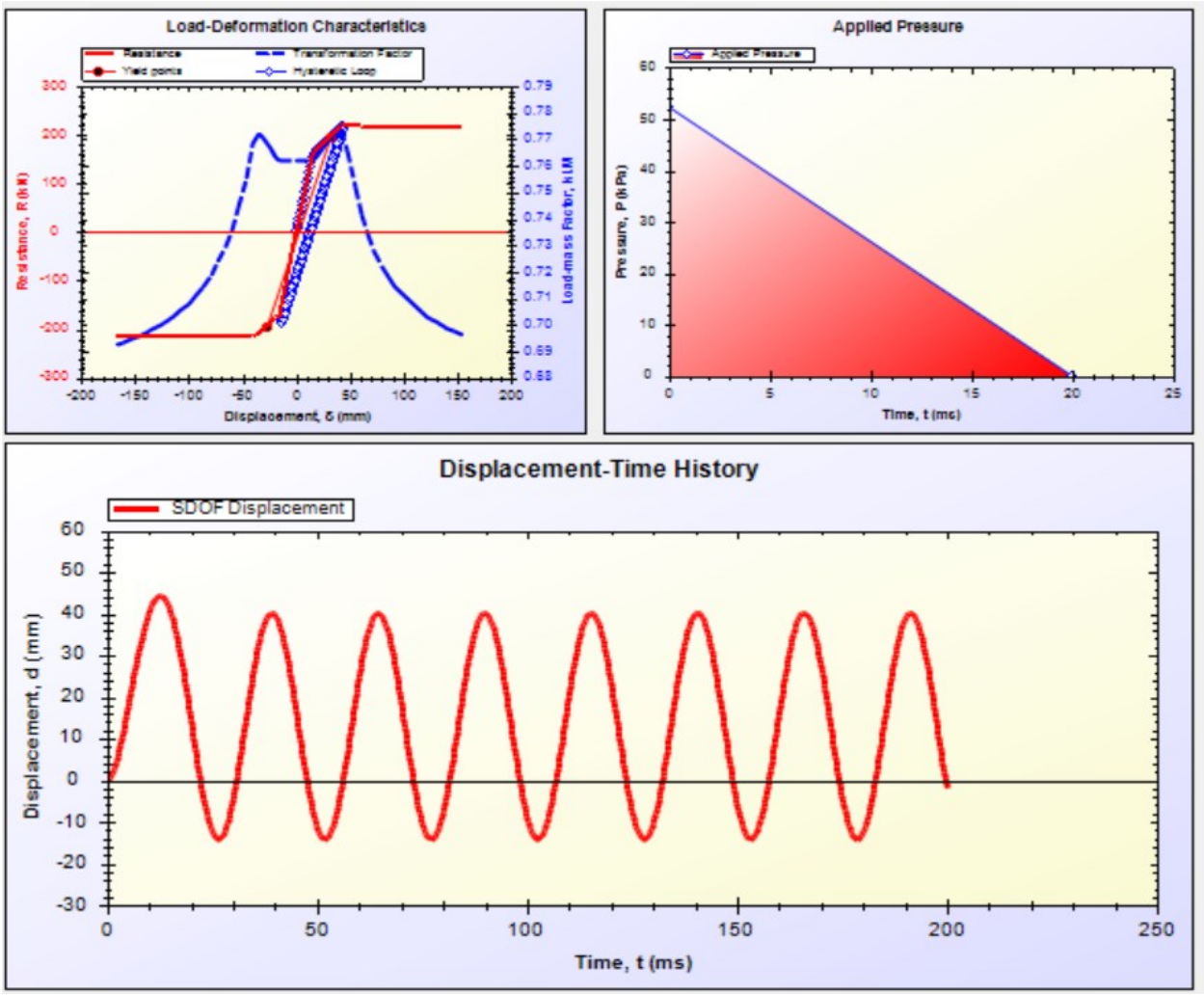

B 11: SDOF for specimen M-4FH – Blast 3

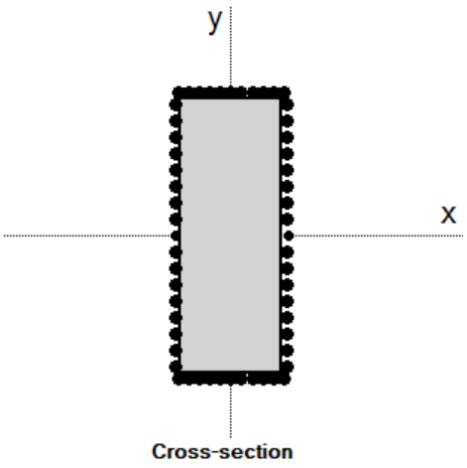

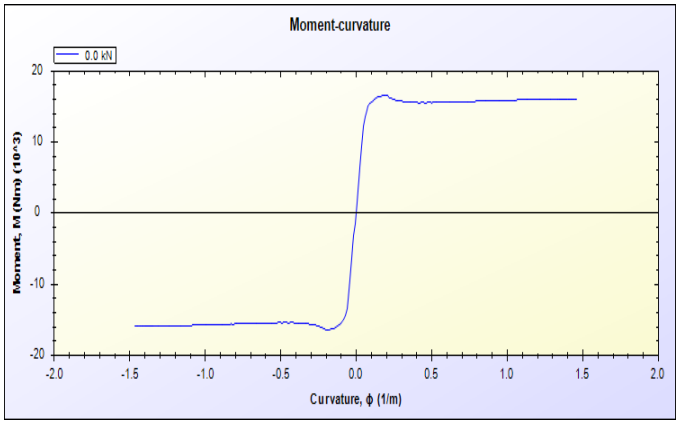

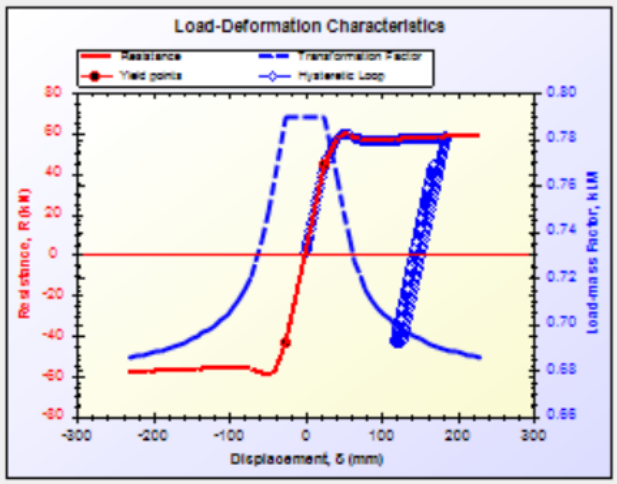

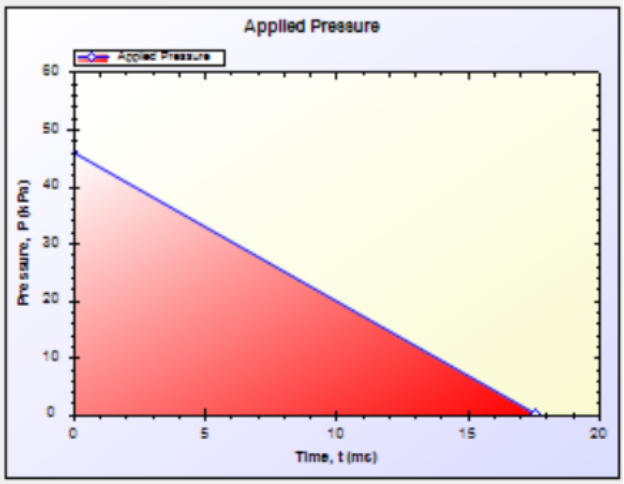

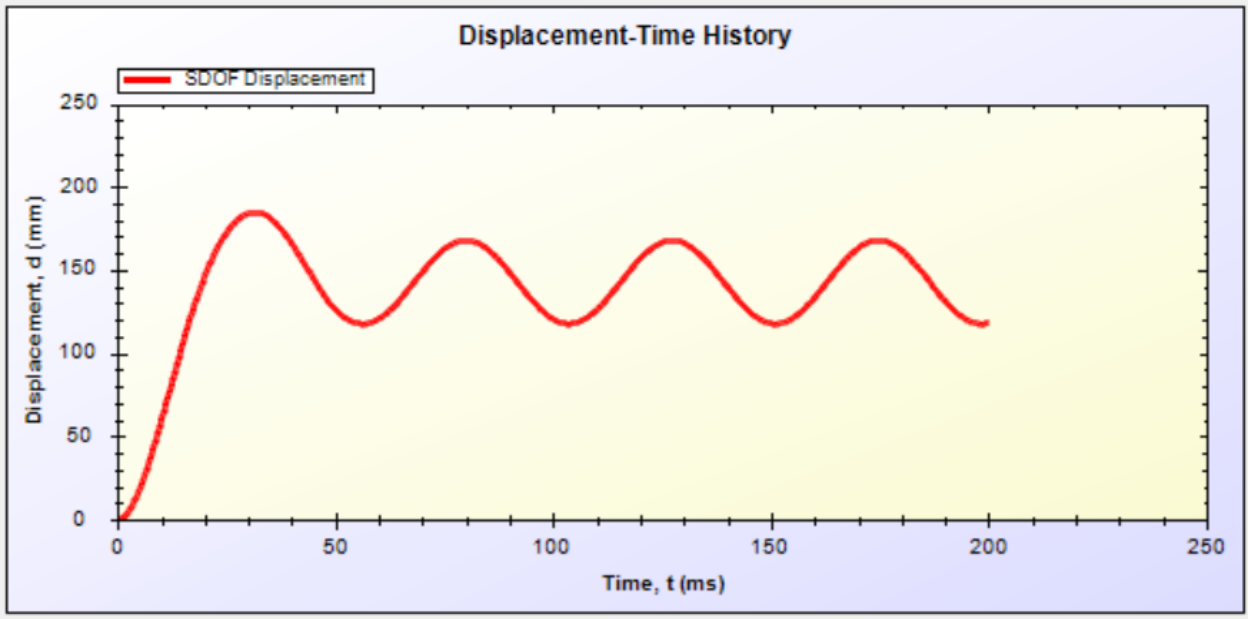

B 12: SDOF for specimen M-5F – Blast 1

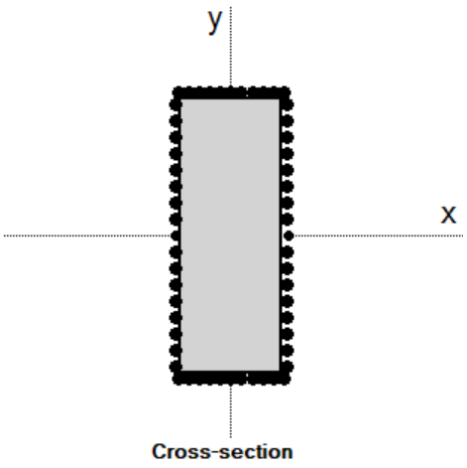

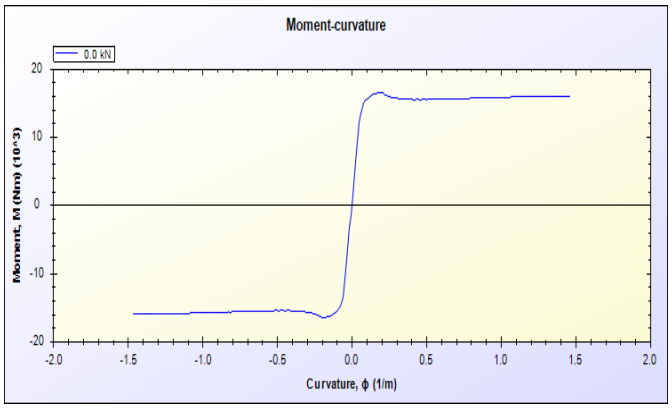

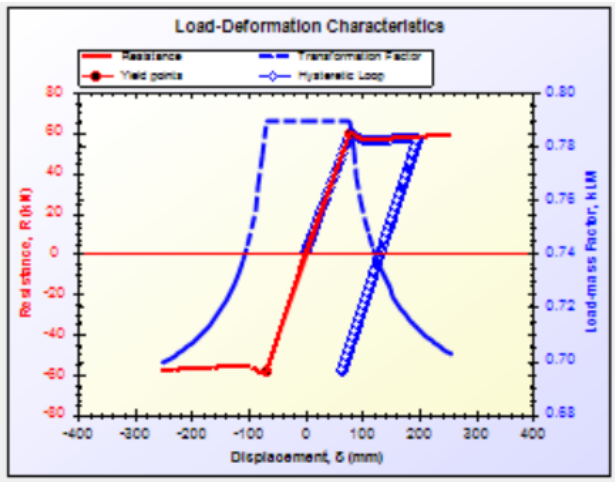

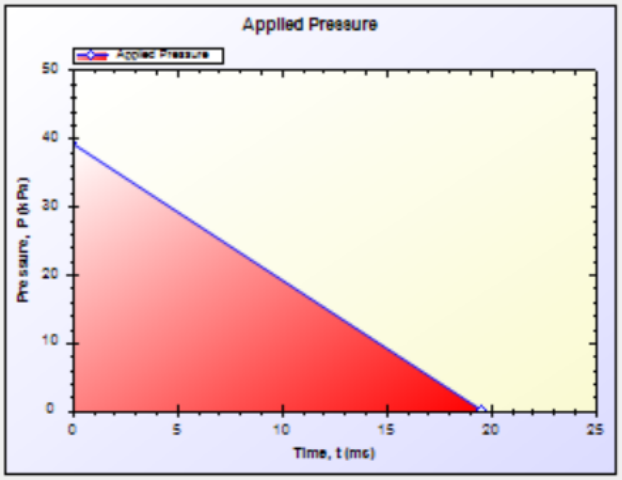

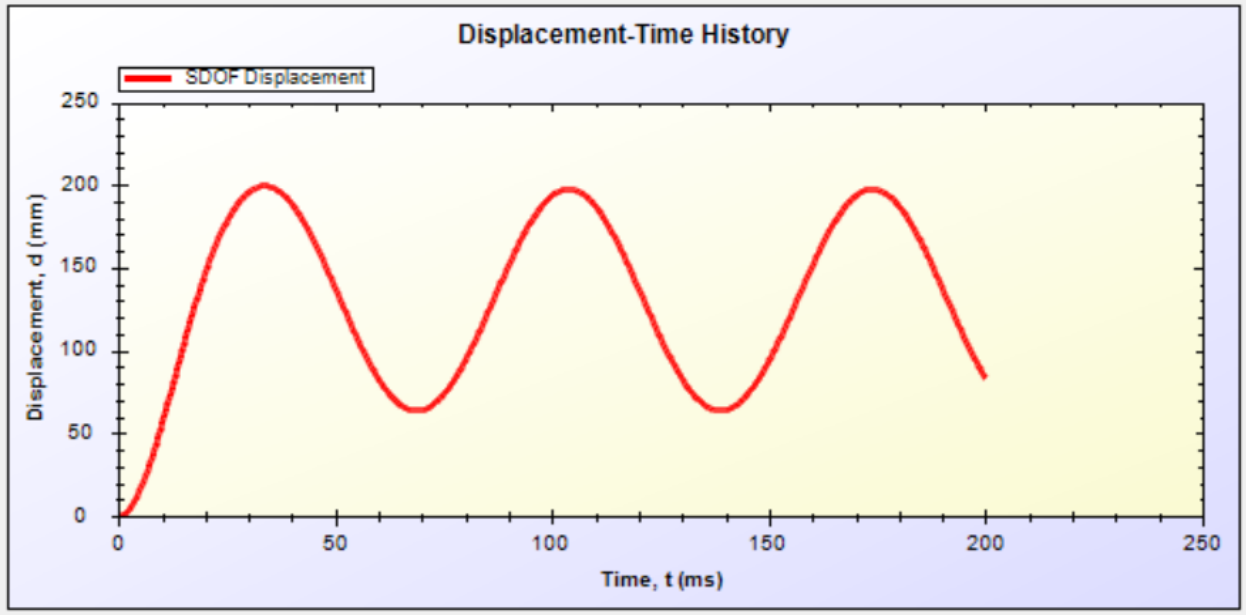

B 13: SDOF for specimen M-5F – Blast 2

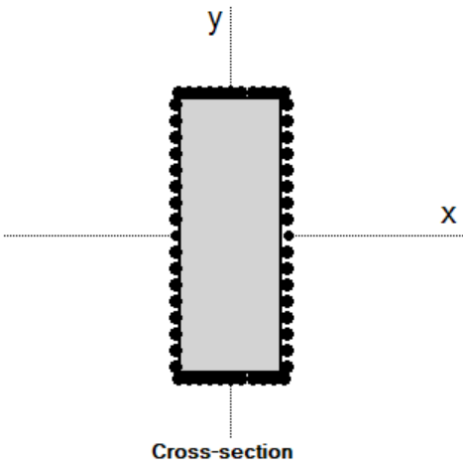

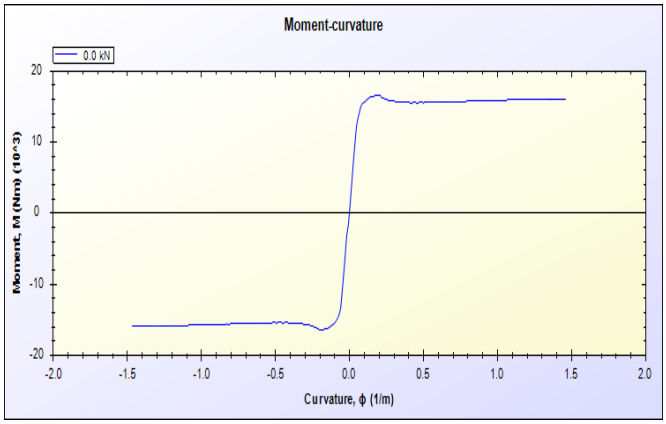

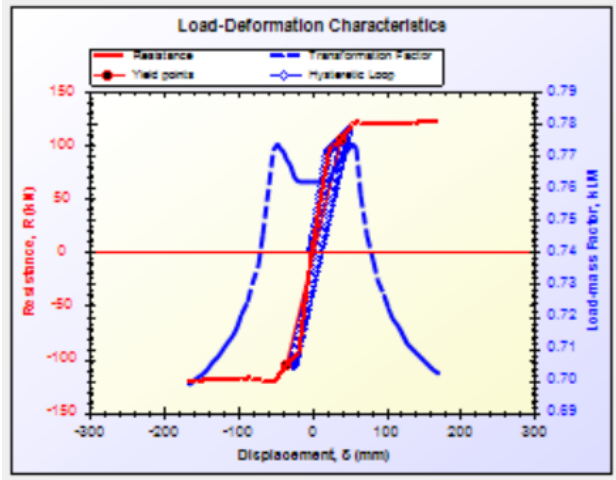

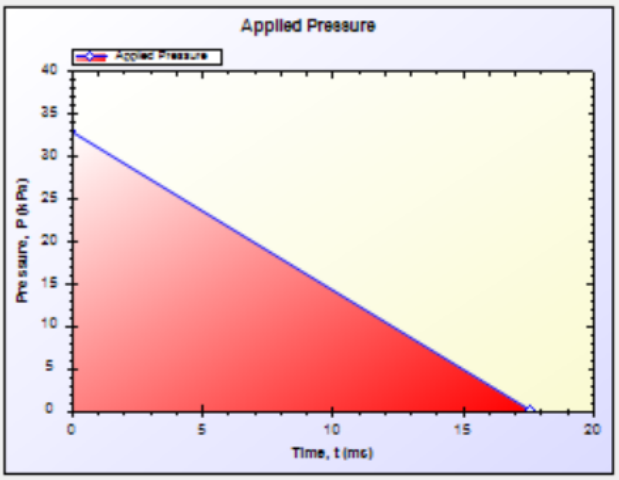

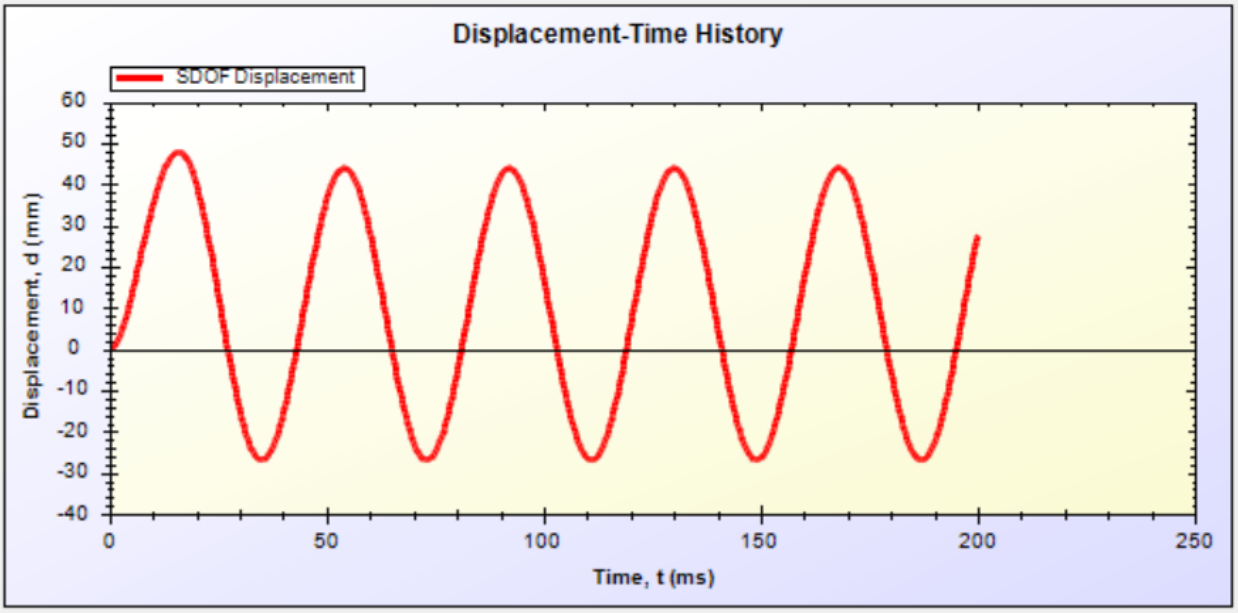

B 14: SDOF for specimen M-6F – Blast 1

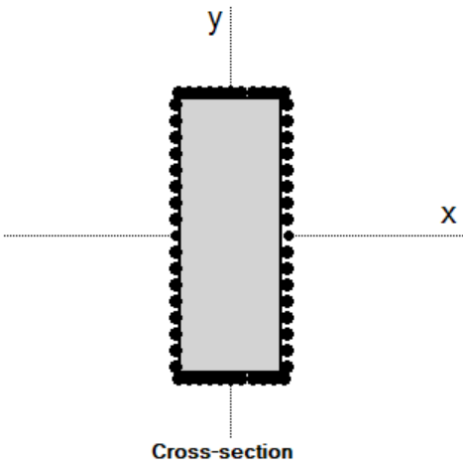

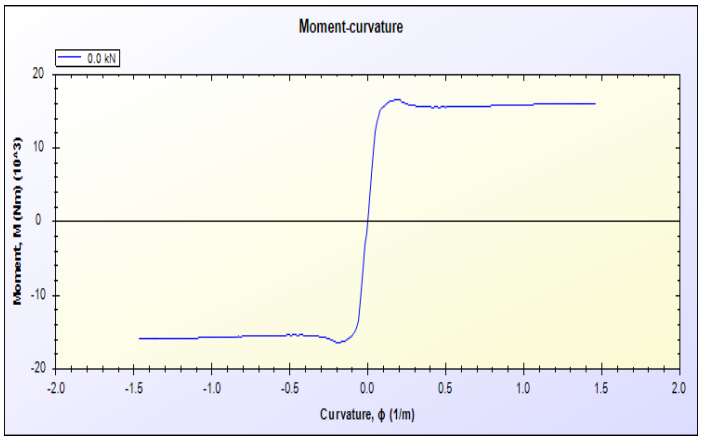

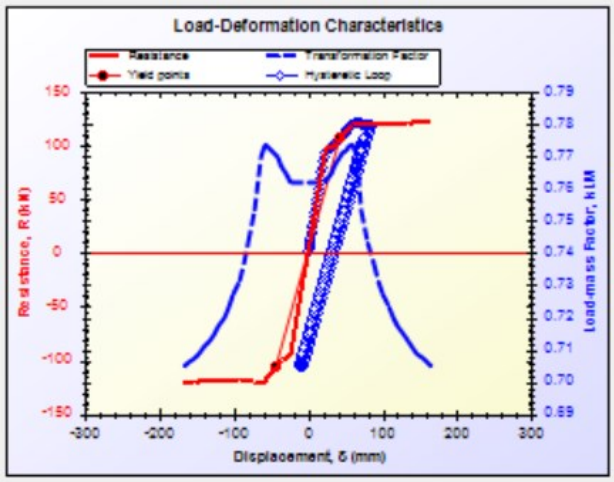

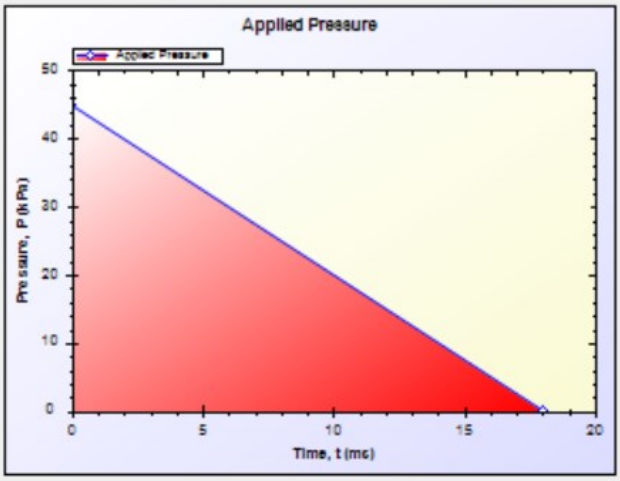

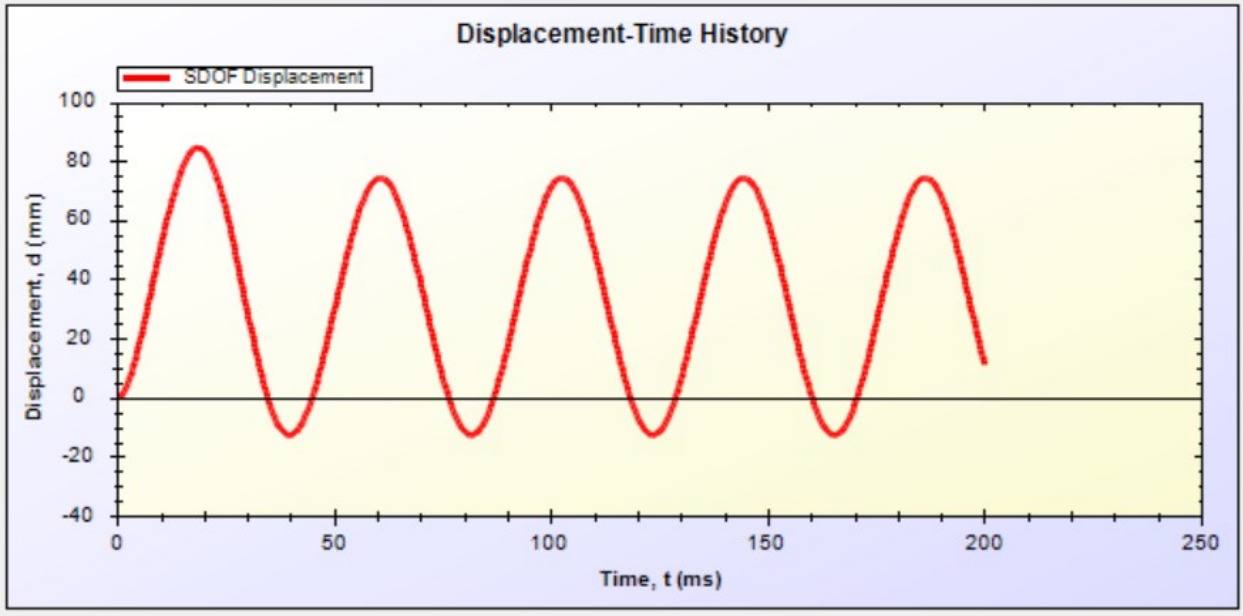

B 15: SDOF for specimen M-6F – Blast *2*

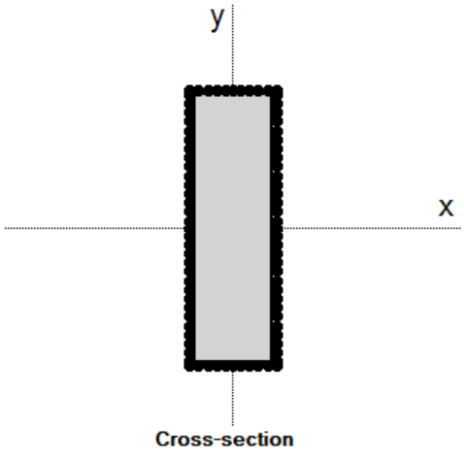

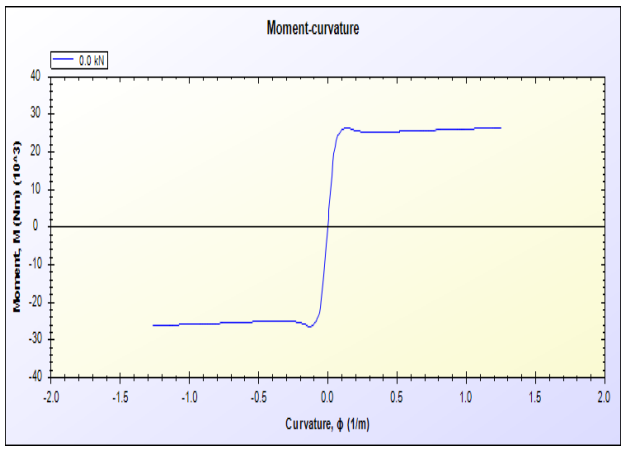

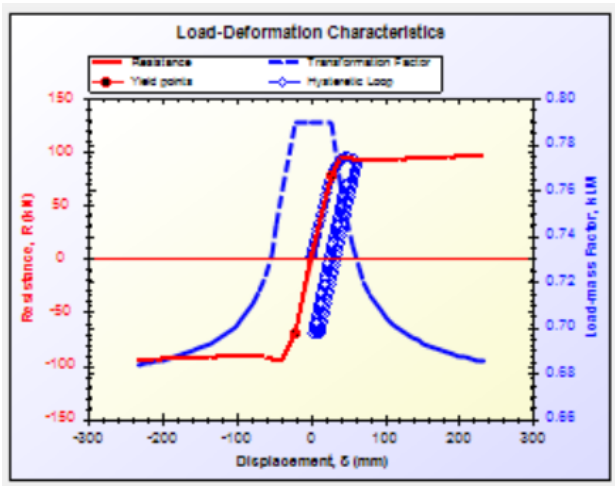

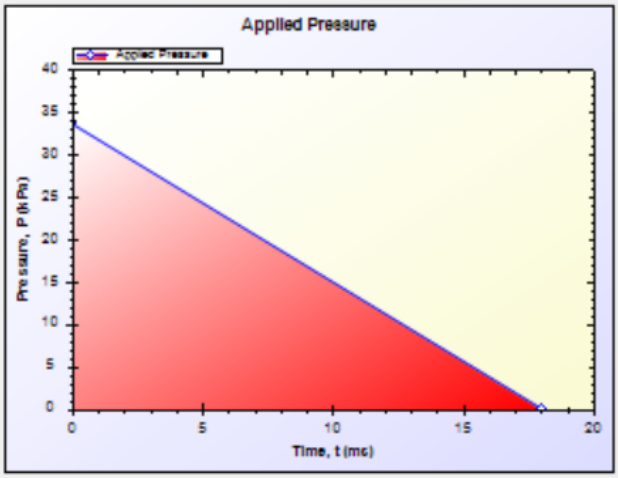

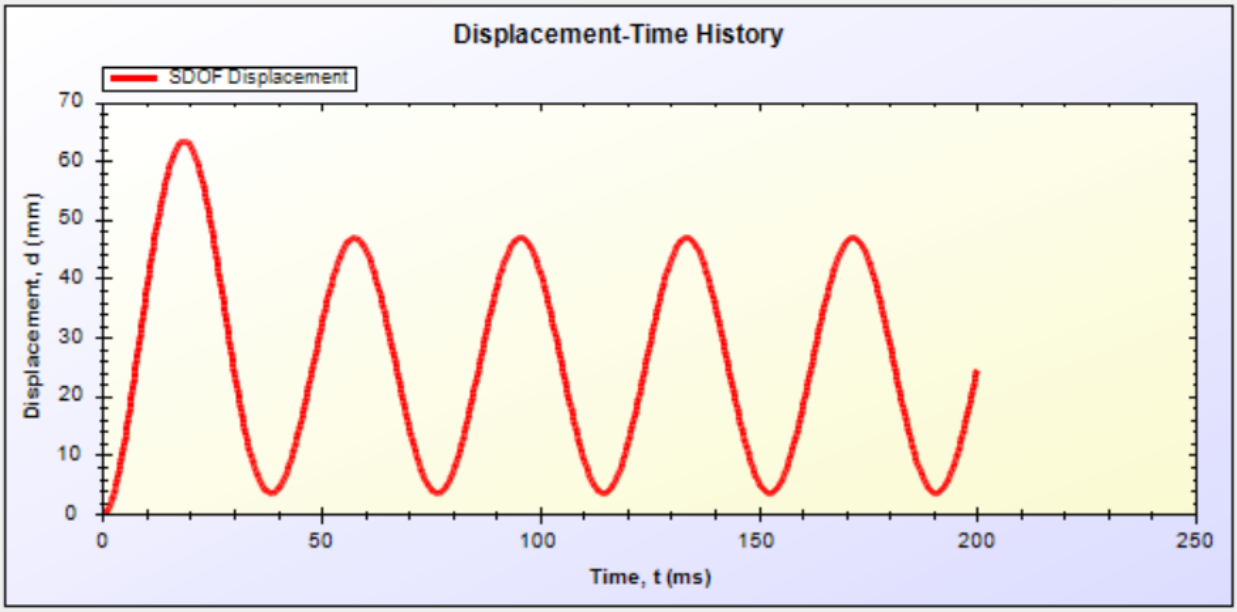

B 16: SDOF for specimen M-7F – Blast 1

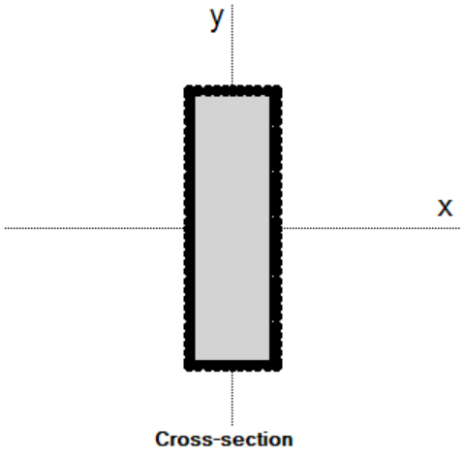

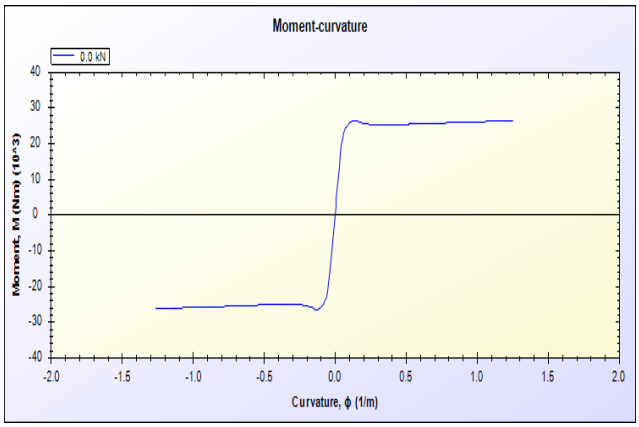

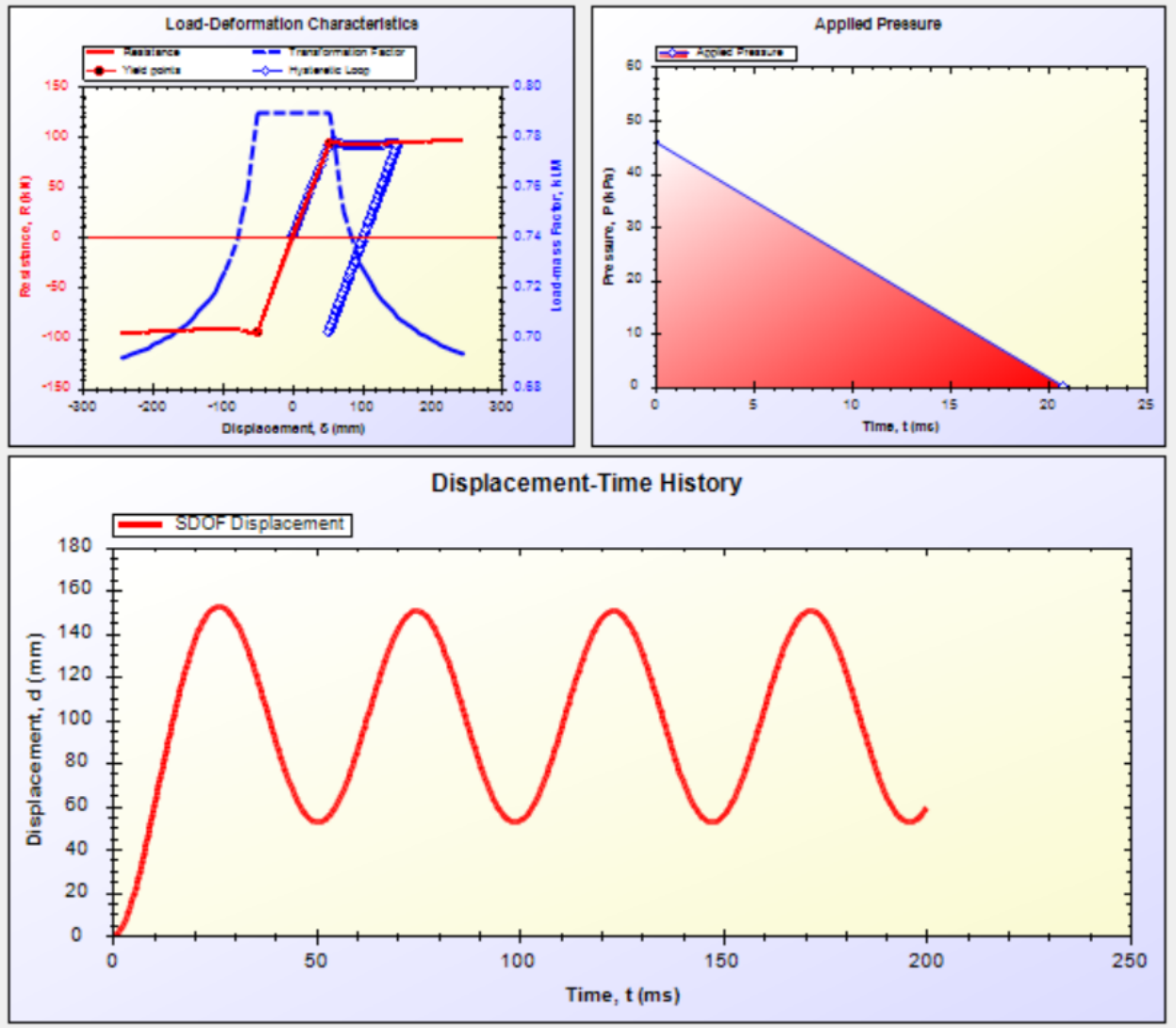

B 17: SDOF for specimen M-7F – Blast 2

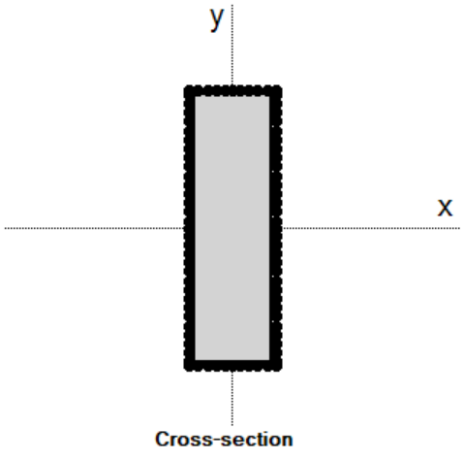

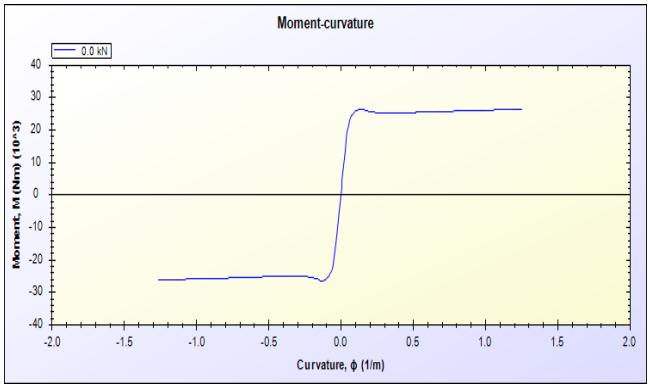

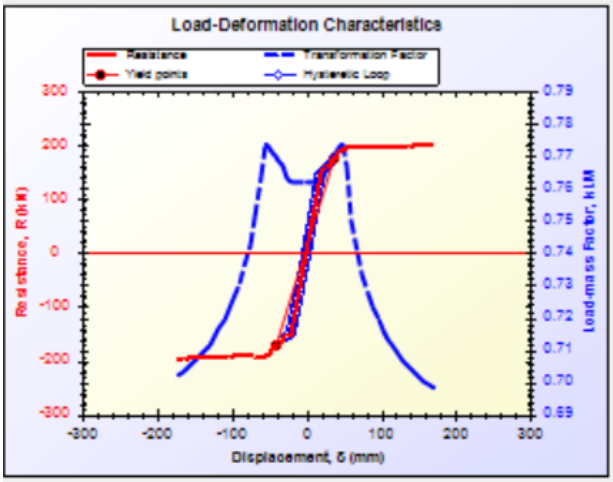

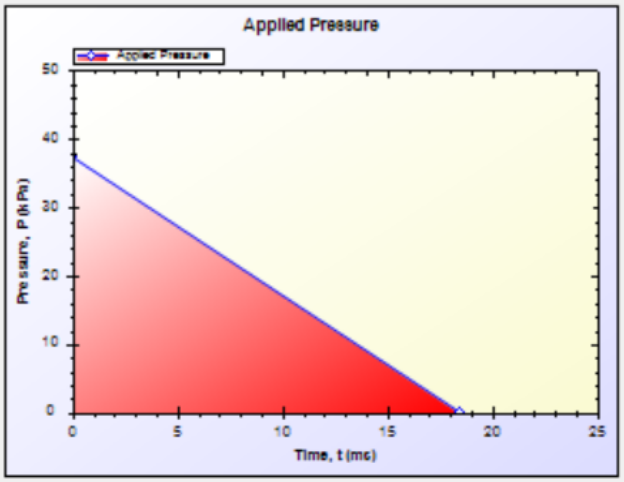

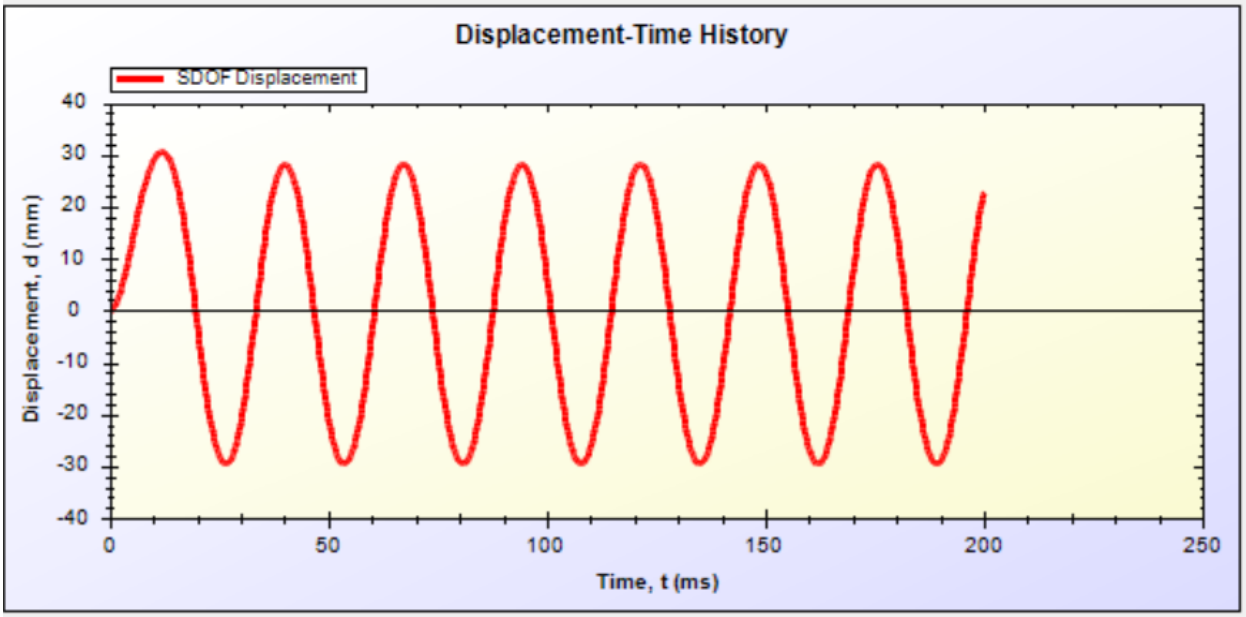

B 18: SDOF for specimen M-8F – Blast 1

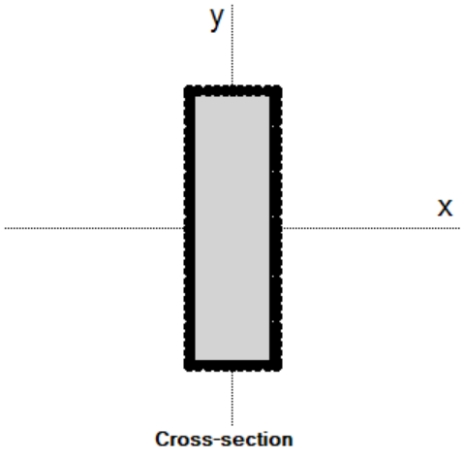

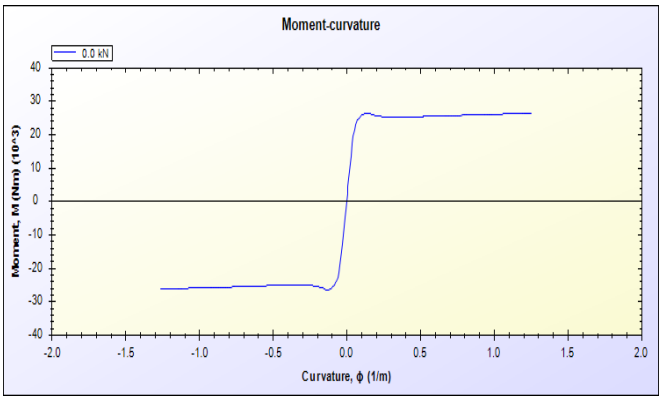

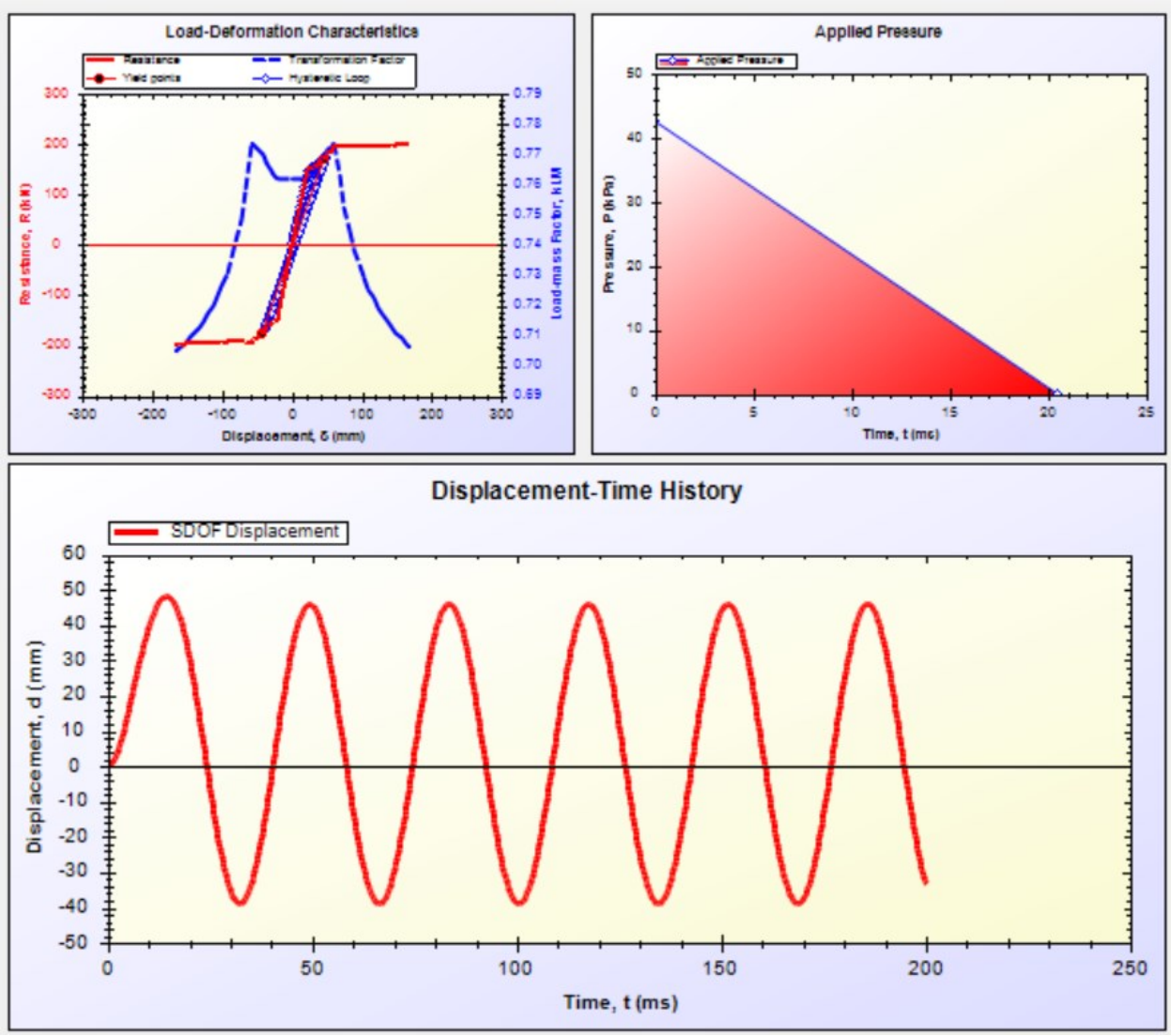

B 19: SDOF for specimen M-8F – Blast 2

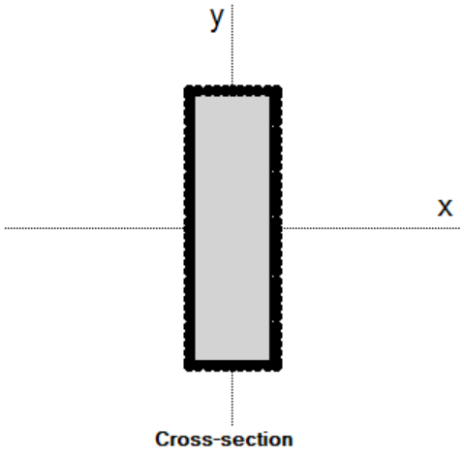

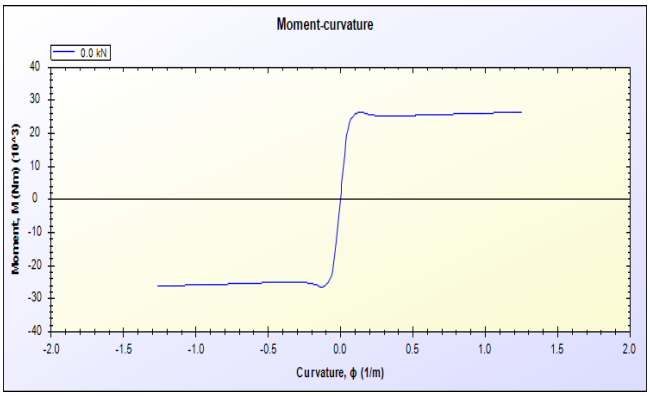

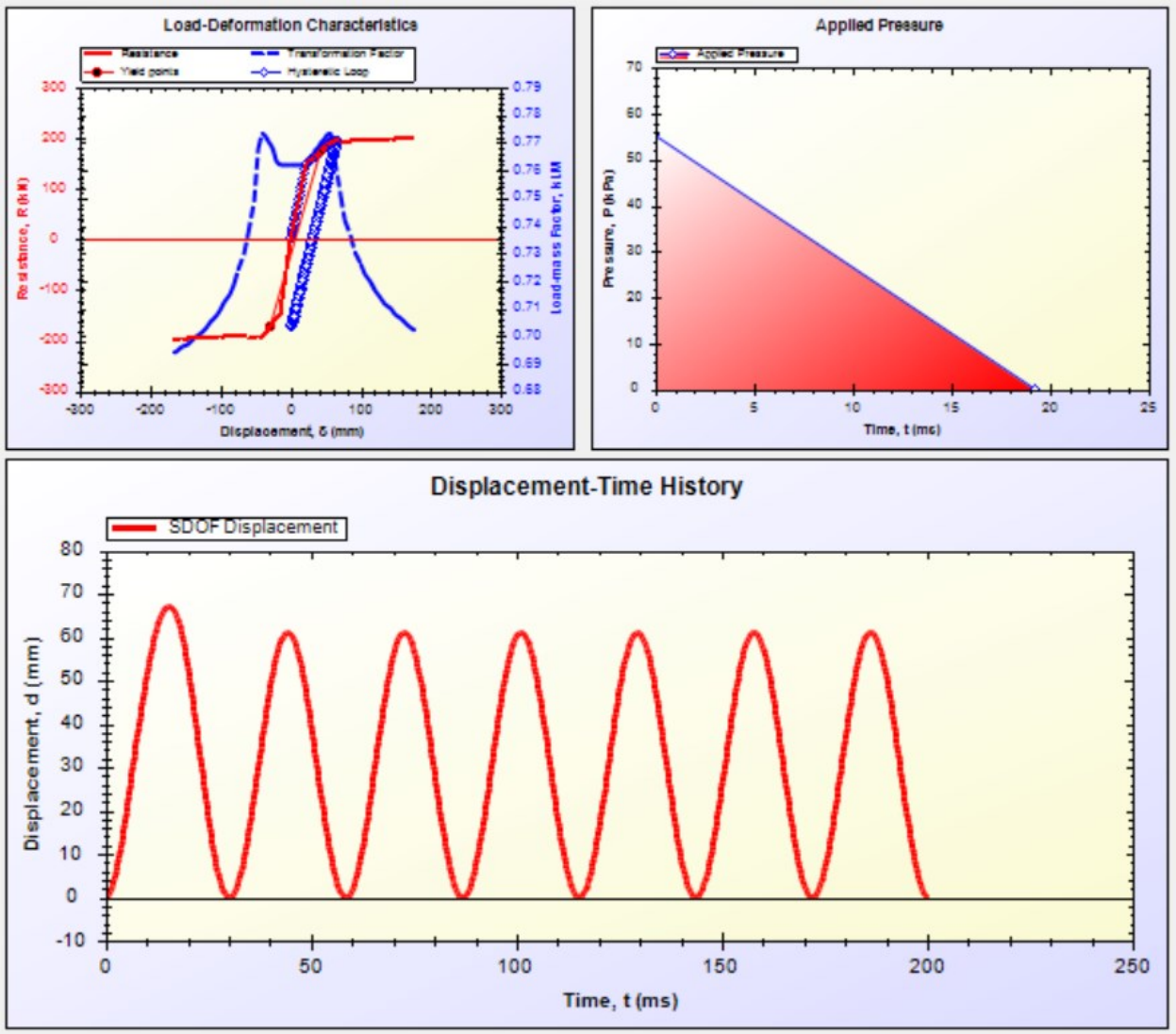

B 20: SDOF for specimen M-8F – Blast 3

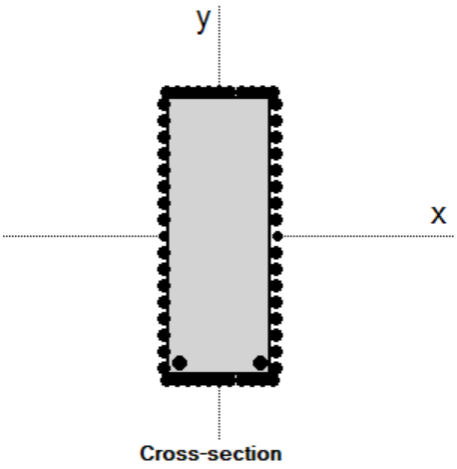

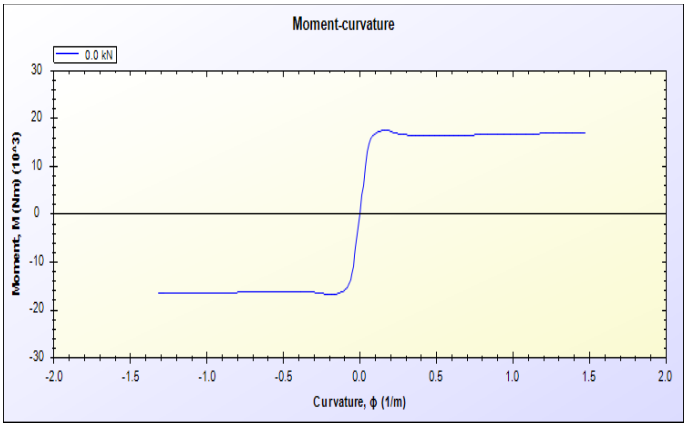

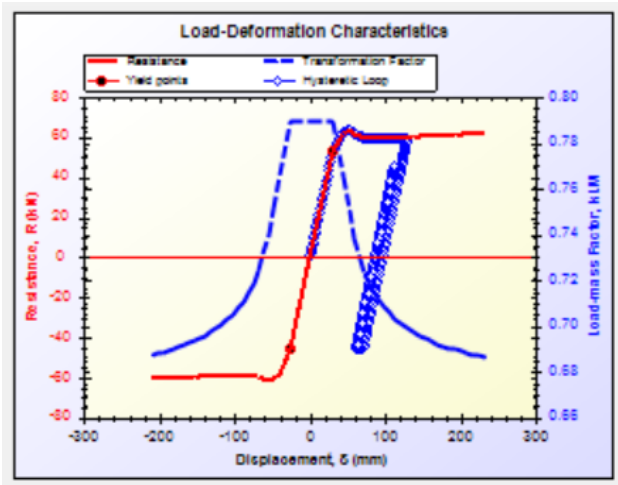

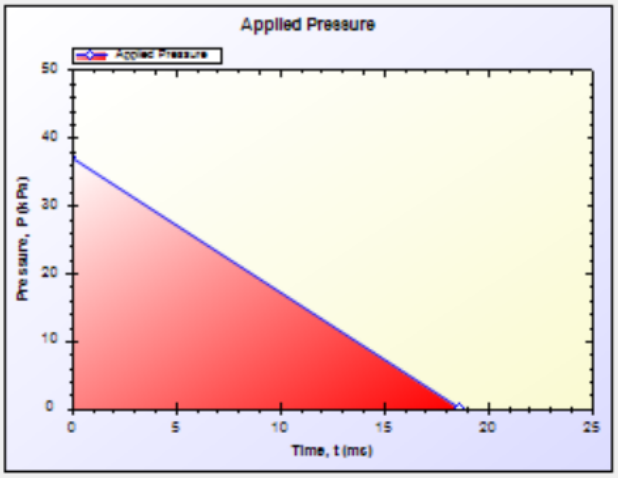

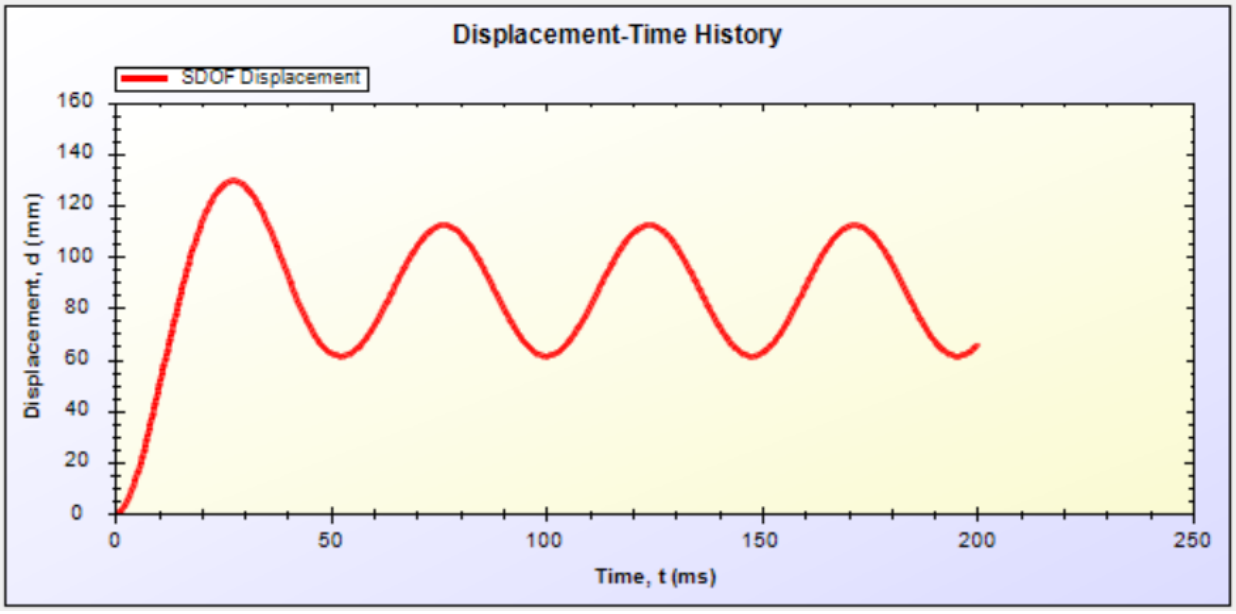

B 21: SDOF for specimen M-9FH – Blast 1

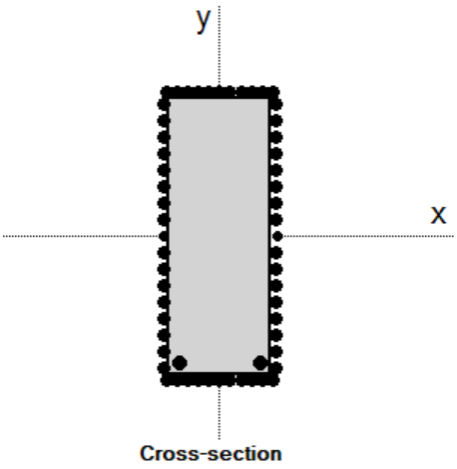

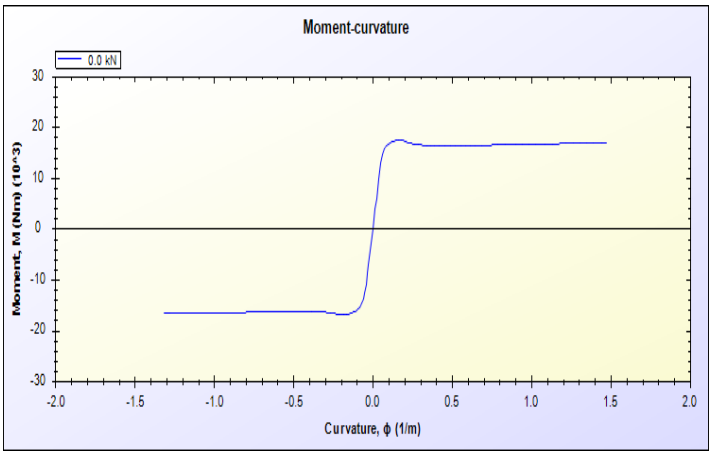

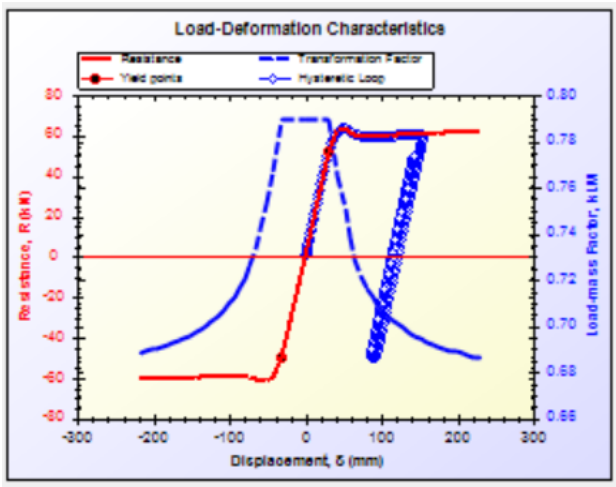

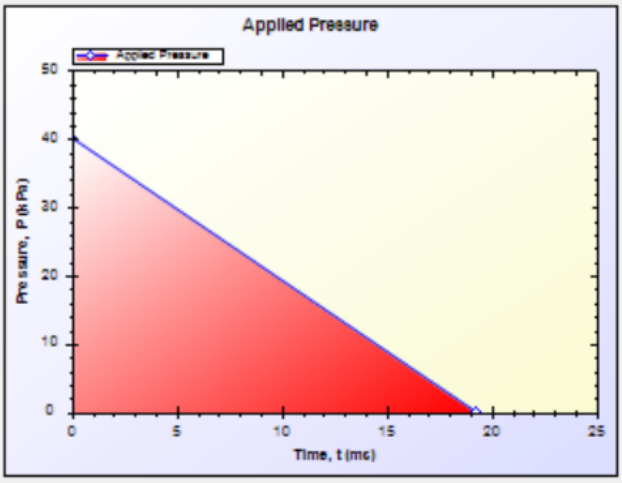

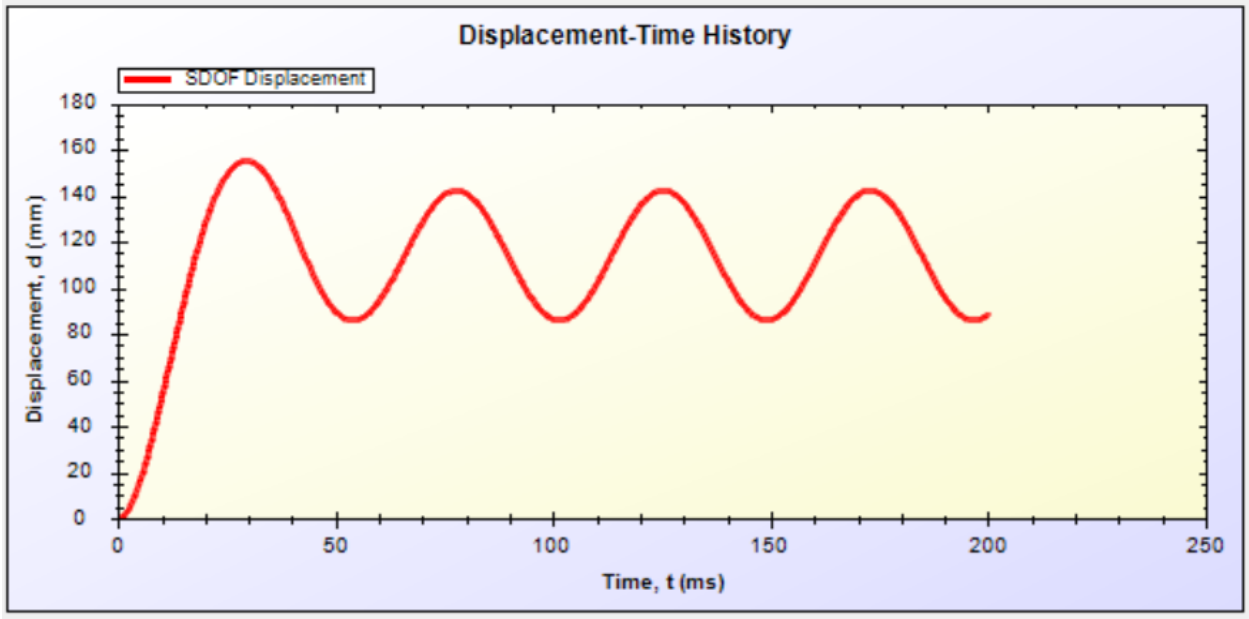

B 22: SDOF for specimen M-9FH – Blast 2

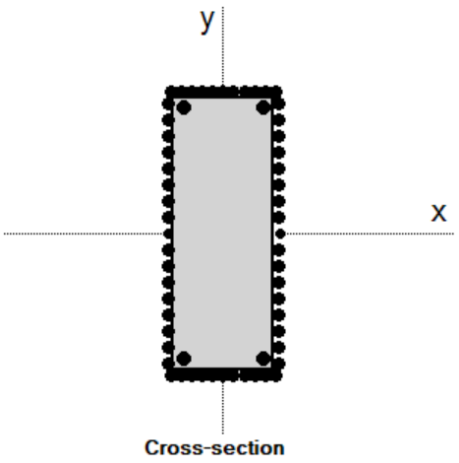

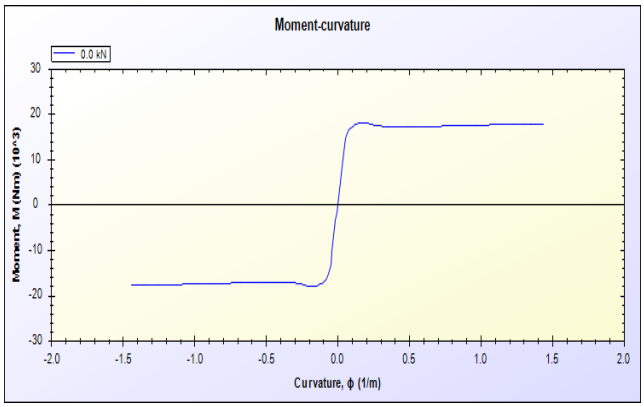

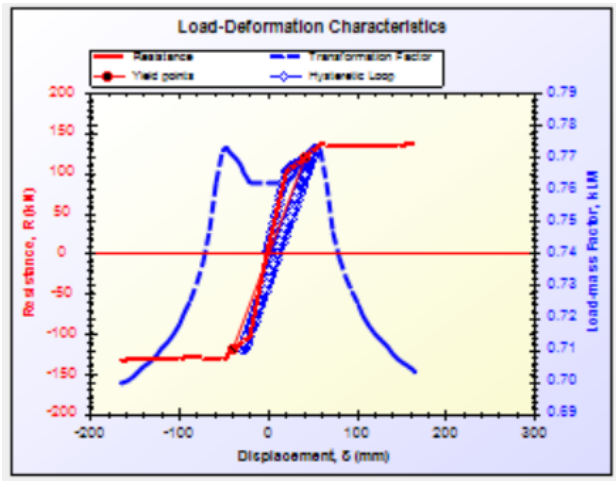

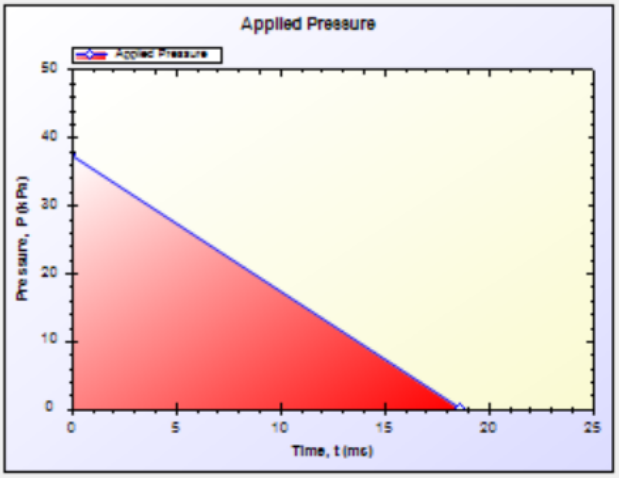

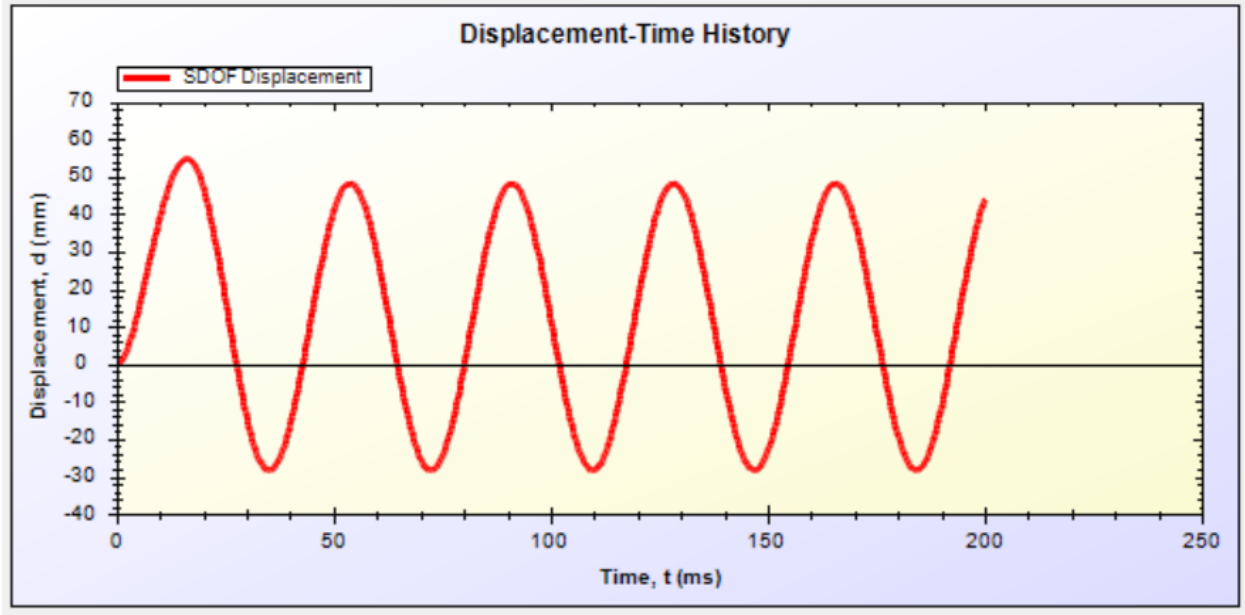

B 23: SDOF for specimen M-10FH – Blast 1

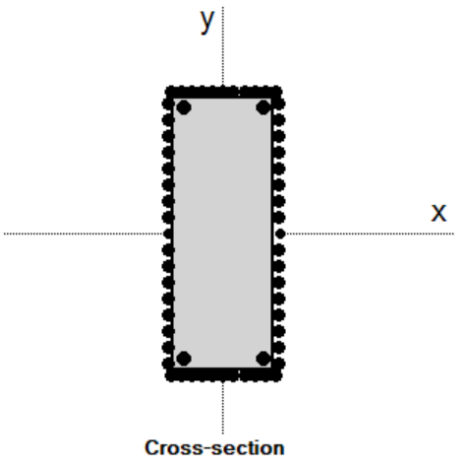

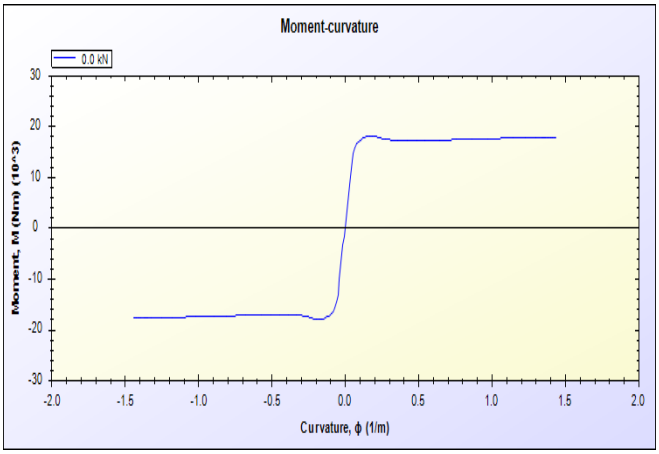

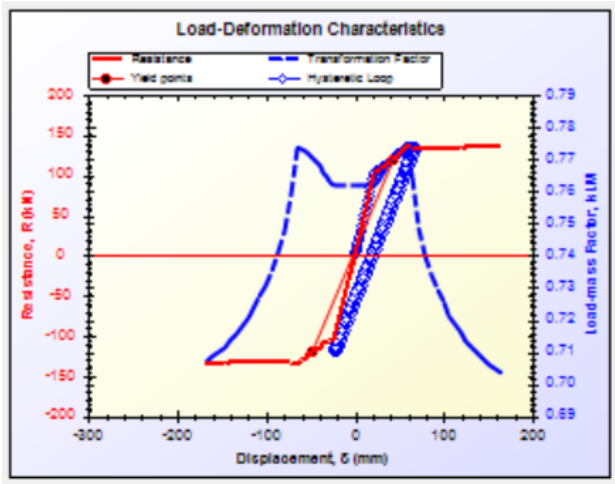

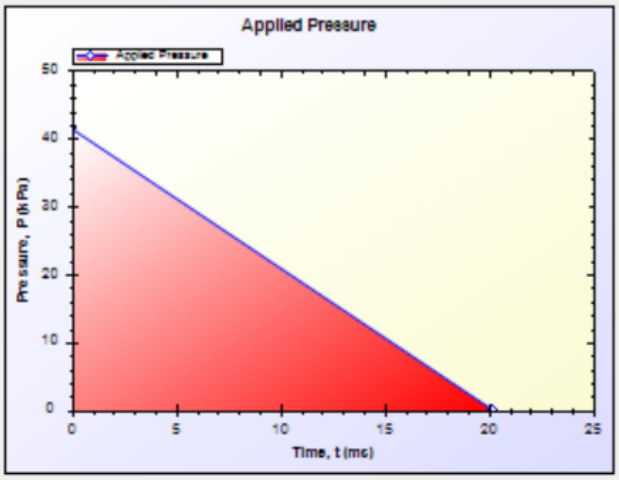

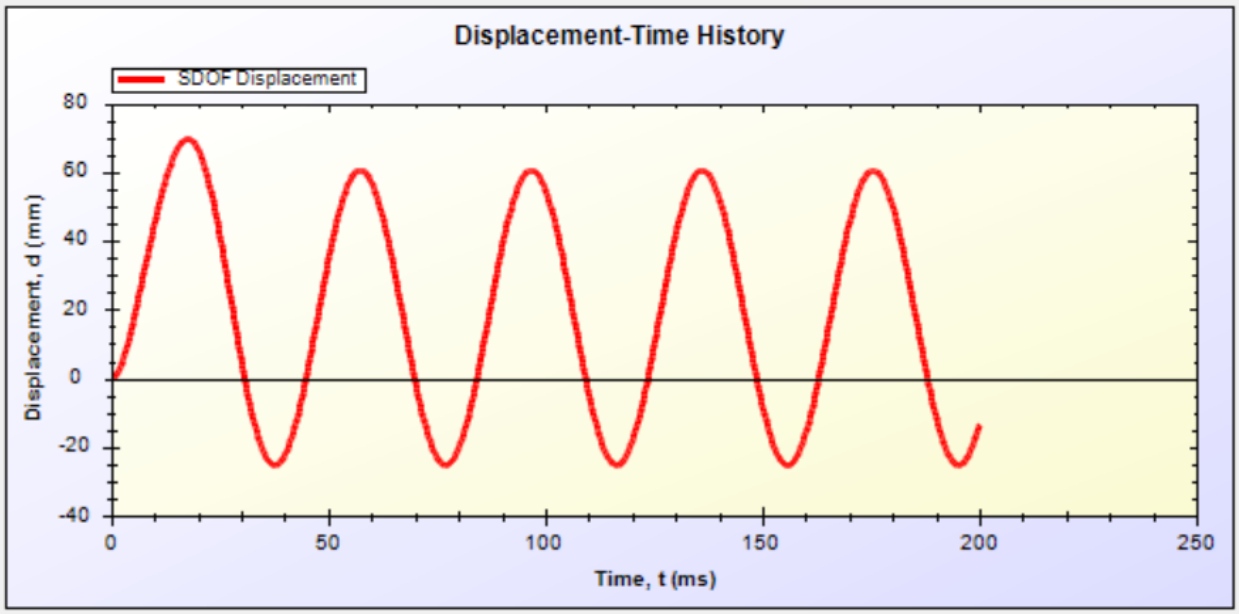

B 24: SDOF for specimen M-10FH – Blast 2

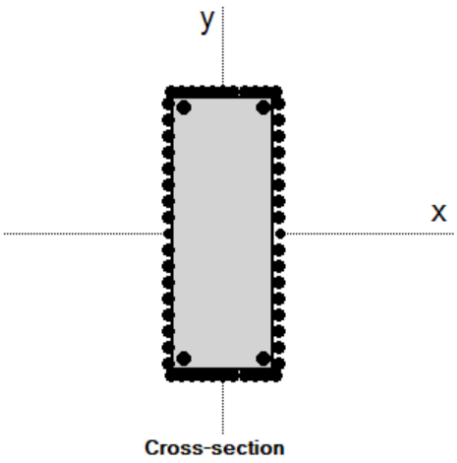

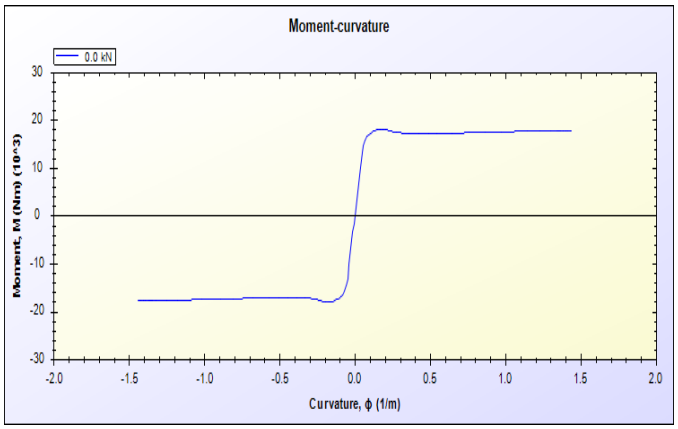

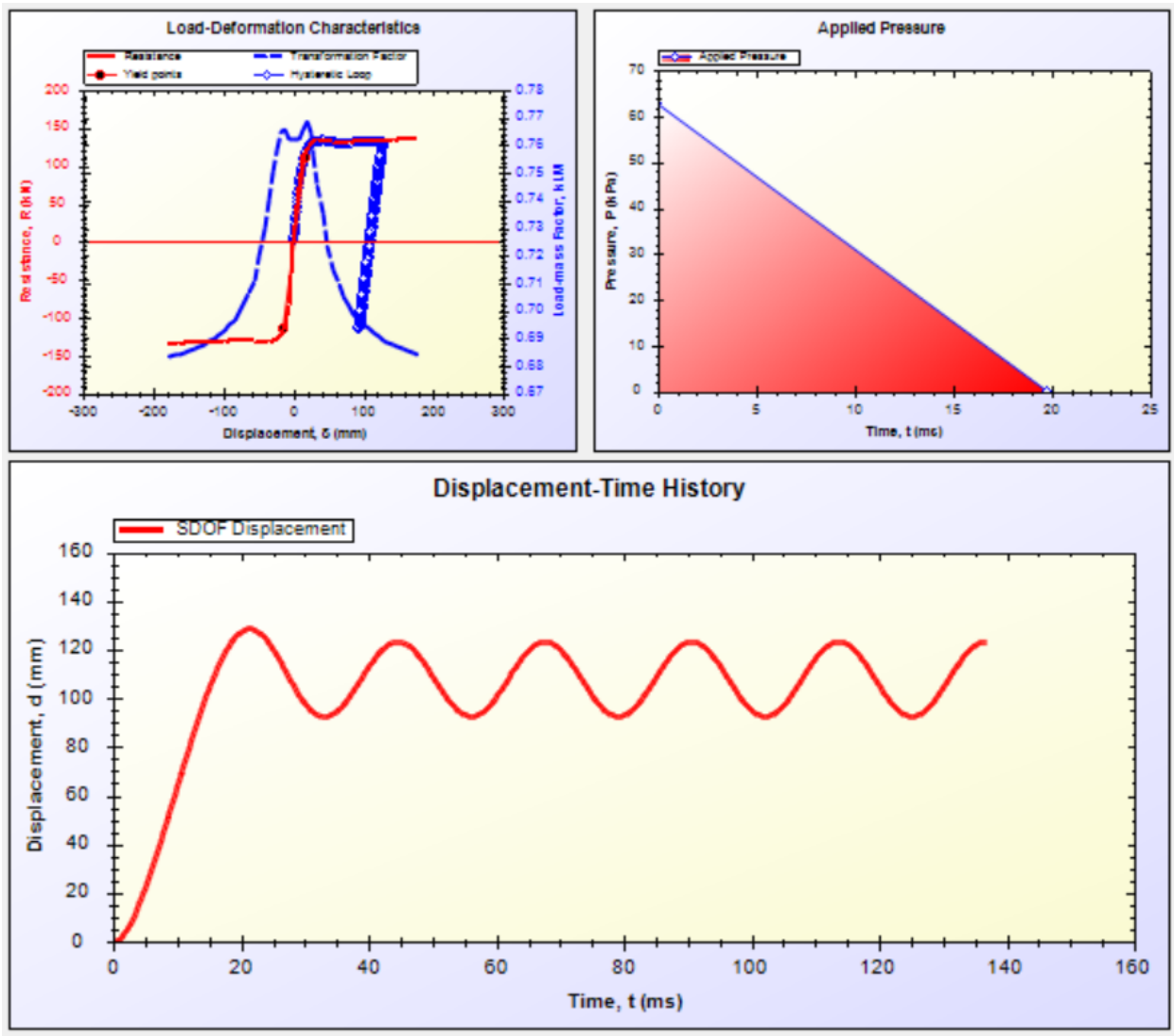

B 25: SDOF for specimen M-10FH – Blast 3

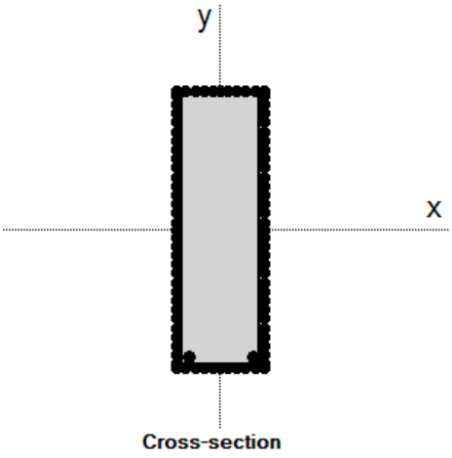

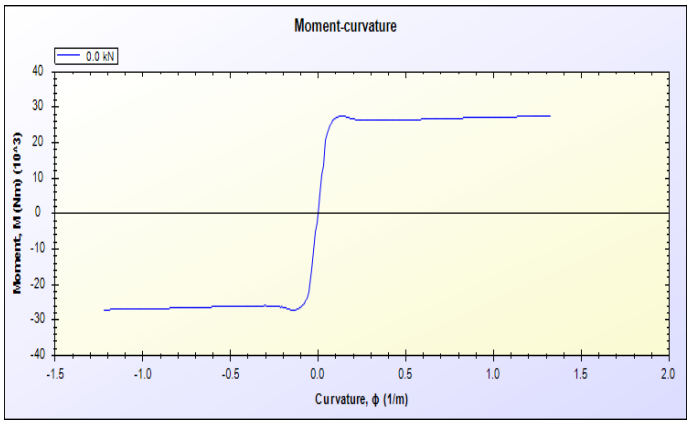

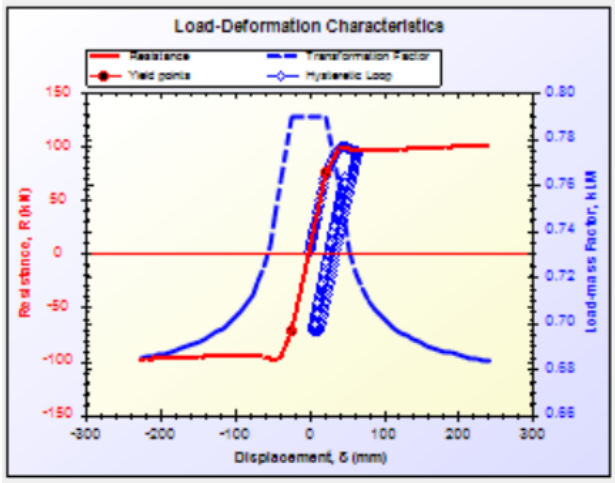

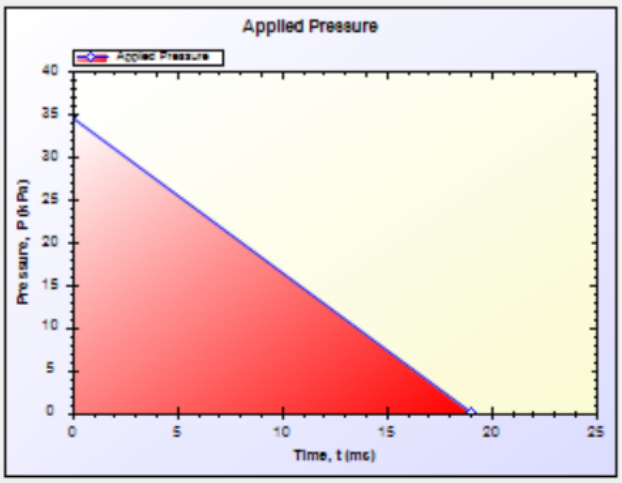

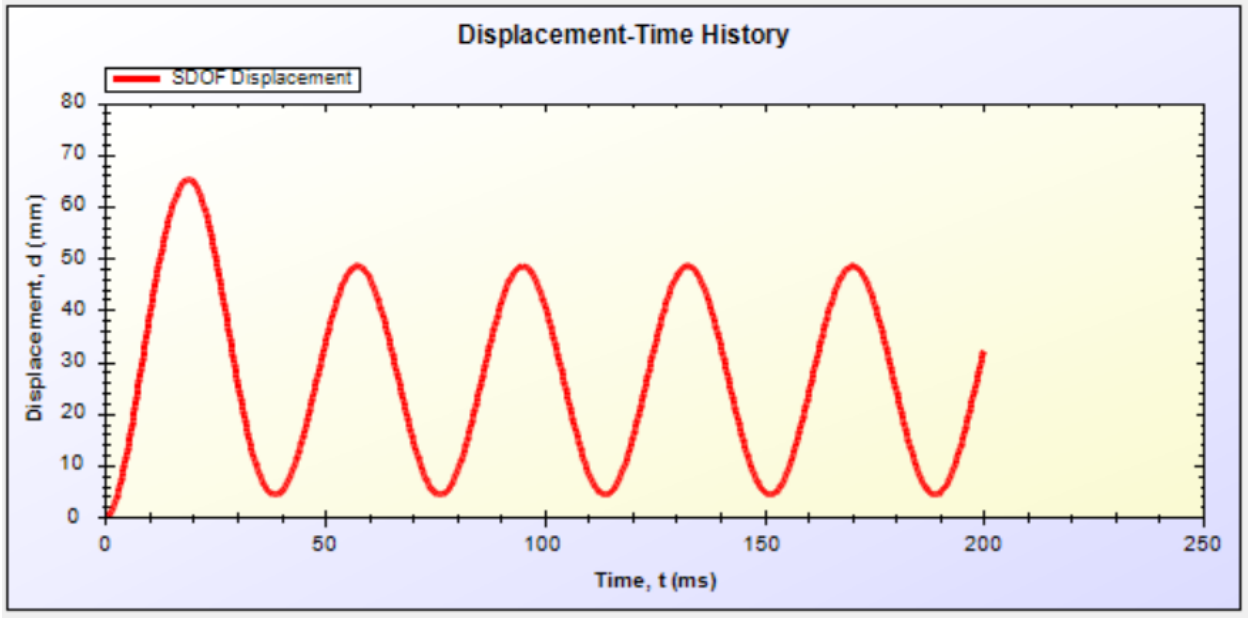

B 26: SDOF for specimen M-11FH – Blast 1

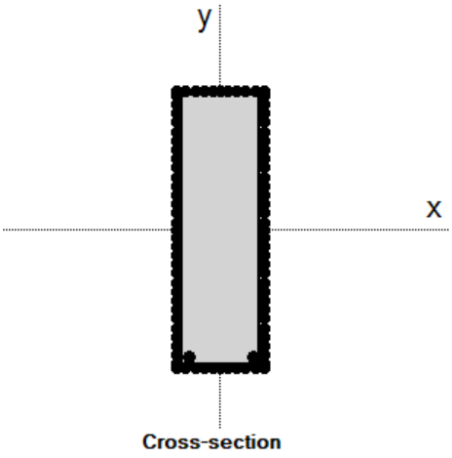

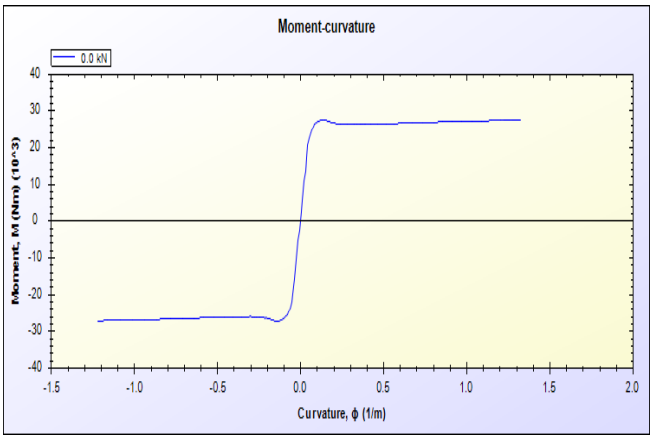

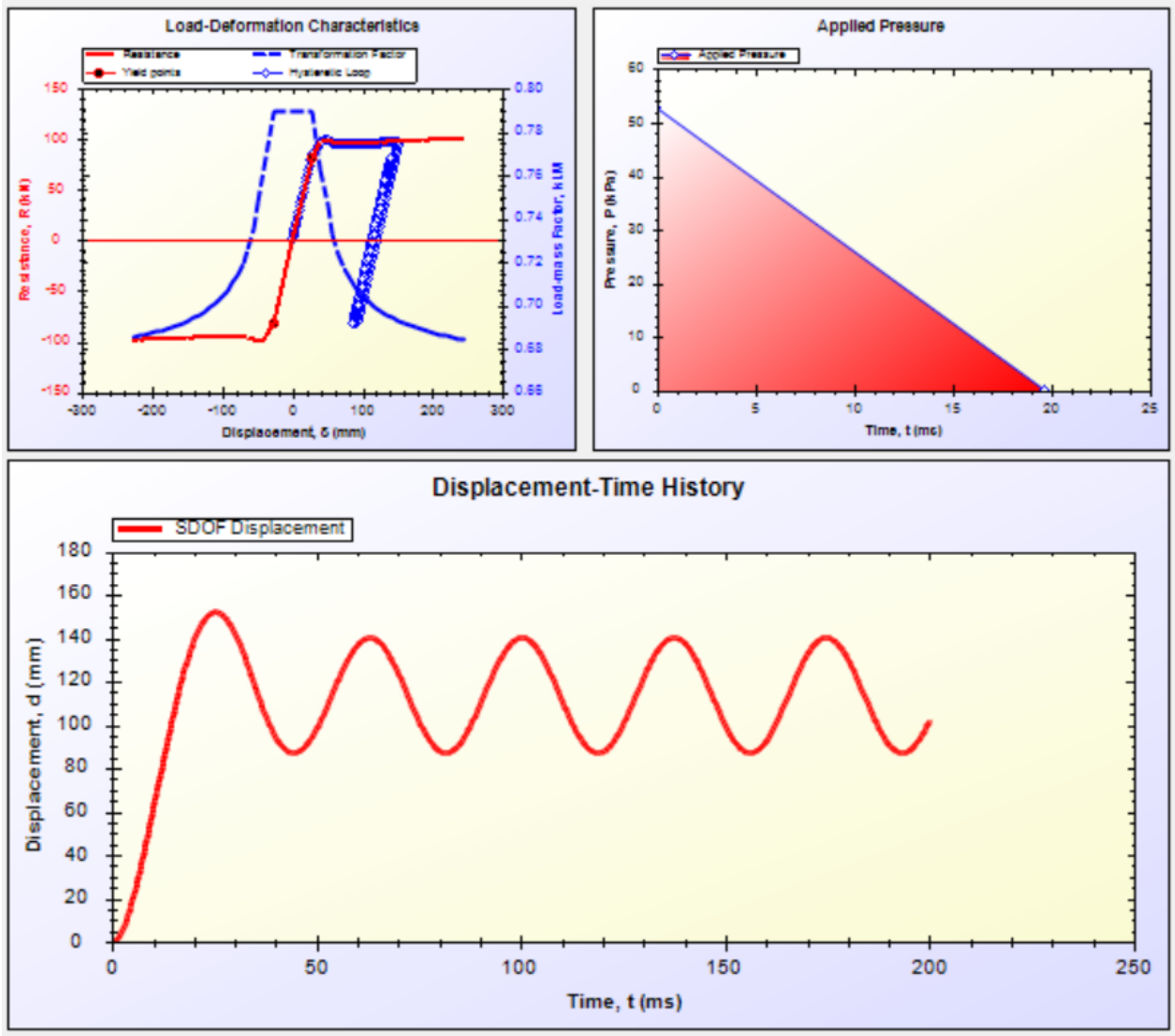

B 27: SDOF for specimen M-11FH – Blast 2

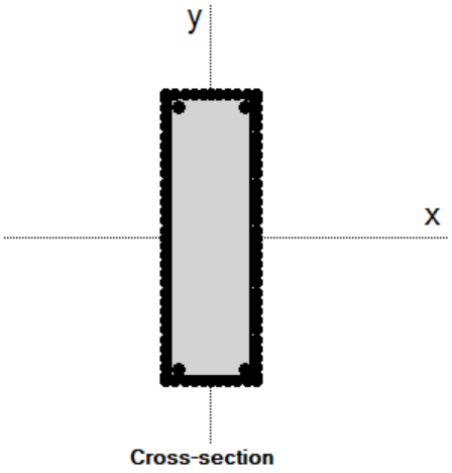

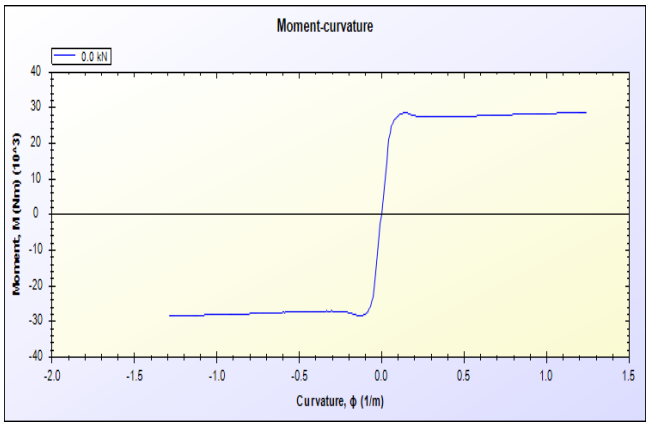

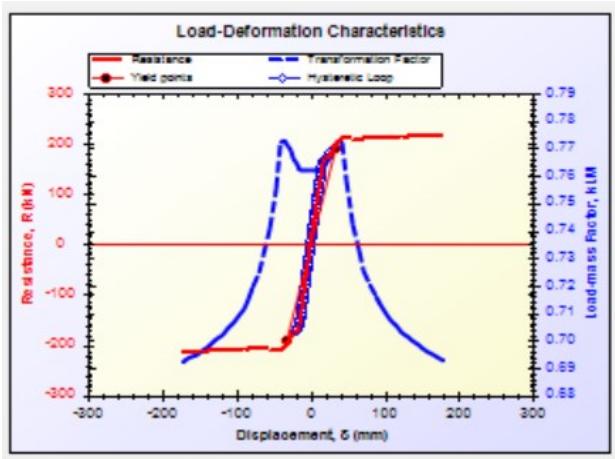

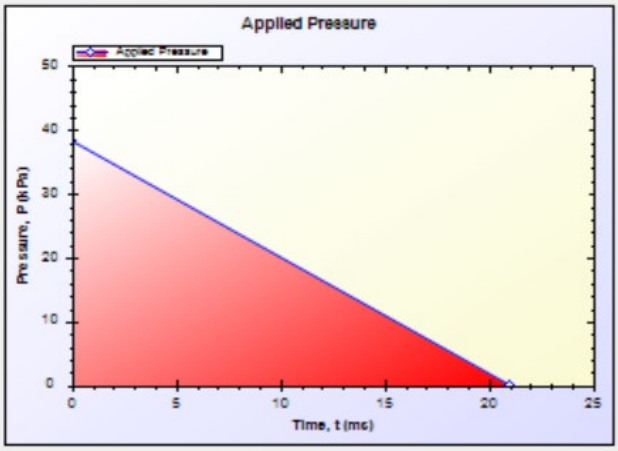

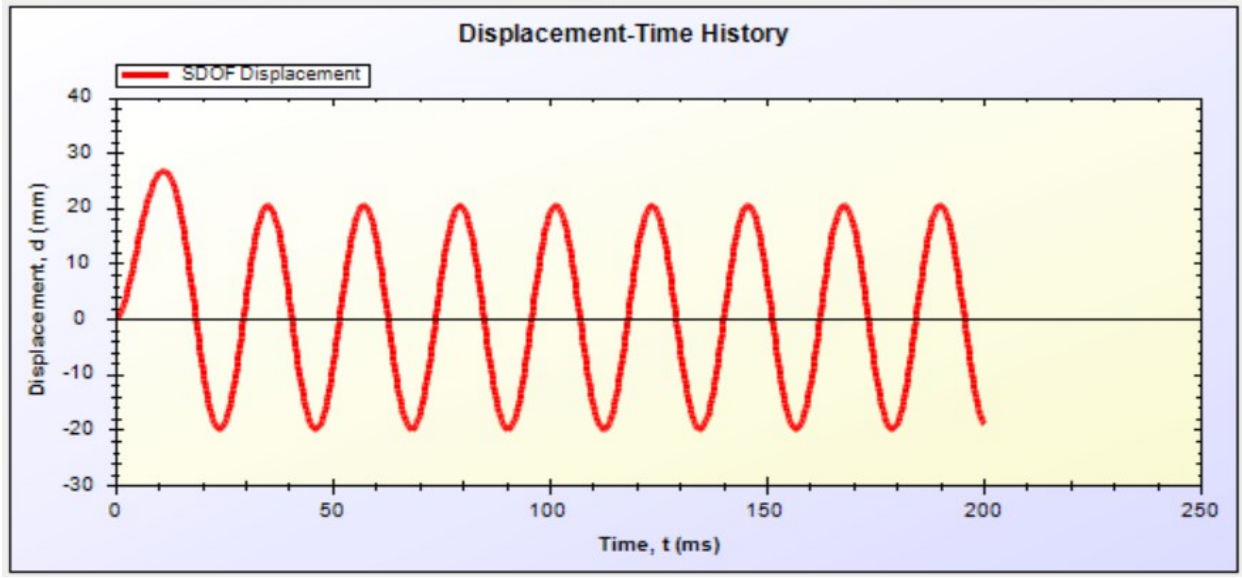

B 28: SDOF for specimen M-12FH – Blast 1

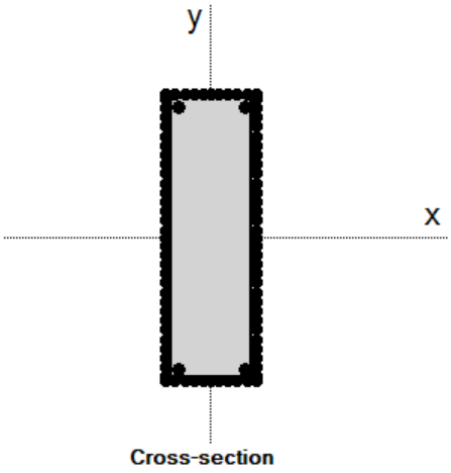

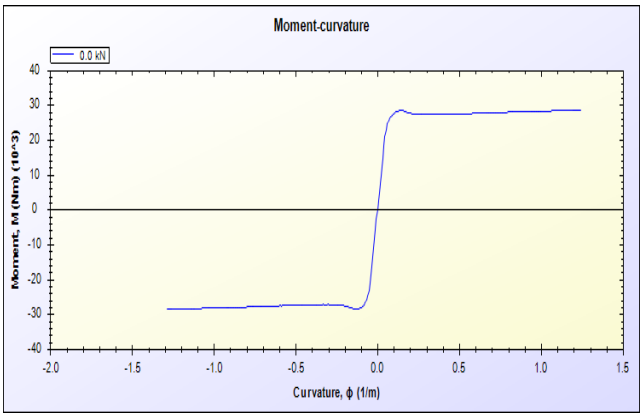

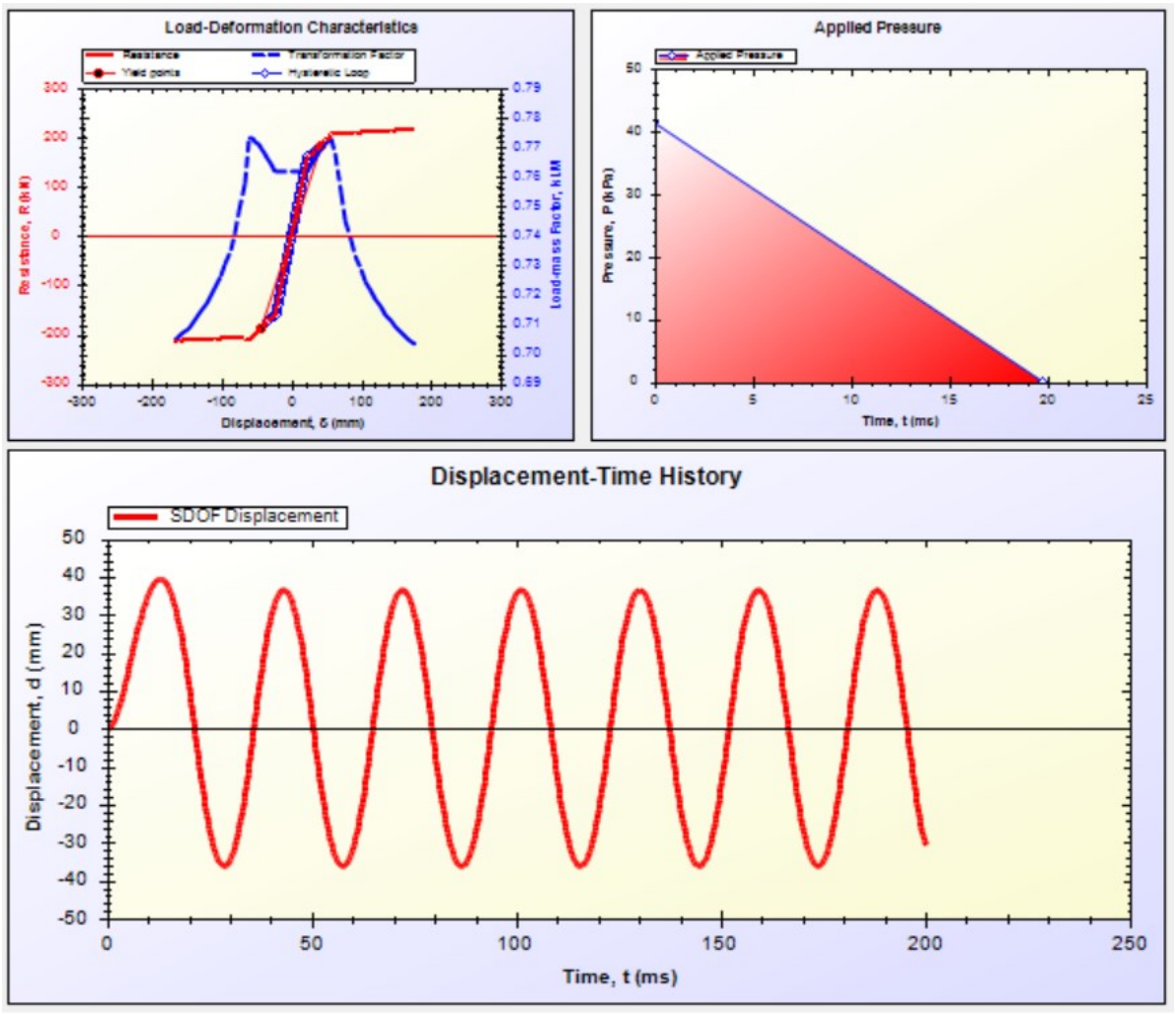

B 29: SDOF for specimen M-12FH – Blast 2

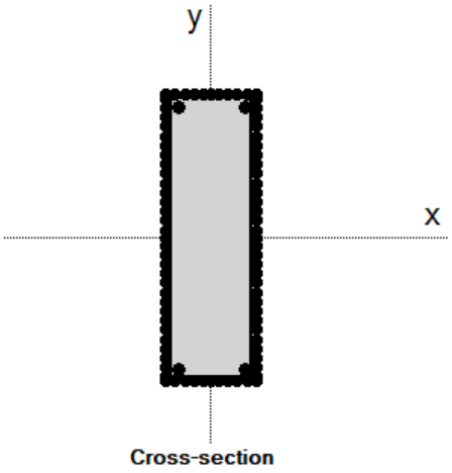

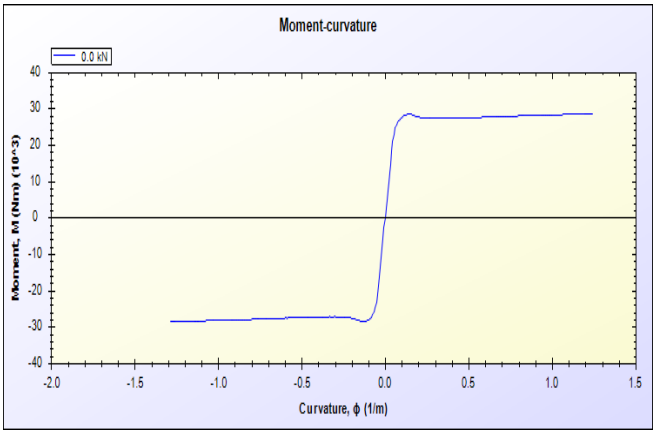

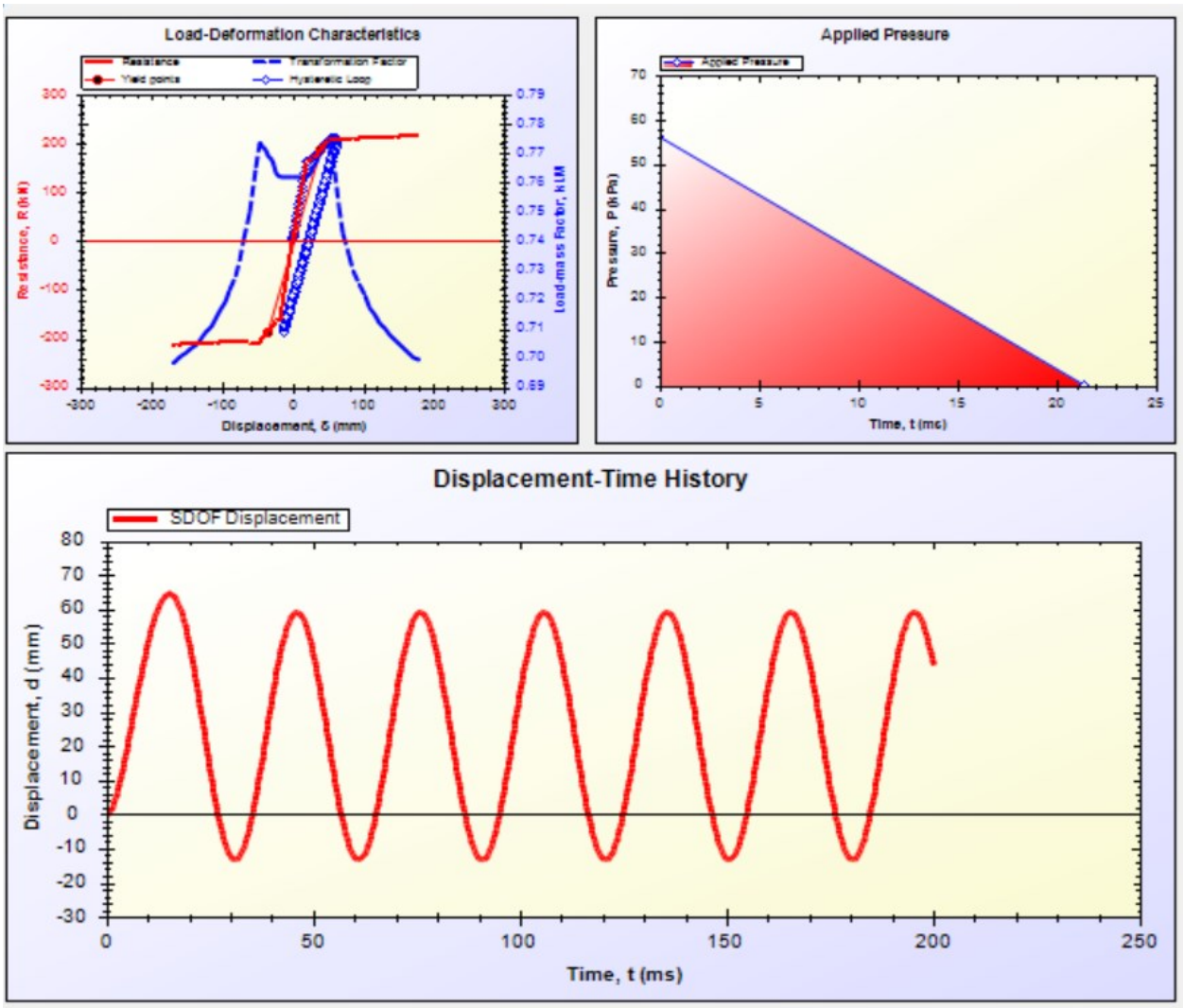

B 30: SDOF for specimen M-12FH – Blast 3

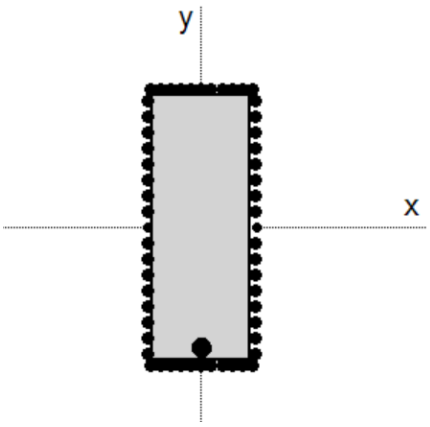

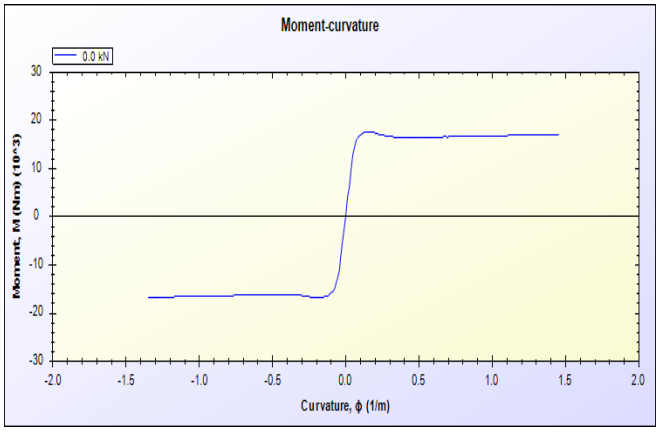

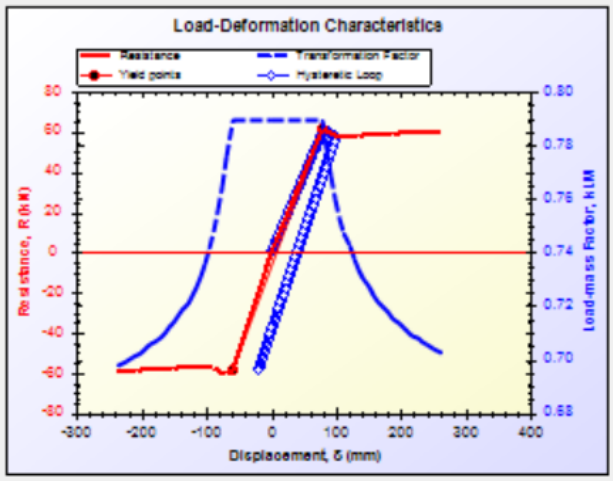

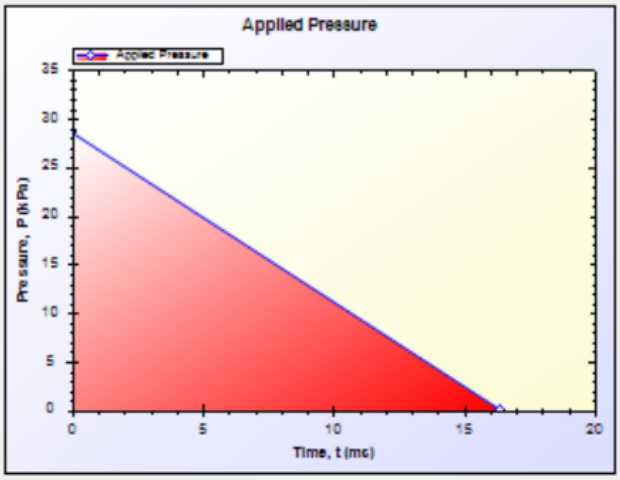

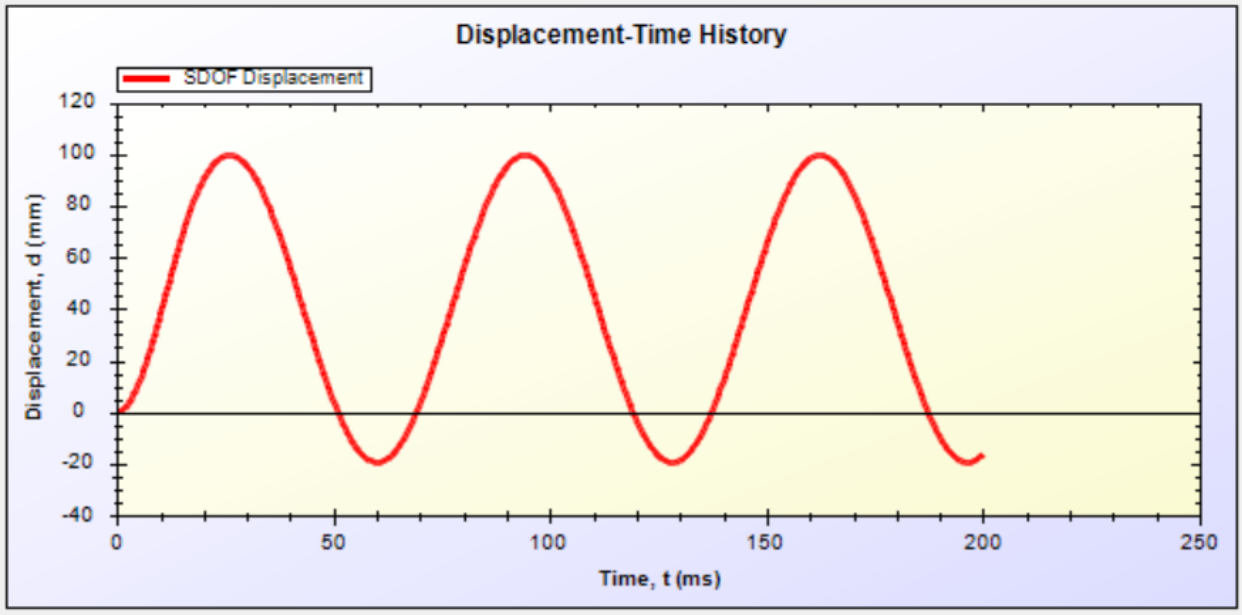

B 31: SDOF for specimen M-13FH – Blast 1

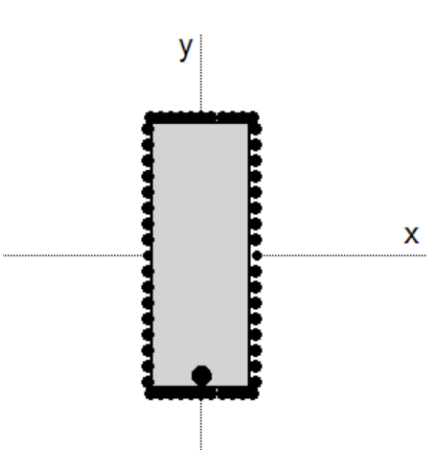

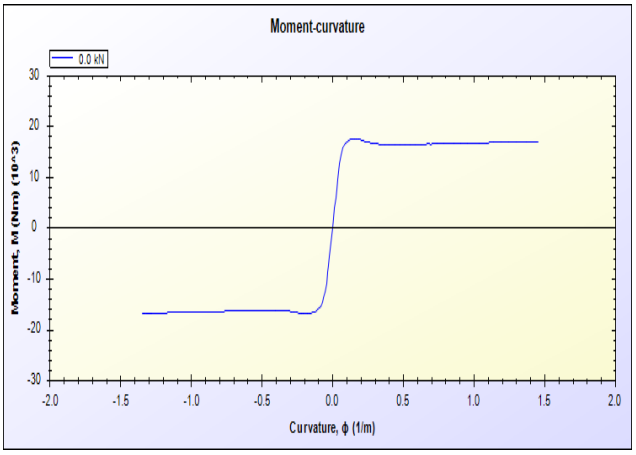

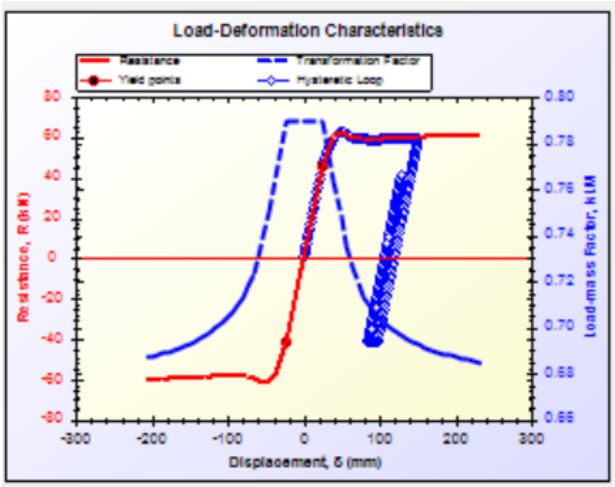

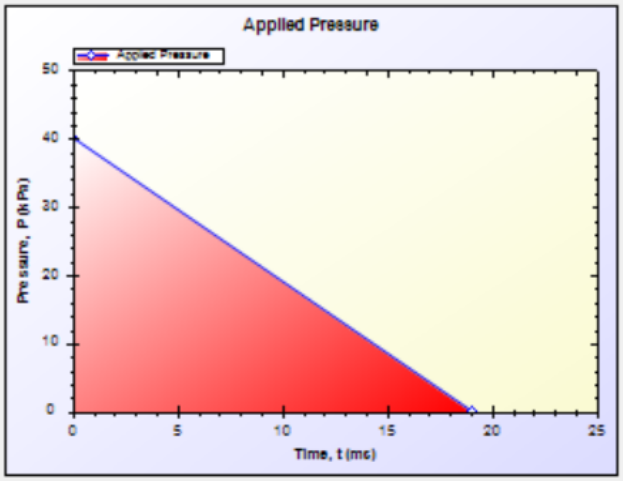

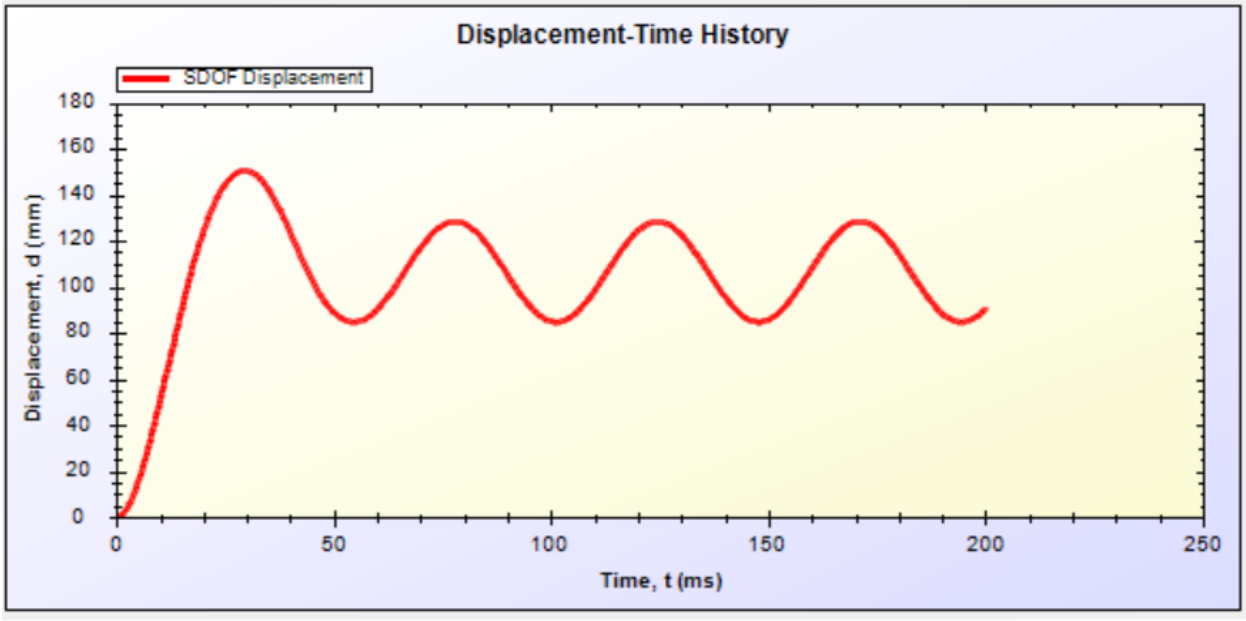

B 32: SDOF for specimen M-13FH – Blast 2

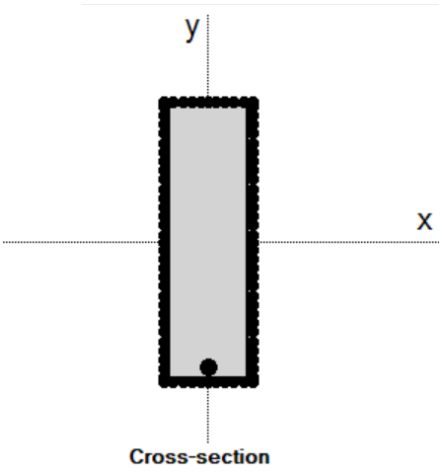

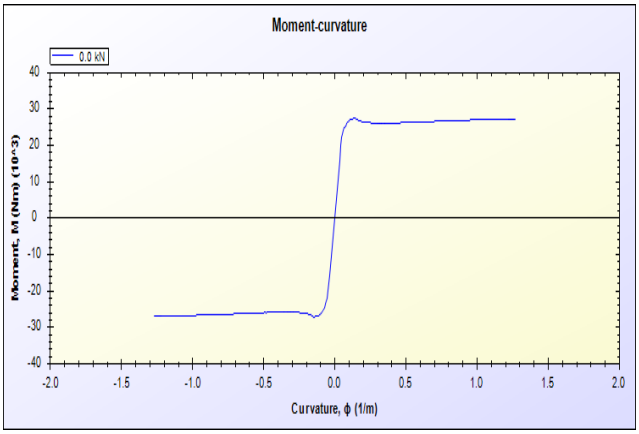

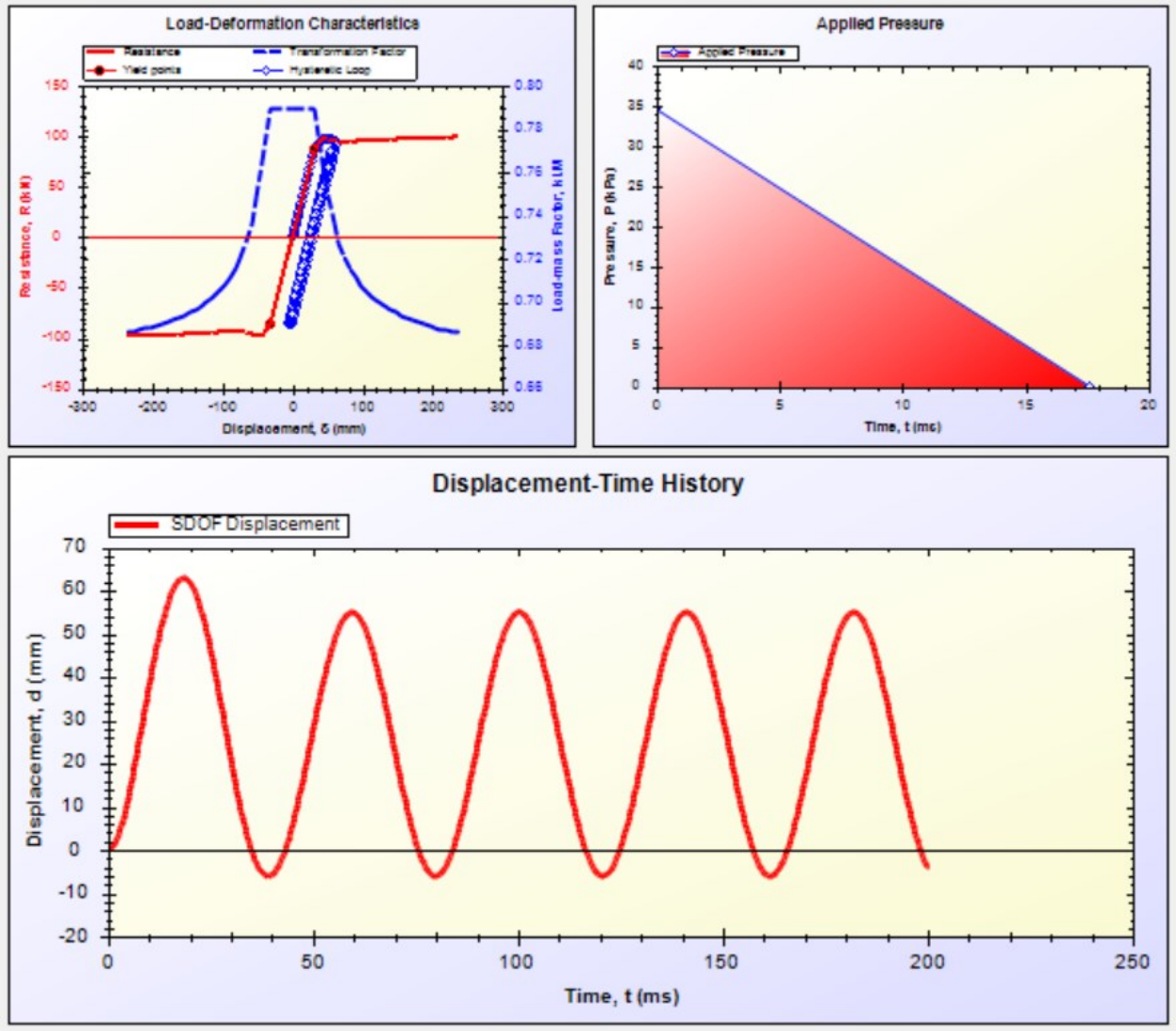

B 33: SDOF for specimen M-14FH – Blast 1

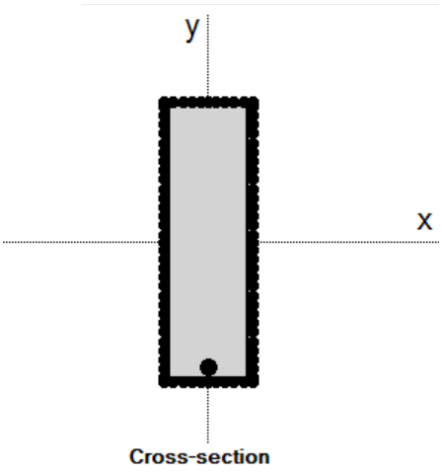

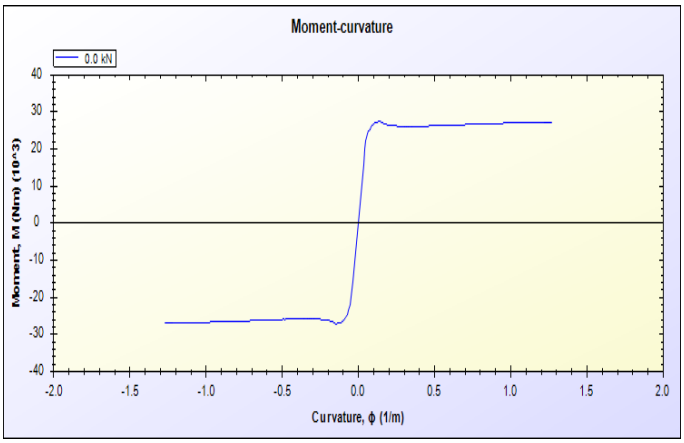

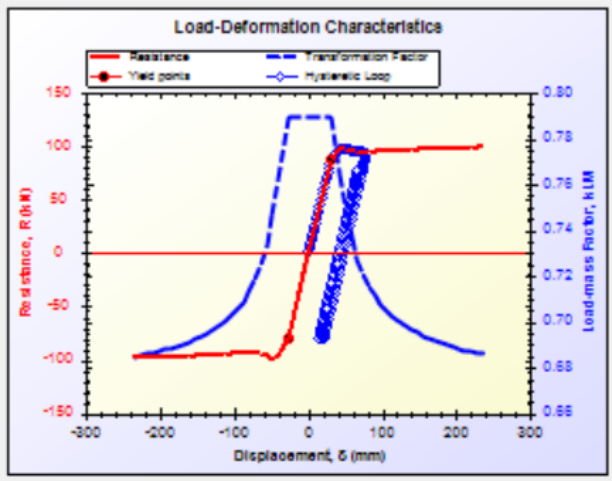

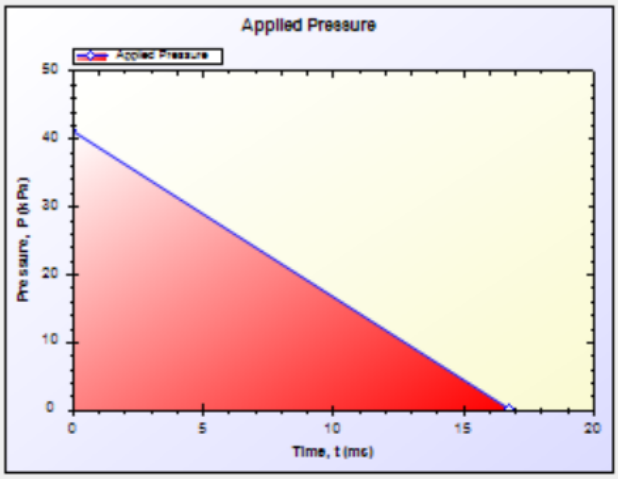

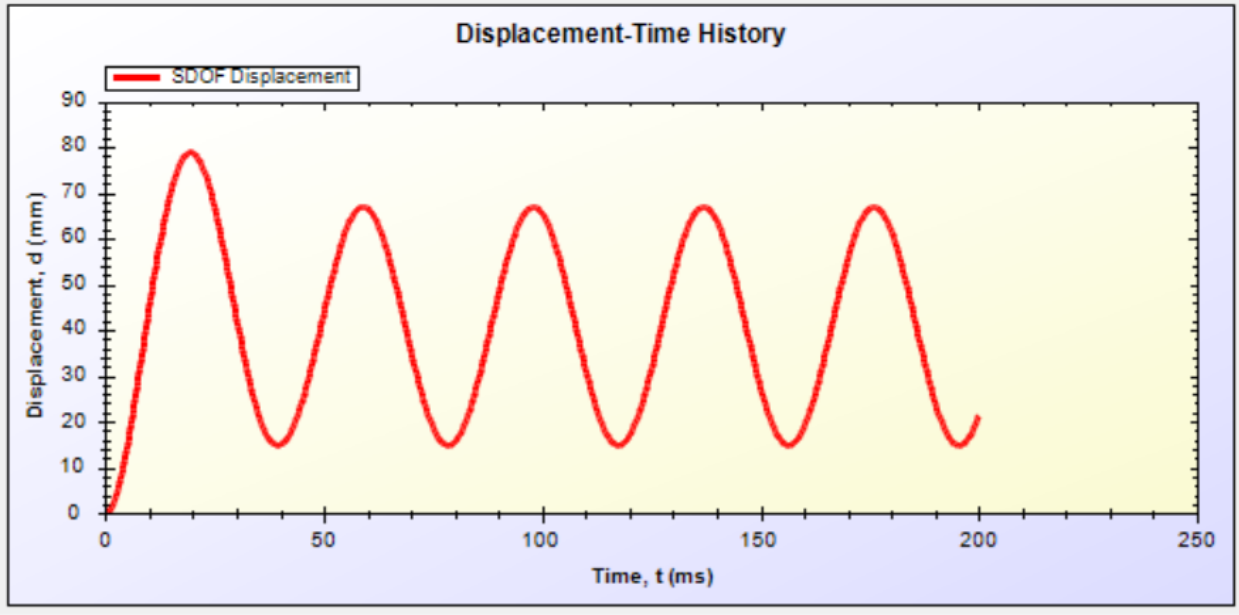

B 34: SDOF for specimen M-14FH – Blast 2

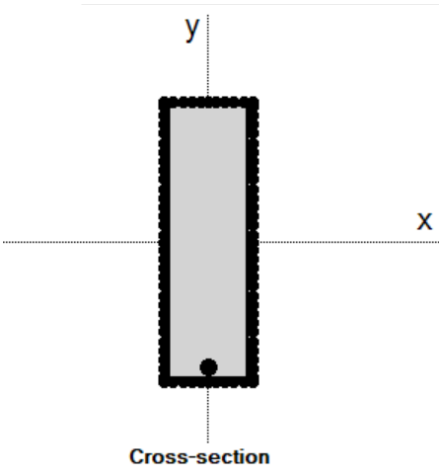

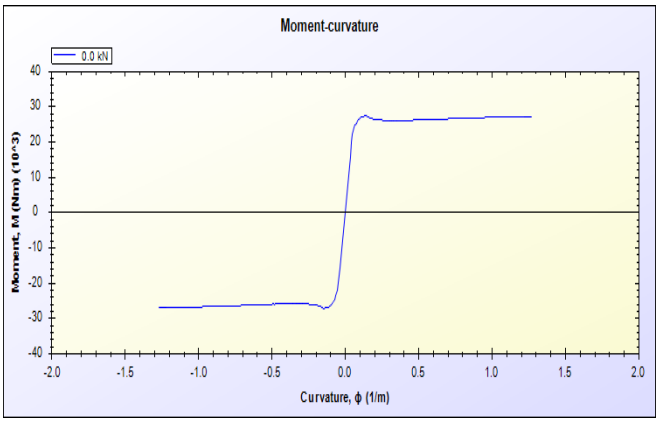

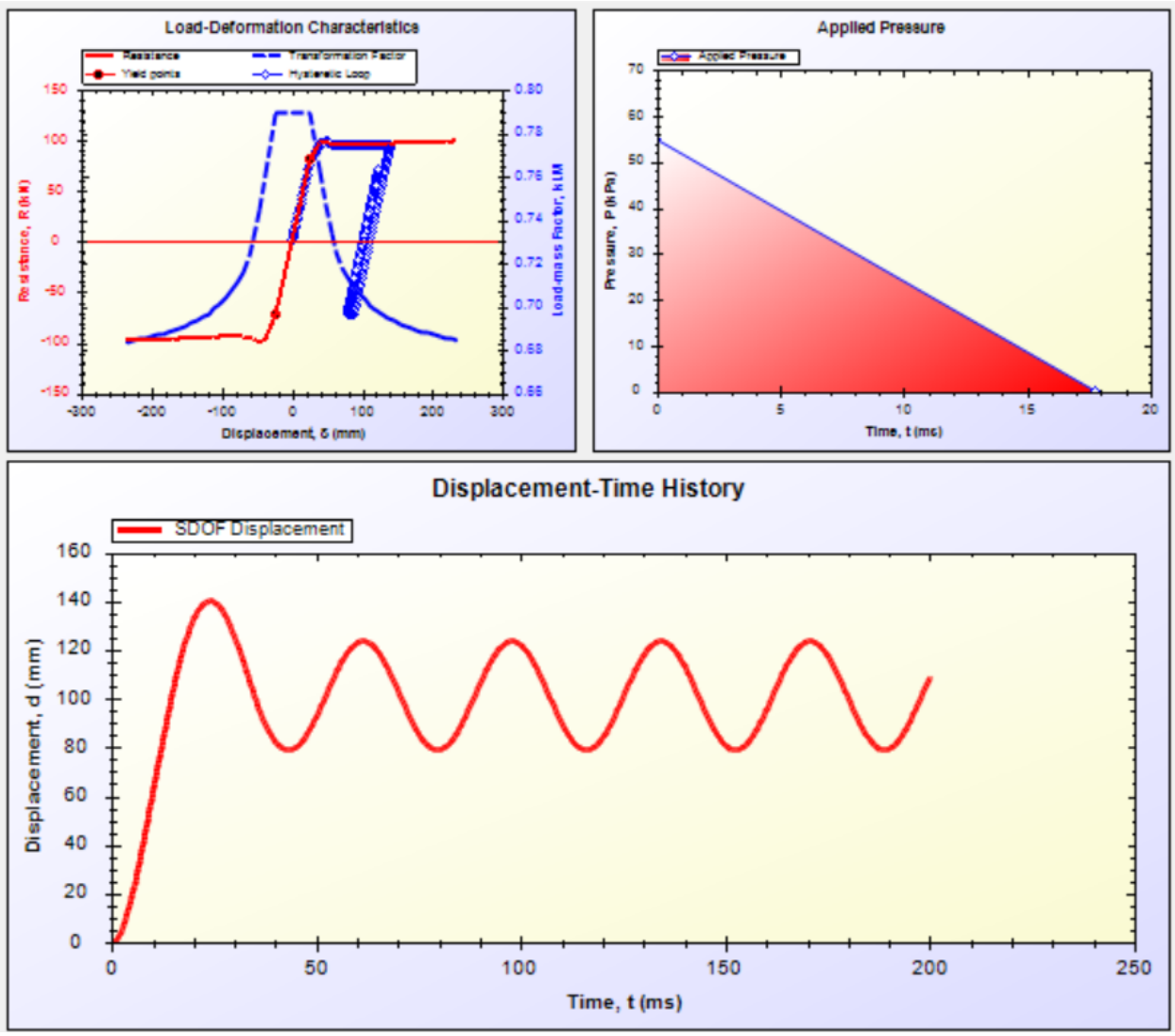

B 35: SDOF for specimen M-14FH – Blast 3

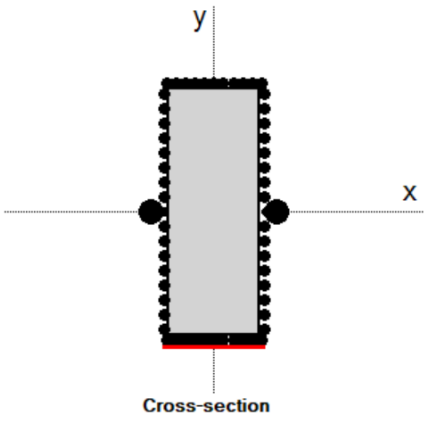

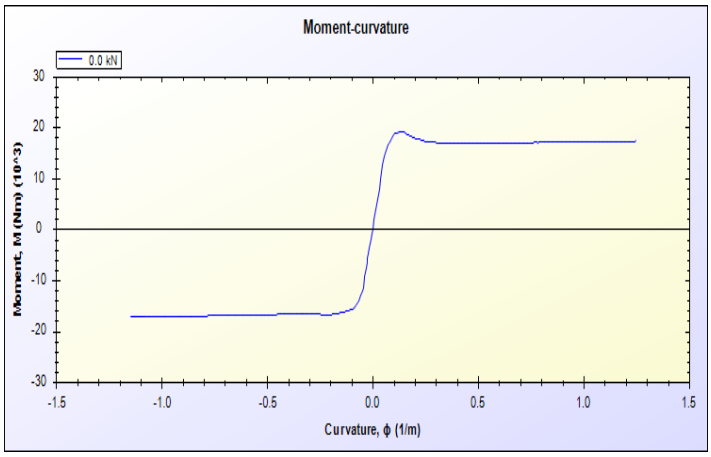

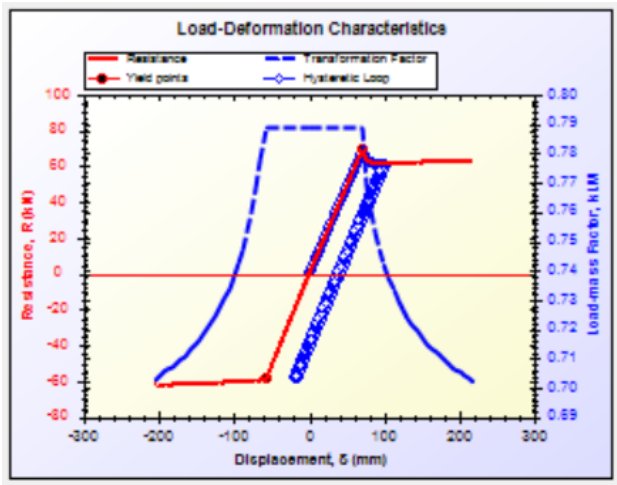

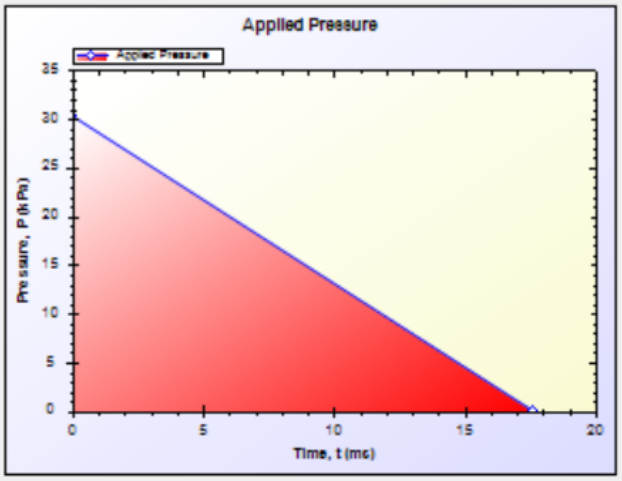

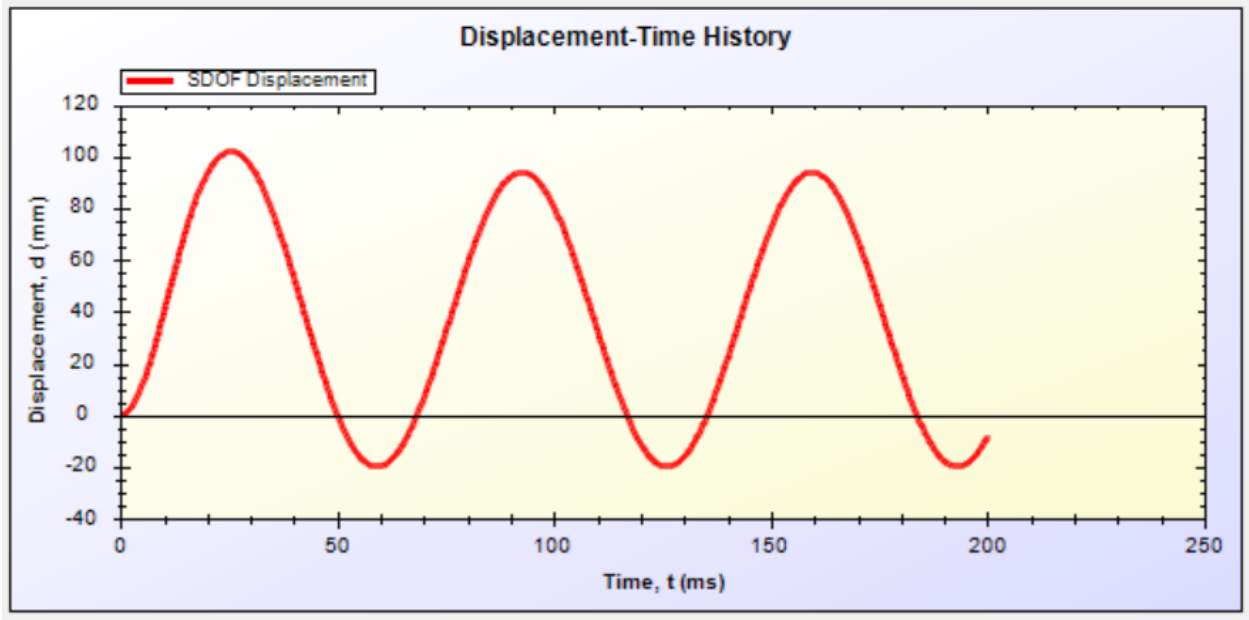

B 36: SDOF for specimen M-15FR – Blast 1

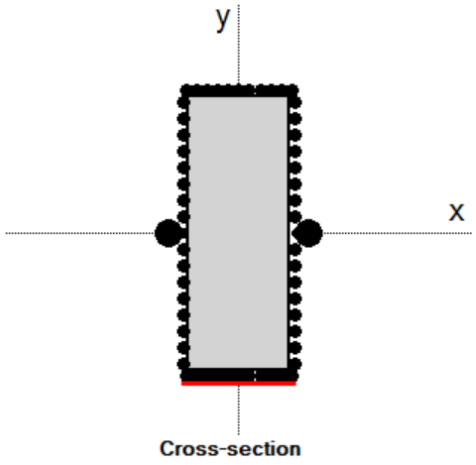

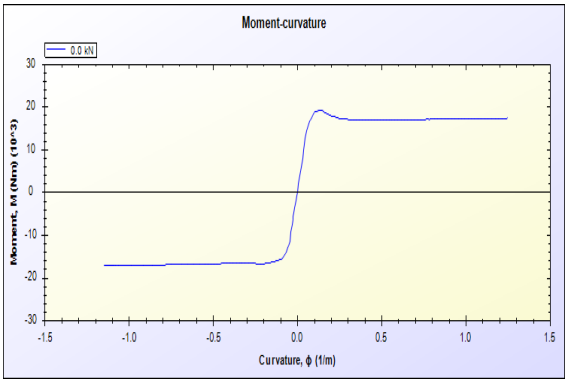

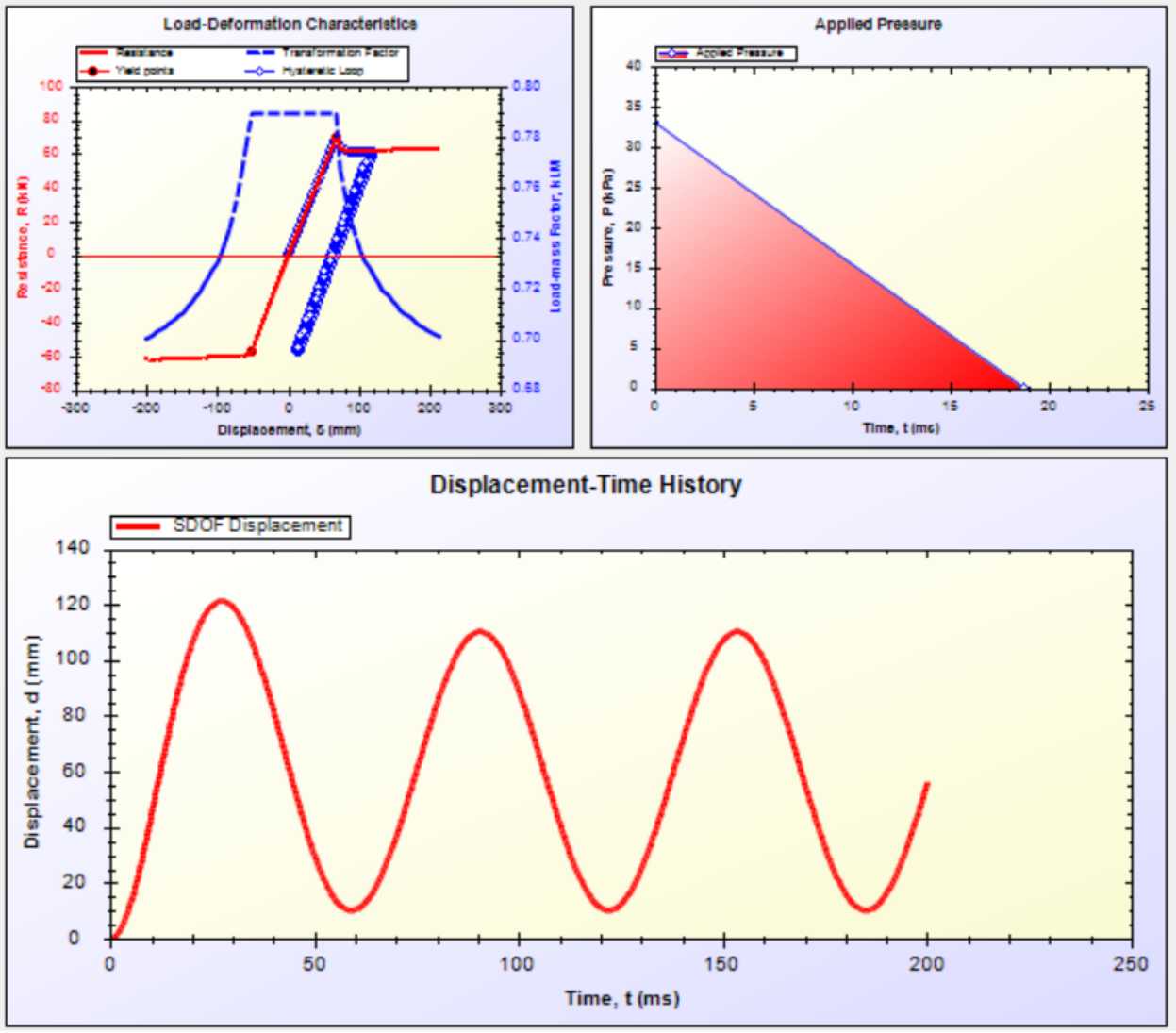

B 37: SDOF for specimen M-15FR – Blast 2

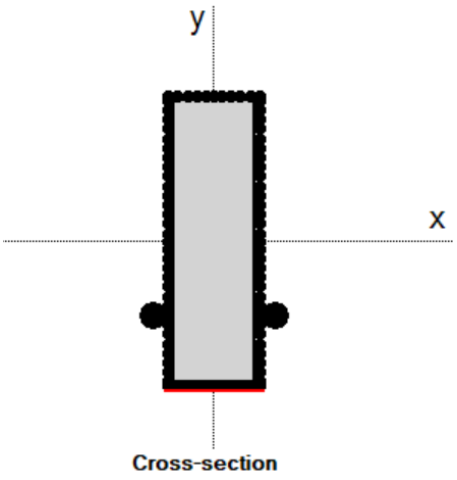

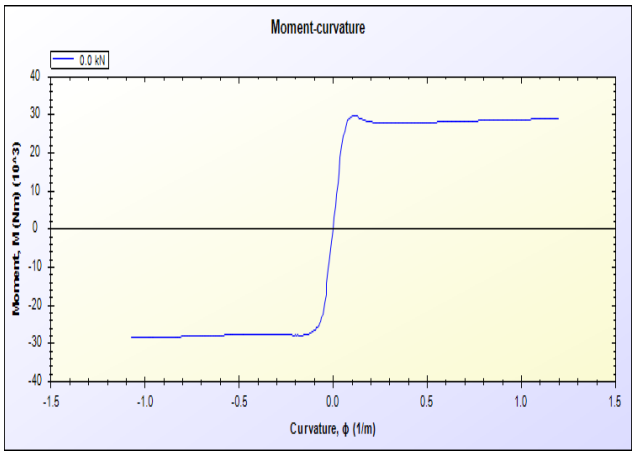

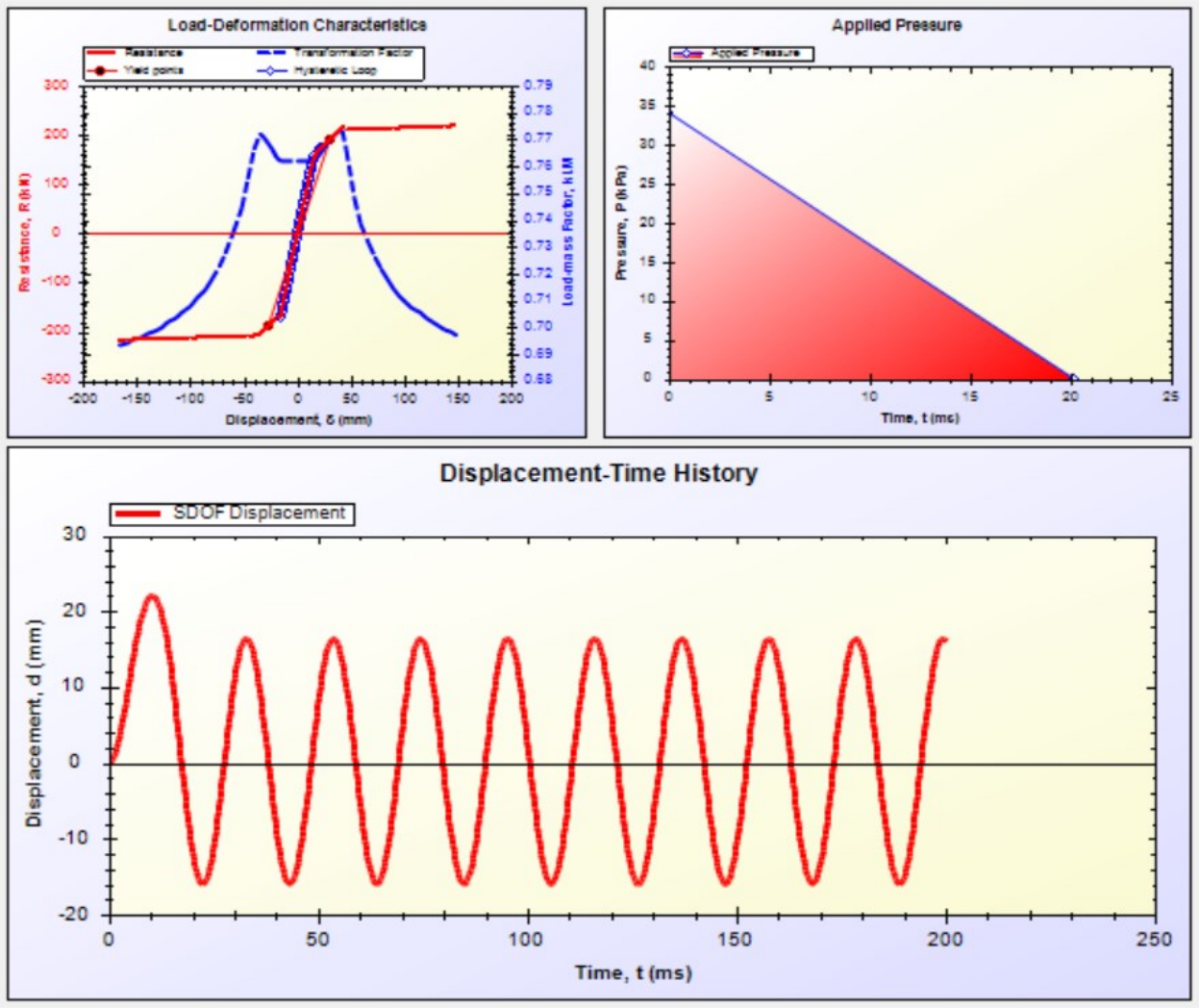

B 38: SDOF for specimen M-16FR – Blast 1

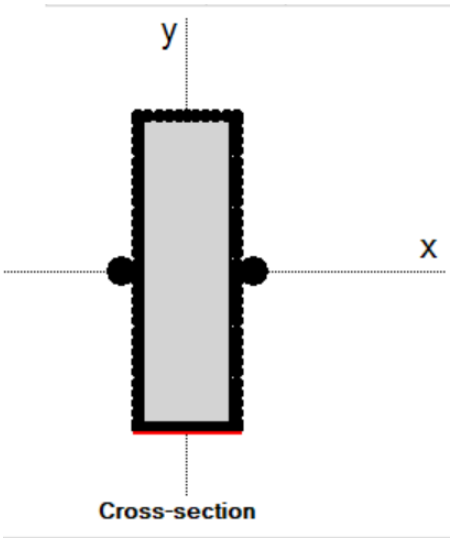

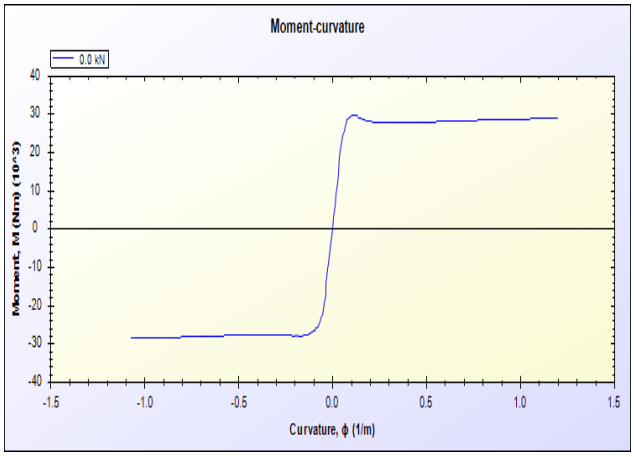

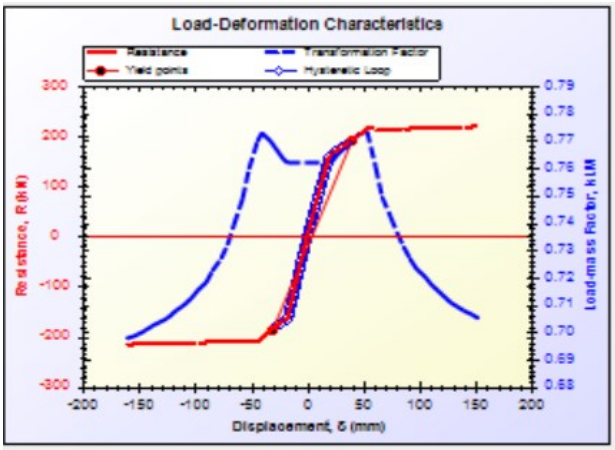

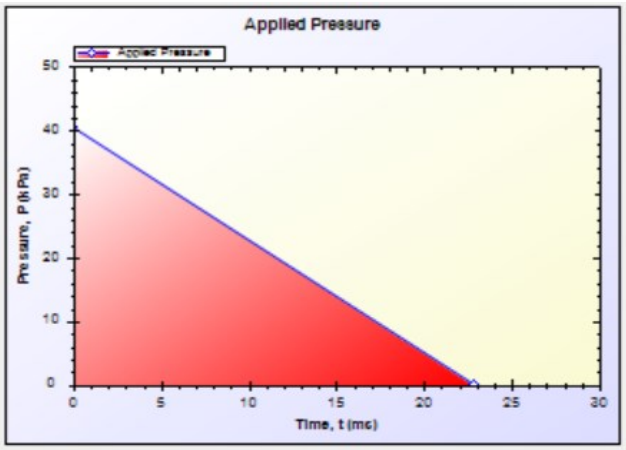

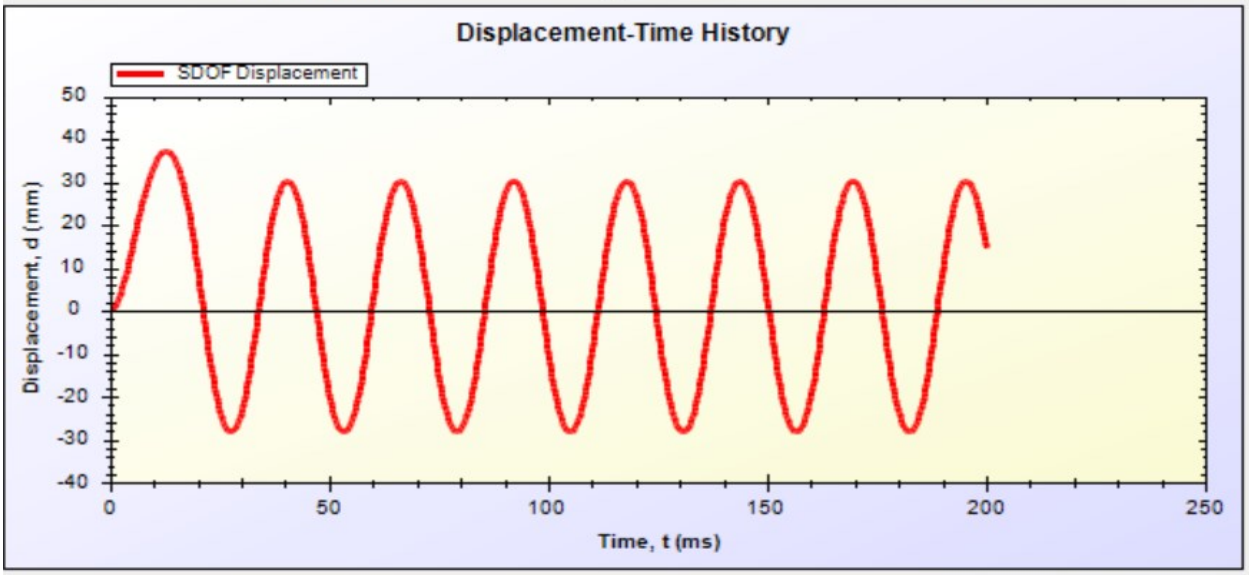

B 39: SDOF for specimen M-16FR – Blast 2

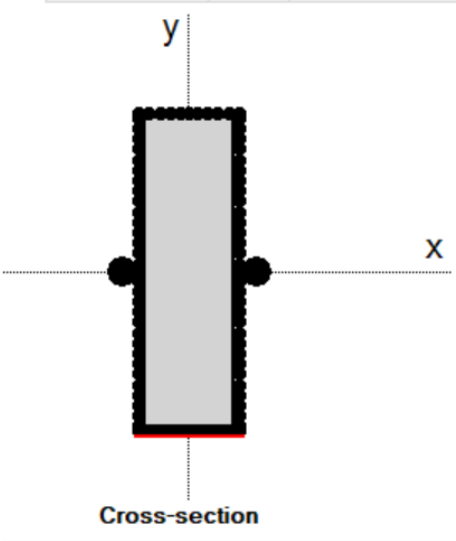

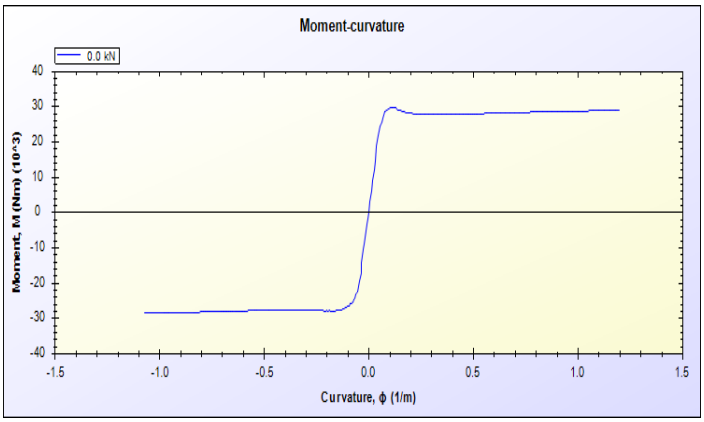

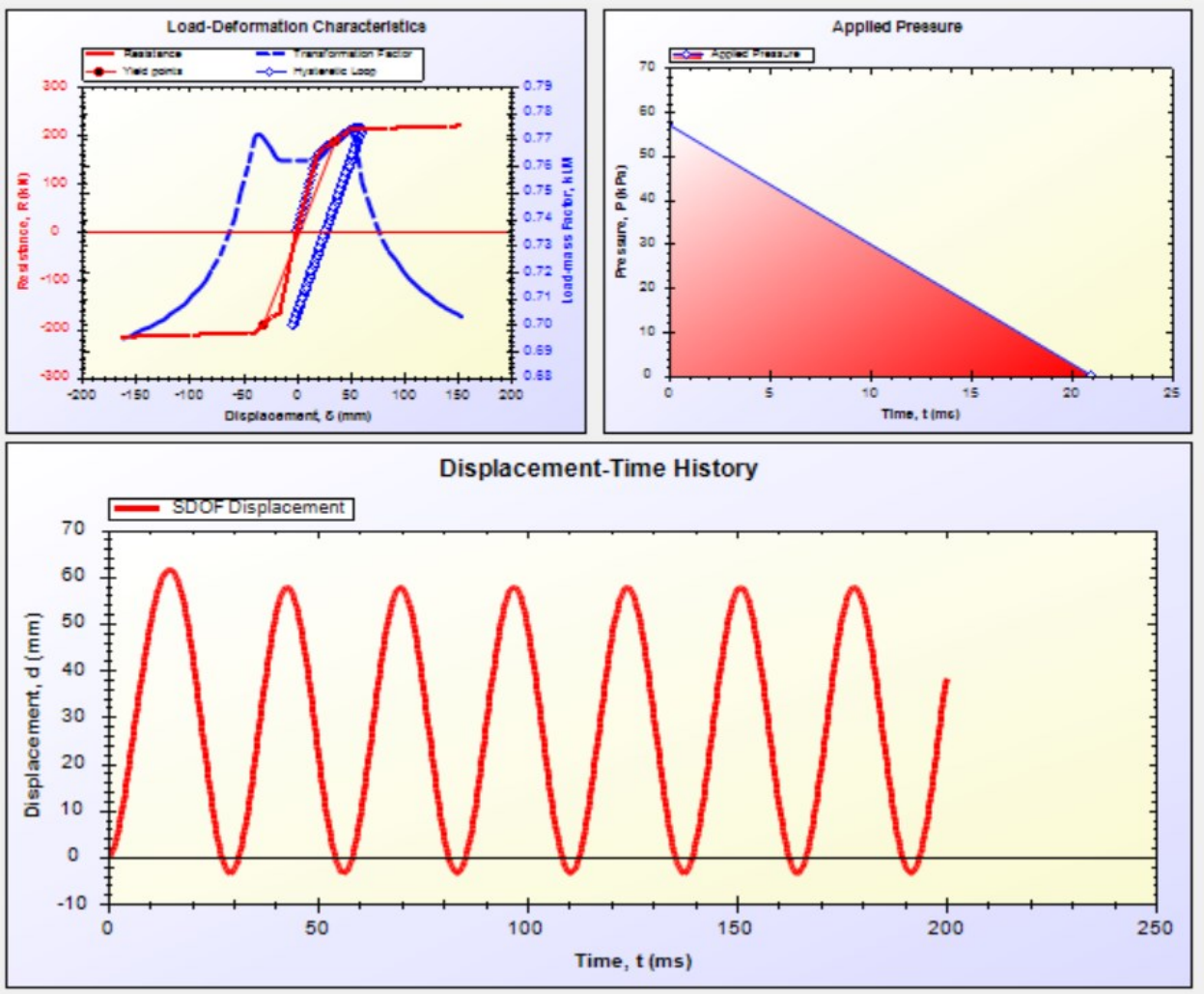

B 40: SDOF for specimen M-16FR – Blast 3

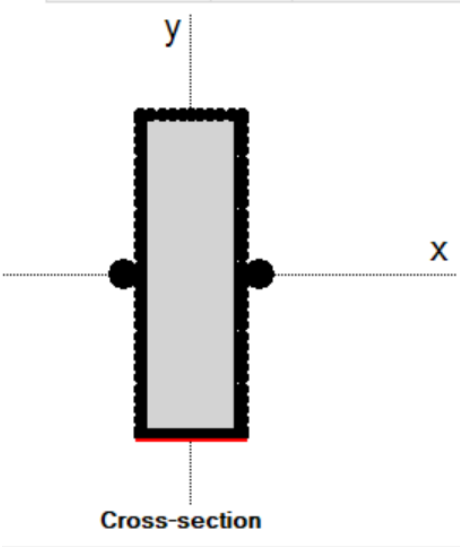

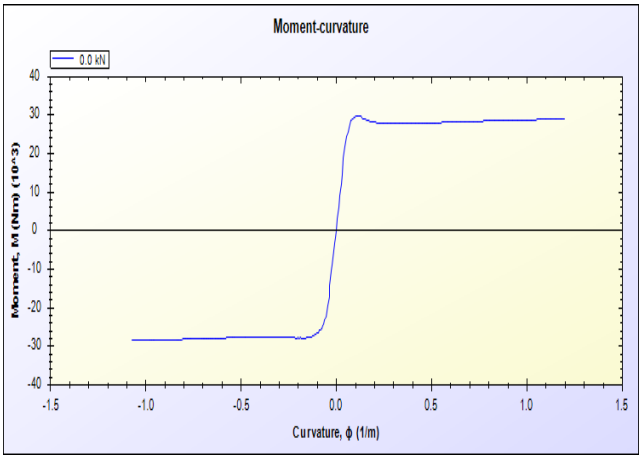

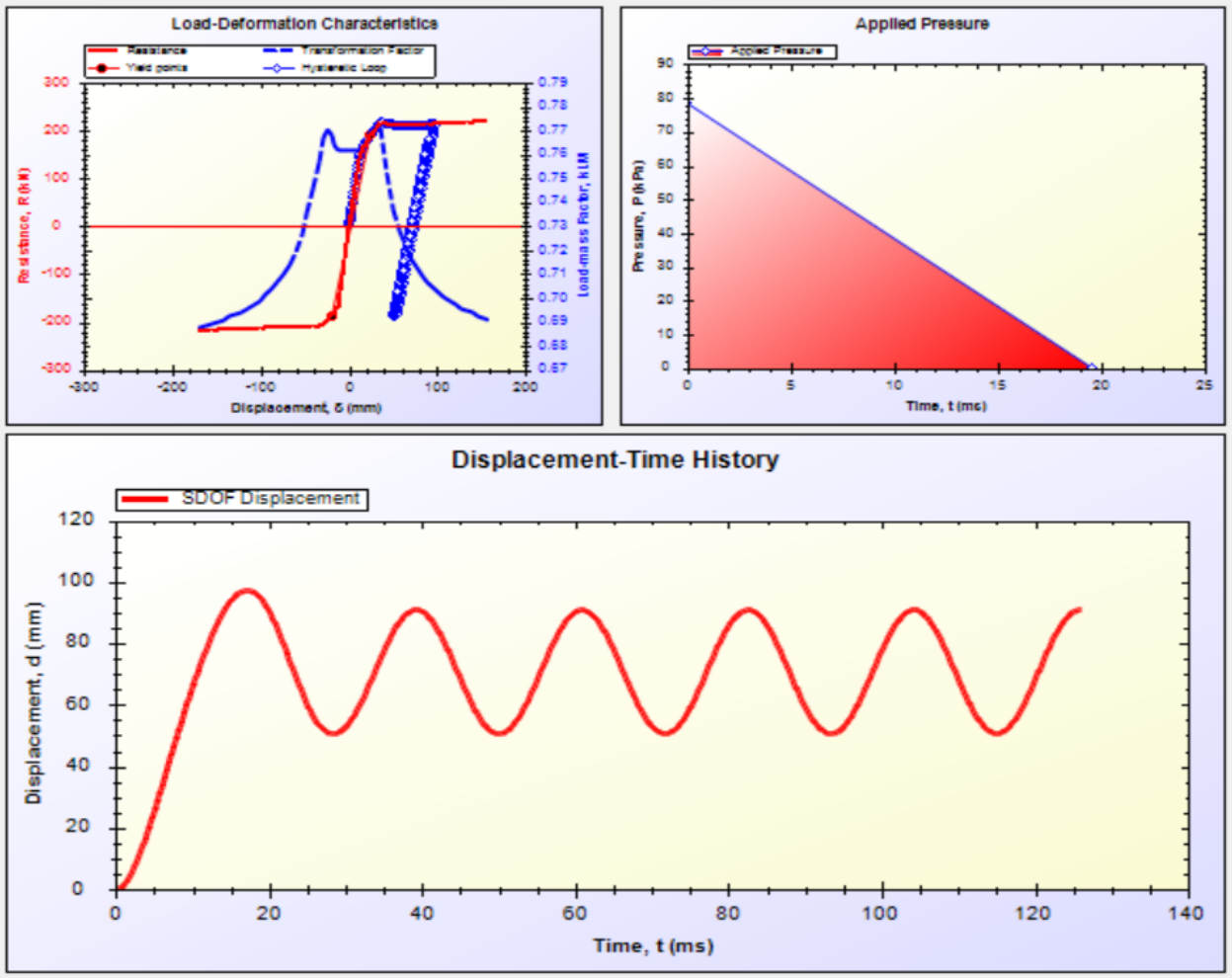

B 41: SDOF for specimen M-16FR – Blast 4

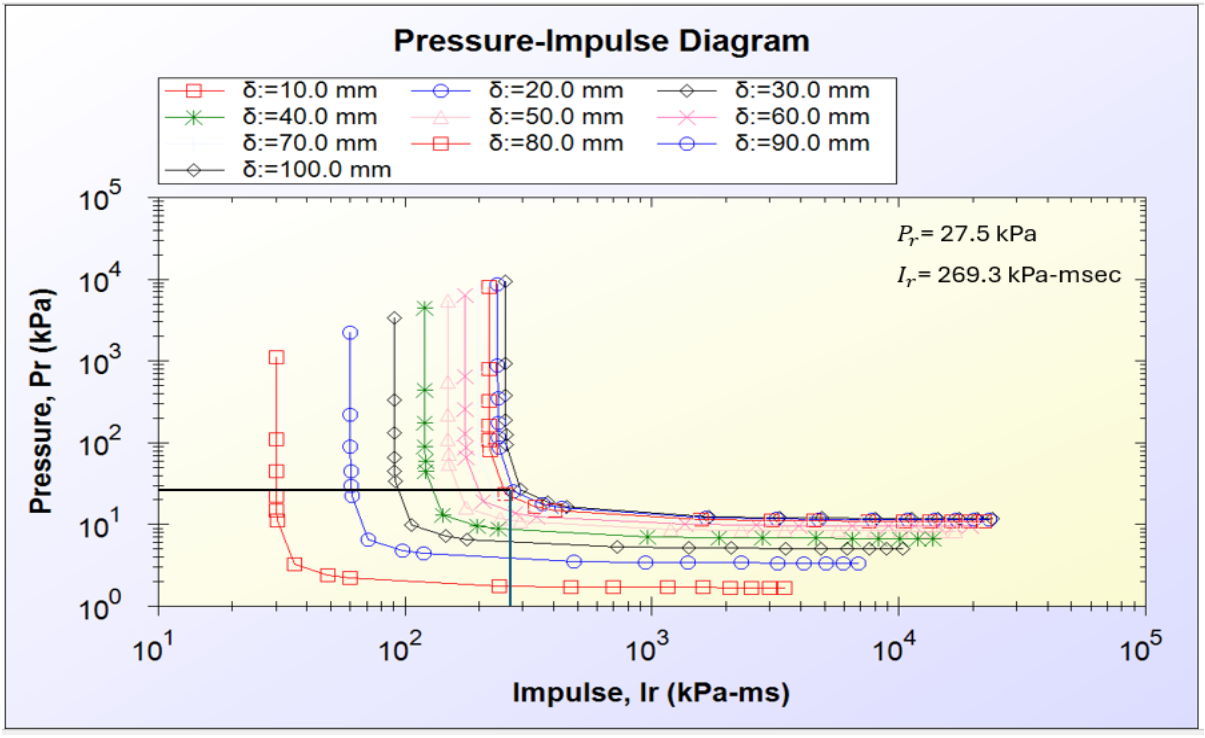

B 42: Pressure-Impulse (P-I) Diagram -M-1F – Blast 1

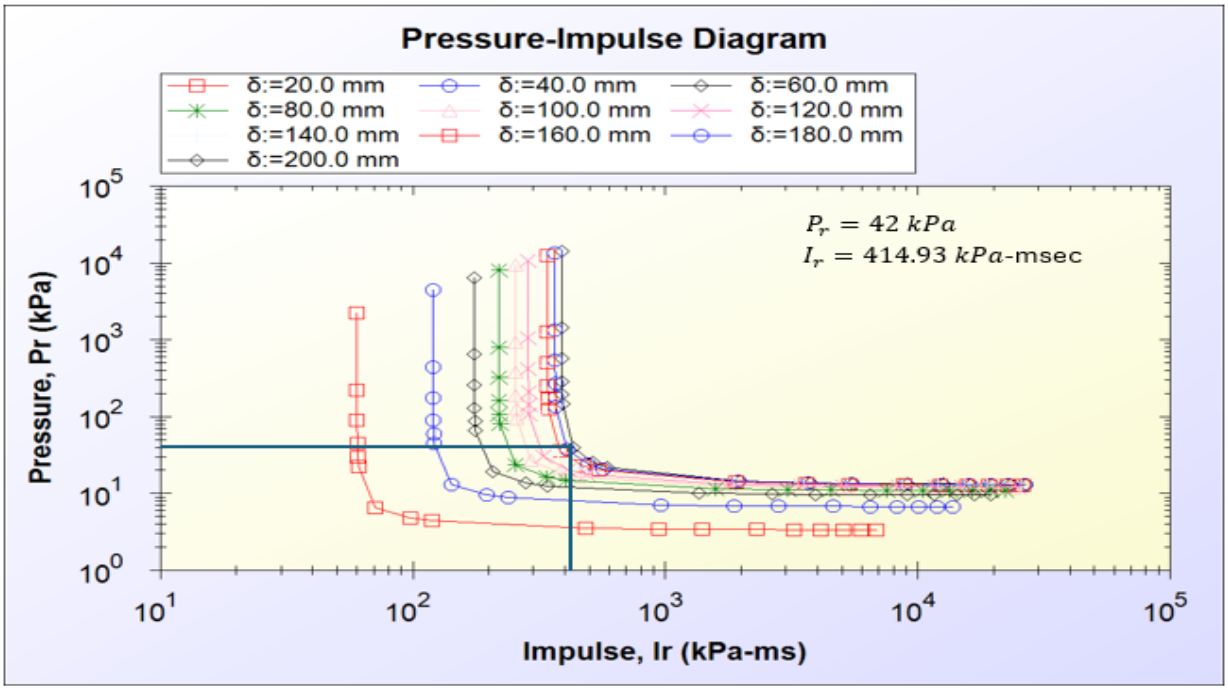

B 43: Pressure-Impulse (P-I) Diagram -M-1F – Blast 2

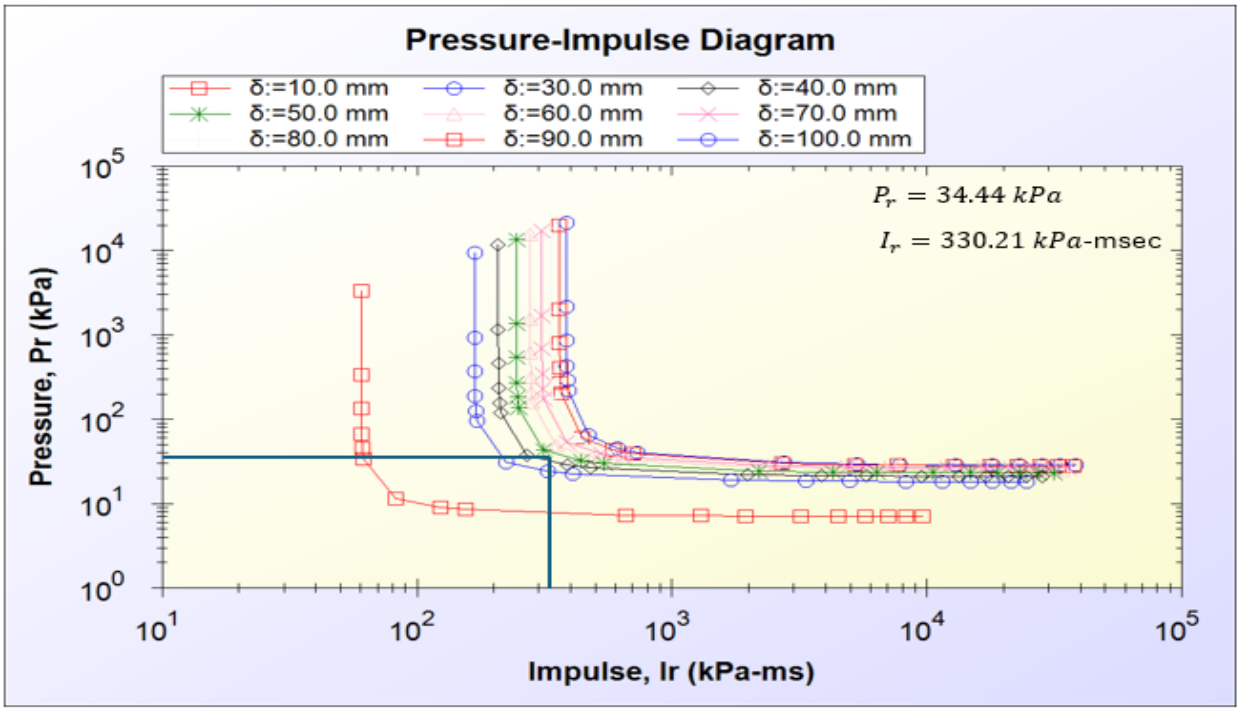

B 44: Pressure-Impulse (P-I) Diagram -M-2FR – Blast 1

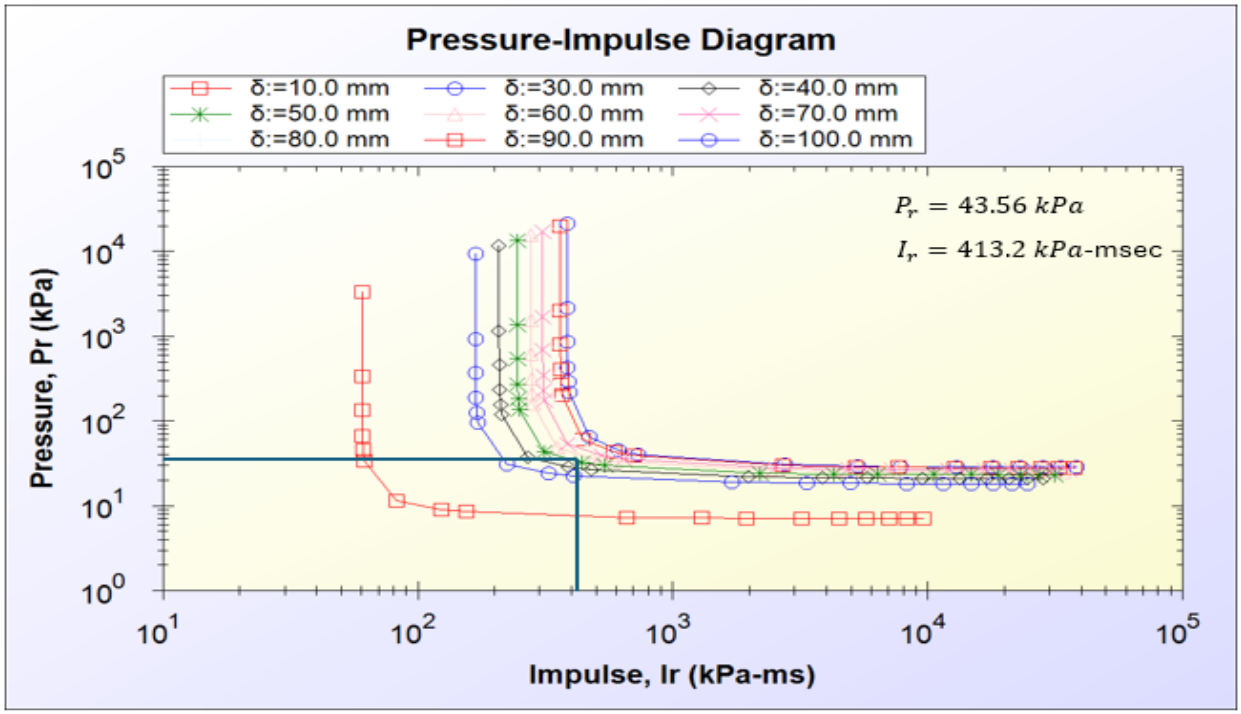

B 45: Pressure-Impulse (P-I) Diagram -M-2FR – Blast 2

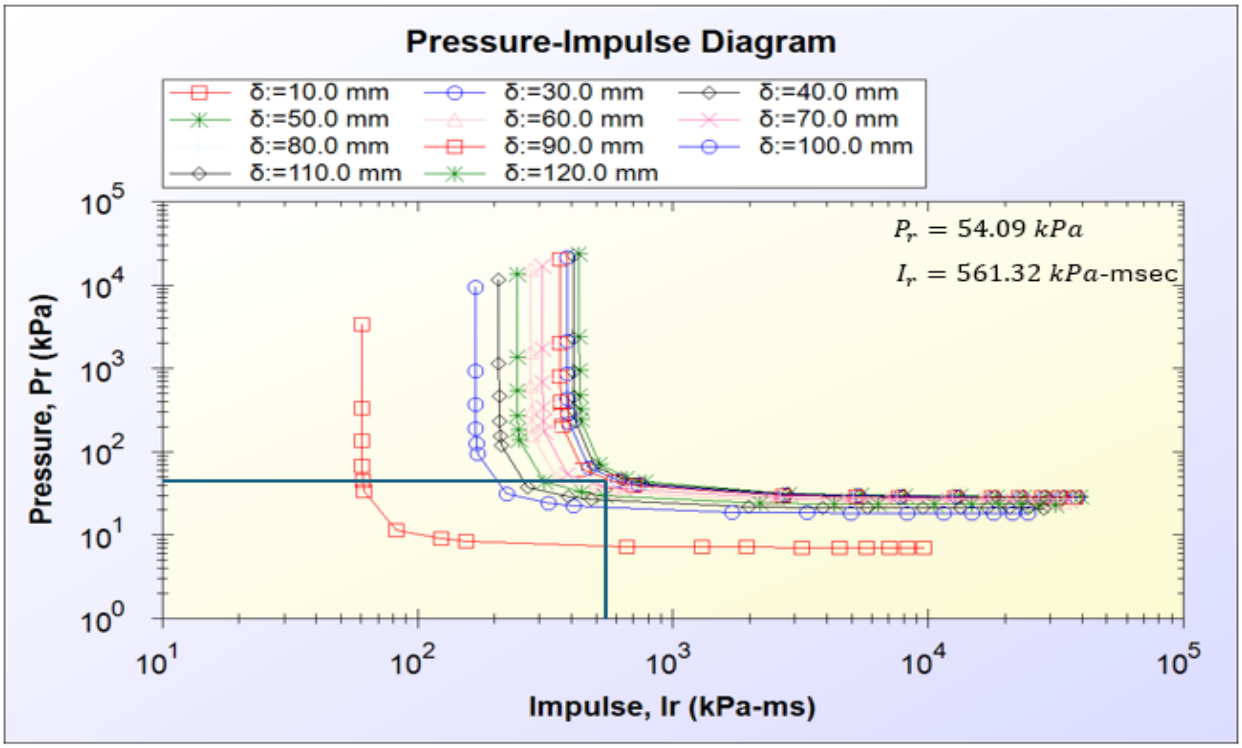

B 46: Pressure-Impulse (P-I) Diagram -M-2FR – Blast 3

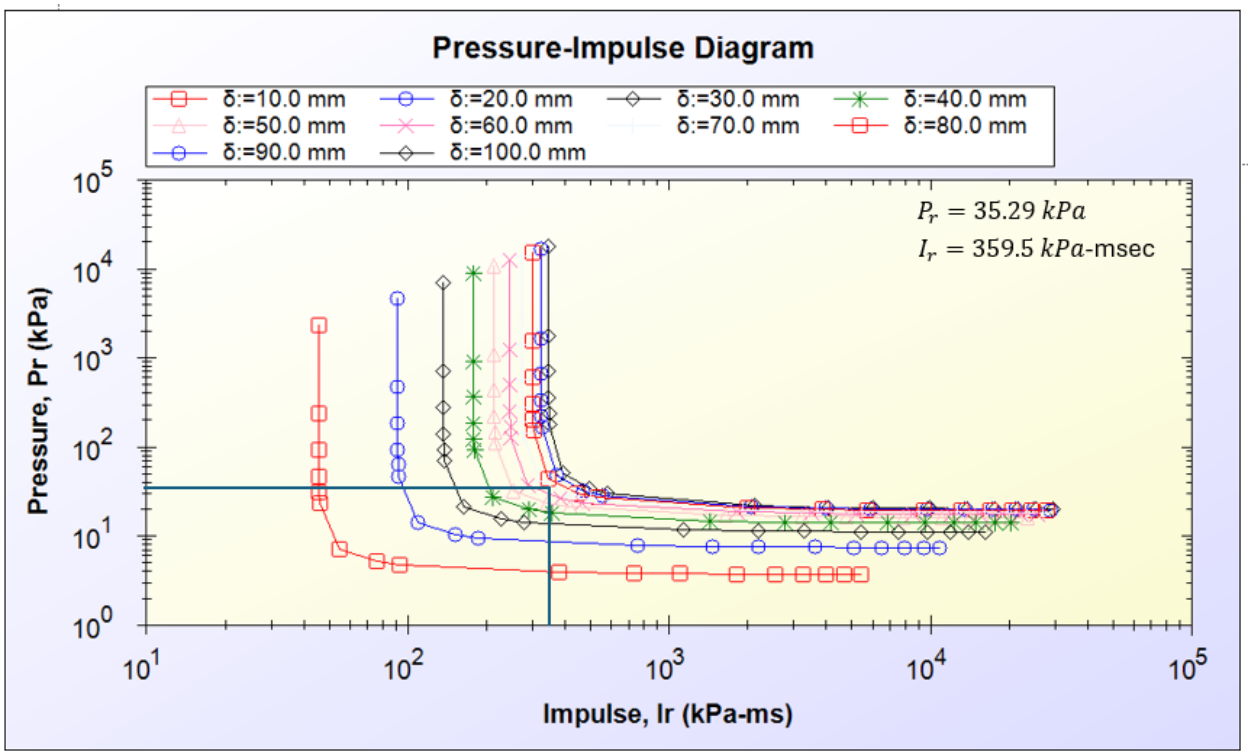

B 47: Pressure-Impulse (P-I) Diagram -M-3F – Blast 1

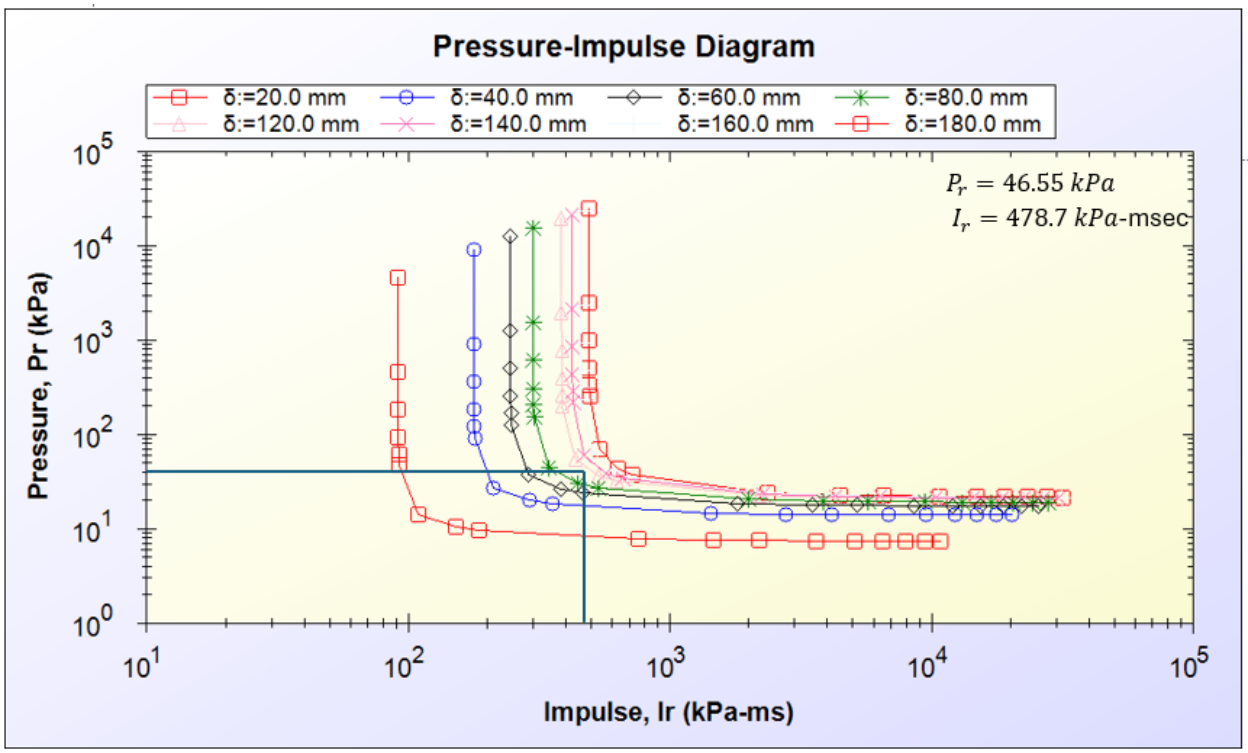

B 48: Pressure-Impulse (P-I) Diagram -M-3F – Blast 2

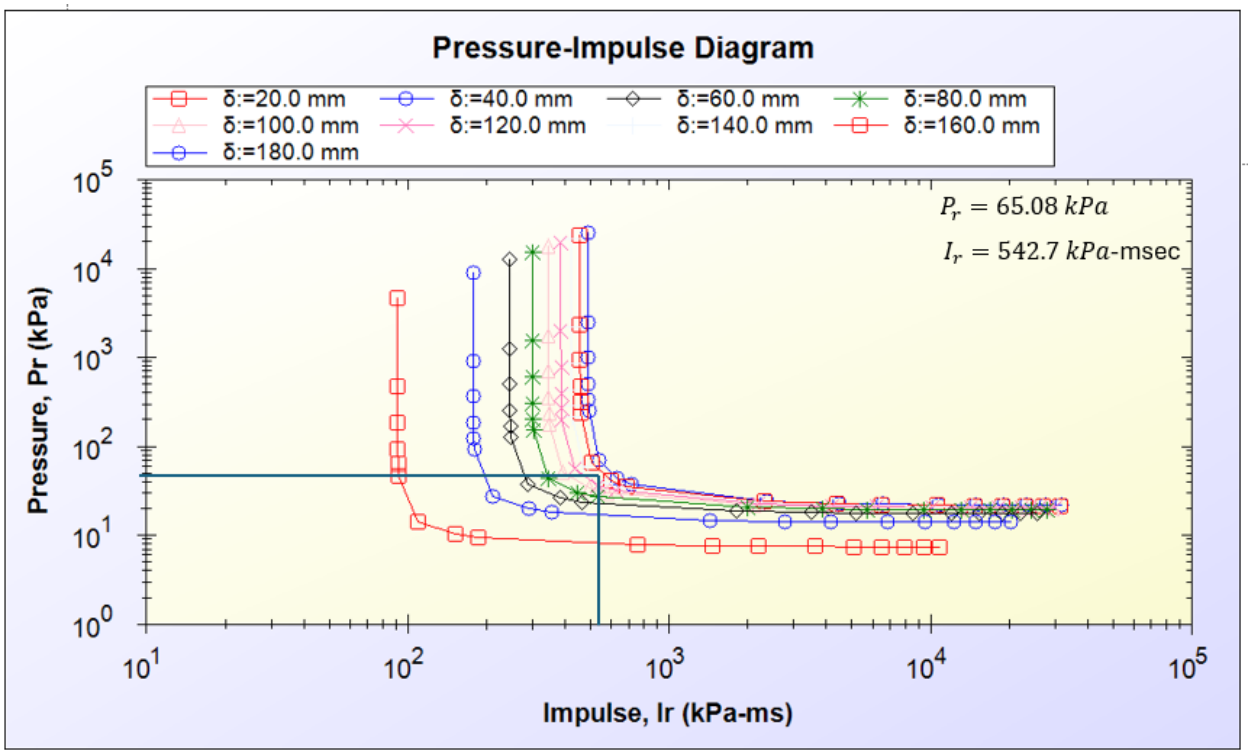

B 49: Pressure-Impulse (P-I) Diagram -M-3F – Blast 3

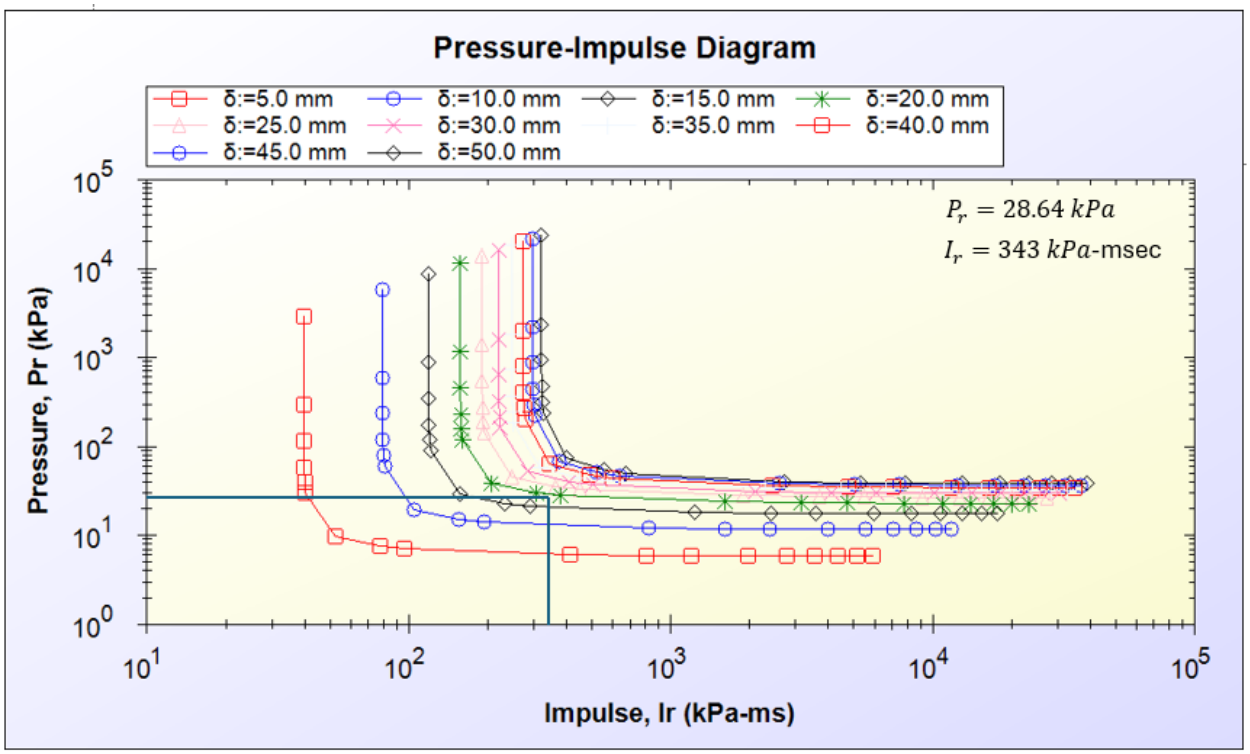

B 50: Pressure-Impulse (P-I) Diagram -M-4FR – Blast 1

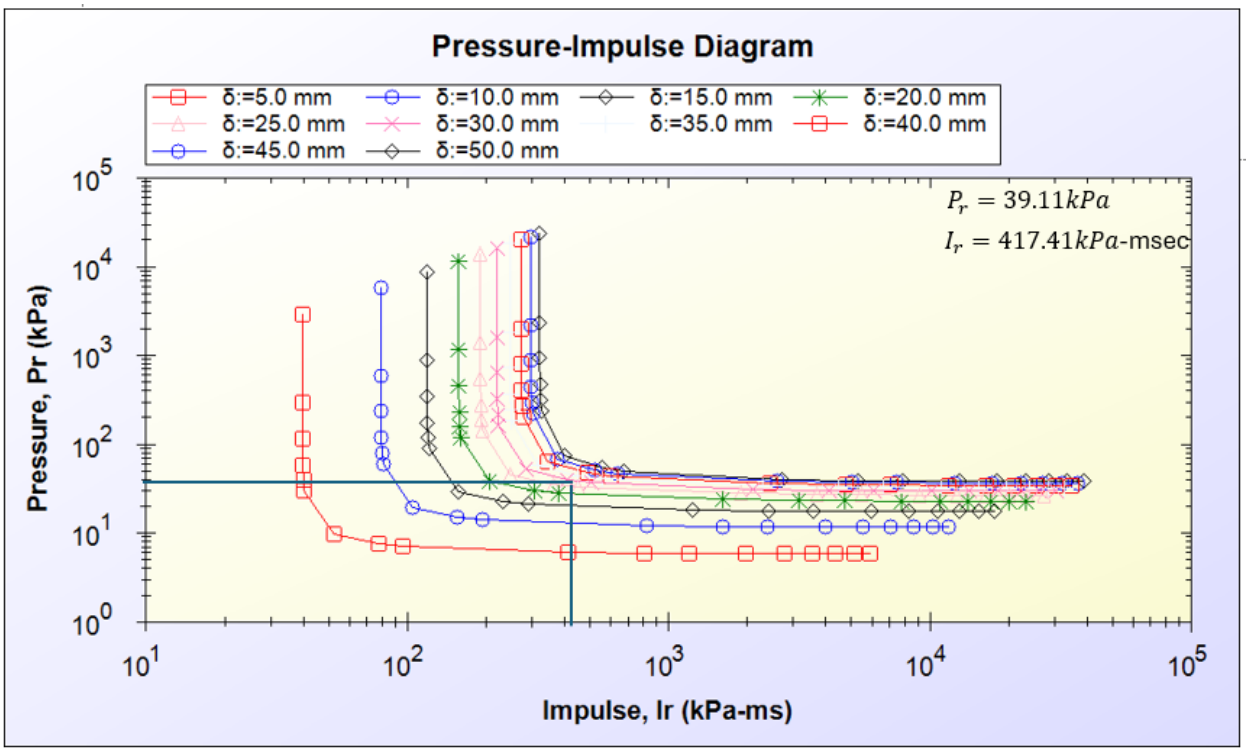

B 51: Pressure-Impulse (P-I) Diagram -M-4FR – Blast 2

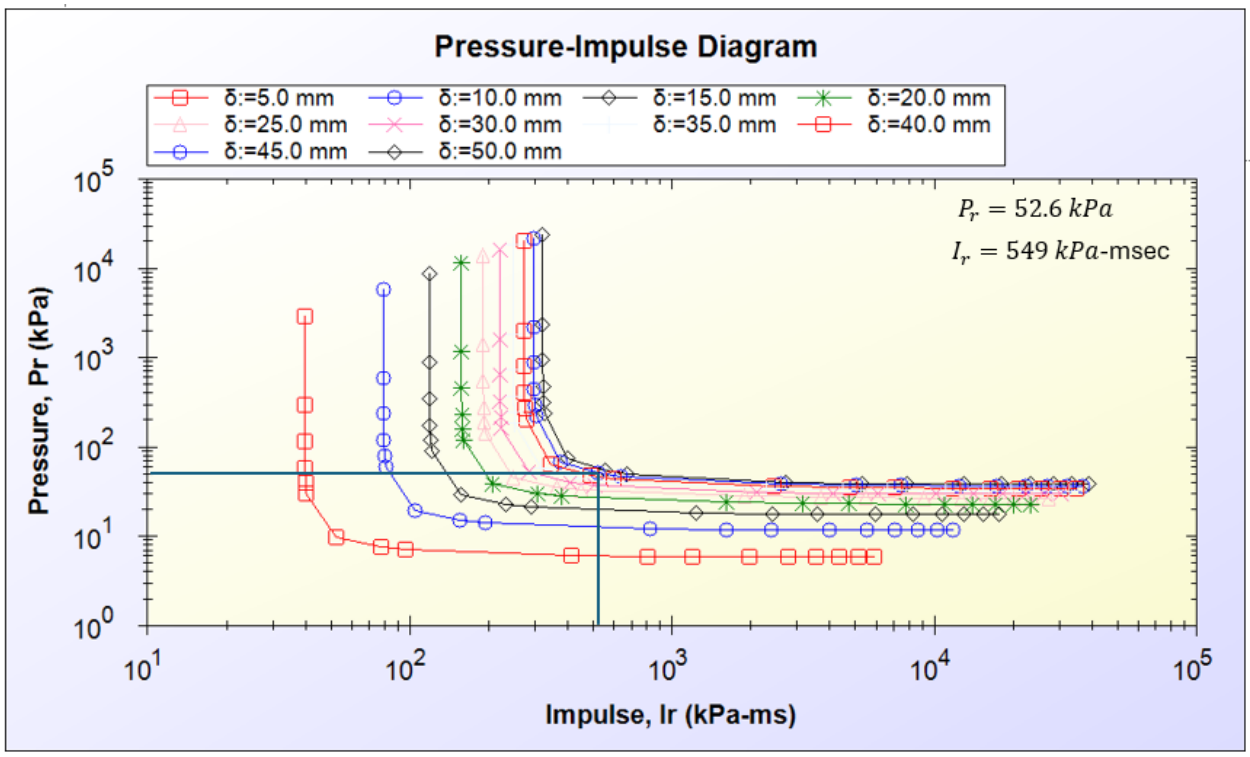

B 52: Pressure-Impulse (P-I) Diagram -M-4FR – Blast 3

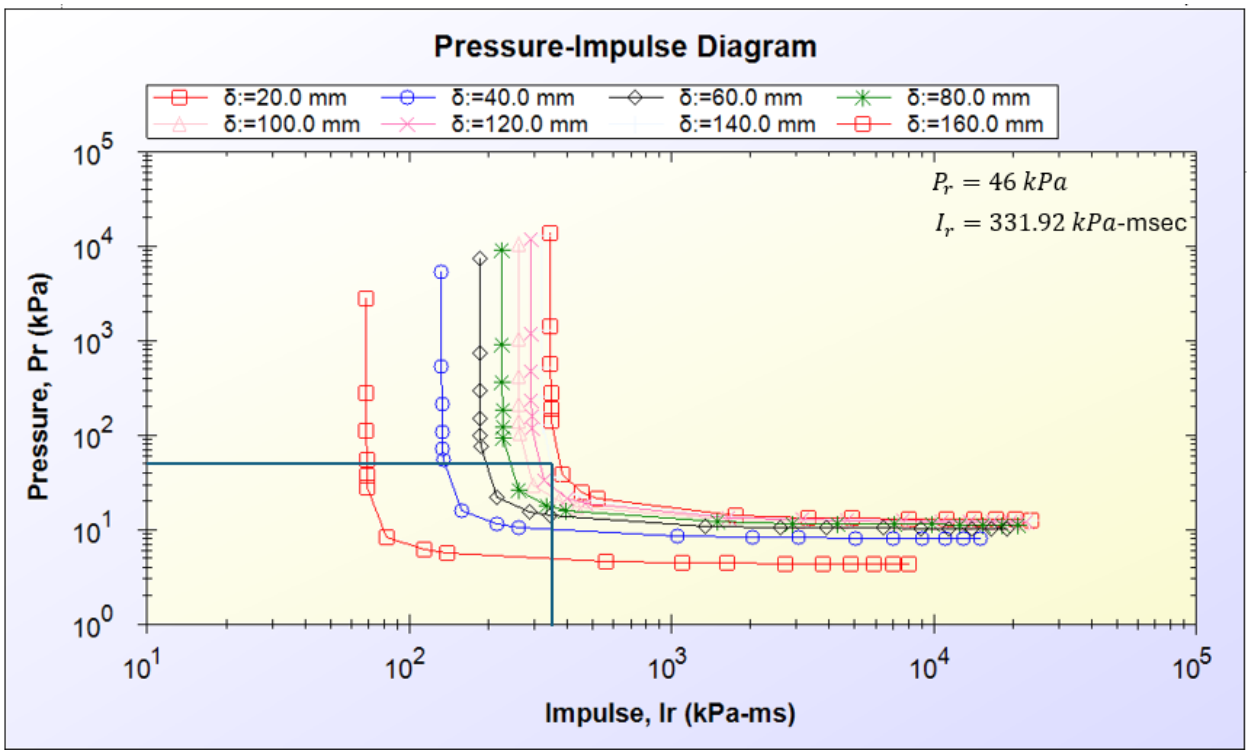

B 53: Pressure-Impulse (P-I) Diagram -M-5F – Blast 1

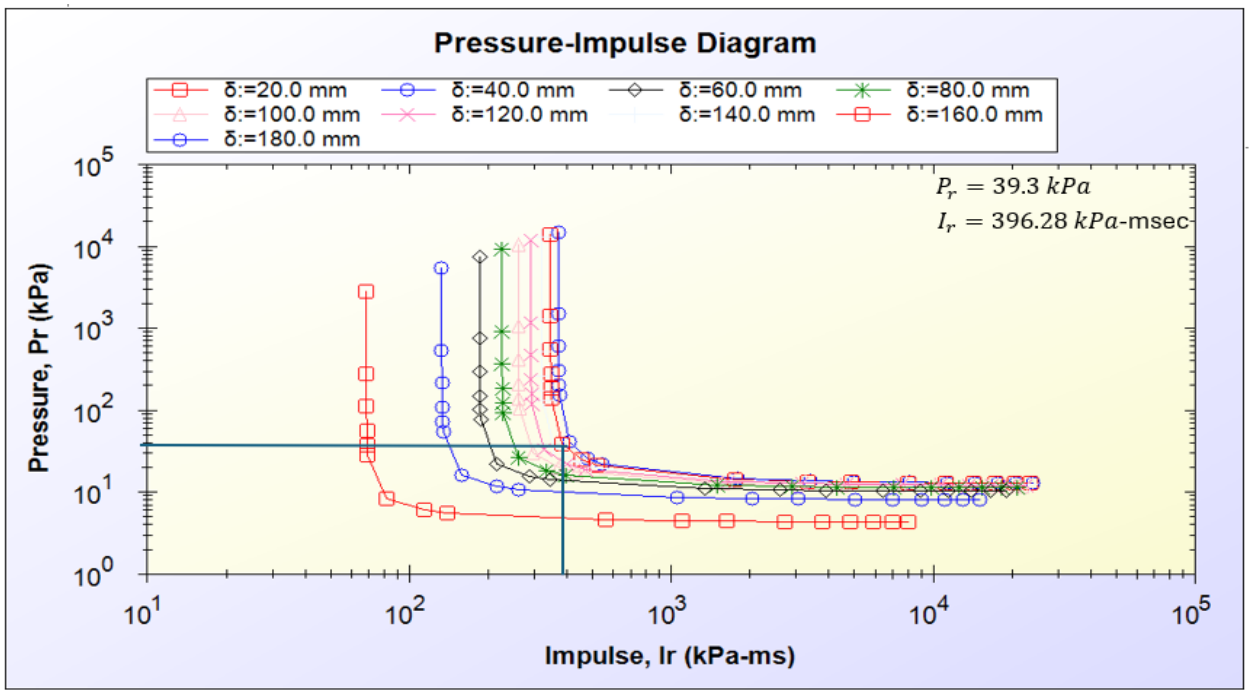

B 54: Pressure-Impulse (P-I) Diagram - M-5F – Blast 2

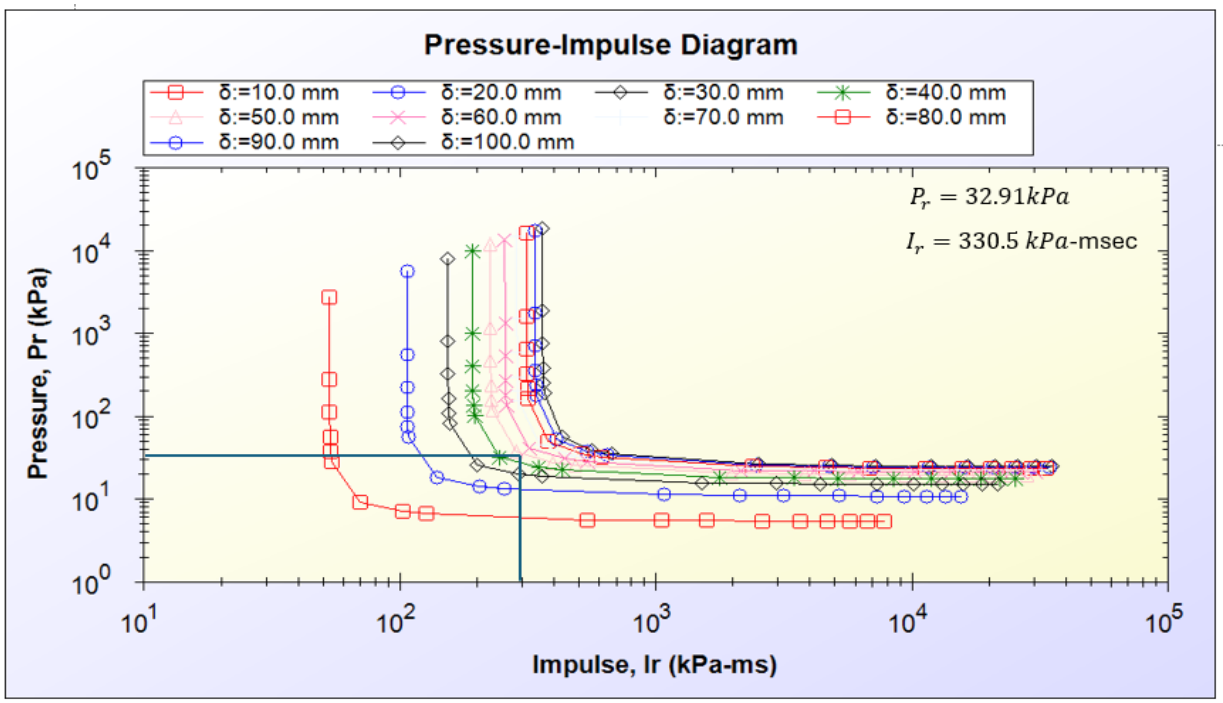

B 55: Pressure-Impulse (P-I) Diagram -M-6F – Blast 1

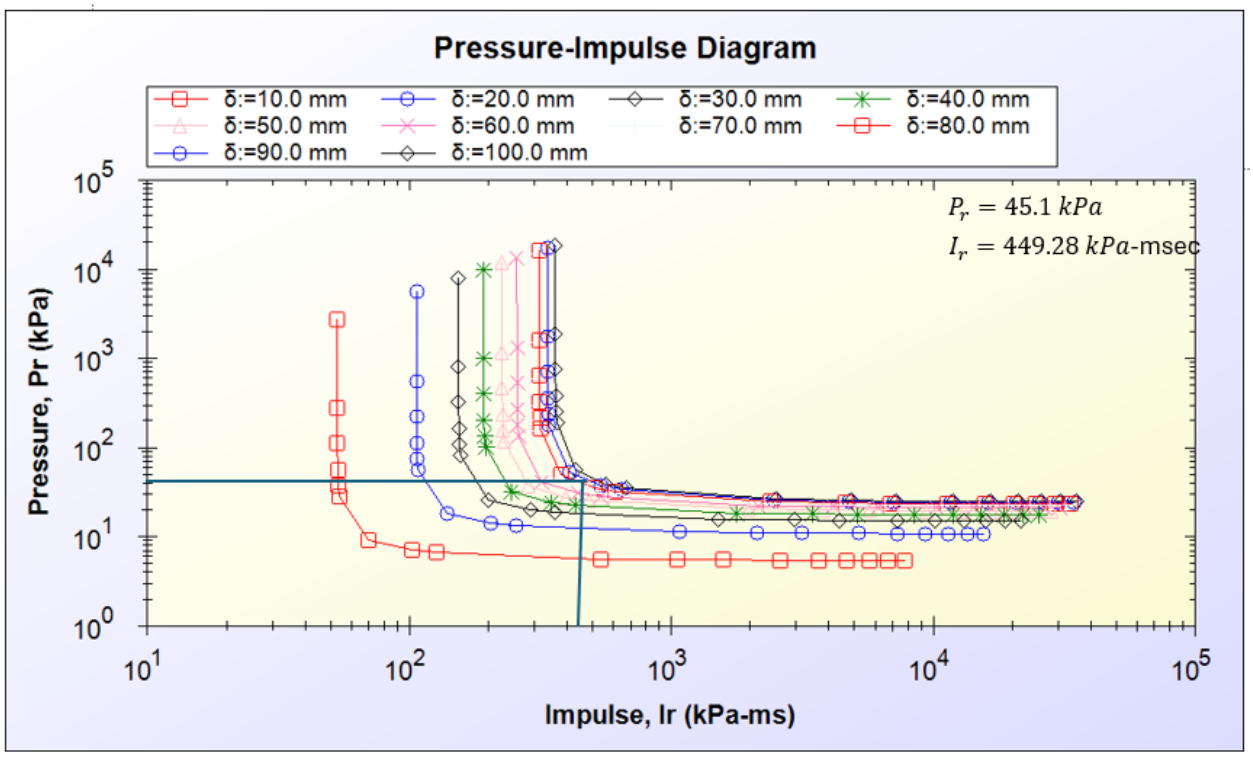

B 56: Pressure-Impulse (P-I) Diagram - M-6F – Blast 2

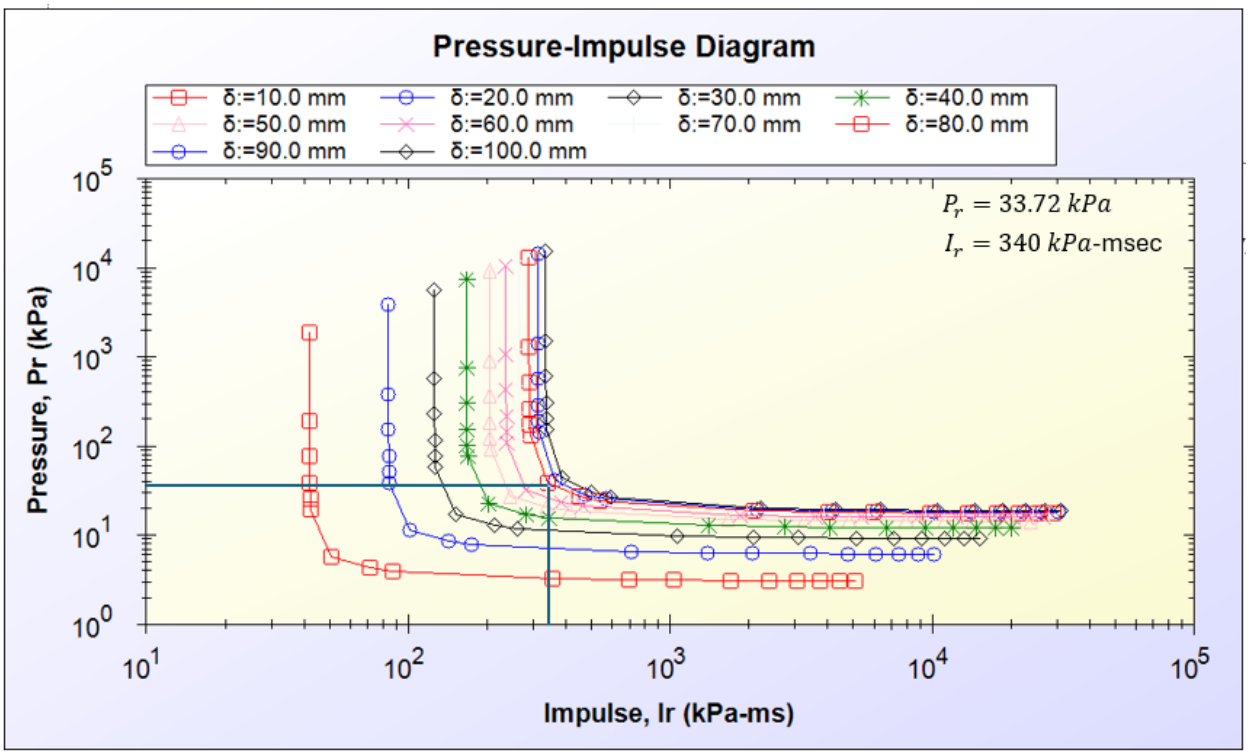

B 57: Pressure-Impulse (P-I) Diagram -M-7F – Blast 1

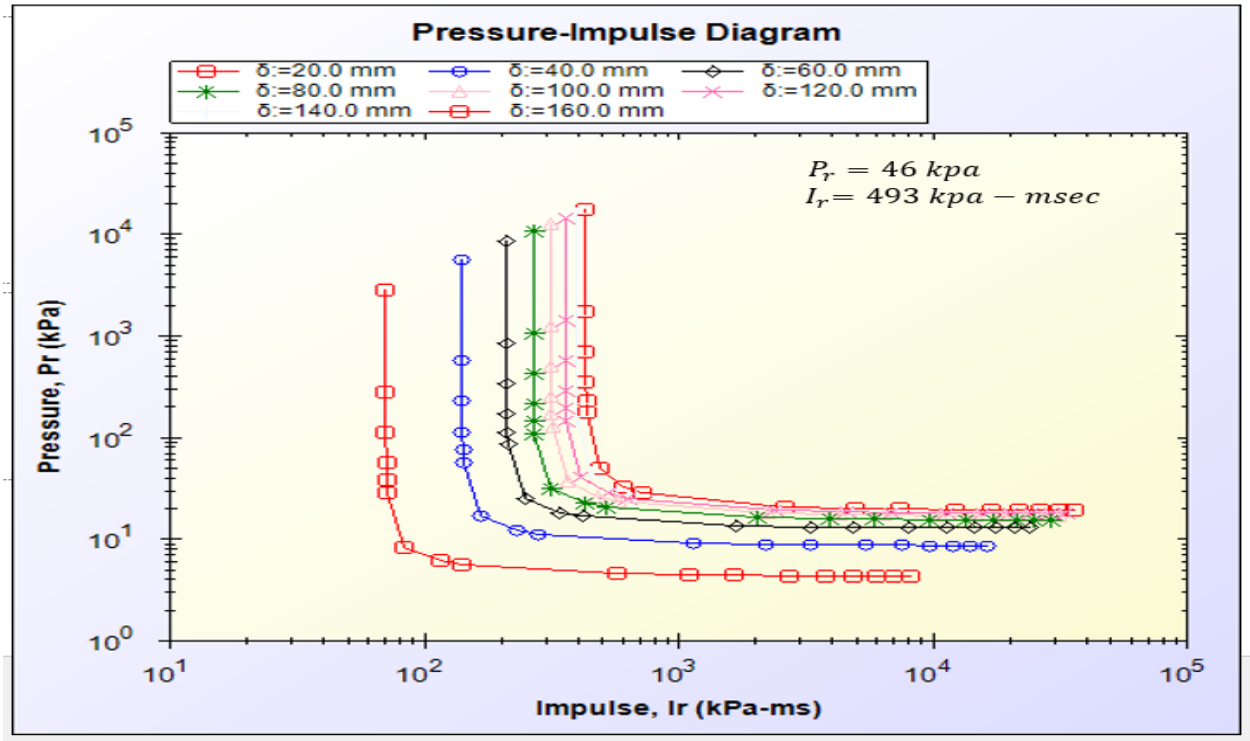

B 58: Pressure-Impulse (P-I) Diagram - M-7F – Blast 2

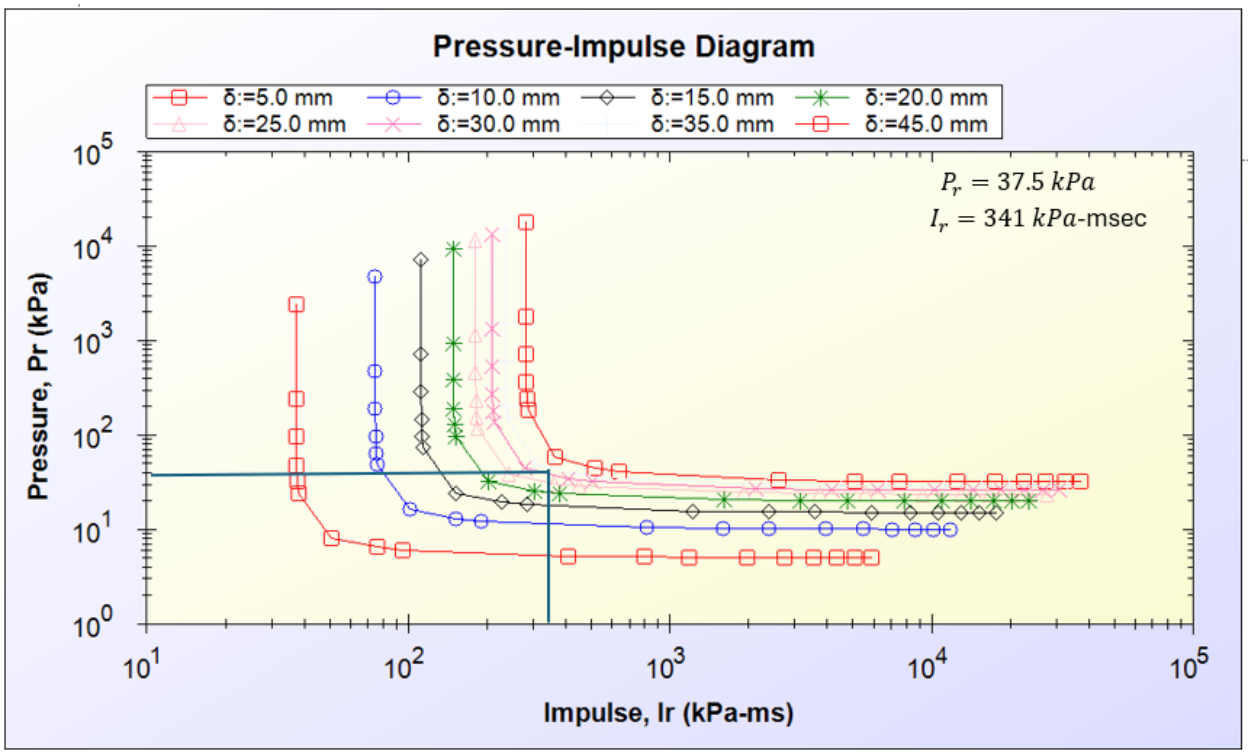

B 59: Pressure-Impulse (P-I) Diagram -M-8F – Blast 1

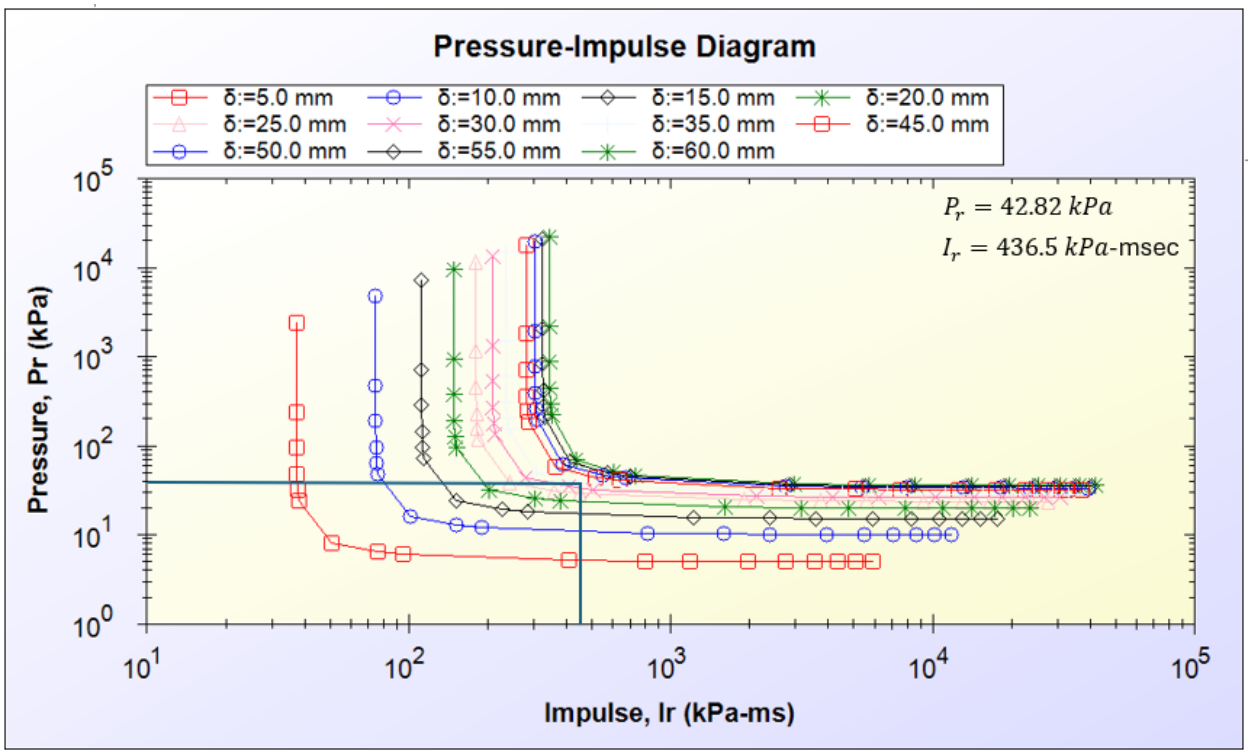

B 60: Pressure-Impulse (P-I) Diagram - M-8F – Blast 2

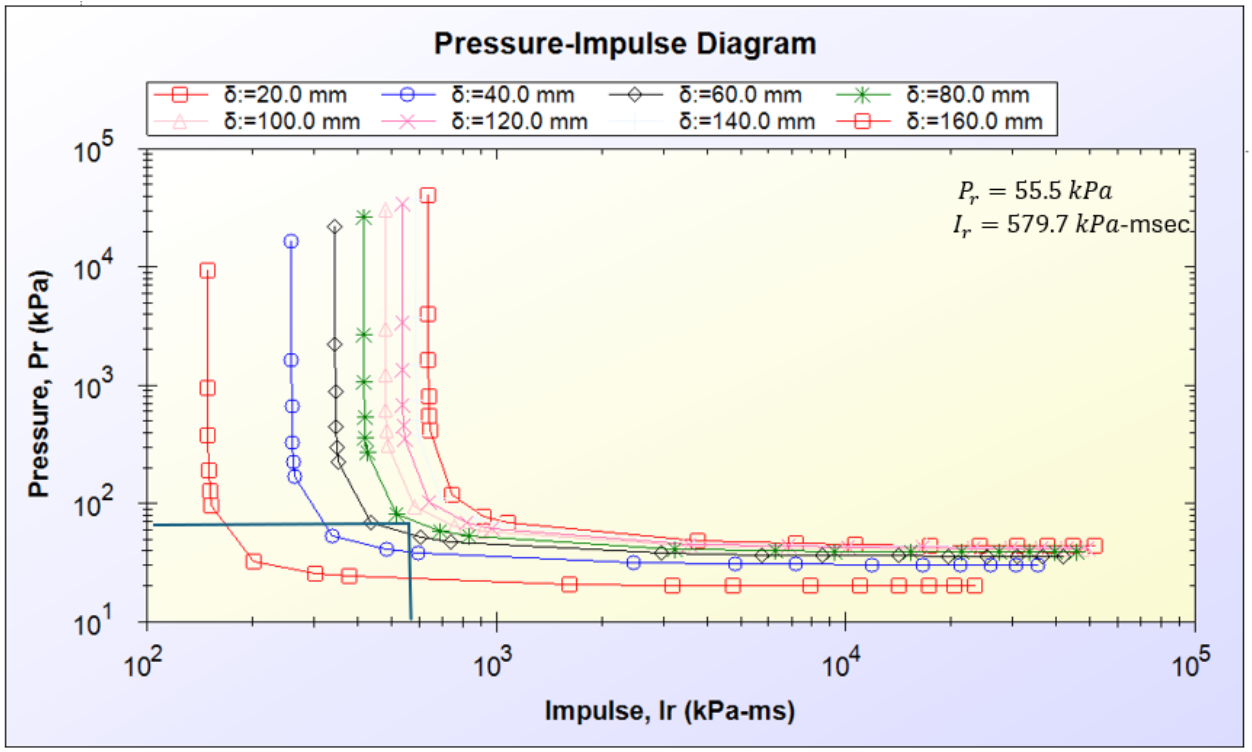

B 61: Pressure-Impulse (P-I) Diagram - M-8F – Blast 3

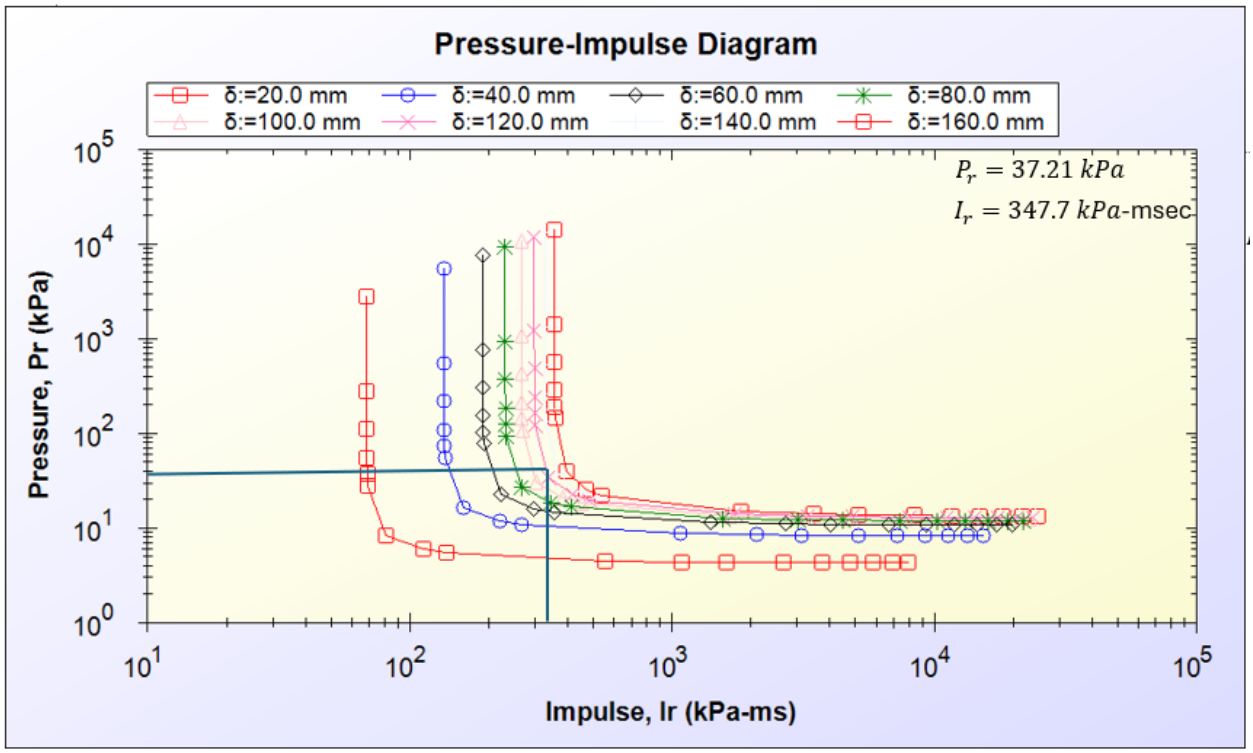

B 62: Pressure-Impulse (P-I) Diagram -M-9FH– Blast 1

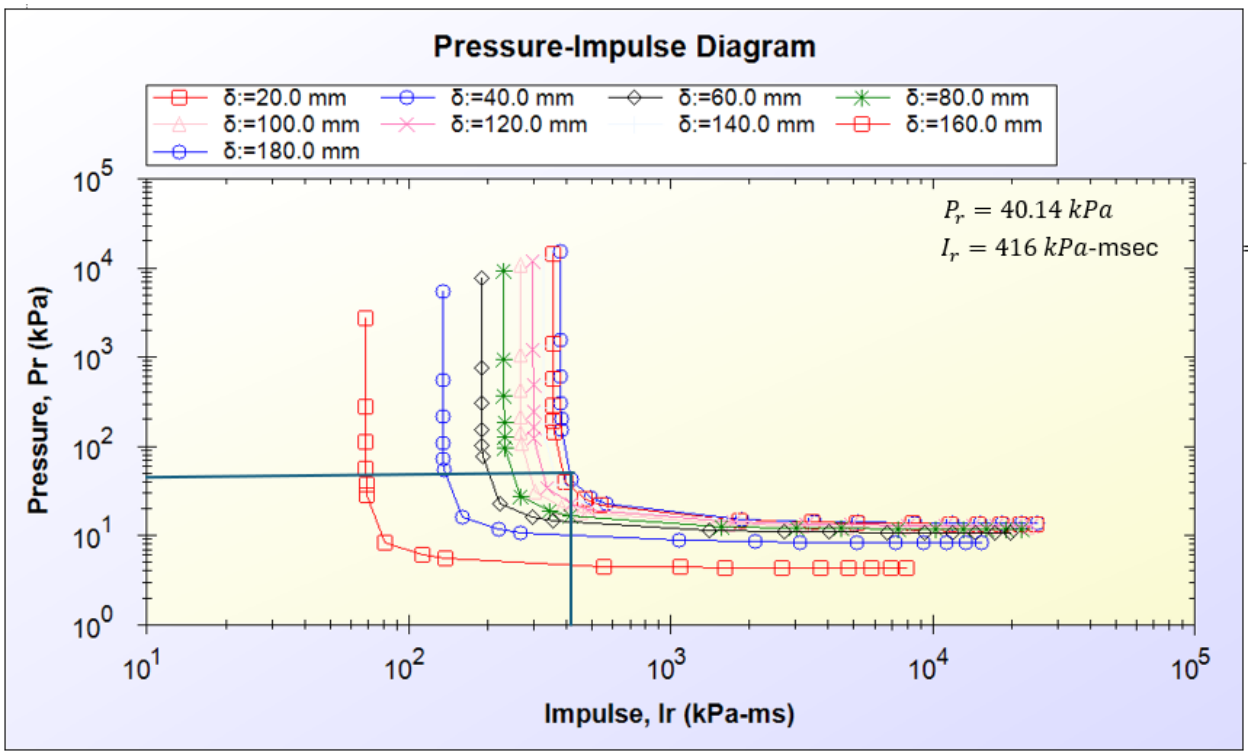

B 63: Pressure-Impulse (P-I) Diagram - M-9FH – Blast 2

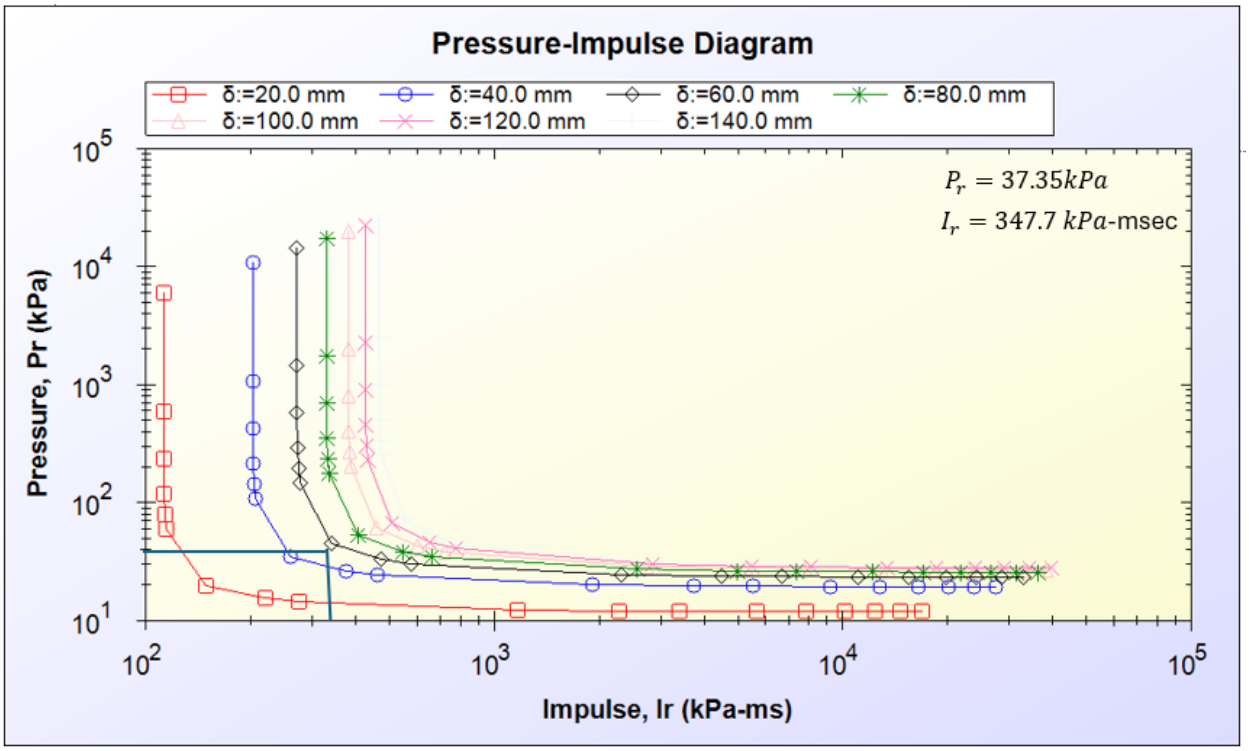

B 64: Pressure-Impulse (P-I) Diagram -M-10FH– Blast 1

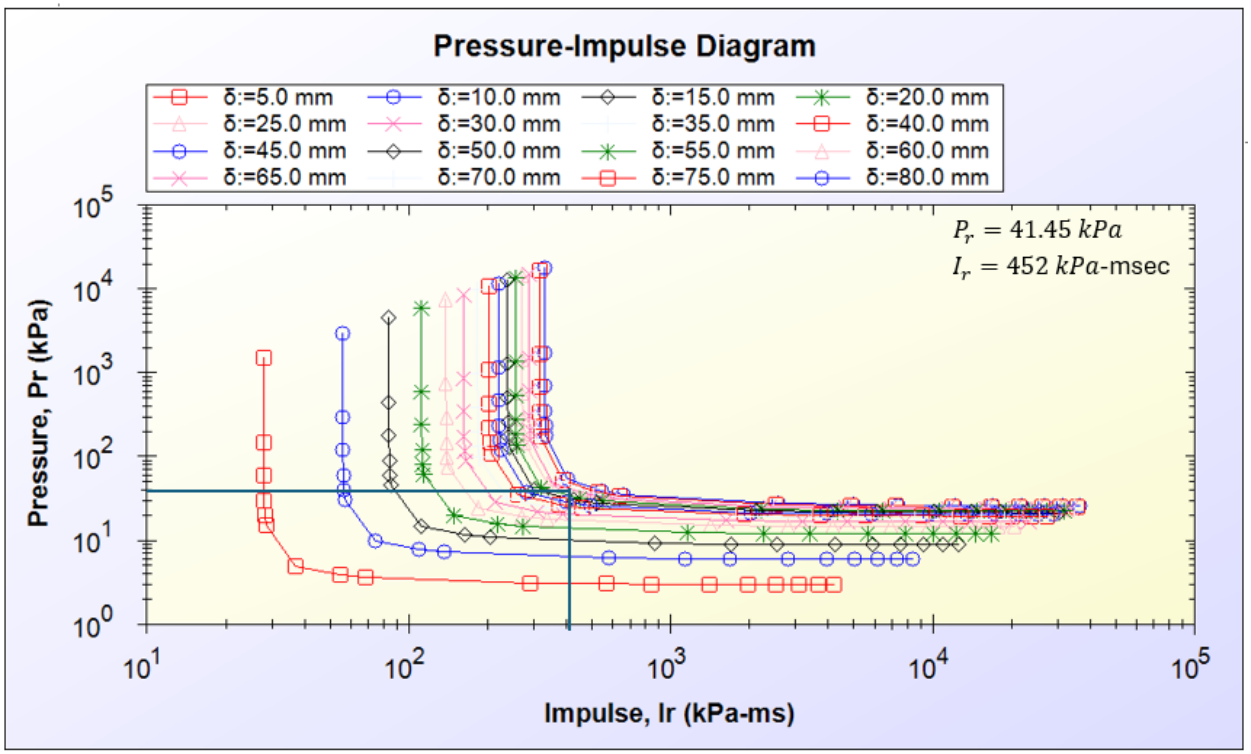

B 65: Pressure-Impulse (P-I) Diagram - M-10FH – Blast 2

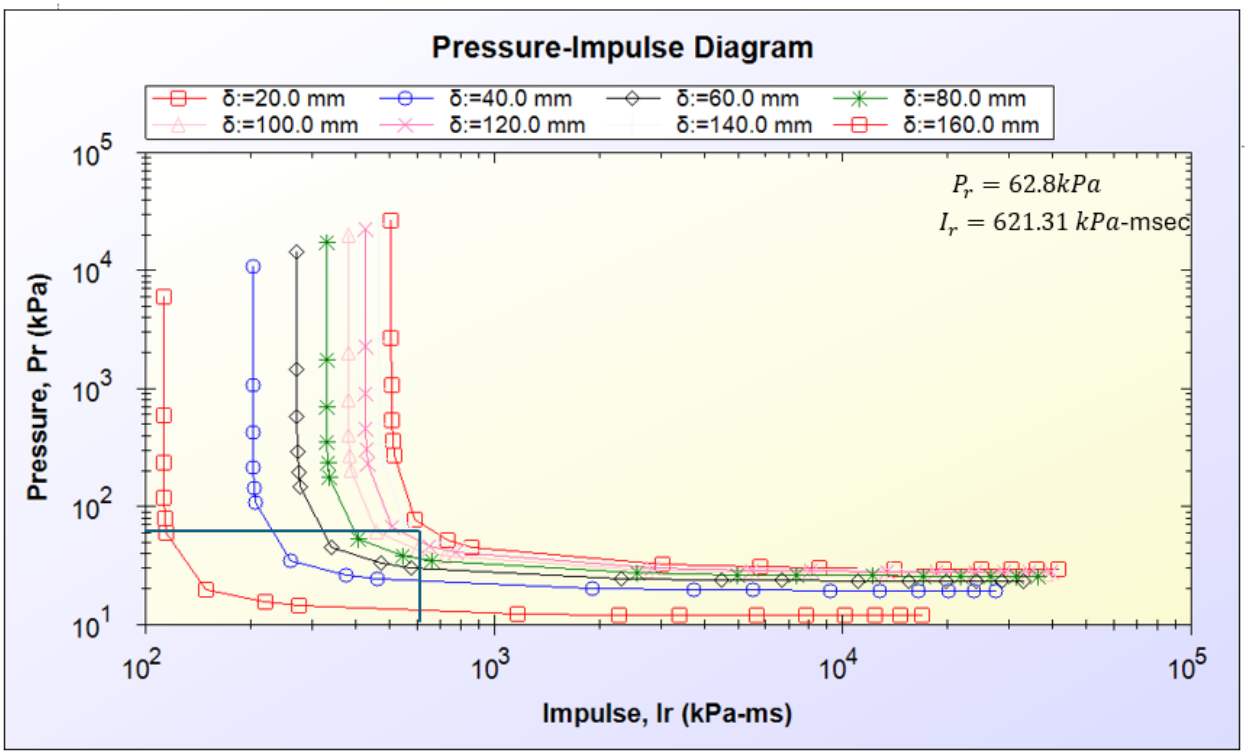

B 66: Pressure-Impulse (P-I) Diagram - M-10FH – Blast 3

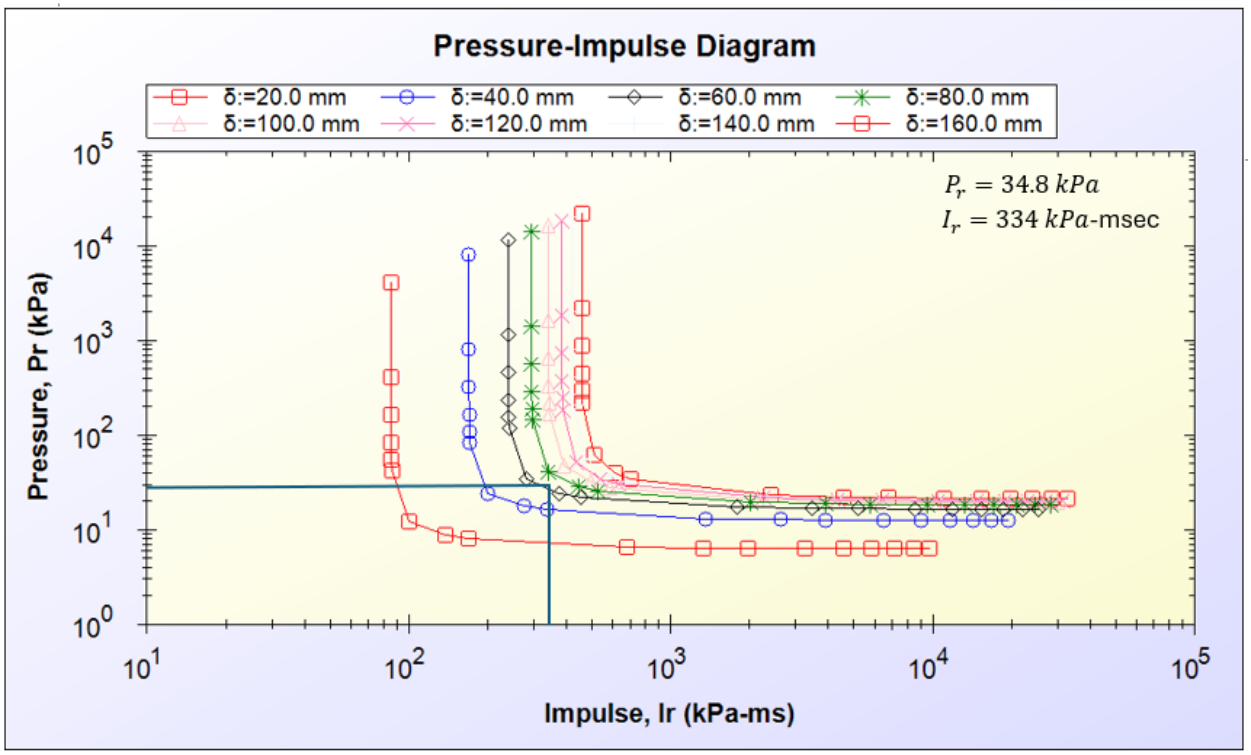

B 67: Pressure-Impulse (P-I) Diagram -M-11FH– Blast 1

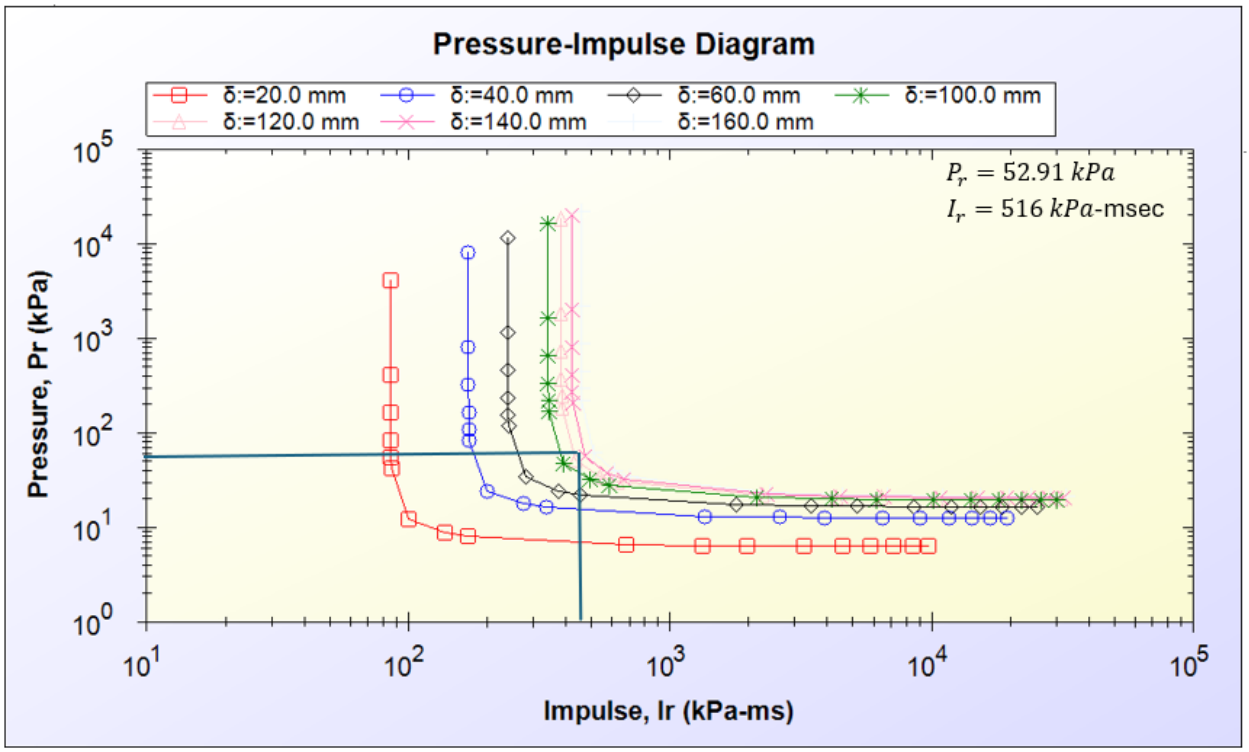

B 68: Pressure-Impulse (P-I) Diagram - M-11FH – Blast 2

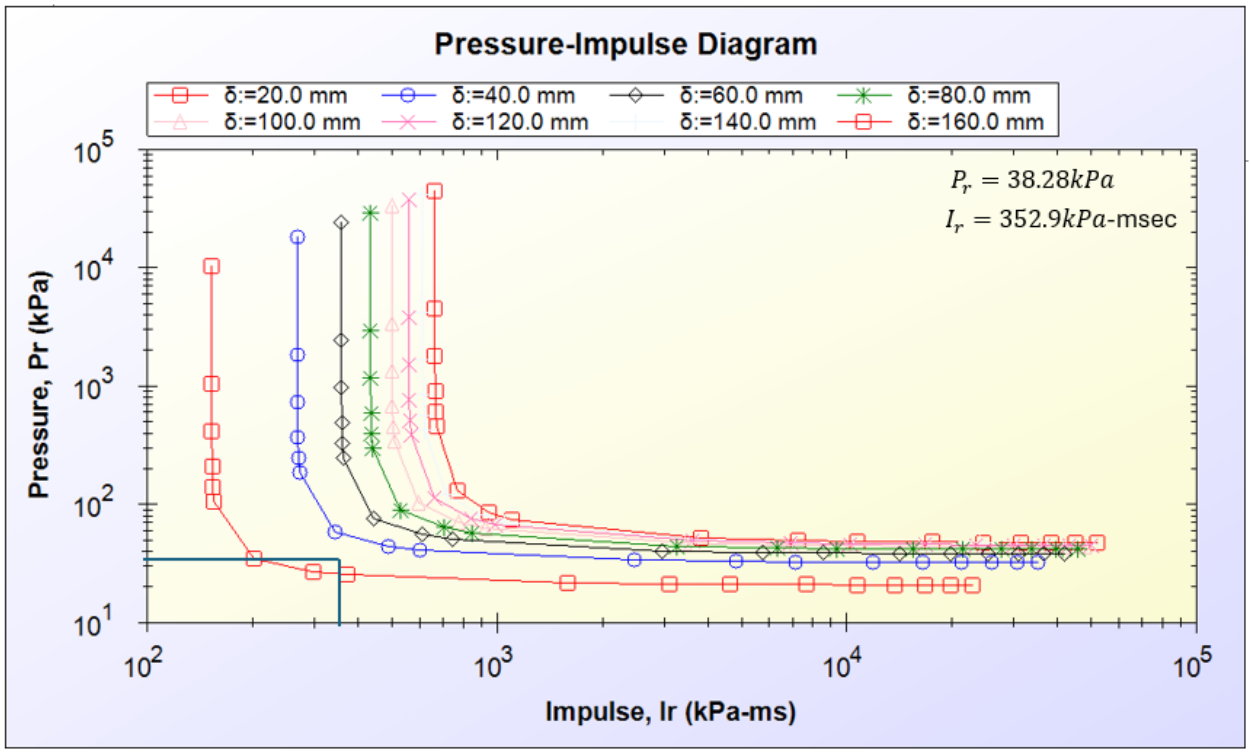

B 69: Pressure-Impulse (P-I) Diagram -M-12FH– Blast 1

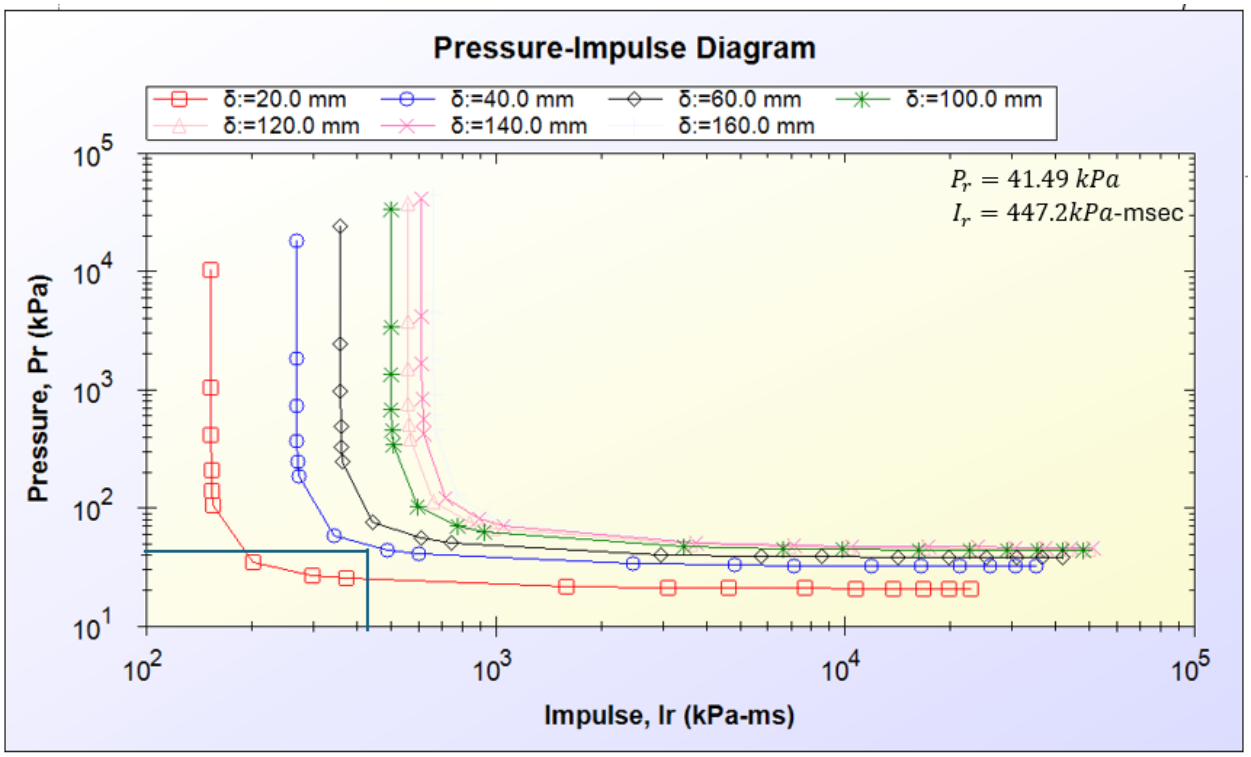

B 70: Pressure-Impulse (P-I) Diagram - M-12FH – Blast 2

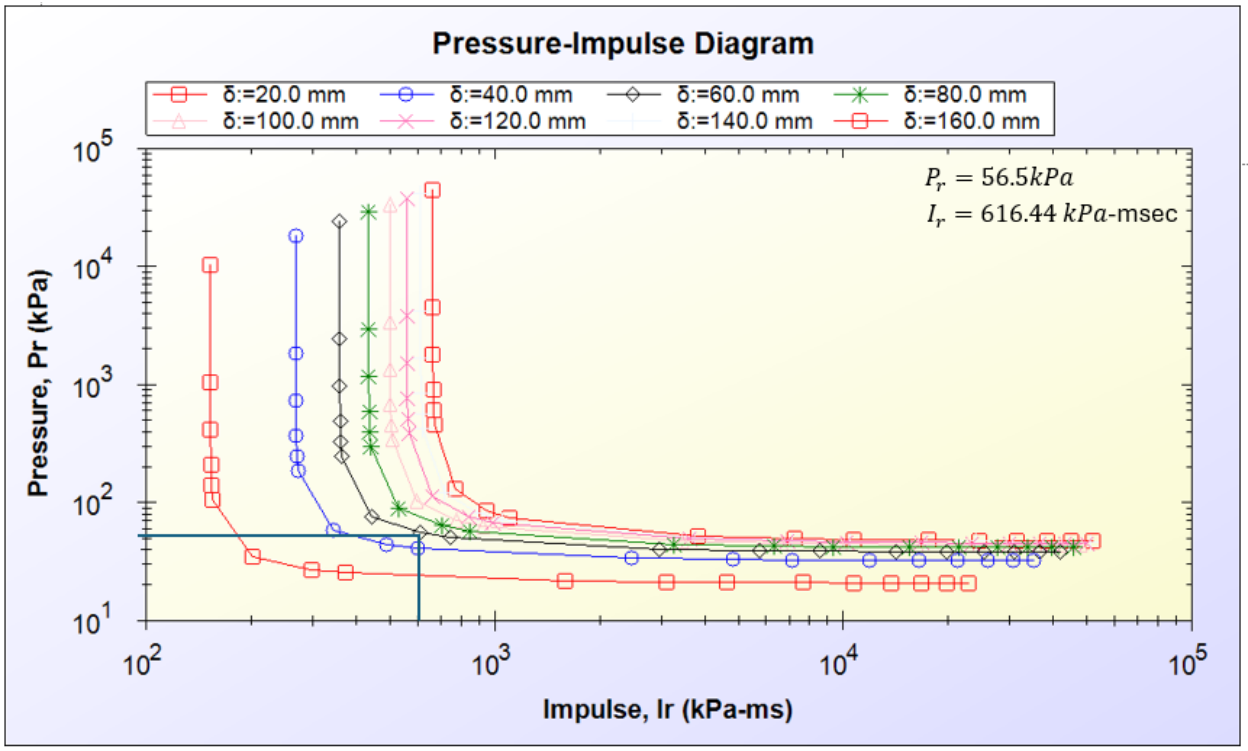

B 71: Pressure-Impulse (P-I) Diagram - M-12FH – Blast 3

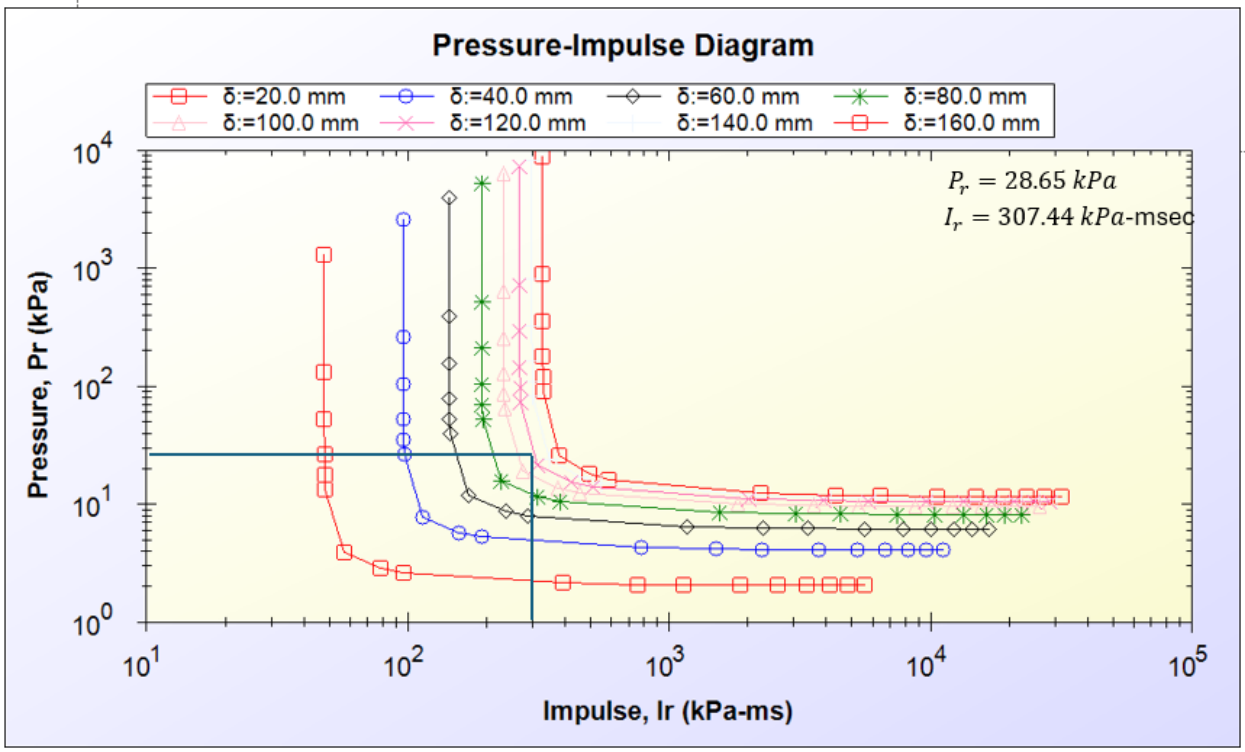

B 72: Pressure-Impulse (P-I) Diagram -M-13FH– Blast 1

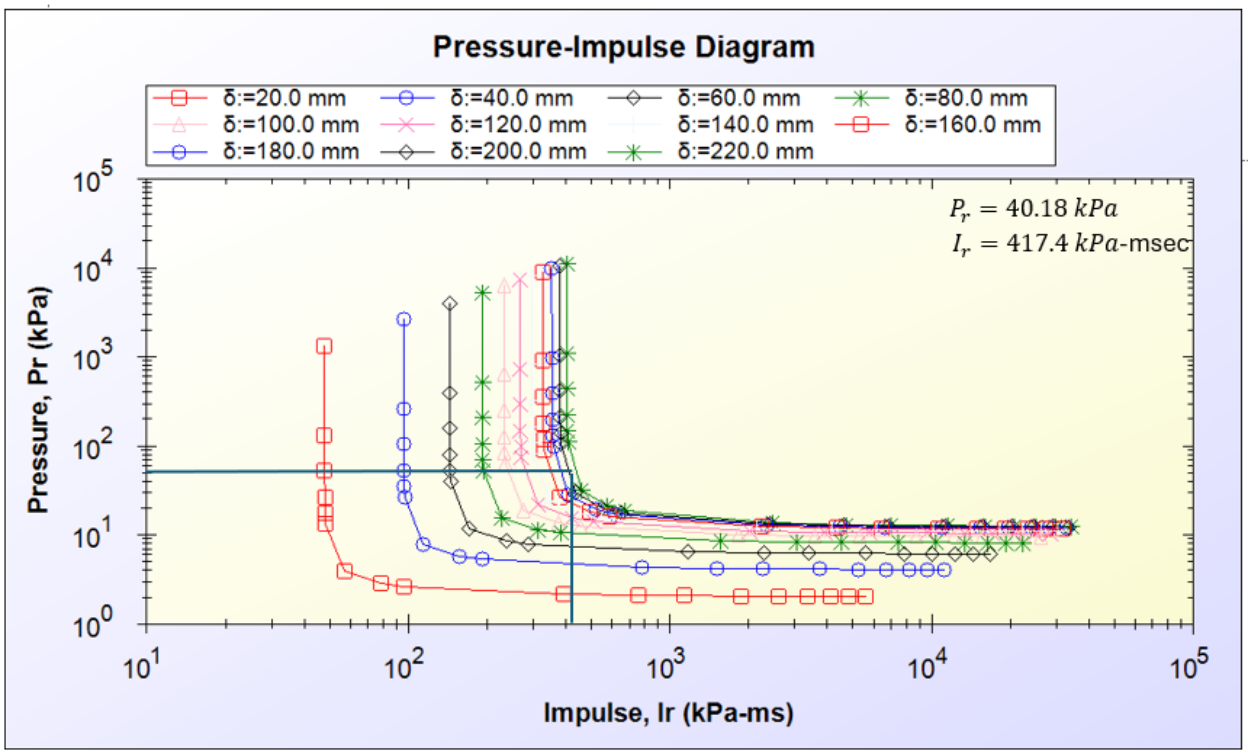

B 73: Pressure-Impulse (P-I) Diagram - M-13FH – Blast 2

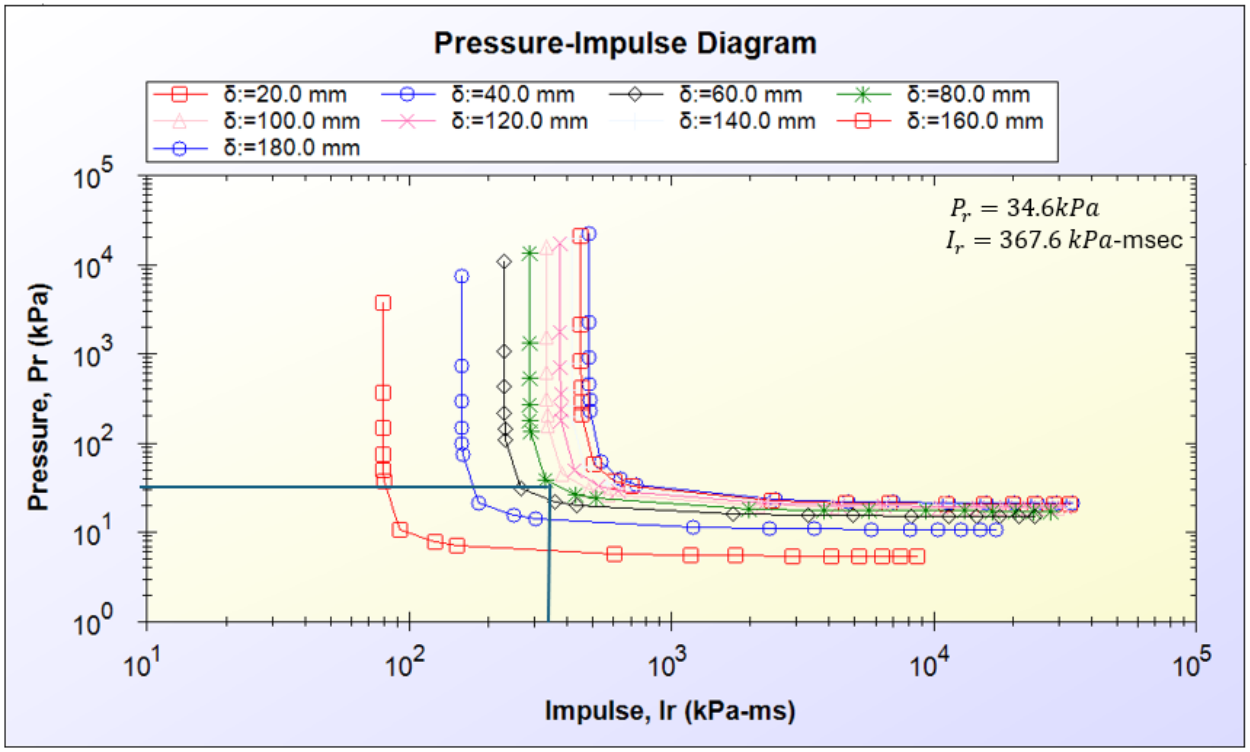

B 74: Pressure-Impulse (P-I) Diagram -M-14FH– Blast 1

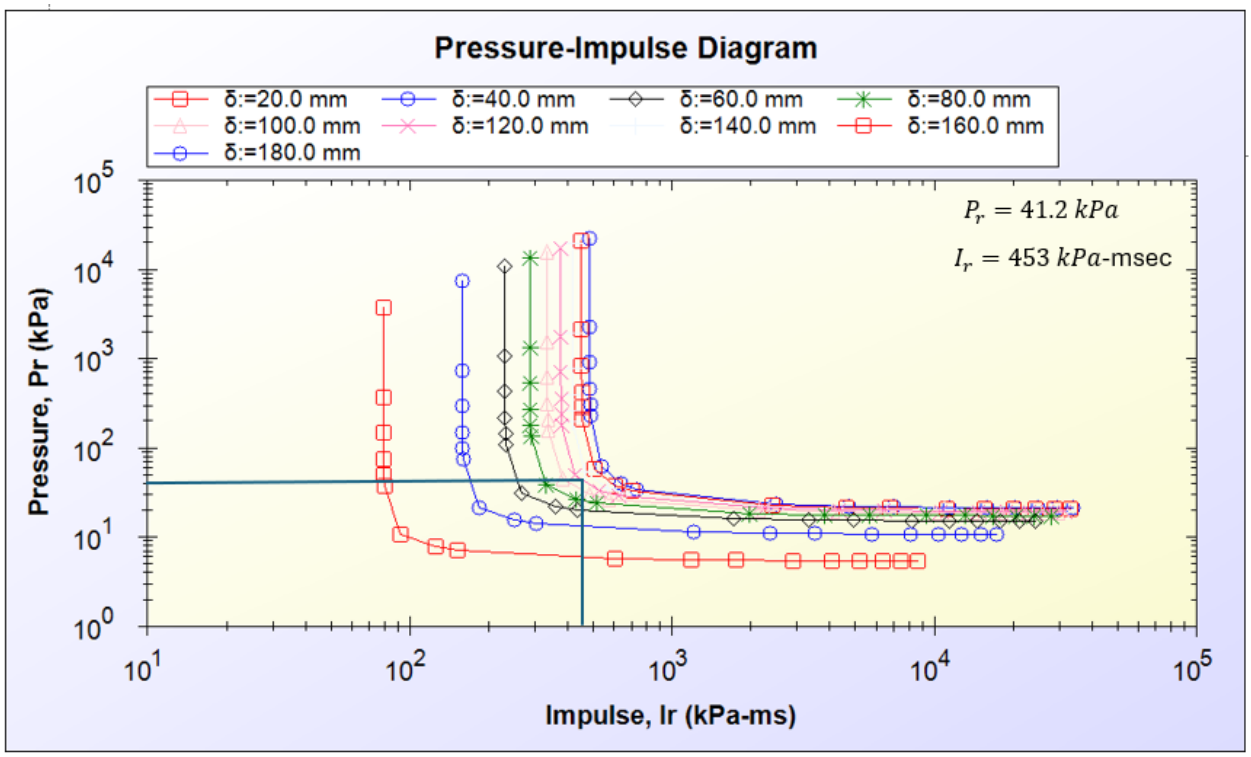

B 75: Pressure-Impulse (P-I) Diagram - M-14FH – Blast 2

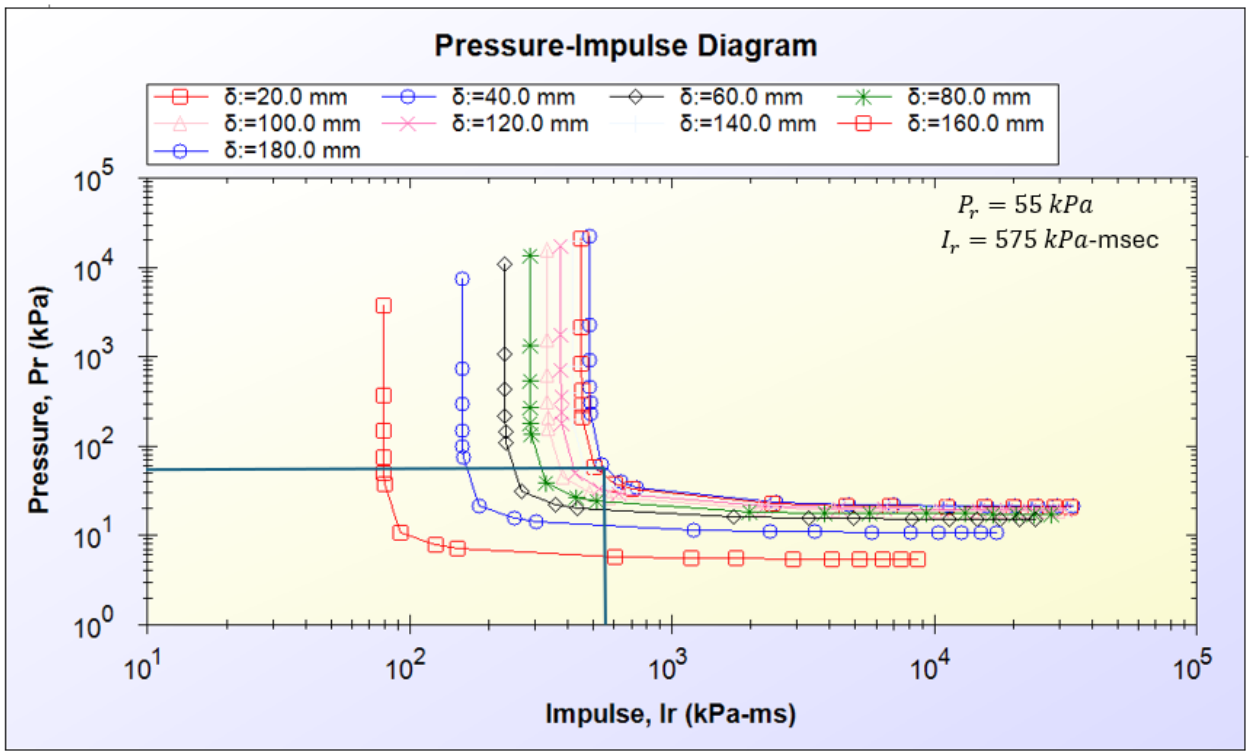

B 76: Pressure-Impulse (P-I) Diagram - M-14FH – Blast 3

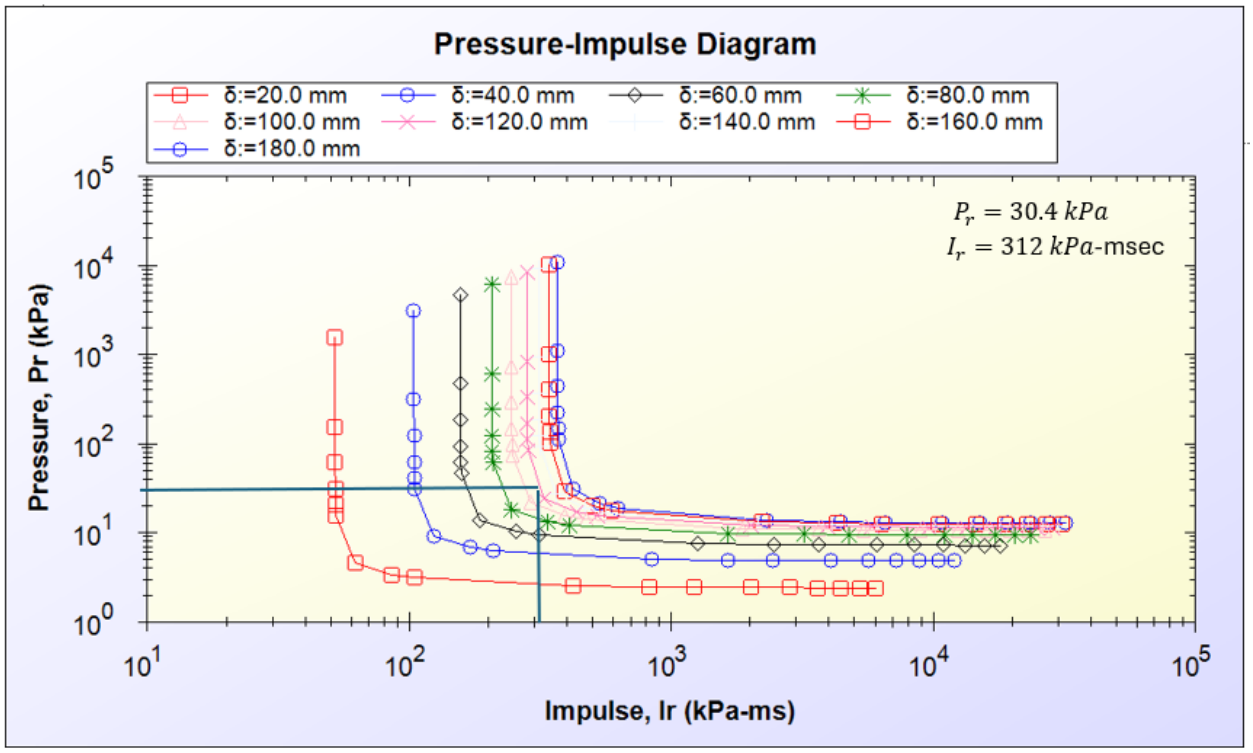

B 77: Pressure-Impulse (P-I) Diagram -M-15FH– Blast 1

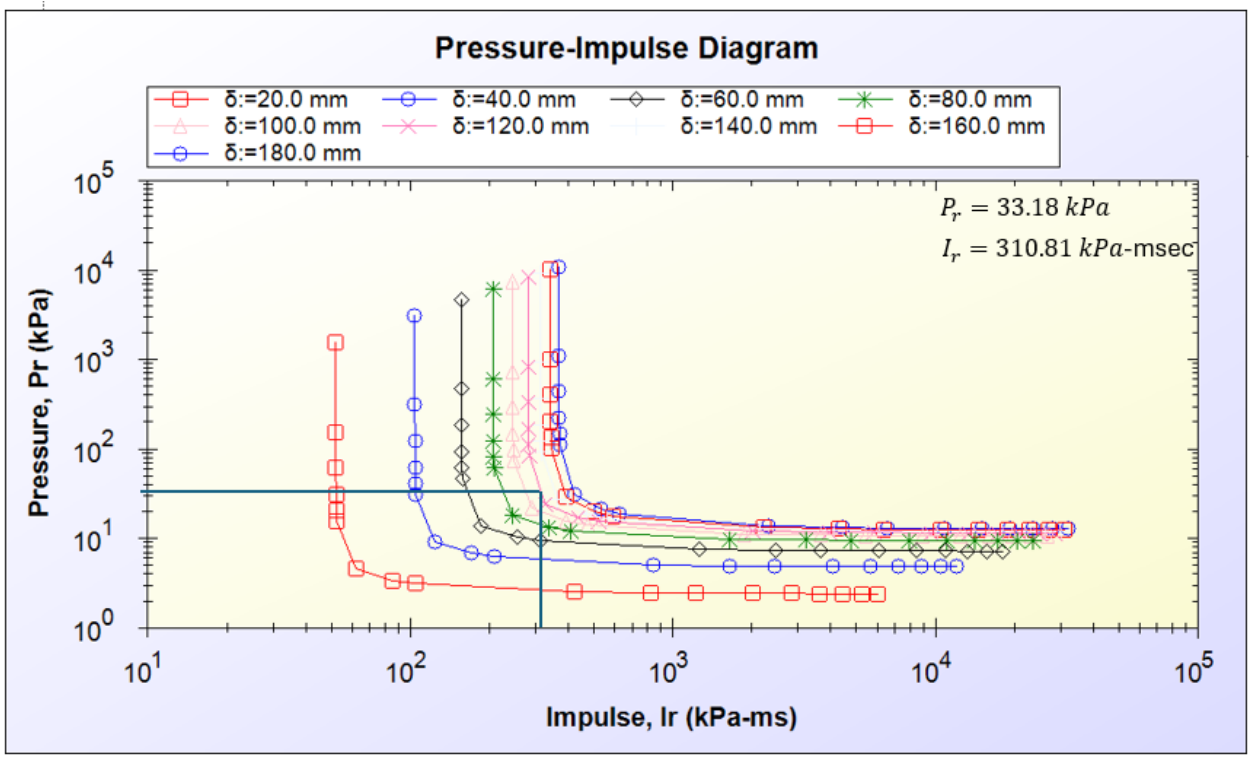

B 78: Pressure-Impulse (P-I) Diagram - M-15FH – Blast 2

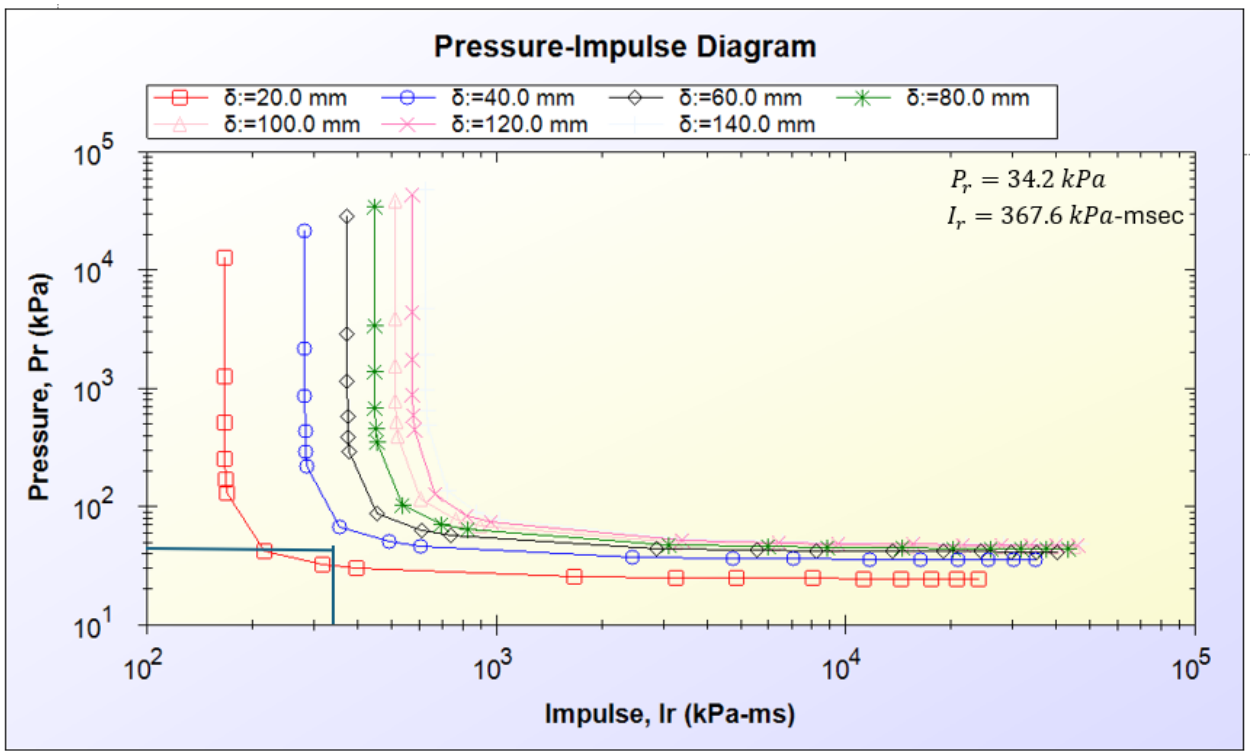

B 79: Pressure-Impulse (P-I) Diagram -M-16FH– Blast 1

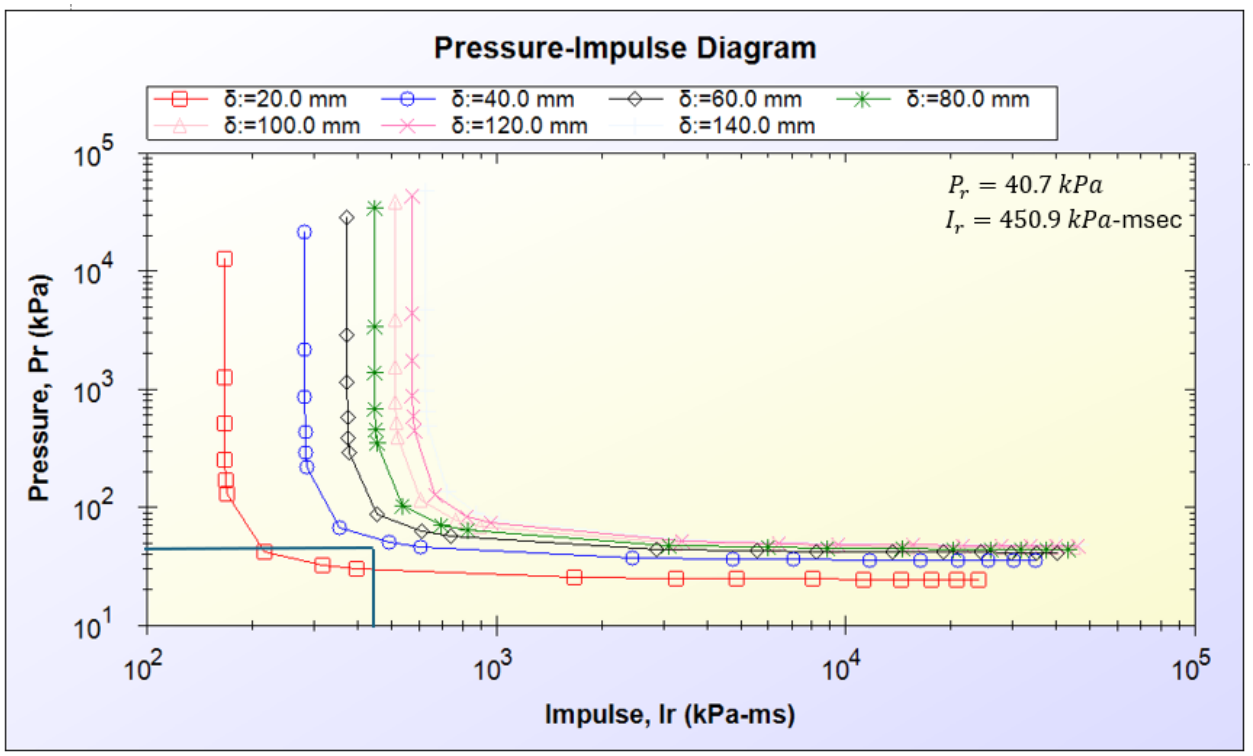

B 80: Pressure-Impulse (P-I) Diagram - M-16FH – Blast 2

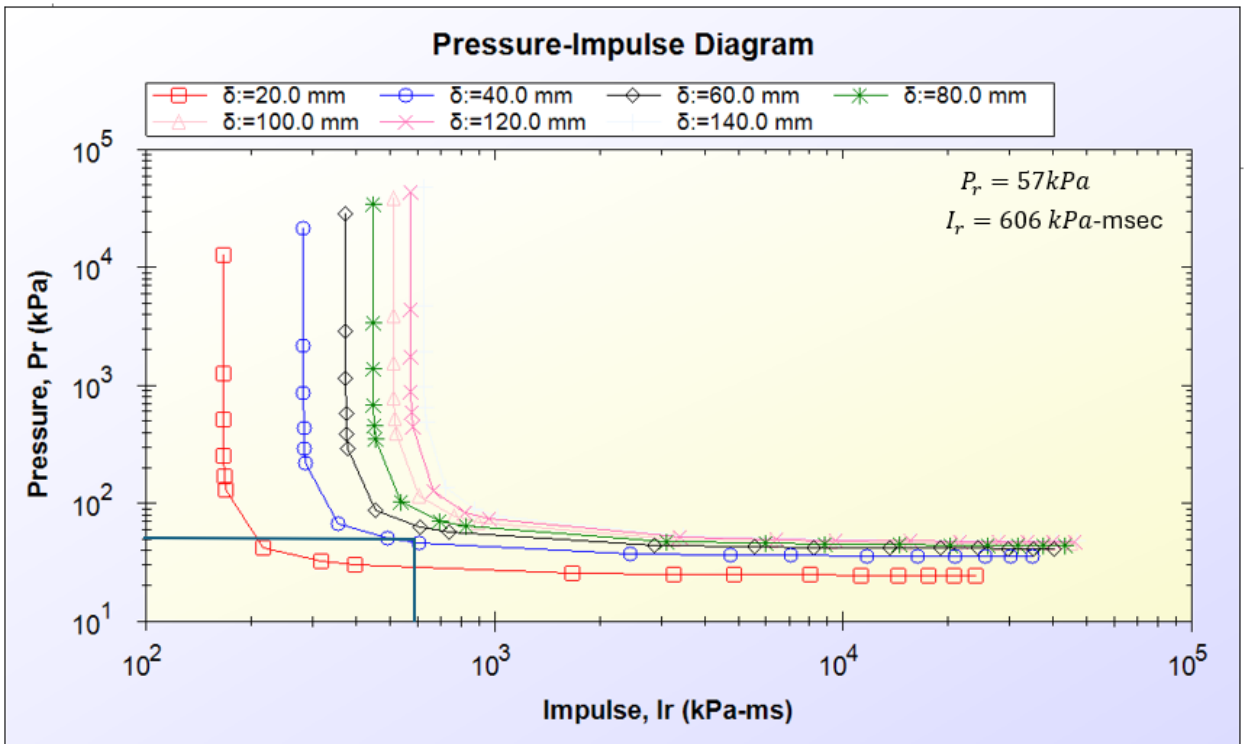

B 81: Pressure-Impulse (P-I) Diagram - M-16FH – Blast 3

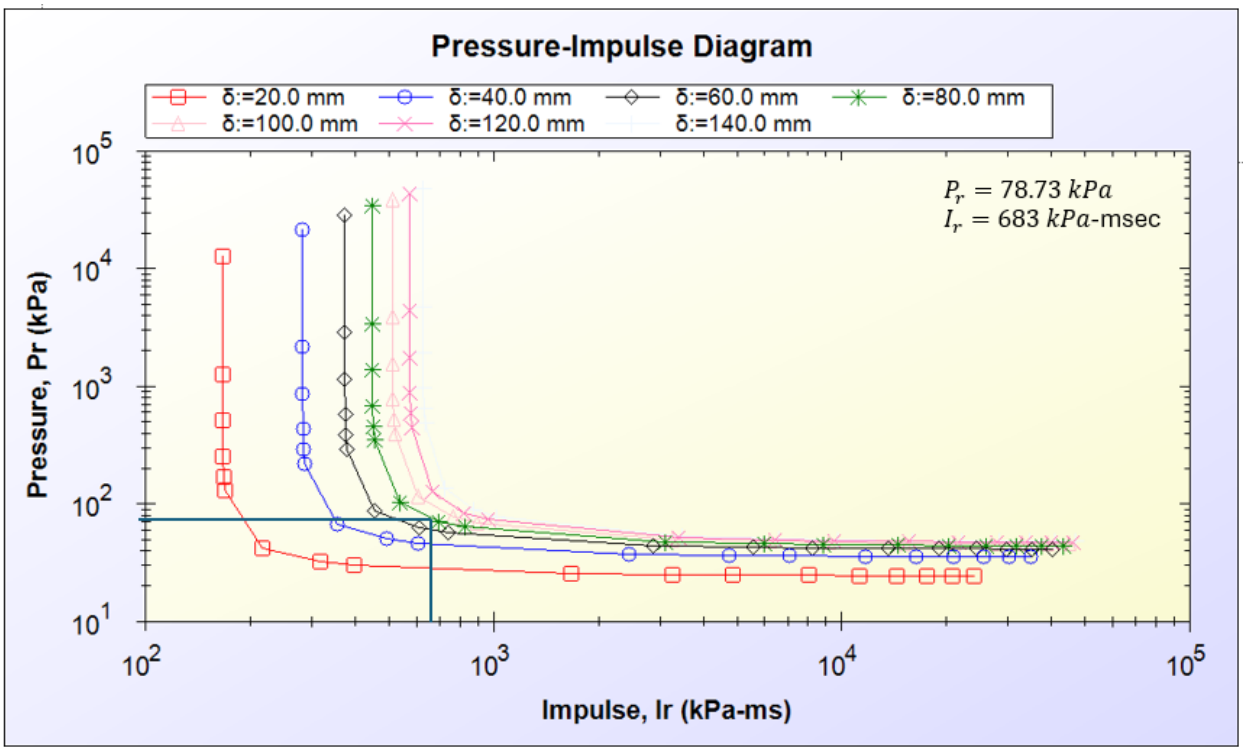

B 82: Pressure-Impulse (P-I) Diagram - M-16FH – Blast 4

Appendix C. UFC Chart calculations

M-1F

Shot 1

R_m= 58.5, U_y=42.6, K_s= $\frac{R_m}{U_y}$ = $\frac{58.5}{42.6}$ =1.37 KN/mm

T_s = 2π$\sqrt{\frac{K_{LM}\ x\ M}{K_s}}$ = 2π$\sqrt{\frac{0.78\ x\ 140.64}{1.37\ x\ 10^6}}$ = 56ms →T_d= $\frac{2\ x\ I_r}{P_r}$ = $\frac{2\ x\ 269.3}{27.5}$ = 19.6 ms, $\frac{T_d}{T_s}$ = 0.35, when μ =1

From the UFC Chart $\frac{R_m}{F_1}$ =1.1, Tributary Area (A_T) = 2.032 x 2.032 = 4.129 m^2,

F_1= P_1 x A_T= 27.5 x 4.129= 113.6 KN

R_m (demand) = 113.6 x 1.1 = 125 KN > R_m (capacity) = 59KN (The specimen is in inelastic zone), Therefore, use K_{LM} = 0.70 (closer to K_{LM} = 0.66)

T_s = 2π$\sqrt{\frac{0.7\ x\ 140.64}{1.37\ x\ 10^6}}$ = 53ms → $\frac{T_d}{T_s}$ = 0.37 → $\frac{R_m}{F_1}$ =0.52 →read μ = 2.3, Um = 42.6 x 2.3 = 97 mm

Shot 2

R_m= 58.5, U_y=42.6, K_s= $\frac{R_m}{U_y}$ = $\frac{58.5}{42.6}$ =1.37 KN/mm

T_s = 2π$\sqrt{\frac{K_{LM}\ x\ M}{K_s}}$ = 2π$\sqrt{\frac{0.78\ x\ 140.64}{1.37\ x\ 10^6}}$ = 56ms →T_d= $\frac{2\ x\ I_r}{P_r}$ = $\frac{2\ x\ 414.9}{42}$ = 19.8 ms, $\frac{T_d}{T_s}$ = 0.35, when μ =1

From the UFC Chart $\frac{R_m}{F_1}$ =0.95 , Tributary Area (A_T) = 2.032 x 2.032 = 4.129 m^2,

F_1= P_1 x A_T= 42 x 4.129= 173.4 KN

R_m (demand) = 173.4 x 1.1 = 191 KN > R_m (capacity) = 59KN (The specimen is in inelastic zone), Therefore, use K_{LM} = 0.70 (closer to K_{LM} = 0.66)

T_s = 2π$\sqrt{\frac{0.7\ x\ 140.64}{1.37\ x\ 10^6}}$ = 53ms → $\frac{T_d}{T_s}$ = 0.37 → $\frac{R_m}{F_1}$ =0.34 →read μ = 5.1, Um = 42.6 x 5.1 = 217 mm

M-2FR

Shot 1

R_{y1}= 99 KN, U_{y1}=17 mm , L= 2100mm K_e= $\frac{384EI}{L^3}$ →K_e= $\frac{R_{y1}}{U_{y1}}$ = $\frac{99}{17}$ = 5.8 KN/mm →EI = 1.4 *10^8

K_{ef}= $\frac{307EI}{L^3}$ = 4.7 KN/mm

T_s = 2π$\sqrt{\frac{K_{LM}\ x\ M}{K_{ef}}}$ = 2π$\sqrt{\frac{0.78\ x\ 140.64}{4.7\ x\ 10^6}}$ = 30.5 ms →T_d= $\frac{2\ x\ I_r}{P_r}$ = $\frac{2\ x\ 330.2}{34.4}$ = 19 ms, $\frac{T_d}{T_s}$ = 0.63, when μ =1 From the UFC Chart $\frac{R_m}{F_1}$ =1.3 , Tributary Area (A_T) = 2.032 x 2.032 = 4.129 m^2,

F_1= P_1 x A_T= 34.44 x 4.129= 142 KN

R_m (demand) = 142 x 1.3 = 185 KN > R_m (capacity) = 141 KN (The specimen is in inelastic zone), Therefore, use K_{LM} = 0.70 (closer to K_{LM} = 0.66)

$T_s = 2\pi\sqrt{\frac{0.7\ x\ 140.64}{4.7\ x\ 10^6}} = 29$ ms → $\frac{T_d}{T_s}$ = 0.67→ $\frac{R_m}{F_1}$ = 0.99 →read μ = 2.1, Um = 17 x 2.1 = 36 mm

Shot 2

R_{y1}= 99 KN, U_{y1}=17 mm , L= 2100mm $K_e = \frac{384EI}{L^3}$ →$K_e = \frac{R_{y1}}{U_{y1}} = \frac{99}{17}$ = 5.8 KN/mm →EI = 1.4 *10^8

$K_{ef} = \frac{307EI}{L^3}$ = 4.7 KN/mm

$T_s = 2\pi\sqrt{\frac{K_{LM}\ X\ M}{K_{ef}}} = 2\pi\sqrt{\frac{0.78\ x\ 140.64}{4.7\ x\ 10^6}}$ = 30.5 ms →$T_d = \frac{2\ x\ I_r}{P_r} = \frac{2\ x\ 413.2}{43.6}$ = 18.9 ms, $\frac{T_d}{T_s}$ = 0.62, when μ =1 From the UFC Chart $\frac{R_m}{F_1}$ =1.29 , Tributary Area (A_T) = 2.032 x 2.032 = 4.129 m^2,

$F_1 = P_1$ x A_T= 43.6 x 4.129= 180 KN

R_m (demand) = 180 x 1.29 = 232 KN > R_m (capacity) = 141 KN (The specimen is in inelastic zone), Therefore, use K_{LM} = 0.70 (closer to K_{LM} = 0.66)

$T_s = 2\pi\sqrt{\frac{0.7\ x\ 140.64}{4.7\ x\ 10^6}} = 29$ ms → $\frac{T_d}{T_s}$ = 0.67 → $\frac{R_m}{F_1}$ = 0.78 →read μ = 2.7, Um = 17 x 2.7 = 46 mm

Shot 3

R_{y1}= 99 KN, U_{y1}=17 mm , L= 2100mm $K_e = \frac{384EI}{L^3}$ →$K_e = \frac{R_{y1}}{U_{y1}} = \frac{99}{17}$ = 5.8 KN/mm →EI = 1.4 *10^8

$K_{ef} = \frac{307EI}{L^3}$ = 4.7 KN/mm

$T_s = 2\pi\sqrt{\frac{K_{LM}\ X\ M}{K_{ef}}} = 2\pi\sqrt{\frac{0.78\ x\ 140.64}{4.7\ x\ 10^6}}$ = 30.5 ms →$T_d = \frac{2\ x\ I_r}{P_r} = \frac{2\ x\ 561.3}{54}$ = 20.7 ms, $\frac{T_d}{T_s}$ = 0.68, when μ =1 From the UFC Chart $\frac{R_m}{F_1}$ =1.35 , Tributary Area (A_T) = 2.032 x 2.032 = 4.129 m^2,

$F_1 = P_1$ x A_T= 54 x 4.129= 223 KN

R_m (demand) = 223 x 1.35 = 287 KN > R_m (capacity) = 141 KN (The specimen is in inelastic zone), Therefore, use K_{LM} = 0.70 (closer to K_{LM} = 0.66)

$T_s = 2\pi\sqrt{\frac{0.7\ x\ 140.64}{4.7\ x\ 10^6}} = 29$ ms → $\frac{T_d}{T_s}$ = 0.72→ $\frac{R_m}{F_1}$ = 0.63 →read μ = 4.5, Um = 17 x 4.5 = 77 mm

M-3F

Shot 1

R_m= 83 KN, U_y=28 mm, K_s= $\frac{R_m}{U_y}$ = $\frac{83}{28}$ =3 KN/mm

T_s = 2π$\sqrt{\frac{K_{LM\ X\ M}}{K_s}}$ = 2π$\sqrt{\frac{0.78\ x\ 148.42}{3\ x\ 10^6}}$ = 39 ms →T_d= $\frac{2\ x\ I_r}{P_r}$ = $\frac{2\ x\ 359.5}{35.3}$ = 20.4 ms, $\frac{T_d}{T_s}$ = 0.52 when μ =1

From the UFC Chart $\frac{R_m}{F_1}$ =1.23 , Tributary Area (A_T) = 2.032 x 2.032 = 4.129 m^2,

F_1= P_1 x A_T= 35.29 x 4.129= 146 KN

R_m (demand) = 146 x 1.32 = 179 KN > R_m (capacity) = 83 KN (The specimen is in inelastic zone), Therefore, use K_{LM} = 0.70 (closer to K_{LM} = 0.66)

T_s = 2π$\sqrt{\frac{0.7\ x\ 148.42}{3\ x\ 10^6}}$ = 37 ms → $\frac{T_d}{T_s}$ = 0.56→ $\frac{R_m}{F_1}$ =0.57 → read μ = 2.8, Um = 28 x 2.8= 78 mm

Shot 2

R_m= 83 KN, U_y=28 mm, K_s= $\frac{R_m}{U_y}$ = $\frac{83}{28}$ =3 KN/mm

T_s = 2π$\sqrt{\frac{K_{LM\ X\ M}}{K_s}}$ = 2π$\sqrt{\frac{0.78\ x\ 148.42}{3\ x\ 10^6}}$ = 39 ms →T_d= $\frac{2\ x\ I_r}{P_r}$ = $\frac{2\ x\ 478.7}{46.6}$ = 20.6 ms, $\frac{T_d}{T_s}$ = 0.53 when μ =1 From the UFC Chart $\frac{R_m}{F_1}$ =1.2 , Tributary Area (A_T) = 2.032 x 2.032 = 4.129 m^2,

F_1= P_1 x A_T= 46.55 x 4.129= 192 KN

R_m (demand) = 192 x 1.2 = 230 KN > R_m (capacity) = 87.5 KN (The specimen is in inelastic zone), Therefore, use K_{LM} = 0.70 (closer to K_{LM} = 0.66)

T_s = 2π$\sqrt{\frac{0.7\ x\ 148.42}{3\ x\ 10^6}}$ = 37 ms → $\frac{T_d}{T_s}$ = 0.56→ $\frac{R_m}{F_1}$ =0.46 → read μ = 4.6 , Um = 28 x 4.6 = 129 mm

Shot 3

R_m= 83 KN, U_y=28 mm, K_s= $\frac{R_m}{U_y}$ = $\frac{83}{28}$ =3 KN/mm

T_s = 2π$\sqrt{\frac{K_{LM\ X\ M}}{K_s}}$ = 2π$\sqrt{\frac{0.78\ x\ 148.42}{3\ x\ 10^6}}$ = 39 ms →T_d= $\frac{2\ x\ I_r}{P_r}$ = $\frac{2\ x\ 542.7}{65}$ = 16.6 ms, $\frac{T_d}{T_s}$ = 0.43 when μ =1 From the UFC Chart $\frac{R_m}{F_1}$ =1.15 , Tributary Area (A_T) = 2.032 x 2.032 = 4.129 m^2,

F_1= P_1 x A_T= 65.08 x 4.129= 269 KN

R_m (demand) = 269 x 1.15 = 309 KN > R_m (capacity) = 83 KN (The specimen is in inelastic zone), Therefore, use K_{LM} = 0.70 (closer to K_{LM} = 0.66)

T_s = 2π$\sqrt{\frac{0.7\ x\ 148.42}{3\ x\ 10^6}}$ = 37 ms → $\frac{T_d}{T_s}$ = 0.45→ $\frac{R_m}{F_1}$ =0.31 → read μ = 7, Um = 28 x 7= 196 mm

M-4FR

Shot 1

R_{y1}= 162 KN, U_{y1} =20 mm , L= 2100mm K_e= $\frac{384EI}{L^3}$ →K_e= $\frac{R_{y1}}{U_{y1}}$ = $\frac{162}{20}$ = 8.1 KN/mm→

EI = 1.95 *10^8, K_{ef}= $\frac{307EI}{L^3}$ = 6.5 KN/mm

T_s = 2π$\sqrt{\frac{K_{LM}\,x\,M}{K_{ef}}}$ = 2π$\sqrt{\frac{0.78\,x\,148.42}{6.5\,x\,10^6}}$ = 26.5 ms →T_d= $\frac{2\,x\,I_r}{P_r}$ = $\frac{2\,x\,343}{28.6}$ = 24 ms, $\frac{T_d}{T_s}$ = 0.9, when μ =1

From the UFC Chart $\frac{R_m}{F_1}$ =1.5 , Tributary Area (A_T) = 2.032 x 2.032 = 4.129 m^2,

F_1= P_1 x A_T= 28.6 x 4.129= 118 KN

R_m (demand) = 118 x 1.5 = 177 KN < R_m (capacity) = 218 KN (The specimen is in elastic zone), Therefore, for μ =1 → Um = 20 x 1 =20 mm

Shot 2

R_{y1}= 162 KN, U_{y1} =20 mm, L= 2100mm K_e= $\frac{384EI}{L^3}$ →K_e= $\frac{R_{y1}}{U_{y1}}$ = $\frac{162}{20}$ = 8.1 KN/mm→

EI = 1.95 *10^8, K_{ef}= $\frac{307EI}{L^3}$ = 6.5 KN/mm

T_s = 2π$\sqrt{\frac{K_{LM}\,x\,M}{K_{ef}}}$ = 2π$\sqrt{\frac{0.78\,x\,148.42}{6.5\,x\,10^6}}$ = 26.5 ms →T_d= $\frac{2\,x\,I_r}{P_r}$ = $\frac{2\,x\,417.4}{39.1}$ = 21.3 ms, $\frac{T_d}{T_s}$ = 0.8, when μ =1

From the UFC Chart $\frac{R_m}{F_1}$ =1.45 , Tributary Area (A_T) = 2.032 x 2.032 = 4.129 m^2,

F_1= P_1 x A_T= 39.1 x 4.129= 161 KN

R_m (demand) = 161 x 1.45 = 234 KN > R_m (capacity) = 218 KN (The specimen is in inelastic zone), Therefore, use K_{LM} = 0.70 (closer to K_{LM} = 0.66)

T_s = 2π$\sqrt{\frac{0.7\,x\,148.42}{6.5\,x\,10^6}}$ = 25 ms → $\frac{T_d}{T_s}$ = 0.85 → $\frac{R_m}{F_1}$ = 1.35→read μ = 1.4 , Um = 20 x 1.4 = 28 mm

Shot 3

R_{y1}= 162 KN, U_{y1} =20 mm, L= 2100mm K_e= $\frac{384EI}{L^3}$ →K_e= $\frac{R_{y1}}{U_{y1}}$ = $\frac{162}{20}$ = 8.1 KN/mm→

EI = 1.95 *10^8, K_{ef}= $\frac{307EI}{L^3}$ = 6.5 KN/mm

T_s = 2π$\sqrt{\frac{K_{LM}\,x\,M}{K_{ef}}}$ = 2π$\sqrt{\frac{0.78\,x\,148.42}{6.5\,x\,10^6}}$ = 26.5 ms →T_d= $\frac{2\,x\,I_r}{P_r}$ = $\frac{2\,x\,549}{52.6}$ = 20.8 ms, $\frac{T_d}{T_s}$ = 0.79, when μ =1

From the UFC Chart $\frac{R_m}{F_1}$ =1.49 , Tributary Area (A_T) = 2.032 x 2.032 = 4.129 m^2,

F_1= P_1 x A_T= 52.6 x 4.129= 217 KN

R_m (demand) = 217 x 1.49 = 323 KN > R_m (capacity) = 218 KN (The specimen is in inelastic zone), Therefore, use K_{LM} = 0.70 (closer to K_{LM} = 0.66)

T_s = 2π$\sqrt{\frac{0.7\ x\ 148.42}{6.5\ x\ 10^6}}$ = 25 ms → $\frac{T_d}{T_s}$ = 0.83 → $\frac{R_m}{F_1}$ = 1→read μ = 2.2, Um = 20 x 2.2 = 44 mm

M-5F

Shot 1

R_m= 56 KN, U_y=46 mm, K_s= $\frac{R_m}{U_y}$ = $\frac{56}{46}$ =1.22 KN/mm

T_s = 2π$\sqrt{\frac{K_{LM\ X\ M}}{K_s}}$ = 2π$\sqrt{\frac{0.78\ x\ 143.46}{1.22\ x\ 10^6}}$ = 60 ms →T_d= $\frac{2\ x\ I_r}{P_r}$ = $\frac{2\ x\ 331.9}{46}$ = 14.4 ms, $\frac{T_d}{T_s}$ = 0.24 when μ =1

From the UFC Chart $\frac{R_m}{F_1}$ =0.7, Tributary Area (A_T) = 2.032 x 2.032 = 4.129 m^2,

F_1= P_1 x A_T= 46 x 4.129= 190 KN

R_m (demand) = 190 x 0.7 =133 KN > R_m (capacity) = 56 KN (The specimen is in inelastic zone),

Therefore, use K_{LM} = 0.70 (closer to K_{LM} = 0.66)

T_s = 2π$\sqrt{\frac{0.7\ x\ 143.46}{1.22x\ 10^6}}$ = 57 ms → $\frac{T_d}{T_s}$ = 0.25 → $\frac{R_m}{F_1}$ = 0.29 → read μ = 3.9, Um = 46 x 3.9= 180 mm

Shot 2

R_m= 56 KN, U_y= 46 mm, K_s= $\frac{R_m}{U_y}$ = $\frac{56}{46}$ =1.2 KN/mm

T_s = 2π$\sqrt{\frac{K_{LM\ X\ M}}{K_s}}$ = 2π$\sqrt{\frac{0.78\ x\ 143.46}{1.22\ x\ 10^6}}$ = 60 ms →T_d= $\frac{2\ x\ I_r}{P_r}$ = $\frac{2\ x\ 396.3}{39.3}$ = 20 ms, $\frac{T_d}{T_s}$ = 0.33 when μ =1

From the UFC Chart $\frac{R_m}{F_1}$ =0.9, Tributary Area (A_T) = 2.032 x 2.032 = 4.129 m^2,

F_1= P_1 x A_T= 39.3 x 4.129= 162 KN

R_m (demand) = 162 x 0.9 =130 KN > R_m (capacity) = 56 KN (The specimen is in inelastic zone),

Therefore, use K_{LM} = 0.70 (closer to K_{LM} = 0.66)

T_s = 2π$\sqrt{\frac{0.7\ x\ 143.46}{1.22x\ 10^6}}$ = 57 ms → $\frac{T_d}{T_s}$ = 0.35 → $\frac{R_m}{F_1}$ = 0.35 → read μ = 4.3, Um = 46 x 4.3= 198 mm

M-6F

Shot 1

R_{y1}= 93 KN, U_{y1} =25 mm, L= 2100mm K_e= $\frac{384EI}{L^3}$ →K_e= $\frac{R_{y1}}{U_{y1}}$ = $\frac{93}{25}$ = 3.7 KN/mm→

EI = 8.9 *10^7, K_{ef}= $\frac{307EI}{L^3}$ = 2.9 KN/mm

T_s = 2π$\sqrt{\frac{K_{LM\ X\ M}}{K_{ef}}}$ = 2π$\sqrt{\frac{0.78\ x\ 143.46}{2.9\ x\ 10^6}}$ = 38.5 ms $\rightarrow T_d = \frac{2\ x\ I_r}{P_r} = \frac{2\ x\ 330.5}{32.9}$ = 20 ms, $\frac{T_d}{T_s}$ = 0.52, when μ =1

From the UFC Chart $\frac{R_m}{F_1}$ =1.25 , Tributary Area (A_T) = 2.032 x 2.032 = 4.129 m^2,

$F_1 = P_1$ x A_T= 32.9 x 4.129= 136 KN

R_m (demand) = 136 x 1.25 = 170 KN > R_m (capacity) = 120 KN (The specimen is in inelastic zone), Therefore, use K_{LM} = 0.70 (closer to K_{LM} = 0.66)

T_s = 2π$\sqrt{\frac{0.7\ x\ 143.46}{2.9\ x\ 10^6}}$ = 36.4 ms → $\frac{T_d}{T_s}$ = 0.6 → $\frac{R_m}{F_1}$ = 0.9 →read μ = 1.9, Um = 25 x 1.9 = 48 mm

Shot 2

R_{y1}= 93 KN, U_{y1} =25 mm, L= 2100mm $K_e = \frac{384EI}{L^3} \rightarrow K_e = \frac{R_{y1}}{U_{y1}} = \frac{93}{25}$ = 3.7 KN/mm→

EI = 8.9 *10^7, $K_{ef} = \frac{307EI}{L^3}$ = 2.9 KN/mm

T_s = 2π$\sqrt{\frac{K_{LM\ X\ M}}{K_{ef}}}$ = 2π$\sqrt{\frac{0.78\ x\ 143.46}{2.9\ x\ 10^6}}$ = 38.5 ms $\rightarrow T_d = \frac{2\ x\ I_r}{P_r} = \frac{2\ x\ 449.3}{45.1}$ = 20 ms, $\frac{T_d}{T_s}$ = 0.52, when μ =1

From the UFC Chart $\frac{R_m}{F_1}$ =1.24 , Tributary Area (A_T) = 2.032 x 2.032 = 4.129 m^2,

$F_1 = P_1$ x A_T= 45.1 x 4.129= 186 KN

R_m (demand) = 186x 1.24 = 230 KN > R_m (capacity) = 120 KN (The specimen is in inelastic zone), Therefore, use K_{LM} = 0.70 (closer to K_{LM} = 0.66)

T_s = 2π$\sqrt{\frac{0.7\ x\ 143.46}{2.9\ x\ 10^6}}$ = 36.4 ms → $\frac{T_d}{T_s}$ = 0.55 → $\frac{R_m}{F_1}$ = 0.64 →read μ = 2.5, Um = 25 x 2.5 = 63 mm

M-7F

Shot 1

R_m= 86 KN, U_y=35 mm, $K_s = \frac{R_m}{U_y} = \frac{86}{35}$ =2.46 KN/mm

T_s = 2π$\sqrt{\frac{K_{LM\ X\ M}}{K_s}}$ = 2π$\sqrt{\frac{0.78\ x\ 151.45}{2.46x\ 10^6}}$ = 43.5 ms $\rightarrow T_d = \frac{2\ x\ I_r}{P_r} = \frac{2\ x\ 340}{33.7}$ =20 ms , $\frac{T_d}{T_s}$ = 0.46 when μ =1

From the UFC Chart $\frac{R_m}{F_1}$ =1.19, Tributary Area (A_T) = 2.032 x 2.032 = 4.129 m^2,

$F_1 = P_1$ x A_T= 33.72 x 4.129= 139 KN

R_m (demand) = 139 x 1.19 =165.5 KN > R_m (capacity) = 86 KN (The specimen is in inelastic zone), Therefore, use K_{LM} = 0.70 (closer to K_{LM} = 0.66)

T_s = 2π$\sqrt{\frac{0.7\ x\ 152.45}{2.46\ x\ 10^6}}$ = 41 ms → $\frac{T_d}{T_s}$ = 0.49 → $\frac{R_m}{F_1}$ = 0.62 → read μ = 1.9, Um = 35 x 1.9= 67 mm

Shot 2

R_m= 86 KN, U_y=35 mm, K_s= $\frac{R_m}{U_y}$ = $\frac{86}{35}$ =2.46 KN/mm

T_s = 2π$\sqrt{\frac{K_{LM}\,x\,M}{K_s}}$ = 2π$\sqrt{\frac{0.78\,x\,151.45}{2.46x\,10^6}}$ = 43.5 ms →T_d= $\frac{2\,x\,I_r}{P_r}$ = $\frac{2\,x\,493}{46}$ =21.4 ms, $\frac{T_d}{T_s}$ = 0.49 when μ =1

From the UFC Chart $\frac{R_m}{F_1}$ =1.19, Tributary Area (A_T) = 2.032 x 2.032 = 4.129 m^2,

F_1= P_1 x A_T= 46 x 4.129= 190 KN

R_m (demand) = 190 x 1.19 =226 KN > R_m (capacity) = 86 KN (The specimen is in inelastic zone), Therefore, use K_{LM} = 0.70 (closer to K_{LM} = 0.66)

T_s = 2π$\sqrt{\frac{0.7\,x\,152.45}{2.46x\,10^6}}$ = 41.3 ms → $\frac{T_d}{T_s}$ = 0.52 → $\frac{R_m}{F_1}$ = 0.5 → read μ = 3.5, Um = 35 x 3.5= 123 mm

M-8F

Shot 1

R_{y1}= 150 KN, U_{y1} =24 mm, L= 2100mm K_e= $\frac{384EI}{L^3}$ →K_e= $\frac{R_{y1}}{U_{y1}}$ = $\frac{150}{24}$ = 6.3 KN/mm→

EI = 1.5 *10^7, K_{ef}= $\frac{307EI}{L^3}$ = 4.9 KN/mm

T_s = 2π$\sqrt{\frac{K_{LM}\,x\,M}{K_{ef}}}$ = 2π$\sqrt{\frac{0.78\,x\,151.45}{4.9\,x\,10^6}}$ = 30.5 ms →T_d= $\frac{2\,x\,I_r}{P_r}$ = $\frac{2\,x\,341}{37.5}$ = 18 ms, $\frac{T_d}{T_s}$ = 0.59, when μ =1

From the UFC Chart $\frac{R_m}{F_1}$ =1.3 , Tributary Area (A_T) = 2.032 x 2.032 = 4.129 m^2,

F_1= P_1 x A_T= 37.5 x 4.129= 155 KN

R_m (demand) = 155 x 1.3 = 201 KN > R_m (capacity) = 193 KN (The specimen is in inelastic zone), Therefore, use K_{LM} = 0.70 (closer to K_{LM} = 0.66)

T_s = 2π$\sqrt{\frac{0.7\,x\,151.45}{4.9\,x\,10^6}}$ = 29 ms → $\frac{T_d}{T_s}$ = 0.63 → $\frac{R_m}{F_1}$ = 1.25 →read μ = 1.25, Um = 24 x 1.25 = 30 mm

Shot 2

R_{y1}= 150 KN, U_{y1} =24 mm, L= 2100mm K_e= $\frac{384EI}{L^3}$ →K_e= $\frac{R_{y1}}{U_{y1}}$ = $\frac{150}{24}$ = 6.3 KN/mm→

EI = 1.5 *10^7, K_{ef}= $\frac{307EI}{L^3}$ = 4.9 KN/mm

T_s = 2π$\sqrt{\frac{K_{LM}\,x\,M}{K_{ef}}}$ = 2π$\sqrt{\frac{0.78\,x\,151.45}{4.9\,x\,10^6}}$ = 30.5 ms →T_d= $\frac{2\,x\,I_r}{P_r}$ = $\frac{2\,x\,438.5}{42.8}$ = 20 ms, $\frac{T_d}{T_s}$ = 0.67, when μ =1

From the UFC Chart $\frac{R_m}{F_1}$ =1.35 , Tributary Area (A_T) = 2.032 x 2.032 = 4.129 m^2,

F_1= P_1 x A_T= 42.8 x 4.129= 177 KN

R_m (demand) = 177 x 1.35 = 2339 KN > R_m (capacity) = 193 KN (The specimen is in inelastic zone), Therefore, use K_{LM} = 0.70 (closer to K_{LM} = 0.66)

$T_s = 2\pi\sqrt{\frac{0.7\ x\ 151.45}{4.9\ x\ 10^6}} = 28.9$ ms → $\frac{T_d}{T_s}$ = 0.7 → $\frac{R_m}{F_1}$ = 1.1 →read μ = 1.7, Um = 24 x 1.7 = 41 mm

Shot 3

R_{y1}= 150 KN, U_{y1} =24 mm, L= 2100mm K_e= $\frac{384EI}{L^3}$ →K_e= $\frac{R_{y1}}{U_{y1}}$ = $\frac{150}{24}$ = 6.3 KN/mm→

EI = 1.5 *10^7, K_{ef}= $\frac{307EI}{L^3}$ = 4.9 KN/mm

$T_s = 2\pi\sqrt{\frac{K_{LM}\ X\ M}{K_{ef}}} = 2\pi\sqrt{\frac{0.78\ x\ 151.45}{4.9\ x\ 10^6}}$ = 30.5 ms →T_d= $\frac{2\ x\ I_r}{P_r}$ = $\frac{2\ x\ 579.7}{55}$ = 21 ms, $\frac{T_d}{T_s}$ = 0.68, when μ =1

From the UFC Chart $\frac{R_m}{F_1}$ =1.45, Tributary Area (A_T) = 2.032 x 2.032 = 4.129 m^2,

F_1= P_1 x A_T= 55.5 x 4.129= 229 KN

R_m (demand) = 229 x 1.45 = 232 KN > R_m (capacity) = 193 KN (The specimen is in inelastic zone), Therefore, use K_{LM} = 0.70 (closer to K_{LM} = 0.66)

$T_s = 2\pi\sqrt{\frac{0.7\ x\ 151.45}{4.9\ x\ 10^6}} = 28.9$ ms → $\frac{T_d}{T_s}$ = 0.72 → $\frac{R_m}{F_1}$ = 0.84 →read μ = 2.5, Um = 24 x 2.5 = 60 mm

M-9FH

Shot 1

R_m = 60 KN, U_y=37 mm, K_s= $\frac{R_m}{U_y}$ = $\frac{60}{37}$ =1.6 KN/mm

$T_s = 2\pi\sqrt{\frac{K_{LM}\ X\ M}{K_s}} = 2\pi\sqrt{\frac{0.78\ x\ 144.22}{1.6\ x\ 10^6}}$ = 52.3 ms →T_d= $\frac{2\ x\ I_r}{P_r}$ = $\frac{2\ x\ 347.7}{37.2}$ =18.7 ms, $\frac{T_d}{T_s}$ = 0.36 when μ =1 From the UFC Chart $\frac{R_m}{F_1}$ =0.99, Tributary Area (A_T) = 2.032 x 2.032 = 4.129 m^2,

F_1= P_1 x A_T= 37.21 x 4.129= 154 KN

R_m (demand) = 154 x 0.99 =152 KN > R_m (capacity) = 60 KN (The specimen is in inelastic zone), Therefore, use K_{LM} = 0.70 (closer to K_{LM} = 0.66)

$T_s = 2\pi\sqrt{\frac{0.7\ x\ 144.22}{1.6\ x\ 10^6}}$ = 49 ms → $\frac{T_d}{T_s}$ = 0.38 → $\frac{R_m}{F_1}$ = 0.39 → read μ =3.5, Um = 37 x 3.5= 129 mm

Shot 2

R_m = 60 KN, U_y=37 mm, K_s= $\frac{R_m}{U_y}$ = $\frac{60}{37}$ =1.6 KN/mm

T_s = 2π$\sqrt{\frac{K_{LM\ X\ M}}{K_s}}$ = 2π$\sqrt{\frac{0.78\ x\ 144.22}{1.6\ x\ 10^6}}$ = 52.3 ms $\rightarrow T_d = \frac{2\ x\ I_r}{P_r} = \frac{2\ x\ 416}{40.1}$ =20.8 ms, $\frac{T_d}{T_s}$ = 0.42 when μ =1

From the UFC Chart $\frac{R_m}{F_1}$ =1.15, Tributary Area (A_T) = 2.032 x 2.032 = 4.129 m^2,

$F_1 = P_1$ x A_T= 40.14 x 4.129= 190 KN

R_m (demand) = 190 x 1.15 =191 KN > R_m (capacity) = 60 KN (The specimen is in inelastic zone), Therefore, use K_{LM} = 0.70 (closer to K_{LM} = 0.66)

T_s = 2π$\sqrt{\frac{0.7\ x\ 144.22}{1.6\ x\ 10^6}}$ = 49 ms $\rightarrow \frac{T_d}{T_s}$ = 0.42 → $\frac{R_m}{F_1}$ = 0.36 → read μ =4.3, Um = 37 x 4.3= 159 mm

M-10FH

Shot 1

R_{y1}= 102 KN, U_{y1} =25 mm, L= 2100mm $K_e = \frac{384EI}{L^3} \rightarrow K_e = \frac{R_{y1}}{U_{y1}} = \frac{102}{25}$ = 4 KN/mm→

EI = 9.8 *10^7, $K_{ef} = \frac{307EI}{L^3}$ = 3.3 KN/mm

T_s = 2π$\sqrt{\frac{K_{LM\ X\ M}}{K_{ef}}}$ = 2π$\sqrt{\frac{0.78\ x\ 144.36}{3.3\ x\ 10^6}}$ = 37 ms $\rightarrow T_d = \frac{2\ x\ I_r}{P_r} = \frac{2\ x\ 347.7}{37.4}$ = 19 ms, $\frac{T_d}{T_s}$ = 0.5, when μ =1

From the UFC Chart $\frac{R_m}{F_1}$ =1.2, Tributary Area (A_T) = 2.032 x 2.032 = 4.129 m^2,

$F_1 = P_1$ x A_T= 37.4 x 4.129= 154 KN

R_m (demand) = 154 x 1.2 = 185 KN > R_m (capacity) = 134 KN (The specimen is in inelastic zone), Therefore, use K_{LM} = 0.70 (closer to K_{LM} = 0.66)

T_s = 2π$\sqrt{\frac{0.7\ x\ 144.36}{3.3\ x\ 10^6}}$ = 35 ms → $\frac{T_d}{T_s}$ = 0.53 → $\frac{R_m}{F_1}$ = 0.87 →read μ = 1.9, Um = 25 x 1.9 = 48 mm

Shot 2

R_{y1}= 102 KN, U_{y1} =25 mm, L= 2100mm $K_e = \frac{384EI}{L^3} \rightarrow K_e = \frac{R_{y1}}{U_{y1}} = \frac{102}{25}$ = 4 KN/mm→

EI = 9.8 *10^7, $K_{ef} = \frac{307EI}{L^3}$ = 3.3 KN/mm

T_s = 2π$\sqrt{\frac{K_{LM\ X\ M}}{K_{ef}}}$ = 2π$\sqrt{\frac{0.78\ x\ 144.36}{3.3\ x\ 10^6}}$ = 37 ms $\rightarrow T_d = \frac{2\ x\ I_r}{P_r} = \frac{2\ x\ 452}{41.5}$ = 21 ms, $\frac{T_d}{T_s}$ = 0.59, when μ =1

From the UFC Chart $\frac{R_m}{F_1}$ =1.25, Tributary Area (A_T) = 2.032 x 2.032 = 4.129 m^2,

$F_1 = P_1$ x A_T= 41.5 x 4.129= 171 KN

R_m (demand) = 171 x 1.25 = 214 KN > R_m (capacity) = 134 KN (The specimen is in inelastic zone), Therefore, use K_{LM} = 0.70 (closer to K_{LM} = 0.66)

T_s = 2π$\sqrt{\frac{0.7\ x\ 144.36}{3.3\ x\ 10^6}}$ = 35 ms → $\frac{T_d}{T_s}$ = 0.62 → $\frac{R_m}{F_1}$ = 0.78 →read μ = 1.85, Um = 25 x 1.85 = 47 mm

Shot 3

R_{y1}= 102 KN, U_{y1} =25 mm, L= 2100mm K_e= $\frac{384EI}{L^3}$ →K_e= $\frac{R_{y1}}{U_{y1}}$ = $\frac{102}{25}$ = 4 KN/mm→

EI = 9.8 *10^7, K_{ef}= $\frac{307EI}{L^3}$ = 3.3 KN/mm

T_s = 2π$\sqrt{\frac{K_{LM}\,x\,M}{K_{ef}}}$ = 2π$\sqrt{\frac{0.78\,x\,144.36}{3.3\,x\,10^6}}$ = 37 ms →T_d= $\frac{2\,x\,I_r}{P_r}$ = $\frac{2\,x\,621.3}{62.8}$ = 19.8 ms, $\frac{T_d}{T_s}$ = 0.54, when μ =1

From the UFC Chart $\frac{R_m}{F_1}$ =1.23, Tributary Area (A_T) = 2.032 x 2.032 = 4.129 m^2,

F_1= P_1 x A_T= 62.8 x 4.129= 259 KN

R_m (demand) = 259 x 1.23 = 324 KN > R_m (capacity) = 134 KN (The specimen is in inelastic zone), Therefore, use K_{LM} = 0.70 (closer to K_{LM} = 0.66)

T_s = 2π$\sqrt{\frac{0.7\,x\,144.36}{3.3\,x\,10^6}}$ = 35 ms → $\frac{T_d}{T_s}$ = 0.57 → $\frac{R_m}{F_1}$ = 0.52 →read μ = 4, Um = 25 x 4 = 100 mm

M-11FH

Shot 1

R_m= 90 KN, U_y=36 mm, K_s= $\frac{R_m}{U_y}$ = $\frac{90}{36}$ =2.5 KN/mm

T_s = 2π$\sqrt{\frac{K_{LM}\,x\,M}{K_s}}$ = 2π$\sqrt{\frac{0.78\,x\,152}{2.5\,x\,10^6}}$ = 43 ms →T_d= $\frac{2\,x\,I_r}{P_r}$ = $\frac{2\,x\,334}{34.8}$ =19.8 ms , $\frac{T_d}{T_s}$ = 0.44 when μ =1

From the UFC Chart $\frac{R_m}{F_1}$ =1.18, Tributary Area (A_T) = 2.032 x 2.032 = 4.129 m^2,

F_1= P_1 x A_T= 34.8 x 4.129= 144 KN

R_m (demand) = 144 x 1.18 =170 KN > R_m (capacity) = 90 KN (The specimen is in inelastic zone), Therefore, use K_{LM} = 0.70 (closer to K_{LM} = 0.66)

T_s = 2π$\sqrt{\frac{0.7\,x\,152}{2.5\,x\,10^6}}$ = 41 ms → $\frac{T_d}{T_s}$ = 0.47 → $\frac{R_m}{F_1}$ = 0.63 → read μ = 1.95, Um = 36 x 1.95 = 70 mm

Shot 2

R_m= 90 KN, U_y=36 mm, K_s= $\frac{R_m}{U_y}$ = $\frac{90}{36}$ =2.5 KN/mm

T_s = 2π$\sqrt{\frac{K_{LM}\,x\,M}{K_s}}$ = 2π$\sqrt{\frac{0.78\,x\,152}{2.5\,x\,10^6}}$ = 42 ms →T_d= $\frac{2\,x\,I_r}{P_r}$ = $\frac{2\,x\,516}{52.9}$ =19.5 ms , $\frac{T_d}{T_s}$ = 0.45 when μ =1

From the UFC Chart $\frac{R_m}{F_1}$ =1.2, Tributary Area (A_T) = 2.032 x 2.032 = 4.129 m^2,

F_1= P_1 x A_T= 52.91 x 4.129= 218 KN

R_m (demand) = 218 x 1.2 =262 KN > R_m (capacity) = 90 KN (The specimen is in inelastic zone), Therefore, use K_{LM} = 0.70 (closer to K_{LM} = 0.66)

T_s = 2π$\sqrt{\frac{0.7\ x\ 152}{2.5\ x\ 10^6}}$ = 40 ms $\rightarrow$ $\frac{T_d}{T_s}$ = 0.48 → $\frac{R_m}{F_1}$ = 0.41 → read μ = 4.2, Um = 36 x 4.2 = 151 mm

M-12FH

Shot 1

R_{y1}= 162 KN, U_{y1} =23 mm, L= 2100mm K_e= $\frac{384EI}{L^3}$ →K_e= $\frac{R_{y1}}{U_{y1}}$ = $\frac{162}{23}$ = 7 KN/mm→

EI = 1.7 *10^8, K_{ef}= $\frac{307EI}{L^3}$ = 5.6 KN/mm

T_s = 2π$\sqrt{\frac{K_{LM}\ X\ M}{K_{ef}}}$ = 2π$\sqrt{\frac{0.78\ x\ 152.96}{5.6\ x\ 10^6}}$ = 28.9 ms →T_d= $\frac{2\ x\ I_r}{P_r}$ = $\frac{2\ x\ 352.9}{38.3}$ = 18.4 ms, $\frac{T_d}{T_s}$ = 0.64, when μ =1 From the UFC Chart $\frac{R_m}{F_1}$ =1.45, Tributary Area (A_T) = 2.032 x 2.032 = 4.129 m^2,

F_1= P_1 x A_T= 38.3 x 4.129= 158 KN

R_m (demand) = 158 x 1.45 = 229 KN > R_m (capacity) = 212 KN (The specimen is in inelastic zone), Therefore, use K_{LM} = 0.70 (closer to K_{LM} = 0.66)

T_s = 2π$\sqrt{\frac{0.7\ x\ 152.96}{5.6\ x\ 10^6}}$ = 27 ms → $\frac{T_d}{T_s}$ = 0.67 → $\frac{R_m}{F_1}$ = 1.34 →read μ = 1.35, Um = 23 x 1.35 = 31 mm

Shot 2

R_{y1}= 162 KN, U_{y1} =23 mm, L= 2100mm K_e= $\frac{384EI}{L^3}$ →K_e= $\frac{R_{y1}}{U_{y1}}$ = $\frac{162}{23}$ = 7 KN/mm→

EI = 1.7 *10^8, K_{ef}= $\frac{307EI}{L^3}$ = 5.6 KN/mm

T_s = 2π$\sqrt{\frac{K_{LM}\ X\ M}{K_{ef}}}$ = 2π$\sqrt{\frac{0.78\ x\ 152.96}{5.6\ x\ 10^6}}$ = 28.9 ms →T_d= $\frac{2\ x\ I_r}{P_r}$ = $\frac{2\ x\ 447.2}{41.9}$ = 21 ms, $\frac{T_d}{T_s}$ = 0.74, when μ =1 From the UFC Chart $\frac{R_m}{F_1}$ =1.46, Tributary Area (A_T) = 2.032 x 2.032 = 4.129 m^2,

F_1= P_1 x A_T= 41.9 x 4.129= 173 KN

R_m (demand) = 173 x 1.46 = 252 KN > R_m (capacity) = 212 KN (The specimen is in inelastic zone), Therefore, use K_{LM} = 0.70 (closer to K_{LM} = 0.66)

T_s = 2π$\sqrt{\frac{0.7\ x\ 152.96}{5.6\ x\ 10^6}}$ = 27 ms → $\frac{T_d}{T_s}$ = 0.78 → $\frac{R_m}{F_1}$ = 1.23 →read μ = 1.4, Um = 23 x 1.4= 32 mm

Shot 3

R_{y1}= 162 KN, U_{y1} =23 mm, L= 2100mm K_e= $\frac{384EI}{L^3}$ →K_e= $\frac{R_{y1}}{U_{y1}}$ = $\frac{162}{23}$ = 7 KN/mm→

EI = 1.7 *10^8, K_{ef}= $\frac{307EI}{L^3}$ = 5.6 KN/mm

T_s = 2π$\sqrt{\frac{K_{LM\ X\ M}}{K_{ef}}}$ = 2π$\sqrt{\frac{0.78\ x\ 152.96}{5.6\ x\ 10^6}}$ = 28.9 ms $\rightarrow T_d = \frac{2\ x\ I_r}{P_r} = \frac{2\ x\ 616.4}{56.5}$ = 22 ms, $\frac{T_d}{T_s}$ = 0.75, when μ =1

From the UFC Chart $\frac{R_m}{F_1}$ =1.49, Tributary Area (A_T) = 2.032 x 2.032 = 4.129 m^2,

$F_1 = P_1$ x A_T= 56.5 x 4.129= 233 KN

R_m (demand) = 233 x 1.49 = 347 KN > R_m (capacity) = 212 KN (The specimen is in inelastic zone), Therefore, use K_{LM} = 0.70 (closer to K_{LM} = 0.66)

T_s = 2π$\sqrt{\frac{0.7\ x\ 152.96}{5.6\ x\ 10^6}}$ = 27 ms → $\frac{T_d}{T_s}$ = 0.79 → $\frac{R_m}{F_1}$ = 0.91 →read μ = 2.2, Um = 23 x 2.2 = 50 mm

M-13FH

Shot 1

R_m= 64m KN, U_y= 77 mm, K_s= 0.83 KN/mm

T_s = 2π$\sqrt{\frac{K_{LM\ X\ M}}{K_s}}$ = 2π$\sqrt{\frac{0.78\ x\ 147.58}{0.83\ x\ 10^6}}$ = 74 ms $\rightarrow T_d = \frac{2\ x\ I_r}{P_r} = \frac{2\ x\ 307.4}{28.7}$ =21.5 ms , $\frac{T_d}{T_s}$ = 0.29 when μ =1

From the UFC Chart $\frac{R_m}{F_1}$ = 0.8, Tributary Area (A_T) = 2.032 x 2.032 = 4.129 m^2,

$F_1 = P_1$ x A_T= 28.65 x 4.129= 118 KN

R_m (demand) = 118 x 0.8 =94 KN > R_m (capacity) = 64 KN (The specimen is in inelastic zone),

Therefore, use K_{LM} = 0.70 (closer to K_{LM} = 0.66)

T_s = 2π$\sqrt{\frac{0.7\ x\ 147.58}{0.83\ x\ 10^6}}$ = 70 ms → $\frac{T_d}{T_s}$ = 0.3 → $\frac{R_m}{F_1}$ = 0.54 → read μ = 1.45, Um = 77 x 1.45= 111 mm

Shot 2

R_m= 64m KN, U_y= 77 mm, K_s= 0.83 KN/mm

T_s = 2π$\sqrt{\frac{K_{LM\ X\ M}}{K_s}}$ = 2π$\sqrt{\frac{0.78\ x\ 147.58}{0.83\ x\ 10^6}}$ = 74 ms $\rightarrow T_d = \frac{2\ x\ I_r}{P_r} = \frac{2\ x\ 417.4}{40.2}$ =20.7 ms , $\frac{T_d}{T_s}$ = 0.28 when μ =1

From the UFC Chart $\frac{R_m}{F_1}$ = 0.8, Tributary Area (A_T) = 2.032 x 2.032 = 4.129 m^2,

$F_1 = P_1$ x A_T= 40.18 x 4.129= 166 KN

R_m (demand) = 166 x 0.8 =132 KN > R_m (capacity) = 64 KN (The specimen is in inelastic zone),

Therefore, use K_{LM} = 0.70 (closer to K_{LM} = 0.66)

T_s = 2π$\sqrt{\frac{0.7\ x\ 147.58}{0.83\ x\ 10^6}}$ = 70 ms → $\frac{T_d}{T_s}$ = 0.3 → $\frac{R_m}{F_1}$ = 0.38 → read μ = 2.01, Um = 77 x 2.01 = 155 mm

M-14FH

Shot 1

R_m= 94 KN, U_y= 43 mm, K_s= 2.18 KN/mm

$T_s = 2\pi\sqrt{\frac{K_{LM}\,X\,M}{K_s}} = 2\pi\sqrt{\frac{0.78\ x\ 153.92}{2.18\ x\ 10^6}}$ = 46.5 ms $\rightarrow T_d = \frac{2\ x\ I_r}{P_r} = \frac{2\ x\ 345.3}{34.6}$ =20 ms , $\frac{T_d}{T_s}$ = 0.43 when μ =1

From the UFC Chart $\frac{R_m}{F_1}$ = 1.19, Tributary Area (A_T) = 2.032 x 2.032 = 4.129 m^2,

$F_1 = P_1$ x A_T= 34.6 x 4.129= 143 KN

R_m (demand) = 143 x 1.19 =170 KN > R_m (capacity) = 94 KN (The specimen is in inelastic zone),

Therefore, use K_{LM} = 0.70 (closer to K_{LM} = 0.66)

$T_s = 2\pi\sqrt{\frac{0.7\ x\ 153.92}{2.18\ x\ 10^6}}$ = 44 ms $\rightarrow \frac{T_d}{T_s}$ = 0.45 → $\frac{R_m}{F_1}$ = 0.66 → read μ = 1.5, Um = 43 x 1.49 = 64 mm

Shot 2

R_m= 94 KN, U_y= 43 mm, K_s= 2.18 KN/mm

$T_s = 2\pi\sqrt{\frac{K_{LM}\,X\,M}{K_s}} = 2\pi\sqrt{\frac{0.78\ x\ 153.92}{2.18\ x\ 10^6}}$ = 46.5 ms $\rightarrow T_d = \frac{2\ x\ I_r}{P_r} = \frac{2\ x\ 453}{41.2}$ =22 ms , $\frac{T_d}{T_s}$ = 0.47 when μ =1

From the UFC Chart $\frac{R_m}{F_1}$ = 1.2, Tributary Area (A_T) = 2.032 x 2.032 = 4.129 m^2,

$F_1 = P_1$ x A_T= 41.2 x 4.129= 170 KN

R_m (demand) = 170 x 1.2 = 204 KN > R_m (capacity) = 94 KN (The specimen is in inelastic zone),
Therefore, use K_{LM} = 0.70 (closer to K_{LM} = 0.66)

$T_s = 2\pi\sqrt{\frac{0.7\ x\ 153.92}{2.18\ x\ 10^6}}$ = 44 ms $\rightarrow \frac{T_d}{T_s}$ = 0.5 → $\frac{R_m}{F_1}$ = 0.55 → read μ = 2.25, Um = 43 x 2.25 = 96mm

Shot 3

R_m= 94 KN, U_y= 43 mm, K_s= 2.18 KN/mm

$T_s = 2\pi\sqrt{\frac{K_{LM}\,X\,M}{K_s}} = 2\pi\sqrt{\frac{0.78\ x\ 153.92}{2.18\ x\ 10^6}}$ = 46.5 ms $\rightarrow T_d = \frac{2\ x\ I_r}{P_r} = \frac{2\ x\ 575}{55}$ =21.5 ms , $\frac{T_d}{T_s}$ = 0.44 when μ =1

From the UFC Chart $\frac{R_m}{F_1}$ = 1.15, Tributary Area (A_T) = 2.032 x 2.032 = 4.129 m^2,

$F_1 = P_1$ x A_T= 55 x 4.129= 227 KN

R_m (demand) = 2277 x 1.15 = 261 KN > R_m (capacity) = 94 KN (The specimen is in inelastic zone),
Therefore, use K_{LM} = 0.70 (closer to K_{LM} = 0.66)

$T_s = 2\pi\sqrt{\frac{0.7\ x\ 153.92}{2.18\ x\ 10^6}}$ = 44 ms $\rightarrow \frac{T_d}{T_s}$ = 0.47 → $\frac{R_m}{F_1}$ = 0.41 → read μ = 4.1, Um = 43 x 4.1 = 176 mm

M-15FH

Shot 1

R_m= 70 KN, U_y= 71 mm, K_s= 0.98 KN/mm

$T_s = 2\pi\sqrt{\frac{K_{LM}\,X\,M}{K_s}} = 2\pi\sqrt{\frac{0.78\ x\ 148.5}{0.98\ x\ 10^6}}$ = 68 ms→T_d= $\frac{2\ x\ I_r}{P_r}$ = $\frac{2\ x\ 312.8}{30.2}$ =20.5 ms , $\frac{T_d}{T_s}$ = 0.3 when μ =1 From the UFC Chart $\frac{R_m}{F_1}$ = 0.85, Tributary Area (A_T) = 2.032 x 2.032 = 4.129 m^2,

F_1= P_1 x A_T= 30.4 x 4.129= 126 KN

R_m (demand) = 126 x 0.85 = 106 KN > R_m (capacity) = 70 KN (The specimen is in inelastic zone), Therefore, use K_{LM} = 0.70 (closer to K_{LM} = 0.66)

$T_s = 2\pi\sqrt{\frac{0.7\ x\ 148.5}{0.98\ x\ 10^6}}$ = 64 ms → $\frac{T_d}{T_s}$ = 0.31 → $\frac{R_m}{F_1}$ = 0.56 → read μ = 1.55, Um = 71 x 1.55 = 110 mm

Shot 2

R_m= 70 KN, U_y= 71 mm, K_s= 0.98 KN/mm

$T_s = 2\pi\sqrt{\frac{K_{LM}\,X\,M}{K_s}} = 2\pi\sqrt{\frac{0.78\ x\ 148.5}{0.98\ x\ 10^6}}$ = 68 ms→T_d= $\frac{2\ x\ I_r}{P_r}$ = $\frac{2\ x\ 310.8}{33.2}$ =18.7 ms , $\frac{T_d}{T_s}$ = 0.28 when μ =1
From the UFC Chart $\frac{R_m}{F_1}$ = 0.8, Tributary Area (A_T) = 2.032 x 2.032 = 4.129 m^2,

F_1= P_1 x A_T= 33.18 x 4.129= 137 KN

R_m (demand) = 137 x 0.97 = 116 KN > R_m (capacity) = 70 KN (The specimen is in inelastic zone), Therefore, use K_{LM} = 0.70 (closer to K_{LM} = 0.66)

$T_s = 2\pi\sqrt{\frac{0.7\ x\ 148.5}{0.98\ x\ 10^6}}$ = 64 ms → $\frac{T_d}{T_s}$ = 0.29 → $\frac{R_m}{F_1}$ = 0.5 → read μ = 1.75 Um = 71 x 1.75 = 124 mm

M-16FH

Shot 1

R_{y1}= 154 KN, U_{y1} =21 mm, L= 2100mm K_e= $\frac{384EI}{L^3}$ →K_e= $\frac{R_{y1}}{U_{y1}}$ = $\frac{154}{21}$ = 7.7 KN/mm→

EI = 1.86 *10^8, K_{ef}= $\frac{307EI}{L^3}$ = 6.1 KN/mm

$T_s = 2\pi\sqrt{\frac{K_{LM}\,X\,M}{K_{ef}}} = 2\pi\sqrt{\frac{0.78\ x\ 152}{6.1\ x\ 10^6}}$ = 27.6 ms →T_d= $\frac{2\ x\ I_r}{P_r}$ = $\frac{2\ x\ 367.6}{34.2}$ = 21.5 ms, $\frac{T_d}{T_s}$ = 0.78, when μ =1
From the UFC Chart $\frac{R_m}{F_1}$ =1.4, Tributary Area (A_T) = 2.032 x 2.032 = 4.129 m^2,

F_1= P_1 x A_T= 34.2 x 4.129= 141 KN

R_m (demand) = 141 x 1.4 = 347 KN > R_m (capacity) = 198 KN (The specimen is in inelastic zone), Therefore, use K_{LM} = 0.70 (closer to K_{LM} = 0.66)

T_s = 2π$\sqrt{\frac{0.7\ x\ 152}{6.1\ x\ 10^6}}$ = 27 ms → $\frac{T_d}{T_s}$ = 0.82 → $\frac{R_m}{F_1}$ = 1.5 →read μ = 1, Um = 21 x 1 = 21 mm

Shot 2

R_{y1}= 154 KN, U_{y1} =21 mm, L= 2100mm K_e= $\frac{384EI}{L^3}$ →K_e= $\frac{R_{y1}}{U_{y1}}$ = $\frac{154}{21}$ = 7.7 KN/mm→

EI = 1.86 *10^8, K_{ef}= $\frac{307EI}{L^3}$ = 6.1 KN/mm

T_s = 2π$\sqrt{\frac{K_{LM}\ X\ M}{K_{ef}}}$ = 2π$\sqrt{\frac{0.78\ x\ 152}{6.1\ x\ 10^6}}$ = 27.6 ms →T_d= $\frac{2\ x\ I_r}{P_r}$ = $\frac{2\ x\ 450.9}{40.7}$ = 22 ms, $\frac{T_d}{T_s}$ = 0.8, when μ =1

From the UFC Chart $\frac{R_m}{F_1}$ =1.42, Tributary Area (A_T) = 2.032 x 2.032 = 4.129 m^2,

F_1= P_1 x A_T= 40.7 x 4.129= 166 KN

R_m (demand) = 166 x 1.42 = 236 KN > R_m (capacity) = 216 KN (The specimen is in inelastic zone), Therefore, use K_{LM} = 0.70 (closer to K_{LM} = 0.66)

T_s = 2π$\sqrt{\frac{0.7\ x\ 152}{6.1\ x\ 10^6}}$ = 26 ms → $\frac{T_d}{T_s}$ = 0.86 → $\frac{R_m}{F_1}$ = 1.3 →read μ = 1.4, Um = 21 x 1.4 = 29 mm

Shot 3

R_{y1}= 154 KN, U_{y1} =21 mm, L= 2100mm K_e= $\frac{384EI}{L^3}$ →K_e= $\frac{R_{y1}}{U_{y1}}$ = $\frac{154}{21}$ = 7.7 KN/mm→

EI = 1.86 *10^8, K_{ef}= $\frac{307EI}{L^3}$ = 6.1 KN/mm

T_s = 2π$\sqrt{\frac{K_{LM}\ X\ M}{K_{ef}}}$ = 2π$\sqrt{\frac{0.78\ x\ 152}{6.1\ x\ 10^6}}$ = 27.6 ms →T_d= $\frac{2\ x\ I_r}{P_r}$ = $\frac{2\ x\ 606}{57}$ = 22 ms, $\frac{T_d}{T_s}$ = 0.8, when μ =1

From the UFC Chart $\frac{R_m}{F_1}$ =1.43, Tributary Area (A_T) = 2.032 x 2.032 = 4.129 m^2,

F_1= P_1 x A_T= 57 x 4.129= 235 KN

R_m (demand) = 235 x 1.43 = 337 KN > R_m (capacity) = 216 KN (The specimen is in inelastic zone), Therefore, use K_{LM} = 0.70 (closer to K_{LM} = 0.66)

T_s = 2π$\sqrt{\frac{0.7\ x\ 152}{6.1\ x\ 10^6}}$ = 26 ms → $\frac{T_d}{T_s}$ = 0.81 → $\frac{R_m}{F_1}$ = 0.92 →read μ = 1.85, Um = 21 x 1.85 = 39 mm

Shot 4

R_{y1}= 154 KN, U_{y1} =21 mm, L= 2100mm K_e= $\frac{384EI}{L^3}$ →K_e= $\frac{R_{y1}}{U_{y1}}$ = $\frac{154}{21}$ = 7.7 KN/mm→

EI = 1.86 *10^8, K_{ef}= $\frac{307EI}{L^3}$ = 6.1 KN/mm

T_s = 2π$\sqrt{\frac{K_{LM\ X\ M}}{K_{ef}}}$ = 2π$\sqrt{\frac{0.78\ x\ 152}{6.1\ x\ 10^6}}$ = 27.6 ms →T_d= $\frac{2\ x\ I_r}{P_r}$ = $\frac{2\ x\ 683}{78.7}$ = 17 ms, $\frac{T_d}{T_s}$ = 0.63, when μ =1

From the UFC Chart $\frac{R_m}{F_1}$ =1.46, Tributary Area (A_T) = 2.032 x 2.032 = 4.129 m^2,

F_1= P_1 x A_T= 578.7 x 4.129= 2 KN

R_m (demand) = 235 x 1.46 = 474 KN > R_m (capacity) = 216 KN (The specimen is in inelastic zone), Therefore, use K_{LM} = 0.70 (closer to K_{LM} = 0.66)

T_s = 2π$\sqrt{\frac{0.7\ x\ 152}{6.1\ x\ 10^6}}$ = 26 ms → $\frac{T_d}{T_s}$ = 0.67 → $\frac{R_m}{F_1}$ = 0.67 →read μ = 4, Um = 21 x 4 = 84 mm